


Recent Advances in Physical Layer Technologies for 5G-Enabled Internet of Things 2021

Lead Guest Editor: Xingwang Li

Guest Editors: Yuan Ding and Omprakash Kaiwartya





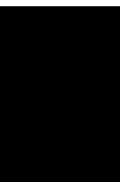
**Recent Advances in Physical Layer
Technologies for 5G-Enabled Internet of
Things 2021**

Wireless Communications and Mobile Computing

**Recent Advances in Physical Layer
Technologies for 5G-Enabled Internet of
Things 2021**

Lead Guest Editor: Xingwang Li

Guest Editors: Yuan Ding and Omprakash
Kaiwartya





Copyright © 2021 Hindawi Limited. All rights reserved.

This is a special issue published in “Wireless Communications and Mobile Computing.” All articles are open access articles distributed under the Creative Commons Attribution License, which permits unrestricted use, distribution, and reproduction in any medium, provided the original work is properly cited.

Chief Editor









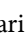






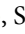







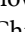








Zhipeng Cai , USA

Associate Editors

Ke Guan , China
Jaime Lloret , Spain
Maode Ma , Singapore

Academic Editors

Muhammad Inam Abbasi, Malaysia
Ghufran Ahmed , Pakistan
Hamza Mohammed Ridha Al-Khafaji ,
Iraq
Abdullah Alamoodi , Malaysia
Marica Amadeo, Italy
Sandhya Aneja, USA
Mohd Dilshad Ansari, India
Eva Antonino-Daviu , Spain
Mehmet Emin Aydin, United Kingdom
Parameshchhari B. D. , India
Kalapraveen Bagadi , India
Ashish Bagwari , India
Dr. Abdul Basit , Pakistan
Alessandro Bazzi , Italy
Zdenek Becvar , Czech Republic
Nabil Benamar , Morocco
Olivier Berder, France
Petros S. Bithas, Greece
Dario Bruneo , Italy
Jun Cai, Canada
Xuesong Cai, Denmark
Gerardo Canfora , Italy
Rolando Carrasco, United Kingdom
Vicente Casares-Giner , Spain
Brijesh Chaurasia, India
Lin Chen , France
Xianfu Chen , Finland
Hui Cheng , United Kingdom
Hsin-Hung Cho, Taiwan
Ernestina Cianca , Italy
Marta Cimitile , Italy
Riccardo Colella , Italy
Mario Collotta , Italy
Massimo Condoluci , Sweden
Antonino Crivello , Italy
Antonio De Domenico , France
Floriano De Rango , Italy



Antonio De la Oliva , Spain
Margot Deruyck, Belgium
Liang Dong , USA
Praveen Kumar Donta, Austria
Zhuojun Duan, USA
Mohammed El-Hajjar , United Kingdom
Oscar Esparza , Spain
Maria Fazio , Italy
Mauro Femminella , Italy
Manuel Fernandez-Veiga , Spain
Gianluigi Ferrari , Italy
Luca Foschini , Italy
Alexandros G. Fragkiadakis , Greece
Ivan Ganchev , Bulgaria
Óscar García, Spain
Manuel García Sánchez , Spain
L. J. García Villalba , Spain
Miguel Garcia-Pineda , Spain
Piedad Garrido , Spain
Michele Girolami, Italy
Mariusz Glabowski , Poland
Carles Gomez , Spain
Antonio Guerrieri , Italy
Barbara Guidi , Italy
Rami Hamdi, Qatar
Tao Han, USA
Sherief Hashima , Egypt
Mahmoud Hassaballah , Egypt
Yejun He , China
Yixin He, China
Andrej Hrovat , Slovenia
Chunqiang Hu , China
Xuexian Hu , China
Zhenghua Huang , China
Xiaohong Jiang , Japan
Vicente Julian , Spain
Rajesh Kaluri , India
Dimitrios Katsaros, Greece
Muhammad Asghar Khan, Pakistan
Rahim Khan , Pakistan
Ahmed Khattab, Egypt
Hasan Ali Khattak, Pakistan
Mario Kolberg , United Kingdom
Meet Kumari, India
Wen-Cheng Lai , Taiwan

Jose M. Lanza-Gutierrez, Spain
Pavlos I. Lazaridis , United Kingdom
Kim-Hung Le , Vietnam
Tuan Anh Le , United Kingdom
Xianfu Lei, China
Jianfeng Li , China
Xiangxue Li , China
Yaguang Lin , China
Zhi Lin , China
Liu Liu , China
Mingqian Liu , China
Zhi Liu, Japan
Miguel López-Benítez , United Kingdom
Chuanwen Luo , China
Lu Lv, China
Basem M. ElHalawany , Egypt
Imadeldin Mahgoub , USA
Rajesh Manoharan , India
Davide Mattera , Italy
Michael McGuire , Canada
Weizhi Meng , Denmark
Klaus Moessner , United Kingdom
Simone Morosi , Italy
Amrit Mukherjee, Czech Republic
Shahid Mumtaz , Portugal
Giovanni Nardini , Italy
Tuan M. Nguyen , Vietnam
Petros Nicolitidis , Greece
Rajendran Parthiban , Malaysia
Giovanni Pau , Italy
Matteo Petracca , Italy
Marco Picone , Italy
Daniele Pinchera , Italy
Giuseppe Piro , Italy
Javier Prieto , Spain
Umair Rafique, Finland
Maheswar Rajagopal , India
Sujan Rajbhandari , United Kingdom
Rajib Rana, Australia
Luca Reggiani , Italy
Daniel G. Reina , Spain
Bo Rong , Canada
Mangal Sain , Republic of Korea
Praneet Saurabh , India

Hans Schotten, Germany
Patrick Seeling , USA
Muhammad Shafiq , China
Zaffar Ahmed Shaikh , Pakistan
Vishal Sharma , United Kingdom
Kaize Shi , Australia
Chakchai So-In, Thailand
Enrique Stevens-Navarro , Mexico
Sangeetha Subbaraj , India
Tien-Wen Sung, Taiwan
Suhua Tang , Japan
Pan Tang , China
Pierre-Martin Tardif , Canada
Sreenath Reddy Thummaluru, India
Tran Trung Duy , Vietnam
Fan-Hsun Tseng, Taiwan
S Velliangiri , India
Quoc-Tuan Vien , United Kingdom
Enrico M. Vitucci , Italy
Shaohua Wan , China
Dawei Wang, China
Huaqun Wang , China
Pengfei Wang , China
Dapeng Wu , China
Huaming Wu , China
Ding Xu , China
YAN YAO , China
Jie Yang, USA
Long Yang , China
Qiang Ye , Canada
Changyan Yi , China
Ya-Ju Yu , Taiwan
Marat V. Yuldashev , Finland
Sherali Zeadally, USA
Hong-Hai Zhang, USA
Jiliang Zhang, China
Lei Zhang, Spain
Wence Zhang , China
Yushu Zhang, China
Kechen Zheng, China
Fuhui Zhou , USA
Meiling Zhu, United Kingdom
Zhengyu Zhu , China





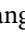
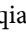
Contents

A Carrier Parameter Decoupling Algorithm for High Order APSK Modulation

Xiangchuan Gao, Xupeng Zhang , Linlin Duan, Kexian Gong, Peng Sun, Wei Wang , Hua Jiang, and Zhongyong Wang

Research Article (10 pages), Article ID 1685260, Volume 2021 (2021)

Performance Analysis of MEC Based on NOMA under Imperfect CSI with Eavesdropper

Xuehua Li , Yingjie Pei , Huan Jiang , Xinwei Yue , Yafei Wang , and Yuqiao Suo 




Research Article (10 pages), Article ID 2700843, Volume 2021 (2021)

Beam Selection Assisted UAV-BS Deployment and Trajectory for Beamspace mmWave Systems

Xingxuan Zuo, Jiankang Zhang , Sheng Chen, and Xiaomin Mu







Research Article (21 pages), Article ID 1363586, Volume 2021 (2021)

A Survey on Transmission Schemes on Large-Scale Internet of Things with Nonorthogonal Multiple Access

Wenyu Zhou, Rui Zhao , Fusheng Zhu , Lijia Lai , and Xutao Li

Review Article (11 pages), Article ID 8555761, Volume 2021 (2021)

Reduced-Complexity LDPC Decoding for Next-Generation IoT Networks

Muhammad Asif , Wali Ullah Khan , H. M. Rehan Afzal , Jamel Nebhen , Inam Ullah , Ateeq Ur Rehman , and Mohammed K. A. Kaabar 



Research Article (10 pages), Article ID 2029560, Volume 2021 (2021)

Outage Performance of Full-Duplex Relay Networks Powered by RF Power Station in Ubiquitous Electric Internet of Things

Yu Zhang , Xiaofei Di , Hongliang Duan , Xi Yang , Peng Wu , and Baoguo Shan 



Research Article (9 pages), Article ID 9983433, Volume 2021 (2021)

Power Allocation in Massive MIMO-HWSN Based on the Water-Filling Algorithm

Zhe Li , Sahil Verma , and Machao Jin



Research Article (11 pages), Article ID 8719066, Volume 2021 (2021)

Energy-Efficient Routing Using Fuzzy Neural Network in Wireless Sensor Networks

Rajesh Kumar Varun, Rakesh C. Gangwar, Omprakash Kaiwartya , and Geetika Aggarwal 

Research Article (13 pages), Article ID 5113591, Volume 2021 (2021)

Low-Cost and Long-Range Node-Assisted WiFi Backscatter Communication for 5G-Enabled IoT Networks

Zhimin Wang , Li Feng , Shumin Yao, Kan Xie, and Yuqiang Chen


Research Article (9 pages), Article ID 8540457, Volume 2021 (2021)

Secrecy Performance Analysis of a Cognitive Network for IoT over k - μ Channels

Junxia Li , Hui Zhao , and Michael Johnson

Research Article (12 pages), Article ID 5548428, Volume 2021 (2021)

CR-NOMA Networks over Nakagami- m Fading: CSI Imperfection Perspective

Anh-Tu Le  and Dinh-Thuan Do


Research Article (10 pages), Article ID 9915974, Volume 2021 (2021)

Relay Selection for Security Improvement in Cognitive Radio Networks with Energy Harvesting

Khuong Ho-Van  and Thiem Do-Dac 

Research Article (16 pages), Article ID 9921782, Volume 2021 (2021)

Physical Layer Secrecy Analysis of Multihop Hybrid Satellite-Terrestrial Relay Networks with Jamming

Xiaoqi Wang , Hanwei Zhang , and Zheng Hou 

Research Article (13 pages), Article ID 9931174, Volume 2021 (2021)

Application Status and Prospects of 5G Technology in Distribution Automation Systems

Zhaoyun Zhang  and Qitong Wang

Review Article (9 pages), Article ID 5553159, Volume 2021 (2021)

Research Article

A Carrier Parameter Decoupling Algorithm for High Order APSK Modulation

Xiangchuan Gao, Xupeng Zhang , Linlin Duan, Kexian Gong, Peng Sun, Wei Wang , Hua Jiang, and Zhongyong Wang

School of Information Engineering, Zhengzhou University, Zhengzhou 450000, China

Correspondence should be addressed to Wei Wang; iewwang@zzu.edu.cn

Received 15 August 2021; Revised 18 October 2021; Accepted 26 November 2021; Published 16 December 2021

Academic Editor: Omprakash Kaiwartya

Copyright © 2021 Xiangchuan Gao et al. This is an open access article distributed under the Creative Commons Attribution License, which permits unrestricted use, distribution, and reproduction in any medium, provided the original work is properly cited.

In satellite communication, carrier parameter estimation usually uses a serial structure, and the accuracy of frequency offset estimation (FOE) will greatly affect the accuracy of phase offset estimation (POE). A new carrier synchronization mode (NCSM) can realize the decoupling of carrier FOE and POE to a certain extent, but this mode is based on multibase phase shift keying (MPSK) modulation analysis, the decoupling performance is poor when uses in amplitude phase shift keying (APSK) modulation, and the decoupling performance of NCSM has a low tolerance of frequency offset. An improved carrier parameter estimation decoupling technique is proposed to solve these problems. The simulation results show that, compared with the original method, under the premise of ensuring the accuracy of carrier parameter estimation, the proposed method is more robust to the modulation mode, the POE has stronger antioffset ability, and the normalized FOE range has been significantly enhanced.

1. Introduction

With the increasing demand of satellite communication system, satellite communications are also more closely linked to fifth generation (5G) wireless networks. On the one hand, security is an important factor in wireless communication systems [1, 2]. On the other hand, high-speed and reliable wireless communication is a hot research topic in academia and industry, and various related researches have been carried out for different communication scenarios [3]. In [4], the authors qualitatively analyse the research progress of geocast routing (GR) in intelligent transportation systems and also analyse some future research challenges of GR. In [5], the authors proposed a predictive distributed cluster mechanism that has further improved the transmission performance of wireless sensor network devices. In order to further improve the transmission performance of satellite communication, the role of high-order modulation in satellite communication is becoming more and more important. Compared with

QAM modulation signal, MAPSK modulation signal is widely used in satellite communication because it is more suitable for nonlinear communication channels. The latest generation of digital video broadcasting standards (Digital Video Broadcasting-Second Generation Extensions, DVB-S2X) adds a variety of high-order APSK modulations on the basis of the original modulation mode, among which the highest order of APSK is up to 256 [6]. Due to the existence of multiple amplitudes and narrower phase discrimination of APSK signals, the synchronization algorithm of high-order modulated signals is challenging, and there are urgent needs to design advanced synchronization algorithm for high-order modulation signals in satellite communication.

In satellite communication, carrier frequency error of receiver mainly comes from Doppler frequency shift and carrier frequency difference introduced by the crystal oscillator error of receiver [7, 8]. At the same time, due to the sudden nature of satellite communication, pilots are usually introduced to help achieve fast acquisition and FOE, but

the limited spectrum resources limit the pilot frequency overhead. Therefore, the large Doppler shift and pilot cost are the two main factors affecting the performance of coherent demodulation of satellite communication. Aiming at the above problems, various carrier synchronization algorithms have been proposed in many literatures. Classical forward frequency offset estimation includes algorithms such as M&M [9], L&R [10], and Fitz [11]. These estimation algorithms can only approach the Cramer Rao Lower Bound (CRLB) at high SNR, and it is difficult to take into account both the accuracy of FOE and the range of FOE. In [12, 13], the authors propose a maximum likelihood iterative synchronization based on the expected maximum algorithm. By combining carrier synchronization with the decoder, accurate synchronization could be obtained, but the synchronization range cannot be guaranteed and the complexity is impractical. In [14], the authors propose a code-assisted carrier synchronization method based on frequency search, whose complexity is less than the original EM algorithm. Although the abovementioned coding-assisted carrier synchronization algorithms can work at low signal-to-noise ratios, the scope of application of such algorithms is limited. In [15], the authors propose a fast Fourier transform (FFT) frequency offset estimation algorithm based on interpolation and binary search. In [16], an improved Discrete Fourier Transform (DFT) frequency offset estimation algorithm is proposed, which solves the problem of the limited estimation range of Candan algorithm. In [17], the authors use coarse estimation based on discrete Fourier transform and fine estimation based on golden section search algorithm to improve the performance of frequency offset estimation. Although the performances of the abovementioned FFT-based frequency offset estimation algorithm are quite good, the complexity of this type of algorithm is still high. In order to reduce complexity, the authors in [18] proposed the maximum likelihood carrier FOE method based on the equal-interval pilot symbol, leading to higher estimation accuracy and lower SNR threshold, nevertheless, the synchronization range is still quite small. In [19], the carrier synchronization is carried out by structure of autocorrelation plus cross-correlation to achieve high accuracy and wide estimation range. Unfortunately, the estimated performance becomes worse when the pilot interval is large. In [20, 21], the authors consider the case that the first sampling time of the receiver is placed in the middle of the burst structure and gives the Cramer-Rao Bound (CRB) for the joint FOE of this case and the traditional case, respectively. However, in practical application, it is impossible to set the sampling zero time position artificially. Moreover, the possible influence of this structure on carrier synchronization performance has not been further discussed in [20, 21]. The authors in [22] proposed a frequency phase decoupling technique based on autocorrelation operator under MPSK modulation. However, the direct transplant to APSK or other high-order modulation signals will lead to poor performance.

To solve the above issues, this paper proposes a new carrier phase decoupling technique for high-order APSK signals. We firstly obtain the decoupling factor by the product of the signal of modulation removal and the autocorrelation

function. Then, we add a phase unwrapping module to overcome the influence of high FO on the decoupling factor. Using the above decoupling factor, we change the order of *arg* operator and summation to get the phase offset estimation, eliminating the influence of amplitude of modulated signal to POE. Simultaneously, we also carry out FOE with the autocorrelation function. The simulation results demonstrate that the decoupling performance of the proposed method is better than NCSM, and the FOE has high estimation accuracy and large estimation range.

2. Signal Model

For the convenience of readers, we list and explain all the symbols used in this paper in Table 1.

In a Gaussian channel, the baseband discrete signal after ideal timing synchronization can be expressed as

$$r(k) = c(k)e^{j(2\pi f_d T k + \theta)} + n(k), k \in \kappa, \quad (1)$$

where $c(k)$ is known modulated signal, f_d and θ are frequency offset (FO) and phase offset (PO) generated during signal reception, T is the symbol period, $n(k)$ is the complex Gaussian random variable, its mean is zero, and its variance is $\sigma = N_0/2$. $\kappa \triangleq \{N, N+1, \dots, N+L-1\}$ is sampling time set corresponding to the pilot symbol in the data frame, and $|\kappa| = L$. The data frame structure is shown in Figure 1, where L is pilot length, and N and \hat{N} are the pilot start position and the total length of the “data-pilot” structure.

We multiply both sides of (1) by $c^*(k)$ to remove the modulation information of the received signal, yielding

$$z(k) = r(k)c^*(k) = a(k)e^{j(2\pi f_d T k + \theta)} + d(k), \quad (2)$$

where $z(k)$ is called unmodulated information signal, $d(k) = c^*(k)n(k)$ is Gaussian white noise, and $a(k) = c(k)c^*(k)$ is a real constant.

The principle block diagram of the traditional carrier synchronization mode (TCSM) is shown in Figure 2. First, the pilot information is used to estimate the FO, then, the result of FOE is compensated to the demodulation signal, and finally, the POE is performed. In this mode, the accuracy of the FOE will affect the backward POE. In order to ensure the accuracy of the FOE, more pilot overhead is usually needed. Therefore, this processing method is not applicable to the communication environment with limited spectrum resources.

In [22], the authors proposed the NCSM suitable for MPSK, and it can realize the decoupling of FO and PO to a certain extent. The structure diagram of NCSM is shown in Figure 3.

The autocorrelation operator formula based on the demodulation signal can be obtained from (2) (for MPSK signals, $|a(k)| = 1$).

$$R(\alpha) = \frac{1}{L-\alpha} \sum_{k=N}^{N+L-\alpha-1} z^*(k)z(k+\alpha) = e^{j2\pi f_d T \alpha} + \psi(\alpha), \quad (3)$$

TABLE 1: Symbol description.

$r(k)$	Received signal
$c(k)$	Known modulated signal
f_d	Frequency offset
θ	Phase offset
\hat{f}_d	Estimated frequency offset
$\hat{\theta}$	Estimated phase offset
$n(k)$	Complex Gaussian random variable
T	Symbol period
N	Pilot start position
\tilde{N}	Total length of data
$z(k)$	Unmodulated information signal
$d(k)$	Gaussian white noise
$a(k)$	Signal energy
$R(\alpha)$	Autocorrelation operator
$D(k)$	Decoupling factor
$\psi(a)$	Noise interference term
$\Psi(\alpha)$	Noise interference term
$\hat{\Psi}(k)$	Noise interference term
$Z_s(k)$	Phase angles of $z(k)$
$R_s(\alpha)$	Phase angles of $R(\alpha)$

where $\psi(a)$ is the sum of noise terms

$$\begin{aligned} \psi(\alpha) &= \frac{1}{L-\alpha} \sum_{k=0}^{L-\alpha-1} e^{-j2\pi f_d T(k+N)} d(k+\alpha+N) \\ &\quad + e^{j2\pi f_d T(k+\alpha+N)} d^*(k+N) + d(k+\alpha+N) d^*(k+N). \end{aligned} \quad (4)$$

The decoupling factor $D(k)$ is expressed as

$$D(k) = z(k) \cdot R^*(\tilde{\alpha}) \Big|_{\tilde{\alpha}=L-1/2} = z(k) \cdot \left[e^{-j2\pi f_d T \tilde{\alpha}} + \Psi^*(\tilde{\alpha}) \right] \Big|_{\tilde{\alpha}=L-1/2}. \quad (5)$$

Then, the decoupling factor $D(k)$ of carrier parameter estimation is sent to the PO estimator based on maximum likelihood criterion to obtain the PO

$$\begin{aligned} \hat{\theta} &= \arg \left\{ \sum_{k=N}^{N+L-1} D(k) \right\} = \arg \left\{ e^{j\theta} e^{j2\pi f_d T N} \sum_{k=0}^{L-1} e^{j2\pi f_d T(k-L-1/2)} + \tilde{\psi} \right\} \\ &= \arg \left\{ e^{j\theta} e^{j2\pi f_d T N} \frac{\sin(\pi f_d T L)}{\sin(\pi f_d T)} + \tilde{\psi} \right\}. \end{aligned} \quad (6)$$

When the signal-to-noise ratio (SNR) of the received sig-

nal is high, we get $|\tilde{\psi}| \approx 0$, then, $\hat{\theta}$ is approximately

$$\hat{\theta} \approx \begin{cases} \theta, & N=0 \text{ and } \frac{|f_d T| \leq 1}{L}, \\ H_1(\theta, f_d, N, L), & N \neq 0 \text{ or } \frac{|f_d T| > 1}{L}, \end{cases} \quad (7)$$

where $H_1(\theta, f_d, N, L)$ is a function representing phase ambiguity, and its value is related to the PO, the FO, the pilot initial position, and the pilot length. We can see from (7) that when the FO is small, the estimated value of PO is still approximately equal to the true value. However, when the received signal is APSK, the derivation of (6) is not valid. In order to make the decoupling method suitable for different modulation modes, we improved NCSM and proposed an improved carrier parameter estimation decoupling technique (ICPEDT). The specific structure is introduced in next section.

3. ICPEDT Based on Parameter Correcting

Figure 4 is the block diagram of ICPEDT. Compared to NCSM, the ICPEDT changed the function of the comparator and added unwrapping operator. The specific analysis is as follows.

For APSK modulation, the $|a(k)| \neq 1$ in (2), so the autocorrelation operator formula of demodulation signal is changed as

$$R(\alpha) = \frac{1}{L-\alpha} \sum_{k=N}^{N+L-\alpha-1} z^*(k) z(k+\alpha) = \gamma_\alpha e^{j2\pi f_d T \alpha} + \Psi(\alpha), \quad (8)$$

where $\gamma_\alpha = a^*(k) a(k+\alpha)$, $\Psi(\alpha)$ is noise interference term

$$\begin{aligned} \Psi(\alpha) &= \frac{1}{L-\alpha} \sum_{k=0}^{L-\alpha-1} \underbrace{c^2(k+N) c(k+\alpha+N)}_{\lambda_1(\alpha)} e^{-j2\pi f_d T(k+N)} n(k+\alpha+N) \\ &\quad + \underbrace{c(k+N) c^2(k+\alpha+N)}_{\lambda_2(\alpha)} e^{j2\pi f_d T(k+\alpha+N)} n^*(k+N) \\ &\quad + \underbrace{c(k+\alpha+N) c(k+N)}_{\lambda_3(\alpha)} n(k+\alpha+N) n^*(k+N). \end{aligned} \quad (9)$$

The $D(k)$ can be expressed as

$$D(k) = z(k) \cdot R^*(\tilde{\alpha}) \Big|_{\tilde{\alpha}=L-1/2} = z(k) \cdot \left[\gamma_{\frac{L-1}{2}} e^{-j2\pi f_d T(L-1/2)} + \Psi^* \left(\frac{L-1}{2} \right) \right]. \quad (10)$$

The expression of POE is

$$\hat{\theta} = \frac{1}{L} \sum_{k=N}^{N+L-1} \arg\{D(k)\} = \frac{1}{L} \sum_{k=N}^{N+L-1} \arg\left\{ a_k \gamma_{L-1/2} e^{j(2\pi f_d T(k-L-1/2)+\theta)} + \hat{\Psi}(k) \right\}, \quad (11)$$

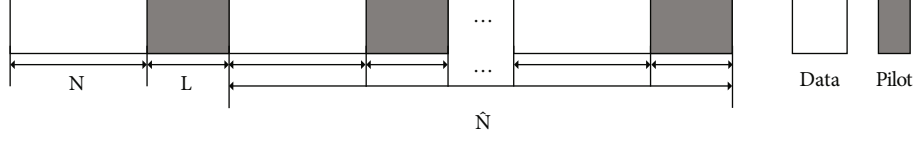


FIGURE 1: The data-pilot frame structure.

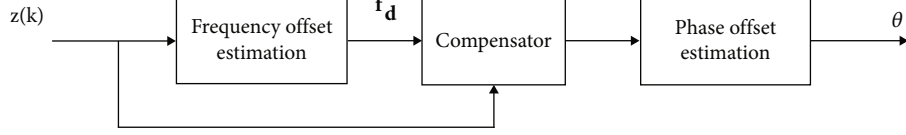


FIGURE 2: Serial carrier synchronization mode.

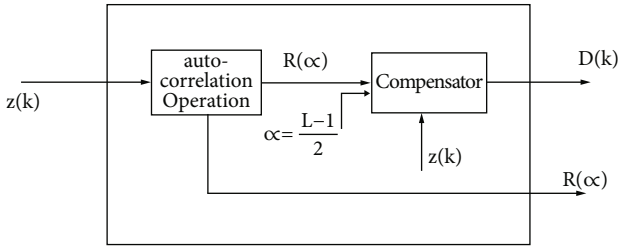


FIGURE 3: The principle block diagram of NCSM.

where $\widehat{\Psi}(k)$ is still the noise interference term. Comparing (9) and (4), each term of $\Psi(\alpha)$ is multiplied by a real number $\lambda_i(\alpha)$. We set $\lambda_i(\alpha) \leq \lambda_{\max}$, then, let $\Psi_1(\alpha)$ be denoted as

$$\begin{aligned} \Psi_1(\alpha) &= \lambda_{\max} \Psi(\alpha) = \frac{1}{L-\alpha} \sum_{k=0}^{L-\alpha-1} \lambda_{\max} e^{-j2\pi f_d T(k+N)} n(k+\alpha+N) \\ &\quad + \lambda_{\max} e^{j2\pi f_d T(k+\alpha+N)} n^*(k+N) + \lambda_{\max}(\alpha) n(k+\alpha+N) n^*(k+N). \end{aligned} \quad (12)$$

From (12), we know that $|\Psi(\alpha)| \leq |\Psi_1(\alpha)|$. Because $|\psi(\alpha)| \approx 0$ holds in (4) under high SNR, the value of $|\Psi(\alpha)|$ also approaches zero at this time. By analogy, $|\widehat{\Psi}(k)| \approx 0$ is true when the SNR is high, the result of POE is

$$\widehat{\theta} \approx \begin{cases} \theta, & N=0 \text{ and } \frac{|f_d T| \leq 1}{(L-1)}, \\ H_2(\theta, f_d, N, L), & N \neq 0 \text{ or } \frac{|f_d T| > 1}{(L-1)}, \end{cases} \quad (13)$$

where $H_2(\theta, f_d, N, L)$ is still a function representing phase ambiguity. Different from (6), we first calculate the phase angle of $D(k)$ in (10), and then sum $D(k)$. In this way, we can eliminate the influence of signal amplitude information on POE. When $|f_d T| > 1/(L-1)$, the POE performance of (11) is still very poor. The reason is that larger FO results will cause phase folding of $\arg\{D(k)\}$. If we can compensate for the folding phase of $\arg\{D(k)\}$, the POE will not be affected by the pilot overhead. This means

that PO estimator can still accurately estimate the PO under a larger FO.

3.1. Phase Unwrapping. In this paper, we use a phase unwrapping method. This method can not only eliminate the phase folding caused by the FO but also greatly reduce the probability of incorrect interval switching caused by the simultaneous presence of noise and FO.

Assume $\vartheta(k) = \widehat{\vartheta}(k) + \Lambda(k)$, where $\widehat{\vartheta}(k)$ is the estimated phase value at time k , $\vartheta(k)$ is the estimated phase value after phase unwrapping, and $\Lambda(k)$ is the phase compensation parameter. The concrete calculation steps are as follows.

- (i) Initialization, $\Lambda(0) = 0$, $\vartheta(0) = \widehat{\vartheta}(0)$
- (ii) $k = k + 1$

$$\Lambda(k) = \begin{cases} \Lambda(k-1) + 2\pi, & \widehat{\vartheta}(k) - \widehat{\vartheta}(k-1) < -\pi, \\ \Lambda(k-1) - 2\pi, & \widehat{\vartheta}(k) - \widehat{\vartheta}(k-1) > \pi, \\ \Lambda(k-1), & \text{Other}; \end{cases} \quad (14)$$

- (iii) $\vartheta(k) = \widehat{\vartheta}(k) + \Lambda(k)$
- (iv) Repeat step (ii)

The variation of $\Lambda(k)$ is determined by the phase difference between time k and time $k-1$. If the random noise at the moment of k is large, the PO error exceeding π will cause $\Lambda(k)$ to change 2π . If the random noise disappears at $k+k_0$ ($k_0 \geq 1$), this will cause the phase estimation difference to exceed $-\pi$ and cause $\Lambda(k)$ to reversely change 2π . In this case, the carrier phase error will only occur between k and k_0-1 . Therefore, the method is also applicable to the case of low SNR.

3.2. POE Based on ICPEDT. In order to further reduce the influence of FO on POE, phase angles of $z(k)$ and $R(\alpha)$ were

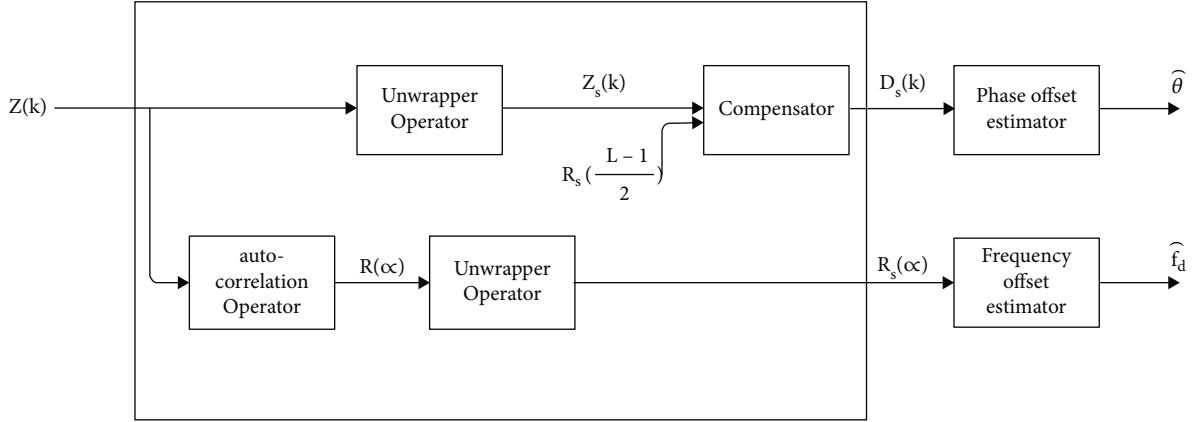


FIGURE 4: The block diagram of ICPEDT.

TABLE 2: Algorithmic complexity comparison of phase offset estimation.

	Multiplication	Addition	Complex angle
NCSM	$\frac{3L^2 + 10L + 8}{2}$	$2L^2 + 4L + 3$	$\frac{1}{2}L$
ICPEDT	$\frac{3L^2 + 18L}{2}$	$2L^2 + \frac{17}{2}L + 1$	$\frac{3}{2}L$

calculated, and phase correction was performed

$$Z_s(k) \triangleq \text{unwrap}\{\arg\{z(k)\}\}, \quad (15)$$

$$R_s(\alpha) \triangleq \text{unwrap}\{\arg\{R(\alpha)\}\}. \quad (16)$$

Then, (11) can be written into

$$\begin{aligned} \hat{\theta} &= \frac{1}{L} \sum_{k=N}^{N+L-1} D_s(k) = \frac{1}{L} \sum_{k=N}^{N+L-1} Z_s(k) - R_s\left(\frac{L-1}{2}\right) \\ &= \frac{1}{L} \sum_{k=N}^{N+L-1} \arg\{a_k e^{j(2\pi f_d T k + \theta)} + d(k)\} \\ &\quad - \arg\left\{ \gamma_{L-1/2} e^{j2\pi f_d T L - 1/2} + \Psi\left(\frac{L-1}{2}\right) \right\}. \end{aligned} \quad (17)$$

If the noise interference terms $d(k)$ and $\Psi(L-1/2)$ are ignored, we can get

$$\hat{\theta} \approx \begin{cases} \theta, & N = 0, \\ H_3(\theta, f_d, N), & N \neq 0, \end{cases} \quad (18)$$

where $H_3(\theta, f_d, N)$ is still a function representing phase ambiguity. From (18), the result of POE is no longer limited by the pilot overhead, so the POE based on ICPEDT has greater antifrequency offset ability after phase unwrapping. At the same time, comparing (11), (17) only needs one real number multiplication operation, so the algorithm complexity is greatly reduced after phase unwrapping. Therefore, the computational complexity of the algorithm in this paper is

only a little higher than that of the NCSM. More in detail, the complexity comparison between NCSM and ICPEDT is explained in Table 2.

3.3. FOE Based on ICPEDT. The FO can be estimated directly by the intermediate variable $R_s(\alpha)$. $R_s(\alpha)$ is the correction term after phase unwrapping of the autocorrelation operator $R(\alpha)$, and (16) can be expanded as

$$R_s(\alpha) = \text{unwrap}\{\arg\{R(\alpha)\}\} = 2\pi f_d T \alpha + \Psi(\alpha), \quad (19)$$

where $\alpha \in [1, L-1/2]$. Sum both ends of (19) separately

$$\sum_{\alpha=1}^{L-1/2} R_s(\alpha) = \sum_{\alpha=1}^{L-1/2} 2\pi f_d T \alpha + \Psi(\alpha) = \frac{(L-1)(L+1)}{8} (2\pi f_d T + \Psi(\alpha)). \quad (20)$$

If the influence of noise term is ignored, then

$$\hat{f}_d = \frac{4}{(L-1)(L+1)\pi T} \sum_{\alpha=1}^{L-1/2} R_s(\alpha). \quad (21)$$

Because the phase of the autocorrelation factor $R_s(\alpha)$ is corrected, the phase of $R_s(\alpha)$ is the actual FO. Therefore, the estimation range of FOE using $R_s(\alpha)$ is no longer affected by the pilot overhead. Theoretically, the frequency offset estimation range is up to $(-0.5, 0.5)$.

4. Simulation and Analysis

ICPEDT can solve the problem that the FOE directly affects the POE in TCSM and realizes the parallel estimation of FO and PO. According to (18), the selection of the initial position of pilot will affect the accuracy of POE. Therefore, first simulate the influence of the initial position of the pilot on the performance of ICPEDT.

4.1. The Selection of Initial Position N of Pilot. Assume that the modulation mode is QPSK, assume $f_d T = 0.08$, and $\theta = 3\pi/8$, the pilot overhead is set to be $L = 35$. Figure 5 shows the MSE of POE for different N .

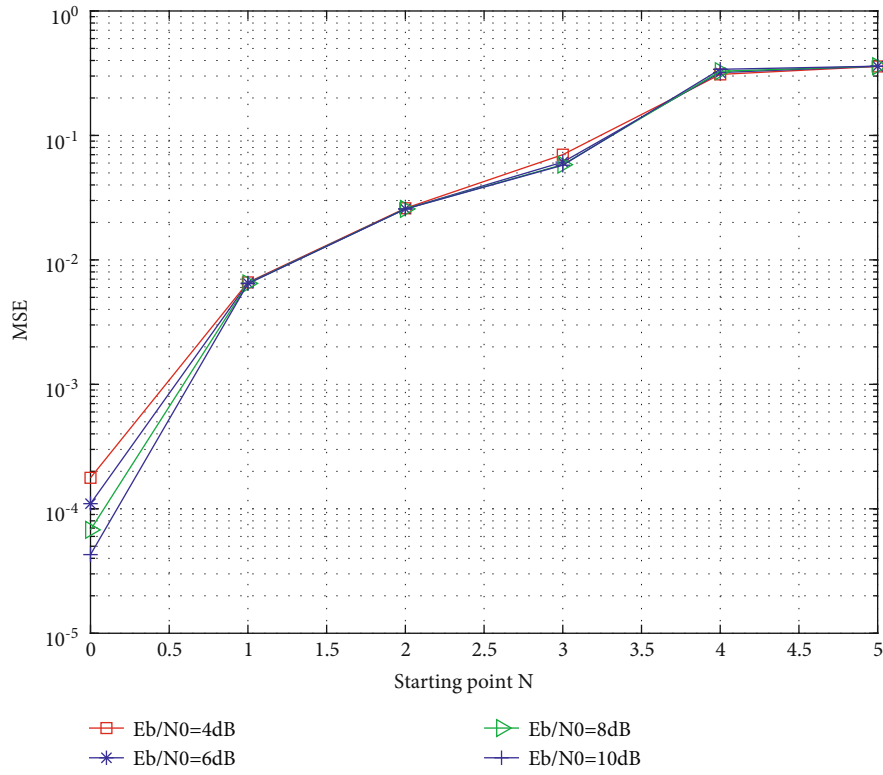


FIGURE 5: The MSE performance of the POE of the ICPEDT at different N .

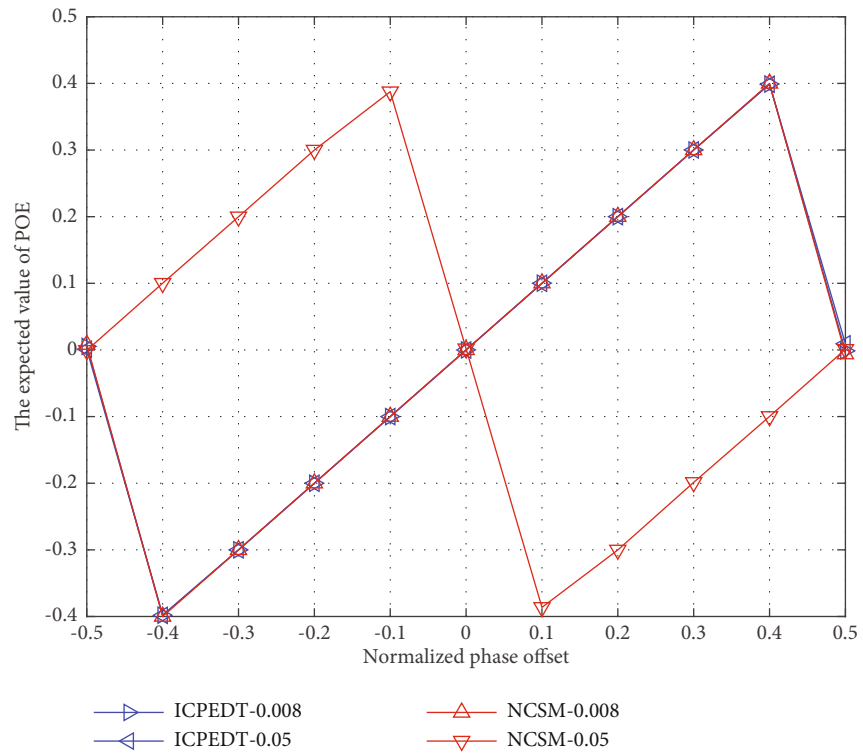


FIGURE 6: The expectation of the POEs under different POs (QPSK modulation).

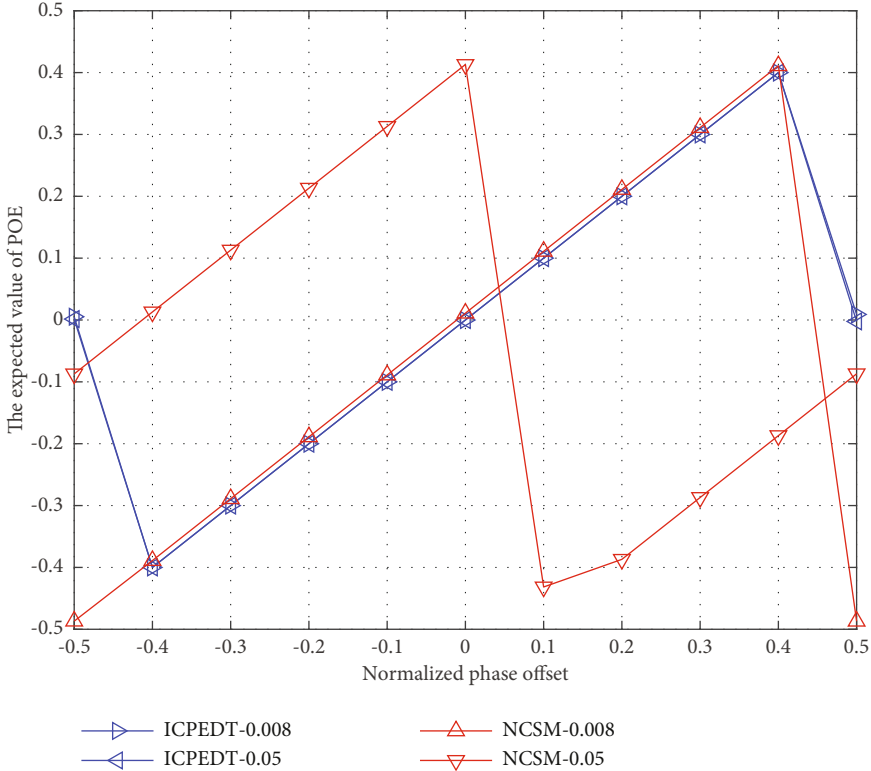


FIGURE 7: The expectation of the POEs under different POs (32APSK modulation).

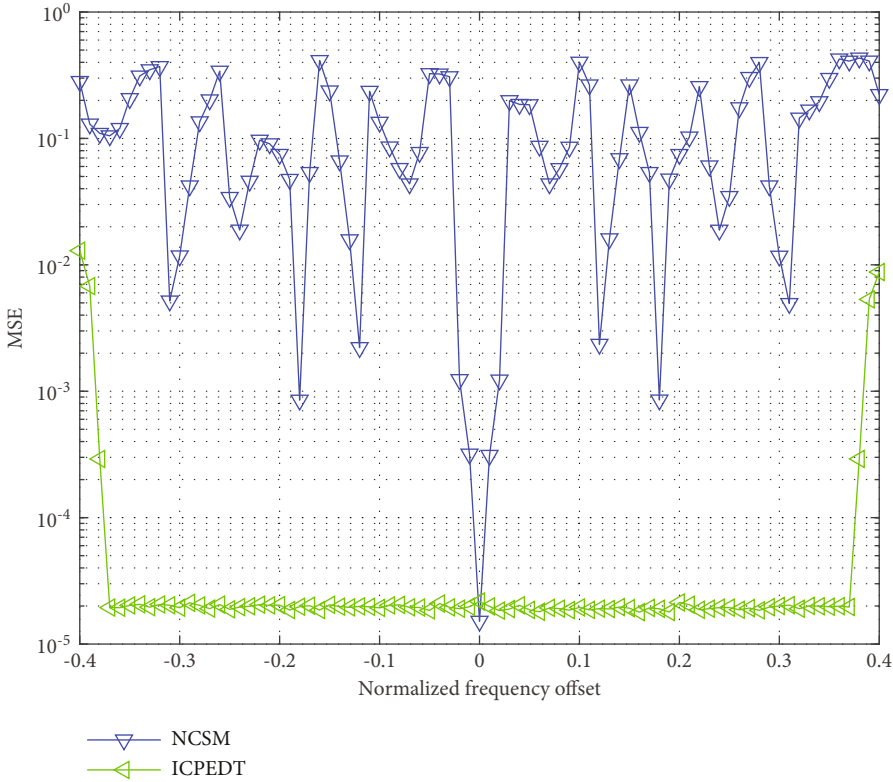


FIGURE 8: The influence of different FOs on POE.

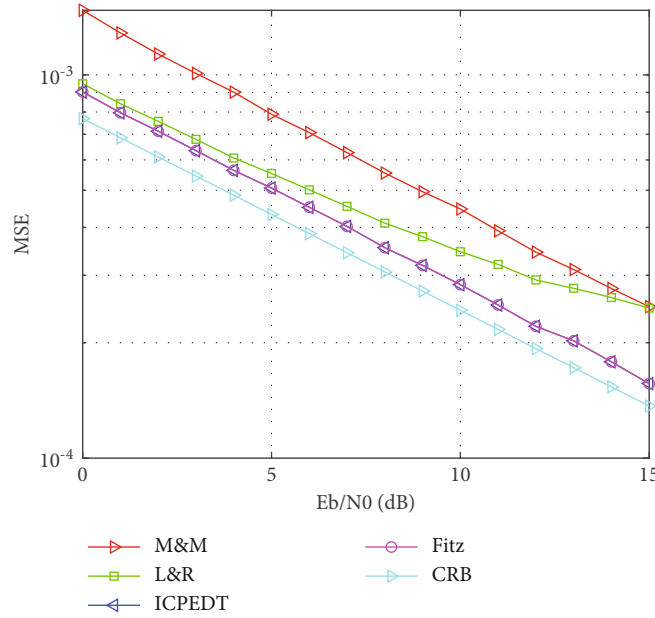


FIGURE 9: The accuracy of different FOE algorithms.

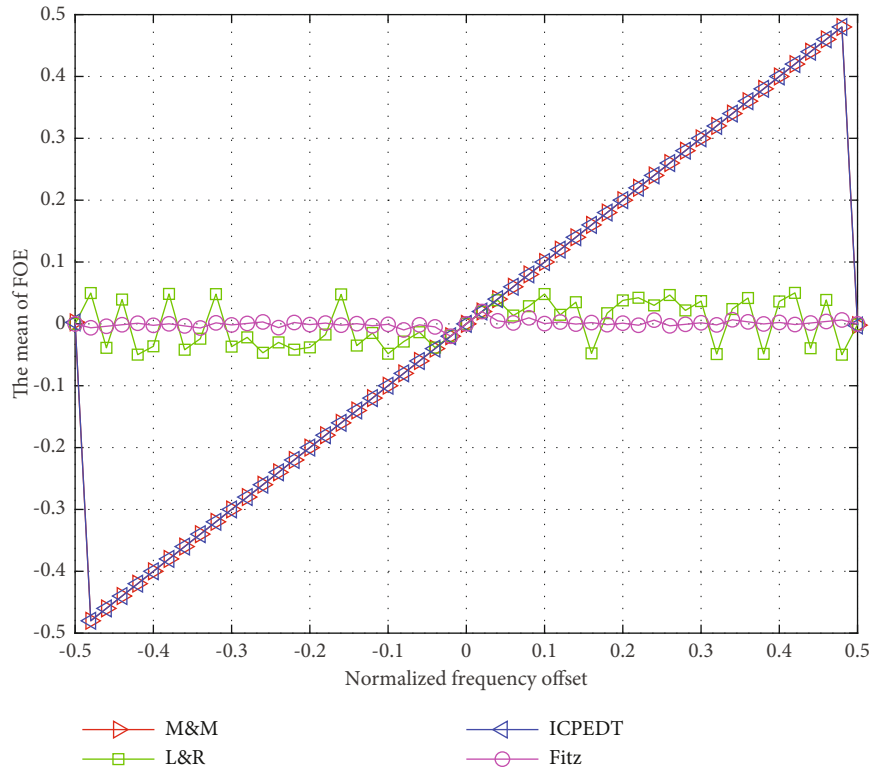


FIGURE 10: The estimation range of different FOE algorithms.

It can be seen from Figure 5, under different SNR, the POE has the best performance at the initial pilot position $N = 0$, and the performance of POE deteriorates with the increase of the initial pilot position. Therefore, in order to obtain the best performance under large FO, the starting point N should be set to zero. In the simulation parameters below, the pilot overhead L is set to 35 and $N = 0$.

4.2. *The Performance of POE under Different Modulation System.* First, assume the modulation system is QPSK, $f_d T = 0.008, 0.05$, the normalized PO $\theta \in (-0.5, 0.5]$, $E_b/N_0 = 8$ dB. Then, set the modulation system to 32APSK, $E_b/N_0 = 15$ dB, and other simulation conditions remain unchanged. Figures 6 and 7 show the expectation of POE of ICPEDT and NCSM for different PO.

We can see from Figures 6 and 7, in the case of QPSK modulation and the normalized FO is 0.008, the value of POE of NCSM basically coincides with the actual PO. But when the normalized FO is 0.05, the result of POE of NCSM has a large deviation from the actual PO. The reason is that NCSM's precise estimation range is limited. It can be seen from (6) that when $L = 35$, the POE range of NCSM is $(-0.0286, 0.0286)$. So when FO is 0.05, NCSM's estimation deviation is very large. When the signal is 32APSK, the overall performance of NCSM's POE decreases, and the estimation accuracy deteriorates. However, the estimated value of POE of ICPEDT under different modulations is very close to the actual PO, and the estimation accuracy does not deteriorate with the increase of the frequency deviation, which is consistent with the conclusion of (18).

4.3. The MSE of POE under Different Normalized FO. Assume the modulation is 64APSK, $f_d T = [-0.4, 0.4]$, $\theta = 3\pi/8$, and $E_b/N_0 = 15dB$, Figure 8 shows the MSE of the POE of ICPEDT and NCSM under different FOs.

It can be seen from the simulation results in Figure 8 that the decoupling performance of NCSM is poor under 64APSK modulation, and the PO can be accurately estimated only when FO is small. However, ICPEDT's POE can still work well under large FO. The method in this paper has strong robust. This is because the phase unwrapping module eliminates the estimation error caused by phase folding, thereby significantly reducing the influence of FOE on the performance of POE.

4.4. The FOE Accuracy of Different Algorithms. Assume the modulation method of the signal is 64APSK, $f_d T = 0.02$, and $\theta = 3\pi/8$. Figure 9 shows the estimation accuracy performance curve of different algorithms.

The simulation curves show that the M&M [3] algorithm has the worst estimate accuracy. The estimation performance of L&R [4] algorithm gradually deteriorates with the increase of E_b/N_0 . The main reason is that the L&R algorithm does not consider the impact of signal amplitude information on POE. The estimation accuracy of FOE based on ICPEDT is close to the performance of Fitz [5] algorithm, which is better than L&R and M&M algorithms. Its performance is close to the lower bound of FOE performance CRB. This shows that the autocorrelation FOE algorithm based on equation (21) is unbiased.

4.5. The FOE Range of Different Algorithms. Assume the simulation signal is 64APSK, $f_d T \in (-0.5, 0.5]$, $\theta = 3\pi/8$, and $E_b/N_0 = 15dB$. Figure 10 shows the estimated range of different FOE algorithms.

We can see from Figure 10 that the Fitz algorithm has the smallest estimation range of FO, which is about $(-0.028, 0.028)$, followed by the L&R algorithm. The estimated range of FOE based on ICPEDT is consistent with the estimated range of the M&M algorithm, which is close to $(-0.5, 0.5]$. The simulation results are consistent with the conclusion derived from (21).

5. Conclusions

According to the characteristics of satellite communication, we propose a strong robust carrier parameter decoupling technique suitable for high-order APSK modulation. This technique can realize parallel estimation of FO and PO. Both theory and simulation show that, compared with the existing methods, the method in this paper is more robust to the decoupling of high-order APSK modulated signals, and the POE of the method in this paper has better estimation performance and stronger antifrequency offset ability. The accuracy of the FOE in this paper is equivalent to the Fitz method, but it has a larger FOE range. The range of FOE in this paper is close to $(-0.5, 0.5]$, but the computational complexity is similar to the Fitz algorithm. Therefore, this method has good engineering practical value.

Data Availability

No data were used to support this study.

Conflicts of Interest

The authors declare that there are no conflicts of interest regarding the publication of this paper.

Acknowledgments

This work is also supported in part by the National Key Research and Development Program under Grant 2019QY0302, in part by the Key Young Teachers Project of Henan Province under Grant 2018GGJS006, and in part by the Key Scientific Research Project of Colleges and Universities in Henan Province under Grant 20A510010 and Grant 20A510007.

References

- [1] X. Li, M. Zhao, M. Zeng et al., "Hardware impaired ambient backscatter NOMA systems: reliability and security," *IEEE Transactions on Communications*, vol. 69, no. 4, pp. 2723–2736, 2021.
- [2] W. U. Khan, M. A. Javed, T. N. Nguyen, S. Khan, and B. M. Elhalawany, "Energy-efficient resource allocation for 6G backscatter-enabled NOMA IoV networks," *IEEE Transactions on Intelligent Transportation Systems*, pp. 1–11, 2021.
- [3] J. Xia, D. Deng, and D. Fan, "A note on implementation methodologies of deep learning-based signal detection for conventional MIMO transmitters," *IEEE Transactions on Broadcasting*, vol. 66, no. 3, pp. 744–745, 2020.
- [4] K. Omprakash and K. Sushil, "Geocast routing: recent advances and future challenges in vehicular adhoc networks," *2014 International Conference on Signal Processing and Integrated Networks, SPIN*, 2014, pp. 291–296, Noida, India, 2014.
- [5] A. Sikandar, R. Agrawal, M. K. Tyagi, A. L. N. Rao, M. Prasad, and M. Binsawad, "Toward green computing in wireless sensor networks: prediction-oriented distributed clustering for non-uniform node distribution," *Journal on Wireless Communications and Networking*, vol. 2020, no. 1, p. 183, 2020.
- [6] ETSI E, *Digital Video Broadcasting (DVB): Second Generation Framing Structure, Channel Coding and Modulation Systems*

- for Broadcasting, Interactive Services, New Gathering and Other Broadband Satellite Applications, Part2:DVB-S2 Extensions(DVB-S2X), 2014.
- [7] X. Li, H. Mengyan, Y. Liu, V. G. Menon, A. Paul, and Z. Ding, "I/Q imbalance aware nonlinear wireless-powered relaying of B5G networks: security and reliability analysis," *IEEE Transactions on Network Science and Engineering*, vol. 8, no. 4, pp. 2995–3008, 2021.
- [8] W. U. Khan, F. Jameel, X. Li, M. Bilal, and T. A. Tsiftsis, "Joint spectrum and energy optimization of NOMA-enabled small-cell networks with QoS guarantee," *IEEE Transactions on Vehicular Technology*, vol. 70, no. 8, pp. 8337–8342, 2021.
- [9] U. Mengali and M. Morelli, "Data-aided frequency estimation for burst digital transmission," *IEEE Transactions on Communications*, vol. 45, no. 1, pp. 23–25, 1997.
- [10] M. Luise and R. Reggiannini, "Carrier frequency recovery in all-digital modems for burst-mode transmissions," *IEEE Transactions on Communications*, vol. 43, no. 2/3/4, pp. 1169–1178, 1995.
- [11] M. Fitz, "Further results in the fast estimation of a single frequency," *IEEE Transactions on Communications*, vol. 42, no. 2/3/4, pp. 862–864, 1994.
- [12] N. Noels, C. Herzet, A. Dejonghe et al., "Turbo synchronization: an EM algorithm interpretation," in *IEEE International Conference on Communications, 2003. ICC '03*, vol. 4, pp. 2933–2937, Anchorage, AK, USA, 2003.
- [13] N. Noels, V. Lottici, A. Dejonghe et al., "A theoretical framework for soft-information-based synchronization in iterative (turbo) receivers," *EURASIP Journal on Wireless Communications and Networking*, vol. 2005, no. 1, 2005.
- [14] M. Zhengke, Z. Haoliang, W. Wei, and Z. Shenghua, "A simplified code-aided carrier synchronization algorithm," in *2019 2nd International Conference on Safety Produce Informatization (IICSPI)*, pp. 283–286, Chongqing, China, 2019.
- [15] C. Wang, Y. Li, and K. Li, "An high-precision FFT frequency offset estimation algorithm based on interpolation and binary search," in *2019 IEEE 3rd information technology, networking, Electronic and Automation Control Conference (ITNEC)*, pp. 437–442, Chengdu, China, 2019.
- [16] T. Li, Y. Zhang, and B. Tang, "An improved DFT frequency offset estimation algorithm with high accuracy," in *2019 IEEE 3rd information technology, networking, Electronic and Automation Control Conference (ITNEC)*, pp. 175–179, Chengdu, China, 2019.
- [17] J. Fan, Y. Ren, X. Luo, and J. Joung, "Iterative carrier frequency offset estimation scheme for faster-than-Nyquist signaling systems," *IEEE Photonics Technology Letters*, vol. 32, no. 18, pp. 1203–1206, 2020.
- [18] Z. Yong-gang, Y. Fu-qiang, L. Yong-xiang, Z. Yi, and P. Wei, "ML-based carrier frequency offset estimation and its low SNR threshold," *Systems Engineering and Electronics*, vol. 33, pp. 427–431, 2011.
- [19] Z. Yu, J. Sun, B. Bai, and X. Wu, "A phase increment-based frequency estimator for general psam in burst communications," in *2016 IEEE 83rd Vehicular Technology Conference (VTC Spring)*, pp. 1–5, Nanjing, China, 2016.
- [20] F. Rice, "Carrier-phase and frequency-estimation bounds for transmissions with embedded reference symbols," *IEEE Transactions on Communications*, vol. 54, no. 2, pp. 221–225, 2006.
- [21] N. Noels, H. Steendam, M. Moeneclaey, and H. Bruneel, "Carrier phase and frequency estimation for pilot-symbol assisted transmission: bounds and algorithms," *IEEE Transactions on Signal Processing*, vol. 53, no. 12, pp. 4578–4587, 2005.
- [22] H. Xu, Z. Yu, H. Zhu, M. Xu, and Z. Luo, "Frequency-phase decoupling method for carrier synchronization in space communications," *IEEE Wireless Communications Letters*, vol. 8, no. 4, pp. 1293–1296, 2019.

Research Article

Performance Analysis of MEC Based on NOMA under Imperfect CSI with Eavesdropper

Xuehua Li ^{1,2,3} Yingjie Pei ^{1,2,3} Huan Jiang ^{1,2,3} Xinwei Yue ^{1,2,3} Yafei Wang ^{1,2,3}
and Yuqiao Suo ⁴

¹School of Information and Communication Engineering, Beijing Information Science and Technology University, Beijing 100101, China

²Institute of Intelligent Communication and Computing (BISTU-IICC), Beijing 100101, China

³Key Laboratory of Modern Measurement & Control Technology, Ministry of Education, Beijing 100101, China

⁴College of Science, Changchun University of Science and Technology, Changchun 130022, China

Correspondence should be addressed to Huan Jiang; 18611256787@163.com

Received 19 July 2021; Revised 29 October 2021; Accepted 10 November 2021; Published 6 December 2021

Academic Editor: Xingwang Li

Copyright © 2021 Xuehua Li et al. This is an open access article distributed under the Creative Commons Attribution License, which permits unrestricted use, distribution, and reproduction in any medium, provided the original work is properly cited.

Mobile edge computing (MEC) is becoming more and more popular because of improving computing power in virtual reality, augmented reality, unmanned driving, and other fields. This paper investigates a nonorthogonal multiple access- (NOMA-) based MEC system, which is under imperfect channel state information (ipCSI). In this system model, a pair of users offloads their tasks to the MEC server with the existence of an eavesdropper (Eve). To evaluate the impact of Eve on the performance of the NOMA-MEC system, the secrecy outage probability (SOP) expressions for two users with the conditions of imperfect CSI and perfect channel state information (pCSI) are derived. In addition, both throughput and energy efficiency are discussed in the delay-limited transmission mode. Simulation results reveal that (1) due to the influence of channel estimation errors, the secrecy outage behaviors of two users under ipCSI conditions are worse than those of users with pCSI; (2) the secrecy performance of NOMA-MEC is superior to orthogonal multiple access- (OMA-) aided MEC systems; and (3) the NOMA-MEC systems have the ability to attain better system throughput and energy efficiency compared with OMA-MEC.

1. Introduction

As the mobile communication systems develop rapidly, the technical standards have constantly evolved. The 4th-generation communication system relies on orthogonal frequency division multiple access to operate, and the data service transmission rate reaches even 1,000 megabits per second. However, with the large-scale popularization and application of intelligent terminals, the requirements for new mobile services are increasing. The transmission rate of wireless communication will have difficulty in meeting the application requirements of future mobile communication. To improve the spectrum efficiency of the 5th-generation (5G) mobile communication technology, the industry recommends a new method of multiple access multiplexing, the nonorthogonal multiple access (NOMA). Only

a single radio resource can be distributed to one user in orthogonal multiple access (OMA), while NOMA is capable of allocating one resource to multiple users at the same frequency, time, or code domain. In some scenarios like near-remote effect and large coverage multinode access cases, especially uplink communication scenarios, the nonorthogonal method with power reuse has obvious performance advantages over traditional orthogonal access.

Considerable research efforts have been devoted to investigate NOMA performance. For the downlink communications, the authors in [1] considered joint user pairing and power allocation issues, where the achievable total rate was optimized according to the minimum rate constraint of all users. To study the large cellular networks, a new analysis framework was developed to evaluate the outage performance and obtained the closed-form expressions of outage

probability [2]. The authors in [3] proposed a power allocation algorithm for a multiuser scheme to ensure successful and low-complexity successive interference cancellation (SIC) decoding and evaluated the proposed performance under different user weight ratio scenarios. As a further advance, the optimal user grouping of the downlink NOMA system was studied to make the sum rate maximal [4]. To further enhance the performance of the system, an advanced multiple-input multiple-output NOMA-aided unmanned aerial vehicle framework was proposed in [5], where the outage probability and diversity order were surveyed in depth. For the uplink communications, the authors studied the NOMA system with imperfect SIC, considered to minimize the total power consumption with the constraints of quality of service, and evaluated the impact of imperfect SIC on system performance [6]. For the cognitive Internet of Things (IoT) supporting the 6th-generation mobile communication technology, the authors of [7] proposed a hybrid spectrum access scheme based on NOMA to maximize the average data transmission rate of the cognitive IoT. The above scenarios are assumed under the ideal condition; however, the loss of distance and path is inevitable during the transmission process in actual scenarios. Thus, it is necessary to research the imperfect channel state information (ipCSI). A new method to solve the problem of multiuser detection was proposed in [8], where the receiver problem of ipCSI scenarios caused by channel estimation errors was discussed carefully. The user ending (UE) signatures presented by forward error correction channel codes under different arrangements were adopted to distinguish the desired useful signals from interfering UEs and provide robustness for channel state information (CSI) errors. Similarly, the authors of [9] designed a system model based on an ipCSI scenario, obtained the closed-form solution of the outage probability, and analyzed the performance of the NOMA system. For a cooperative NOMA system, the authors in [10] considered the influence of residual transceiver hardware damage on the system and deduced the expressions of interruption probability, traversal capacity, and energy efficiency, which proved the superiority of outage performance of cooperative NOMA. On this basis, considering the challenge of large-scale connection in IoT, the author investigated the performance of NOMA for cooperative synchronization of wireless signals and power transmission in a large-scale IoT system [11].

With the popularization of 5G, new applications have higher requirements for computing capabilities. With the core technology of mobile communication networks, mobile edge computing (MEC) sinks computing resources and storage resources closer to users and handles resource-intensive and delay-sensitive tasks at the edge of the network, which tackles the problems of extended communication resource processing time and high energy consumption. Due to the high requirements of MEC on latency and energy consumption, a mass of literature has regarded these two problems as optimization objectives. Considering the resource constraints and interference between multiple users, the authors of [12] designed an

iterative MEC resource allocation algorithm which operated heuristically to make dynamic offloading decisions and confirmed that this method overmatches the cloud computing solutions in the field of execution delay and offloading efficiency. To achieve the requirements of ultra-reliability and low delay in mission-critical applications, the authors of [13] proposed a new system design, where the applications of extreme value theory to exact probability were used for local computing and task offloading. The combined application of NOMA and MEC is a pivotal solution technology. In [14], the authors comprehensively considered the uplink and downlink communication where NOMA cooperated with MEC. It indicated that NOMA-MEC can greatly reduce the delay and energy consumption of the offloading process. The authors in [15] jointly optimized the power and time distribution to cut down computing and offloading energy consumption and then obtained the closed-form expression of optimal power and time allocation solution. In [16], the partial offloading scheme based on NOMA minimized the average power consumption and realized the dynamic power delay trade-off for MEC offloading by using the Lyapunov method. To improve the offloading efficiency of edge users, a NOMA-assisted MEC system was introduced in [17], where a joint communication and computation resource iterative optimization algorithm with low complexity was proposed to minimize the energy consumption. In the full-duplex mode, edge users utilize NOMA to transfer part of the computing workload to two MEC servers. The energy consumption of the whole system was effectively reduced through the cooperation scheme, and the resources of different MEC servers were balanced to improve the experience quality of edge users. Regarding energy efficiency, the authors of [18] studied joint user association and resource allocation and proposed a matching method to reduce the energy consumption of each user in NOMA-MEC networks. It was proven that this method effectively lessens the energy consumption and iterations times. In [19], a NOMA-MEC task delay minimization problem was investigated, where a bisection search iterative algorithm is applied to tackle the nonconvex optimization issue. It is observed that the cooperation between NOMA and MEC can significantly improve energy/power efficiency.

Physical layer security (PLS) is expected to be a complementary role of wireless communication security in the future. Compared with traditional key encryption measures, PLS technology makes full use of the diversity, time variation, and heterogeneity of wireless channels to ensure that legitimate users receive private and useful information safely. Considering the existence of eavesdroppers (Eves), the author in [20] optimized the allocation of time, power, and subchannels to acquire safe and energy-saving transmission among multiple users. The authors of [21] studied the secure communications via full-duplex wiretap with wireless power supply and proposed an iterative algorithm, which was capable of achieving higher total security rate and anti-interference ability of wiretap. To enhance the security of computing task offloading, the authors in [22]

researched the security behaviors of NOMA for MEC-aware networks, considered passive eavesdropping schemes, measured the security performance of computing offload by using security interruption probability, and deduced the semiclosed form expression of the optimal solution. In order to further evaluate the eavesdropping ability of users without knowing the CSI of the Eve, the authors in [23] proposed an effective iterative algorithm to maximize the minimum antieavesdropping ability of uplink NOMA users by jointly formulating the security rate, locally calculating bits, and allocating power. To solve the delay problem of NOMA in the presence of malicious Eves, an algorithm based on binary search was proposed, which can ensure the security rate and make the maximum task delay of uplink NOMA users minimal [24]. The authors of [25] considered the transmission scenarios of single-antenna and multiantenna devices at the same time, where the exact secrecy outage probability (SOP) expressions for two antenna-aided scenarios were derived. Furthermore, the authors employed stochastic geometry to model legitimate users and Eves and studied the impact of physical layer confidentiality on the performance of a unified NOMA framework [26], where the external and internal eavesdropping scenarios were checked carefully. Given the backscatter component, the PLS of the environmental backscatter NOMA system with the actual assumptions of residuary hardware damage, channel estimation error, and imperfect SIC were studied in [27].

This paper mainly investigates the integration of NOMA and MEC by taking ipCSI and perfect channel state information (pCSI) into account, i.e., considering the Eve in the NOMA uplink-assisted MEC scenarios with channel estimation errors. The treatises of [28, 29] have studied the impact of Eves on NOMA-MEC system performance. To the best of the authors' knowledge, the NOMA-based MEC secure problem is always considered in the pCSI condition. Little is known, however, about the security performance analysis of MEC based on NOMA under ipCSI. This motivates us to evaluate the damaging influence of ipCSI for NOMA-based MEC secure communication, since pCSI is hardly obtained due to channel fading and channel estimate errors in reality. We sum up the contributions of this paper as follows:

- (1) We concentrate on the secrecy performance of NOMA-MEC in the presence of an Eve. We derive the exact expressions of SOP of NOMA-MEC under ipCSI/pCSI conditions. To obtain more insights, we further derive the expressions of the asymptotic SOP at high signal-to-noise ratios (SNRs) and provide diversity orders of the legitimate user
- (2) The results of system performance are also evaluated by simulation, which reveal that in the presence of the Eve, the SOP under ipCSI conditions is greater than that under the ideal condition. We also analyze the effect of channel estimation errors and the Eve's

SNR on system performance. Under both ipCSI and pCSI conditions, the secrecy performance of the nearby user for NOMA-MEC overmatches that of the remote user and OMA-MEC

- (3) We discuss the system throughput and energy efficiency in delay-limited transmission mode. We confirmed that NOMA-MEC is capable of attaining the greater system throughput and energy efficiency relative to OMA-MEC. As the channel estimation errors increase, the system throughput and energy efficiency of NOMA-MEC decrease seriously

2. System Model

We consider the uplink NOMA-assisted MEC communication framework as shown in Figure 1, in which the tasks are offloaded by M legitimate users to a single MEC server in the presence of an Eve, assuming that all devices are equipped with a single antenna and work in a half-duplex mode. Each link in the system experiences Rayleigh fading and will be bothered by additive white Gaussian noise (AWGN). Then n -th user and m -th user are selected from M users to offload tasks, where Eve wiretaps the communication between the users and MEC server. $\hat{h}_i \sim \mathcal{CN}(0, \hat{\Omega}_i)$ denotes the channel parameters of links between the user and MEC server, and $\hat{h}_{Eve,i} \sim \mathcal{CN}(0, \hat{\Omega}_{Eve,i})$ represents the channel parameters of links between the user and Eve, $i \in \{1, 2, \dots, M\}$, $\hat{\Omega}_i = \hat{\Omega}_{Eve,i} = 1$.

Due to the existence of channel estimation errors, it is hard to achieve perfect CSI in actual scenarios. In order to evaluate the impact of Eve under ipCSI on the NOMA-MEC system, the channel factor of the i -th user and MEC server is modeled as $\hat{h}_i = h_i + \omega e_i$, and the channel parameter of the i -th user and Eve is modeled as $\hat{h}_{Eve,i} = h_{Eve,i} + \omega e_{Eve,i}$, where $\omega \in (0, 1)$, h_i , and $h_{Eve,i}$ represent the channel gain under pCSI. $\omega = 0$ represents that the system is able to acquire the pCSI, and $\omega = 1$ represents that the system cannot acquire the pCSI and will sustain from the channel estimation error $e_i \sim \mathcal{CN}(0, \sigma_{e_i}^2)$ and $e_{Eve,i} \sim \mathcal{CN}(0, \sigma_{e_{Eve,i}}^2)$.

In this paper, the n -th and m -th users are paired to perform a nonorthogonal transmission scheme and offload their missions to the MEC server simultaneously. Moreover, the n -th/ m -th user is regarded as a nearby/remote user, which is close/far to the MEC server and Eve. Therefore, the channel gains between users and the MEC server can be classified as $|h_{\wedge m}|^2 \leq |h_{\wedge n}|^2$, and the channel gains between users and the Eve can be classified as $|h_{\wedge Eve,m}|^2 \leq |h_{\wedge Eve,n}|^2$ [30]. According to the principle of NOMA, the received signals at the MEC server and the Eve are given by

$$y_{MEC} = (h_m + \omega e_m) \sqrt{P_m} x_m + (h_n + \omega e_n) \sqrt{P_n} x_n + n_{MEC}, \quad (1)$$

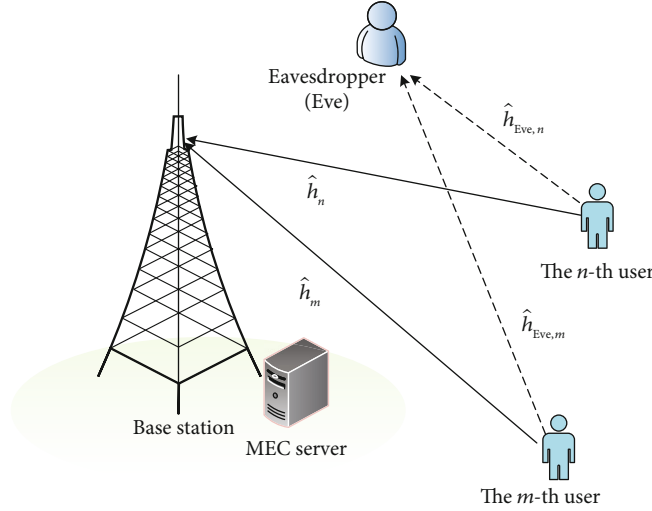


FIGURE 1: System model of uplink NOMA-assisted MEC communications.

$$y_{\text{Eve}} = (h_{\text{Eve},m} + \omega e_{\text{Eve},m})\sqrt{P_m}x_m + (h_{\text{Eve},n} + \omega e_{\text{Eve},n})\sqrt{P_n}x_n + n_{\text{Eve}}, \quad (2)$$

respectively, where x_j represents the j -th user's signal of offloading task, $j \in (m, n)$. $n_{\text{MEC}} \sim \mathcal{CN}(0, \sigma_{\text{MEC}}^2)$ and $n_{\text{Eve}} \sim \mathcal{CN}(0, \sigma_{\text{Eve}}^2)$ represent the AWGN at the MEC server and Eve, respectively. The transmission power of the j -th user is represented as P_j , $P_j = a_j P$, while P is the total transmission power of the paired users. In order to ensure reasonable fairness among users, we assume that $a_m > a_n$, $a_m + a_n = 1$. Hence, the signal-to-interference-plus-noise ratios (SINRs) for the MEC server to decode the information of two users are derived as

$$\gamma_n = \frac{a_n \rho |h_n|^2}{\omega \theta_n + 1}, \quad (3)$$

$$\gamma_m = \frac{a_m \rho |h_m|^2}{a_n \rho |h_n|^2 + \omega(\theta_n + \theta_m) + 1}, \quad (4)$$

respectively.

The SINR expressions of n -th and m -th tapped by Eve are given by

$$\gamma_{\text{Eve},n} = \frac{a_n \rho_{\text{Eve}} |h_{\text{Eve},n}|^2}{\omega \theta_{\text{Eve},n} + 1}, \quad (5)$$

$$\gamma_{\text{Eve},m} = \frac{a_m \rho_{\text{Eve}} |h_{\text{Eve},m}|^2}{a_n \rho_{\text{Eve}} |h_{\text{Eve},n}|^2 + \omega(\theta_{\text{Eve},n} + \theta_{\text{Eve},m}) + 1}, \quad (6)$$

respectively, where $\rho \triangleq P/\sigma_{\text{MEC}}^2$ and $\rho_{\text{Eve}} \triangleq P/\sigma_{\text{Eve}}^2$ represent the transmit SNR of the MEC server and Eve, $\theta_i = \sigma_{e_i}^2 a_i \rho$, $\theta_{\text{Eve},i} = \sigma_{e_{\text{Eve},i}}^2 a_i \rho_{\text{Eve}}$, $i \in \{m, n\}$.

3. Performance Analysis

In this section, the secrecy outage behaviors with an Eve under ipCSI and pCSI in the uplink NOMA-MEC system are analyzed. The new exact expressions of SOP and the asymptotic SOP are derived in the high SNR region. In addition, we acquire the diversity orders and evaluate throughput as well as energy efficiency to further explore the security in NOMA-MEC.

3.1. Secrecy Outage Probability. The secrecy outage means that users cannot complete the offloading tasks within a certain time slot in the presence of the Eve. As a consequence, the secrecy outage performance for the users under the two conditions of ipCSI and pCSI with Eve is analyzed in detail.

Considering that the n -th user and the m -th user offload tasks to the MEC server at the same time, the secret rate of the two users can be defined as

$$C_n = [\log_2(1 + \gamma_n) - \log_2(1 + \gamma_{\text{Eve},n})]^+, \quad (7)$$

$$C_m = [\log_2(1 + \gamma_m) - \log_2(1 + \gamma_{\text{Eve},m})]^+, \quad (8)$$

respectively, where $(x)^+ = \max\{0, x\}$.

Assuming that the target secrecy rate of the n -th user is V_n , when its actual secrecy rate C_n is less than V_n , the n -th user has an outage behavior. Thus, the SOP of the n -th user with the ipCSI condition is expressed as

$$P_n = \Pr(C_n < V_n) = \int_0^\infty f_{\gamma_{\text{Eve},n}}(x) F_{\gamma_n}(2^{V_n}(1+x) - 1) dx. \quad (9)$$

Theorem 1. Under the condition of ipCSI, the exact SOP expression of the n -th user in the NOMA-MEC system with

Eve can be given by

$$P_{ipCSI}^n = \frac{M!}{(M-n)!(n-1)!} (\theta_{Eve,n} + 1) \sum_{i=0}^{M-n} \sum_{r=0}^{n+i} \binom{M-n}{i} \binom{n+i}{r} \frac{(-1)^{i+r}}{n+i} \\ \times e^{-((2^{V_n-1})(\omega\theta_n+1)r/a_n\rho\Omega_n)} \frac{\rho\Omega_n}{(\theta_{Eve,n} + 1)\rho\Omega_n + 2^{V_n}(\theta_n + 1)r\rho_{Eve}\Omega_{Eve,n}}, \quad (10)$$

where $\omega = 1$.

Proof. The SINR of the n -th user in the process of offloading to the MEC server γ_n and the SINR wiretapped by Eve $\gamma_{Eve,n}$ can be obtained in (3) and (5), respectively. According to order statistics, the CDF of the n -th user's sorted channel gain and the PDF of the n -th user's unsorted channel gain are given by

$$F_{\gamma_n}(x) = \frac{M!}{(M-n)!(n-1)!} \sum_{i=0}^{M-n} \sum_{r=0}^{n+i} \binom{M-n}{i} \binom{n+i}{r} \frac{(-1)^{i+r}}{n+i} e^{-r(\omega\theta_n+1)x}, \quad (11)$$

$$f_{\gamma_{Eve,n}}(x) = \frac{\omega\theta_{Eve,n} + 1}{a_n\rho_{Eve}\Omega_{Eve,n}} e^{-((\omega\theta_{Eve,n}+1)x/a_n\rho_{Eve}\Omega_{Eve,n})}, \quad (12)$$

respectively. Substituting (11) and (12) into (9) and doing

some arithmetic operations, we can get (10), which completes the proof. \square

Corollary 2. Upon substituting $\omega = 0$ into (10), the exact SOP expression of the n -th user under the circumstance of pCSI with Eve is shown as

$$P_{pCSI}^n = \frac{M!}{(M-n)!(n-1)!} \sum_{i=0}^{M-n} \sum_{r=0}^{n+i} \binom{M-n}{i} \\ \cdot \binom{n+i}{r} \frac{(-1)^{i+r}}{n+i} e^{-((2^{V_n-1})r/a_n\rho\Omega_n)} \frac{\rho\Omega_n}{\rho\Omega_n + 2^{V_n}r\rho_{Eve}\Omega_{Eve,n}}. \quad (13)$$

According to the SIC principle, the MEC server first decodes the task x_m by regarding the task x_n as an interference. By this time, a secrecy outage event occurs when the actual secrecy rate C_m is lower than the target secrecy rate $V_m = \log(1 + \gamma_m)$. Therefore, the SOP under ipCSI with Eve can be given by

$$P_m = \Pr(C_m < V_m) = \int_0^\infty f_{\gamma_{Eve,m}}(y) F_{\gamma_m}(2^{V_m}(1+y) - 1) dy. \quad (14)$$

Theorem 3. Under the condition of ipCSI, the exact SOP expression of the m -th user with Eve is shown as

$$P_{ipCSI}^m = \frac{M!}{(M-m)!(m-1)!} \frac{M!}{(M-n)!(n-1)!} \sum_{i=0}^{M-m} \sum_{s=0}^{m+i} \sum_{r=0}^{M-n} \sum_{k=0}^{n+r-1} \binom{M-m}{i} \binom{m+i}{s} \binom{M-n}{r} \\ \times \binom{n+r-1}{k} \frac{(-1)^{i+s+r+k}}{m+i} \int_0^\infty \left(\frac{\omega(\theta_{Eve,n} + \theta_{Eve,m}) + 1}{\rho_{Eve}(a_m\Omega_{Eve,m} + \Omega_{Eve,n}\gamma a_n)} + \frac{a_n a_m \Omega_{Eve,m} \Omega_{Eve,n}}{(a_m\Omega_{Eve,m} + \Omega_{Eve,n}\gamma a_n)^2} \right) \\ \times e^{-y(\omega(\theta_{Eve,n} + \theta_{Eve,m}) + 1)/a_m\rho_{Eve}\Omega_{Eve,m}} e^{-s(2^{V_m}(1+y)-1)[\omega(\theta_n + \theta_m) + 1]/a_n\rho\Omega_m} \frac{a_m\Omega_m}{(1+k)a_m\Omega_m + s(2^{V_m}(1+y)-1)a_n\Omega_n} dy, \quad (15)$$

where $\omega = 1$.

Proof. See the appendix. \square

Corollary 4. Upon substituting $\omega = 0$ into (15), the exact SOP expression of the m -th user under the pCSI condition with Eve can be given by

$$P_{pCSI}^m = \frac{M!}{(M-m)!(m-1)!} \frac{M!}{(M-n)!(n-1)!} \sum_{i=0}^{M-m} \sum_{s=0}^{m+i} \sum_{r=0}^{M-n} \sum_{k=0}^{n+r-1} \binom{M-m}{i} \binom{m+i}{s} \binom{M-n}{r} \\ \times \binom{n+r-1}{k} \frac{(-1)^{i+s+r+k}}{m+i} \int_0^\infty \left(\frac{1}{\rho_{Eve}(a_m\Omega_{Eve,m} + \Omega_{Eve,n}\gamma a_n)} + \frac{a_n a_m \Omega_{Eve,m} \Omega_{Eve,n}}{(a_m\Omega_{Eve,m} + \Omega_{Eve,n}\gamma a_n)^2} \right) \\ \times e^{-y/a_m\rho_{Eve}\Omega_{Eve,m}} e^{-s(2^{V_m}(1+y)-1)/a_n\rho\Omega_m} \frac{a_m\Omega_m}{(1+k)a_m\Omega_m + s(2^{V_m}(1+y)-1)a_n\Omega_n} dy. \quad (16)$$

3.2. Diversity Order. In this subsection, we acquire the diversity orders of users under the two CSI conditions with Eve, which is defined as follows:

$$\mu = - \lim_{\rho \rightarrow \infty} \frac{\log [P^{\infty}(\rho)]}{\log \rho}, \quad (17)$$

where $P^{\infty}(\rho)$ denotes the SOP at high SNRs.

Corollary 5. *The asymptotic SOP of the n -th user at high SNR region under ipCSI condition with Eve is given as follows:*

$$P_{ipCSI}^{n,\infty} = \frac{M!}{(M-n)!(n-1)!} (\theta_{Eve,n} + 1) \sum_{i=0}^{M-n} \sum_{r=0}^{n+i} \binom{M-n}{i} \binom{n+i}{r} \frac{(-1)^{i+r}}{n+i} \times \left(1 - \frac{(2^{V_n} - 1)(\theta_n + 1)r}{a_n \rho \Omega_n} \right) \frac{\rho \Omega_n}{(\theta_{Eve,n} + 1) \rho \Omega_n + 2^{V_n} (\theta_n + 1) r \rho_{Eve} \Omega_{Eve,n}}. \quad (18)$$

Remark 6. Substituting (18) into (17), the diversity order for the n -th user under ipCSI condition with Eve $\mu_{n,ipCSI} = 0$ is acquired.

Corollary 7. *Substituting $\rho \rightarrow \infty$ into (13), asymptotic SOP of the n -th user at a high SNR region under the pCSI condition with Eve is shown as*

$$P_{pCSI}^{n,\infty} = \frac{M!}{(M-n)!(n-1)!} \sum_{i=0}^{M-n} \sum_{r=0}^{n+i} \binom{M-n}{i} \binom{n+i}{r} \frac{(-1)^{i+r}}{n+i} \cdot \left(1 - \frac{(2^{V_n} - 1)r}{a_n \rho \Omega_n} \right) \frac{\rho \Omega_n}{\rho \Omega_n + 2^{V_n} r \rho_{Eve} \Omega_{Eve,n}}. \quad (19)$$

Remark 8. Substituting (19) into (17), the diversity order for the n -th user under the pCSI condition with Eve $\mu_{n,pCSI} = n$ is obtained.

3.3. Throughput Analysis. In this subsection, we discuss the system throughput in the delay-limited transmission mode of the system.

Under the condition of ipCSI, we also derive the throughput for the users with Eve, which is given by

$$R_{ipCSI} = \left(1 - P_{ipCSI}^n \right) V_n + \left(1 - P_{ipCSI}^m \right) V_m, \quad (20)$$

where P_{ipCSI}^n and P_{ipCSI}^m have been obtained in (10) and (15), respectively.

Under the condition of pCSI, we may derive the throughput for the users with Eve, which is given by

$$R_{pCSI} = \left(1 - P_{pCSI}^n \right) V_n + \left(1 - P_{pCSI}^m \right) V_m, \quad (21)$$

where P_{pCSI}^n and P_{pCSI}^m have been obtained in (13) and (16), respectively.

3.4. Energy Efficiency. Given the previous analysis of system throughput, we focus on the energy efficiency in NOMA-MEC in this subsection. Energy efficiency had been defined in [31].

In view of the results obtained above, the system energy efficiencies under the ipCSI and pCSI conditions with Eve are shown as

$$\eta_{ipCSI} = \frac{R_{ipCSI}}{TP}, \quad (22)$$

$$\eta_{pCSI} = \frac{R_{pCSI}}{TP}, \quad (23)$$

respectively, where T denotes the time of the whole transmission process and η_{ipCSI} and η_{pCSI} are the energy efficiency of the system under the ipCSI and pCSI conditions, respectively.

4. Results and Discussion

In this section, the simulation results verify the rationality of the theoretical expressions deduced above. The secrecy performance under the ipCSI and pCSI conditions with Eve is further evaluated seriously. We assume that the path loss factor is $\alpha = 2$ and the power allocation parameters are $a_n = 0.2$ and $a_m = 0.8$. The target secrecy rates of the users are $V_n = 2$ bits/s and $V_m = 0.05$ bits/s.

Figure 2 indicates the relationship between SOP for the two users and the transmit SNR. The channel estimation errors are set to $\sigma_{e_n}^2 = -10$ dB, $\sigma_{e_m}^2 = -10$ dB, $\sigma_{e_{Eve,n}}^2 = 0$ dB, and $\sigma_{e_{Eve,m}}^2 = -20$ dB. According to (10) and (13) and (15) and (16), the exact theoretical SOP curves of the paired users under the ipCSI and pCSI conditions with Eve are drawn, respectively. Error floors of SOP exist under the ipCSI for the NOMA-MEC system. The reason lies in the existence of interference of channel estimation errors in communication transmission. One can also observe that the error floor exists in a remote user under pCSI since the MEC server will suffer from interference of the near user while detecting the remote user's message.

As indicated in Figure 3, we study the system throughput versus SNR under ipCSI and pCSI conditions in the delay-limited transmission case with Eve. The channel estimation errors are set to $\sigma_{e_n}^2 = -10$ dB and $\sigma_{e_m}^2 = -10$ dB. The solid curves represent the throughput in the NOMA-MEC system under ipCSI and pCSI with Eve. The dashed curves stand for the throughput in the OMA-MEC under ipCSI and pCSI with Eve. It can be observed that the throughput of NOMA-MEC under pCSI is higher than that under ipCSI. This is because the user's SOP under the pCSI condition is lower than that of the ipCSI condition, which proves that channel estimation errors and the Eve will indeed affect system performance.

Figure 4 depicts the system energy efficiency versus the SNR for the paired users under ipCSI and pCSI conditions in the delay-limited transmission case with Eve. The solid curves indicate the energy efficiency for the NOMA-MEC

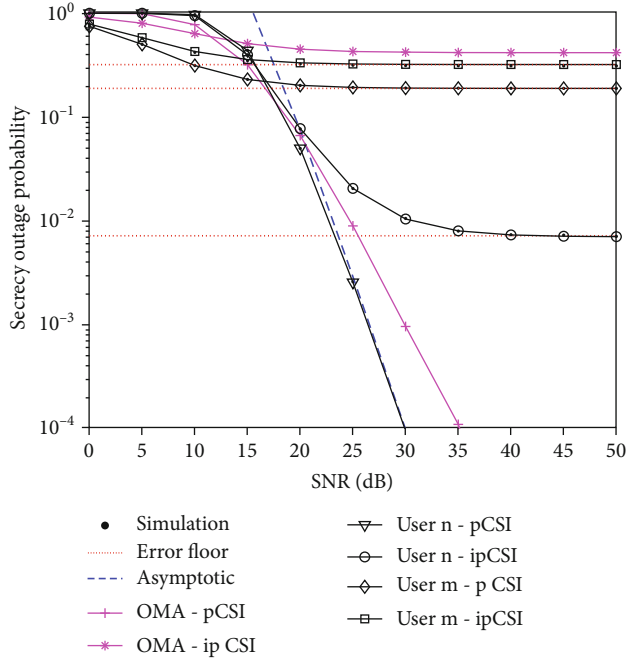


FIGURE 2: SOP for paired users versus SNR.

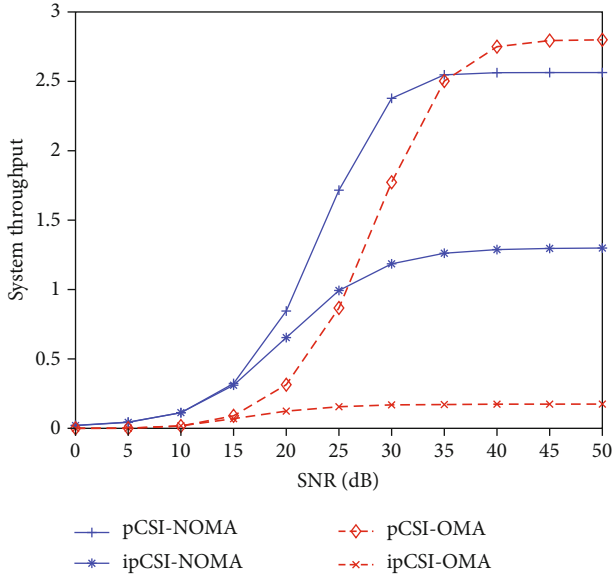


FIGURE 3: System throughput versus SNR in delay-limited transmission mode.

system. At high SNRs, under the same conditions, NOMA-MEC obtains higher energy efficiency than OMA-MEC. Meanwhile, the energy efficiency with channel estimation error is superior to that without channel estimation error since the pCSI condition is capable of achieving much greater throughput than ipCSI condition.

In Figure 5, the SOP for the paired users with channel estimation errors from $\sigma_{e_n}^2 = \sigma_{e_m}^2 = -10$ dB to $\sigma_{e_n}^2 = \sigma_{e_m}^2 = 0$ dB is illustrated. We can observe that the quality of communication condition is improved as SNR increases. Moreover, the n -th user is closer to MEC server than the m -th user, so

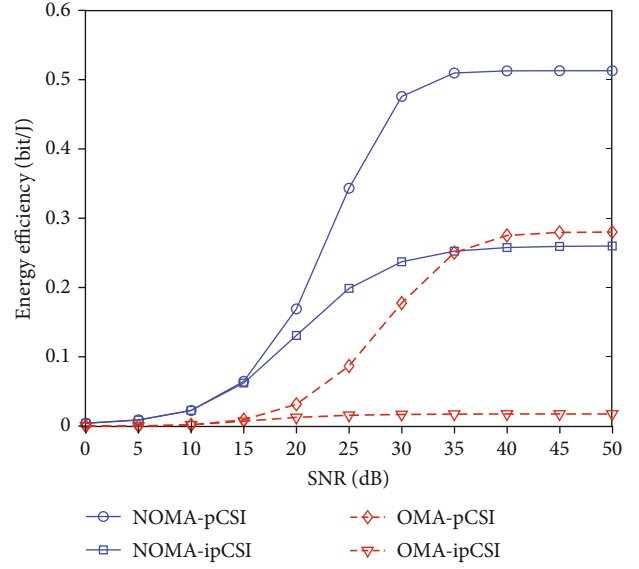
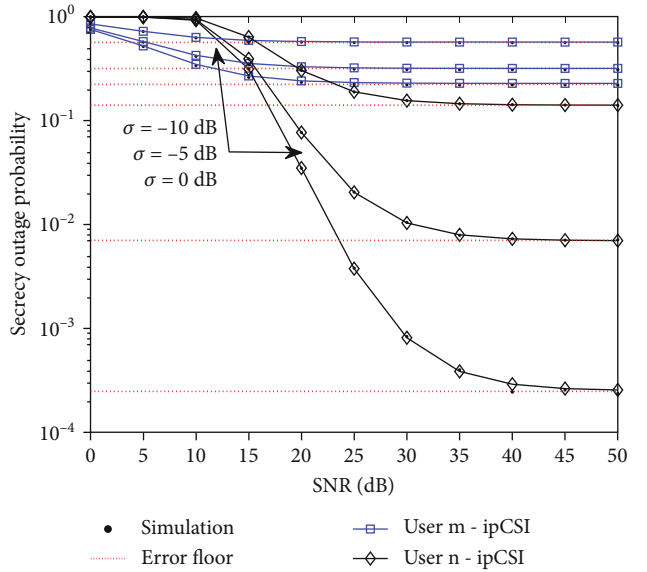

 FIGURE 4: System energy efficiency versus SNR in delay-limited transmission mode, $P = 5$ W, and $T = 1$ s.


FIGURE 5: SOP versus SNR with different values of channel estimation errors.

the improvement in SOP performance of the n -th user is much more obvious. One can also observe that the SOP rises with the increase of the channel estimation error values, and the influence on the nearby user is more obvious than the remote user on account of the interference from the nearby user, the Eve, and the channel estimation error. Meanwhile, the nearby user is only disturbed by the Eve and the channel estimation error.

Figure 6 plots the SOP for the n -th user and m -th user versus various values of target secrecy rate. When $V_m = 0.05$ bits/s, $V_n = 2$ bits/s, $V_m = 0.3$ bits/s, $V_n = 3$ bits/s, $V_m = 0.7$ bits/s, and $V_n = 4$ bits/s, it is observed that with the simultaneous increase of target secrecy rate for both users, SOP rises

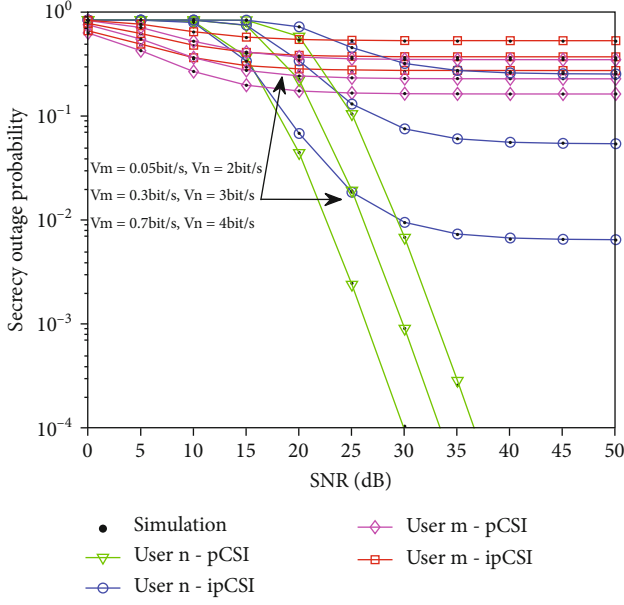


FIGURE 6: SOP versus SNR with various values of target secrecy rate.

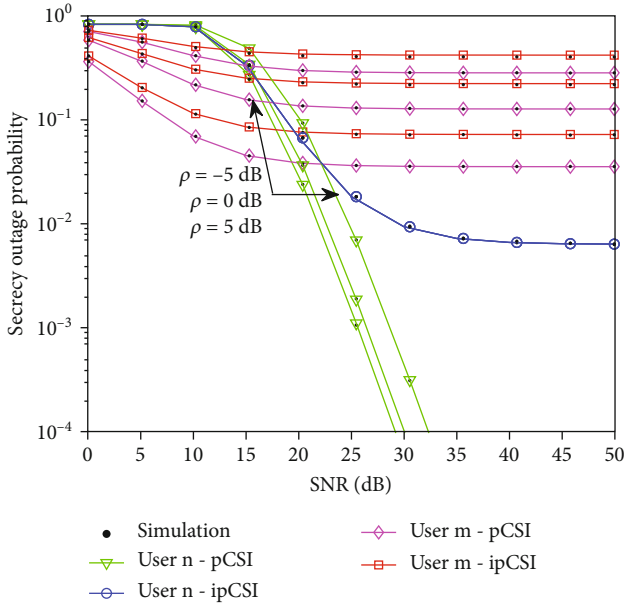


FIGURE 7: SOP versus SNR with different SNR values of the Eve.

as well. As a result, the influence of the target secrecy rate of users must be taken into consideration in the practical system.

Figure 7 indicates the SOP versus different SNR values of the Eve. $\rho_{Eve} = -5$ dB, $\rho_{Eve} = 0$ dB, and $\rho_{Eve} = 5$ dB. It can be seen that when the SNR values of the Eve rises, the SOP also gradually increases. That is because when the SNR of the Eve increases, it will strengthen the interference to users, which will lead to the degradation of users' secrecy performance.

5. Conclusions

We have studied the secrecy performance of uplink NOMA-MEC under ipCSI and pCSI conditions with an Eve. New exact and approximate expressions of SOP are derived for NOMA-MEC systems. The analysis results have revealed that the SOP of NOMA-MEC with pCSI performs better than that of OMA-MEC. Due to the influence of channel estimation errors, the secrecy behaviors of NOMA-MEC with ipCSI are inferior to that of pCSI. As the increase of channel estimation errors, the SOP of NOMA-MEC is getting worse. Moreover, the throughput and energy efficiency in the system have been studied under ipCSI and pCSI conditions with the Eve.

Appendix

A.1. Proof of Theorem 3

The SINR of the m -th user in the process of offloading to the MEC server γ_m and the SINR wiretapped by Eve $\gamma_{Eve,m}$ can be obtained in (4) and (6), respectively. The CDF of the m -th user's unsorted channel gain is given by

$$\begin{aligned}
 F_{\gamma_{Eve,m}}(y) &= \Pr(\gamma_{Eve,m} < y) \\
 &= \Pr\left(\frac{a_m \rho_{Eve} |h_{Eve,m}|^2}{a_n \rho_{Eve} |h_{Eve,n}|^2 + \omega(\theta_{Eve,n} + \theta_{Eve,m}) + 1} < y\right) \\
 &= \Pr\left(|h_{Eve,m}|^2 < \frac{y(a_n \rho_{Eve} |h_{Eve,n}|^2 + \omega(\theta_{Eve,n} + \theta_{Eve,m}) + 1)}{a_m \rho_{Eve}}\right).
 \end{aligned} \tag{A.1}$$

With some simple operations, the above expression can be rewritten as

$$F_{\gamma_{Eve,m}}(y) = 1 - e^{-(y(\omega(\theta_{Eve,n} + \theta_{Eve,m}) + 1)/a_m \rho_{Eve} \Omega_{Eve,m})} \frac{a_m \Omega_{Eve,m}}{a_m \Omega_{Eve,m} + \Omega_{Eve,n} y a_n}. \tag{A.2}$$

Taking the derivative of (A.2), the PDF expression $f_{\gamma_{Eve,m}}$ can be obtained:

$$f_{\gamma_{Eve,m}}(y) = \left(\frac{\omega(\theta_{Eve,n} + \theta_{Eve,m}) + 1}{\rho_{Eve}(a_m \Omega_{Eve,m} + \Omega_{Eve,n} y a_n)} + \frac{a_n a_m \Omega_{Eve,m} \Omega_{Eve,n}}{(a_m \Omega_{Eve,m} + \Omega_{Eve,n} y a_n)^2} \right) e^{-(y(\omega(\theta_{Eve,n} + \theta_{Eve,m}) + 1)/a_m \rho_{Eve} \Omega_{Eve,m})}. \tag{A.3}$$

The CDF of sorted F_{γ_m} is expressed as

$$\begin{aligned} F_{\gamma_m}(y) &= \Pr(\gamma_m < y) = \Pr\left(\frac{a_m \rho |h_m|^2}{a_n \rho |h_n|^2 + \bar{\omega}(\theta_n + \theta_m) + 1} < y\right) \\ &= \Pr\left(|h_m|^2 < \frac{y(a_n \rho |h_n|^2 + \bar{\omega}(\theta_n + \theta_m) + 1)}{a_m \rho}\right). \end{aligned} \quad (\text{A.4})$$

Similarly, the sorted CDF expression F_{γ_m} of the m -th user can be expressed as

$$\begin{aligned} F_{\gamma_m}(y) &= \frac{M!}{(M-m)!(m-1)!} \frac{M!}{(n-1)!(M-n)!} \sum_{i=0}^{M-m} \sum_{s=0}^{m+i} \sum_{r=0}^{M-n} \sum_{k=0}^{n+r-1} \\ &\cdot \binom{M-m}{i} \binom{m+i}{s} \times \binom{M-n}{r} \\ &\cdot \binom{n+r-1}{k} \frac{(-1)^{i+s+r+k}}{m+i} e^{-(sy(\bar{\omega}(\theta_n + \theta_m) + 1)/a_m \rho \Omega_m)} \frac{a_m \Omega_m}{(1+k)a_m \Omega_m + sy a_n \Omega_n}. \end{aligned} \quad (\text{A.5})$$

Substituting (A.3) and (A.5) into (14), (15) can be attained easily.

Data Availability

The data used to support the findings of this study are available from the corresponding author upon request.

Conflicts of Interest

The authors declare that they have no conflicts of interest.

Acknowledgments

This work was supported in part by the Natural Science Foundation of Beijing Municipality under Grants 4204099, L182039, and KZ201911232046; in part by the Science and Technology Project of the Beijing Municipal Education Commission under Grant KM202011232003; and in part by the Supplementary and Supportive Project for Teachers at Beijing Information Science and Technology University (2019-2021) under Grant 5111911147.

References

- [1] L. Zhu, J. Zhang, Z. Xiao, X. Cao, and D. O. Wu, "Optimal user pairing for downlink non-orthogonal multiple access (NOMA)," *IEEE Wireless Communications Letters*, vol. 8, no. 2, pp. 328–331, 2019.
- [2] J. Wang, B. Xia, K. Xiao, and Z. Chen, "Performance analysis and power allocation strategy for downlink NOMA systems in large-scale cellular networks," *IEEE Transactions on Vehicular Technology*, vol. 69, no. 3, pp. 3459–3464, 2020.
- [3] P. Sindhu, K. S. Deepak, and K. M. Abdul Hameed, "A novel low complexity power allocation algorithm for downlink NOMA networks," in *2018 IEEE Recent Advances in Intelligent Computational Systems (RAICS)*, Thiruvananthapuram, India, 2018.
- [4] J. Kang and I. Kim, "Optimal user grouping for downlink NOMA," *IEEE Wireless Communications Letters*, vol. 7, no. 5, pp. 724–727, 2018.
- [5] T. Hou, Y. Liu, Z. Song, X. Sun, and Y. Chen, "Multiple antenna aided NOMA in UAV networks: a stochastic geometry approach," *IEEE Transactions on Communications*, vol. 67, no. 2, pp. 1031–1044, 2019.
- [6] Z. Ming, W. Hao, O. A. Dobre, Z. Ding, and H. V. Poor, "Power minimization for multi-cell uplink NOMA with imperfect SIC," *IEEE Wireless Communications Letters*, vol. 9, no. 12, pp. 2030–2034, 2020.
- [7] X. Liu, H. Ding, and S. Hu, "Uplink resource allocation for NOMA-based hybrid spectrum access in 6G-enabled cognitive internet of things," *IEEE Internet of Things Journal*, vol. 8, no. 20, pp. 15049–15058, 2021.
- [8] P. Li, Z. Ding, and K. Feng, "Enhanced receiver based on FEC code constraints for uplink NOMA with imperfect CSI," *IEEE Transactions on Wireless Communications*, vol. 18, no. 10, pp. 4790–4802, 2019.
- [9] S. Schiessl, M. Skoglund, and J. Gross, "NOMA in the uplink: delay analysis with imperfect CSI and finite-length coding," *IEEE Transactions on Wireless Communications*, vol. 19, no. 6, pp. 3879–3893, 2020.
- [10] X. Li, J. Li, Y. Liu, Z. Ding, and A. Nallanathan, "Residual transceiver hardware impairments on cooperative NOMA networks," *IEEE Transactions on Wireless Communications*, vol. 19, no. 1, pp. 680–695, 2020.
- [11] X. Li, Q. Wang, M. Liu et al., "Cooperative wireless-powered NOMA relaying for B5G IoT networks with hardware impairments and channel estimation errors," *IEEE Internet of Things Journal*, vol. 8, no. 7, pp. 5453–5467, 2021.
- [12] Z. Ning, P. Dong, X. Kong, and F. Xia, "A cooperative partial computation offloading scheme for mobile edge computing enabled internet of things," *IEEE Internet of Things Journal*, vol. 6, no. 3, pp. 4804–4814, 2019.
- [13] C. Liu, M. Bennis, M. Debbah, and H. V. Poor, "Dynamic task offloading and resource allocation for ultra-reliable low-latency edge computing," *IEEE Transactions on Communications*, vol. 67, no. 6, pp. 4132–4150, 2019.
- [14] Z. Ding, P. Fan, and H. V. Poor, "Impact of non-orthogonal multiple access on the offloading of mobile edge computing," *IEEE Transactions on Communications*, vol. 67, no. 1, pp. 375–390, 2019.
- [15] Z. Ding, J. Xu, O. A. Dobre, and H. V. Poor, "Joint power and time allocation for NOMA-MEC offloading," *IEEE Transactions on Vehicular Technology*, vol. 68, no. 6, pp. 6207–6211, 2019.
- [16] N. Nouri, A. Entezari, J. Abouei, M. Jaseemuddin, and A. Anpalagan, "Dynamic power-latency tradeoff for mobile edge computation offloading in NOMA-based networks," *IEEE Internet of Things Journal*, vol. 7, no. 4, pp. 2763–2776, 2020.
- [17] X. Duan, B. Li, and W. Zhao, "Energy consumption minimization for near-far server cooperation in NOMA-assisted mobile edge computing system," *IEEE Access*, vol. 8, pp. 133269–133282, 2020.
- [18] G. Zheng, C. Xu, and L. Tang, "Joint user association and resource allocation for NOMA-based MEC: a matching-coalition approach," in *2020 IEEE Wireless Communications and Networking Conference (WCNC)*, Seoul, Korea (South), 2020.

- [19] F. Fang, Y. Xu, Z. Ding, C. Shen, M. Peng, and G. K. Karagiannis, "Optimal resource allocation for delay minimization in NOMA-MEC networks," *IEEE Transactions on Communications*, vol. 68, no. 12, pp. 7867–7881, 2020.
- [20] L. Lei, Z. Chang, Y. Hu, T. Ristaniemi, Y. Yuan, and S. Chatzinotas, "Energy-efficient resource optimization with wireless power transfer for secure NOMA systems," in *2018 IEEE/CIC International Conference on Communications in China (ICCC)*, Beijing, China, 2018.
- [21] Q. Li and D. Xu, "Secure communication with a wireless powered full-duplex eavesdropper," in *2019 IEEE 19th International Conference on Communication Technology (ICCT)*, Xi'an, China, 2019.
- [22] W. Wu, F. Zhou, R. Q. Hu, and B. Wang, "Energy-efficient resource allocation for secure NOMA-enabled mobile edge computing networks," *IEEE Transactions on Communications*, vol. 68, no. 1, pp. 493–505, 2020.
- [23] W. Wu, X. Wang, F. Zhou, K. Wong, C. Li, and B. Wang, "Resource allocation for enhancing offloading security in NOMA-enabled MEC networks," *IEEE Systems Journal (Early Access)*, vol. 15, pp. 1–4, 2020.
- [24] X. Wang, W. Wu, B. Lyu, and H. Wang, "Delay minimization for secure NOMA mobile-edge computing," in *2019 IEEE 19th International Conference on Communication Technology (ICCT)*, Xi'an, China, 2019.
- [25] Y. Liu, Z. Qin, M. ElKashlan, Y. Gao, and L. Hanzo, "Enhancing the physical layer security of non-orthogonal multiple access in large-scale networks," *IEEE Transactions on Wireless Communications*, vol. 16, no. 3, pp. 1656–1672, 2017.
- [26] X. Yue, Y. Liu, Y. Yao, X. Li, R. Liu, and A. Nallanathan, "Secure communications in a unified non-orthogonal multiple access framework," *IEEE Transactions on Wireless Communications*, vol. 19, no. 3, pp. 2163–2178, 2020.
- [27] X. Li, M. Zhao, M. Zeng et al., "Hardware impaired ambient backscatter NOMA systems: reliability and security," *IEEE Transactions on Communications*, vol. 69, no. 4, pp. 2723–2736, 2021.
- [28] W. Wu, F. Zhou, P. Li, P. Deng, B. Wang, and V. C. M. Leung, "Energy-efficient secure NOMA-enabled mobile edge computing networks," in *ICC 2019-2019 IEEE International Conference on Communications (ICC)*, Shanghai, China, 2019.
- [29] H. Jiang, Y. Wang, X. Yue, and X. Li, "Performance analysis of NOMA-based mobile edge computing with imperfect CSI," *EURASIP Journal on Wireless Communications and Networking*, vol. 2020, no. 1, 2020.
- [30] H. A. David and H. N. Nagaraja, *Order Statistics*, Wiley, New York, NY, USA, 3rd edition, 2003.
- [31] X. Yue, Y. Liu, S. Kang, A. Nallanathan, and Z. Ding, "Exploiting full/half-duplex user relaying in NOMA systems," *IEEE Transactions on Communications*, vol. 66, no. 2, pp. 560–575, 2018.

Research Article

Beam Selection Assisted UAV-BS Deployment and Trajectory for Beamspace mmWave Systems

Xingxuan Zuo,¹ Jiankang Zhang², Sheng Chen,³ and Xiaomin Mu¹

¹School of Information Engineering, Zhengzhou University, Zhengzhou 450001, China

²Department of Computing & Informatics, Bournemouth University, BH12 5BB, UK

³School of Electronics and Computer Science, University of Southampton, SO17 1BJ Southampton, UK

Correspondence should be addressed to Jiankang Zhang; jzhang3@bournemouth.ac.uk

Received 8 August 2021; Accepted 7 September 2021; Published 30 September 2021

Academic Editor: Xingwang Li

Copyright © 2021 Xingxuan Zuo et al. This is an open access article distributed under the Creative Commons Attribution License, which permits unrestricted use, distribution, and reproduction in any medium, provided the original work is properly cited.

Exploiting unmanned aerial vehicles (UAVs) as base stations (UAV-BS) can enhance capacity, coverage, and energy efficiency of wireless communication networks. To fully realize this potential, millimeter wave (mmWave) technology can be exploited with UAV-BS to form mmWave UAV-BS. The major difficulty of mmWave UAV-BS, however, lies in the limited energy of UAV-BS and the multiuser interference (MUI). Beam division multiple access with orthogonal beams can be employed to alleviate the MUI. Since each user has dominant beams around the line of sight direction, beam selection can reduce the power consumption of radio frequency chain. In this paper, we formulate the problem of maximizing the sum rate of all users by optimizing the beam selection for beamspace and UAV-BS deployment in the mmWave UAV-BS system. This nonconvex problem is solved in two steps. First, we propose a signal-to-interference plus noise ratio-based greedy beam selection scheme to ensure that all the ground users in the given area can be served by the UAV-BS, where a zero forcing precoding scheme is used to eliminate the MUI. Then, we utilize the continuous genetic algorithm to find the optimal UAV-BS deployment and beam pattern to maximize the sum rate of all users. Moreover, considering the mobility of the UAV-BS, the UAV-BS trajectory and beam selection for beamspace are optimized in the mmWave UAV-BS system. The simulation results demonstrate the effectiveness of the proposed design for the mmWave UAV-BS system.

1. Introduction

Unmanned aerial vehicles (UAVs) have drawn growing attention in a wide range of applications, such as disaster rescue, surveillance and monitoring, aerial imaging, and cargo delivery [1, 2]. Wireless communication utilizing UAVs is a promising technology to achieve fast deployment and flexible reconfiguration [3, 4]. Specifically, UAVs as different types of wireless communication platforms, such as UAV base stations (UAV-BS), aerial relays, and UAV swarms, assist and enhance terrestrial communications [5, 6]. Employing UAV-BS in particular is a cost-effective solution to assist the existing terrestrial communication infrastructure by providing seamless coverage and improving the network performance. Recent researches on UAV-BS can be divided into two main categories.

In the first category, UAVs are considered aerial quasi-stationary BSs. The altitude and horizontal positions of UAVs can be separately or jointly optimized to obtain a better air-ground channel for meeting different requirements of ground users [7–9]. Specifically, in [7], the altitude of the UAV-BS was optimized to achieve the maximum coverage for the terrestrial users. By contrast, with the fixed altitude, the horizontal placement of UAV-BS was jointly optimized with the user association in [8]. Furthermore, the joint optimization of altitude and horizontal positions of UAV-BS was investigated in [9], where the aim of the UAV-BS placement is to maximize the number of covered users with minimum transmit power.

For the second category, UAVs are considered mobile BSs. By exploiting the mobility of UAV-BS, the communication

distance between the UAV-BS and terrestrial users can be significantly shortened via careful design on the trajectory of UAV-BS. In [10], a joint optimization of the UAV-BS trajectory and transmit power for multiple users was developed to dynamically establish short-distance line of sight (LoS) links and thus to improve the throughput of the system. A joint optimization of the UAV-BS trajectory and user scheduling for a UAV-enabled secure system was proposed in [11] to maximize the minimum secrecy rate under the required constraints of UAV-BS and ground users. In [12], a joint optimization of the UAV trajectory and nonorthogonal multiple access (NOMA) precoding was investigated for a UAV-assisted NOMA network, where the UAV trajectory and NOMA precoding are jointly optimized to maximize the sum rate of users served by the UAV-BS and NOMA-network BS.

Early researches mainly focused on the UAV-BS working in microwave frequencies with a single antenna owing to the strict constraint of size. Because the UAV-BS also has limited on-board energy, the signals of a single antenna may be significantly attenuated due to the long communication distance between the UAV-BS and ground users [13]. However, by exploiting the small wavelengths of millimeter wave (mmWave) signals, mmWave frequencies can be adopted to the UAV-BS to pack large antenna arrays in small dimensions [14, 15].

The combination of UAV-BS and mmWave communication technology therefore offers advantages of enhancing coverage, improving energy efficiency, and providing sufficient bandwidth [16]. An UAV-BS mmWave system can naturally establish LoS links between UAV-BS and ground users to support the connectivity of existing ground wireless networks [17]. Because of limited scattering of air-to-ground links in the mmWave band, the path loss is dominant by LoS. The authors of [18] developed a 3D beamforming approach to achieve efficient and flexible coverage in mmWave UAV-BS communications. In [19], the impact of adaptive navigation on mmWave UAV-BSs was investigated to enhance the system performance. Furthermore, the mmWave UAV-BS deployment optimization is an important issue to improve the performance. In [20], the optimized mmWave UAV-BS deployment, which includes the optimal height, horizontal coordinates, and coverage radius, was analyzed by taking into account human body blockage. Xiao et al. [21] presented a mmWave UAV-BS deployment optimization with a constant modulus beamforming to maximize the sum rate of all ground users. However, since mmWave UAV-BSs place large antenna arrays in a small area, the power consumption of radio frequency (RF) chains is considerable [22], but UAV-BSs typically have limited energy supply. In addition, to support simultaneous transmissions between the mmWave UAV-BS and ground users, the multi-user interference (MUI) mitigation is necessary.

Since mmWave UAV-BS signals propagate mainly through LoS paths, users from different directions can be simultaneously served by orthogonal beams, which is known as beam division multiple access (BDMA) [16]. By employing orthogonal beams, MUI can be effectively decreased to improve the system performance [23]. In particular, the discrete lens array (DLA), which points signals in different directions, was employed in BDMA to transform the conventional spatial channel into a beamspace

channel [24]. To exploit the sparsity of the beamspace channel, beam selection was investigated in [25] to achieve near-optimal performance with fewer RF chains. In [26], a comparison among different kinds of beam selection schemes was evaluated, in terms of the required number of RF chains as well as the trade-off between spectral efficiency and energy efficiency. Furthermore, the power allocation for BDMA transmission was analyzed in [27] with only statistical channel state information (CSI). In [28], considering the power leakage and the imperfect channel statistics estimation, the RF chains were further reduced after the beamspace transformation in the lens antenna array.

There exist increasing interests in the use of the genetic algorithm (GA) for wireless communication and signal processing [29–31], since GA can attain the global optimal solutions of challenging optimization problems with affordable computational complexity and it does not require derivative information [32]. The work [31] applied several evolutionary algorithms, including continuous GA (CGA), to solve the difficult problem of joint channel estimation and turbo multiuser detection/decoding. Compared with discrete GA [32], CGA has high precision, low storage, and high speed without the requirement of prior decoding. In [33], GA was utilized to find the optimal deployment of drones to cover the target area with the lowest cost. However, the method of [33] is based on the single transmit antenna, which can be improved by taking the multiple transmit antennas and MUI into account.

The comparison of the recent researches in UAV-BS and BDMA is summarized in Table 1. Inspired by the existing research, we focus on the mmWave UAV-BS system, where the mmWave-frequency antenna array and DLA are employed by the UAV-BS to direct signals to different directions and to form the beamspace channel. We propose a beam selection optimization for beamspace and UAV-BS deployment to maximize the sum rate of all ground users. Due to the sparse nature of the beamspace channel in BDMA, the dominant beams are near the LoS directions of the ground users. By properly designing the horizontal positions of the mmWave UAV-BS, not only can the better channel gain be achieved but also the interfering channel distance among the ground users can be enlarged to alleviate the MUI, while imposing lower number of RF chains. However, this design problem is nonconvex and difficult to solve directly. To tackle this challenging optimization problem, we decompose it into two subproblems by first designing the beam selection scheme for beamspace and then finding the optimal positions and beam pattern of the mmWave UAV-BS. For the first subproblem, we propose a signal-to-interference plus noise ratio- (SINR-) based greedy beam selection scheme. When the UAV-BS communicates with its served users, if the served users have different dominant beams, the UAV-BS will naturally select their corresponding dominant beams. However, in the scenario that two or more users have the same dominant beam, the UAV-BS can select the beams to users according to the SINR-based greedy beam selection scheme. Zero forcing (ZF) precoding is used to further eliminate the MUI. Given the SINR-based greedy beam selection, we design a CGA to solve the second subproblem, namely, the optimal deployment of the mmWave UAV-BS system. Similarly, considering the mobility of the mmWave

TABLE 1: Reference comparison of recent researches.

	[7] 2016	[8] 2019	[9] 2017	[10] 2018	[11] 2018	[12] 2019	[18] 2019	[20] 2018	[21] 2020	[25] 2016	[26] 2015	[28] 2018	[33] 2019
UAV-BS	√	√	√	√	√	√	√	√	√				
Deployment	√	√	√						√				
3D deployment			√				√	√					√
Trajectory				√	√	√							
mmWave							√	√	√	√	√		
Beamforming						√	√		√	√	√		
BDMA										√	√	√	
ZF						√				√	√		
Beam selection										√	√	√	
SINR				√		√					√		
Multuser		√	√	√	√	√	√	√	√	√	√	√	√
Multuser interference						√				√	√		
GA													√

UAV-BS, we also optimize the trajectory of the mmWave UAV-BS by the CGA scheme, given the SINR-based greedy beam selection. The main contributions of this paper are recapped below.

- (1) In this paper, we consider a mmWave UAV-BS, which is equipped with the lens antenna array to serve the multiple ground users. Aimed at maximizing the sum rate of all ground users, the optimization problem of beam selection and UAV deployment is complicated to solve, which is decomposed into two subproblems
- (2) First, we propose an SINR-based greedy beam selection scheme for the users which share the same dominant beams, where ZF precoding is employed to further minimize the MUI. Then, the CGA of UAV-BS deployment is designed to optimize the UAV deployment and beam pattern by maximizing the sum rate of ground users
- (3) We also formulate an optimization problem of beam selection and UAV-BS trajectory in the multiuser mmWave system to maximize the sum rate of all ground users with the speed constraint of UAV-BS. Given the suboptimal SINR-based greedy beam selection, the CGA-based mmWave UAV-BS trajectory optimization is proposed

The paper is structured as follows. Section 2 introduces the system model and problem formulation. The optimizations of beam selection in beamspace as well as mmWave UAV-BS deployment and trajectory are addressed in Section 3. The design analysis and achievable performance are provided and discussed in Section 4. Section 5 concludes the paper.

In this paper, \mathbb{R} and \mathbb{C} denote the real and complex number fields, respectively. The boldfaced lowercase and uppercase letters stand for vectors and matrices, respectively. $\|\cdot\|$ denotes the Euclidean norm, while the transpose and Hermitian trans-

pose operators are denoted by $(\cdot)^T$ and $(\cdot)^H$, respectively. The inverse operation is denoted by $(\cdot)^{-1}$, while $\text{tr}(\cdot)$ represents the trace operation. The operator $\mathcal{A} \setminus \mathcal{B}$ denotes the set consisting of all elements in \mathcal{A} excluding those in \mathcal{B} . The integer ceiling operation is denoted by $\lceil \cdot \rceil$, $\mathbf{0}_K$ is the K -dimensional zero vector, and \mathbf{I}_K is the $(K \times K)$ -dimensional identity matrix, while $\mathbf{A}(i, :)_{i \in \mathcal{I}}$ denotes the submatrix consisting of the rows of \mathbf{A} with the row indices given by the index set \mathcal{I} . The cardinality of the set \mathcal{I} is denoted by $|\mathcal{I}|$, and the j th element of \mathcal{I} is denoted as $\mathcal{I}(j)$, while $\mathbf{w}_{(k, \cdot)}$ and $\mathbf{w}_{(\cdot, k)}$ denote the k th row and k th column of \mathbf{W} , respectively.

2. System Model and Problem Formulation

As illustrated in Figure 1, we consider an mmWave downlink multiuser communication system, where a rotary-wing UAV-BS employs N_t transmit antennas and N_{RF} RF chains to simultaneously communicate with K terrestrial users. The different users are served by different beams. Each ground user is equipped with a single antenna, and the horizontal coordinate of the k th ground user is given by $\mathbf{u}_k = [x_k y_k]^T \in \mathbb{R}^{2 \times 1}$, $1 \leq k \leq K$. We assume that the UAV-BS flies at a constant altitude H (m) above the ground and the location of UAV-BS projected on the ground in the 3D rectangular coordinate system is defined by $\mathbf{q} = [q_x q_y]^T \in \mathbb{R}^{2 \times 1}$.

2.1. Channel Model. Owing to the flexibility of the UAV-BS, the LoS can be naturally established in low-altitude platforms [34], and scattering is relatively rare in mmWave frequencies for the air-to-ground links. Thus, we assume that the wireless links between the UAV-BS and the ground users are dominant by the LoS paths [18, 35]. Then, the effective channel model between the UAV-BS and the k th ground user can be expressed as [36]

$$\mathbf{h}_k = \beta_k \mathbf{a}(\theta_k), \quad (1)$$

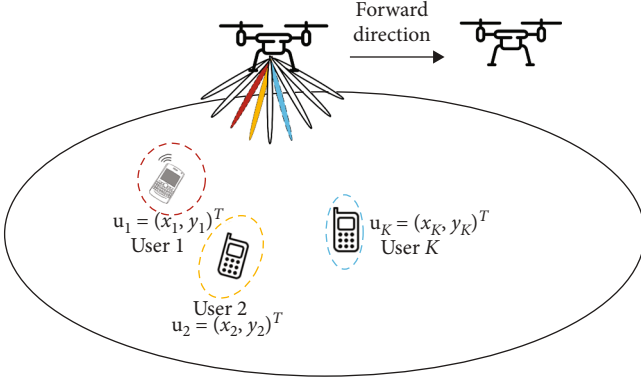


FIGURE 1: A mmWave UAV-BS serving multiple ground users.

where $\mathbf{a}(\theta_k) \in \mathbb{C}^{N_t \times 1}$ is the array steering vector of the k th ground user and β_k is the gain of the LoS path for this ground user. The channel coefficient β_k depends on the path loss at the mmWave frequency and is given by [37, 38]

$$\beta_k = \frac{1}{(4\pi f_{m,m} \times 10^9 / c) \cdot d_k^{\alpha_L}}, \quad (2)$$

where $d_k = \sqrt{H^2 + \|\mathbf{q} - \mathbf{u}_k\|^2}$ is the distance between the UAV-BS and the k th ground user, $c = 3 \times 10^8$ m/s is the speed of light, $f_{m,m}$ is the carrier frequency, and α_L is the parameter of the LoS path loss model. In our investigation, $f_{m,m} = 28$ GHz is allocated and $\alpha_L = 0.95$ is adopted. In addition, the spatial direction θ_k is defined as $\theta_k = \cos(\phi_k)$, where ϕ_k is the real angle of departure of the k th ground user. Hence, the range of θ_k is $[-1, 1]$. A uniform linear array (ULA) is employed in the mmWave UAV-BS, and the array steering vector for the k th ground user is expressed as [26]

$$\mathbf{a}(\theta_k) = \left[e^{-j2\pi \frac{d}{\lambda} \left(\frac{1-N_t}{2}\right) \theta_k} \dots e^{-j2\pi \frac{d}{\lambda} \left(l - \frac{N_t-1}{2}\right) \theta_k} \dots e^{-j2\pi \frac{d}{\lambda} \left(\frac{N_t-1}{2}\right) \theta_k} \right]^T, \quad l = 0, 1, \dots, N_t - 1, \quad (3)$$

where λ is the signal wavelength and $d = \lambda/2$ is the antenna element spacing.

2.1.1. UAV-BS Deployment. For the mmWave UAV-BS deployment, the spatial direction of the k th user θ_k is related to the placement of the UAV-BS, given as the cosine value of the direction vector from the k th ground user to the UAV-BS and the UAV-BS forward direction vector $[100]^T$ [21]. Thus, the spatial direction θ_k is defined as

$$\begin{aligned} \theta_k &= \frac{\left([x_k y_k 0] - [q_x q_y H] \right) \cdot [100]^T}{\left\| [x_k y_k 0]^T - [q_x q_y H]^T \right\| \cdot \left\| [100]^T \right\|} \\ &= \frac{x_k - q_x}{\sqrt{(x_k - q_x)^2 + (y_k - q_y)^2 + H^2}}. \end{aligned} \quad (4)$$

2.1.2. UAV-BS Trajectory. To take into account the mobile nature of the UAV-BS, the UAV-BS trajectory should be considered. Specifically, the fly-hover communication protocol [39] of rotary-wing UAV-BS can be adopted to realize the communication with users. The UAV-BS serves the ground users with a constant mission time T , which can be equally divided into $N + 1$ time slots. For this fly-hover communication protocol, the UAV-BS successively visits the N optimized hovering locations and communicates with the ground users when it is hovering at the optimized locations. Since the UAV-BS flies at a constant altitude H , the horizontal coordinate in the n th time slot is defined as $\mathbf{q}[n] = [q_x[n] q_y[n]]^T$, $n = 0, 1, \dots, N + 1$. In practice, the trajectory of the UAV-BS should satisfy the following constraints:

$$\mathcal{A}_{\text{tra}} = \begin{cases} \mathbf{q}[0] = \mathbf{q}_I, \mathbf{q}[N + 1] = \mathbf{q}_F, \\ \|\mathbf{q}[n + 1] - \mathbf{q}[n]\| \leq v_{\max}, 0 \leq n \leq N, \\ \mathbf{q}[n] \in [q_{x,l}, q_{x,h}] \times [q_{y,l}, q_{y,h}], \forall n, \end{cases} \quad (5)$$

where $\mathbf{q}_I, \mathbf{q}_F \in \mathbb{R}^{2 \times 1}$ denote the initial and final horizontal locations of the UAV-BS, respectively, and v_{\max} is the maximum speed of the UAV-BS, that is, the UAV-BS velocity $v \leq v_{\max}$, while $[q_{x,l}, q_{x,h}] \times [q_{y,l}, q_{y,h}]$ denotes the UAV-BS flying area. The forward direction vector of the UAV-BS is related to the location of the next time slot and is defined as $\mathbf{q}_f[n] = [(q_x[n + 1] - q_x[n]) (q_y[n + 1] - q_y[n]) 0]^T$, $n = 0, 1, \dots, N$. Thus, the spatial direction of the k th user at the n th time slot can be expressed as

$$\theta_{k,n} = \frac{\left([x_k y_k 0] - [q_x q_y H] \right) \cdot \mathbf{q}_f[n]}{\left\| [x_k y_k 0]^T - [q_x q_y H]^T \right\| \cdot \left\| \mathbf{q}_f[n] \right\|}. \quad (6)$$

2.2. Beamspace Representation. By employing an elaborately designed DLA, the traditional channel (1) in the spatial domain can be translated into an equivalent one in the beamspace or angular domain [40]. In particular, let $\mathbf{U} \in \mathbb{C}^{N_t \times N_t}$ be the spatial discrete Fourier transform (DFT) matrix representing the operation of the DLA, which is acquired by the steering vectors at the N_t fixed spatial frequencies with uniform spacing [41, 42]. Thus, the DFT matrix \mathbf{U} , which contains the N_t orthogonal beams that cover the whole space, is defined as

$$\mathbf{U} = \frac{1}{\sqrt{N_t}} \left[\mathbf{a}(\psi_1) \mathbf{a}(\psi_2) \dots \mathbf{a}(\psi_{N_t}) \right], \quad (7)$$

where $\psi_n = 1/N_t (n - ((N_t + 1)/2))$, $n = 1, 2, \dots, N_t$, are the predefined spatial directions. The DFT matrix \mathbf{U} forms the basis of the N_t -dimensional spatial orthogonal signal space.

Let $\mathbf{x} \in \mathbb{C}^{K \times 1}$ be the transmitted symbol vector to the K ground users and $\mathbf{y} \in \mathbb{C}^{K \times 1}$ be the received signal vector at the K ground users. Then, the system model in the beamspace domain can be expressed as

$$\mathbf{y} = \tilde{\mathbf{H}}^H \mathbf{W} \mathbf{x} + \mathbf{n}, \quad (8)$$

where $\mathbf{n} \sim \mathcal{CN}(\mathbf{0}_K, \sigma_n^2 \mathbf{I}_K)$ is the additive white Gaussian noise (AWGN) vector with the covariance matrix $\sigma_n^2 \mathbf{I}_K$, $\mathbf{W} \in \mathbb{C}^{N_t \times K}$ is the precoding matrix, and the beamspace channel $\tilde{\mathbf{H}} \in \mathbb{C}^{N_t \times K}$ is defined as

$$\tilde{\mathbf{H}} = [\mathbf{h}_{b,1} \mathbf{h}_{b,2} \cdots \mathbf{h}_{b,K}] = [\mathbf{U} \mathbf{h}_1 \mathbf{U} \mathbf{h}_2 \cdots \mathbf{U} \mathbf{h}_K] = \mathbf{U} \mathbf{H}, \quad (9)$$

where $\mathbf{H} \in \mathbb{C}^{N_t \times K}$ is the spatial channel for all the K users and $\mathbf{h}_{b,k} \in \mathbb{C}^{N_t \times 1}$ is the beamspace channel of the k th user. The beamspace channel $\tilde{\mathbf{H}}$ indicates that the signals of each user are mapped in the N_t orthogonal beams, and each element of $\mathbf{h}_{b,k}$ denotes one of the N_t beams supported by the DLA.

2.3. Problem Formulation

2.3.1. UAV-BS Deployment Problem Formulation. Let the UAV hovering area \mathcal{A}_{dep} be defined by

$$q_{x,l} \leq q_x \leq q_{x,u}, \quad q_{y,l} \leq q_y \leq q_{y,u}, \quad (10)$$

where $q_{x,l}$ and $q_{y,l}$ denote the minimum values of q_x and q_y , respectively, while $q_{x,u}$ and $q_{y,u}$ represent the maximum values of q_x and q_y , respectively. The UAV-BS deployment problem is to determine the position $\mathbf{q} \in \mathcal{A}_{\text{dep}}$ to deploy the UAV-BS. Due to the sparse nature of the beamspace channel [24], there are only a few dominant entries of the beamspace channel for each user. The use of the beamspace channel allows us to select the corresponding beams to reduce the dimension of the mmWave UAV-BS system without significant performance loss. The reduced system model in the beamspace domain is given by

$$\tilde{\mathbf{y}} = \tilde{\mathbf{H}}_r^H \mathbf{W}_r \mathbf{x} + \mathbf{n}, \quad (11)$$

where $\tilde{\mathbf{H}}_r = \tilde{\mathbf{H}}(b, :)|_{b \in \mathcal{B}}$ and \mathcal{B} consists of the indices of the selected beams, while \mathbf{W}_r is the precoding matrix with the corresponding reduced dimension. Thus, the received signal at the k th user can be expressed as

$$\tilde{y}_k = \tilde{\mathbf{h}}_{r(k,:)}^H \mathbf{w}_{r(:,k)}^* x_k + \sum_{j=1, j \neq k}^K \tilde{\mathbf{h}}_{r(k,:)}^H \mathbf{w}_{r(:,j)}^* x_j + n_k, \quad (12)$$

where \tilde{y}_k is the k th element of $\tilde{\mathbf{y}}$. Based on the above discussion, for the UAV-BS transmission with multiple users, the average achievable rate of the k th user is

$$R_k = \log_2 \left(1 + (P_t/K) \left\| \frac{\tilde{\mathbf{h}}_{r(k,:)}^H \mathbf{w}_{r(:,k)}}{\sigma_n^2 + (P_t/K) \sum_{j=1, j \neq k}^K \|\tilde{\mathbf{h}}_{r(k,:)}^H \mathbf{w}_{r(:,j)}\|^2} \right\|^2 \right), \quad (13)$$

where P_t is the total transmission power of the UAV-BS. Thus, the sum rate of all the users is $R_{\text{sum}} = \sum_{k=1}^K R_k$.

Note that the beamspace channel $\tilde{\mathbf{H}}$ is a function of the UAV-BS position \mathbf{q} , and hence, \mathcal{B} also depends on \mathbf{q} as well as the way of beam selection. Therefore, R_{sum} depends on both \mathbf{q} and \mathcal{B} , and the UAV-BS placement problem in the beamspace domain can be formulated as

$$\begin{aligned} & \max_{\mathbf{q}, \mathcal{B}} R_{\text{sum}}(\mathbf{q}, \mathcal{B}), \\ & \text{s.t.} \quad \mathbf{q} \in \mathcal{A}_{\text{dep}}. \end{aligned} \quad (14)$$

2.3.2. UAV-BS Trajectory Problem Formulation. The UAV-BS trajectory problem is to determine the mission trajectory $\{\mathbf{q}[n]\}_{n=0}^N \in \mathcal{A}_{\text{tra}}$ of the UAV-BS. At the n th time slot, given the UAV-BS position $\mathbf{q}[n]$, the beamspace channel $\tilde{\mathbf{H}}$ is known. Let $\mathcal{B}[n]$ be the corresponding selected beam set. In order to study the performance of the UAV-BS trajectory, we consider the sum rate of the k th user served by the UAV-BS in the n th time slot of a mission, which is expressed as

$$R_k[n] = \log_2 \left(1 + (P_t/K) \left\| \frac{\tilde{\mathbf{h}}_{r(k,:)}^H[n] \mathbf{w}_{r(:,k)}^*[n]}{\sigma_n^2 + (P_t/K) \sum_{j=1, j \neq k}^K \|\tilde{\mathbf{h}}_{r(k,:)}^H[n] \mathbf{w}_{r(:,j)}^*[n]\|^2} \right\|^2 \right), \quad (15)$$

where $\tilde{\mathbf{h}}_{r(k,:)}[n]$ is the reduced beamspace channel vector of the k th user in the n th time slot, P_t denotes the transmit power at the UAV-BS for each time slot, and $\mathbf{w}_{r(:,k)}[n]$ is the reduced precoding vector of the k th user in time slot n . Therefore, the sum rate for all the users over the $N+1$ time slots can be expressed as $R_{\text{sum},N} = \sum_{k=1}^K \sum_{n=0}^N R_k[n]$.

Based on the above discussion, we can formulate the sum rate maximization problem for the UAV-BS trajectory as

$$\begin{aligned} & \max_{\{\mathbf{q}[n]\}_{n=0}^N, \{\mathcal{B}[n]\}_{n=1}^N} R_{\text{sum},N}(\{\mathbf{q}[n]\}_{n=0}^N, \{\mathcal{B}[n]\}_{n=1}^N), \\ & \text{s.t.} \quad \{\mathbf{q}[n]\}_{n=0}^N \in \mathcal{A}_{\text{tra}}. \end{aligned} \quad (16)$$

$\{\mathcal{B}[n]\}_{n=1}^N$ depends on the UAV-BS trajectory $\{\mathbf{q}[n]\}_{n=1}^N$ and how the beams are selected at each time slot n .

3. Solution of the Problem

By evaluating the Hessian matrices of the objective functions for the problems (14) and (16), it can be seen that both the optimization problems are nonconvex and highly complex. Therefore, it is challenging to solve the problems (14) and (16) by the existing optimization tools. We focus on the optimization problem of UAV-BS deployment first by separating the problem (14) into two subproblems. The ‘‘inner’’ subproblem determines the selected beam set \mathcal{B} giving the UAV-BS position \mathbf{q} . A suboptimal SINR beam selection algorithm is introduced to incrementally maximize the sum rate of the mmWave UAV-BS system. With this SINR beam selection scheme, the ‘‘outer’’ subproblem then solves the UAV-BS deployment by employing the CGA algorithm.

Next, we solve the optimization problem (16) for UAV-BS trajectory in a similar way. Specifically, the CGA is designed to optimize the UAV-BS trajectory with the proposed suboptimal SINR beam selection scheme.

3.1. Beam Selection. Given the UAV-BS position \mathbf{q} , the beamspace channel $\tilde{\mathbf{H}}$ is known. The proposed SINR beam selection scheme is composed of two parts. The ground users having unique dominant beams can select the dominant beams to communicate with the UAV-BS, while the users having overlap dominant beams will search for the proper beams from the unselected beams by incrementally maximizing the SINR of the mmWave UAV-BS system, where ZF is utilized to further eliminate the MUI.

Due to the sparse structure of the beamspace channel in the mmWave UAV-BS system, the beamspace channel for the k th user has dominant values near the LoS direction [25]. Since the dominant beams have the most transmission power, they can be selected for the transmission to reduce the number of RF chains with minor performance loss. In order to reduce the number of RF chains N_{RF} to the minimum, we consider that each user is served by only one beam, and hence, $N_{\text{RF}} = K$. Let the index of the selected dominant beam for user k be $\mathcal{B}_{\text{max},k}$, which is defined as [43]

$$\mathcal{B}_{\text{max},k} = \left\{ i^* = \arg \max_{1 \leq i \leq N_t} |h_{b,k}^i|^2 \right\}, \quad (17)$$

where $h_{b,k}^i$ denotes the i th element of the k th column of the beamspace channel $\tilde{\mathbf{H}}$.

Given the beamspace channel vectors $\mathbf{h}_{b,k}$ and the corresponding selected beam indexes (17) for $1 \leq k \leq K$, the K users can be assigned into the two groups, the nonoverlap group \mathcal{E}_N and the overlap groups \mathcal{E}_O . The group \mathcal{E}_N includes the users having the unique dominant beams, while a user in the group \mathcal{E}_O has the same selected beam with some other users in \mathcal{E}_O . In particular, the selected beam set or index of a nonoverlap user i satisfies $\mathcal{B}_{\text{max},i} \cap (\cup_{j \neq i, 1 \leq j \leq K} \mathcal{B}_{\text{max},j}) = \emptyset$. On the other hand, if $\mathcal{B}_{\text{max},i} \cap (\cup_{j \neq i, 1 \leq j \leq K} \mathcal{B}_{\text{max},j}) \neq \emptyset$, the i 'th user is an overlap user and is assigned to \mathcal{E}_O . Obviously, \mathcal{E}_N and \mathcal{E}_O satisfy $\mathcal{E}_N \cup \mathcal{E}_O = \{1, 2, \dots, K\}$ and $\mathcal{E}_O \cap \mathcal{E}_N = \emptyset$. We consider an example of $K = 6$ and $N_t = 8$, where $\mathcal{B}_{\text{max},1} = \{1\}$, $\mathcal{B}_{\text{max},2} = \{4\}$, $\mathcal{B}_{\text{max},3} = \{7\}$, $\mathcal{B}_{\text{max},4} = \{7\}$, $\mathcal{B}_{\text{max},5} = \{8\}$, and $\mathcal{B}_{\text{max},6} = \{8\}$. Then, $\mathcal{E}_N = \{1, 2\}$ and $\mathcal{E}_O = \{3, 4, 5, 6\}$.

For nonoverlap user $k \in \mathcal{E}_N$, the beam with index $\mathcal{B}_{\text{max},k}$ will be directly selected, since this dominant beam contains most of the transmission power and causes few interferences to other users. Let $\mathcal{B}_{\mathcal{E}_N}$ denote the selected beams for the nonoverlap users in \mathcal{E}_N . For the overlap users in \mathcal{E}_O , the beams should be reselected to communicate with the UAV-BS by maximizing the sum rate of all users. To incrementally maximize the sum rate, the beams which result in the maximum increase in SINR should be selected. In order to mitigate the MUI with the user group \mathcal{E}_N , the beams for the users in \mathcal{E}_O are selected from the beam set $\mathcal{B}_R = \{1, 2,$

$\dots, N_t\} \setminus \mathcal{B}_{\mathcal{E}_N}$. Let $\mathcal{B}_{\mathcal{E}_O}$ denote the selected beams for the overlap users in \mathcal{E}_O .

The precoding matrix \mathbf{W}_r for all the users with the selected beams $\mathcal{B}_{\text{sel}} = \mathcal{B}_{\mathcal{E}_O} \cup \mathcal{B}_{\mathcal{E}_N}$ can be expressed as

$$\mathbf{W}_r = \alpha \mathbf{F}_r, \quad (18)$$

where α is the power normalization factor given by

$$\alpha = \sqrt{\frac{P_t}{\text{tr}(\mathbf{F}_r \mathbf{F}_r^H)}}, \quad (19)$$

and \mathbf{F}_r is the ZF precoding matrix expressed as

$$\mathbf{F}_r = \tilde{\mathbf{H}}_r (\tilde{\mathbf{H}}_r^H \tilde{\mathbf{H}}_r)^{-1}, \quad (20)$$

in which $\tilde{\mathbf{H}}_r = \tilde{\mathbf{H}}(b, :)_{b \in \mathcal{B}_{\text{sel}}}$. The SINR with the ZF precoding for user k can be expressed as [44]

$$\text{SINR}_{k,ZF} = \frac{P_t |\alpha|^2}{K \sigma_n^2}. \quad (21)$$

Thus, the maximization of the SINR can be transformed to the maximization of the normalization factor α with respect to the selected beam set $\mathcal{B}_{\mathcal{E}_O}$ for the overlap users in \mathcal{E}_O .

Hence, we can select the required beams for the overlap users in \mathcal{E}_O one by one based on a greedy-type beam selection algorithm that identifies the beams with the maximal gains in terms of SINR. Specifically, at each selection stage, a beam is selected for an overlap user in \mathcal{E}_O which maximizes the gain in the SINR. This greedy beam selection algorithm is summarized in Algorithm 1.

3.2. Continuous Genetic Algorithm for UAV-BS Deployment. For given \mathbf{q} , we use Algorithm 1 to select the beam set $\mathcal{B}_{\text{dep}}(\mathbf{q}) = \mathcal{B}_{\text{sel}}(\mathbf{q})$. Express the objective function of the UAV-BS deployment problem for this beam selection scheme as $f_{\text{dep}}(\mathbf{q}) = R_{\text{sum}}(\mathbf{q}, \mathcal{B}_{\text{dep}}(\mathbf{q}))$. Hence, with this greedy SINR-based beam selection scheme, the optimization of the UAV-BS deployment can be expressed as

$$\mathbf{q}^* = \arg \max_{\mathbf{q} \in \mathcal{A}_{\text{dep}}} f_{\text{dep}}(\mathbf{q}). \quad (22)$$

We propose to apply the CGA [30, 45, 46] to solve this optimization problem. With P_{dep} denoting the population size and g being the generation index, the procedure of the CGA-based UAV-BS deployment is detailed below.

- (1) Initialization: at $g = 0$, the initial population of P_{dep} chromosomes or candidate UAV-BS locations $\{\mathbf{q}_{g,p}\}_{p=1}^{P_{\text{dep}}}$ are randomly generated over the UAV hovering area \mathcal{A}_{dep} . Algorithm 1 is utilized to select the beam set $\mathcal{B}_{\text{dep}}(\mathbf{q}_{g,p})$ for every chromosome $\mathbf{q}_{g,p}$

```

Input:  $\tilde{\mathbf{H}}, \mathcal{B}_{\max,k}$  for  $1 \leq k \leq K$ 
Output:  $\mathcal{B}_{\text{sel}}, \tilde{\mathbf{H}}_r$ 
1: for  $k = 1 \rightarrow K$ 
2:   if  $\mathcal{B}_{\max,k} \cap (\cup_{k' \neq k, 1 \leq k' \leq K} \mathcal{B}_{\max,k'}) = \emptyset$ 
3:      $k \in \mathcal{G}_N$ 
4:   else
5:      $k \in \mathcal{G}_O$ 
6: end
7:  $\mathcal{B}_{\mathcal{G}_N} = \cap_{k \in \mathcal{G}_N} \mathcal{B}_{\max,k}$ 
8:  $\mathcal{B}_{\mathcal{G}_O} = \emptyset$ 
9:  $\mathcal{B}_R = \{1, 2, \dots, N_t\} \setminus \mathcal{B}_{\mathcal{G}_N}$ 
10: for  $j' = 1 \rightarrow K - |\mathcal{G}_N|$ 
11:    $j = \{\{1, 2, \dots, K\} \setminus \mathcal{G}_N\}(j')$ 
12:   for  $i' = 1 \rightarrow |\mathcal{B}_R|$ 
13:      $i = \mathcal{B}_R(i')$ 
14:      $\mathbf{C}^{(i)} = \tilde{\mathbf{H}}(b, \cdot)_{b \in (\mathcal{B}_{\mathcal{G}_N} \cup \mathcal{B}_{\mathcal{G}_O} \cup i)}$ 
15:      $\mathbf{F}^{(i)} = \mathbf{C}^i ((\mathbf{C}^{(i)})^H \mathbf{C}^{(i)})^{-1}$ 
16:      $\alpha^{(i)} = \sqrt{P_t / \text{tr}(\mathbf{F}^{(i)} (\mathbf{F}^{(i)})^H)}$ 
17:   end
18:    $i_j^* = \arg \max_{i'} |\alpha^{(i)}|^2$ 
19:    $\mathcal{B}_{\mathcal{G}_O} = \mathcal{B}_{\mathcal{G}_O} \cup i_j^*$ 
20:    $\mathcal{B}_R \leftarrow \mathcal{B}_R \setminus \mathcal{B}_R(i_j^*)$ 
21: end
22:  $\mathcal{B}_{\text{sel}} = \mathcal{B}_{\mathcal{G}_O} \cup \mathcal{B}_{\mathcal{G}_N}$ 
23:  $\tilde{\mathbf{H}}_r = \tilde{\mathbf{H}}(b, \cdot)_{b \in \mathcal{B}_{\text{sel}}}$ 

```

ALGORITHM 1: Greedy SINR-based beam selection.

, and then, the fitness value $F_{\text{dep},g,p} = f_{\text{dep}}(\mathbf{q}_{g,p})$ is calculated, for $1 \leq p \leq P_{\text{dep}}$. The P_{dep} chromosomes are ranked from top to bottom according to their fitness values. Denote this ranked population as $\{\mathbf{q}_{g,p}; F_{\text{dep},g,p}\}_{p=1}^{P_{\text{dep}}}$ with the fitness values $F_{\text{dep},g,1} \geq F_{\text{dep},g,2} \geq \dots \geq F_{\text{dep},g,P_{\text{dep}}}$.

- (2) Selection: set $g = g + 1$. The $P_{\text{keep},d}$ previous chromosomes with the highest fitness values will survive into the next generation, i.e., $\{\mathbf{q}_{g,p} = \mathbf{q}_{g-1,p}; F_{\text{dep},g,p} = F_{\text{dep},g-1,p}\}_{p=1}^{P_{\text{keep},d}}$, and these high-fitness chromosomes also form a mating pool, where $P_{\text{keep},d} = P_{\text{dep}} \cdot \gamma_{\text{dep}}$ is the size of the mating pool. The selection ratio γ_{dep} decides how many chromosomes are to be chosen for the mating pool from the total P_{dep} chromosomes. The mating pool is used to select parents to provide $P_{\text{dep}} - P_{\text{keep},d}$ offspring for the next generation to maintain a constant-size population

The rank weighting, a roulette wheel weighting [30], is used to choose chromosomes for mating. With this weighting, the chromosome with the largest fitness has the greatest probability of mating, while the chromosome with the smallest

fitness has the lowest probability of mating. Let P_m^{dep} be the probability of selecting the m th chromosome for mating from the $P_{\text{keep},d}$ chromosomes, which is calculated as

$$P_m^{\text{dep}} = \frac{P_{\text{keep},d} - m + 1}{\sum_{m=1}^{P_{\text{keep},d}} m}, 1 \leq m \leq P_{\text{keep},d}. \quad (23)$$

Then, P_m^{dep} is turned into the cumulative probability $P_{c,m}^{\text{dep}}$ for deciding which chromosome can be selected as a parent. In particular, when a random number P_{mum} between 0 and 1 is generated, if $P_{c,m-1}^{\text{dep}} < P_{\text{mum}} \leq P_{c,m}^{\text{dep}}$, the m th chromosome will be selected as a parent (mum). For instance, let $P_{\text{keep},d} = 4$, and the corresponding $P_m^{\text{dep}} \in \{0.4, 0.3, 0.2, 0.1\}$. Then, $P_{c,m}^{\text{dep}} \in \{0.4, 0.7, 0.9, 1\}$. If $P_{\text{mum}} = 0.33$, the first chromosome is selected as ‘‘mum.’’ Similarly, the ‘‘dad’’ chromosome is chosen in the same manner. We adopt two parents producing two offspring as a common form of mating. Thus, $P_{\text{dep}} - P_{\text{keep},d}$ parents are required for mating to create new offspring. We will assume that $P_{\text{dep}} - P_{\text{keep},d}$ is an even number, and we have selected $(P_{\text{dep}} - P_{\text{keep},d})/2$ pairs of parents.

- (3) Crossover: each pair of parents selected for the crossover operation can be expressed as

$$\begin{cases} \mathbf{q}_{g,\text{mum}} = [q_{x,g,\text{mum}} q_{y,g,\text{mum}}]^T, \\ \mathbf{q}_{g,\text{dad}} = [q_{x,g,\text{dad}} q_{y,g,\text{dad}}]^T. \end{cases} \quad (24)$$

They are used to produce two offspring $\mathbf{q}_{g,\text{os1}}$ and $\mathbf{q}_{g,\text{os2}}$.

The single crossover point scheme is utilized to combine the parents’ information. A crossover point q_{p_c} is randomly selected between x and y . If y is selected as the crossover point, i.e., $q_{p_c} = y$, the two new offspring are produced as

$$\begin{cases} \mathbf{q}_{g,\text{os1}} = [q_{x,g,\text{mum}} q_{p_c,g,\text{os1}}]^T, \\ \mathbf{q}_{g,\text{os2}} = [q_{x,g,\text{dad}} q_{p_c,g,\text{os2}}]^T, \end{cases} \quad (25)$$

with

$$\begin{cases} q_{p_c,g,\text{os1}} = q_{p_c,g,\text{mum}} - \mu(q_{p_c,g,\text{mum}} - q_{p_c,g,\text{dad}}) = q_{y,g,\text{mum}} - \mu(q_{y,g,\text{mum}} - q_{y,g,\text{dad}}), \\ q_{p_c,g,\text{os2}} = q_{p_c,g,\text{dad}} + \mu(q_{p_c,g,\text{mum}} - q_{p_c,g,\text{dad}}) = q_{y,g,\text{dad}} + \mu(q_{y,g,\text{mum}} - q_{y,g,\text{dad}}), \end{cases} \quad (26)$$

where μ is a random value uniformly selected in the range of $(0, 1)$. Similarly, if x is selected as the crossover point, i.e., $q_{p_c} = x$, the crossover operation produces the two corresponding offspring from the pair of parents.

Algorithm 1 selects the beam set for every offspring, and its fitness value is calculated. After the crossover, the new generation of the chromosomes include the $P_{\text{keep},d}$ elitist

chromosomes from the previous generation and their $P_{\text{dep}} - P_{\text{keep},d}$ offspring. These P_{dep} chromosomes are ranked from top to bottom according to their fitness values as $\{\mathbf{q}_{g,p}; F_{\text{dep},g,p}\}_{p=1}^{P_{\text{dep}}}$.

- (4) Mutation: the element $q_{p_m, g, p}$ of chromosome $\mathbf{q}_{g,p}$ is randomly selected to mutate; thereby, the mutated element is replaced by a new random value $q_{p_m, l} \leq q_{p_m, g, p} \leq q_{p_m, u}$, where $p_m = x$ or y , while $2 \leq p \leq P_{\text{dep}}$. We opt to not mutate the best chromosome with the highest fitness found so far, i.e., $\mathbf{q}_{g,1}$. The number of elements that will mutate in each generation is governed by a mutation probability M_{dep} [45, 46]. Thus, the total number of mutated elements is $2(P_{\text{dep}} - 1)M_{\text{dep}}$ since each chromosome has 2 elements. The mutation operation is crucial to providing sufficient diversity for the CGA

Algorithm 1 then selects the beam sets for the mutated chromosomes, and their fitness values are calculated. Afterward, the mutated population of the P_{dep} chromosomes is ranked again from top to bottom according to their fitness values as $\{\mathbf{q}_{g,p}; F_{\text{dep},g,p}\}_{p=1}^{P_{\text{dep}}}$.

- (5) Termination: if $g > G_{\text{max,dep}}$, where $G_{\text{max,dep}}$ is the maximum number of generations, the procedure stops and the chromosome with the highest fitness is chosen as the solution, i.e., $\mathbf{q}^* = \mathbf{q}_{g,1}$. Otherwise, the procedure repeats from step (2)

The CGA-based UAV-BS deployment algorithm is summarized in Algorithm 2. The population size P_{dep} , the maximum number of generations $G_{\text{max,dep}}$, the selection ratio γ_{dep} , and the mutation probability M_{dep} are the problem-dependent algorithmic parameters, which need to be carefully chosen.

3.3. Continuous Genetic Algorithm for UAV-BS Trajectory. With the initial and final locations \mathbf{q}_I and \mathbf{q}_F fixed, the UAV-BS trajectory has N locations, which is expressed as

$$\mathbf{q}_N = [\mathbf{q}^T[1] \mathbf{q}^T[2] \cdots \mathbf{q}^T[N]]^T. \quad (27)$$

For given $\mathbf{q}[n]$ at time slot n , we use Algorithm 1 to select the beam set $\mathcal{B}_{\text{tra}}(\mathbf{q}[n]) = \mathcal{B}_{\text{sel}}(\mathbf{q}[n])$. Denote the overall beam set selected for \mathbf{q}_N by Algorithm 1 as $\mathcal{B}_{\text{tra}}(\mathbf{q}_N) = \{\mathcal{B}_{\text{sel}}(\mathbf{q}[n])\}_{n=1}^N$. Then, the optimization of the UAV-BS trajectory is reduced to

$$\mathbf{q}_N^* = \arg \max_{\mathbf{q}_N \in \mathcal{A}_{\text{tra}}} f_{\text{tra}}(\mathbf{q}_N), \quad (28)$$

where the objective function of the UAV-BS trajectory problem is $f_{\text{tra}}(\mathbf{q}_N) = R_{\text{sum},N}(\mathbf{q}_N, \mathcal{B}_{\text{tra}}(\mathbf{q}_N))$. We also apply the CGA to solve this optimization problem. From (27), each chromosome has $2N$ coordinates, and the p th chromosome in the g th generation can be expressed as

$$\mathbf{q}_{N,g,p} = \left\{ \mathbf{q}_{g,p}[n] \right\}_{n=1}^N = \left[q_{x,g,p}[1] q_{y,g,p}[1] q_{x,g,p}[2] q_{y,g,p}[2] \cdots q_{x,g,p}[N] q_{y,g,p}[N] \right]^T. \quad (29)$$

With the population size P_{tra} , the procedure of the CGA for the UAV-BS trajectory is now detailed.

- (1) Initialization: at $g = 0$, the initial population of P_{tra} chromosomes $\{\mathbf{q}_{N,g,p}\}_{p=1}^{P_{\text{tra}}}$ is randomly generated, constrained inside \mathcal{A}_{tra} . Algorithm 1 then selects the beam sets $\{\mathcal{B}_{\text{tra}}(\mathbf{q}_{N,g,p})\}_{p=1}^{P_{\text{tra}}}$, and the corresponding fitness values $\{F_{\text{tra},g,p} = f_{\text{tra}}(\mathbf{q}_{N,g,p})\}_{p=1}^{P_{\text{tra}}}$ are calculated. Then, these P_{tra} chromosomes are ranked from top to bottom according to their fitness values as $\{\mathbf{q}_{N,g,p}; F_{\text{tra},g,p}\}_{p=1}^{P_{\text{tra}}}$ with the fitness values $F_{\text{tra},g,1} \geq F_{\text{tra},g,2} \geq \cdots \geq F_{\text{tra},g,P_{\text{tra}}}$
- (2) Selection: set $g = g + 1$, and retain the $P_{\text{keep},t}$ previous chromosomes with the highest fitness values in the next generation as $\{\mathbf{q}_{N,g,p} = \mathbf{q}_{N,g-1,p}; F_{\text{tra},g,p} = F_{\text{tra},g-1,p}\}_{p=1}^{P_{\text{keep},t}}$, which also form a mating pool, where $P_{\text{keep},t} = P_{\text{tra}} \cdot \gamma_{\text{tra}}$ with γ_{tra} being the selection ratio. As usual, the mating pool is used to select parents to provide $P_{\text{tra}} - P_{\text{keep},t}$ offspring for the next generation to maintain a constant-size population

The rank weight is also adopted to select parents from the mating pool. The probability P_m^{tra} of the m th chromosome to be selected from the mating pool is again defined by

$$P_m^{\text{tra}} = \frac{P_{\text{keep},t} - m + 1}{\sum_{m=1}^{P_{\text{keep},t}} m}, \quad 1 \leq m \leq P_{\text{keep},t}, \quad (30)$$

and P_m^{tra} is converted into the cumulative probability $P_{c,m}^{\text{tra}}$ to choose chromosomes as parents from the mating pool.

- (3) Crossover: the mating strategy with two parents producing two new offspring is utilized, and hence, a total of $(P_{\text{tra}} - P_{\text{keep},t})/2$ pairs of parents are selected. A generic pair of two parents selected from the mating pool can be expressed as

$$\begin{cases} \mathbf{q}_{N_{g,\text{mum}}} = [q_{x,g,\text{mum}}[1]q_{y,g,\text{mum}}[1] \cdots q_{x,g,\text{mum}}[n]q_{y,g,\text{mum}}[n] \cdots q_{x,g,\text{mum}}[N]q_{y,g,\text{mum}}[N]]^T, \\ \mathbf{q}_{N_{g,\text{dad}}} = [q_{x,g,\text{dad}}[1]q_{y,g,\text{dad}}[1] \cdots q_{x,g,\text{dad}}[n]q_{y,g,\text{dad}}[n] \cdots q_{x,g,\text{dad}}[N]q_{y,g,\text{dad}}[N]]^T. \end{cases} \quad (31)$$

Input: $\mathcal{A}_{\text{dep}}, P_{\text{dep}}, \gamma_{\text{dep}}, G_{\text{max,dep}}, M_{\text{dep}}$

Output: $\mathbf{q}^*, \mathcal{B}_{\text{dep}}(\mathbf{q}^*)$

1: Set $g = 0$, randomly generate P_{dep} chromosomes $\mathbf{q}_{g,p} \in \mathcal{A}_{\text{dep}}$, determine $\mathcal{B}_{\text{dep}}(\mathbf{q}_{g,p})$ with Algorithm 1, and calculate fitness values $F_{\text{dep},g,p}$, for $1 \leq p \leq P_{\text{dep}}$

2: Rank P_{dep} chromosomes according to their fitness values from top to bottom as $\{\mathbf{q}_{g,p}; F_{\text{dep},g,p}\}_{p=1}^{P_{\text{dep}}}$

3: $P_{\text{keep},d} = P_{\text{dep}} \cdot \gamma_{\text{dep}}$

4: **while** $g \leq G_{\text{max,dep}}$

5: $g = g + 1$

6: $\{\mathbf{q}_{g,p}; F_{\text{dep},g,p}\}_{p=1}^{P_{\text{keep},d}} = \{\mathbf{q}_{g-1,p}; F_{\text{dep},g-1,p}\}_{p=1}^{P_{\text{keep},d}}$

7: $P_m^{\text{dep}} = P_{\text{keep},d} - m + 1 / \sum_{m=1}^{P_{\text{keep},d}} m$, $P_m^{\text{dep}} \rightarrow P_{c,m}^{\text{dep}}$, $1 \leq m \leq P_{\text{keep},d}$

8: **for** $i = 1 \rightarrow P_{\text{dep}} - P_{\text{keep},d} / 2$

9: Select pair of parents with $P_{c,m}^{\text{dep}}$ from mating pool

10: Use single-point crossover to generate two offspring

11: Calculate their beam sets and fitness values

12: **end for**

13: Rank $P_{\text{keep},d}$ survivals and $P_{\text{dep}} - P_{\text{keep},d}$ offspring according to their fitness values from top to bottom as $\{\mathbf{q}_{g,p}; F_{\text{dep},g,p}\}_{p=1}^{P_{\text{dep}}}$

14: **for** $p = 2 \rightarrow P_{\text{dep}}$

15: Mutate $\mathbf{q}_{g,p}$ with mutation probability M_{dep}

16: If mutated, re-calculate beam set and fitness value

17: **end for**

18: Rank mutated population according to their fitness values from top to bottom as $\{\mathbf{q}_{g,p}; F_{\text{dep},g,p}\}_{p=1}^{P_{\text{dep}}}$

19: **if** $g > G_{\text{max,dep}}$

20: $\mathbf{q}^* = \mathbf{q}_{g,1}$, $\mathcal{B}_{\text{dep}}(\mathbf{q}^*) = \mathcal{B}_{\text{dep}}(\mathbf{q}_{g,1})$ **break**

21: **end if**

22: **end while**

ALGORITHM 2: Continuous GA for UAV-BS deployment.

The number of crossover points depends on the UAV-BS flying area $[q_{x,l}q_{x,h}] \times [q_{y,l}q_{y,h}]$ and the maximum speed constraint v_{max} . In particular, the longest straight flying distance is the diagonal line $\sqrt{(q_{x,h} - q_{x,l})^2 + (q_{y,h} - q_{y,l})^2}$; thereby, the minimum required number of time slots to fly across the UAV-BS flying area can be expressed as

$$N_l = \left\lceil \frac{\sqrt{(q_{x,h} - q_{x,l})^2 + (q_{y,h} - q_{y,l})^2}}{v_{\text{max}}} \right\rceil - 1. \quad (32)$$

Thus, the $2N_l$ -point crossover scheme is utilized to

guarantee the offspring satisfying the constraints \mathcal{A}_{tra} . Specifically, the first crossover point n is randomly selected from $\{1, 2, \dots, N - N_l + 1\}$, and the two offspring produced can be expressed, respectively, as

$$\begin{aligned} \mathbf{q}_{N_{g,os1}} &= \begin{bmatrix} q_{x,g,mum}[1]q_{y,g,mum}[1] \cdots q_{x,g,mum}[n-1]q_{y,g,mum}[n-1] \\ q_{x,g,os1}[n]q_{y,g,os1}[n]q_{x,g,os1}[n+1] \cdots q_{x,g,os1}[n+N_l-1] \\ q_{y,g,os1}[n+N_l-1] \left| \begin{matrix} q_{x,g,dad}[n+N_l]q_{y,g,dad}[n+N_l] \\ \cdots q_{x,g,dad}[N]q_{y,g,dad}[N] \end{matrix} \right. \cdot \mathbf{q}_{N_{g,os2}} \end{bmatrix} \\ &= \begin{bmatrix} q_{x,g,dad}[1]q_{y,g,dad}[1] \cdots q_{x,g,dad}[n-1]q_{y,g,dad}[n-1] \\ q_{x,g,os2}[n]q_{y,g,os2}[n]q_{x,g,os2}[n+1] \cdots q_{x,g,os2}[n+N_l-1] \\ q_{y,g,os2}[n+N_l-1] \left| \begin{matrix} q_{x,g,mum}[n+N_l]q_{y,g,mum}[n+N_l] \\ \cdots q_{x,g,mum}[N]q_{y,g,mum}[N] \end{matrix} \right. \end{bmatrix}^T. \end{aligned} \quad (33)$$

Each offspring contains portions of the ‘‘genes’’ from both parents. Specifically, offspring os1 has mum’s genes before the first crossover point n and dad’s genes after the last crossover point $n + N_l - 1$, while offspring os2 has dad’s genes before the first crossover point n and mum’s genes after the last crossover point $n + N_l - 1$. The new coordinates q_x and q_y at the crossover points are the combinations of the coordinates from both parents, which can be expressed as

$$\begin{cases} q_{x/y,g,os1}[n_l] = q_{x/y,g,mum}[n_l] - \mu \left(q_{x/y,g,mum}[n_l] - q_{x/y,g,dad}[n_l] \right), \\ q_{x/y,g,os2}[n_l] = q_{x/y,g,dad}[n_l] + \mu \left(q_{x/y,g,mum}[n_l] - q_{x/y,g,dad}[n_l] \right), \end{cases} \quad (34)$$

for $n \leq n_l \leq n + N_l - 1$, where μ is a random value uniformly selected from $(0, 1)$. If the new coordinates produced do not satisfy the maximum speed constraint of \mathcal{A}_{tra} , μ is reselected until the new coordinates meet the requirements of \mathcal{A}_{tra} .

The beam set of every offspring is then selected using Algorithm 1, and its fitness value is calculated. The new generation of the chromosomes, including the $P_{\text{keep},t}$ elitist chromosomes from the previous generation and their $P_{\text{tra}} - P_{\text{keep},t}$ offspring, is ranked from top to bottom according to their fitness values as $\{\mathbf{q}_{N_{g,p}}; F_{\text{tra}_{g,p}}\}_{p=1}^{P_{\text{tra}}}$.

- (4) Mutation: the chromosomes $\mathbf{q}_{N_{g,p}}$, $2 \leq p \leq P_{\text{tra}}$, are subject to random mutation with the mutation probability M_{tra} to explore other area of \mathcal{A}_{tra} so as to avoid local maxima. Specially, $2N_l$ points of a chromosome, $q_{x,g,p}[n], q_{y,g,p}[n], \dots, q_{x,g,p}[n+N_l-1], q_{y,g,p}[n+N_l-1]$, are randomly chosen to be mutated. If the mutated chromosome does not satisfy the requirement of \mathcal{A}_{tra} , the chromosome is remutated

until the constraints \mathcal{A}_{tra} are met. Given the mutation probability M_{tra} , a total of $2M_{\text{tra}}N(P_{\text{tra}} - 1)$ elements will be mutated

The beam sets for the mutated chromosomes are selected with Algorithm 1, and their fitness values are calculated. The mutated population of the P_{tra} chromosomes is ranked again from top to bottom according to their fitness values as $\{\mathbf{q}_{N_{g,p}}; F_{\text{tra}_{g,p}}\}_{p=1}^{P_{\text{tra}}}$.

- (5) Termination: if $g > G_{\text{max,tra}}$, where $G_{\text{max,tra}}$ denotes the maximum number of generations, the procedure stops with the solution $\mathbf{q}_N^* = \mathbf{q}_{N_{g,1}}$. Otherwise, the procedure repeats from step (2)

This CGA for the UAV-BS trajectory optimization is summarized in Algorithm 3.

3.4. Complexity Analysis. The complexity of the proposed CGA for the UAV-BS deployment optimization with the aid of the greedy SINR beam selection algorithm is specified by the number $N_{\text{GA,dep}}$ of the cost function evaluations and the complexity per cost function evaluation. Given the population size P_{dep} and the maximum number of generation $G_{\text{max,dep}}$, we have $N_{\text{GA}} = P_{\text{dep}} \cdot G_{\text{max,dep}}$, whereas the complexity per cost function is derived according to R_{sum} and the greedy SINR beam selection algorithm. The complexity evaluations of R_{sum} and the greedy SINR beam selection algorithm are listed in Table 2.

Thus, the complexity of the proposed CGA for the UAV-BS deployment optimization with the aid of the greedy SINR beam selection algorithm is $N_{\text{GA,dep}} \cdot \{(K - |\mathcal{E}_N|) \sum_{i=1}^{K-|\mathcal{E}_N|} (N_t - |\mathcal{E}_N| - i)[3(|\mathcal{E}_N| + i)^3 + 4(|\mathcal{E}_N| + i)^2 + 1] + 2K^2 + (N_t + 1)K\}$. In a similar way, the number $N_{\text{GA,tra}}$ of the cost function evaluations of the proposed CGA for the UAV-BS trajectory optimization with the aid of the greedy SINR beam selection algorithm is $N_{\text{GA,tra}} = P_{\text{tra}} \cdot G_{\text{max,tra}}$, and the complexity of the proposed CGA for the UAV-BS trajectory optimization with the aid of the greedy SINR beam selection algorithm is $N \cdot N_{\text{GA,tra}} \cdot \{(K - |\mathcal{E}_N|) \sum_{i=1}^{K-|\mathcal{E}_N|} (N_t - |\mathcal{E}_N| - i)[3(|\mathcal{E}_N| + i)^3 + 4(|\mathcal{E}_N| + i)^2 + 1] + 2K^2 + (N_t + 1)K\}$.

4. Performance Analysis

We evaluate the performance of the proposed CGA for the UAV-BS deployment optimization and the proposed CGA for the UAV-BS trajectory optimization, with the aid of the greedy SINR beam selection algorithm. We consider an UAV-BS simultaneously serving several (K) ground users in a mmWave system. The terrestrial users are randomly distributed in the square area of $[0, 100] \times [0, 100]$ (m^2), and the UAV-BS deployment area/flying area is also this $[0, 100] \times [0, 100]$ (m^2) square area. The main default parameters of this simulated UAV-BS mmWave system are listed in Table 3.

4.1. Performance of the CGA for UAV-BS Deployment. We first quantify the performance of the proposed CGA-based

Input: $\mathcal{A}_{tra}, N_l, P_{tra}, \gamma_{tra}, G_{max,tra}, M_{tra}$
Output: $\mathbf{q}_N^*, \mathcal{B}_{tra}(\mathbf{q}_N^*)$
1: Set $g = 0$, randomly generate P_{tra} chromosomes $\mathbf{q}_{N_{g,p}} \in \mathcal{A}_{tra}$, determine $\mathcal{B}_{tra}(\mathbf{q}_{N_{g,p}})$ with Algorithm 1, and calculate fitness values $F_{tra_{g,p}}$, for $1 \leq p \leq P_{tra}$
2: Rank P_{tra} chromosomes according to their fitness values from top to bottom as $\{\mathbf{q}_{N_{g,p}}; F_{tra_{g,p}}\}_{p=1}^{P_{tra}}$
3: $P_{keep,t} = P_{tra} \cdot \gamma_{tra}$
4: **while** $g \leq G_{max,tra}$
5: $g = g + 1$
6: $\{\mathbf{q}_{N_{g,p}}; F_{tra_{g,p}}\}_{p=1}^{P_{keep,t}} = \{\mathbf{q}_{N_{g-1,p}}; F_{tra_{g-1,p}}\}_{p=1}^{P_{keep,t}}$
7: $P_m^{tra} = P_{keep,t} - m + 1 / \sum_{m=1}^{P_{keep,t}} \boxtimes m, P_m^{tra} \rightarrow P_{c,m}^{tra}, 1 \leq m \leq P_{keep,t}$
8: **for** $i = 1 \rightarrow P_{tra} - P_{keep,t} / 2$
9: Select pair of parents with $P_{c,m}^{tra}$ from mating pool
10: **repeat**
11: Randomly generate μ
12: Use $2N_l$ -points crossover to produce two offspring $\mathbf{q}_{N_{g,os1}}, \mathbf{q}_{N_{g,os2}}$
13: **until** $\mathbf{q}_{N_{g,os1}}, \mathbf{q}_{N_{g,os2}} \in \mathcal{A}_{tra}$
14: Calculate beam sets and fitness values of two offspring
15: **end for**
16: Rank survivals and offspring according to their fitness values from top to bottom as $\{\mathbf{q}_{N_{g,p}}; F_{tra_{g,p}}\}_{p=1}^{P_{tra}}$
17: **for** $p = 2 \rightarrow P_{tra}$
18: Select $\mathbf{q}_{N_{g,p}}$ with probability M_{tra}
19: **repeat**
20: Randomly mutate $2N_l$ elements of $\mathbf{q}_{N_{g,p}}$
21: **until** Mutated chromosome satisfies \mathcal{A}_{tra}
22: Calculate beam set and fitness value of mutated chromosome
23: **end for**
24: Rank mutated population according to their fitness values from top to bottom as $\{\mathbf{q}_{N_{g,p}}; F_{tra_{g,p}}\}_{p=1}^{P_{tra}}$
25: **if** $g > G_{max,tra}$
26: $\mathbf{q}_N^* = \mathbf{q}_{N_{g,1}}, \mathcal{B}_{tra}(\mathbf{q}_N^*) = \mathcal{B}_{tra}(\mathbf{q}_{N_{g,1}})$ **break**
27: **end if**
28: **end while**

ALGORITHM 3: Continuous GA for UAV-BS trajectory.

TABLE 2: Complexity in number of operations.

	Number of operations
$ h_{b,k}^i ^2 \forall i, k$	$N_t K$
F	$(K - \mathcal{E}_N) \sum_{i=1}^{K- \mathcal{E}_N } (N_t - \mathcal{E}_N - i) [3(\mathcal{E}_N + i)^3 + 2(\mathcal{E}_N + i)^2]$
α	$(K - \mathcal{E}_N) \sum_{i=1}^{K- \mathcal{E}_N } (N_t - \mathcal{E}_N - i) (2(\mathcal{E}_N + i)^2 + 1)$
R_{sum}	$2K^2 + K$

UAV-BS deployment with the aid of the greedy SINR beam selection scheme.

Figure 2 depicts the achievable sum rate as the function of the number of users for the proposed CGA-optimized UAV-BS deployment, in comparison with the performance attained by the random UAV-BS deployment. Both deployments are aided by the greedy SINR beam selection. The system has the total transmission power $P_t = 20$ dBm. The position of the mmWave UAV-BS in the random deploy-

ment is randomly chosen in the square area of $[0,100] \times [0,100] \text{ m}^2$. As expected, the CGA-optimized UAV-BS deployment outperforms the random deployment. In particular, for the system with $K = 8$ users, the sum rate attained by the proposed optimized approach is about 5 bits/s/Hz higher than that of the random deployment.

We also evaluate the achievable sum rates as the functions of the transmit power P_t for our CGA-optimized UAV-BS deployment and the random UAV-BS deployment

TABLE 3: Default system parameters.

	Parameter	Value
Network	Height of UAV-BS H	100 m
	Number of transmit antennas at UAV-BS N_t	16
	AWGN σ_n^2	-94 dBm
	Frequency $f_{m,m}$	28 GHz
	LoS parameter α_L	0.95
UAV-BS deployment	Population size P_{dep}	20
	Mutation probability M_{dep}	0.2
	Selection ratio γ_{dep}	0.5
	Number of generation $G_{\text{max,dep}}$	50
	Population size P_{tra}	100
UAV-BS trajectory	Mutation probability M_{tra}	0.05
	Number of time slots N	10
	Maximum speed of UAV-BS v_{max}	50 (m/s)
	Selection ratio γ_{tra}	0.5
	Number of generation $G_{\text{max,tra}}$	50

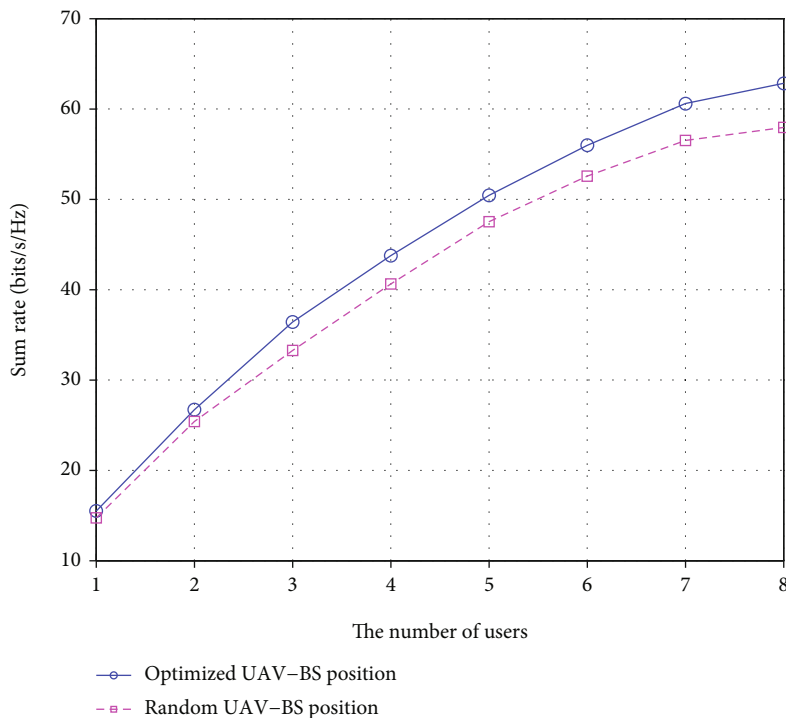


FIGURE 2: Comparison of achievable sum rates versus number of users for the CGA-optimized deployment and random deployment, both with the aid of the greedy SINR beam selection, given total transmission power $P_t = 20$ dBm.

in Figure 3, for the system of $K = 4$ ground users. Again, the greedy SINR beam selection is utilized by both deployments. It can be seen that our CGA-optimized UAV-BS deployment outperforms the random deployment by around 8 bits/s/Hz.

Next, we investigate the convergence performance of the proposed CGA with the aid of the greedy SINR beam selection for UAV-BS deployment. The system has $K = 4$ ground users with the total transmission power $P_t = 20$ dBm. Figure 4 depicts the maximum sum rate and the mean sum

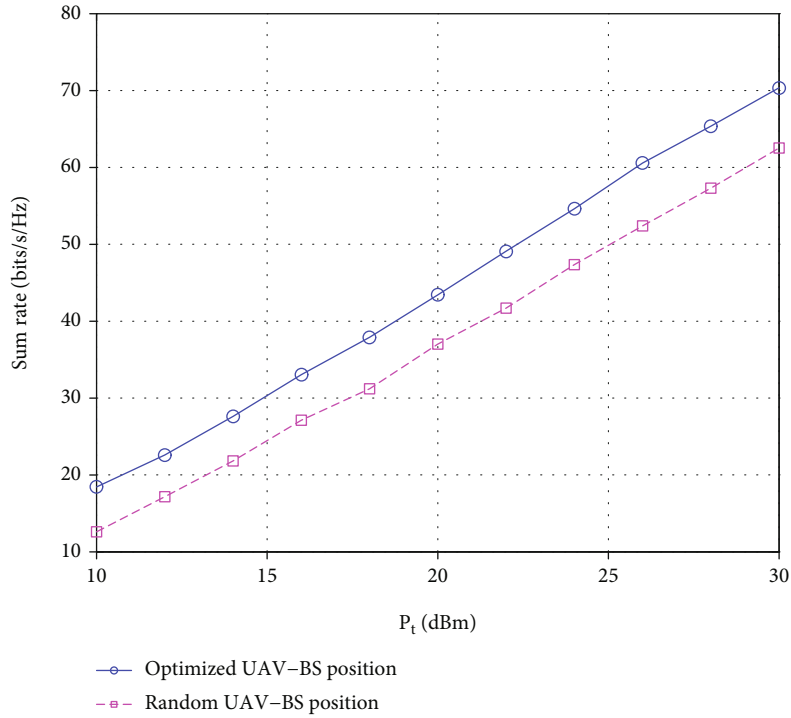


FIGURE 3: Comparison of achievable sum rates versus total transmit power P_t for the CGA-optimized deployment and random deployment, both with the aid of the greedy SINR beam selection, given $K = 4$ ground users.

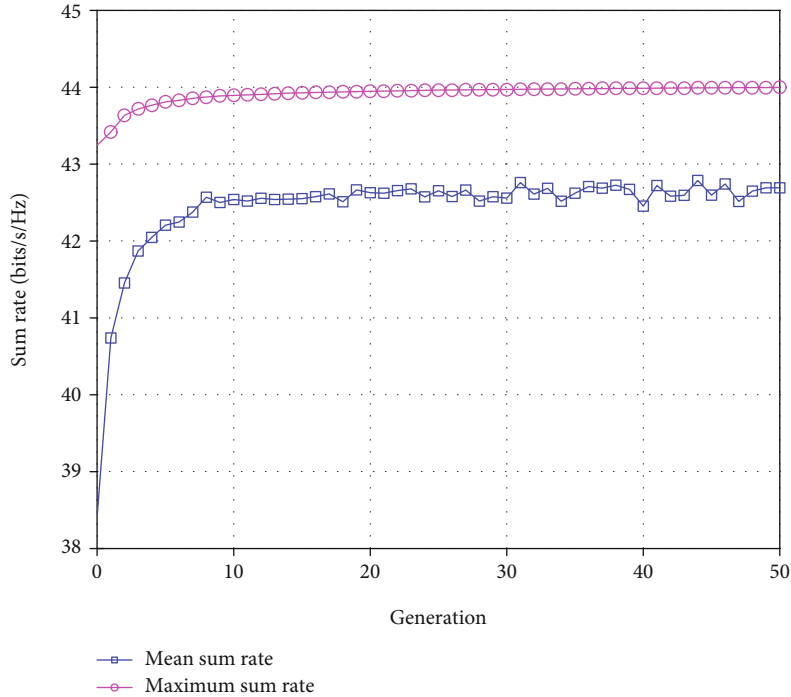


FIGURE 4: Convergence performance of the CGA with the aid of greedy SINR beam selection for optimizing UAV-BS deployment, averaged over 100 runs. The system has $K = 4$ ground users and total transmission power $P_t = 20$ dBm.

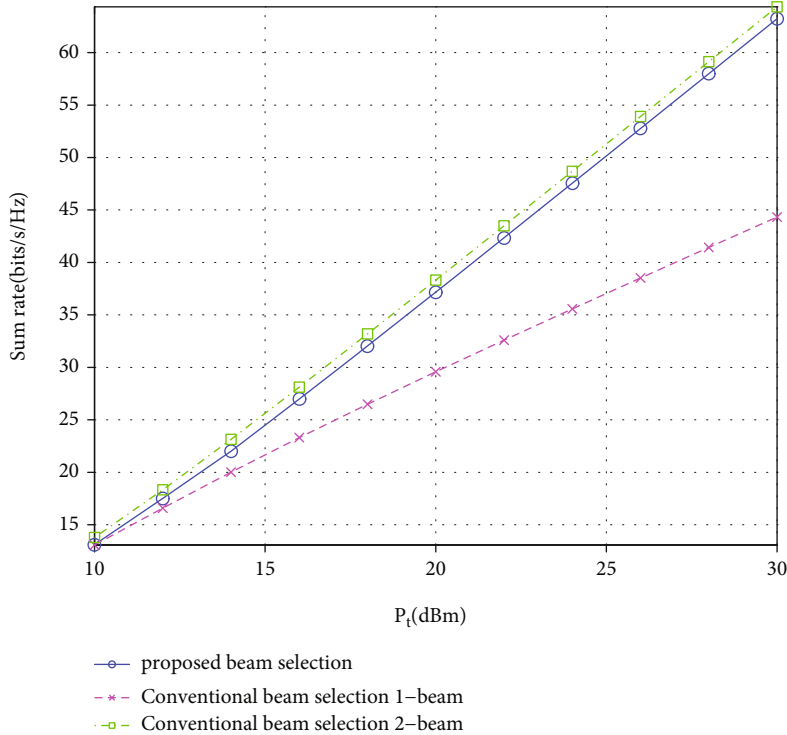


FIGURE 5: Comparison of achievable sum rates versus total transmit power P_t for three beam selection schemes. The system has $K = 4$ ground users, and the UAV-BS is deployed at the CGA-optimized position.

rate of the population as the function of the number of generations, averaged over 100 independent deployments. It can be observed from Figure 4 that the CGA converges within 30 generations.

Our greedy SINR beam selection scheme selects one beam per user by incrementally maximizing the SINR, and it requires $N_{\text{RF}} = K$ RF chains. The maximum channel magnitude selection (MCMS) scheme in [43] is selected as a reference to the proposed greedy SINR beam selection scheme. For the MCMS scheme, by calculating the $|h_{b,k}^i|$ for each beam, m strongest beams can be chosen for each user. To demonstrate its effectiveness, we compare its sum rate performance versus the system transmit power P_t with those of the MCMS scheme with 1 beam per user and 2 beams per user. Again, the system has $K = 4$ ground users. For fair comparison, the CGA-optimized UAV-BS position is used for all the three cases. To mitigate MUI and for a fair comparison, the ZF precoding is also employed in the MCMS scheme. The MCMS scheme chooses the required number of dominant beams for each user, which may result in selecting the same beam for different users. Note that for the scheme with 2 beams per user, the required RF chains are $N_{\text{RF}} = 2K$. Figure 5 compares the sum rate performance of these three beam selection schemes as the functions of the transmission power P_t . Observe that our proposed beam selection scheme, which has 1 beam per user, significantly outperforms the MCMS scheme with 1 beam per user. Given $P_t = 25$ dBm, for example, the sum rate of our greedy SINR selection scheme is 13 bits/s/Hz higher than that of the

latter. This is because this MCMS scheme selects the strongest beam of each user. But some users may share the same strongest beam, and hence, this scheme may result in interference from selecting the same beams for different users. It was further observed that the sum rate of the MCMS scheme with 2 beams per user is only marginally better than that of our greedy SINR selection scheme of 1 beam per user. This is because although utilizing the second strongest beam for each user is beneficial for enhancing the achievable rate of the individual user, some second strongest beams may be shared by different users too, resulting in the increased interference. Hence, the performance gain of the MCMS scheme by using 2 beams per user is very slight compared with our greedy SINR beam selection scheme.

In order to see the trade-off between sum rate performance and RF complexity, we need to investigate the transmit energy efficiency, which is defined by [47]

$$\eta = \frac{R}{P_t + N_{\text{RF}} \cdot P_{\text{RF}}} \text{ (bits/s/Hz/W)}, \quad (35)$$

where R (bits/s/Hz) is the sum rate and P_{RF} (W) represents the power consumed in each RF chain, and $P_{\text{RF}} = 34.4$ mW is adopted as the practical value [47]. For the same system setup as in Figures 5 and 6, compare the energy efficiency against the total transmit power P_t achieved by the three beam selection schemes. As observed from Figure 6, the energy efficiency of the MCMS scheme with 2 beams per user is far inferior to that of its counterpart of 1 beam per

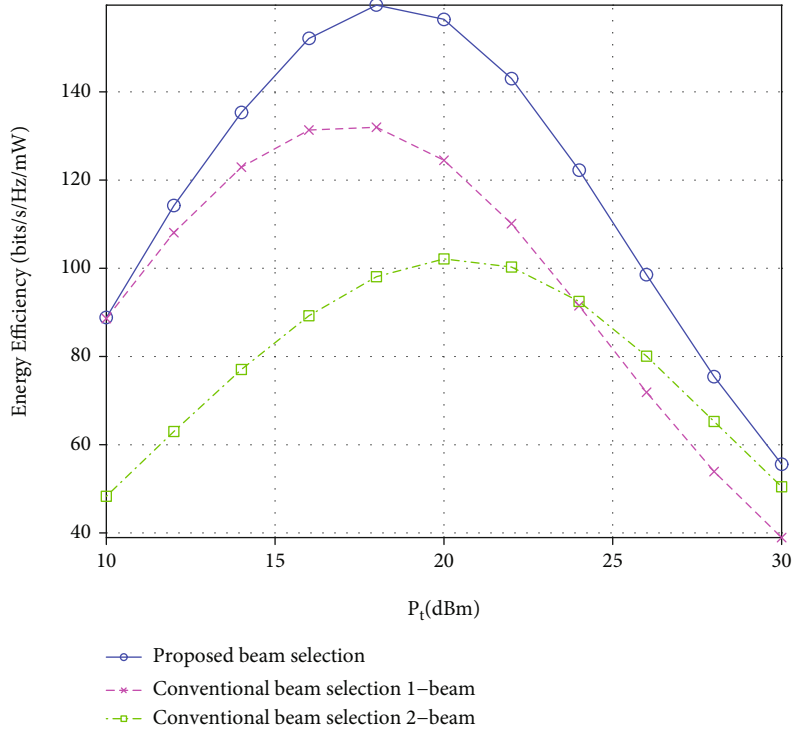


FIGURE 6: Comparison of energy efficiency performance versus total transmit power P_t for three beam selection schemes. The system has $K = 4$ ground users, and the UAV-BS is deployed at the CGA-optimized position.

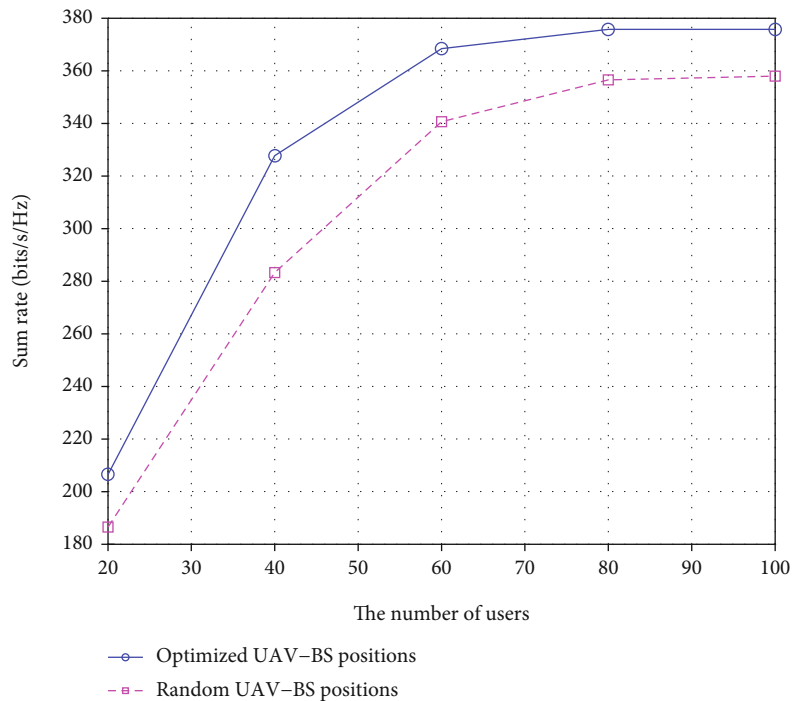


FIGURE 7: Comparison of achievable sum rates versus number of users for the CGA-optimized deployment and random deployment, both with the aid of the greedy SINR beam selection, given total transmission power $P_t = 20$ dBm and $N_t = 256$.

user, except for high P_t situation. Our greedy SINR selection scheme with 1 beam per user significantly outperforms both MCMS schemes, in terms of energy efficiency. In particular,

for $P_t = 20$ dB, although the sum rate of the MCMS scheme with 2 beams per user is about 1 bit/s/Hz better than that of our scheme of 1 beam per user, as shown in Figure 5,

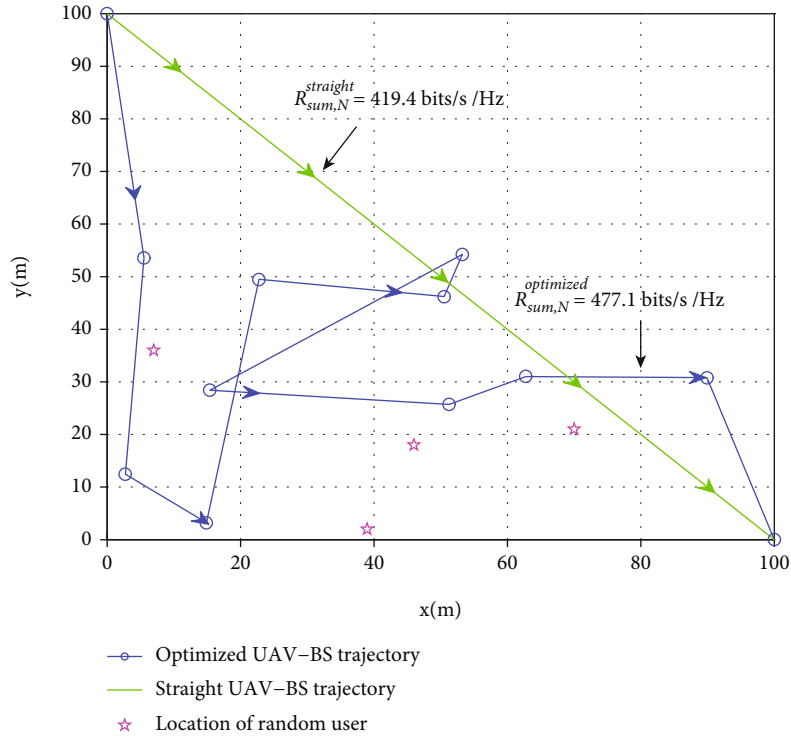


FIGURE 8: Comparison of the CGA-optimized UAV-BS trajectory and the shortest straight-line UAV-BS trajectory, both with the aid of the greedy SINR beam selection scheme. The system has $K = 4$ ground users, and the transmit power per time slot is $P_{t1} = 20 \text{ dBm}$.

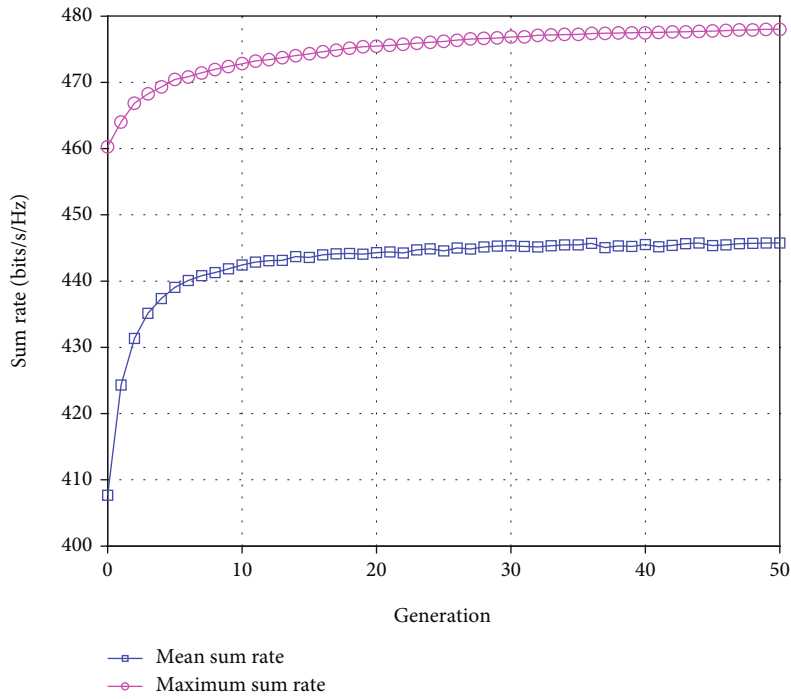


FIGURE 9: Convergence performance of the CGA with the aid of greedy SINR beam selection for optimizing UAV-BS trajectory, averaged over 100 runs. The system has $K = 4$ ground users, and transmit power per time slot is $P_{t1} = 20 \text{ dBm}$.

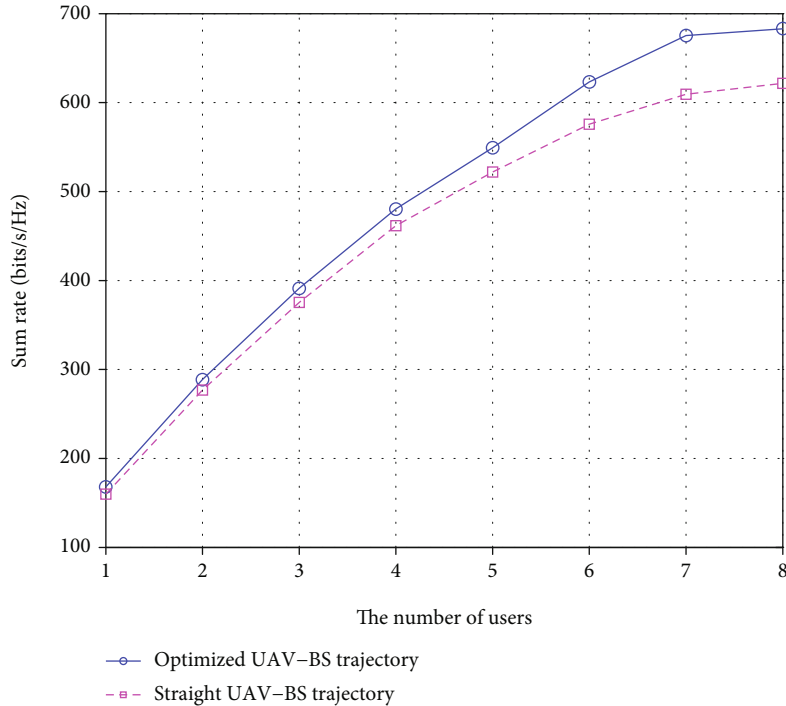


FIGURE 10: Comparison of achievable sum rates versus number of users for the CGA-optimized UAV-BS trajectory and straight-line UAV-BS trajectory, both with the aid of greedy SINR beam selection, given transmit power per time slot $P_{t1} = 20$ dBm.

the energy efficiency of our greedy SINR beam selection scheme is 57 bits/s/Hz/mW higher than that of the former.

Figure 7 shows the achievable sum rate of the proposed CGA-optimized UAV-BS deployment and the random UAV-BS deployment when $N_t = 256$. Both deployments are aided by the greedy SINR beam selection. The system has the total transmission power $P_t = 20$ dBm. As shown in Figure 7, when the number of users is 100, the sum rate of the CGA-optimized UAV-BS deployment is better than that of the random deployment. It can conclude that the proposed CGA-optimized UAV-BS deployment is still robust when the number of users is 100.

4.2. Performance of the CGA for UAV-BS Trajectory. In the first experiment, there are $K = 4$ randomly located ground users, whose locations are indicated in Figure 8. The UAV-BS flying trajectory starts from $\mathbf{q}_I = [0100]^T$ and ends at $\mathbf{q}_F = [1000]^T$. The transmit power of the UAV-BS for each time slot is $P_{t1} = 20$ dBm. Figure 8 depicts the CGA-optimized UAV-BS trajectory and the straight-line UAV-BS trajectory, both with the aid of the greedy SINR beam selection scheme. For the CGA-optimized UAV-BS trajectory, the UAV-BS is able to serve the ground users better by flying closer to them to achieve a higher sum rate. Specifically, the sum rate of the CGA-optimized UAV-BS trajectory is more than 57 bits/s/Hz higher than that achieved by the straight-line trajectory.

In Figure 9, we investigate the convergence performance of the CGA for optimizing UAV-BS trajectory with the aid of the greedy SINR beam selection scheme for the same

system of $K = 4$ ground users with the transmit power per time slot $P_{t1} = 20$ dBm. The curves of the maximum sum rate and mean sum rate in Figure 9 are averaged over 100 runs. It can be seen that the CGA converges within 50 generations. Evidently, the UAV-BS trajectory optimization is much more challenging than the UAV-BS deployment optimization.

Figure 10 compares the achievable sum rates as the functions of the number of users K for the CGA-optimized UAV-BS trajectory and the straight-line UAV-BS trajectory, both adopting the greedy SINR beam selection. The transmit power per time slot is $P_{t1} = 20$ dBm. The UAV-BS's initial and final coordinates are $\mathbf{q}_I = [0100]^T$ and $\mathbf{q}_F = [1000]^T$, respectively. As shown in Figure 10, the CGA-optimized UAV-BS trajectory outperforms the straight-line UAV-BS trajectory considerably. Furthermore, the sum rate gain of the CGA-optimized UAV-BS trajectory over the straight-line UAV-BS trajectory increases with K .

Figure 11 compares the achievable sum rates as the functions of transmit power per time slot P_{t1} for the CGA-optimized UAV-BS trajectory and the straight-line UAV-BS trajectory, both adopting the greedy SINR beam selection. $K = 4$ ground users are randomly distributed in the square area of $[0,100] \times [0,100] \text{ m}^2$. From the results of Figure 11, we observe that the sum rate of the CGA-optimized UAV-BS trajectory is consistently more than 60 bits/s/Hz higher than that achieved by the straight-line UAV-BS trajectory, over the whole range of P_{t1} evaluated. When the target sum rate is 600 bits/s/Hz, the CGA-optimized UAV-BS trajectory attains 2.5 dBm gain in P_{t1} compared with the straight-line UAV-BS trajectory.

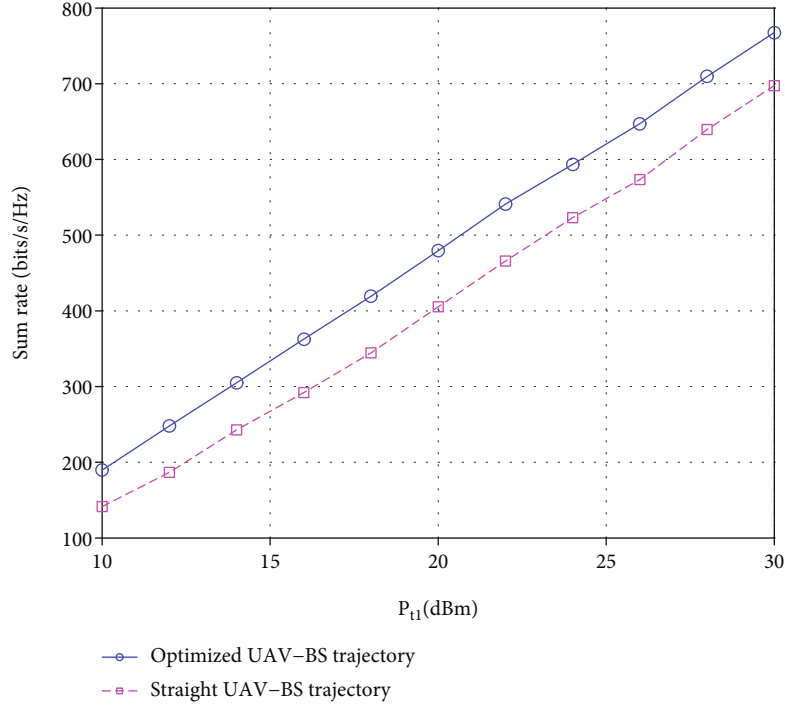


FIGURE 11: Comparison of achievable sum rates versus transmit power per time slot P_{t1} for the CGA-optimized UAV-BS trajectory and straight-line UAV-BS trajectory, both adopting greedy SINR beam selection. The system has $K = 4$ ground users.

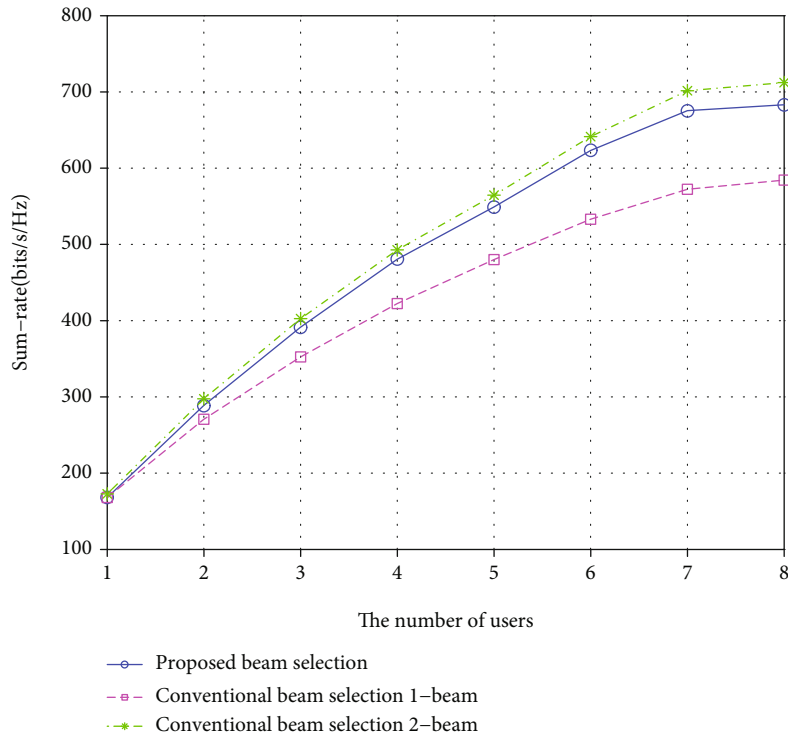


FIGURE 12: Comparison of sum rates versus number of users K for three beam selection schemes, given the system with the CGA-optimized UAV-BS trajectory and transmit power per time slot $P_{t1} = 20$ dBm.

For the system adopting the CGA-optimized UAV-BS trajectory with the transmit power per time slot $P_{t1} = 20$ dBm, Figure 12 compares the sum rates versus the number

of ground users for the three beam selection schemes, namely, the proposed greedy SINR beam selection with 1 beam per user as well as the MCMS scheme with 1 beam

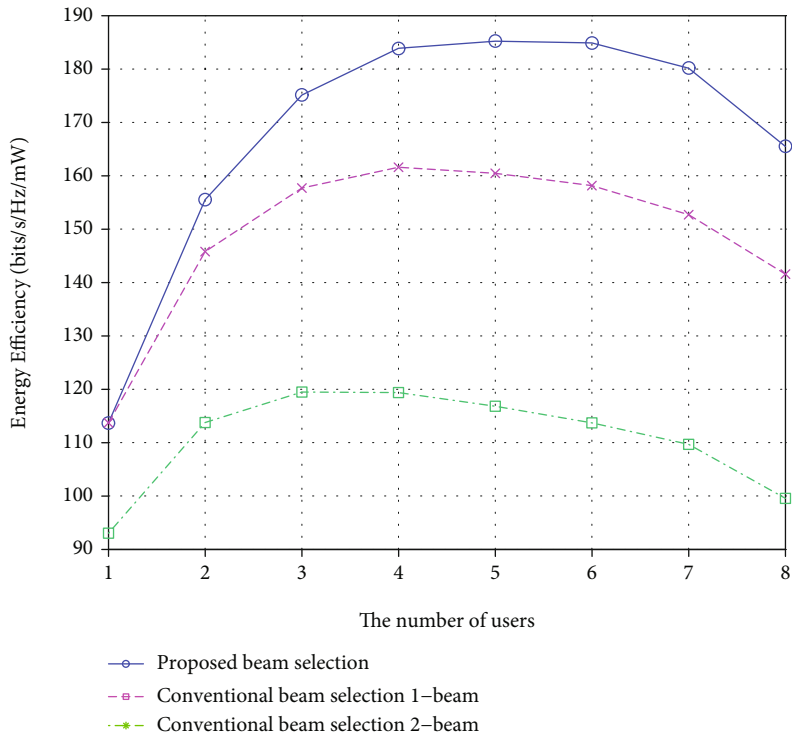


FIGURE 13: Comparison of energy efficiency performance versus number of users for three beam selection schemes for the system with the CGA-optimized UAV-BS trajectory and transmit power per time slot $P_{t1} = 20$ dBm.

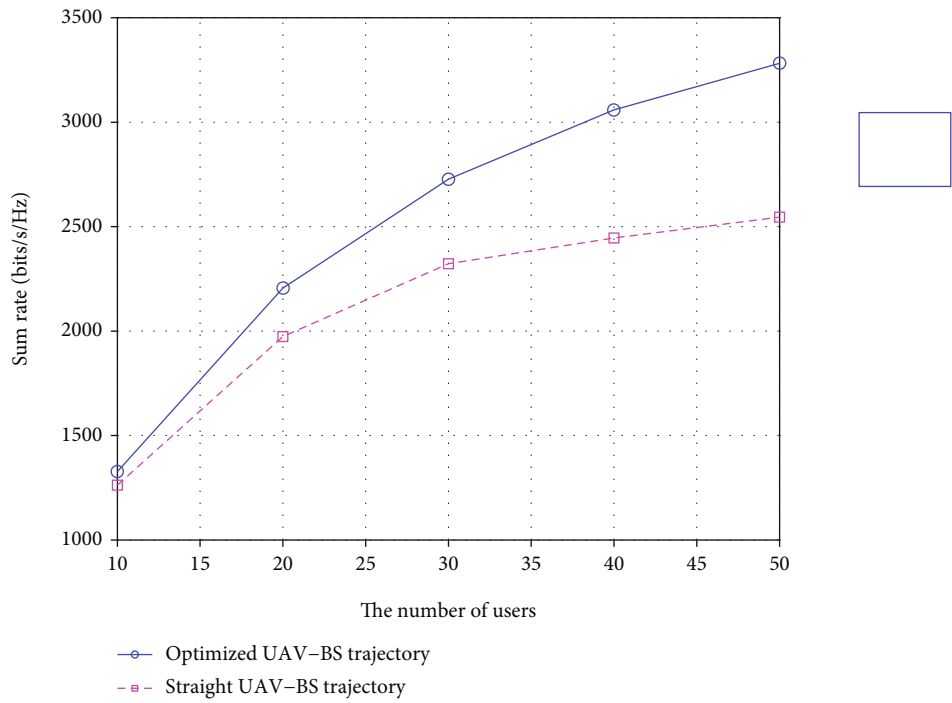


FIGURE 14: Comparison of achievable sum rates versus number of users for the CGA-optimized UAV-BS trajectory and straight-line UAV-BS trajectory, both with the aid of greedy SINR beam selection, given transmit power per time slot $P_{t1} = 20$ dBm and $N_t = 256$.

per user and 2 beams per user. It can be seen from Figure 12 that the MCMS scheme with 2 beams per user achieves a slightly better sum rate than our greedy SINR beam selection scheme with 1 beam per user, while our beam selection scheme significantly outperforms the MCMS scheme with 1 beam per user, in terms of sum rate. Our greedy SINR beam selection is the most energy-efficient scheme, while the MCMS scheme with 2 beams per user has the worst energy efficiency, as shown in Figure 13.

Figure 14 compares the achievable sum rates of the CGA-optimized UAV-BS trajectory and the straight-line UAV-BS trajectory with $N_t = 256$. Both schemes employ the greedy SINR beam selection. The transmit power per time slot is $P_{t1} = 20$ dBm. The UAV-BS's initial and final coordinates are $\mathbf{q}_I = [0100]^T$ and $\mathbf{q}_F = [1000]^T$, respectively. As shown in Figure 10, when the number of users is 50, the sum rate of the CGA-optimized UAV-BS trajectory outperforms that of the straight-line UAV-BS trajectory.

5. Conclusions

In this paper, we have investigated the challenging problems of optimizing the UAV-BS deployment and the UAV-BS trajectory in mmWave systems. We have formulated the optimal deployment/trajectory problem as the one that maximizes the sum rate among the ground users subject to the deployment/trajectory constraints. To solve this highly complex and nonconvex problem, we have decomposed it into two subproblems. First, we have proposed a greedy SINR beam selection scheme for the mmWave UAV-BS multiuser system with one beam per user. Specifically, the users with the unique nonsharing dominant beams use their dominant beams, while the other users select the beams by incrementally maximizing the SINR. With the aid of this greedy SINR beam selection, we have proposed to use the CGA to solve the deployment/trajectory optimization problem to maximize the sum rate. The sum rate and energy efficiency as well as convergence performance have been evaluated for the proposed CGA-optimized UAV-BS deployment and CGA-optimized UAV-BS trajectory. Our studies have demonstrated that the proposed solutions achieve excellent performance, in terms of both sum rate and energy efficiency. The results have also shown that the CGA converges sufficiently fast even for the very challenging UAV-BS trajectory optimization.

Our future work will consider that each user is equipped with multiple antennas. The receive beamforming and beam selection can be designed to compensate for the path loss in mmWave frequency.

Data Availability

The simulation data used to support the findings of this study are included within the article. The MATLAB code data used to support the findings of this study are available from the corresponding author upon request.

Conflicts of Interest

The authors declare that they have no conflicts of interest.

References

- [1] Z. Xiao, P. Xia, and X.-G. Xia, "Enabling UAV cellular with millimeter-wave communication: potentials and approaches," *IEEE Communications Magazine*, vol. 54, no. 5, pp. 66–73, 2016.
- [2] J. Zhang, T. Chen, S. Zhong et al., "Aeronautical *ad hoc* networking for the internet-above-the-clouds," *Proceedings of the IEEE*, vol. 107, no. 5, pp. 868–911, 2019.
- [3] Y. Zeng, R. Zhang, and T. J. Lim, "Wireless communications with unmanned aerial vehicles: opportunities and challenges," *IEEE Communications Magazine*, vol. 54, no. 5, pp. 36–42, 2016.
- [4] X. Li, Q. Wang, Y. Liu, T. A. Tsiftsis, Z. Ding, and A. Nallanathan, "UAV-aided multi-way NOMA networks with residual hardware impairments," *IEEE Wireless Communications Letters*, vol. 9, no. 9, pp. 1538–1542, 2020.
- [5] C. Pan, H. Ren, Y. Deng, M. ElKashlan, and A. Nallanathan, "Joint blocklength and location optimization for URLLC-enabled UAV relay systems," *IEEE Communications Letters*, vol. 23, no. 3, pp. 498–501, 2019.
- [6] Z. Yang, C. Pan, K. Wang, and M. Shikh-Bahaei, "Energy efficient resource allocation in UAV-enabled mobile edge computing networks," *IEEE Transactions on Wireless Communications*, vol. 18, no. 9, pp. 4576–4589, 2019.
- [7] M. M. Azari, F. Rosas, K.-C. Chen, and S. Pollin, "Optimal UAV positioning for terrestrial-aerial communication in presence of fading," in *Proc. GLOBECOM 2016*, pp. 1–7, Washington, DC, USA, 2016.
- [8] X. Xi, X. Cao, P. Yang, J. Chen, T. Quek, and D. Wu, "Joint user association and UAV location optimization for UAV-aided communications," *IEEE Wireless Communications Letters*, vol. 8, no. 6, pp. 1688–1691, 2019.
- [9] M. Alzenad, A. El-Keyi, F. Lagum, and H. Yanikomeroglu, "3-D placement of an unmanned aerial vehicle base station (UAV-BS) for energy-efficient maximal coverage," *IEEE Wireless Communications Letters*, vol. 6, no. 4, pp. 434–437, 2017.
- [10] Q. Wu, Y. Zeng, and R. Zhang, "Joint trajectory and communication design for multi-UAV enabled wireless networks," *IEEE Transactions on Wireless Communications*, vol. 17, no. 3, pp. 2109–2121, 2018.
- [11] Y. Cai, F. Cui, Q. Shi, M. Zhao, and G. Y. Li, "Dual-UAV-enabled secure communications: joint trajectory design and user scheduling," *IEEE Journal on Selected Areas in Communications*, vol. 36, no. 9, pp. 1972–1985, 2018.
- [12] N. Zhao, X. Pang, Z. Li et al., "Joint trajectory and precoding optimization for UAV-assisted NOMA networks," *IEEE Transactions on Communications*, vol. 67, no. 5, pp. 3723–3735, 2019.
- [13] Y. Zeng and R. Zhang, "Energy-efficient UAV communication with trajectory optimization," *IEEE Transactions on Wireless Communications*, vol. 16, no. 6, pp. 3747–3760, 2017.
- [14] M. R. Akdeniz, Y. Liu, M. K. Samimi et al., "Millimeter wave channel modeling and cellular capacity evaluation," *IEEE Journal on Selected Areas in Communications*, vol. 32, no. 6, pp. 1164–1179, 2014.
- [15] S. Rangan, T. S. Rappaport, and E. Erkip, "Millimeter-wave cellular wireless networks: potentials and challenges," *Proceedings of the IEEE*, vol. 102, no. 3, pp. 366–385, 2014.
- [16] C. Zhang, W. Zhang, W. Wang, L. Yang, and W. Zhang, "Research challenges and opportunities of UAV millimeter-

- wave communications,” *IEEE Wireless Communications*, vol. 26, no. 1, pp. 58–62, 2019.
- [17] M. Mozaffari, W. Saad, M. Bennis, Y. H. Nam, and M. Debbah, “A tutorial on UAVs for wireless networks: applications, challenges, and open problems,” *IEEE Communications Surveys and Tutorials*, vol. 21, no. 3, pp. 2334–2360, 2019.
- [18] L. Zhu, J. Zhang, Z. Xiao, X. Cao, D. O. Wu, and X. G. Xia, “3-D beamforming for flexible coverage in millimeter-wave UAV communications,” *IEEE Wireless Communications Letters*, vol. 8, no. 3, pp. 837–840, 2019.
- [19] N. Tafintsev, M. Gerasimenko, D. Moltchanov et al., “Improved network coverage with adaptive navigation of mmWave-based drone-cells,” in *Proc. GLOBECOM 2018 Workshops*, pp. 1–7, Abu Dhabi, United Arab Emirates, 2018.
- [20] M. Gapeyenko, I. Bor-Yaliniz, S. Andreev, H. Yanikomeroglu, and Y. Koucheryavy, “Effects of blockage in deploying mmWave drone base stations for 5G networks and beyond,” in *Proc. ICC 2018 Workshops*, pp. 1–6, Kansas City, MO, USA, 2018.
- [21] Z. Xiao, H. Dong, L. Bai, D. O. Wu, and X. G. Xia, “Unmanned aerial vehicle base station (UAV-BS) deployment with millimeter-wave beamforming,” *IEEE Internet of Things Journal*, vol. 7, no. 2, pp. 1336–1349, 2020.
- [22] X. Li, M. Zhao, M. Zeng et al., “Hardware impaired ambient backscatter NOMA systems: reliability and security,” *IEEE Transactions on Communications*, vol. 69, no. 4, pp. 2723–2736, 2021.
- [23] R. Jia, X. Chen, C. Zhong, D. W. Ng, H. Lin, and Z. Zhang, “Design of non-orthogonal beamspace multiple access for cellular Internet-of-things,” *IEEE Journal of Selected Topics in Signal Processing*, vol. 13, no. 3, pp. 538–552, 2019.
- [24] J. Brady, N. Behdad, and A. M. Sayeed, “Beamspace MIMO for millimeter-wave communications: system architecture, modeling, analysis, and measurements,” *Institute of Electrical and Electronics Engineers*, vol. 61, no. 7, pp. 3814–3827, 2013.
- [25] X. Gao, L. Dai, Z. Chen, Z. Wang, and Z. Zhang, “Near-optimal beam selection for beamspace mmWave massive MIMO systems,” *IEEE Communications Letters*, vol. 20, no. 5, pp. 1054–1057, 2016.
- [26] P. V. Amadori and C. Masouros, “Low RF-complexity millimeter-wave beamspace-MIMO systems by beam selection,” *IEEE Transactions on Communications*, vol. 63, no. 6, pp. 2212–2223, 2015.
- [27] C. Sun, X. Gao, and Z. Ding, “BDMA in multicell massive MIMO communications: power allocation algorithms,” *IEEE Transactions on Signal Processing*, vol. 65, no. 11, pp. 2962–2974, 2017.
- [28] Z. Jiang, S. Zhou, and Z. Niu, “Optimal discrete spatial compression for beamspace massive MIMO signals,” *IEEE Transactions on Signal Processing*, vol. 66, no. 9, pp. 2480–2493, 2018.
- [29] S. Chen, Y. Wu, and S. McLaughlin, “Genetic algorithm optimization for blind channel identification with higher order cumulant fitting,” *IEEE Transactions on Evolutionary Computation*, vol. 1, no. 4, pp. 259–265, 1997.
- [30] K. Yen and L. Hanzo, “Genetic algorithm assisted joint multiuser symbol detection and fading channel estimation for synchronous CDMA systems,” *IEEE Journal on Selected Areas in Communications*, vol. 19, no. 6, pp. 985–998, 2001.
- [31] J. Zhang, S. Chen, X. Mu, and L. Hanzo, “Evolutionary-algorithm-assisted joint channel estimation and turbo multiuser detection/decoding for OFDM/SDMA,” *IEEE Transactions on Vehicular Technology*, vol. 63, no. 3, pp. 1204–1222, 2014.
- [32] R. L. Haupt and S. E. Haupt, *Practical Genetic Algorithms*, John Wiley & Sons, New Jersey, USA, 2nd edition, 2004.
- [33] F. Al-Turjman, J. P. Lemayian, S. Alturjman, and L. Mostarda, “Enhanced deployment strategy for the 5G drone-BS using artificial intelligence,” *IEEE Access*, vol. 7, pp. 75999–76008, 2019.
- [34] H. Ren, C. Pan, K. Wang, Y. Deng, M. ElKashlan, and A. Nallanathan, “Achievable data rate for URLLC-enabled UAV systems with 3-D channel model,” *IEEE Wireless Communications Letters*, vol. 8, no. 6, pp. 1587–1590, 2019.
- [35] Z. Xiao, L. Zhu, J. Choi, P. Xia, and X. G. Xia, “Joint power allocation and beamforming for non-orthogonal multiple access (NOMA) in 5G millimeter wave communications,” *IEEE Transactions on Wireless Communications*, vol. 17, no. 5, pp. 2961–2974, 2018.
- [36] A. Alkhateeb, O. El Ayach, G. Leus, and R. W. Heath, “Channel estimation and hybrid precoding for millimeter wave cellular systems,” *IEEE Journal of Selected Topics in Signal Processing*, vol. 8, no. 5, pp. 831–846, 2014.
- [37] T. S. Rappaport, Y. Xing, M. C. GR, A. F. Molisch, E. Mellios, and J. Zhang, “Overview of millimeter wave communications for fifth-generation (5G) wireless networks—with a focus on propagation models,” *Institute of Electrical and Electronics Engineers*, vol. 65, no. 12, pp. 6213–6230, 2017.
- [38] C. Yan, L. Fu, J. Zhang, and J. Wang, “A comprehensive survey on UAV communication channel modeling,” *IEEE Access*, vol. 7, pp. 107769–107792, 2019.
- [39] Y. Zeng, J. Xu, and R. Zhang, “Energy minimization for wireless communication with rotary-wing UAV,” *IEEE Transactions on Wireless Communications*, vol. 18, no. 4, pp. 2329–2345, 2019.
- [40] D. Tse and P. Viswanath, *Fundamentals of Wireless Communication*, Cambridge University Press, Cambridge, U.K., 2005.
- [41] A. M. Sayeed and N. Behdad, “Continuous aperture phased MIMO: a new architecture for optimum line-of-sight links,” in *Proc. APSURSI 2011*, pp. 293–296, Spokane, WA, USA, 2011.
- [42] A. M. Sayeed, “Deconstructing multiantenna fading channels,” *IEEE Transactions on Signal Processing*, vol. 50, no. 10, pp. 2563–2579, 2002.
- [43] A. Sayeed and J. Brady, “Beamspace MIMO for high-dimensional multiuser communication at millimeter-wave frequencies,” in *Proc. GLOBECOM 2013*, pp. 3679–3684, Atlanta, GA, USA, 2013.
- [44] C. Masouros, M. Sellathurai, and T. Ratnarajah, “Large-scale MIMO transmitters in fixed physical spaces: the effect of transmit correlation and mutual coupling,” *IEEE Transactions on Communications*, vol. 61, no. 7, pp. 2794–2804, 2013.
- [45] M. Mitchell, *An Introduction to Genetic Algorithms*, MIT press, Cambridge, MA, 1998.
- [46] L. Hanzo, L.-L. Yang, E. Kuan, and K. Yen, *Single- and Multi-Carrier DS-CDMA: Multi-User Detection, Space-Time Spreading, Synchronisation, Networking and Standards*, John Wiley & Sons, New Jersey, USA, 2003.
- [47] C. Masouros, M. Sellathurai, and T. Ratnarajah, “Computationally efficient vector perturbation precoding using thresholded optimization,” *IEEE Transactions on Communications*, vol. 61, no. 5, pp. 1880–1890, 2013.

Review Article

A Survey on Transmission Schemes on Large-Scale Internet of Things with Nonorthogonal Multiple Access

Wenyu Zhou,¹ Rui Zhao ,² Fusheng Zhu ,³ Lijia Lai ,² and Xutao Li⁴

¹School of Management, Hefei University of Technology, Hefei, Anhui, China

²School of Computer Science, Guangzhou University, Guangzhou, China

³Guangdong New Generation Communication and Network Innovative Institute (GDCNi), Guangzhou, China

⁴Department of Electronic Engineering, Shantou University, Shantou, Guangdong, China

Correspondence should be addressed to Rui Zhao; 2111806073@e.gzhu.edu.cn and Fusheng Zhu; zhufusheng@gdcni.cn

Received 28 July 2021; Revised 28 August 2021; Accepted 4 September 2021; Published 28 September 2021

Academic Editor: Xingwang Li

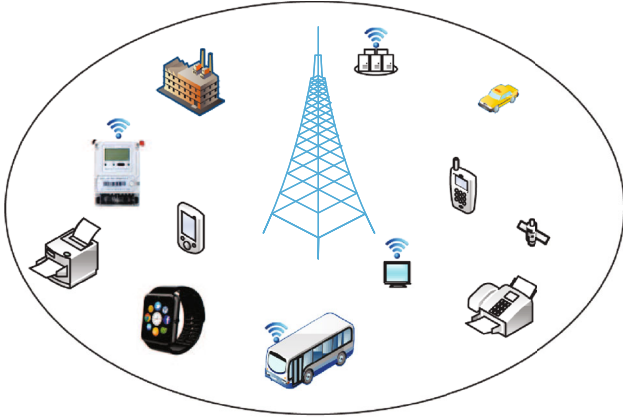
Copyright © 2021 Wenyu Zhou et al. This is an open access article distributed under the Creative Commons Attribution License, which permits unrestricted use, distribution, and reproduction in any medium, provided the original work is properly cited.

This paper performs a comprehensive survey on transmission schemes for the large-scale Internet of things (IoT) networks with nonorthogonal multiple access (NOMA). By solving the interference among users, NOMA can significantly improve the frequency reuse efficiency and support multiple users to use the same frequency resources. It is considered to be one of the most effective technologies for the next-generation wireless communication. However, there are still many challenges on the transmission schemes for the large-scale NOMA system, including the short-data packet transmission, active user detection, channel estimation, and data detection. In order to meet these challenges, this paper first reviews the short-packet transmission in the large-scale NOMA systems and then reviews the active user detection and channel estimation technologies of the considered systems.

1. Introduction

The application of Internet of things (IoT) has promoted a significant increase in data traffic of wireless networks [1–3]. For machine-type communication (MTC) or mission-critical communication (autonomous driving, drones, and augmented/virtual reality), all of them have proposed new development requirements on capacity, latency, reliability, and scalability. In particular, the massive machine-type communication (mMTC) and mass access are considered as two very important scenarios of the fifth-generation (5G) and beyond 5G (B5G) wireless communications [4–8]. As a typical application of mMTC, large-scale IoT-enabled cellular networks are widely used in intelligent buildings, intelligent cities, intelligent medical treatment, factory automation, automatic driving, intelligent meters, and other fields. It has been recognized that large-scale IoT can significantly reduce the system operation cost [9, 10].

As shown in Figure 1, only a short number of unknown users are active at any given time in the large-scale IoT model. This communication mode is mainly designed with the purpose of energy saving. Generally, developing future cellular IoT faces many challenges, such as adapting to more users with low latency requirements, dynamically identifying active users, and reliably receiving their information [11]. For the traditional authorization-based random access scheme, uncoordinated users can compete for physical layer resource blocks for data transmission. Each active user randomly selects one from a set of predefined orthogonal preamble sequences to notify the base station (BS) that the user is active [12, 13]. As to each activation preamble, the BS responds to the corresponding user as permission for the subsequent transmission. Each user who receives a response to its preamble transmission sends a connection request for the required resources of the subsequent data transmission [14–16]. When only one user in the system




 Denoting active users, and others are idle users.

FIGURE 1: System model of large-scale IoT sporadic communications.

selects the current preamble sequence, the BS authorizes the user's connection request and sends a contention resolution message to notify the reserved resource user to send suspended data. If two or more users select the same preamble sequence, the connection request will send conflicts [17–19].

When the BS detects a conflict, it will not reply to the contention resolution message. The affected user restarts the random access process after the timer expires. For the authorized access scheme, the user needs to handshake four times with the BS, which increases the control signaling overhead and latency. On the contrary, users can start data transmission in the unauthorized protocol without shaking hands with the BS, which can meet the low latency requirements of large-scale IoT. In addition, the nonorthogonal multiple access (NOMA) technology allows multiple users to share the same resource block (including time and spectrum resources) to establish more connections.

At present, there are still some challenges, such as the nonorthogonal transmission scheme for short data packets (or short packets), large-scale pilot sequences, active user detection, channel estimation, and multiple optimal design and analysis of user data detection. Recently, it has been recognized that a reliable nonorthogonal transmission scheme and effective multiuser detection can improve the spectrum efficiency of the system. Therefore, the license-free NOMA can effectively combine the low access latency of the license-free protocol with the advantages of large numbers of connections of NOMA and the high spectrum efficiency, which can meet the communication requirements of the large-scale IoT networks that realize the low latency and reliable communication. The cochannel interference of NOMA, especially in the IoT networks with large-scale multiple access, dramatically limits the system performance. Hence, designing an appropriate license-free NOMA scheme is very critical.

Due to the requirements of low transmission latency, the data packet length and pilot sequence of IoT users are limited, the scale of users is enormous, and it is challenging to meet the needs of all users for the orthogonal spectrum

resources and pilot sequence. Therefore, nonorthogonal transmission schemes and nonorthogonal pilot sequences, such as Gaussian and Reed Muller (RM) sequences, have been widely studied. In addition, signal detection plays a vital role in the design of a license-free NOMA system. This is because with no coordination, multiple users can transmit information to BS in parallel and BS needs to detect these signals efficiently. In particular, BS needs to detect signals from some unknown users among a large number of potential users. The signal detection problem of large-scale IoT networks involves three essential parts: identifying active users, channel estimation, and multiuser data detection [20, 21]. The signal detection of large-scale IoT can be divided into two successive stages: channel training and data transmission, in which active user detection, channel estimation, and data decoding will be performed. The paper implementation plan includes the following steps: (1) performing the channel estimation and then performing the joint detection of the data of active users and multiuser and (2) performing the channel estimation and active users jointly and then detecting the multiuser data. For the single-phase transmission scheme, data information is embedded in a pilot sequence or pilot symbols are embedded in a data packet and the BS can jointly detect active users and their data in a phase. This scheme does not require particular channel estimation and can reduce the system overhead and transmission latency. However, the signal transmission and reception scheme need to be carefully designed.

Due to the broadcast characteristics of wireless transmission, ten large-scale IoT networks are vulnerable to interference and attack by illegal users, so physical layer security is very important. In [22, 23], the authors analyze the physical layer security of the cooperative NOMA system and a two-stage relay scheme is proposed. The closed expression of outage probability and the asymptotic expression of outage probability under signal-to-noise ratios (SNRs) are derived. In [24], the authors propose a security-enhanced user pairing scheme under weak security constraints to achieve high-frequency spectral efficiency and weak system confidentiality. In [25], the authors study the outage probability and secret outage probability in two-user NOMA systems. Based on the concept of NOMA, the interruption behavior of trusted users under the constraint of security outage probability is studied.

Most researches on IoT data transmission are based on the Shannon theory [26–29]. In practice, the data packets of IoT users are tiny and different users have different business requirements. In addition, signal detection mainly uses compressed sensing (CS) or linear inversion technology, which ignores the changing characteristics of sparse signals [30–33]. Therefore, researches based on the large-scale IoT transmission characteristics and different business requirements are not systematic and complete. This paper studies the nonorthogonal transmission and signal detection of large-scale IoT from the following three aspects: (1) from the perspective of short-data packet transmission, we design a reliable nonorthogonal transmission scheme for the cellular IoT uplink and downlink and analyze the system error performance and its influencing factors, (2) we study the

characteristics of fast fading of nonzero elements of sparse signals and design efficient and reliable active user detection algorithms to reduce the false alarm rate of IoT user activity detection, thereby improving the utilization of spectrum resources, and (3) from the structural characteristics of double signal sparsity, we use Bayesian inference and optimization theory to design estimation algorithms for the user activity, channel jointly, and data, reducing the pilot overhead for reliable information transmission. However, for the large-scale NOMA, a series of topics such as the design of nonorthogonal transmission scheme with a short data packet, reliable detection algorithm with low complexity, and the reduction of system signaling overhead and transmission latency are very challenging. The problems mentioned above have essential theory and application value for the planning and deploying the large-scale multiple access technology in IoT networks.

2. Recent Progress and Challenges

It is essential to design the large-scale IoT signal transmission and detection solutions to meet a series of requirements such as large-scale connections, reliable transmission of short data packets, high spectrum efficiency, and low signal overhead. In particular, the reliable transmission design and performance analysis of short data packets and the design of large-scale signal detection algorithms are the keys to IoT researches. To fully understand the existing problems and limitations of the IoT research, we will analyze the relevant research status and development of the trend in the following.

2.1. Short-Data Packet Transmission in Large-Scale Multiple Access. In the third-generation partnership project (3GPP) IoT standard, the uplink of the narrow-band IoT (NB-IoT) uses single-carrier frequency division multiple access (SC-FDMA) and the downlink uses orthogonal frequency division multiple access (OFDMA). Although the transmission and reception schemes of IoT can be simplified, the spectrum efficiency of the system is low. Therefore, it is necessary to design new multiple-access schemes to improve IoT network spectrum efficiency further. In fact, the performance of the large-scale IoT networks is determined by the channel estimation, uplink data transmission, and downlink data transmission. At present, some researchers have optimized designs for a system that couples two or three parts of channel estimation, uplink data transmission, and downlink data transmission. In the literature, the researchers considered the channel estimation and uplink data transmission of a single-cell uplink in the large-scale multi-antenna system, jointly optimized the pilot length and transmission power, and then obtained an optimized design with an optimal pilot length equal to the user number [34]. In addition, for the three-stage transmission, a cellular IoT transmission protocol can be designed for large-scale access by optimizing the transmission time of three stages to maximize the rate and speed. They proposed a reliable transmission scheme based on NOMA, analyzed the relationship between packet rate and interruption of the performance, and optimized the

transmission power of the system [35]. Specifically, the current optimized design for IoT uplink and downlink data transmission is based on the Shannon theory which is given by [36],

$$C = \log_2(1 + \gamma), \quad (1)$$

where γ represents the received SNR. Although the Shannon theory defines the theoretical upper bound of the communication rate without transmission error, it theoretically requires an infinite amount of code to implement. In practice, the amount of data transmitted by IoT users is short and the short-packet transmission requires a low transmission latency. Therefore, the Shannon capacity cannot accurately characterize the reliability and latency of the large-scale IoT short-data packet transmission.

To accurately describe the channel capacity under the finite code length, the finite coding system can be designed for the additive white Gaussian noise (AWGN) channel. The approximate relationship between the achievable rate r , the code length L , and the packet error rate ε can be derived as

$$r \approx \log_2(1 + \gamma) - \sqrt{\frac{1}{L} \left(1 - \frac{1}{(1 + \gamma)^2}\right)} \frac{Q^{-1}(\varepsilon)}{\ln 2}, \quad (2)$$

where $Q^{-1}(\bullet)$ is the inverse function of function $Q(x) = \int_x^{+\infty} 1/\sqrt{2\pi}e^{-t^2/2} dt$. Although equation (2) is an approximation of the upper bound of the achievable rate under a finite code length, most of existing researches have verified that equation (2) is very accurate.

For the research on the nonorthogonal transmission system of short packets of large-scale IoT, there is still no complete theoretical framework and the design and performance analysis of the large-scale IoT short-data packet nonorthogonal transmission scheme based on the finite coding has not been studied. The influence of channel estimation error propagation, data encoding length, and the number of message bits on system performance are also to be further studied.

2.2. Active User Detection and Channel Estimation for Large-Scale Multiple Access. In order to estimate the active users and their channel information, a practical approach is to use the ‘‘sporadic’’ nature of the large-scale IoT communication to model the received signal in the training phase as a sparse signal recovery problem and then solve the problem based on the CS technology or a Bayesian inference framework. In [37], Du et al. considered a joint design scheme for the active user detection and channel estimation for a single antenna system, where the received pilot signal is portrayed as a single measurement vector problem. They proposed a joint iterative algorithm based on the message passing and block sparse Bayesian learning to design high-precision and low-complexity algorithms to solve the sparse signal recovery problem. In addition, for a system with analog-to-digital converters (ADC), He et al. [38] proposed an active user detection and channel estimation based on a

generalized expectation-consistent signal recovery algorithm, which allows the output mapping of the signal to be of the arbitrary form. The above findings show that the single antenna system can serve thousands of IoT users and requires long lead sequences. Therefore, the large-scale antenna system is considered to improve system connectivity. The joint active user detection and channel estimation problem for the large-scale receive antenna system is described as a multiple measurement vector problem [39]. The authors use the approximate message passing (AMP) algorithm with multiple measurement vectors to solve the problem and use the approximate message passing algorithm based on state evolution to analyze the limiting performance of the system.

However, most of the existing algorithms for active user detection are based on the derivative frequency matrix, which satisfies the finite isometric property or has low inter-correlation. In addition, the active user detection algorithm is based on the prior distribution of the large-scale fading of the user or the exact large-scale fading information. In practice, the AMP and the CS-based active user detection algorithms are not suitable for highly correlated derivative matrices and the oversampled discrete cosine transform matrix has very high intercorrelation under individual parameters. In contrast, the AMP algorithm performs poorly in the same setting. In addition, during the active user detection and channel estimation phase, it is not practical to assume that the statistical characteristics of the channel are known to the receiver.

Based on the in-depth analysis of the sparse structure of the received signal in a large-scale multiple access system, the design of active user detection and channel estimation scheme is of great significance for further improving the accuracy of active user detection. However, there is little research on this aspect.

2.3. Data Detection Algorithms for Large-Scale Multi Access.

In the large-scale IoT network based on unauthorized NOMA, multiuser data detection plays a vital role, as multiple users can transmit data simultaneously without coordination [40]. Although only a tiny fraction of users is active, the potential user base is large. Hence, the BS needs to obtain a priori information of the data detection of multiple users with the unknown active user. Moreover, two factors need to be considered when designing a data detection scheme for the large-scale multiple access. On the one hand, the impact of the active user detection and the accuracy of the channel estimation on the data detection give a large number of potential users. On the other hand, the computational complexity of the algorithm is reduced while ensuring the accuracy of the algorithm.

In the large-scale IoT networks, the multiuser data detection involves two key components, the active user detection and the channel estimation. In [41], the authors jointly designed the algorithm which can detect the low-complexity active user and data under the assumption that the complete channel information is known [42]. To characterize the impact of incomplete channel information on the multiuser data detection, Liu et al. [43] first jointly designed

the active user detection and channel estimation algorithm, based on the estimated active user and channel information, using the traditional minimum mean square error (MMSE) and least squares (LS) for data detection. However, for the two design schemes mentioned above, the accuracy of active user detection and channel estimation affects the performance of multiuser data detection to a great extent. In addition, when the number of active users is large, the computational complexity that MMSE and LS detection required is high because they are designed to find the inverse of the matrix. Moreover, the existing works focus on the packet synchronization transmission system that users can only change their activity status at the beginning of each coherent time. During the packet transmission, the packet alignment among a large number of users will result in significant overhead and the user who fails to align their packets can disrupt the entire multiuser data detection process.

Currently, in order to further reduce the system overhead and detection error rate and improve the spectral efficiency of the system, Ding et al. [44] concentrated the three parts of active user detection, channel estimation, and data detection in a phase and used blind detection and semiblind detection algorithms to solve the multiuser data detection problem. However, the dual sparsity of the signal and channel has not been fully exploited in this algorithm. Moreover, it will be more challenging as it can be seen from the three-part joint design scheme that the BS needs only a phase-based data signal to identify the active users, estimate the channel, and decode the user data. In this sense, symbolic synchronous transmission is more suitable for the unlicensed multiple access system to minimize the user coordination cost and improve reliability. However, depending on the structure of the symbol synchronous system, it is more challenging to design for the active user identification, channel estimation, and data decoding using the dual-block sparsity performance.

In summary, the current researches on the multiaccess scheme for the large-scale IoT networks mainly focus on active user detection and channel estimation. Although many effective mechanisms and algorithms have been proposed, the current researches rely more on traditional signal detection methods for multiuser data detection. In particular, in the large-scale NOMA system with two-phase or three-phase signal transmission, although there have been many results on the optimal design of active user detection, channel estimation, and data transmission, a complete theory and technology system has not yet been formed and there are still many key issues to be solved:

- (1) Firstly, for the nonorthogonal transmission scheme of short packets for the large-scale IoT networks, most of the existing researches are based on the Shannon theory for optimal design. In practice, the quality of service requirements of large-scale IoT users is different. In the smart home scenario, most of the data packets received by the user equipment are very short, which requires low latency and high-reliability transmission. For the fax service

scenario, it requires a lot of data transmission. Therefore, the design of a signal transmission and reception scheme that can meet the needs of large-scale IoT services and realize short packets, low latency, and reliable transmission is worthy of further research

- (2) Secondly, for the NOMA-based large-scale IoT research, most of the existing signal processing schemes mostly focus on active user detection and channel estimation. Regarding the false-positive rate and false-negative rate of active users, the relevant research only finds a compromise between them and does not consider handling the false-positive rate and false-negative rate separately based on the characteristics of active user signals. Meanwhile, the traditional MMSE detection is more in consideration for multiuser data detection. However, this detection scheme is only applicable to the case of a short number of active users. If the number of the potential user base and active users is still large, the detection requires a low-complexity algorithm. This prompts us to study a more reliable and more widely applicable detection scheme, which considers signal characteristics, user's prior information, and each user's guide frequency sequence to propose effective active users and data detection algorithms
- (3) Finally, for the data joint detection scheme and active users of the large-scale IoT networks, the related literature only uses the CS or linear model inversion technology to configure the system without considering the specific signal transmission, reception scheme, and the structure of the signal processing problem. The relevant algorithm or mechanism has much room for improvement. Therefore, how to study the signal detection model of the large-scale multiple access based on the characteristics of the received signal and reduce the system detection error rate, the transmission latency, and the system overhead also needs further investigation

3. Research Plan

3.1. Research Plan to Be Adopted. This paper studies how to design an effective nonorthogonal transmission and reception scheme under the condition of limited spectrum and energy resources. The objective is to realize low latency and reliable transmission in large-scale IoT networks, improve the system user access rate and spectrum efficiency, and save the system cost. Drawing on the research progress and thought methods in related fields such as NOMA, large-scale IoT, and signal processing and combining the characteristics of large-scale multiple access and IoT, the technical solution shown in Figure 2 has been proposed and the performance of the adopted solution and its impact factors are comprehensively analyzed and simulated to verify the system platform. In the following, the specific technical lines and the associated research schemes will be

presented for each research component. In particular, the problem description, system modeling, and the research plans will be provided.

3.2. Nonorthogonal Transmission and Reception Scheme of Large-Scale IoT Short Data Packets Based on Finite Coding. In large-scale IoT networks, especially the cellular IoT, the system performance is mainly determined by the channel estimation and uplink and downlink data transmission. Based on the traditional time division duplex (TDD) mode of cellular IoT, the uplink and downlink of the system are transmitted on different time slots of the same frequency resource. The system only needs to estimate the uplink channel information to take advantage of the channel reciprocity in the coherent time. However, since the BS and IoT users have different processing capabilities and higher requirements for the implementation of the NOMA scheme, a hybrid multiple-access scheme is needed for the large-scale IoT uplink and downlink communication modes and characteristics. The specific technical solution is shown in Figure 3.

A cellular IoT model, as shown in Figure 4, includes N short-packet transmission users and a central BS where all user terminals are equipped with a single antenna and a low-resolution ADC.

The BS preassigns a dedicated nonorthogonal spreading sequence $S_n \in \mathbb{C}^{L_p \times 1}$ to each user, where the length of the sequence L_p is shorter than the total number of users N and each element of the sequence is independently and equally probabilistically selected from the set $\{-1, 1\}$. In the uplink, an authorization-free NOMA scheme is used, i.e., each user can access the network and transmit data without being authorized. Therefore, the BS needs to estimate the active users and their channel information before detecting the uplink data. In addition, due to the high computational power of the BS, algorithms with higher accuracy can be used to jointly detect multiuser information. However, users in large-scale IoT networks have very limited computational power. In the downlink nonorthogonal transmission, if the information of all active users is superimposed and broadcast, the performance of each user will decrease and the detection complexity will increase. Therefore, it is necessary to consider the active user pairing and grouping strategies and use a nonorthogonal transmission scheme within a group of users and orthogonal resources between groups, such as subcarriers. Moreover, in the nonorthogonal transmission scheme for downlink packet data, the obtainable capacity can be expressed as a function of code length and error block rate using the finite code length capacity. For user n , the signals of other users are usually considered as interference. Thus, in the group with N users, the signal-to-interference-plus-noise ratio (SINR) of the n th user when decoding its own signal is

$$\gamma_{n \rightarrow n} = \frac{\alpha_n |h_{\Lambda_n}|^2}{|h_{\Lambda_n}|^2 \sum_{k=1,2,\dots,N, k \neq n} \alpha_k + \sigma_\epsilon^2 + 1/\rho}, \quad (3)$$

where $\alpha_k = p_k/P$, $P = \sum_{k=1,2,\dots,N} p_k$, and $\rho = P/\sigma_d^2$ denote the

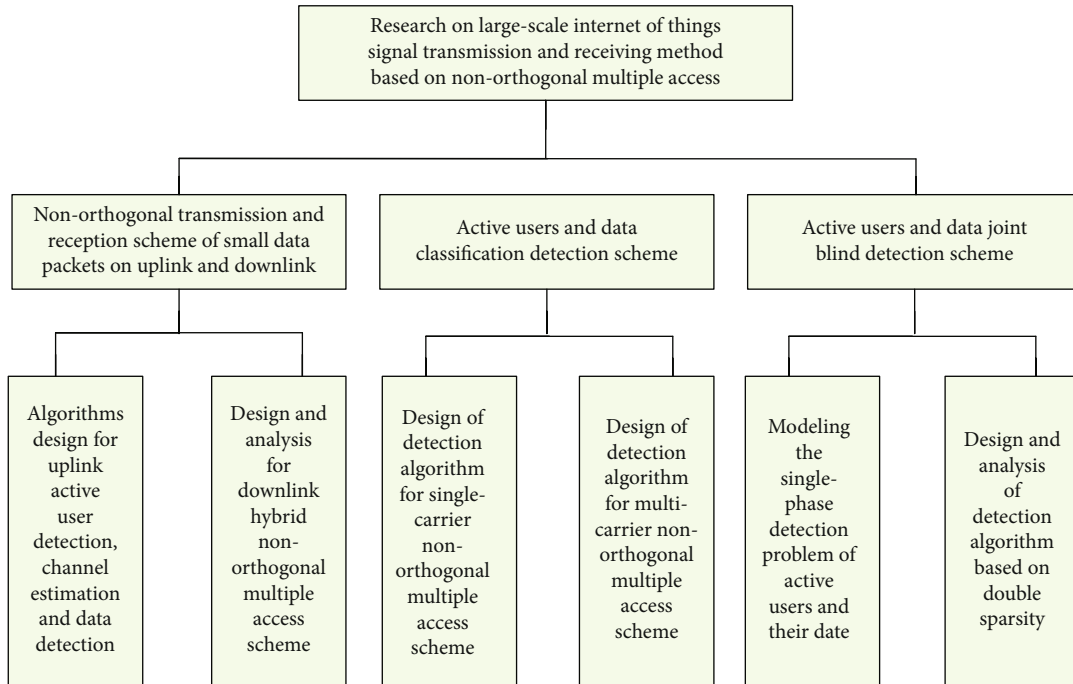


FIGURE 2: Proposed research framework.

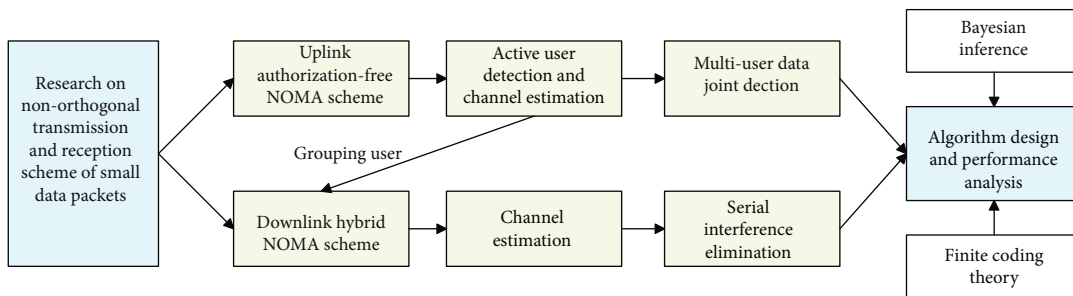


FIGURE 3: Technical solution of nonorthogonal transmission and reception scheme for large-scale IoT short data packets.

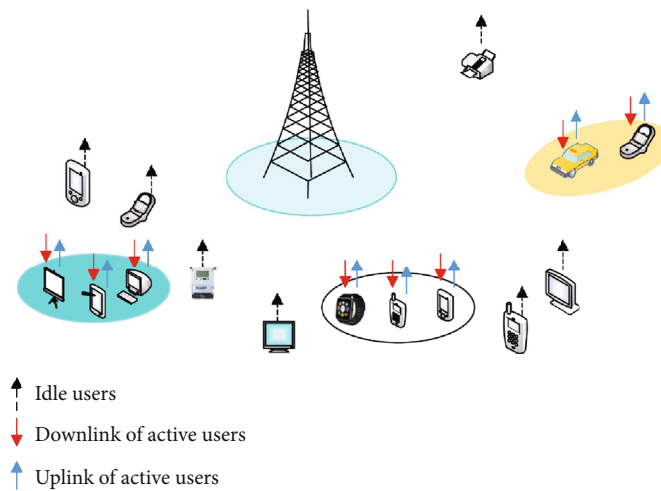


FIGURE 4: Nonorthogonal transmission model for large-scale IoT uplink and downlink in cellular networks.

transmission signal-to-noise ratio (SNR), \hat{h}_n is the estimated channel, and σ_e^2 is the variance of the channel estimation error. Accordingly, the instantaneous error block rate of user n is approximated by

$$\varepsilon_n \approx Q \left(\frac{c(\gamma_{n \rightarrow n}) - (B_n/L^d)}{\sqrt{V(\gamma_{n \rightarrow n})/L^d}} \right), \quad (4)$$

where $c(\gamma_{n \rightarrow n}) = \log_2(1 + \gamma_{n \rightarrow n})$ is the Shannon capacity and $V(\gamma_{n \rightarrow n}) = (1 - (1/(1 + \gamma_{n \rightarrow n})^2))(\log_2 e)^2$ denotes the channel dispersion. When the probability density function of $\gamma_{n \rightarrow n}$ is $f_{\gamma_{n \rightarrow n}}(x)$, the average error block rate of user n can be written as

$$\bar{\varepsilon}_n \approx \int_0^\infty Q \left(\frac{c(\gamma_{n \rightarrow n}) - (B_n/L_n)}{\sqrt{V(\gamma_{n \rightarrow n})/L_n}} \right) f_{\gamma_{n \rightarrow n}}(x) dx. \quad (5)$$

In the uplink pilot frequency and data transmission phase, since the receiver with low-resolution ADC is considered, the received signal is quantized, which cannot provide good statistical information. At present, most of the approximate information transmission algorithms are not suitable for the model's active user detection, channel estimation, and data detection. The algorithms for this part need to be redesigned. In addition, for this model, the impact of analog-to-digital conversion bits on the system performance needs to be studied. On the other hand, in the downlink nonorthogonal transmission, the downlink channel needs to be estimated before analyzing the error block rate performance of the system. Meanwhile, the performance of the user grouping strategy for the nonorthogonal transmission should be discussed and analyzed to obtain a more explicit user grouping criterion, which will be the key issue to be investigated. Firstly, we will model the short-packet nonorthogonal transmission system for the cellular IoT uplink and downlink; design the uplink active user, channel estimation, and multiuser detection algorithms; and analyze the performance of uplink based on the short packet transmission and its impact factors. For the downlink, the downlink channel estimation method should be proposed to derive the error block rate performance of the short-packet nonorthogonal transmission and the impact of channel estimation error, information bits, coding length, and other factors on the performance of short-packet nonorthogonal transmission in the downlink is analyzed. Meanwhile, using the power domain NOMA theory, we analyze the short-packet nonorthogonal transmission performance under different cellular IoT transmission service requirements and discuss the variation of system performance under different user groupings. This guides the design of short-packet nonorthogonal schemes for the cellular IoT.

3.3. Large-Scale IoT's Active Users and Data Grading Detection Scheme Based on Reliable Information Transmission. In the signal coherent detection of large-scale IoT uplink, i.e., license-free NOMA, active users, and

data detection are the two key parts, in particular, data detection can be performed through estimation of active users and channels first or active users and data detection can be combined. In the coherent detection, if a joint detection scheme of active users and data is used, the channel information needs to be estimated in advance. However, in the case of unknown active users, the channel of active users should be estimated, which increases the complexity of the detection algorithm and leads to a degradation in the performance of active users and data detection. Therefore, for active user and hierarchical coherent detection schemes, the characteristics of sparse signals should be exploited to obtain the reliable iterative first, and then, the information iterative steps can be optimized and higher detection accuracy can be obtained at the cost of more computational complexity. The specific technical solution is shown in Figure 5.

Assuming that the summarized users are synchronized in a frame structure and are active or dormant for the entire frame, a single-cell IoT uplink license-free single/multicarrier NOMA system is considered. Moreover, a block fading channel is considered, i.e., the channel coefficients remain unchanged within a frame. Since only a short part of users is active in the coherent time, without loss of generality, it is assumed that the BS knows the distribution of each user activity indicator α_n or the total number of active users, where $K(K \ll N)$, α_n obeys Bernoulli distribution, i.e., $\Pr(\alpha_n = 1) = \epsilon$ and $\Pr(\alpha_n = 0) = 1 - \epsilon$, for a certain frame $K/N \approx \epsilon$. In a certain frame, the active user sends a pilot symbol followed by L_d data symbols, while the inactive user stays dormant throughout the frame.

In the training phase, at the BS, the pilot measurement of the l th ($l = 1, 2, \dots, L$) subcarrier is

$$\mathbf{y}_l^p = \sum_{n=1}^N \zeta_p \mathbf{s}_n \alpha_n h_{nl} + \mathbf{z}_l^p = \mathbf{S}(\text{diag}(\mathbf{a})\mathbf{h}_l) + \mathbf{z}_l^p, \quad (6)$$

where ζ_p is the energy normalization factor of the pilot in the spread sequence, $\mathbf{S} = \zeta_p[\mathbf{s}_1, \mathbf{s}_2, \dots, \mathbf{s}_N]$ is the pilot observation matrix, and $\mathbf{a} = (\alpha_1, \alpha_2, \dots, \alpha_N)^T \in \{0, 1\}^N$ is the user activity indicator vector. Notation $\mathbf{h} = (h_{1l}, h_{2l}, \dots, h_{Nl})^T$ is the channel vector, where $h_{nl} \sim \mathcal{CN}(0, \sigma_h^2)$, and $\mathbf{z}_l^p \sim \mathcal{CN}(0, \sigma_p^2 \mathbf{I}_{L_p})$ represents the additive white Gaussian noise vector.

In the uplink transmission phase, at the BS, the j th data symbol received by the l th subcarrier is

$$y_{lj}^d = \sum_{n=1}^N x_{n,j} \alpha_n h_{nl} + z_{lj}^d. \quad (7)$$

Thus, the signals received by all subcarriers can be expressed as

$$\mathbf{y}_j^d = \mathbf{H}(\mathbf{a})\mathbf{x}_j + \mathbf{z}_j^d, \quad (8)$$

where $\mathbf{y}_j^d \triangleq (y_{1j}^d, y_{2j}^d, \dots, y_{Lj}^d)^T$, $\mathbf{H} \triangleq [\mathbf{h}_1, \mathbf{h}_2, \dots, \mathbf{h}_L]^T$, and $\mathbf{x}_j = (x_{1,j}, x_{2,j}, \dots, x_{N,j})^T$. The license-free single/multicarrier NOMA system can provide a large number of links and

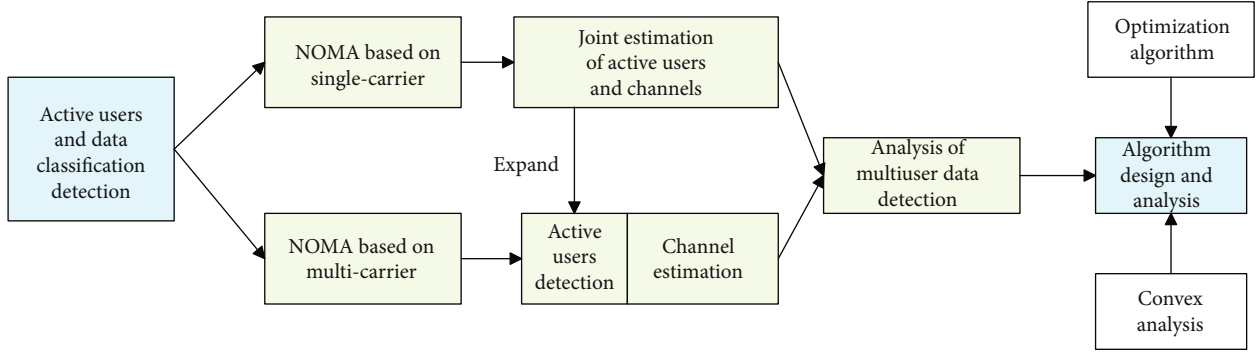


FIGURE 5: Technical solution of the activity user and data classification detection solution in the large-scale IoT.

low access latency and has a wide range of applications in the cellular IoT. However, due to a large number of potential users and that these users use nonorthogonal pilot sequences, the key challenges existing in the unlicensed connection scenarios for large-scale IoT users are channel estimation, active user detection, and data decoding. A fundamental question is, in addition to active user detection, how to design a receiver to perform the channel estimation and/or multiuser data detection effectively.

We intend to solve how to exploit the nonzero element characteristics of sparse signals and the sparse structure of system blocks to effectively improve the system's channel estimation, active user detection, and data decoding. To take advantage of the fast attenuation characteristics of nonzero components in the sparse signals, the traditional least absolute shrinkage and selection operator (LASSO) problem can be transformed into an iterative weighting problem

$$\begin{aligned} \min_{\bar{\mathbf{h}}_l \in \mathbb{C}^L} \quad & \|\bar{\mathbf{h}}_l\|_{1,w} \\ \text{s.t.} \quad & \|\mathbf{y}_l^p - \mathbf{S}\bar{\mathbf{h}}_l\|_2 \leq \varepsilon, \end{aligned} \quad (9)$$

where $\|\bar{\mathbf{h}}_l\|_{1,w} = \sum_{n=1}^J \omega_n |\bar{h}_{nl}| \bar{h}_{nl} \triangleq \alpha_n h_{nl}$, $\omega_n = 0$, $n \in \Lambda$, $\omega_n = 1$, $n \notin \Lambda$, ε is the tolerable estimation error and the set Λ is defined as $\Lambda = \{n : \bar{h}_{nl}\} \neq 0$. Since the information of the nonzero element part of the sparse signals is more reliable, the estimation of some nonzero elements can be stopped after several iterations. In addition, the active user set is updated based on the symbol energy of unreliable information and the accurate or approximate total number of active users known by the BS. This can not only reduce the false alarm rate but also reduce the missed detection rate and even achieve a complete detection of active users. For the uplink transmission stage, the multiple user signals received by the BS are decomposed into linear combinations of different signal vectors and the maximum likelihood (ML) detection problem is transformed into two separable subproblems, using alternate minimization algorithm. By analyzing the information of each iteration, the inversion of large-scale matrices is avoided, thereby reducing the computational complexity of multiuser data detection.

3.4. Joint Blind Detection Scheme of Large-Scale IoT Activity Users and Data Based on Double-Sparse Learning. Due to the transmission latency requirement, it is necessary to further reduce the pilot symbol transmission. Different from the active user and data classification detection scheme, the active user and data joint blind detection scheme based on the double-sparsity learning needs to be devised into the data packet as the user's identity, and at the same time, the activity can be completed in one transmission stage for user and data detection. We need not to estimate the channel information firstly, which can help reduce the transmission latency further. The specific technical solution is shown in Figure 6. Therefore, considering the symbol synchronization and authorization-free uplink NOMA system, users are allowed to initiate data packet transmission at the beginning of any symbol interval. Whenever the user wants to transmit a message, it generates a data packet that carries the message and the identity of the sending user. Once activated, the user transmits the data packet to the BS at L consecutive symbol intervals. Assume that the j th data packet of user n is denoted by $\mathbf{c}_n^{(j)} \in \mathbb{C}^{L \times 1}$ and $s_{n,t}$ represents the transmission symbol of user n in the t th symbol interval. As shown in Figure 7, $t_n^{(t)}$ represents the symbol interval at which user n starts to transmit the j th data packet, $s_{n,t} = c_n^{(j)}(k)$, $k = 1, 2, \dots, L$. The symbol of the dormant user can be represented by zero. Therefore, when $t_n^{(j)} \leq t \leq t_n^{(j)} + L$ holds, the transmission symbol of user n is $s_{n,t} = c_n^{(j)}(t - t_n^{(j)} + 1)$; otherwise $s_{n,t} = 0$. For the data packet $c_n^{(j)}$, the channel from user n to the BS can be expressed by $\mathbf{h}_n^{(j)} = \sqrt{\beta_n} \mathbf{g}_n^{(j)}$, where β_n and $\mathbf{g}_n^{(j)}$ represent large-scale and short-scale fading, respectively. The channel state remains unchanged during the entire transmission period of the data packet $c_n^{(j)}$, which is the block fading channel.

In the t th symbol interval, the signal received by the BS can be expressed as

$$\mathbf{y}_t = \mathbf{H}_t \mathbf{s}_t + \mathbf{w}_t \in \mathbb{C}^{M \times 1}, \quad (10)$$

where $\mathbf{H}_t = [\mathbf{h}_{1,t}, \mathbf{h}_{2,t}, \dots, \mathbf{h}_{N,t}]$ and $\mathbf{s}_t = (s_{1,t}, s_{2,t}, \dots, s_{N,t})^T$. If $t_n^{(j)} \leq t \leq t_n^{(j)} + L$ holds, then, we have $\mathbf{h}_{n,t} = \mathbf{h}_n^{(j)}$. Otherwise, $\mathbf{h}_{n,t} = \mathbf{0}$.

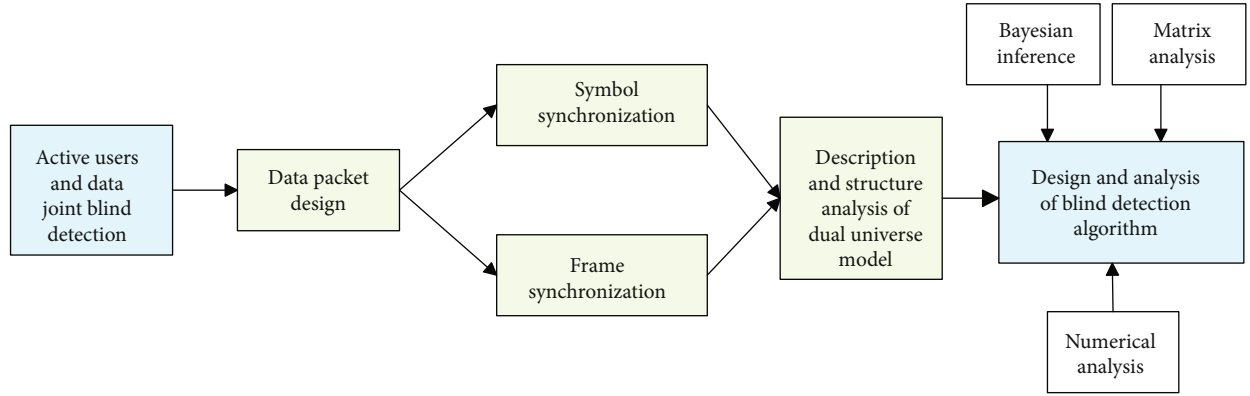


FIGURE 6: Technical design of joint blind detection solution for large-scale IoT activity users and data.

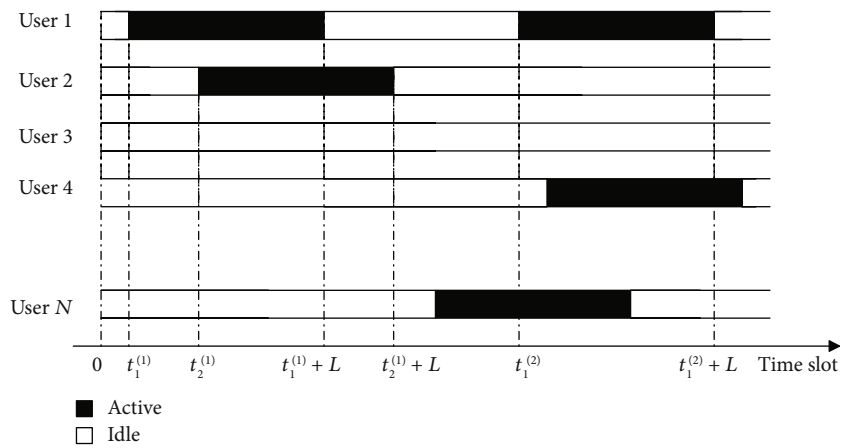


FIGURE 7: User activity status within the symbol interval.

$= 0$. This problem combines active user detection, channel estimation, and data detection, which can help reduce the system's transmission latency. Note that the representations of the channel and the signal are both sparse, so that this problem is also called as the double-sparsity problem. The performance analysis of the model and the use of the double sparsity of the received signal model to design detection algorithms should be developed.

We firstly use the double sparsity of the received signal model to describe the iterative information of the estimated channel and data estimation as a conditionally independent random distribution and use a blind detection algorithm to estimate the signal in each sparse block. Secondly, a low-complexity information iterative algorithm is used between the independent sparse blocks, which can make good use of the sparseness of the signals to improve the system performance and reduce system transmission latency. Finally, numerical results should be provided to verify the reliability of the above theoretical results and correctness.

4. Conclusions

In this paper, we performed a comprehensive survey on the transmission schemes for large-scale IoT with NOMA, which could support multiple users to use the same fre-

quency resources as long as the interference among users could be addressed. The NOMA technique could help improve the frequency reuse efficiency significantly and was viewed as one of the most efficient candidate of the techniques for the next-generation wireless communications. However, there still existed a lot of challenges on the transmission schemes for large-scale NOMA systems, including the short-data packet transmission, active user detection, channel estimation, and data detection. To address these challenges, we firstly reviewed the short-data packet transmission in the large-scale NOMA system and then reviewed the active user detection and channel estimation techniques for the considered system. We further described the data detection algorithms for large-scale NOMA systems. In future works, we will incorporate some intelligent algorithms, such as the deep learning-based algorithm [45–47], deep Q-network-based algorithms [48], federated algorithms [49, 50], and transfer learning-based algorithms [51], to the considered system to enhance the system transmission performance.

Data Availability

The data in this work can be available through email to the authors of this paper.

Conflicts of Interest

The authors declare that they have no conflicts of interest.

Acknowledgments

This work was supported by the Key-Area Research and Development Program of Guangdong Province (no. 2018B010124001), by the International Science and Technology Cooperation Projects of Guangdong Province (no. 2020A0505100060), by the National Natural Science Foundation of China (no. 61471229), by the Key Field Projects of Colleges and Universities of Guangdong Province (no. 2019KTSCX040), by the Natural Science Foundation of Guangdong Province (no. 2021A1515011392), and in part by the research program of Guangzhou University (nos. YK2020008 and YJ2021003).

References

- [1] J. Xia, "Secure cache-aided multi-relay networks in the presence of multiple eavesdroppers," *IEEE Transactions on Communications*, vol. 67, no. 11, pp. 7672–7685, 2019.
- [2] B. Wang, F. Gao, S. Jin, H. Lin, and G. Y. Li, "Spatial- and frequency-wideband effects in millimeter-wave massive MIMO systems," *IEEE Trans. Signal Processing*, vol. 66, no. 13, pp. 3393–3406, 2018.
- [3] X. Hu, C. Zhong, Y. Zhu, X. Chen, and Z. Zhang, "Programmable metasurface-based multicast systems: design and analysis," *IEEE Journal on Selected Areas in Communications*, vol. 38, no. 8, pp. 1763–1776, 2020.
- [4] K. He, "Ultra-reliable MU-MIMO detector based on deep learning for 5G/B5G-enabled IoT," *Phys. Commun.*, vol. 43, pp. 1–7, 2020.
- [5] X. Hu, J. Wang, and C. Zhong, "Statistical CSI based design for intelligent reflecting surface assisted MISO systems," *Science China: Information Science*, vol. 63, no. 12, 2020.
- [6] J. Zhao, X. Sun, Q. Li, and X. Ma, "Edge caching and computation management for real-time Internet of vehicles: an online and distributed approach," *IEEE Transactions on Intelligent Transportation Systems*, vol. 22, no. 4, pp. 2183–2197, 2021.
- [7] Y. Xu, C. Shen, D. Cai, and G. Zhu, "Latency constrained non-orthogonal packets scheduling with finite blocklength codes," *IEEE Transactions on Vehicular Technology*, vol. 69, no. 10, pp. 12312–12316, 2020.
- [8] Z. Na, Y. Liu, J. Shi, C. Liu, and Z. Gao, "Uav-supported clustered noma for 6g-enabled Internet of things: trajectory planning and resource allocation," *IEEE Internet of Things Journal*, vol. 12, pp. 1–1, 2020.
- [9] C. Li, "Dynamic offloading for multiuser multi-CAP MEC networks: a deep reinforcement learning approach," *IEEE Transactions on Vehicular Technology*, vol. 70, no. 3, pp. 2922–2927, 2021.
- [10] X. Pang, J. Tang, N. Zhao, X. Zhang, and Y. Qian, "Energy-efficient design for mmwave-enabled noma-uav networks," *Science China Information Sciences*, vol. 64, no. 4, 2021.
- [11] L. Yang, F. Meng, J. Zhang, M. O. Hasna, and M. D. Renzo, "On the performance of ris-assisted dual-hop UAV communication systems," *IEEE Transactions on Vehicular Technology*, vol. 69, no. 9, pp. 10385–10390, 2020.
- [12] Z. Wang, "An adaptive deep learning-based UAV receiver design for coded MIMO with correlated noise," *Physical Communication*, vol. 45, no. 101295, pp. 1–8, 2021.
- [13] Y. Guo and S. Lai, "Emergency semantic feature vector extraction from WiFi signals for in-home monitoring of elderly," *IEEE Journal of Selected Topics in Signal Processing*, vol. 23, pp. 1–12, 2021.
- [14] X. Lai, "Secure mobile edge computing networks in the presence of multiple eavesdroppers," *IEEE Transactions on Communications*, vol. 65, pp. 1–12, 2021.
- [15] Y. Zhang and J. Wang, "CV-3DCNN: complex-valued deep learning for CSI prediction in FDD massive MIMO systems," *IEEE Wireless Communications Letters*, vol. 10, no. 2, pp. 266–270, 2021.
- [16] X. Li, H. Mengyan, Y. Liu, V. G. Menon, A. Paul, and Z. Ding, "I/Q imbalance aware nonlinear wireless-powered relaying of B5G networks: security and reliability analysis," *IEEE Transactions on Network Science and Engineering*, vol. 5, no. 33, pp. 1–1, 2020.
- [17] W. Zhou, "PSO based offloading strategy for cache-enabled mobile edge computing UAV networks," *Cluster Computing*, vol. 53, pp. 1–8, 2021.
- [18] M. Liu and F. Tang, "6G: opening new horizons for integration of comfort, security, and intelligence," *IEEE Wireless Communications*, vol. 27, no. 5, pp. 126–132, 2020.
- [19] X. Li, Q. Wang, and M. Liu, "Cooperative wireless-powered NOMA relaying for B5G IoT networks with hardware impairments and channel estimation errors," *IEEE Internet of Things Journal*, vol. 8, no. 7, pp. 5453–5467, 2021.
- [20] S. Tang, "Dilated convolution based CSI feedback compression for massive MIMO systems," *IEEE Transactions on Vehicular Technology*, vol. 61, pp. 1–5, 2021.
- [21] X. Li, M. Zhao, M. Zeng et al., "Hardware impaired ambient backscatter NOMA systems: reliability and security," *IEEE Transactions on Communications*, vol. 69, no. 4, pp. 2723–2736, 2021.
- [22] A. Li, "Enhancing the physical layer security of cooperative NOMA system," in *2019 IEEE 3rd ITNEC*, vol. 343no. 34, pp. 2194–2198, 2019.
- [23] Y. Cao, N. Zhao, F. R. Yu et al., "Optimization or alignment: secure primary transmission assisted by secondary networks," *IEEE Journal on Selected Areas in Communications*, vol. 36, no. 4, pp. 905–917, 2018.
- [24] T. Zhao, G. Li, G. Zhang, and C.-X. Zhang, "Security-enhanced user pairing for MISO-NOMA downlink transmission," *2018 IEEE GLOBECOM*, vol. 68, no. 36, pp. 1–6, 2018.
- [25] B. M. ElHalawany and K. Wu, "Physical-layer security of NOMA systems under untrusted users," in *2018 IEEE Global Communications Conference (GLOBECOM)*, vol. 534no. 43, pp. 1–6, 2018.
- [26] J. Xia, D. Deng, and D. Fan, "A note on implementation methodologies of deep learning-based signal detection for conventional MIMO transmitters," *IEEE Transactions on Broadcasting*, vol. 66, no. 3, pp. 744–745, 2020.
- [27] S. Lai, "Intelligent secure mobile edge computing for beyond 5G wireless networks," *Physical Communication*, vol. 45, no. 101283, pp. 1–8, 2021.
- [28] G. Gui, F. Liu, J. Sun, J. Yang, Z. Zhou, and D. Zhao, "Flight delay prediction based on aviation big data and machine learning," *IEEE Transactions on Vehicular Technology*, vol. 69, no. 1, pp. 140–150, 2020.

- [29] X. Li, M. Zhao, Y. Liu, L. Li, Z. Ding, and A. Nallanathan, "Secrecy analysis of ambient backscatter NOMA systems under I/Q imbalance," *IEEE Transactions on Vehicular Technology*, vol. 69, no. 10, pp. 12286–12290, 2020.
- [30] R. Zhao, "Deep reinforcement learning based mobile edge computing for intelligent Internet of things," *Physical Communication*, vol. 43, pp. 1–7, 2020.
- [31] X. Hu, C. Zhong, Y. Zhang, X. Chen, and Z. Zhang, "Location information aided multiple intelligent reflecting surface systems," *IEEE Transactions on Communications*, vol. 68, no. 12, pp. 7948–7962, 2020.
- [32] J. Zhao and S. Ni, "Multiband cooperation for 5G hetnets: a promising network paradigm," *IEEE Vehicular Technology Magazine*, vol. 14, no. 4, pp. 85–93, 2019.
- [33] J. Yang, D. Ruan, J. Huang, X. Kang, and Y. Shi, "An embedding cost learning framework using GAN," *IEEE Transactions on Information Forensics and Security*, vol. 15, pp. 839–851, 2020.
- [34] Z. Zhou, H. Yu, S. Mumtaz, S. Al-Rubaye, A. Tsourdos, and R. Q. Hu, "Power control optimization for large-scale multi-antenna systems," *IEEE Transactions on Wireless Communications*, vol. 19, no. 11, pp. 7339–7352, 2020.
- [35] M. D. Renzo and P. Guan, "Stochastic geometry modeling and systemlevel analysis of uplink heterogeneous cellular networks with multi-antenna base stations," *IEEE Transactions on Communications*, vol. 64, no. 6, pp. 2453–2476, 2016.
- [36] C. E. Shannon, "A mathematical theory of communication," *Bell Systems Technical Journal*, vol. 27, no. 4, pp. 623–656, 1948.
- [37] Y. Du, B. Dong, W. Zhu et al., "Joint channel estimation and multiuser detection for uplink grant-free NOMA," *IEEE Wireless Communications Letters*, vol. 7, no. 4, pp. 682–685, 2018.
- [38] H. He, C. Wen, and S. Jin, "Bayesian optimal data detector for hybrid mmwave MIMO-OFDM systems with low-resolution adcs," *IEEE Journal of Selected Topics in Signal Processing*, vol. 12, no. 3, pp. 469–483, 2018.
- [39] T. Hara and K. Ishibashi, "Grant-free non-orthogonal multiple access with multiple-antenna base station and its efficient receiver design," *IEEE Access*, vol. 7, pp. 175717–175726, 2019.
- [40] D. Cai, "Active user and data detection for uplink grant-free NOMA systems," *China Communications*, vol. 17, no. 11, pp. 22–38, 2020.
- [41] B. Wang, L. Dai, Y. Zhang, T. Mir, and J. Li, "Dynamic compressive sensing-based multi-user detection for uplink grant-free NOMA," *IEEE Wireless Communications Letters*, vol. 20, no. 11, pp. 2320–2323, 2016.
- [42] Q. Zou, H. Zhang, D. Cai, and H. Yang, "A low-complexity joint user activity, channel and data estimation for grant-free massive mimo systems," *IEEE Signal Processing Letters*, vol. 27, no. 33, 2020.
- [43] T. Liu, S. Jin, C.-K. Wen, M. Matthaiou, and X. You, "Generalized channel estimation and user detection for massive connectivity with mixedadc massive MIMO," *IEEE Transactions on Wireless Communications*, vol. 18, no. 6, pp. 3236–3250, 2019.
- [44] T. Ding, X. Yuan, and S. C. Liew, "Sparsity learning-based multiuser detection in grant-free massive-device multiple access," *IEEE Transactions on Wireless Communications*, vol. 18, no. 7, pp. 3569–3582, 2019.
- [45] J. Xia and L. Fan, "Computational intelligence and deep reinforcement learning for next-generation industrial IoT," *IEEE Transactions on Network Science and Engineering*, vol. 99, pp. 1–12, 2021.
- [46] L. He and K. He, "Towards optimally efficient search with deep learning for large-scale mimo systems," *IEEE Transactions on Communications*, vol. 76, pp. 1–12, 2022.
- [47] K. He, "Learning based signal detection for MIMO systems with unknown noise statistics," *IEEE Transactions on Communications*, vol. 69, no. 5, pp. 3025–3038, 2021.
- [48] S. Tang, "Battery-constrained federated edge learning in UAV-enabled IoT for B5G/6G networks," *Physical Communication*, vol. 47, no. 101381, pp. 1–9, 2021.
- [49] Y. Guo, "Efficient and flexible management for industrial Internet of things: a federated learning approach," *Computer Networks*, vol. 192, pp. 1–9, 2021.
- [50] Z. Zhao, "System optimization of federated learning networks with a constrained latency," *IEEE Transactions on Vehicular Technology*, vol. 21, pp. 1–5, 2021.
- [51] L. Chen, "Intelligent ubiquitous computing for future UAV-enabled MEC network systems," *Cluster Computing*, vol. 48, no. 99, pp. 1–8, 2021.

Research Article

Reduced-Complexity LDPC Decoding for Next-Generation IoT Networks

Muhammad Asif ¹, Wali Ullah Khan ², H. M. Rehan Afzal ³, Jamel Nebhen ⁴,
Inam Ullah ⁵, Ateeq Ur Rehman ⁶, and Mohammed K. A. Kaabar ^{7,8,9}

¹College of Electronics and Information Engineering, Shenzhen University, Shenzhen, Guangdong, 518060, China

²Interdisciplinary Centre for Security, Reliability and Trust (SnT), University of Luxembourg, 1855 Luxembourg City, Luxembourg

³School of Electrical Engineering and Computing, University of Newcastle, NSW, Australia

⁴School of Computer Science and Engineering, Prince Sattam Bin Abdulaziz University, Alkharj 11942, Saudi Arabia

⁵College of Internet of Things (IoT) Engineering, Hohai University, Changzhou, China

⁶Department of Electrical Engineering, Government College University, Lahore 54000, Pakistan

⁷Jabalia Camp, United Nations Relief and Works Agency (UNRWA) Palestinian Refugee Camp, Gaza Strip Jabalya, State of Palestine

⁸Gofa Camp, Near Gofa Industrial College and German Adebabay, Nifas Silk-Lafto, 26649 Addis Ababa, Ethiopia

⁹Institute of Mathematical Sciences, Faculty of Science, University of Malaya, Kuala Lumpur 50603, Malaysia

Correspondence should be addressed to Mohammed K. A. Kaabar; mohammed.kaabar@wsu.edu

Received 15 April 2021; Revised 19 May 2021; Accepted 24 August 2021; Published 22 September 2021

Academic Editor: Simone Morosi

Copyright © 2021 Muhammad Asif et al. This is an open access article distributed under the Creative Commons Attribution License, which permits unrestricted use, distribution, and reproduction in any medium, provided the original work is properly cited.

Low-density parity-check (LDPC) codes have become the focal choice for next-generation Internet of things (IoT) networks. This correspondence proposes an efficient decoding algorithm, dual min-sum (DMS), to estimate the first two minima from a set of variable nodes for check-node update (CNU) operation of min-sum (MS) LDPC decoder. The proposed architecture entirely eliminates the large-sized multiplexing system of sorting-based architecture which results in a prominent decrement in hardware complexity and critical delay. Specifically, the DMS architecture eliminates a large number of comparators and multiplexors while keeping the critical delay equal to the most delay-efficient tree-based architecture. Based on experimental results, if the number of inputs is equal to 64, the proposed architecture saves 69%, 68%, and 52% area over the sorting-based, the tree-based, and the low-complexity tree-based architectures, respectively. Furthermore, the simulation results show that the proposed approach provides an excellent error-correction performance in terms of bit error rate (BER) and block error rate (BLER) over an additive white Gaussian noise (AWGN) channel.

1. Introduction

Internet of things (IoT) will be one of the major trends in next-generation wireless networks for connecting billions of devices to the Internet [1–4]. These communication devices will provide a high data rate with low transmission delay and energy consumption [5–8]. In this regard, low-density parity-check (LDPC) codes [9–15] are one of the most promising candidates in the list of error-control codes and adopted as a primary choice for next-generation IoT networks [16–19].

Compared to other error-correction codes, like Bose-Chaudhuri-Hocquenghem (BCH) codes, Reed Solomon (RS) codes, and turbo codes, LDPC codes have many advantages, e.g., very low error floor, high-speed encoder and decoder, and more varieties in code construction [20–23]. Therefore, LDPC codes have become the focal choice for many communication standards, such as 10-Gigabit Ethernet (802.3an) [24] and Wi-Fi (802.11n/ac/ad) [25–27].

To obtain an optimal performance, LDPC codes are usually decoded with an iterative process between the two

decoding phases, i.e., check-node update and variable-node update. Among various decoding algorithms, sum-product (SP) [28] algorithm provides a tremendous decoding performance close to Shannon capacity. However, it suffers from large complexity because of logarithmic and multiplicative functions involved in CNU operation. For hardware implementation of decoder, an area-efficient approximation of SP called min-sum (MS) [29] algorithm was proposed which provides implementation advantages over SP algorithm by computing two minimum values from a set of messages arriving at check nodes. But it suffers from performance degradation. The normalized min-sum (NMS) and offset min-sum (OMS) [30], modified versions of MS, significantly improve the performance of MS by introducing additional normalization and offset factors, respectively.

In hardware implementation of MS decoder, each iteration involves two operations, i.e., CNU and variable-node update (VNU). For CNU, a minimum-value unit (mvu), also called minimum finder, is required to estimate the first two minima (Min_1, Min_2) and index of the first minimum value. For large block-length LDPC codes required in high data rate applications, a huge number of minimum-value units are needed to estimate the first two minima and index of Min_1 which significantly increases the complexity of CNU operation. Existing methods require circuitry with high complexity in terms of comparators, multiplexors, latency, and area time. Thus, a low cost algorithm is greatly desired to reduce the complexity of CNU operation of MS decoder.

Recently, some attempts have been utilized to estimate the first two minima from a set of messages arriving at check node. In [31], a single minimum min-sum (smMS) algorithm was proposed which only computes the absolute minimum value and the second minimum value is computed by adding a corrective constant in the first minimum. The smMS provides a significant reduction in hardware complexity of CNU processor, but it suffers from performance degradation. Wang et al. proposed a modification factor min-sum (mfMS) algorithm in [32]; the mfMS algorithm improves the performance of smMS by introducing a modification factor in absolute minimum value. Zhang et al. used the mfMS approach to design a flexible LDPC decoder for multigigabit per second applications [33]. A variable-weight min-sum (vwMS) algorithm was proposed by Angarita et al. in [29] by introducing a variable iteration-based correction factor; the performance of vwMS is better than smMS and mfMS. A simplified variable-weight min-sum (svwMS) is also proposed in [29] which requires low computational cost to determine if more than one input message shares the same first minimum value. In [29, 31–33], the absolute minimum value is calculated first, and then, the second minimum is estimated by applying a modification or correction factor to absolute minimum value. Researches have also investigated various problems on the other related topics of communications [34–44].

Besides the single minimum-based algorithms, some efforts have been made to propose architectures which compute the two minima from a set of messages for CNU operation [45–49]. A sorting-based architecture was proposed by Xie et al. in [46] for finding two minima, but it suffers from

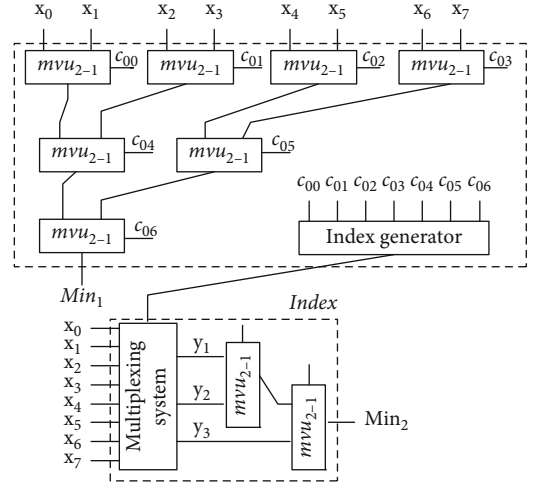


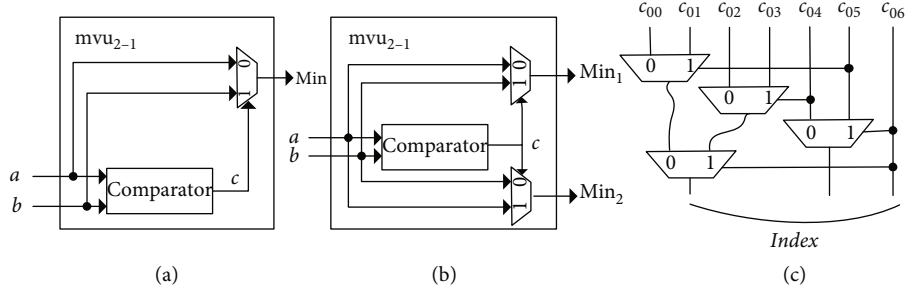
FIGURE 1: Sorting-based search module architecture.

large critical delay. Chen-Long et al. proposed a tree-based architecture in [47] which requires some additional complexity but provides critical delay less than that of sorting-based architecture. A low-complexity tree-based architecture [48] was proposed by Lee et al. which reduces some hardware complexity of tree-based structure while keeping the critical delay between those of the sorting-based and tree-based architectures. This manuscript presents an efficient approach, known as dual min-sum (DMS) architecture, for finding the first two minima (Min_1 and Min_2) from a set of variable nodes participating in CNU operation. Compared to existing sorting-based and tree-based architectures, the proposed scheme efficiently eliminates a large number of comparators and multiplexors while keeping the critical delay almost equal to the tree-based architecture. Based on experimental results, if the number of inputs is equal to 64, the proposed architecture saves 69%, 68%, and 52% area over the sorting-based, tree-based, and low-complexity tree-based architectures, respectively. Furthermore, the simulation results show that the proposed approach outperforms its counterparts by providing an excellent error-correction performance close to NMS algorithm over an additive white Gaussian noise (AWGN) channel.

The remainder of this correspondence is arranged as follows. In Section 2, the basic concepts about LDPC codes and min-sum decoding are given. A detailed review of the state-of-the-art architectures for finding the first two minima is given in Section 3. Section 4 presents a proposed architecture to find the first two minima for CNU operation of min-sum LDPC decoder. The performance analysis and hardware implementation of the proposed architecture are given in Section 5, and the conclusion of this correspondence is presented in Section 6.

2. Min-Sum LDPC Decoding

An (N, K) LDPC code can be described by the null space of a $M \times N$ sparse parity-check matrix H , where M denotes to


 FIGURE 2: Detailed structure of three component units. (a) mvu_{2-1} ; (b) mvu_{2-2} ; (c) index generator.

the number of parity-checks and N denotes to the block length of code. It can also be specified by a bipartite graph or Tanner graph having M check nodes and N variable nodes. The check nodes $\{c_1, \dots, c_M\}$ specify the rows of H and variable nodes $\{v_1, \dots, v_N\}$ specify the columns of H . The degree of check node (d_c) is equal to the number of nonzero entries in a row of H , and the degree of variable node (d_v) is equal to the number of nonzero entries in a column of H .

Let $N_m = \{n : H_{mn} = 1\}$ denote the set of variable nodes involve in check node c_m and $M_n = \{m : H_{mn} = 1\}$ denote the set of check nodes connected to variable node v_n . Also, let $N_{m \setminus n}$ represent the set N_m with excluding the variable node n and set $M_{n \setminus m}$ represents exclusion of check node m from the set M_n . The log-likelihood ratio (LLR) for a random variable can be defined as $\ln((1-\gamma)/\gamma)$, where γ represents the probability of transmitted bit being equal to zero. In addition, let $\varphi_{n \rightarrow m}^{(j)}$ denote the LLR message for bit n , sent from variable node v_n to check node c_m in the j th iteration. Similarly, $\psi_{m \rightarrow n}^{(j)}$ denotes the LLR message for bit n , sent from check node c_m to variable node v_n in the j th iteration. Finally, $w = [w_1, w_2, \dots, w_N]$ and $r = [r_1, r_2, \dots, r_N]$ denote the transmitted and the received codewords, respectively. Also, let us assume that $\ell = [\ell_1, \ell_2, \dots, \ell_N]$ denote the intrinsic reliability provided by the channel. The MS decoding consist of the following steps:

- (1) Initialize $j = 1, \dots, J_{\max}$, where J_{\max} represents the maximum number of iterations
- (2) Initialize $\psi_{m \rightarrow n}^{(j=0)} = 0, \forall m \in \{1, \dots, M\}, \forall n \in N_m$
- (3) VNU function: $\forall n \in \{1, \dots, N\}, \forall m \in M_n$

$$\varphi_{n \rightarrow m}^{(j)} = \ell_n + \sum_{m' \in M_{n \setminus m}} \psi_{m' \rightarrow n}^{(j-1)}. \quad (1)$$

- (4) CNU function: $\forall m \in \{1, \dots, M\}, \forall n \in N_m$

$$\psi_{m \rightarrow n}^{(j)} = \min_{n' \in N_{m \setminus n}} \left| \varphi_{n' \rightarrow m}^{(j)} \right| \prod_{n' \in N_{m \setminus n}} \text{sign} \left(\varphi_{n' \rightarrow m}^{(j)} \right). \quad (2)$$

- (5) Hard decision: applying a hard decision to compute the transmitted sequence $\hat{W} = (\hat{w}_1, \hat{w}_2, \dots, \hat{w}_N)$ as

$$\begin{aligned} \mu_n &= \ell_n + \sum_{m' \in M_n} \psi_{m' \rightarrow n}^{(j)}, \\ \hat{w}_n &= \begin{cases} 0, & \text{if } \mu_n \geq 0, \\ 1, & \text{otherwise.} \end{cases} \end{aligned} \quad (3)$$

If $\hat{W}H^T = 0$ or the maximum number of iteration J_{\max} is reached, move to Step 6; otherwise, set $j = j + 1$ and go back to Step 3.

- (6) Output: declare the estimated sequence $W \wedge^{(j)}$ as the decoder output

As compared to conventional SP and NMS algorithms, although the performance of MS algorithm is lower, it requires much simpler hardware circuitry for CNU operation performed in check-node update processor. In practical implementation of MS decoder, instead of finding the minimum value in (2), two minimum values are computed from the set of messages arriving at check node and a suitable one is selected depending upon the information received at the check node. Thus, the MS decoder reduces the hardware complexity and provides implementation advantages in terms of area and delay. In the next section, we introduce some existing architectures to find the first two minima for CNU operation of MS decoder.

3. Related Architectures

Generally, the hardware circuit used to find the first two minima from a set of messages arriving at check node is known as search module (SM). Let, for a given set of mw -bit messages received at check node, $X = \{x_0, x_1, \dots, x_{m-1}\}$; SM generates three outputs: (1) the first minimum value of set $\{X\}$, (2) the second minimum value of $\{X\}$, and (3) the index of the first minimum value. For hardware realization, two 2-input units, mvu_{2-1} and mvu_{2-2} , are used as the fundamental units of a search module. mvu_{2-1} , as shown in Figure 1(a), consists of one comparator and one w -bit 2-to-1 multiplexer and it returns the smaller value from two inputs. mvu_{2-2} consists of one comparator and two w -bit 2-to-1 multiplexers, and it returns both smaller and larger values,

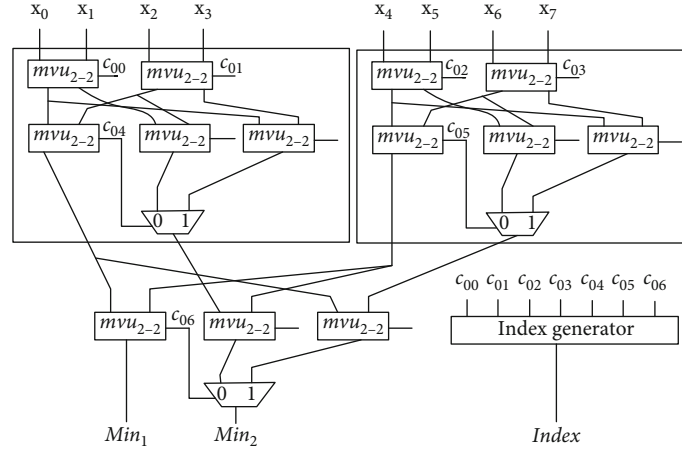


FIGURE 3: Tree-based search module architecture.

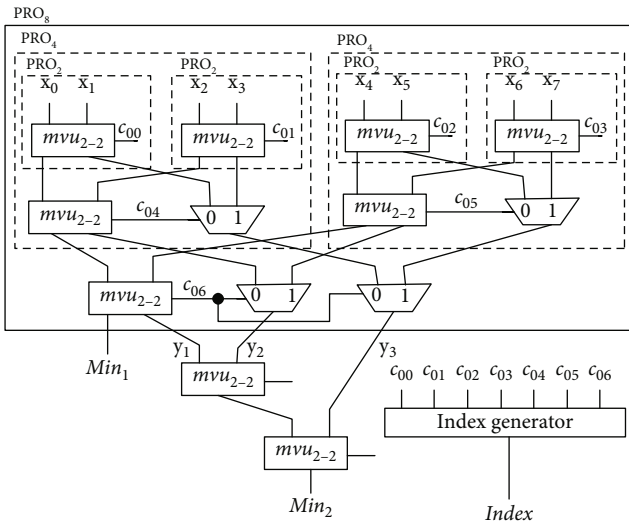


FIGURE 4: Low-complexity tree-based search module architecture.

as depicted in Figure 1(b). Also, assume m inputs of SM be a power of 2, i.e., $m = 2^k$. If m is not a power of 2, then such SM can be obtained by pruning some leaf nodes of the balanced SM having 2^k inputs as described in previous literatures [45–47]. Next, we present some state-of-the-art architectures to find the first two minima and index of the first minimum value.

The sorting-based SM architecture for eight inputs is depicted in Figure 2. The overall process of sorting-based SM is partitioned into two steps: (1) Min_1 is computed with the binary search tree and (2) an index-controlled multiplexing system is used to compute Min_2 . In Figure 1(c), the index of Min_1 can be estimated from comparison results. A set of candidates, $Y = \{y_1, y_2, y_3\}$, is computed by the multiplexing system which employs three 8-to-1 multiplexers to estimate the value of Min_2 . Once the set Y is in hand, two mvu_{2-1} are required to compute Min_2 . Consequently, the sorting-based SM requires nine 2-to-1 multiplexers, nine comparators, and three 8-to-1 multiplexers for processing

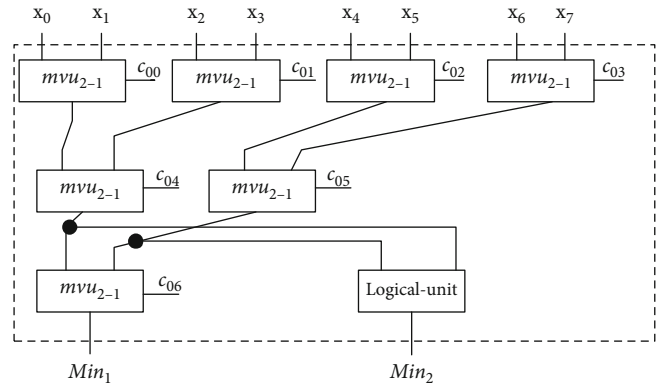


FIGURE 5: The proposed search module for DMS architecture.

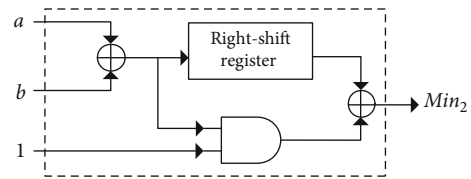


FIGURE 6: Detailed structure of logical unit for DMS architecture.

eight inputs. But it causes the long critical delay due to serially connected multiplexing system.

The sorting-based architecture is not feasible for high-speed applications because it induces a large critical delay due to serially connected multiplexing system. A tree-based architecture, as depicted in Figure 3, was proposed in [47] for high-speed realization. In tree-based SM, Min_1 and Min_2 have almost the same processing time due to the hierarchical tree architecture. Compared to sorting-based SM, it requires more comparators and multiplexers for finding Min_2 . Three mvu_{2-1} and one 2-to-1 multiplexer are additionally required for combining two subtrees. But the serially connected multiplexing system is completely removed which reduces the critical delay.

Input: a set X of m positive values.

for $j = 1: m$ **do**

Step 1

Partition set X into pairs of values and find the minimum value of each pair. Continue partitioning, and find Min_1 from the last pair of values.

Step 2

Input the last pair of values in Step 1 to logical unit, and estimate $\text{Min}_{\sim 2}$.

end for

Output: $X_{\min} = \{\text{Min}_1, \text{Min}_{\sim 2}\}$

ALGORITHM 1: DMS algorithm.

The tree-based architecture provides implementation advantages over sorting-based architecture in terms of critical delay, but it is not cost-effective for large block-length LDPC codes. Thus, it has higher hardware complexity that arises from large number of comparators and multiplexers. A low-complexity tree-based architecture was proposed in [48] which reduces the number of comparators while keeping the critical delay between those of the sorting-based and tree-based architectures. A low-complexity tree-based SM, referred to as SM_{pro} , for eight inputs is depicted in Figure 4 where a PRO_8 unit provides a candidate set, $Y = \{y_1, y_2, y_3\}$, for finding Min_2 . A tree structure composed of two mvu_{2-1} is required to find Min_2 from candidate set Y . SM_{pro} requires nine comparators and twenty 2-to-1 multiplexers to process eight inputs. Therefore, the existing sorting-based and tree-based search modules are not cost-effective for large block-length LDPC codes. Hence, a low-cost SM architecture is greatly needed for hardware implementation of MS-LDPC decoder. Next, we present SM, known as DMS architecture, which reduces the hardware complexity of MS decoder for large block-length LDPC codes.

4. Proposed Architecture

The complexity of comparators and multiplexers is considerable for hardware realization of the MS-LDPC decoder. A DMS-based SM is presented which reduces a large number of comparators and multiplexers while keeping the critical delay almost equal to the tree-based architecture. The proposed SM is conceptually similar to sorting-based SM. But the serially connected multiplexing system for finding Min_2 is completely removed which reduces the hardware complexity and critical delay. The proposed DMS-based SM estimates the $\text{Min}_{\sim 2}$ value using a logical unit, as depicted in Figure 5. The complexity and delay of logical unit are much less than those of the serially connected multiplexing system. The hardware complexity of both the proposed and sorting-based architectures is the same to find Min_1 . But the DMS-based SM estimates the $\text{Min}_{\sim 2}$ using a logical unit which reduces the hardware complexity.

The DMS-based SM for eight inputs is depicted in Figure 5, where seven comparators and seven 2-to-1 multiplexers are required to find Min_1 . The logical unit, as depicted in Figure 6, requires two adders, one right-shift register, and one AND gate for estimating Min_2 . The first

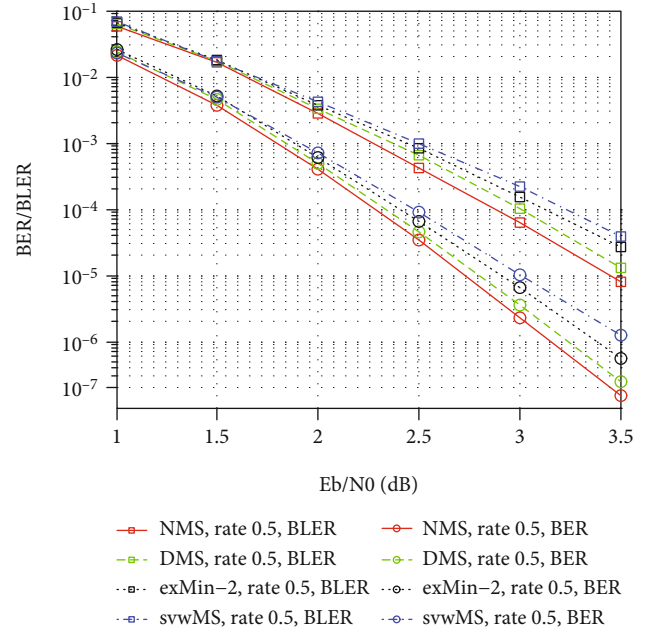


FIGURE 7: Error-correction performance of the proposed approach and its competitors for the IEEE802.16e (2304, 1152) LDPC code.

step of DMS approach is to replace the CNU function in (2) with

$$\psi_{m \rightarrow n}^{(j)} = \min_{n' \in N_m} \left| \psi_{n' \rightarrow m}^{(j)} \right| \prod_{n'' \in N_m} \text{sign} \left(\psi_{n'' \rightarrow m}^{(j)} \right). \quad (4)$$

In other words, the sign and output magnitudes are estimated from all N_m variable nodes arriving at check node c_m . The next step is to find the first two minimum values for CNU operation. Let $\lambda_{\min}^{(j)}$ and $\lambda_{\text{sub}}^{(j)}$ denote Min_1 and Min_2 , respectively. The magnitude of check-node output is computed as

$$\left| \psi_{m \rightarrow n}^{(j)} \right| = \begin{cases} \lambda_{\text{sub}} = \left\lceil \frac{1}{2}(a + b) \right\rceil, & \text{if } \varphi_{n \rightarrow m}^{(j)} = \lambda_{\min}, \\ \lambda_{\min}, & \text{otherwise,} \end{cases} \quad (5)$$

where a and b denote the variable nodes participating in the last mvu_{2-1} of DMS architecture. Thus, the DMS

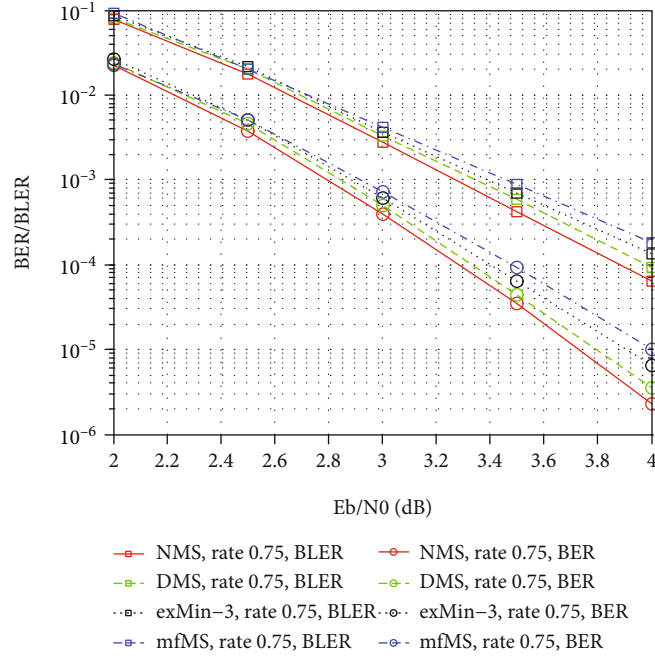


FIGURE 8: Error-correction performance of the proposed approach and its competitors for the IEEE802.16e (2304, 576) standard LDPC code.

architecture reduces the hardware complexity for CNU operation of the MS-LDPC decoder.

As an illustrative example, assume a set X of eight input values, $X = \{2, 8, 1, 6, 5, 3, 7, 4\}$. Based on Step 1 of the DMS algorithm, set X as partitioned into pair of values as $R = \{\{2, 8\}, \{1, 6\}, \{5, 3\}, \{7, 4\}\}$. Finding the minimum value of each pair, a subset is obtained as $X_1 = \{2, 1, 3, 4\}$. Again, partitioned subset X_1 into a pair of values as $R_1 = \{\{2, 1\}, \{3, 4\}\}$. Finding the minimum value of each pair, we obtain the last pair of values as $\{1, 3\}$ which returns the first minimum value as $\text{Min}_1 = \{1\}$. According to Step 2 of the DMS algorithm, the last pair of values, $\{1, 3\}$, is passed to the logical unit for finding $\text{Min}_{\sim 2}$. Based on (5), $\text{Min}_{\sim 2}$ can be estimated as $\lceil (1/2)(1+3) \rceil = 2$. Afterward, the DMS algorithm returns the output as $X_{\min} = \{1, 2\}$. It is important to mention that the DMS algorithm returns Min_1 which is always the first minimum value of set X , but it returns $\text{Min}_{\sim 2}$ which is the estimated second minimum value among the values of X ; it may or may not be the exact second minimum value. Consequently, the DMS algorithm provides an efficient architecture which is more cost-effective for large block-length LDPC codes.

5. Experimental Results

5.1. Performance Analysis. In this section, the error-correction performance of the proposed DMS approach in terms of bit error rate (BER) and block error rate (BLER) is compared with its counterparts under the same conditions. The standard IEEE802.16e LDPC codes with code rates 0.5 and 0.75 having a block length of 2304 are used for evaluating the performance of the proposed and some other existing algorithms. The performance of the proposed

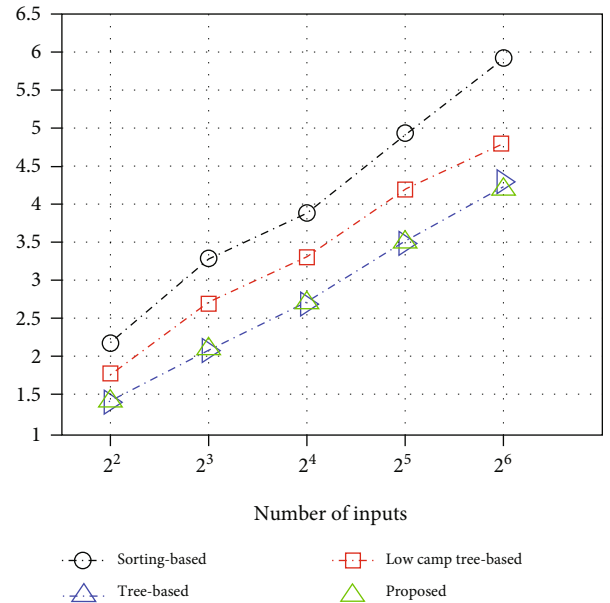


FIGURE 9: Critical delay of the proposed architecture and its counterparts for different numbers of inputs.

approach is compared with the NMS, mfMs, svwMS, and exMin- n [49] algorithms with maximum number of decoding iterations equal to 50. Binary phase-shift keying (BPSK) transmission is assumed over an AWGN channel. Figures 7 and 8 depict the performance analysis for the (2304, 1152) and (2304, 576) IEEE802.16e LDPC codes.

Figure 7 compares the error-correction performance of the proposed DMS algorithm with NMS, svwMS, and

TABLE 1: Comparisons of hardware complexity for different search modules.

Architecture	Sorting based [46]	Tree based [47]	Low-complexity tree based [48]	Proposed
Comparators	$2^k + k - 2$	$2^{k+1} - 3$	$2^k + k - 2$	$2^k - 1$
Multiplexors (2-to-1)	$2^k + k - 2$	$3 \cdot 2^k - 4$	$3 \cdot 2^k - 4$	$2^k - 1$
Multiplexors (2^k -to-1)	k	0	0	0
(Adders, shift registers)	0	0	0	(2, 1)
Critical delay	$(k + \lceil \log_2 k \rceil) \tau_c + \tau_{Mk} + (k + \lceil \log_2 k \rceil) \tau_{M2}$	$k \tau_c + (2k - 1) \tau_{M2}$	$(k + \lceil \log_2 k \rceil) \tau_c + (k + 1 \lceil \log_2 k \rceil) \tau_{M2}$	$k * \tau_c + \tau_{Lu} + k * \tau_{M2}$

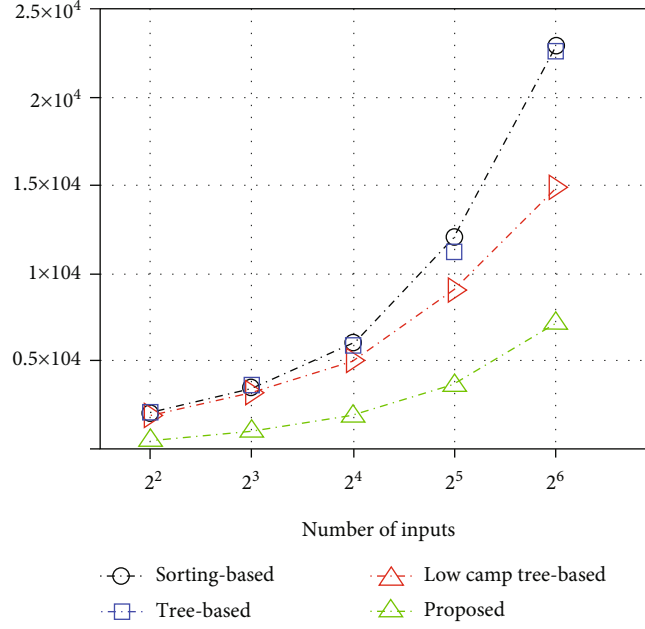


FIGURE 10: Area complexity of the proposed architecture and its counterparts for different numbers of inputs.

exMin- n , for $n = 2$. Numerical results show that the DMS algorithm provides an excellent error performance close to the NMS algorithm with code rate 0.5 and code length of 2304 for IEEE802.16e standard LDPC code. At a BER of 10^{-6} , the DMS algorithm performs very close to NMS with a degradation of 0.09 dB. On the other hand, the exMin-2 and swMS algorithms perform with a degradation of 0.20 dB and 0.30 dB, respectively.

Similarly, the error-correction performance of the DMS algorithm is also compared with NMS, mfMS, and exMin- n , for $n = 3$, for IEEE802.16e standard LDPC code with code rate 0.75 and a code length of 2304. Figure 9 reveals that the DMS algorithm performs close to the NMS algorithm with a degradation of 0.06 dB at BER of 10^{-5} . But the exMin-3 and mfMS algorithms provide a performance loss of 0.22 dB and 0.26 dB, respectively. As a result, the proposed DMS algorithm outperforms its counterparts under the same conditions by providing an error-correction performance very close to the NMS algorithm.

5.2. Complexity and Speed Performance. As compared to the state-of-the-art architectures [46–48], the proposed DMS architecture reduces the computational complexity for CNU operation of the MS-LDPC decoder. According to Table 1, a comparison of the hardware complexity and critical delay of DMS architecture with sorting- and tree-based architectures is shown, where τ_c , τ_{M2} , τ_{Mk} , and τ_{Lu} denote the delay of comparator, multiplexor (2-to-1), multiplexor (2^k -to-1), and logical unit, respectively. The sorting-based [46] and low-complexity tree-based [48] architectures require $2^k + k - 2$ comparators, and the tree-based [47] architecture requires $2^{k+1} - 3$ comparators to find the first two minima. As the DMS architecture completely removes the multiplexing system inevitable for sorting-based SM, it

requires $2^k - 1$ comparators for finding two minima. The sorting-based SM requires $2^k + k - 2$ 2-to-1 and $k2^k$ -to-1 multiplexors, where the tree- and low-complexity tree-based architectures require $3 \cdot 2^k - 4$ comparators to find the first two minima. But the DMS architecture requires $2^k - 1$ multiplexors for finding Min_1 and Min_2 . Also, the DMS architecture additionally requires two adders, one right-shift register, and one AND gate for the implementation of logical unit, but it keeps the critical delay almost equal to that of the tree-based architecture. Consequently, if the number of input values is equal to 16, for example, the DMS architecture eliminates 16.66% comparators compared with the sorting-based and low-complexity tree-based architectures and 48.27% comparators compared with the tree-based architecture. Also, the proposed architecture requires 65.90% less multiplexors compared with the tree-based and low-complexity tree-based architectures.

For fair comparison, four types of architectures are implemented in 6-bit CMOS standard cell library process: the sorting-based [46], tree-based [47], low-complexity tree-based [48], and proposed DMS architectures. Figure 9 depicts the critical delay for four architectures against different numbers of inputs. To the best of our knowledge, the tree-based [47] architecture is assumed to be the best architecture in literature for high-speed realization. Figure 9 shows that the critical delay of the DMS architecture is almost the same as that of the tree-based [47] architecture.

The most area-efficient architecture was proposed by Lee et al. in [48]. Figure 10 shows that when k is equal to 6, the proposed architecture saves 69%, 68%, and 52% area over the sorting-based, tree-based, and low-complexity tree-based architectures, respectively. Consequently, the proposed architecture is proved to be the most area-efficient architecture for high-speed realization. Consequently, the

DMS architecture reduces the hardware complexity of the MS-LDPC decoder for CNU operation.

6. Conclusion

An efficient approach has been proposed to find the first two minima for CNU operation of the MS-LDPC decoder. The proposed architecture is conceptually similar to the sorting-based architecture, but it completely removes the large-sized multiplexing system which results in a prominent reduction in hardware complexity and critical delay. The proposed architecture estimates the second minimum value by utilizing a logical unit circuit having complexity and delay less than those of the multiplexing system. Based on the experimental results, the proposed architecture provides a critical delay almost the same as that of the tree-based architecture. More specifically, the proposed SM eliminates a large number of comparators and multiplexors for CNU operation of the MS-LDPC decoder. Therefore, the DMS architecture saves 69%, 68%, and 52% area over the sorting-based, tree-based, and low-complexity tree-based architectures, respectively. Furthermore, simulation results show that the proposed approach outperforms its competitors in terms of bit error rate (BER) and block error rate (BLER) by providing an excellent error-correction performance over an AWGN channel.

Data Availability

No data were used to support this study.

Conflicts of Interest

The authors declare that they have no conflicts of interest.

References

- [1] W. U. Khan, J. Liu, F. Jameel, V. Sharma, R. Jantti, and Z. Han, "Spectral efficiency optimization for next generation NOMA-enabled IoT networks," *IEEE Transactions on Vehicular Technology*, vol. 69, no. 12, pp. 15284–15297, 2020.
- [2] X. Li, Q. Wang, M. Liu et al., "Cooperative wireless-powered NOMA relaying for B5G IoT networks with hardware impairments and channel estimation errors," *IEEE Internet of Things Journal*, vol. 8, no. 7, pp. 5453–5467, 2021.
- [3] W. U. Khan, F. Jameel, M. A. Jamshed, H. Pervaiz, S. Khan, and J. Liu, "Efficient power allocation for NOMA-enabled IoT networks in 6G era," *Physical Communication*, vol. 39, 2020.
- [4] A. Junejo, M. K. A. Kaabar, and S. Mohamed, "Future Robust Networks: Current Scenario and Beyond for 6G," *IMCC Journal of Science*, vol. 1, pp. 67–81, 2021.
- [5] X. Li, M. Zhao, Y. Liu, L. Li, Z. Ding, and A. Nallanathan, "Secrecy analysis of ambient backscatter NOMA systems under I/Q imbalance," *IEEE Transactions on Vehicular Technology*, vol. 69, no. 10, pp. 12286–12290, 2020.
- [6] W. U. Khan, F. Jameel, N. Kumar, R. Jantti, and M. Guizani, "Backscatter-enabled efficient V2X communication with non-orthogonal multiple access," *IEEE Transactions on Vehicular Technology*, vol. 70, no. 2, pp. 1724–1735, 2021.
- [7] X. Li, Y. Zheng, W. U. Khan et al., "Physical layer security of cognitive ambient backscatter communications for green Internet-of-things," *IEEE Transactions on Green Communications and Networking*, vol. 5, no. 3, pp. 1066–1076, 2021.
- [8] W. U. Khan, X. Li, M. Zeng, and O. A. Dobre, "Backscatter-enabled NOMA for future 6G systems: a new optimization framework under imperfect SIC," *IEEE Communications Letters*, vol. 25, no. 5, pp. 1669–1672, 2021.
- [9] H. H. Attar, A. A. A. Solyman, M. R. Khosravi, L. Qi, M. Alhihi, and P. Tavallali, "Bit and packet error rate evaluations for half-cycle stage cooperation on 6G wireless networks," *Physical Communication*, vol. 44, p. 101249, 2020.
- [10] R. G. Gallager, *Low-Density Parity-Check Codes*, MIT Press, Cambridge, MA, USA, 1963.
- [11] D. J. C. MacKay and R. M. Neal, "Near Shannon limit performance of low density parity check codes," *Electronics Letters*, vol. 33, no. 6, pp. 457–458, 1997.
- [12] M. Asif, W. Zhou, M. Ajmal, and N. A. Khan, "A construction of high performance quasicyclic LDPC codes: a combinatoric design approach," *Wireless Communications and Mobile Computing*, vol. 2019, 10 pages, 2019.
- [13] M. Asif, W. Zhou, Q. Yu, X. Li, and N. A. Khan, "A deterministic construction for jointly designed quasicyclic LDPC coded-relay cooperation," *Wireless Communications and Mobile Computing*, vol. 2019, 12 pages, 2019.
- [14] M. Asif, W. Zhou, Q. Yu, S. Adnan, and M. S. Iqbal, "Jointly designed quasi-cyclic LDPC-coded cooperation with diversity combining at receiver," *International Journal of Distributed Sensor Networks*, vol. 16, no. 7, 2020.
- [15] M. Asif, W. Zhou, J. S. Ally, and N. A. Khan, "An algebraic construction of quasi-cyclic LDPC codes based on the conjugates of primitive elements over finite fields," in *IEEE International Conference on Communication Technology (ICCT)*, pp. 115–119, 2018.
- [16] W. U. Khan, N. Imtiaz, and I. Ullah, "Joint optimization of NOMA-enabled backscatter communications for beyond5G IoT networks," *Internet Technology Letters*, vol. 4, no. 2, 2021.
- [17] F. Jameel, "Time slot management in backscatter systems for large-scale IoT networks," in *Wireless-Powered Backscatter Communications for Internet of Things*, pp. 51–65, Springer, Cham, 2021.
- [18] W. U. Khan, "NOMA-enabled wireless powered backscatter communications for secure and green IoT networks," in *Wireless-Powered Backscatter Communications for Internet of Things*, pp. 103–131, Springer, Cham, 2021.
- [19] F. Jameel, "Multi-tone carrier backscatter communications for massive IoT networks," in *Wireless-Powered Backscatter Communications for Internet of Things*, pp. 39–50, Springer, Cham, 2021.
- [20] B. Oudjani, H. Tebbikh, and N. Doghmane, "Modification of extrinsic information for parallel concatenated Gallager/convolutional code to improve performance/complexity trade-offs," *AEU-International Journal of Electronics and Communications*, vol. 83, no. 1, pp. 484–491, 2018.
- [21] E. M. Ar-Reyouchi, Y. Chatei, K. Ghomid, M. Hammouti, and B. Hajji, "Efficient coding techniques algorithm for cluster-heads communication in wireless sensor networks," *AEU-International Journal of Electronics and Communications*, vol. 82, no. 12, pp. 294–304, 2017.
- [22] J. Liu and R. C. De-Lamare, "Rate-compatible LDPC codes with short block lengths based on puncturing and extension techniques," *AEU-International Journal of Electronics and Communications*, vol. 69, no. 11, pp. 1582–1589, 2015.

- [23] A. Kadi, S. Najah, and M. Mrabti, "An exponential factor appearance probability belief propagation algorithm for regular and irregular LDPC codes," *AEU-International Journal of Electronics and Communications*, vol. 69, no. 6, pp. 933–936, 2015.
- [24] Z. Zhang, V. Anantharam, M. J. Wainwright, and B. Nikolic, "An efficient 10GBASE-T ethernet LDPC decoder design with low error floors," *IEEE Journal of Solid-State Circuits*, vol. 45, no. 4, pp. 843–855, 2010.
- [25] J. Jin and C. Y. Tsui, "An energy efficient layered decoding architecture for LDPC decoder," *IEEE Transactions on Very Large Scale Integration (VLSI) Systems*, vol. 18, no. 8, pp. 1185–1195, 2010.
- [26] T. H. Tran, Y. Nagao, H. Ochi, and M. Kurosaki, "ASIC design of 7.7 Gbps multi-mode LDPC decoder for IEEE 802.11ac," in *Int. Symp., Commun. and Inf. Technologies (ISCIT)*, pp. 259–263, Incheon, 2014.
- [27] S. Ajaz and H. Lee, "Multi-Gb/s multi-mode LDPC decoder architecture for IEEE 802.11ad standard," in *Asia Pacific Conf., Circuits and Systems (APCCAS)*, pp. 153–156, Ishigaki, Japan, 2014.
- [28] J. Chen, A. Dholakia, E. Eleftheriou, M. P. C. Fossorier, and X. Y. Hu, "Reduced-complexity decoding of LDPC codes," *IEEE Transactions on Communications*, vol. 53, no. 8, pp. 1288–1299, 2005.
- [29] F. Angarita, J. Valls, V. Almenar, and V. Torres, "Reduced-complexity min-sum algorithm for decoding LDPC codes with low error-floor," *IEEE transactions on circuits and systems I*, vol. 61, no. 7, pp. 2150–2158, 2014.
- [30] J. Chen and M. Fossorier, "Density evolution for two improved BP-based decoding algorithms of LDPC codes," *IEEE Communications Letters*, vol. 6, no. 5, pp. 208–210, 2002.
- [31] A. Darabiha, A. Carusone, and F. Kschischang, "A bit-serial approximate min-sum LDPC decoder and FPGA implementation," in *in Proc. IEEE Int. Symp. Circuits Syst*, pp. 149–152, 2006.
- [32] Q. Wang, K. Shimizu, T. Ikenaga, and S. Goto, "A power-saved 1Gbps irregular LDPC decoder based on simplified min-sum algorithm," in *in Proc. Int. Symp. VLSI Des., Autom. Test*, pp. 1–4, 2007.
- [33] C. Zhang, Z. Wang, J. Sha, L. Li, and J. Lin, "Flexible LDPC decoder design for multigigabit-per-second applications," *IEEE transactions on circuits and systems I*, vol. 57, no. 1, pp. 116–124, 2010.
- [34] W. U. Khan, Z. Yu, S. Yu, G. A. S. Sidhu, and J. Liu, "Efficient power allocation in downlink multi-cell multi-user NOMA networks," *IET Communications*, vol. 13, no. 4, pp. 396–402, 2018.
- [35] W. U. Khan, F. Jameel, T. Ristaniemi, S. Khan, G. A. S. Sidhu, and J. Liu, "Joint spectral and energy efficiency optimization for downlink NOMA networks," *IEEE Transactions on Cognitive Communications and Networking*, vol. 6, no. 2, pp. 645–656, 2019.
- [36] F. Jameel, "Towards intelligent IoT networks: reinforcement learning for reliable backscatter communications," in *2019 IEEE Globecom Workshops (GC Wkshps)*, Waikoloa, HI, USA, 2019.
- [37] W. U. Khan, F. Jameel, G. A. S. Sidhu, M. Ahmed, X. Li, and R. Jantti, "Multiobjective optimization of uplink NOMA-enabled vehicle-to-infrastructure communication," *IEEE Access*, vol. 8, pp. 84467–84478, 2020.
- [38] F. Jameel, S. Zeb, W. U. Khan, S. A. Hassan, Z. Chang, and J. Liu, "NOMA-enabled backscatter communications: toward battery-free IoT networks," *IEEE Internet of Things Magazine*, vol. 3, no. 4, pp. 95–101, 2020.
- [39] W. U. Khan, "Secure backscatter communications in multi-cell NOMA networks: enabling link security for massive IoT networks," in *IEEE INFOCOM 2020-IEEE Conference on Computer Communications Workshops (INFOCOM WKSHPS)*, Toronto, ON, Canada, 2020.
- [40] F. Jameel, "Efficient power-splitting and resource allocation for cellular V2X communications," in *IEEE Transactions on Intelligent Transportation Systems*, 2020.
- [41] F. Jameel, "Reinforcement learning for scalable and reliable power allocation in SDN-based backscatter heterogeneous network," in *IEEE INFOCOM 2020-IEEE Conference on Computer Communications Workshops (INFOCOM WKSHPS)*, Toronto, ON, Canada, 2020.
- [42] M. Nawaz, W. U. Khan, Z. Ali, A. Ihsan, O. Waqar, and G. A. S. Sidhu, "Resource optimization framework for physical layer security of dual-hop multi-carrier decode and forward relay networks," *IEEE Open Journal of Antennas and Propagation*, vol. 2, pp. 634–645, 2021.
- [43] S. Yu, W. U. Khan, X. Zhang, and J. Liu, "Optimal power allocation for NOMA-enabled D2D communication with imperfect SIC decoding," *Physical Communication*, vol. 46, p. 101296, 2021.
- [44] K. Bakht, F. Jameel, Z. Ali et al., "Power allocation and user assignment scheme for beyond 5G heterogeneous networks," *Wireless Communications and Mobile Computing*, vol. 2019, 11 pages, 2019.
- [45] X. Qian, C. Zhixiang, P. Xiao, and G. Satoshi, "A sorting-based architecture of finding the first two minimum values for LDPC decoding," in *IEEE, Int. Coll. on Signal Processing and its Applications*, pp. 95–98, 2001.
- [46] Q. Xie, Z. Chen, X. Peng, and S. Goto, "A sorting based architecture of finding the first two minimum values for LDPC decoding," in *in Proc. IEEE CSPA*, pp. 95–98, 2011.
- [47] W. Chen-Long, S. Ming-Der, and L. Shin-Yo, "Algorithms of finding the first two minimum values and their hardware implementation," *IEEE transactions on circuits and systems I*, vol. 55, no. 11, pp. 3430–3437, 2008.
- [48] Y. Lee, B. Kim, J. Jun, and P. In-Cheol, "Low-complexity tree architecture for finding the first two minima," *IEEE Transactions on Circuits and Systems II, Express Briefs*, vol. 62, no. 1, pp. 61–64, 2015.
- [49] I. Tsatsaragkos and V. Paliouras, "Approximate algorithms for identifying minima on min-sum LDPC decoders and their hardware implementation," *IEEE Transactions on Circuits and Systems II, Express Briefs*, vol. 62, no. 8, pp. 766–770, 2015.

Research Article

Outage Performance of Full-Duplex Relay Networks Powered by RF Power Station in Ubiquitous Electric Internet of Things

Yu Zhang ¹, Xiaofei Di ², Hongliang Duan ^{3,4}, Xi Yang ^{5,6}, Peng Wu ¹
and Baoguo Shan ¹

¹Institute of Economics and Energy Supply and Demand, State Grid Energy Research Institute Co., Ltd., Beijing 102209, China

²School of Software Engineering, Beijing Jiaotong University, Beijing 100044, China

³School of Mechanical Engineering, Northwestern Polytechnical University, Xi'an 710072, China

⁴Beijing Institute of Space Long March Aerospace Vehicle, Beijing 100076, China

⁵School of Information, Beijing Wuzi University, Beijing 101149, China

⁶Beijing Intelligent Logistics System Collaborative Innovation Center, Beijing 101149, China

Correspondence should be addressed to Xiaofei Di; xfdi@bjtu.edu.cn

Received 31 March 2021; Revised 17 June 2021; Accepted 16 July 2021; Published 10 August 2021

Academic Editor: Yuan Ding

Copyright © 2021 Yu Zhang et al. This is an open access article distributed under the Creative Commons Attribution License, which permits unrestricted use, distribution, and reproduction in any medium, provided the original work is properly cited.

This paper investigates a full-duplex relay network assisted by radio frequency (RF) power station in ubiquitous electric Internet of Things (UEIoT), where a wireless sensor on high voltage transmission line collects electric data and then transmits data to a destination via a full-duplex decode-and-forward relay. The destination receives and processes the data to inspect the state of high voltage transmission line. Both the sensor and relay do not have fixed energy source; so, they first have to harvest energy from a RF power station and then complete information transmission by using the harvested energy. As the line-of-sight (LOS) propagations often exist in outdoor application scenarios of UEIoT, the Rician fading channel is adopted in the network. To explore the system outage performance, the explicit expressions of the outage probability and throughput of the system are derived by using mathematical analysis. Simulation results validate the correctness of our theoretical analysis and also evaluate the effects of system parameters and deployment position of power station on the outage performance.

1. Introduction

The ubiquitous electric Internet of Things (UEIoT) aims to realize the interconnection of all things and human-computer interaction in the power system by integrating modern information technologies, including wireless sensor networks, artificial intelligence, and advanced communication technologies [1]. The State Grid Corporation of China has planned to initially build UEIoT by 2021 to support the development of grid business and some other emerging businesses. By 2024, UEIoT will be established to form an energy internet ecosystem with joint construction, cogovernance, and sharing [2, 3]. UEIoT has attracted much attention from academia to industry [4, 5].

The UEIoT can be applied to a large number of outdoor and field application scenarios, such as field power line inspection. Unfortunately, although wireless sensors are deployed on the high-voltage line, they cannot be driven directly by the power of the high-voltage line. So, recently passive Internet of Things [6] has attracted attention and become an important part of UEIoT, where the sensors can be wirelessly charged by harvesting energy of the radio frequency (RF) signals emitted by wireless power stations [7–9]. The authors in [7] realized a practical wireless powered sensor network and investigated the efficiency of RF energy harvesting (EH). In [8, 9], an IoT powered by a static and mobile base station was, respectively, studied, where a number of wireless sensors first harvested

energies from base station and then transmit their information to the base station. The works in [6–9] considered the linear EH model, while [10, 11] further considered a more practical nonlinear EH model. In [10], a wireless powered cognitive radio sensor network was studied, where two primary users communicate to each other with the help of a sensor node with nonlinear energy harvester and accurate expressions of the outage probability and throughput were derived for the primary system. [11] considered a downlink nonorthogonal multiple access (NOMA) network, where the near user was equipped with a nonlinear energy harvester, and the outage probabilities and throughput for both the far and near users were derived.

On the other hand, to complete information delivery, wireless sensors generally communicate by using relaying mode due to the long distance among sensors in IoT [12]. Compared with traditional half-duplex relay, full-duplex relay can use the same frequency band to simultaneously receive and transmit information; so, the transmission delay and system spectrum efficiency are greatly improved [13, 14]. Owing to these merits, full-duplex relay has attracted increasing interest [15–17]. In [15], an optimal beamformer design was proposed for a full-duplex decode-and-forward (DF) relay system with self-energy recycling. [16] extended the one-way relay system in [15] to two-way relay one and analyzed outage performance of the system. The authors in [17] studied effect of residual self-interference (SI) on the stability performance of the full-duplex amplify-and-forward (AF) relay system.

To inherit the benefits of RF EH and full-duplex relaying, some exiting works have investigated the full-duplex relay networks powered by RF EH, see e.g., [18–21]. In [18], some full-duplex AF relays first harvested energy from a source and then received and forwarded the information of the source to a destination by using the harvested energy. The achievable information rate was maximized by designing optimal power allocation and relay selection policy [18]. The authors in [19] further studied two-way relay system and derived closed-form expressions of the throughput and outage probability over Rayleigh fading channels. In [20], a multidestination relay network was considered, where a source first emitted energy to a full-duplex DF relay and then the relay further used the harvested energy to forward the information of the source to multiple destinations, and the spectral efficiency of system was enhanced by jointly optimizing the time allocation, subcarriers, and transmission power of the source and relay. Different from the works [18–21] considered a relay network consisting of a source, a DF relay and a destination, as well as a power station, where the source and relay first harvested energy from the power station and then cooperatively transmit information to the destination.

This paper also considers a full-duplex relay network assisted by a dedicated power station in the UEIoT, as shown in Figure 1. A wireless sensor (S) on high voltage transmission line collects electric data and then transmits data to a base station (D) via a dual antenna full-duplex DF relay (R). D receives and processes the data to inspect the state of high voltage transmission line. Both S and R do not have fixed energy source; so, they first have to harvest energy from a RF power station and then complete information transmission by using the harvested energy. Different from [21], the Rician fading

channel model is better suited in outdoor roadside scenario with RF energy harvesting, according to the experimental result [22]. As UEIoT is usually deployed in outdoor roadside scenario, the Rician fading channel model is adopted in this paper.

For such a network, our contributions are summarized as follows. Firstly, the EH process and information transmission are modeled for the full-duplex relay network powered by RF power station. Then, the explicit expressions of the outage probability and throughput of the system are derived by using mathematical analysis in order to explore the system outage performance. Simulation results validate the correctness of our theoretical analysis, and the effects of system parameters on the outage probability are also discussed. Finally, the optimal deployment position of power station is also investigated, which may provide some useful insights on the future practical applications of UEIoT.

The rest of this paper is organized as follows. In section 2, the system model is presented. Section 3 derives the outage probability and throughput of the system. Section 4 shows some simulation results to evaluate our theoretical analysis and illustrate the system performance. Finally, this paper is concluded in section 5.

2. System Model

We consider a full-duplex relay network assisted by RF power station (PS) in UEIoT, as shown in Figure 1, which is composed of a source (S), a relay (R), and a destination (D), as well as a dedicated RF PS. S desires to transmit information to D with the help of R . S and R do not have fixed energy source; so, they have to harvest energy from PS and then use the harvested energy to accomplish information transmission. R adopts the decode-and-forward (DF) protocol. As the decoding processing power required at R is much less than its transmit power, its decoding processing power is thus ignored. PS, S , and D are equipped with single antenna. R is equipped with two antennas, one is the receiving antenna used to receive information from S or harvest energy from PS, and the other is the transmitting antenna used to forward received information to D in the full-duplex mode.

Figure 2 illustrates the time frame of the transmission protocol. It is assumed that each time frame is with the time period of T , which is divided into two parts, where the first part is used for energy transfer and the second one is for information transmission with full-duplex relaying. Considering there exist line-of-sight (LOS) propagations between the nodes in the outdoor UEIoT, the links between any two nodes are modeled as Rician fading channels. The channel coefficients are assumed to be unchanged in each time frame T , but may change independently between any two adjacent time frames.

Specifically, during the first part with time interval of αT , PS broadcasts energy to S and R , where α is the time division factor satisfying $0 \leq \alpha \leq 1$. The energy harvested by S and R can be, respectively, expressed by

$$E_S = \alpha T \eta P_B d_1^{-m} |h_1|^2, \quad (1)$$

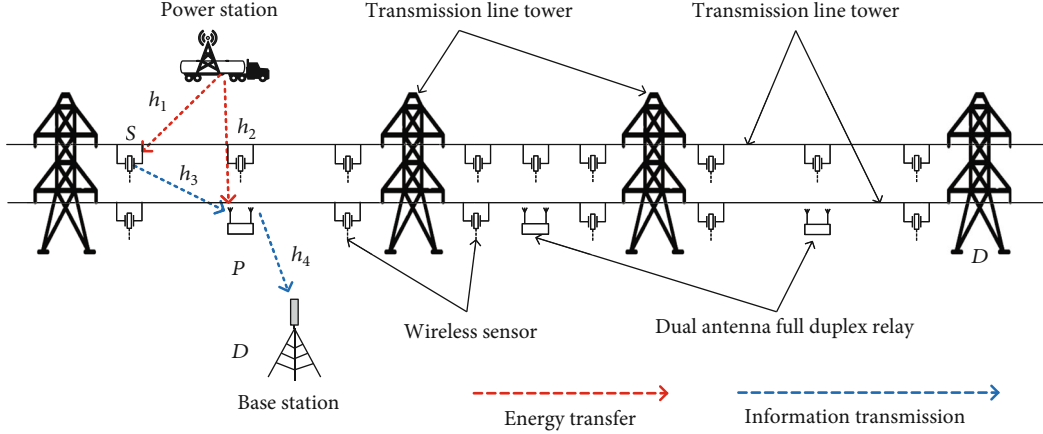


FIGURE 1: System model of full-duplex relay network in UEIoT.

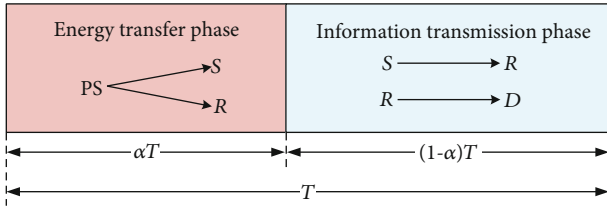


FIGURE 2: Time frame of the transmission protocol.

$$E_R = \alpha T \eta P_B d_2^{-m} |h_2|^2, \quad (2)$$

where h_1 and h_2 are the channel coefficients of the links from PS to S (PS-S) and from PS to R (PS-R), respectively. d_1 and d_2 denote the distances between PS and S and between PS and R, respectively. P_B denotes the transmit power of PS. m represents the path loss exponent. η is the energy harvesting efficiency satisfying $0 \leq \eta \leq 1$.

During the second part with time interval of $(1 - \alpha)T$, by using the harvested energies, S and R cooperatively transmit information to D with the full-duplex mode; that is, S transmits information to R, and R simultaneously receives information of S and forwards the information to D. From (1) and (2), the available transmit power at S and R can be, respectively, expressed by

$$P_S = \frac{E_S}{(1 - \alpha)T} = \frac{\eta \alpha P_B d_1^{-m} |h_1|^2}{(1 - \alpha)}, \quad (3)$$

$$P_R = \frac{E_R}{(1 - \alpha)T} = \frac{\eta \alpha P_B d_2^{-m} |h_2|^2}{(1 - \alpha)}. \quad (4)$$

Let x_S and x_R , respectively, represent the signals transmitted by S and R, with $E[|x_S|^2] = P_S$ and $E[|x_R|^2] = P_R$. n_R denotes the additive Gaussian white noise (AWGN) with the mean of 0 and the variance of N_0 at the relay node R. The signal received at R can be expressed as

$$y_R = \sqrt{d_3^{-m}} h_3 x_S + h_{RR} x_R + n_R, \quad (5)$$

where the first term of right part $\sqrt{d_3^{-m}} h_3 x_S$ is the desired signal, and the second term $h_{RR} x_R$ is the self interference (SI). h_3 represents fading coefficient of the link from S to R (S-R). h_{RR} represents the channel coefficient of the link between the transmitting antenna and receiving antenna of R. d_3 is the distance between S and R.

R adopts self-interference cancellation (SIC) technology to eliminate SI. However, it is hard to completely eliminate SI in practice, and therefore, the residual self-interference (RSI) always exists [23], which may limit the system performance of full-duplex mode. In order to describe the RSI, denote it as n_{RSI} , and then the signal received at R can be transformed into [24]

$$y_R = \sqrt{d_3^{-m}} h_3 x_S + n_{RSI} + n_R, \quad (6)$$

where n_{RSI} is modeled as a complex Gaussian distribution with mean of 0 and variance of N_{RSI} [25]. N_{RSI} is proportional to the transmit power P_R of R, that is,

$$N_{RSI} = \Omega P_R, \quad (7)$$

where Ω represents the SIC capability and indicates the strength of the self-interference cancellation capability of relay. The smaller the value Ω is, the stronger the relay SIC capability is.

Simultaneously, R also decodes and forwards signal to D while receiving the signal from S. The signal received at D can be expressed as

$$y_D = \sqrt{d_4^{-m}} h_4 x_R + n_D, \quad (8)$$

where h_4 denotes the fading coefficient of the link from R to D (R-D), and d_4 represents the distance between R and D. n_D represents the AWGN with the mean of 0 and variance of N_0 at D.

Following (6), the received signal-to-interference and noise ratio (SINR) for decoding at R can be given by

$$\gamma_R = \frac{d_3^{-m} P_S |h_3|^2}{N_{RSI} + N_0}. \quad (9)$$

By substituting (3) and (7) into (9), and using some simple mathematical transformations, we can obtain that

$$\gamma_R = \frac{d_1^{-m} d_3^{-m} \varphi_1 \varphi_3}{\Omega d_2^{-m} \varphi_2 + (1/\Phi)}, \quad (10)$$

where $\Phi = \eta\alpha\gamma_0/(1-\alpha)$ with $\gamma_0 = P_B/N_0$, and $\varphi_i = |h_i|^2$ ($i = 1, 2, 3, 4$).

Similarly, by using (4), (7), and (8), and after some mathematical transformations, the received signal-to-noise ratio (SNR) at D can be given by

$$\gamma_D = \Phi d_2^{-m} d_4^{-m} \varphi_2 \varphi_4. \quad (11)$$

3. Outage Performance Analysis

In this section, we analyze the outage probability of the system. As R adopts DF protocol, it will decode the information of S and forward the information to D if the information is correctly decoded. Let γ_{th} be the required SINR for successful transmissions for both S - R link and R - D link. Then, the outage probability of the system can be expressed by

$$P_{\text{out}} = P_r\{\gamma_R < \gamma_{th}\} + (1 - P_r\{\gamma_R < \gamma_{th}\})P_r\{\gamma_D < \gamma_{th}\}, \quad (12)$$

where $P_r\{\gamma_R < \gamma_{th}\}$ is the outage probability of the first hop (i.e., S - R link), and $P_r\{\gamma_D < \gamma_{th}\}$ is the outage probability of the second hop (i.e., R - D link). For convenience, $P_r\{\gamma_R < \gamma_{th}\}$ and $P_r\{\gamma_D < \gamma_{th}\}$ are represented as P_{out_R} and P_{out_D} , respectively.

Define R_{th} (in bps/Hz) as a target transmission rate threshold. According to the Shannon formula, we can have that

$$R_{th} = (1 - \alpha) \log_2(1 + \gamma_{th}), \quad (13)$$

and thus γ_{th} can be calculated as $\gamma_{th} = 2^{R_{th}/(1-\alpha)} - 1$.

To calculate P_{out_R} and P_{out_D} , firstly it can be seen that there are two multiplied random variables φ_i in (10) and (11). Following the Rician distribution, the probability density function (PDF) $f_{\varphi_i}(x)$ and cumulative probability function (CDF) $F_{\varphi_i}(x)$ of the random variable φ_i are, respectively, given by [26]

$$f_{\varphi_i}(x) = \frac{(K_i + 1)e^{-K_i}}{\lambda_i} \sum_{l=0}^{\infty} \left(\frac{K_i + 1}{\lambda_i}\right)^l \frac{K_i^l x^l}{(l!)^2} e^{-\frac{K_i+1}{\lambda_i}x}, \quad (14)$$

$$F_{\varphi_i}(x) = \int_0^x f_{\varphi_i}(x) dx = 1 - e^{-K_i} \sum_{l=0}^{\infty} \sum_{m=0}^l \frac{K_i^l B_i^m x^m}{m! l!} e^{-B_i x}, \quad (15)$$

where $B_i = ((K_i + 1)/\lambda_i)$ ($i = 1, 2, 3, 4$). K_i and λ_i represent the Rician factor and the mean of random variables φ_i , respectively.

In order to facilitate the derivation and analysis, define an auxiliary variable $Y_{ij} = \varphi_i \varphi_j$, and the CDF of Y_{ij} can be expressed as

$$\begin{aligned} F_{Y_{ij}}(y) &= P_r\{Y_{ij} < y\} = P_r\{\varphi_i \varphi_j < y\} \\ &= P_r\left\{\varphi_i < \frac{y}{\varphi_j}\right\} = \int_0^{\infty} F_{\varphi_i}\left(\frac{y}{\varphi_j}\right) f_{\varphi_j}(\varphi_j) d\varphi_j. \end{aligned} \quad (16)$$

By using (14) and (15), the CDF of Y_{ij} in (16) can be further calculated as

$$\begin{aligned} F_{Y_{ij}}(y) &= \int_0^{\infty} \left\{1 - e^{-K_i} \sum_{l=0}^{\infty} \sum_{m=0}^l \frac{K_i^l B_i^m}{l! m!} \left(\frac{y}{\varphi_j}\right)^m e^{-B_i \frac{y}{\varphi_j}}\right\} f_{\varphi_j}(\varphi_j) d\varphi_j \\ &= 1 - \int_0^{\infty} e^{-K_i} \sum_{l=0}^{\infty} \sum_{q=0}^l \frac{K_i^l B_i^q}{l! q!} \left(\frac{y}{\varphi_j}\right)^q e^{-B_i \frac{y}{\varphi_j}} e^{-B_j \varphi_j} \sum_{k=0}^{\infty} \frac{(B_j K_j)^k}{(k!)^2} \cdot \varphi_j^k d\varphi_j \\ &= 1 - 2e^{-(K_i+K_j)} \sum_{l=0}^{\infty} \sum_{k=0}^{\infty} \sum_{q=0}^l \frac{K_i^l K_j^k}{l! q! (k!)^2} (B_i B_j)^{\frac{k+q+1}{2}} K_{k-q+1}(2\sqrt{B_i B_j y}), \end{aligned} \quad (17)$$

where $A_j = B_j e^{-K_j}$ and $K_v(\cdot)$ are the modified Bessel function of the second kind [27].

Then, by using (10) and (17), the outage probability of the first hop can be derived as

$$\begin{aligned} P_{\text{out}_R} &= P_r\left\{\frac{d_1^{-m} d_3^{-m} \varphi_1 \varphi_3}{\Omega_B d_2^{-m} \varphi_2 + (1/\Phi)} < \gamma_{th}\right\} \\ &= P_r\left\{Y_{13} < \frac{\gamma_{th}(\Omega_B d_2^{-m} \varphi_2 + (1/\Phi))}{d_1^{-m} d_3^{-m}}\right\} \\ &= \int_0^{\infty} f_{\varphi_2}(\varphi_2) F_{Y_{13}}\left(\frac{\gamma_{th}(\Omega_B d_2^{-m} \varphi_2 + (1/\Phi))}{d_1^{-m} d_3^{-m}}\right) d\varphi_2 \\ &\triangleq 1 - \Delta, \end{aligned}$$

where

$$\begin{aligned} \Delta &= 2A_2 e^{-(K_1+K_3)} \sum_{q=0}^{\infty} \sum_{l=0}^{\infty} \sum_{k=0}^{\infty} \sum_{z=0}^l \frac{(B_2 K_2)^q K_1^l K_3^k}{l! z! (k!)^2 (q!)^2} \\ &\cdot \int_0^{\infty} \varphi_2^q e^{-B_2 \varphi_2} \left[\frac{B_1 B_3 \gamma_{th} (\Omega_B d_2^{-m} \varphi_2 + (1/\Phi))}{d_1^{-m} d_3^{-m}}\right]^{\frac{k+m+1}{2}} \\ &\cdot K_{k-z+1}\left(2\sqrt{\frac{B_1 B_3 \gamma_{th} (\Omega_B d_2^{-m} \varphi_2 + (1/\Phi))}{d_1^{-m} d_3^{-m}}}\right) d\varphi_2. \end{aligned}$$

Similarly, by using (11) and (17), the outage probability of the second hop can be derived as

TABLE 1: System simulation parameter table.

Parameter	Explanation	Default value/value range
η	Energy harvesting efficiency	0.8/0-1
λ_i	Mean of φ_i	1
d_i	Distance	3 m
m	Path loss coefficient	2
Ω	SIC capability	-20 dB
R_{th}	Transmission rate	0.05 bits/s/Hz/0.01-0.5 bits/s/Hz
α	Time division factor	0.4/0-1
γ_0	Power station transmit power and noise power ratio P_B/N_0	0-50 dB
K_i	Rician factor	2/0-4

$$P_{out_D} = F_{Y_{24}} \left(\frac{\gamma_{th}}{\Phi d_2^{-m} d_4^{-m}} \right) \triangleq 1 - \Theta, \quad (20)$$

where

$$\Theta = 2e^{-(K_2+K_4)} \sum_{p=0}^{\infty} \sum_{t=0}^{\infty} \sum_{n=0}^p \frac{K_2^p K_4^t}{p!n!(t!)^2} \left(\frac{B_2 B_4 \gamma_{th}}{\Phi d_2^{-m} d_4^{-m}} \right)^{\frac{t+n+1}{2}} K_{t-n+1} \left(2 \sqrt{\frac{B_2 B_4 \gamma_{th}}{\Phi d_2^{-m} d_4^{-m}}} \right). \quad (21)$$

Substituting (18) and (20) into (12), we can obtain the outage probability of system as

$$\begin{aligned} P_{out} &= P_r \{ \gamma_R < \gamma_{th} \} + (1 - P_r \{ \gamma_R < \gamma_{th} \}) P_r \{ \gamma_D < \gamma_{th} \} \\ &= (1 - \Delta) + (1 - (1 - \Delta))(1 - \Theta) = 1 - \Delta\Theta. \end{aligned}$$

So, by substituting (19) and (21) into (22), the outage probability of the system is expressed as

$$\begin{aligned} P_{out} &= 1 - 4A_2 e^{-(K_1+K_2+K_3+K_4)} \sum_{q=0}^{\infty} \sum_{l=0}^{\infty} \sum_{k=0}^{\infty} \sum_{z=0}^l \frac{(B_2 K_2)^q K_1^l K_3^k}{l!z!(k!)^2 (q!)^2} \\ &\cdot \int_0^{\infty} \varphi_2^q e^{-B_2 \varphi_2} \left[\frac{B_1 B_3 \gamma_{th} (\Omega d_2^{-m} \varphi_2 + (1/\Phi))}{d_1^{-m} d_3^{-m}} \right]^{\frac{k+z+1}{2}} \\ &\cdot K_{k-z+1} \left(2 \sqrt{\frac{B_1 B_3 \gamma_{th} (\Omega d_2^{-m} \varphi_2 + (1/\Phi))}{d_1^{-m} d_3^{-m}}} \right) d\varphi_2 \\ &\cdot \sum_{p=0}^{\infty} \sum_{t=0}^{\infty} \sum_{n=0}^p \frac{K_2^p K_4^t}{p!n!(t!)^2} \left[\frac{B_2 B_4 \gamma_{th}}{\Phi d_2^{-m} d_4^{-m}} \right]^{\frac{t+n+1}{2}} \\ &K_{t-n+1} \left(2 \sqrt{\frac{B_2 B_4 \gamma_{th}}{\Phi d_2^{-m} d_4^{-m}}} \right). \end{aligned}$$

Finally, the system throughput for a delay limited scenario can be expressed as

$$R = R_{th}(1 - P_{out})(1 - \alpha). \quad (24)$$

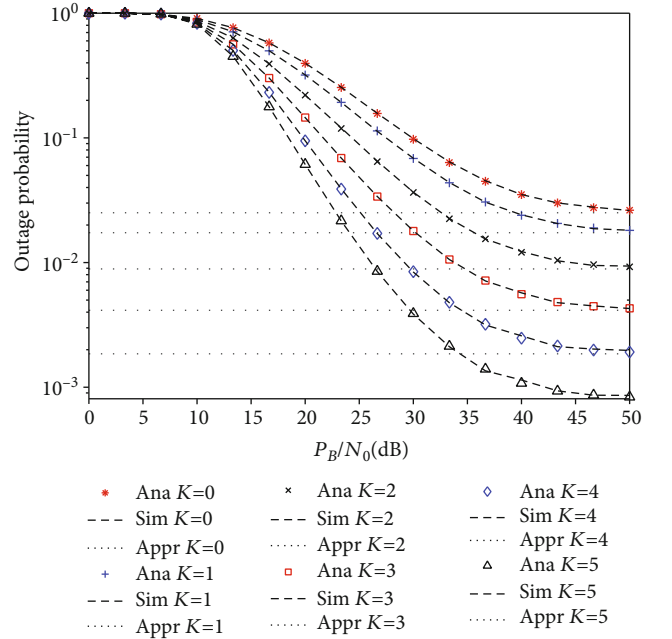


FIGURE 3: The system outage probability versus P_B/N_0 for different Rician factor K .

4. Simulation Result

This section presents some simulation results to verify our obtained theoretical results and demonstrate the system performances. For clarity, the simulation parameters are listed in Table 1. In the figures of the section, the marker of Ana \pm denotes the numerical results calculated by the derived closed expression, the marker of Sim \pm denotes the simulation results obtained by Monte Carlo method, and Appr \pm denotes the numerical asymptote in high SNR regime. In the following, we will discuss the effect of system parameters and PS position on the system performance, respectively.

4.1. The Effect of System Parameters on Performance. Figures 3 and 4 show the effect of the ratio of the PS transmit power to the noise power (i.e., $\gamma_0 = P_B/N_0$) on the system outage probability and throughput with different values of the

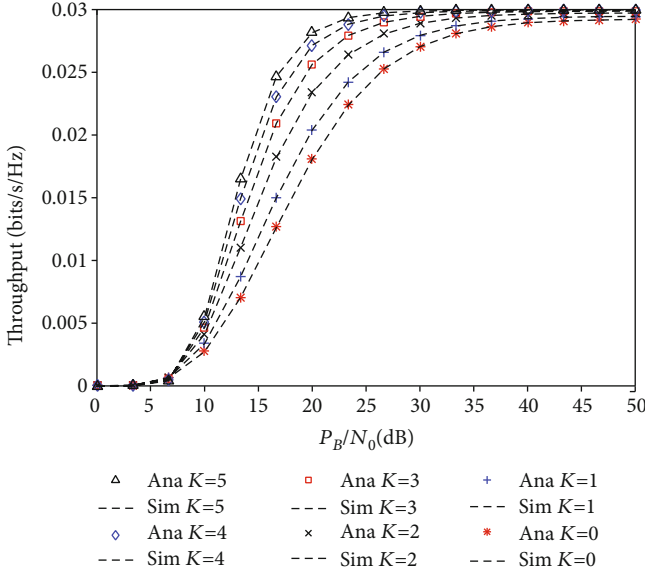


FIGURE 4: The system throughput versus P_B/N_0 for different Rician factor K .

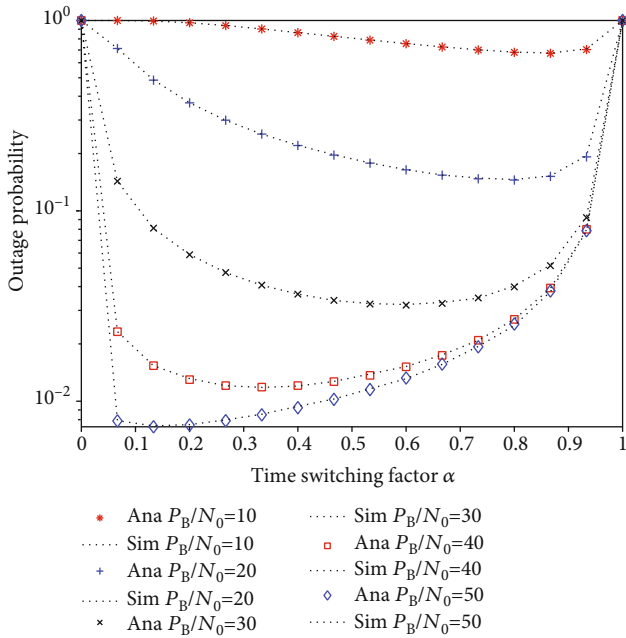


FIGURE 5: The system outage probability versus time switching factor α for different γ_0 .

Rician factor, respectively. From Figures 3 and 4, it can be seen that the results calculated by the closed expression match the results obtained by Monte Carlo simulation well, which demonstrates the correctness of our obtained theoretical results.

From Figures 3 and 4, one can also find that for a fixed Rician factor K , the greater the value of γ_0 is, the smaller the system outage probability becomes, and the larger the system throughput becomes. This is because with the increment of

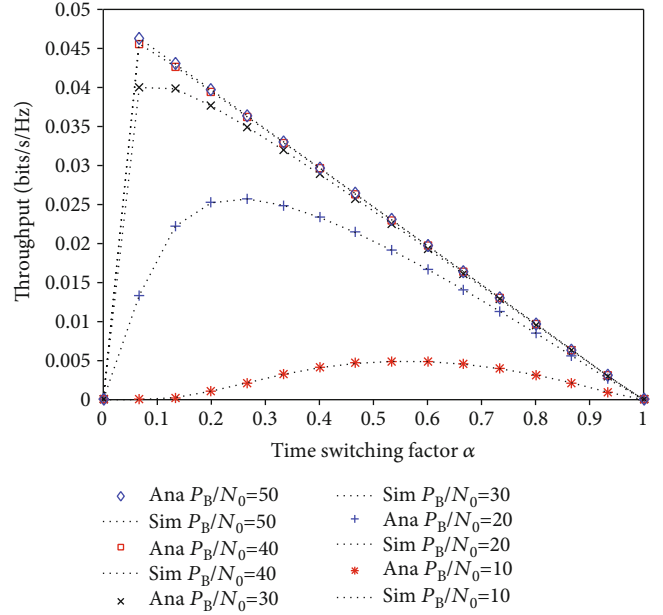


FIGURE 6: The system throughput versus time switching factor α for different γ_0 .

γ_0 for given N_0 , the energy harvested by S and R increases, which yields higher SINR of both R and D . It can also be found that for fixed γ_0 , the greater the value of the Rician factor is, the lower the outage probability of the system becomes, and the larger the system throughput becomes. The reason is that the larger Rician factor means the stronger LOS, which increases the energy harvested by both S and R . Finally, from Figure 3, it can be seen that the outage probability gradually approaches an numerical asymptote in high SNR regime. This indicates that increasing the transmit power of PS cannot infinitely decrease the outage probability of the system.

Figures 5 and 6 show the effects of the time division factor α on the system outage probability and throughput for different values of γ_0 , respectively. The results calculated by the closed expression fit well with those obtained by Monte Carlo simulation, confirming that the derived closed-form solution of the system outage probability is completely accurate again. One can see that for a fixed α , the larger γ_0 is, the lower outage probability is and the larger throughput is, which agrees with Figures 3 and 4.

From Figure 5, one can see that for a fixed γ_0 , with the increment of the value of α , the outage probability decreases first and then increases. On one hand, when the value of α is close to 0, the time allocated for energy harvesting is relatively short. In this case, the less energy can be harvested by S and R and therefore, the outage probability of system is close to 1. On the other hand, when the value of α approaches to 1, the time assigned for information relaying transmission becomes very short, and thus the outage probability of system tends to be 1. In addition, it can be found that there is an optimal value of α , which makes the outage probability of system reach the lowest. For example, for $\gamma_0 = 30$, when α is equal to about 0.6, the system achieves the best outage performance.

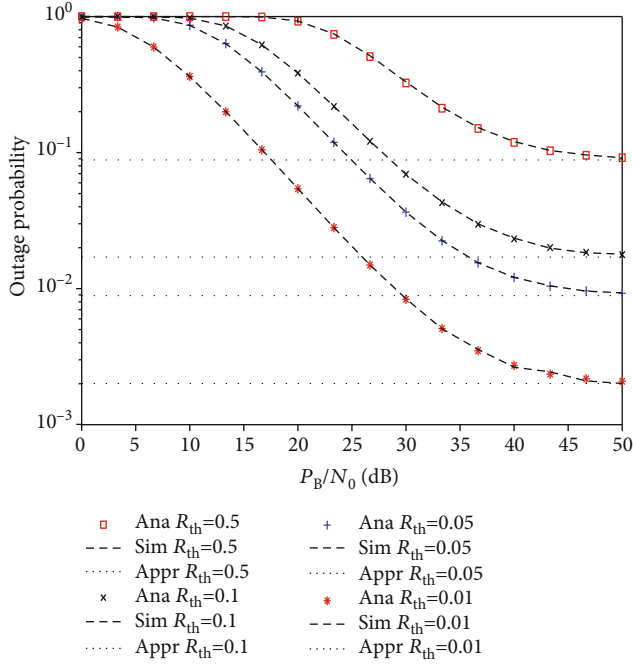


FIGURE 7: The system outage probability versus P_B/N_0 for different transmission rate threshold R_{th} .

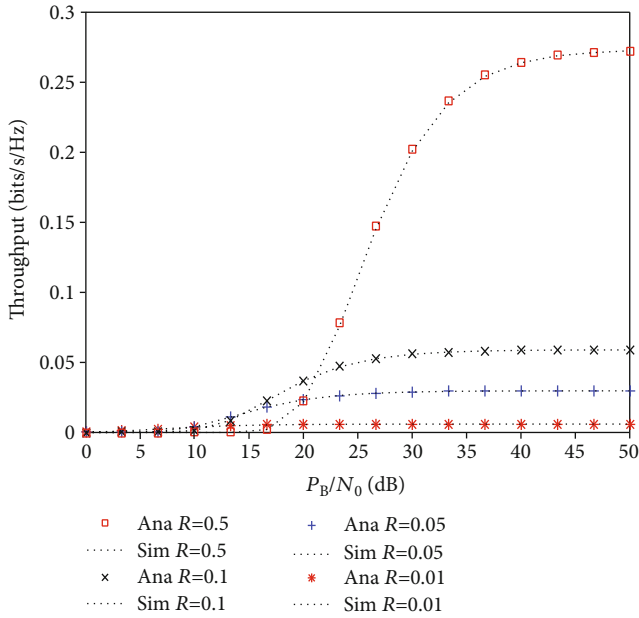


FIGURE 8: The system throughput versus P_B/N_0 for different transmission rate threshold R_{th} .

From Figure 6, one can also see that for a fixed γ_0 , with the increment of the value of α , the system throughput increases first and then decreases. The reason is as follows. When the value of α is close to 0, S and R do not have energy to transmit information, while when the value of α is close to 1, S and R do not have time to transmit information. Moreover, it can be found that there is an optimal value of α , which makes the system throughput reach the largest. For example, for $\gamma_0 = 30$,

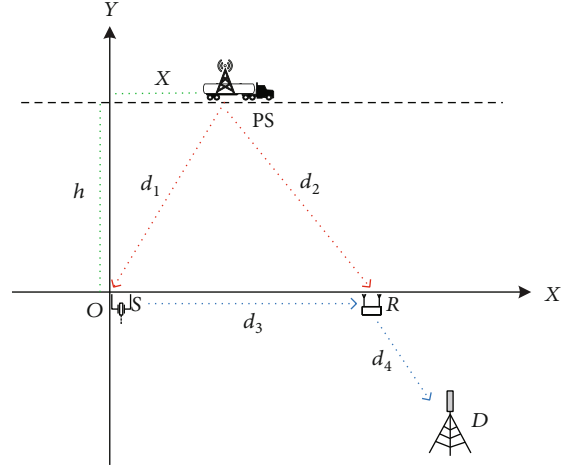


FIGURE 9: The considered coordinate system.

when α is equal to about 0.08, the system achieves the best throughput performance. Finally, by comparing Figure 6 with Figure 5, it can be found that the optimal values of α are different for the best outage probability and throughput.

Figures 7 and 8 discuss the effect of transmission rate threshold R_{th} on the system outage probability and throughput with respect to γ_0 , respectively. It can be seen that for fixed transmission rate threshold R_{th} , as the value of γ_0 increases, the outage probability gradually decreases, and the throughput gradually increases, and they tend to be stable, which is consistent with the results in Figures 3 and 4. Moreover, from Figure 7, one can observe that for a fixed γ_0 , the smaller the value of R_{th} is, the lower the value of system outage probability becomes. This is because when R_{th} becomes smaller, $\gamma_{th} = 2^{R/(1-\alpha)} - 1$ also becomes smaller, which further causes lower outage probability. Finally, from Figure 8, it can be found that the larger the value of R_{th} is, the larger the system throughput becomes. The reason is that from (24) one can see that with the decrement of system outage probability, the throughput gradually increases.

4.2. The Effect of Power Station Position on Performance. In order to discuss the effect of power station position on performance, we consider a coordinate system, as shown in Figure 9. S is located at the origin of coordinate, R is located at the positive X-axis, and their distance d_3 is set to be 10 m. D is located in the fourth quadrant and its distance d_4 from R may be set to 5 m, 10 m, 20 m, or 30 m. PS moves at a straight line whose distance h from the X-axis is set to be 10 m. The X-axis coordinate of PS is denoted by x , which is used to represent the position of PS. Besides, the ratio of PS transmit power to the noise power γ_0 is set to be 40 dB, and other system parameters are set according to Table 1.

Figures 10 and 11 show the system outage probability and system throughput with respect to PS position x for different distances between R and D d_4 , respectively. It can be found that with the increment of the X-axis coordinate of PS x , the outage probability first decreases and then increases while the throughput first increases and then decreases. And there

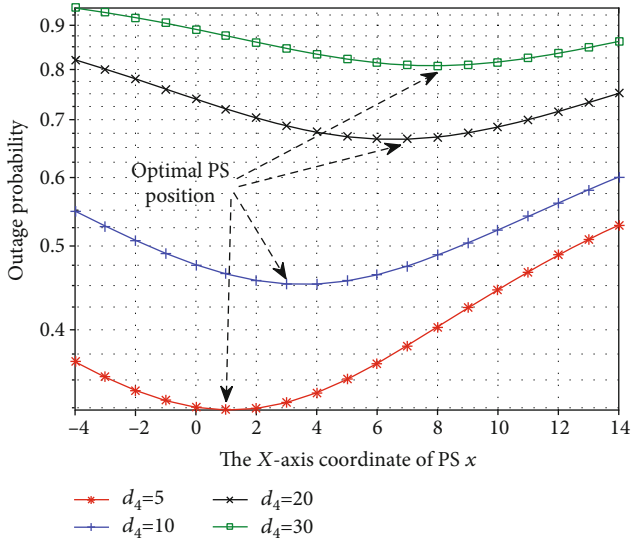


FIGURE 10: The system outage probability versus PS position x for different distances between R and Dd_4 .

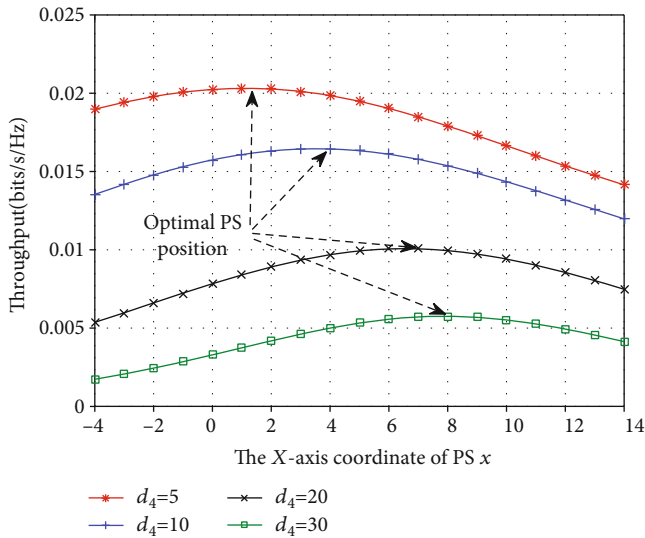


FIGURE 11: The system throughput versus PS position x for different distances between R and Dd_4 .

is an optimal PS position whose X-axis coordinate is located between S and R , which makes the outage probability of system reaches the lowest or system throughput reach the largest. The reason is when the X-axis coordinate of PS is located between S and R , and both hops are balanced, which leads to lower outage probability and larger throughput. It can be also seen that with the increment of distance between R and Dd_4 , the outage probability increases, and the throughput decreases, which is caused by larger path loss from R to D . Finally, one can see that with the increment of distance between R and Dd_4 , the optimal PS position is gradually close to R . This is because when PS is closer to R , it can supply more energy to R to alleviate the effect of larger path loss from R to D .

5. Conclusion

This paper has studied the communication outage performance of full-duplex relay networks powered by RF energy harvesting in UEIoT, where the outdoor Rician fading channel model is adopted and full-duplex relaying protocol is employed. The explicit expression of the outage probability of the system has been derived. Simulation results have validated the correctness of our theoretical analysis and also evaluated the effects of the transmit power of the power station, the Rician factor, the time division factor, and system transmission rate threshold on the system outage probability and throughput. The optimal deployment position of power station is also investigated, which provides some useful insights on the future practical applications of UEIoT.

Data Availability

The data used to support the findings of this study are available from the corresponding author upon request.

Conflicts of Interest

The authors declare that they have no conflicts of interest.

Acknowledgments

This work was supported by the National Natural Science Foundation of China under Grant (no. 61801155) and was supported by the Self-Developed Project of State Grid Energy Research Institute Co., Ltd (Ubiquitous Electric Internet of Things Edge Computing Performance Analysis and Simulation Based on Typical Scenarios, SGN202009014).

References

- [1] Z. Zhai, L. Jia, Y. Wang, Y. Ma, W. Jing, and Z. Zhang, "Research on ubiquitous Power Internet of Things architecture," in *2019 IEEE 3rd Conference on Energy Internet and Energy System Integration (EI2)*, pp. 435–439, Changsha, China, 2019.
- [2] The State Grid Corporation of China, "White paper: Internet of Things in electricity," 2019, <http://news.bjx.com.cn/html/20191014/1012993.shtml>.
- [3] The State Grid Corporation of China, "The state grid outline for the construction of ubiquitous power Internet of Things was officially released," 2019, <http://www.chinasmartgrid.com.cn/news/20190311/632172.shtml>.
- [4] Y. Gong, C. Chen, B. Liu, G. Gong, B. Zhou, and N. K. Mahato, "Research on the ubiquitous electric power internet of things security management based on edge-cloud computing collaboration technology," in *2019 IEEE Sustainable Power and Energy Conference (iSPEC)*, pp. 1997–2002, Beijing, China, 2019.
- [5] Q. Wang and Y. G. Wang, "Research on Power Internet of Things architecture for smart grid demand," in *2018 2nd IEEE Conference on Energy Internet and Energy System Integration (EI2)*, pp. 1–9, Beijing, China, 2018.
- [6] K. Xiong, C. Chen, G. Qu, P. Fan, and K. B. Letaief, "Group cooperation with optimal resource allocation in wireless

- powered communication networks,” *IEEE Transactions on Wireless Communications*, vol. 16, no. 6, pp. 3840–3853, 2017.
- [7] K. W. Choi, L. Ginting, P. A. Rosyady, A. A. Aziz, and D. I. Kim, “Wireless-powered sensor networks: how to realize,” *IEEE Transactions on Wireless Communications*, vol. 16, no. 1, pp. 221–234, 2017.
- [8] J. Liu, K. Xiong, P. Fan, and Z. Zhong, “RF energy harvesting wireless powered sensor networks for smart cities,” *IEEE Access*, vol. 5, pp. 9348–9358, 2017.
- [9] X. Li, G. Zhu, Y. Gong, and K. Huang, “Wirelessly powered data aggregation for IoT via over-the-air function computation: beamforming and power control,” *IEEE Transactions on Wireless Communications*, vol. 18, no. 7, pp. 3437–3452, 2019.
- [10] D. S. Gurjar, H. H. Nguyen, and P. Pattanayak, “Performance of wireless powered cognitive radio sensor networks with non-linear energy harvester,” *IEEE Sensors Letters*, vol. 3, no. 8, pp. 1–4, 2019.
- [11] Y. Liu, Y. Ye, H. Ding, F. Gao, and H. Yang, “Outage performance analysis for SWIPT-based incremental cooperative NOMA networks with non-linear harvester,” *IEEE Communications Letters*, vol. 24, no. 2, pp. 287–291, 2020.
- [12] D. Lecce, A. Grassi, G. Piro, and G. Boggia, “Boosting energy efficiency of NB-IoT cellular networks through cooperative relaying,” in *2018 IEEE 29th Annual International Symposium on Personal, Indoor and Mobile Radio Communications (PIMRC)*, pp. 1–5, Bologna, Italy, 2018.
- [13] T. Riihonen, S. Werner, and R. Wichman, “Comparison of full-duplex and half-duplex modes with a fixed amplify-and-forward relay,” in *2009 IEEE Wireless Communications and Networking Conference*, pp. 1–5, Budapest, Hungary, 2009.
- [14] R. Nikjah and N. Beaulieu, “Achievable rates and fairness in rateless coded decode-and-forward half-duplex and full-duplex opportunistic relaying,” in *2008 IEEE International Conference on Communications*, pp. 3701–3707, Beijing, China, 2008.
- [15] K. Kwon, D. Hwang, and S. S. Nam, “Beamformer design for self-energy recycling in full-duplex decode-and-forward relay systems,” *IEEE Wireless Communications Letters*, vol. 9, no. 9, pp. 1417–1421, 2020.
- [16] J.-H. Lee, S. S. Nam, and Y.-C. Ko, “Outage performance analysis of two-way full-duplex DF relaying networks with beamforming,” *IEEE Transactions on Vehicular Technology*, vol. 69, no. 8, pp. 8753–8763, 2020.
- [17] L. Samara, A. Gouisseem, R. Hamila, M. O. Hasna, and N. Al-Dhahir, “Full-duplex amplify-and-forward relaying under I/Q imbalance,” *IEEE Transactions on Vehicular Technology*, vol. 69, no. 7, pp. 7966–7970, 2020.
- [18] X. Song and S. Xu, “Joint optimal power allocation and relay selection in full-duplex energy harvesting relay networks,” in *2018 10th International Conference on Communication Software and Networks (ICCSN)*, pp. 80–84, Chengdu, China, 2018.
- [19] G. Chen, P. Xiao, J. R. Kelly, B. Li, and R. Tafazolli, “Full-duplex wireless-powered relay in two way cooperative networks,” *IEEE Access*, vol. 5, pp. 1548–1558, 2017.
- [20] Z. Wei, S. Sun, X. Zhu, D. Kim, and D. W. K. Ng, “Resource allocation for wireless-powered full-duplex relaying systems with nonlinear energy harvesting efficiency,” *IEEE Transactions on Vehicular Technology*, vol. 68, no. 12, pp. 12079–12093, 2019.
- [21] B. C. Nguyen, T. M. Hoang, and P. T. Tran, “Performance analysis of full-duplex decode-and-forward relay system with energy harvesting over Nakagami- m fading channels,” *AEU - International Journal of Electronics and Communications*, vol. 98, pp. 114–122, 2019.
- [22] S. Kumar, S. De, and D. Mishra, “RF energy transfer channel models for sustainable IoT,” *IEEE Internet of Things Journal*, vol. 5, no. 4, pp. 2817–2828, 2018.
- [23] K. Yang, H. Cui, L. Song, and Y. Li, “Efficient full-duplex relaying with joint antenna-relay selection and self-interference suppression,” *IEEE Transactions on Wireless Communications*, vol. 14, no. 7, pp. 3991–4005, 2015.
- [24] Q. Wang, Y. Dong, X. Xu, and X. Tao, “Outage probability of full-duplex AF relaying with processing delay and residual self-interference,” *IEEE Communications Letters*, vol. 19, no. 5, pp. 783–786, 2015.
- [25] M. Duarte, C. Dick, and A. Sabharwal, “Experiment-driven characterization of full-duplex wireless systems,” *IEEE Transactions on Wireless Communications*, vol. 11, no. 12, pp. 4296–4307, 2012.
- [26] G. L. Stueber, *Principles of Mobile Communication*, Springer, Norwell, MA USA, 2001.
- [27] I. S. Gradshteyn and I. M. Ryzhik, “Table of integrals series and products,” Academic press, New York, NY, USA, 2007.

Research Article

Power Allocation in Massive MIMO-HWSN Based on the Water-Filling Algorithm

Zhe Li ¹, Sahil Verma ², and Machao Jin³

¹School of Information Engineering, Department of Railway Policing, Railway Police College, Zhengzhou, China

²Chandigarh University, Mohali, India

³Department of Information and Communication, Shanxi Metallurgical Geotechnical Engineering Investigation Co., Ltd., Taiyuan, Shanxi, China

Correspondence should be addressed to Zhe Li; lizhe@rpc.edu.cn

Received 30 April 2021; Revised 1 June 2021; Accepted 10 July 2021; Published 10 August 2021

Academic Editor: Xingwang Li

Copyright © 2021 Zhe Li et al. This is an open access article distributed under the Creative Commons Attribution License, which permits unrestricted use, distribution, and reproduction in any medium, provided the original work is properly cited.

Pilot power allocation for Internet of Things (IoT) devices in massive multi-input multioutput heterogeneous wireless sensor networks (MIMO-HWSN) is studied in this paper. The interference caused by fractional pilot reusing in adjacent cells had a negative effect on the MIMO-HWSN system performance. Reasonable power allocation for users can effectively weaken the interference. Motivated by the water-filling algorithm, we proposed a suboptimal pilot transmission power method to improve the system capacity. Simulation results show that the proposed method can significantly improve the uplink capacity of the system and explain the influence of different pilot transmission power on the performance of the system, but the complexity of the system almost does not increase.

1. Introduction

Due to the continued development of 5G and the gradual proliferation of 6G, the wireless data traffic is estimated to reach the unprecedented quantity. Most of the future data-intensive applications handling a massive number of connected IoT will demand high data rates with low latency in some scenarios (such as vehicle network, smart city, and remote health) [1, 2]. MIMO, millimeter wave (mmWave), nonorthogonal multiple access (NOMA), and heterogeneous cellular network (HetNet) have been broadly investigated from all aspects of academia, research, and industry at home and abroad [3–9]. Massive MIMO technology configures a large number of antennas for multiple base stations (BSs), and the transmitted signals can be dynamically adjusted horizontally and vertically, thus improving the performance of wireless communication systems. The technology was introduced by Bell Laboratories in 2010 [10–12]. Wireless sensor networks (WSNs) play a very important role in telemedicine, electronic instruments, transportation, and many

other fields. WSN is equipped with abundant sensor nodes (SN) which can sense the external environment and perform communication and calculation and connect extensive wireless devices through the wireless systems [13–19]. HWSN usually consists of low power consumption and a tiny village network stack on the macrocell, though the space and spectrum reuse technology upgrades the capacity of the hot spots of the overlay network [20–22]. In this paper, the massive MIMO-HWSN system embodies some small-cell base stations (SBSs) and macrocell base stations (MBSs).

In actual wireless communication systems, the number of orthogonal pilots is often less than active users, so it is impossible for each user to use the orthogonal pilots because of the limited length of the coherence time. When several users in the system use the same pilots, pilot contamination will result in inaccurate channel estimation and the BS cannot obtain accurate channel state information (CSI) [23–29]. In the time-division duplex (TDD) massive MIMO-HWSN system which employs pilots to conduct uplink channel estimation, the pilot contamination seriously hinders the increasing

trend of wireless communication system capacity and delays the process of standardization and industrialization [30, 31].

In the current research, there are many means to mitigate the pilot contamination. In terms of channel estimation, some researchers designed new channel estimation methods or improved the existing channel estimation algorithm according to the characteristics of the system to reduce channel estimation errors and directly alleviate the pilot contamination. In addition to the classical Minimum Mean Square Error (MMSE) and Least Square (LS) channel estimation [32], a variety of channel estimation methods that may become the industry standard of massive MIMO systems has also been proposed. Reference [33] proposes a channel estimation method based on mutual cooperation between base stations (BSs) in the system. This scheme uses additional second-order statistical information of channels to distinguish users. Reference [34] proposes a blind channel estimation method based on subspace projection without mutual cooperation between cells. This blind channel estimation scheme is combined with an appropriate power allocation scheme which can effectively alleviate the pilot contamination in massive MIMO systems. Reference [35] gives a channel estimation method which has no special requirements on the encoding and signal structure of the transmitting end. The channel response vectors corresponding to different users will be close to orthogonality when the number of BS antennas is close to infinity. This scheme uses the feature of the massive MIMO system to decompose the covariance matrix of the received signal by eigenvalue decomposition, so as to achieve the purpose of distinguishing users. References [31, 32, 36–39] gave a channel estimation scheme combined with geographic location information. After the channel estimation based on the uplink pilot sequence, the scheme performs a postprocessing process based on the fast Fourier transform on the steering vector at the BS. Hence, the users with different angles of arrival (AOAs) can be effectively distinguished.

For the pilot allocation, an allocation scheme based on channel covariance matrix is proposed in [36, 37]. References [38–40] proposed a partial pilot sequence (frequency) multiplexing scheme or soft multiplexing scheme. Reference [41] modeled the pilot scheduling problem as an optimal permutation and combination problem and obtained the corresponding low-complexity approximate solution. Reference [42] uses the unique sparse characteristics of broadband system channels in the time domain to distinguish between target users and interfering users and designs a pilot sequence allocation scheme that can randomize pilot pollution in multiple consecutive uplink frames. For mitigating the interference between cells and increase the system capacity in [43], a pilot allocation scheme with cell sectorization is given which ensures that the pilot sequence used in each sector and adjacent cells are orthogonal. Reference [44] grouped cell edge users based on channel AOA information, thus effectively mitigating the adverse effects of interfering users on target users. In [45], the Rice fading channel model is adopted, and the pilot sequence is allocated according to the line-of-sight interference between different users. In [46], a problem is formulated to jointly optimize the number

of BS antennas, power allocation and guide neck sequence allocation are constructed, and a step-by-step solution is proposed.

In this paper, a macrocell SN (MSN) uplink pilot transmit power allocation scheme based on location-aware channel estimation and a novel pilot allocation method is proposed and obtains the effects of different power allocations on improving massive MIMO-HWSN system performance. Inspired by the main idea of power allocation in the water-filling algorithm, that is to say, when MSN has better channel gain, more transmit power will be allocated, we apply the power allocation method according to the constraint conditions and only implement this method for MSNs. In the simulation, the results of pilot power average transmission are compared, which shows that the proposed method can effectively improve the performance of the system.

The remainder of this paper is organized as follows. The massive MIMO-HWSN system and the channel model are presented in Section II. A novel channel estimation method is described in Section III. Section IV proposes a pilot power allocation scheme. The simulation results under different conditions are given in Section V. Finally, we summarize this paper in Section VI.

1.1. Notations. The upper case and lower case boldface represent matrices and vectors, respectively. $(\mathbf{A})^T$ and $(\mathbf{A})^H$ denote the transpose and conjugate transpose of \mathbf{A} , respectively. \mathbb{C} denotes the complex number. $\mathbb{E}\{\mathbf{B}\}$ and $\text{Tr}(\mathbf{B})$ indicate the statistical expectation and the trace of \mathbf{B} for random variables \mathbf{B} .

2. System Model

We consider a heterogeneous multicell multiuser massive MIMO system with C hexagonal macrocells. As shown in Figure 1, there are P covered small cells in each macrocell. At the coherent time, one single-antenna SSN is served in each small cell and K_m single-antenna MSNs in a macrocell. The number of SSNs is far less than that of the MSNs in each cell of this system. The MBS has M antennas in each cell, where $M > K_m$, while the SBS has one antenna.

The time division duplex (TDD) model is applied in the system to reduce the large overhead of training in the MIMO-HWSN system, which is shown in Figure 2. The response vectors of the uplink channel change with time but remain unchanged in the coherent time.

At the uplink training, all MSNs and SSNs from their own cells send the pilot signal to corresponding BSs. $\phi_k = [\phi_{k,1}, \phi_{k,2}, \dots, \phi_{k,\tau}] \in \mathbb{C}^{1 \times \tau}$ is the pilot sequence of the k -th MSN of a cell, $k \in [1, K_m]$, and $E\{\phi_k \phi_k^H\} = 1$. τ is denoted as the length of the pilot sequence. The pilot sequences are orthogonal when k has different values, i.e., $\phi_{k_1} \phi_{k_2}^H = 0$, where $k_1 \neq k_2$ and $k_1, k_2 \in [1, K_m]$. In the MIMO-HWSN system, the k -th SSN reuses the pilot sequences of the s_k -th MSN in the same cell, which is denoted as $\phi_{s_k} \in \{\phi_1, \phi_2, \dots, \phi_{K_m}\}$, where $s_k \in \{1, 2, \dots, K_m\}$ and $k \in [1, P]$.

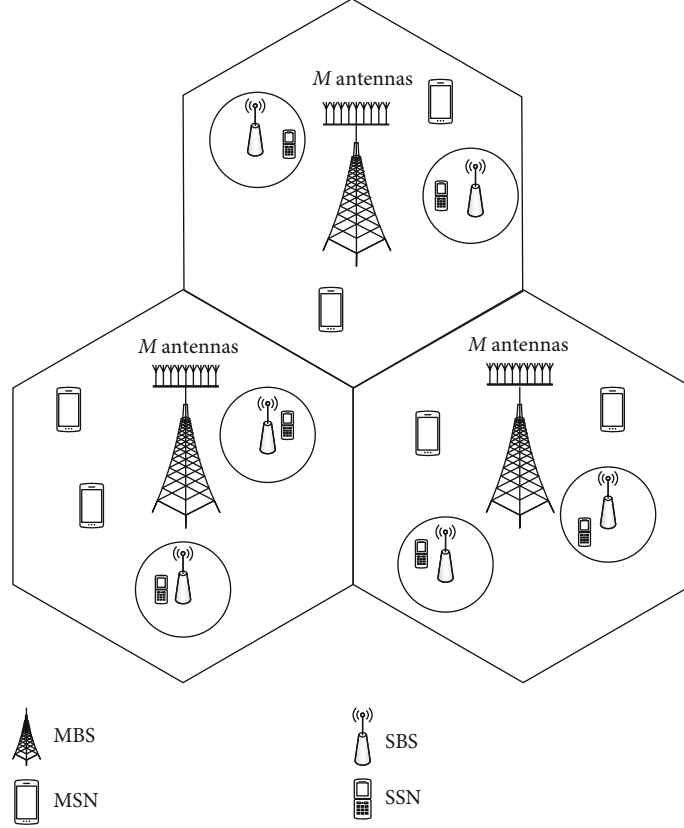
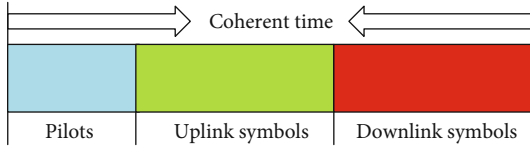

 FIGURE 1: The MIMO-HWSN system model with $C = 3$ and $P = 2$.


FIGURE 2: Coherent time model.

We consider the narrow-band channel which is a commonly used channel model, which can be modeled as

$$\mathbf{h}_{b,c,k} = \frac{1}{\sqrt{Q}} \sum_{q=1}^Q \mathbf{v}(\theta_{b,c,k,q}) \omega_{b,c,k,q}, \quad (1)$$

where $\omega_{b,c,k,q}$ stands for the large-scale fading parameter of the i -th path, which contains the shadow fading and path-loss; Q denotes the path of the k -th MSN in the c -th cell to the b -th MBS; $\mathbf{v}(\theta)$ indicates the steering vector; and $\theta_{b,c,k,q}$ denotes the AOA of the q -th path. The AOA is small and can be assumed in $[\theta_{\min}, \theta_{\max}]$ generally. The steering vector is given in this expression for uniformly spaced linear array as

$$\mathbf{v}(\theta) = \begin{bmatrix} 1 \\ e^{-j2\pi\frac{D}{\lambda} \cos(\theta)} \\ \dots \\ e^{-j2\pi\frac{(M-1)D}{\lambda} \cos(\theta)} \end{bmatrix}, \quad (2)$$

where λ denotes the wavelength, D indicates the antenna spacing at MBS, and $D \leq \lambda/2$. The received signal by the MBS in the c -th cell can be denoted as

$$\mathbf{Y}_b = \sum_{c=1}^C \sum_{k=1}^{K_m} \sqrt{p_{c,k}} \mathbf{h}_{b,c,k} \phi_k + \sum_{c=1}^C \sum_{p=1}^P \sqrt{p'_{c,k}} \mathbf{h}'_{b,c,k} \phi_{s_k} + \mathbf{N}_b, \quad (3)$$

where $\mathbf{Y}_b \in \mathbb{C}^{M \times \tau}$ denotes the received signal matrix and $\mathbf{N}_b \in \mathbb{C}^{M \times \tau}$ indicates the additive white Gaussian noise (AWGN) matrix; p_{c,k_m} and p'_{c,k_s} are pilot transmitted power of the k_m -th MSN and k_s -th SSN in the c -th cell to the b -th MBS, respectively; and $\mathbf{h}_{b,c,k_m} = [h_{b,c,k_m,1}, h_{b,c,k_m,2}, \dots, h_{b,c,k_m,M}]^T$ and $\mathbf{h}'_{b,c,k_s} = [h'_{b,c,k_s,1}, h'_{b,c,k_s,2}, \dots, h'_{b,c,k_s,M}]^T$ denote channels with $h_{b,c,k_m,q}$ and $h'_{b,c,k_s,q}$ which denote the channel coefficient between the k_m -th MSN and k_s -th SSN in the c -th cell and the b -th antenna of the b -th MBS, respectively. The orthogonal pilot sequence is used for the LS channel estimation at the MBS. That is, right multiplying \mathbf{Y}_b by ϕ_k^H can be written as

$$\hat{\mathbf{h}}_{b,b,k} = \frac{\mathbf{Y}_b \boldsymbol{\xi}_k^H}{\sqrt{p_{b,k}}} = \mathbf{h}_{b,b,k} + \sum_{c=1, c \neq b}^C \sqrt{\frac{p_{c,k}}{p_{b,k}}} \mathbf{h}_{b,c,k} + \sum_{c=1}^C \sum_{s_i=k} \sqrt{\frac{p'_{c,i}}{p_{b,k}}} \mathbf{h}'_{b,c,i} + \mathbf{N}_b', \quad (4)$$

where $\mathbf{N}_b' = \mathbf{N}_b \phi_k^H / \sqrt{p_{b,k}}$ indicates the equivalent noise matrix for channel estimation. Obviously, for the k -th MSN in the b -th cell, the part containing the $\mathbf{h}_{b,c,i}'$ denotes the intertier interference from the SSNs using the same pilot as the MSN, while the part that contains $\mathbf{h}_{b,c,k}$ is the intercell interference caused by MSNs in the adjacent cell.

The received signal by the i -th SBS in the b -th macrocell is written as

$$\mathbf{y}_{b,i}' = \sum_{c=1}^C \sum_{k=1}^{K_m} \sqrt{\xi_{b,i,c,k}} g_{b,i,c,k} \phi_k^T + \sum_{c=1}^C \sum_{k=1}^P \sqrt{\xi_{b,i,c,k}'} g_{b,i,c,k}' \phi_{s_k}^T + \gamma_{b,i}, \quad (5)$$

where ξ_{b,i,c,k_m} and ξ_{b,i,c,k_s}' are pilot transmitted powers of the k_m -th MSN and k_s -th SSN, respectively; $g_{b,i,c,k}$ and $g_{b,i,c,k}'$ are the channel coefficients linking the k_m -th MSN and k_s -th SSN of the c -th cell to the i -th SBS of the b -th macrocell, respectively; and $\gamma_{b,i}$ denotes the AWGN vector. Similarly, we can get the channel estimation $\hat{g}_{b,i,b,i}$ which can be denoted as

$$\begin{aligned} \hat{g}_{b,i,b,i} &= \frac{\phi_{s_i}^H \mathbf{y}_{b,i}'}{\sqrt{\xi_{b,i,b,i}}} = \underbrace{\hat{g}_{b,i,b,i} + \sum_{j=1}^C \frac{g_{b,i,c,s_i}}{\sqrt{\xi_{b,i,b,i}}}}_{\text{P1}} \\ &+ \underbrace{\sum_{s_k=s_i, k \neq i} \frac{\hat{g}_{b,i,b,k}}{\sqrt{\xi_{b,i,b,i}}}}_{\text{P2}} + \underbrace{\sum_{j=1, j \neq i}^C \sum_{s_k=s_i} \frac{\hat{g}_{b,i,c,k}}{\sqrt{\xi_{b,i,b,i}}}}_{\text{P3}} + \zeta_{b,i}, \end{aligned} \quad (6)$$

where $\zeta_{b,i} = \phi_{s_i}^H \gamma_{b,i} / \sqrt{\xi_{b,i,b,i}}$ denotes the equivalent noise at the channel estimate. Behind the second equal sign of (4), P1 is the intertier interference caused by the s_i -th MSN of each macrocell. The sum of P2 and P3 denotes the intercell interference which is caused by other SSNs with the same pilot. In this formula, P2 is the intercell interference caused by the SSNs in the same macrocell, and P3 can be denoted as the intercell interference from SSNs in the adjacent macrocell.

Based on the analysis of the above equations, the fundamental cause of pilot contamination is that different MSNs in the system reuse the same pilot sequence. The length of the coherent time in a massive MIMO system is limited, which is shown in Figure 2, and this character limits the length of the pilot sequence. The limited length of pilot sequences also means that the number of orthogonal pilot sequences available in the system is limited. On the other hand, the number of users is generally huge in a massive MIMO system, so it is impossible for all users to allocate mutually orthogonal pilot sequences. In this case, the phenomenon of pilot multiplexing occurs. Moreover, the base station in each cell will not only receive the uplink pilot sequences sent by SNs in the cell but also receive the pilot sequences sent by SNs in other cells. Furthermore, when the channel estimation is conducted at the BS, SNs in other cells using the same pilot sequence will be affected, resulting

in inaccurate channel estimation results. Specifically in this system model, the k -th SN ($k = 1, 2, 3, \dots, K_m$) in each cell reuses the same pilots. The base station in the b -th cell simultaneously receives uplink pilot sequences from SNs in other cells. So the channel estimation result obtained by the BS based on the received pilot signal includes both the channel response parameters of users in the b -th cell and the channel response parameters from users in other cells.

We only consider the process of MSNs to its corresponding MBSs in the stage of transmitting data. Actually, the stages of SSNs are very similar to those of MSNs. The received signal $\mathbf{y}_b \in \mathbb{C}^{M \times 1}$ in b -th can be denoted as

$$\mathbf{y}_b = \sqrt{p_m} \sum_{c=1}^C \sum_{k=1}^{K_m} \mathbf{h}_{b,c,k} x_{b,c,k} + \sqrt{p_s} \sum_{c=1}^C \sum_{k=1}^P \mathbf{h}_{b,c,k}' x_{b,c,k}' + \varepsilon_b, \quad (7)$$

where x_{b,c,k_m} and x_{b,c,k_s}' denote the symbols transmitted by the k_m -th MSN and k_s -th SSN in the c -th cell to b -th MBS, respectively; $E\{|x_{b,c,k}|^2\} = E\{|x_{b,c,k}'|^2\} = 1$; and p_m and p_s are the data transmit power which are assumed to be identical for all MSNs and SSNs, respectively. $\varepsilon_b \in \mathbb{C}^{M \times 1}$ denotes the AWGN vector. The MBS demodulates the data according to the channel estimation $\hat{\mathbf{h}}_{l,l,k}$, which is obtained in the previous stage. In this stage, we consider the matched-filter (MF) detector, and the detected signal from the k -th MSN to l -th MBS in the j -th cell can be modeled as

$$\begin{aligned} \hat{\mathbf{x}}_{b,b,k} &= \frac{(\mathbf{h}^{\wedge}_{b,b,k})^H \mathbf{y}_b}{\sqrt{p_m}} = \underbrace{\sum_{c=1}^C \sum_{k=1}^{K_m} (\mathbf{h}^{\wedge}_{b,b,k})^H \mathbf{h}_{b,c,k} x_{b,c,k}}_{\text{S1}} \\ &+ \underbrace{\sqrt{\frac{p_s}{p_m}} \sum_{j=1}^C \sum_{k=1}^P (\mathbf{h}^{\wedge}_{b,b,k})^H \mathbf{h}_{b,c,k}' x_{b,c,k}'}_{\text{S2}} + \underbrace{\frac{(\mathbf{h}^{\wedge}_{b,b,k})^H \varepsilon_b}{\sqrt{p_m}}}_{\text{S3}}, \end{aligned} \quad (8)$$

where S1 can be expressed as

$$\begin{aligned} \text{S1} &= (\mathbf{h}^{\wedge}_{b,b,k})^H \mathbf{h}_{b,b,k} x_{b,b,k} + \underbrace{\sum_{k' \neq k}^{K_m} (\mathbf{h}^{\wedge}_{b,b,k})^H \mathbf{h}_{b,b,k}' x_{b,b,k}'}_{\text{S1a}} \\ &+ \underbrace{\sum_{c' \neq c}^C \sum_{k=1}^{K_m} (\mathbf{h}^{\wedge}_{b,b,k})^H \mathbf{h}_{b,c'} x_{b,c'}}_{\text{S1b}}, \end{aligned} \quad (9)$$

where S1a represents the interference from MSNs of the same macrocell and S1b denotes the interference from MSNs of the different macrocells. The SINR of the k -th MSN in the b -th macrocell is computed by (10). A channel estimation method will be introduced to get the more accurate $\hat{\mathbf{h}}$.

3. A Novel Location-Aware Channel Estimation Method

$$\text{SINR}_{c,k} = \frac{|(h \wedge_{b,b,k})^H h_{b,b,k}|^2}{\sum_{k' \neq k}^{K_m} |(h \wedge_{b,b,k})^H h_{b,b,k'}|^2 + \sum_{c' \neq c}^C \sum_{k=1}^{K_m} |(h \wedge_{b,b,k})^H h_{b,c',k}|^2 + (P_s/P_m) \sum_{c=1}^C \sum_{k=1}^P |(h \wedge_{b,b,k})^H h_{b,c,k}|^2 + |(h \wedge_{b,b,k})^H \varepsilon_b|^2 / P_m}. \quad (10)$$

$\hat{\mathbf{h}}$ can be rewritten as

$$\hat{\mathbf{h}} = \mathbf{h} + \mathbf{h}_I + \mathbf{n}, \quad (11)$$

where \mathbf{h}_I denotes the sum of all interfering channels, \mathbf{h} is the profitable channel vector, and \mathbf{n} is the AWGN vector. Actually, we regard (2) as a single frequency signal, and its frequency is $f_a = (D/\lambda) \cos(\theta)$ when $M \rightarrow \infty$, and we denote \mathbf{F} as the N -point Fast Fourier Transform (FFT) of $\hat{\mathbf{h}}$. Then, the N -point DFT of $\mathbf{a}(\theta)$ can be written as

$$X(k) = \sum_{m=1}^{M-1} a(m) \exp\left(-j \frac{2\pi}{N} km\right), \quad (12)$$

where $a(m) = \exp(-j2\pi(mD/\lambda) \cos(\theta))$, which is the m -th element of $a(\theta)$, and $m \in [0, M-1]$, $k \in [0, N-1]$, $\max[X(k)] = M$, let $k_{\text{lim}} = \arg\max[X(k)]$, $k \in [0, N-1]$, $k_{\text{lim}} = \lfloor g_N(\theta) \rfloor$, where $\lfloor g_N(\theta) \rfloor$ represents the integer rounding for g_N , and it can be expressed as

$$g_N(\theta) = \begin{cases} N - N \frac{D}{\lambda} \cos(\theta), & \theta \in \left[0, \frac{\pi}{2}\right], \\ -N \frac{D}{\lambda} \cos(\theta), & \theta \in \left[\frac{\pi}{2}, \pi\right]. \end{cases} \quad (13)$$

The large frequency domain values of \mathbf{F} should be in the region $J(k_{\min}, k_{\max})$ when $X(k)$ approaches to the maximal value M , which can be written as

$$J(k_{\min}, k_{\max}) = \begin{cases} [0, k_{\max}] \cup [k_{\min}, N], & \theta_{\min} \in \left[0, \frac{\pi}{2}\right] \\ & \theta_{\max} \in \left[\frac{\pi}{2}, \pi\right] \\ [k_{\min}, k_{\max}], & \text{otherwise} \end{cases} \quad (14)$$

where $k_{\min} = \lfloor g_N(\theta_{\min}) \rfloor$ and $k_{\max} = \lfloor g_N(\theta_{\max}) \rfloor$. The values of \mathbf{F} outside the interval $J(k_{\min}, k_{\max})$ are set to zero, which is equivalent to canceling the signals outside the interval $[\theta_{\min}, \theta_{\max}]$, leading to the interference and the effect of the noise reducing. Then, the Inverse Fast Fourier Transform (IFFT) of \mathbf{F} can be expressed as

$$\mathbf{f} = [f \wedge(0) f \wedge(1) \cdots f \wedge(N-1)]^T, \quad (15)$$

The estimation of the channel coefficient vector can be written as

$$\bar{\mathbf{h}} = [f \wedge(0) f \wedge(1) \cdots f \wedge(M-1)]^T. \quad (16)$$

4. Uplink Pilot Power Allocation Based on Water-Filling Algorithm

First, we introduce a pilot assignment method based location for massive MIMO-HWSN system. The novel channel estimation at the MBSs shown in the previous section is utilized, and some orthogonal pilot sequences could be reused by SSNs so that the idea can support more users simultaneously reducing the interference partly.

In Figure 3, we define $d_{n,k,j}$ as the Euclidean distance between the j -th macrocell and the n -th interfering user. $\mathbf{z}(\theta) = [\cos(\theta) \sin(\theta)]^T$ indicates the directional vector with unit length. In the j -th macrocell, there is a function to measure the interference at the MBS from the k -th MSN to the n -th interfering user, which is written as

$$I_{n,k,c} = \frac{|\mathbf{z}^T(\theta_{n,k,n}) \mathbf{z}(\theta_{n,k,j})|}{d_{n,k,c}^\gamma}, \quad (17)$$

where $\theta_{n,k,j}$ denotes the AOA of the k -th MSN in the j -th macrocell at the n -th MBS, and we denote γ as the pathloss exponent. Then, the interference to all MSNs can be expressed as

$$\mathbf{T}_{\text{MSN}} = \sum_{b=1}^C \sum_{k=1}^{K_m} \sum_{n=1, n \neq b}^C \mathbf{I}_{n,k,c} + \sum_{l=1}^C \sum_{k=1}^{K_m} \sum_{s=k}^{K_m} \mathbf{I}_{i,k,c}, \quad (18)$$

where \mathbf{T}_{MSN} is the interference from MSNs and the second part of \mathbf{T}_{MSN} is the interference from SSNs.

The assignment not applicable to this scenario that the SBSs with only one antenna. Thus, the interference at the SBS is

$$I'_{n,k,c} = \frac{1}{d_{n,k,c}^\gamma}, \quad (19)$$

where $I'_{n,k,j}$ denotes the interference from the k -th SSN to the n -th interfering user in the j -th macrocell. Similarly, the interference to all SSNs can be written as

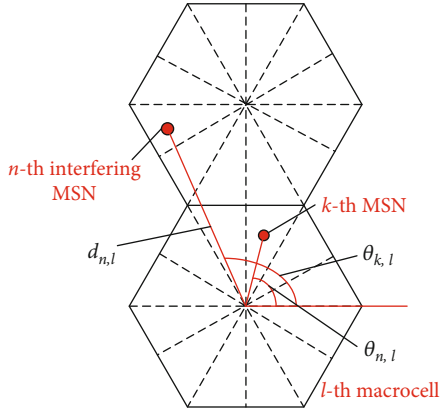


FIGURE 3: Illustration of k -th MSN in l -th macrocell with respect to n -th interfering MSN.

$$\mathbf{T}_{\text{SSN}} = \sum_{b=1}^C \sum_{k=1}^P \sum_{n=1}^C \mathbf{I}'_{n,k,c} + \sum_{b=1}^C \sum_{k=1}^P \sum_{s_i=s_k, i \neq k} \mathbf{I}'_{i,b,k}. \quad (20)$$

The first part of \mathbf{T}_{SSN} is the interference from MSNs, and the second part of \mathbf{T}_{SSN} is the interference from SSNs. All interference in this system can be modeled as $\mathbf{T} = \mathbf{T}_{\text{MSN}} + \mathbf{T}_{\text{SSN}}$.

The traditional optimal mode can find the optimal pilot allocation method with the minimum T value by exhaustively calculating various schemes, but for MIMO-HWSN, this is impossible because its complexity is very high.

In this model, there is a hexagonal macrocell, which is evenly divided into K_m sectors, and there is only one MSN in each sector. We determine the number of MSN K_m supported by each macrocell, but we are not sure where the MSN is located in each sector. Then, we introduce a pilot allocation algorithm to get a suboptimal pilot allocation scheme, which is divided into four steps:

- (1) The same pilot will be assigned to the two sectors which have the least interference between two sectors in an adjacent macrocell
- (2) In the central macrocell, we assign the pilots to each SSN. Since different pilot allocation modes lead to different interferences, the pilot allocation mode can be determined after finding the minimize intertier interference
- (3) We assign the pilots to SSNs in each macrocell and the remaining unallocated sectors through exhaustive search, which depends on ensuring the minimize interference metric \mathbf{I} . When calculating interference from MSNs, only the SSNs in the same macrocell with the MSNs are considered
- (4) Checking for the interference between SSNs and assigning same pilots. A new pilot allocation method is proposed to handle the serious interference

After the four-step pilot assignment algorithm, a suboptimal pilot allocation model with reasonable computational complexity can be determined.

After determining the pilot allocation, the mode of allocating the total pilot transmission power to the MSNs will significantly affect the system capacity. The uplink capacity of the k -th MSN is given by

$$C_{c,k} = E\{\log_2(1 + \text{SINR}_{c,k})\}. \quad (21)$$

The uplink $\text{SINR}_{j,k}$ of the k -th MSN in j -th macrocell can be obtained through (10). In order to achieve a larger average achievable system capacity, the optimization problem can be written as

$$\max_{\{\Delta\}} \sum_{c=1}^C \sum_{k=1}^{K_m} \text{SINR}_{c,k}, \quad (22)$$

$$\text{s.t.} \quad \sum_{c=1}^C \sum_{k=1}^{K_m} P_{c,k} = P_{\text{total}},$$

where $\{\Delta\}$ represents the optimal pilot power allocation schemes. Since it is difficult to get a closed form solution to the optimal problem, we consider proposing a suboptimal power allocation method combined with the traditional water-filling algorithm. The traditional water-filling algorithm allocates the transmit power adaptively according to channel conditions. In general, more power is allocated when the channel condition is good, and less power is allocated when the channel condition is poor, so as to maximize the SINR and transmission rate. Inspired by the water-filling algorithm, we can propose a suboptimal pilot transmit power allocation scheme on the basis of keeping the total power unchanged.

Figure 4 shows the distribution process of the water-filling algorithm. The interference energy is expressed by the reciprocal of the Γ/SINR_n , where Γ represents the difference of the values of SINR. Obviously, the subchannel with a large SINR has a small reciprocal Γ/SINR_n in Figure 4 and, thus, can allocate more energy. Otherwise, it can be allocated less energy. The SINR is too small for channel 3, that is, Γ/SINR_3 is too large, so no energy is allocated to this subchannel.

The result of the “water-filling algorithm” shows that the characteristic subchannel with a large channel gain is allocated with larger power to make its capacity larger; on the contrary, the characteristic subchannel with a small channel gain is allocated with smaller power to maintain a certain capacity to ensure that the characteristic subchannel with good channel conditions can transmit more information. When the conditions of a subchannel are poor to a certain extent, the transmit power may not be allocated for that channel. At this point, the subchannel does not send any data. The water-filling algorithm makes full use of the good channel conditions, discards the poor channels, and avoids the system using most of the transmit power to make up for the poor channel conditions.

Sufficient power is allocated for each WSN to guarantee the successful transmission of pilot sequences. However, when the allocated pilot transmission power is too large, it will affect the system performance of other users, so this

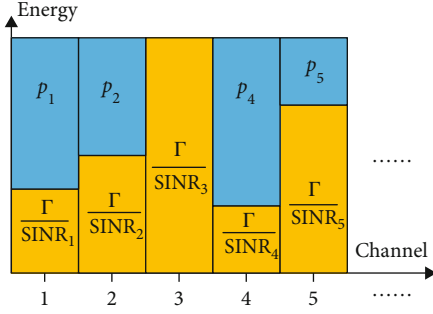


FIGURE 4: Water-filling algorithm of AWGN channel.

condition $p_{c,k} \in [p_{\min}, p_{\max}]$ should be satisfied. The values are $p_{\min} = p_{\text{total}}/2K_m$ and $p_{\max} = 3p_{\text{total}}/2K_m$.

We can set the number of all MSNs to $U = L \cdot K_m$, and the pilot transmission power of MSNs can be written as $P_l = \{p_1, p_2, \dots, p_U\}$, where $p_i = 0$, $i \in 1, 2, \dots, U$. Then, we use the pilot to distribute the transmission power based on the water-filling algorithm, which can be described as follows:

First, the lowest power p_{\min} is assigned to MSNs; that is, for all the elements $p_i = p_{\min}$, $i \in 1, 2, \dots, U$, the power not allocated is

$$p_{\text{rest}} = p_{\text{total}} - U \cdot p_{\min}. \quad (23)$$

Second, a set of numbers as $T = \{t_1, t_2, \dots, t_U\}$ is generated to satisfy both uniform distribution in $[p_{\min}, p_{\max}]$ and the constraint

$$\sum_{u=1}^U t_u = p_{\text{rest}}, \quad (24)$$

where $t_1 > t_2 > \dots > t_U$. Through the previous calculation, we can clearly obtain the channel gain of MSNs, marked as $H_l = \{|h_1|^2, |h_2|^2, \dots, |h_U|^2\}$. The remaining power is allocated to MSNs according to the order of channel gain. $|h_j|^2$ indicates the channel gain of j -th MSN, and the order of values in H_l is $j^\#$. The pilot power of j -th MSN can be given as

$$p_j = p_{\min} + t_{j^\#}. \quad (25)$$

where $t_{j^\#}$ is the $j^\#$ -th value of T .

We can improve the system capacity by the above scheme, while satisfying the constraints in (22).

5. Simulation Result

The performance of our proposed scheme is evaluated via simulations. We propose a multicell multiuser MIMO-HWSN system with $C = 7$ macrocells, which is divided into $S = 12$ sectors evenly. The number of MSNs is set as $K_m = 12$, and $P = 4$ SSNs of the four reused partial orthogonal pilots are randomly distributed. The radio of the macrocell is set as 500 m, the number of paths in the multipath chan-

TABLE 1: Parameters of the simulation system.

Macrocell radius	500 m
Number of orthogonal pilots	12
Path loss exponent	3.5
Number of paths per user Q	50
Angle spread	10 degrees
Variance of shadow fading	8 dB
Transmit power at SSNs	10 mW
Antenna spacing D	$\lambda/2$

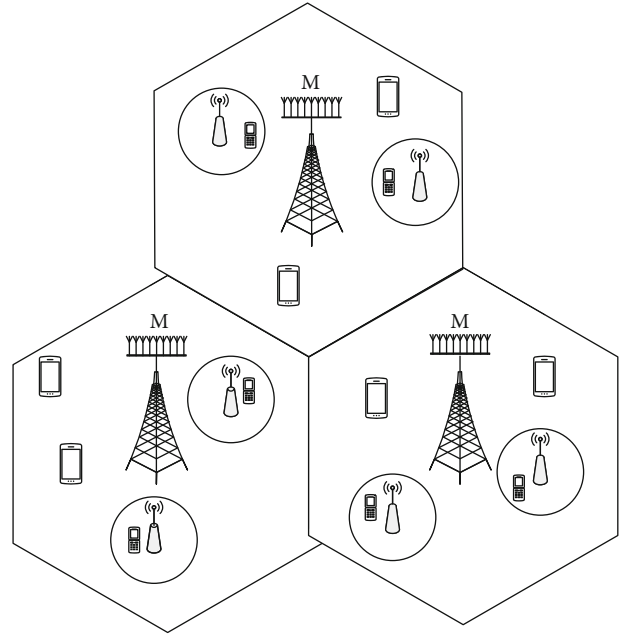


FIGURE 5: The model obtained after assigning the pilots.

nel is 50, and the path loss exponent is 3.5. It is assumed that there are 12 orthogonal pilots and the angle spread is 10 degrees. The transmit power of SSNs is 0 dBm, and the variance of shadow fading is 8 dB. The wavelength $\lambda = 2D$. All of the parameters which are used in simulations are listed in Table 1.

In the location-aware channel estimation, we set $N = 8192$ as the size of FFT. Figure 5 is the model of a massive MIMO-HWSN system using pilot assignment based on location information. In this figure, the red dots represent the randomly distributed small cells, the red numbers indicate the pilot reused by SSN in that small cell, and the black numbers in each sector indicate the pilots to which the sector is assigned. In the allocation process, we ensure that the interference between MSNs using the same pilot is always minimal. In this model, the pilots used by MSNs in each sector of the central macrocell are randomly assigned. The pilot allocation in the central macrocell will affect the pilot types used by other SNs in the system. We assume that the pilot settings in the central macrocell are as shown in the figure.

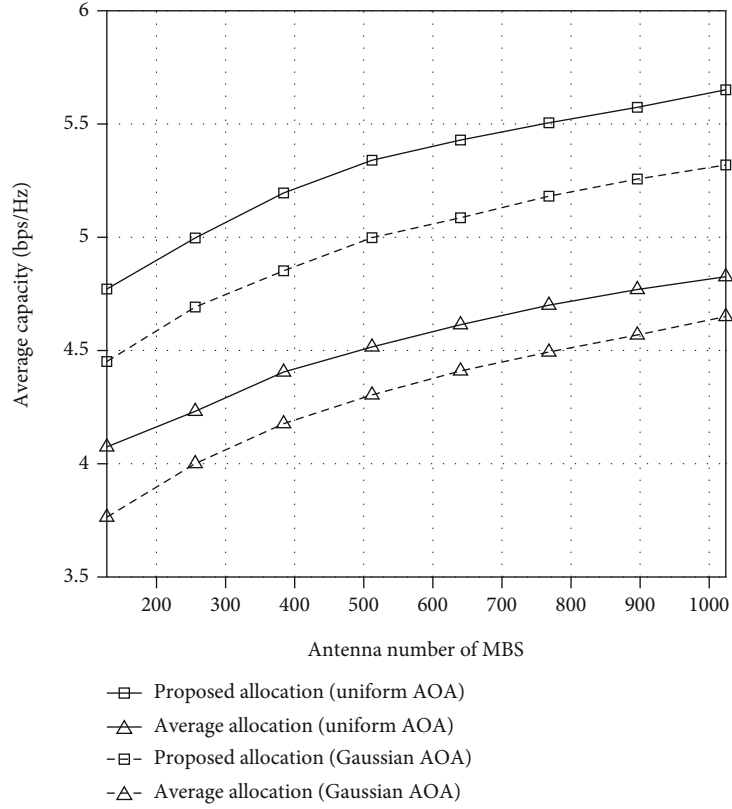


FIGURE 6: Average per SN uplink capacity versus antenna number of MBS.

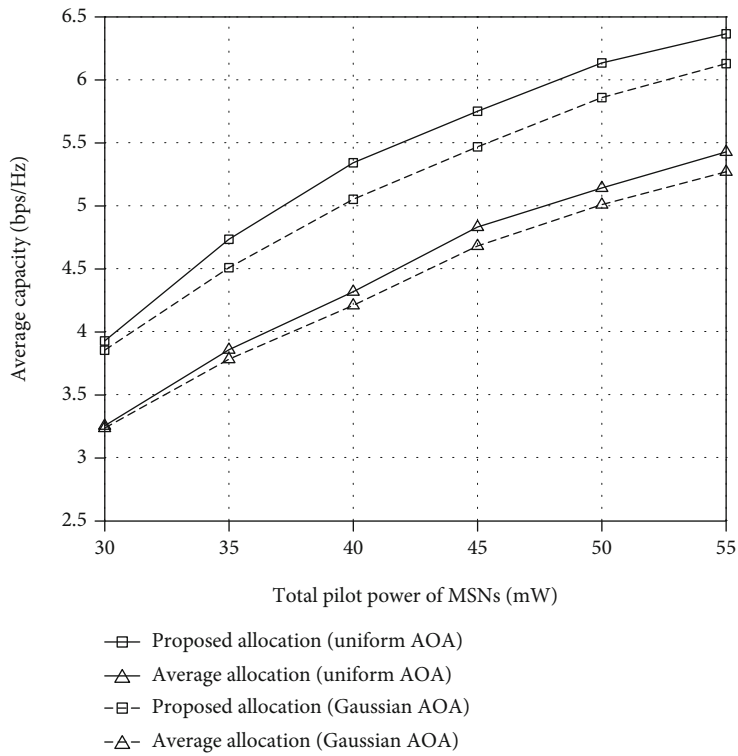


FIGURE 7: Average capacity versus the total pilot power of MSNs.

In the simulation, we use the channel estimation which is proposed in the previous section, and AOAs have Gaussian and uniform distributions. We consider that AOAs have uniform distribution when $\theta \in [\bar{\theta} - \theta_{\Delta}, \bar{\theta} + \theta_{\Delta}]$, where $\bar{\theta}$ is the line of sight AOA and $\theta_{\Delta} = \delta_{\theta}/2$. In another assumption that AOAs are Gaussian random variables, the mean and variance are $\bar{\theta}$ and $(\delta_{\theta}/2)^2$, respectively, where δ_{θ} is the angle spread.

The proposed pilot allocation mode can be evaluated using the average uplink capacity of each user. In Figure 6, the relationship between the average uplink capacity of each MSN and the number of MBSs' antennas in this scheme is shown, and the total pilot power is 40 mW. In the figure, the "average allocation" scheme has poor performance. This is because it equally distributes the pilot transmit power to MSNs without any difference and does not take into account that different MSNs are affected by pilot-related pollution to different degrees. The "proposed allocation" scheme outperforms the "average allocation" scheme because it allocates more pilot transmit power to MSNs with better channel conditions. In two pilot power allocation modes, because some useful paths are filtered out and AOA obeys Gaussian distribution in an interval, so the Gaussian distribution of the AOA average uplink capacity is lower than the uniform distribution of AOA. With the increase of MBS antenna number, each under two kinds of AOA distribution MSN will significantly improve the average uplink transmission capacity. Different AOAs have higher resolutions, and pilot frequency reuse caused by interference will be greatly reduced.

Figure 7 shows the relationship of the average uplink capacity and the total pilot power of MSNs in two schemes, that is, pilot power average and distinguishing allocation. As the total transmitted power of the pilot increases, the average uplink capacity increases significantly. Moreover, regardless of the distribution of AOAs, with the increase of total power, the average power distribution obtained by the proposed power distribution scheme differs greatly from the uplink average capacity. The larger the p_{total} value, the more transmitted power is allocated to the WeChat nodes with better channel gain, which tends to have a fundamental impact on system capacity.

6. Conclusion

In order to improve the uplink capacity of the MIMO-HWSN system, a pilot transmission power scheme based on the traditional water-filling algorithm is proposed. Location-aware pilot allocation and channel estimation are introduced to suppress interference. When the total pilot transmitting power is fixed, based on the proposed pilot transmitting power scheme, more transmitting power can be allocated to a MSN with better channel gain, and the system capacity can be improved. Simulation results show that this method has the ability to significantly improve the uplink capacity when considering the average power allocation. These contributions will certainly improve the performance of 6G systems and make the quality of service of users much higher than 5G and bring some additional benefits.

Data Availability

The reader can contact us to get the paper data.

Conflicts of Interest

The authors declare that they have no conflicts of interest.

References

- [1] Z. Chu, Z. Zhu, F. Zhou, M. Zhang, and N. Al-Dhahir, "Intelligent reflecting surface assisted wireless powered sensor networks for internet of things," *IEEE Transactions on Communications*, vol. 69, no. 7, pp. 4877–4889, 2021.
- [2] S. Jacob, S. Joseph, P. G. Vinoj et al., "A novel spectrum sharing scheme using dynamic long short-term memory with CP-OFDMA in 5G networks," *IEEE Transactions on Cognitive Communications and Networking*, vol. 6, no. 3, pp. 926–934, 2020.
- [3] D. T. Do, T. T. T. Nguyen, C. B. le, M. Voznak, Z. Kaleem, and K. M. Rabie, "UAV relaying enabled NOMA network with hybrid duplexing and multiple antennas," *IEEE Access*, vol. 8, pp. 186993–187007, 2020.
- [4] D. Zhang, Z. Zhou, S. Mumtaz, J. Rodriguez, and T. Sato, "One integrated energy efficiency proposal for 5G IoT communications," *IEEE Internet of Things Journal*, vol. 3, no. 6, pp. 1346–1354, 2016.
- [5] X. Li, M. Zhao, Y. Liu, L. Li, Z. Ding, and A. Nallanathan, "Secrecy analysis of ambient backscatter NOMA systems under I/Q imbalance," *IEEE Transactions on Vehicular Technology*, vol. 69, no. 10, pp. 12286–12290, 2020.
- [6] D. T. Do, M. S. Van Nguyen, T. N. Nguyen, X. Li, and K. Choi, "Enabling multiple power beacons for uplink of NOMA-enabled mobile edge computing in wirelessly powered IoT," *IEEE Access*, vol. 8, pp. 148892–148905, 2020.
- [7] Z. Chu, F. Zhou, Z. Zhu, R. Q. Hu, and P. Xiao, "Wireless powered sensor networks for internet of things: maximum throughput and optimal power allocation," *IEEE Internet of Things Journal*, vol. 5, no. 1, pp. 310–321, 2018.
- [8] H. Niu, Z. Chu, F. Zhou, Z. Zhu, M. Zhang, and K. -K. Wong, "Weighted sum secrecy rate maximization using intelligent reflecting surface," *IEEE Transactions on Communications*, p. 1, 2021.
- [9] X. Li, J. Li, Y. Liu, Z. Ding, and A. Nallanathan, "Residual transceiver hardware impairments on cooperative NOMA networks," *IEEE Transactions on Wireless Communications*, vol. 19, no. 1, pp. 680–695, 2020.
- [10] T. L. Marzetta, "Noncooperative cellular wireless with unlimited numbers of base station antennas," *IEEE Transactions on Wireless Communications*, vol. 9, no. 11, pp. 3590–3600, 2010.
- [11] Z. Zhu, Z. Chu, F. Zhou, H. Niu, Z. Wang, and I. Lee, "Secure beamforming designs for secrecy MIMO SWIPT systems," *IEEE Wireless Communications Letters*, vol. 7, no. 3, pp. 424–427, 2018.
- [12] Z. Zhu, Z. Chu, N. Wang, S. Huang, Z. Wang, and I. Lee, "Beamforming and power splitting designs for AN-aided secure multi-user MIMO SWIPT systems," *IEEE Transactions on Information Forensics and Security*, vol. 12, no. 12, pp. 2861–2874, 2017.
- [13] S. Wang, J. Wan, D. Zhang, D. Li, and C. Zhang, "Towards smart factory for industry 4.0: a self-organized multi-agent

- system with big data based feedback and coordination,” *Computer Networks*, vol. 101, pp. 158–168, 2016.
- [14] X. Wu, H. Wang, D. Wei, and M. Shi, “ANFIS with natural language processing and gray relational analysis based cloud computing framework for real time energy efficient resource allocation,” *Computer Communications*, vol. 150, pp. 122–130, 2020.
- [15] X. Wu, Y. Wei, T. Jiang, Y. Wang, and S. Jiang, “A micro-aggregation algorithm based on density partition method for anonymizing biomedical data,” *Current Bioinformatics*, vol. 14, no. 7, pp. 667–675, 2019.
- [16] J. M. Williams, R. Khanna, J. P. Ruiz-Rosero et al., “Weaving the wireless Web: toward a low-power, dense wireless sensor network for the industrial IoT,” *IEEE Microwave Magazine*, vol. 18, no. 7, pp. 40–63, 2017.
- [17] Z. Zhu, S. Huang, Z. Chu, F. Zhou, D. Zhang, and I. Lee, “Robust designs of beamforming and power splitting for distributed antenna systems with wireless energy harvesting,” *IEEE Systems Journal*, vol. 13, no. 1, pp. 30–41, 2019.
- [18] Z. Zhu, N. Wang, W. Hao, Z. Wang, and I. Lee, “Robust beamforming designs in secure MIMO SWIPT IoT networks with a non-linear channel model,” *IEEE Internet of Things Journal*, vol. 8, no. 3, pp. 1702–1715, 2021.
- [19] I. Khan, F. Belqasmi, R. Glitho, N. Crespi, M. Morrow, and P. Polakos, “Wireless sensor network virtualization: a survey,” *IEEE Communications Surveys & Tutorials*, vol. 18, no. 1, pp. 553–576, 2016.
- [20] M. Kountouris and N. Pappas, “HetNets and massive MIMO: modeling, potential gains, and performance analysis,” in *2013 IEEE-APS Topical Conference on Antennas and Propagation in Wireless Communications (APWC)*, pp. 1319–1322, Turin, Italy, 2013.
- [21] Z. Zhu, W. Ge, N. Wang et al., “AN-based beamforming design in secrecy heterogeneous WSN with MIMO-SWIPT,” in *IEEE international conference on communications workshops (ICC workshops)*, pp. 1–6, Shanghai, China, 2019.
- [22] Z. Chu, F. Zhou, P. Xiao et al., “Resource allocation for secure wireless powered integrated multicast and unicast services with full duplex self-energy recycling,” *IEEE Transactions on Wireless Communications*, vol. 18, no. 1, pp. 620–636, 2019.
- [23] T. X. Vu, T. A. Vu, and T. Q. S. Quek, “Successive pilot contamination elimination in multiantenna multicell networks,” *IEEE Wireless Communications Letters*, vol. 3, no. 6, pp. 617–620, 2014.
- [24] Y. Yao, Z. Zhu, S. Huang, X. Yue, C. Pan, and X. Li, “Energy efficiency characterization in heterogeneous IoT system with UAV swarms based on wireless power transfer,” *IEEE Access*, vol. 8, pp. 967–979, 2020.
- [25] J. K. Tugnait, “Self-contamination for detection of pilot contamination attack in multiple antenna systems,” *IEEE Wireless Communications Letters*, vol. 4, no. 5, pp. 525–528, 2015.
- [26] A. Khansefid and H. Minn, “On channel estimation for massive MIMO with pilot contamination,” *IEEE Communications Letters*, vol. 19, no. 9, pp. 1660–1663, 2015.
- [27] J.-C. Shen, J. Zhang, and K. B. Letaief, “Downlink user capacity of massive MIMO under pilot contamination,” *IEEE Transactions on Wireless Communications*, vol. 14, no. 6, pp. 3183–3193, 2015.
- [28] O. Elijah, C. Y. Leow, T. A. Rahman, S. Nunoo, and S. Z. Iliya, “A comprehensive survey of pilot contamination in massive MIMO—5G system,” *IEEE Communications Surveys Tutorials*, vol. 18, no. 2, pp. 905–923, 2016.
- [29] I. E. Shaalan, A. A. Khattaby, and A. S. Dessouki, “A new joint TSPA/WGC pilot contamination reduction strategy based on exact graph coloring grouping algorithm,” *IEEE Access*, vol. 7, pp. 150552–150564, 2019.
- [30] J. Jose, A. Ashikhmin, T. L. Marzetta, and S. Vishwanath, “Pilot contamination problem in multi-cell TDD systems,” in *2009 IEEE International Symposium on Information Theory*, pp. 2184–2188, Seoul, Korea (South), 2009.
- [31] Z. Wang, P. Zhao, C. Qian, and S. Chen, “Location-aware channel estimation enhanced TDD based massive MIMO,” *IEEE Access*, vol. 4, no. 99, pp. 7828–7840, 2016.
- [32] T. Lian, L. You, W. Zhong, and X. Gao, “Coordinated pilot reuse for multi-cell massive MIMO transmission,” in *International Symposium on Personal, Indoor and Mobile Radio Communications*, pp. 492–496, Washington, DC, USA, 2014.
- [33] H. Yin, D. Gesbert, M. Filippou, and Y. Liu, “A coordinated approach to channel estimation in large-scale multiple-antenna systems,” *IEEE Journal on Selected Areas in Communications*, vol. 31, no. 2, pp. 264–273, 2013.
- [34] R. R. Muller, L. Cottatellucci, and M. Vehkaperä, “Blind pilot decontamination,” *IEEE Journal of Selected Topics in Signal Processing*, vol. 8, no. 5, pp. 773–786, 2014.
- [35] H. Q. Ngo and E. G. Larsson, “EVD-based channel estimation in multicell multiuser MIMO systems with very large antenna arrays,” in *International Conference on Acoustics, Speech and Signal Processing*, pp. 3249–3252, Kyoto, Japan, 2012.
- [36] L. You, X. Gao, X. G. Xia, N. Ma, and Y. Peng, “Pilot reuse for massive MIMO transmission over spatially correlated Rayleigh fading channels,” *IEEE Transactions on Wireless Communications*, vol. 14, no. 6, pp. 3352–3366, 2015.
- [37] L. Su and C. Yang, “Fractional frequency reuse aided pilot decontamination for massive MIMO systems,” in *81st Vehicular Technology Conference, IEEE*, pp. 1–6, Glasgow, UK, 2015.
- [38] I. Atzeni, J. Arnau, and M. Debbah, “Fractional pilot reuse in massive MIMO systems,” in *International Conference on Communication Workshop*, pp. 1030–1035, London, UK, 2015.
- [39] X. Zhu, Z. Wang, C. Qian et al., “Soft pilot reuse and multi-cell block diagonalization precoding for massive MIMO systems,” *IEEE Transactions on Vehicular Technology*, vol. 65, no. 5, pp. 3285–3298, 2016.
- [40] J.-C. Chen, C.-K. Wen, S. Jin, and K.-K. Wong, “A low complexity pilot scheduling algorithm for massive MIMO,” *IEEE Wireless Communications Letters*, vol. 6, no. 1, pp. 18–21, 2017.
- [41] Z. Chen and C. Yang, “Pilot decontamination in massive MIMO systems: exploiting channel sparsity with pilot assignment,” in *IEEE Global Conference on Signal and Information Processing*, pp. 637–641, Atlanta, GA, USA, 2014.
- [42] Z. Zhao, Z. Chen, and Y. Liu, “Cell sectorization-based pilot assignment scheme in massive MIMO systems,” in *IEEE Wireless Telecommunications Symposium*, pp. 1–5, New York, NY, USA, 2015.
- [43] M. Liu, X. Chen, W. Xu, H. Zhang, X. You, and W. Miao, “Grouped pilot reuse for channel estimation in massive MIMO networks,” in *IEEE International Conference on Wireless Communications and Signal Processing*, pp. 1–5, Yangzhou, China, 2016.
- [44] N. Akbar, S. Yan, N. Yang, and J. Yuan, “Mitigating pilot contamination through location-aware pilot assignment in

- massive MIMO networks,” in *IEEE Global Communications Conference Workshop*, pp. 1–6, Washington, DC, USA, 2017.
- [45] V. Saxena, G. Fodor, and E. Karipidis, “Mitigating pilot contamination by pilot reuse and power control schemes for massive MIMO systems,” in *IEEE 81st Vehicular Technology Conference*, pp. 1–6, Glasgow, UK, 2015.
- [46] T. M. Nguyen and L. B. Le, “Joint pilot assignment and resource allocation in multicell massive MIMO network: throughput and energy efficiency maximization,” in *IEEE Wireless Communications and Networking Conference*, pp. 393–398, New Orleans, LA, USA, 2015.

Research Article

Energy-Efficient Routing Using Fuzzy Neural Network in Wireless Sensor Networks

Rajesh Kumar Varun,¹ Rakesh C. Gangwar,² Omprakash Kaiwartya ,³
and Geetika Aggarwal ³

¹Department of Computer Science and Engineering, I. K. Gujral Punjab Technical University, Jalandhar, Punjab, India

²Department of Computer Science and Engineering, Beant College of Engineering & Technology, Gurudaspur, 143521, Punjab, India

³School of Science and Technology, Nottingham Trent University, Nottingham NG11 8NS, UK

Correspondence should be addressed to Omprakash Kaiwartya; omprakash.kaiwartya@ntu.ac.uk

Received 9 April 2021; Revised 30 June 2021; Accepted 21 July 2021; Published 10 August 2021

Academic Editor: Giovanni Pau

Copyright © 2021 Rajesh Kumar Varun et al. This is an open access article distributed under the Creative Commons Attribution License, which permits unrestricted use, distribution, and reproduction in any medium, provided the original work is properly cited.

In wireless sensor networks, energy is a precious resource that should be utilized wisely to improve its life. Uneven distribution of load over sensor devices is also the reason for the depletion of energy that can cause interruptions in network operations as well. For the next generation's ubiquitous sensor networks, a single artificial intelligence methodology is not able to resolve the issue of energy and load. Therefore, this paper proposes an energy-efficient routing using a fuzzy neural network (ERFN) to minimize the energy consumption while fairly equalizing energy consumption among sensors thus as to prolong the lifetime of the WSN. The algorithm utilizes fuzzy logic and neural network concepts for the intelligent selection of cluster head (CH) that will precisely consume equal energy of the sensors. In this work, fuzzy rules, sets, and membership functions are developed to make decisions regarding next-hop selection based on the total residual energy, link quality, and forward progress towards the sink. The developed algorithm ERFN proves its efficiency as compared to the state-of-the-art algorithms concerning the number of alive nodes, percentage of dead nodes, average energy decay, and standard deviation of residual energy.

1. Introduction

Wireless sensor network (WSN) is referred to as a collection of smart sensor nodes that collect data and taken appropriate decisions [1–3]. WSN environment is comprised of smart sensor nodes for detecting some unusual (RFID enabled) that collect data from the confined condition and forward it to the base station. WSN is a group of smart sensor nodes that collect data from encompassing conditions and forward it to the base station for future actions [4–6]. It also overloads the data on cloud applications that are downloaded by users for processing. The sensing field is a sensor-enabled environment that is used in almost all the fields for smart monitoring purposes, such as human or animal tracking, medical, military, automobile industries, natural hazard, environmental monitoring, seismic detection, agriculture, navigation, and surveillance environments [7, 8]. The sensor nodes have a

limited range of energy that is used to communicate and computation. It is highly difficult to recharge these smart nodes or to provide some alternate power source [9–11]. In WSN, few nodes deplete their energy more quickly than may cause degrading the lifetime of the network. The authors proposed an energy efficiency approach where ANT colony with Huffman coding is used to conserve the energy of WSN [12]. Therefore, this paper will look after energy and load of sensor nodes to improve the lifetime of WSN. A load of sensor nodes must be evenly distributed or scheduled to obtain the defined goal. The proposed approach schedules the load among nodes having higher transmission capabilities and computational power.

Routing using route-centric parameters is also a supporting approach used in the past to tackle energy consumption balancing issues. In this approach, the routing is performed into a small network region, and in each region, one sensor

is selected as next hop that will forward the data from other sensors of a sink [13, 14]. Parameter-centric routing further applies geocast techniques to reduce delay and improve the packet delivery ratio. The next-hop plays a significant role in scalable routing to load balancing, enhancing network lifetime [15]. The major feature used for designing a parametric centric routing is optimal selection techniques for next hop sensor for forwarding the data to the sink. Advanced sensor networks are becoming complex day by day; therefore, traditional mathematical models for next hop selection are not appropriate. A fuzzy inference system provides applicable solutions to fabricate a model for the selection of next hop, as it processes the detailed part of general human apprehension in absence of any mathematical tools. In 1965, the basic theory of fuzzy is explained by Zadeh [16]. Then, Takagi and Sugeno followed the fuzzy system and proposed a fuzzy logic modeling to evaluate the mess of different pragmatic applications, namely, as control, inference, prediction, and estimation [17]. There are some advantages with fuzzy modeling like as the capacity to translate immanent indecisive of human feature into linguistic variables and apprehension of outcomes in natural rule portrayal way and in simple augmentation rule with the help of the extension of new postulates and usefulness of the system. The fuzzy logic is also affected with some disadvantages of no proper method to explain human practical knowledge into fuzzy logic databases. It only analyses the rule database. It cannot think out of the box, or we can say, generalization in fuzzy is a little difficult. It is high time to obtain a generalized solution, to tune the membership function to alleviate error rates in order to enhance the accomplishment index, a generalized solution is required. The artificial neural network (ANN) model proposed by McCulloch and Pitts trained various variants of the ANN model as adaptive linear neuron, which is known as adaptive linear element algorithm [18]. The ANN is an analytical model for "connectionist" which analyses by logic neurons of the human cerebrum. Such models acquire knowledge from trained data vectors and input-output of the system [19–24]. It depicts the weight function concerning the problem including the error rate of the system to make a more efficient system. To enlarge the learning algorithm with generalization ability of fuzzy environment is the incorporating concept that is followed here [25]. It obtains logical interpretation to rectify the issues. A hybrid system named neuro-fuzzy system is proposed by Jang, Lin, Berenji, and Nauck [26–33].

In this context, we propose an energy-efficient routing using soft computing-based hybrid system by combining an adaptive neural network and a fuzzy inference system to find an appropriate next hop sensor from the neighboring sensors. The election of next hop relies upon residual energy of each sensor, node degree, and forward progress towards the sink. In each round, a new next hop is selected which supports equalizing the energy consumption to meliorate the lifetime of the network by altering the path each time. The followings are the main contribution of the paper:

- (1) First, a system and energy model is presented to explain the topological configuration of WSN and

to analyze the energy required for transmitting and receiving data throughout the network

- (2) To optimize the performance of the sensor network, routing centric parameters are derived focusing on expected energy consumption, expected node degree, and expected forward progress towards the sink
- (3) Fuzzy-Neural networks have been used which jointly combine three routing centric parameters to efficient next hop selection
- (4) A fuzzy neural network-assisted energy-efficient routing framework is developed based on the energy model and routing centric parameters
- (5) The proposed routing framework is simulated to comparatively evaluate the performance against state-of-the-art routing providing metrics related to sensing environments

The remaining part of the paper is organized as follows: the section presents a review of energy-centric routing with and without heuristics approaches. Section 3 presents energy-efficient routing using a fuzzy neural network for WSN. Section 4 explained the simulation results and analysis for the proposed routing. The conclusion is presented in section 5.

2. Related Works

2.1. Energy Centric Routing without Heuristics. The first hierarchical clustering algorithm is LEACH (low energy adaptive clustering hierarchy) which supports two stages for each clustering round [34]. One deals with cluster head (CH) selection and with cluster formation in a network. Another stage deals with data transmission to CH. When a cluster is formed, all the sensor nodes are assigned with some probability through a probabilistic model to elect CH. A predefined threshold value is defined which plays an important role in electing CH. An arbitrary value between 0-1 is generated for every sensor node which is further compared to the threshold value for electing CH in a particular round. To avoid intercluster interface, each CH floats a message using CSMA. Now the sensor nodes are able to make the decision regarding the data transmission that to which CH they wish to connect. After this, CH piles up data from its member nodes and claims data aggregation technique to lessen data redundancy and forward the filtered data to the intended base station. This is how the LEACH algorithm takes fair decisions for CH selection, and each node gets equal opportunity to become a CH [35]. But the critical concern with the LEACH algorithm is that the energy consumption of the nodes is not considered which is our prime concern. Moreover, LEACH does not look after the asymmetric classification of clusters in networks, and multihop data transmission is also not allowed. Therefore, to overcome the mentioned issues of LEACH, hybrid energy efficiency distribution (HEED) is introduced [36]. This algorithm also supports a probabilistic model for CH selection where the probabilistic is increased twice in between the

rotations. But this algorithm (HEED) has its own issues. In HEED, few sensor nodes are exempted for the selection of CH, and few nodes are not even a part of any cluster and are freely available. To focus on the conservation of energy, a power-efficient gathering in sensor information systems (PEGASIS) is launched that uses greedy. In PEGASIS, every node acquires data from its near node and forwards it to another neighbor node, and fused [37]. The fused data is transmitted to the base station from a specified node. After a specified time slot, random nodes are selected for the designated role. Hence, all the nodes participate equally and deplete their energy evenly. The average energy consumption in each rotation is abated.

2.2. Energy Centric Routing with Fuzzy-Heuristics. A fuzzy logic system plays a significant role in the selection of CH in sensor-enabled IOT environment. Gupta et al. introduced fuzzy logic approach to select CH nodes based on current energy level, the centrality of node, and density [38]. This approach is different from the traditional LEACH approach, as in this scheme the base station is simply accountable for the election of CH node and base station further processes the data using Mamdani type fuzzy inference system that provides output as a plunge to decide favorable node, applicable for CH. After this stage, all the operations are similar to LEACH. CHEF is proposed as a new CH selection scheme that observes the residual energy and local distance as parameters [39]. The local information about the node is gathered from neighboring nodes. This mechanism is localized within a cluster. The base station does not gather information or select CH. LEACH and CHEF share a common set-up phase. CHEF works in residual energy and local distance. Another protocol came which is an improvised version of traditional LEACH names as LEACH-FL (low energy adaptive clustering hierarchy protocol based on fuzzy logic) [40]. It analyses three parameters as fuzzy variables such as node density, energy level, and distance to base station. The base station collects data and applies Mamdani type fuzzy inference system to make decision for CH. Here, expected residual energy and actual residual energy are used to determine the chance of being a CH. This approach is also similar LEACH. The nodes which have extra residual energy along with expected residual energy have high chance of becoming a CH node. For energy prediction technique with fuzzy logic for homogeneous WSN, LEACH-ERE is introduced by Lee and Cheng [41]. This approach presents a concept considering the distance to the base station, concretion of node leads to bumpy energy utilization over a network. The fuzzy logic-based clustering algorithms for wireless sensor networks are presented in papers [42–46]. In this approach [42, 43], the base station is not static and aggregated data is not transmitted to mobile station. This scheme proposed a super CH (SCH), which forwards data to the base station. This approach also makes use of probabilistic model in each CH selection round. Hence, CH is selected through Mamdani type fuzzy inference system. Three main fuzzy descriptors such as residual energy, mobility, and centrality are used for making a decision on CH selection. The node with the highest value of summation of centrality and battery power will get a chance to be CH.

The centrality varies upon mobility if the base station, therefore, fuzzy labels are as additives. The node with a greater probability of becoming a CH will become a super CH. The super CH decreases the transmission value and hence decreases the node dead time, as the number of rounds increases and improves the network survivability. In [43], the improved LEACH has been proposed to enhance the network lifetime and reduce packet loss for mobility-oriented services for WSN. In [44], authors have proposed to enhance clustering hierarchy (ECH) method to improve the energy efficiency using the sleep-wake up duty cycling approach for the sensors which sensed redundant data due to coverage overlapping. In [45], authors have suggested a cluster head selection method using fuzzy logic aiming at energy saving of the sensors to improve the WSN lifetime.

Nayak et al. exhibit the importance of IoT in WSN [46]. All the applications of IoT use different energy-efficient model for enabling various services. The WSN-based environment works in two stages, one is to establish cluster-based model for service followed by designing an energy aware model. This scenario is not performance effective for IoT-enabled environment because IoT devices are considered dynamic in nature. Therefore, it is high time to improvise the algorithms and emphasize fuzzy-based technique with an adaptive neural network that can adapt to a dynamic network as well. An analytical hierarchy process with a fuzzy-based energy management system is proposed for industrial equipment management that displays as an exposé of numerous case studies [47]. A fuzzy-based vehicular physical system is also observed that combines fuzzy and Markov chain for optimizing location-oriented channel access delay. To measure the channel density, two parameters such as signal to inference ratio and channel access delay are used [48]. Qitu et al. also proposed an IoV enabled set-up for communication using fuzzy logic. Here, the velocity of the vehicle, vehicle nearby nodes, and height of antenna are taken as parameters for selection of CH. In this approach, an optimal number of CHs is elected to bridge the communication and enhances the overall throughput [49, 50]. A genetic-based virtualization technique is proposed to tackle the torrent delay and reduce the energy utilization [51]. Kaiwartya et al. [52] developed similar approach for agriculture purposes which works on seven metrics to quantify the quantity measurement of sensor nodes. INDRIYA is a testbed experiment that is used to examine the effectiveness of this algorithm.

The abovementioned approaches are fuzzy logic-based approaches which show promising results for load balancing and energy conservation but these are not suitable for weight fuzzy descriptor to adapt to the environment. In real-time applications where input-output pair changed with the environment, such approaches are not suitable [53]. Therefore, the purpose of introducing a novel energy-efficient routing using fuzzy neural network in WSN is to address the issue of the leaning rate of membership function, reducing energy consumption, and improving the survivability of the sensor networks. The routing approach has potential newer areas of applications including E-mobility route planning [54] and information sharing in traffic environment [55].

3. Energy-Efficient Routing Using Fuzzy Neural Network (ERFN)

In this section, the detail of the proposed ERFN is presented focusing on routing centric parameters. First, the network and energy model of WSN is discussed. Second, the routing centric parameters: residual energy, node degree, and forward distance towards sink are presented. We have concentrated in-depth on constructing the mathematical model of these routing parameters using a probabilistic modeling approach. Thus, the route forming approach by selecting a next hop at each step using a fuzzy neural network is presented.

3.1. Network and Energy Model. We consider that there are N sensors that are placed arbitrarily in network field to monitor the place and its physical features periodically. Each sensor has neighboring sensors, and it transmits data to one of the neighboring sensors. We assume immobile sensors with equal initial energy. The computation capabilities of each sensor are identical. Symmetric radio links are considered between any two neighboring sensors. The sink is located inside the network region. Let the maximum transmission of each sensor is R . Adaptive transmission is considered by using distance between any two neighboring sensors.

The first order radio model to analyze the energy consumption of the proposed routing is discussed. Let m is the size of packet in bits. The energy is needed for transmitting a m bits of packet across d unit distance between a sender sensor and one of its neighboring sensor is expressed by

$$E_{TX}(m, d) = \begin{cases} m * E_{\text{elect}} + m * \varepsilon_{fsp} * d^2 & \text{if } d < d_o, \\ m * E_{\text{elect}} + m * \varepsilon_{mpf} * d^4 & \text{if } d \geq d_o. \end{cases} \quad (1)$$

To receive a m bits of packet, the energy requirement is given by

$$E_{RX}(m) = m * E_{\text{elect}}, \quad (2)$$

where E_{Select} denotes statistics about the energy dissipate for transmitting electrons per bit. Several factors such as acceptable bit-rate, digital coding, and modulation affect the E_{Select} . The ε_{fsp} and ε_{mpf} represent the need of energy in the free-space path and multipath environment, respectively. When two neighboring sensors for which energy usage is calculated are separated with the distance less than or equal to l_o ($l_o = \sqrt{\mathcal{E}_{fsp}/\mathcal{E}_{mpf}}$), the radio model applies (1) otherwise (2) to calculate the energy need for transmitting the data.

3.2. Routing Metric Computation

3.2.1. Degree Distribution of Sensor. The essential feature of a sensor in WSN is the degree of connectivity with neighboring sensors. A sensor with zero degrees cannot transmit data in the network. A sensor with higher degree is healthier against link failure, and it hikes the chances of the data transmission in the network. A neighboring sensor with a higher degree

will be preferred for next hop selection. Here, we compute the degree distribution of a sensor. Let N number of sensors are placed in the network field. The degree of each sensor is the sum of $N - 1$ independent random variables, which follows a binomial distribution. Let p is the probability of a link being present, and the α is representing a random variable of degree. The degree is distribution is given by

$$P(\alpha = k) = \binom{N-1}{k} p^k (1-p)^{N-k-1}. \quad (3)$$

The quantity $\binom{N-1}{k}$ is the number of ways of choosing k link, out of the possible $N - 1$ links, and $p^k (1-p)^{N-k-1}$ is the probability that the k selected links are present and the remaining $N - k - 1$ are not.

(1) *Expected Degree.* Since N is large, replacing $N - 1$ by N does not cause much error. The expected degree of a sensor is given by

$$E(\alpha) \approx pN. \quad (4)$$

For very small p , the probability $P(\alpha = k)$ tends to Poisson distribution and expressed as

$$P(\alpha = k) \cong \frac{((N-1)p)^k}{k!} e^{-((N-1)p)}. \quad (5)$$

The probability of at least node having one degree is defined as

$$P(\alpha \geq 1) \cong 1 - e^{-((N-1)p)}. \quad (6)$$

Now the question is how to compute link probability p , for that we uniform sensor deployment over a network field of the area A . The P be influenced by the broadcasting region of each sensor. The region covered by each sensor is given by $A_B = \pi R^2$. Thus, the probability of a link being present is given by

$$p = \frac{A_B \cap A}{A} \approx \frac{\pi R^2}{A}. \quad (7)$$

The expected degree of a sensor can be determined by substituting p in (4) and is not counting the border sensors.

3.2.2. Forward Progress. The proposed routing selects a next hop sensor from the neighboring sensors which lie in its forward search space. The forward search space is transmission region of a sensor which belongs to the direction of the sink (see Figure 1, red shaded region). To minimize the unnecessary transmissions, here, we define a forwarding search space (FSS) as a region that is a half-circle towards sink as depicted in Figure 1. Now we calculate which neighboring sensor node n_j of a sensor n_i lies in its FSS. Let a point $n_i(x_i, y_i)$ represents

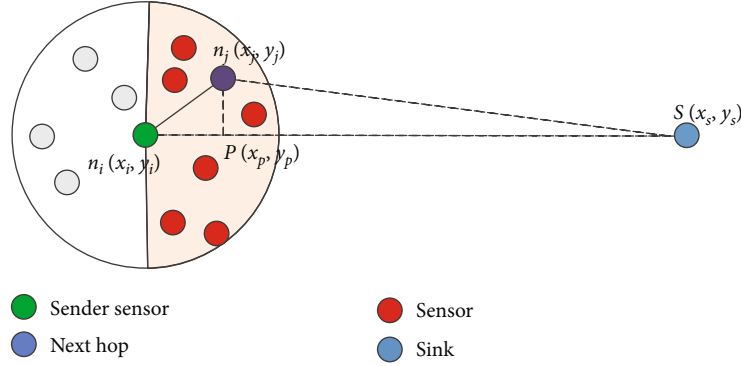


FIGURE 1: Forwarding search space.

that the sensor n_i is located at a position (x_i, y_i) , another point $n_j(x_j, y_j)$ denotes the position of the sensor n_j (cf. Figure 1). The sink s is position at (x_s, y_s) , represented by a point $s(x_s, y_s)$. Equation of line passing through two point $n_i(x_i, y_i)$ and $s(x_s, y_s)$ is given by

$$\left. \begin{aligned} a_1x + b_1y + c_1 &= 0 \\ a_1 &= y_i - y_s \\ b_1 &= x_s - x_i \\ c_1 &= y_i(x_i - x_s) + x_i(y_s - y_i) \end{aligned} \right\}. \quad (8)$$

Find the projection of the point $n_j(x_j, y_j)$ on the line given in eq. (8) to decide its progress towards sink. The projection of $n_j(x_j, y_j)$ is an intersection point between the line given in eq. (8) and a perpendicular drawn from the point $n_j(x_j, y_j)$ to the line (8). The equation of the perpendicular is given by

$$\left. \begin{aligned} a_2x + b_2y + c_2 &= 0 \\ a_2 &= x_i - x_s \\ b_2 &= y_i - y_s \\ c_2 &= x_j(x_s - x_i) + y_j(y_s - y_i) \end{aligned} \right\}. \quad (9)$$

The projection $P(x_p, y_p)$ of the point $n_j(x_j, y_j)$ on the line given in eq. (8) is calculated as

$$(x_p, y_p) = \left(\frac{b_1c_2 - b_2c_1}{a_1b_2 - a_2b_1}, \frac{a_2c_1 - a_1c_2}{a_1b_2 - a_2b_1} \right). \quad (10)$$

A sensor n_j is belonging to the FSS_i of a sensor n_i if the following inequality is satisfied.

$$n_j \in FSS_i \text{ iff,} \quad (11)$$

$$\left. \begin{aligned} \sqrt{(x_i - x_j)^2 + (y_i - y_j)^2} &< r^2 \\ \text{and} \\ \sqrt{(x_s - x_p)^2 + (y_s - y_p)^2} &< \sqrt{(x_s - x_i)^2 + (y_s - y_i)^2} \end{aligned} \right\}, \quad (12)$$

where r is the radius of the circle that represents the transmission range of the sender sensor n_i .

(1) *Forward Progress*. It is defined as distance travel a packet from sensor n_i to a sensor n_j towards sink. It is calculated as the distance between the points $n_i(x_i, y_i)$ and (x_p, y_p) . It is given by

$$F_{ij} = \sqrt{(x_i - x_p)^2 + (y_i - y_p)^2}. \quad (13)$$

(2) *Expected Forward Progress*. To drive expected forward progress of a packet towards sink, let there are n_h number of neighboring sensors are lying in the FSS of a sensor, which has data to send to the sink. Let d_i is distances between the sensor and neighboring sensors, and each neighboring sensor is located at the angles θ_i from the sender to the destination. The forward progress of each neighboring towards destination is X_i where $i = 1, 2 \dots n_h$. To calculate the expected forward, the probability distribution of distance X need to be computed. The neighboring sensor lies anywhere in the range of 0 to r , and 0 to $\pi/2$. Let the probability density function (pdf) $f_{x\theta}(x, \theta)$ of the distance (x) and angle (θ) is expressed by

$$f_{x\theta}(x, \theta) = \frac{2x}{\pi r^2}, \quad (14)$$

where $0 \leq x \leq R$, and $0 \leq \theta \leq \pi/2$. The pdf x can be computed as

$$f_x(x) = \int_0^{\pi/2} \frac{2x}{\pi r^2} d\theta = \frac{x}{r^2}. \quad (15)$$

To maximize the forward progress for neighboring sensor, a farthest neighboring sensor from the sender sensor is preferred as relay for transmitting the packets. Since all x_i are identical independent random variables, each with pdf $f_X(x)$, the pdf of x is

$$f_{X_m}(x) = n_h(F_X(x))^{n_h} f_X(x) = n_h \frac{x^{2n_h-1}}{r^{2n_h}}, \quad (16)$$

where $F_X(x)$ is the cdf of x . The expected forward progress (EFP) of the X_m is

$$\text{EFP} = E(X_m) = \int_0^r x f_{X_m}(x) dx = \frac{n_h}{2n_h + 1} r. \quad (17)$$

3.2.3. Residual Energy. The residual energy of each is remaining amount of energy after a transmission occurred. In this work, we prefer a neighboring sensor that acts as next hop which has the highest energy. A sensor with more energy lives longer. Let initial energy of E_i and after receiving and transmission of a packet of size m bits, the residual energy E_R of a sensor can be given by

$$E_R = E_i - (E_{TX}(m, r) + E_{TR}(m)). \quad (18)$$

(1) *Expected Energy Consumption.* The expected energy consumption $E(E_{\text{total}}(m, r))$ for transmitting of m bits data from a sensor to its next hop sensor using (11) can be expressed as

$$\begin{aligned} E(E_{\text{total}}(m, r)) &= E_{TX}(m, r) + E_{TR}(m) \\ &= \left[2e_{\text{elect}} + e_{\text{efp}} \left(\frac{n_h}{2n_h + 1} r \right)^2 \right] m. \end{aligned} \quad (19)$$

3.3. Single Metric Using Fuzzy Neural Network. Initially, in ERFN, all the routing centric metrics: residual energy, degree of a sensor, and forward progress towards sink are jointly assumed for the purpose of searching the next hop sensor from the FSS. Let NH is considered as a single metric for choosing a next hop from the FSS. The NH is determined by an adaptive neuro-fuzzy inference system (ANFIS). It is much superior than fuzzy logic inference system (FIS), attributable to in contrast to another ANN, ANFIS has higher functionality to follow situational's changes in the learning practice and updates the weight of membership function of FIS and minimizes error rate in deciding the rules in fuzzy logic. Supervised learning is used in ANFIS for the learning process. The ANFIS employs the learning method of the Takagi-Sugeno fuzzy inference system [50]. The simple structural design of ANFIS with three input parameters residual energy (E_R), sensor degree (α), forward progress (F_{ij}), and one output single metric (NH) is shown in Figure 2. Each routing metric has a membership function agreeing to the Takagi-Sugeno fuzzy inference model, which consists of 27 rules. A five-layer architecture of ANFIS that

consists of fuzzy layer, T-norm layer, normalized layer, de-fuzzy layer, and aggregated layer is presented in Figure 2. The first fuzzy layer (is called also called membership/antecedent layer) and fourth de-fuzzy layer (is also known as the consequent layer) are dynamic since they are modified agreeing to results achieved and the rest layers are static in nature.

We define the linguistic variables of the routing centric metrics as residual energy (E_R) = {below, fair, high} and is symbolized by $\{E_1, E_2, E_3\}$, sensor degree (α) = {deficient, medium, compact} that is represented by $\{\alpha_1, \alpha_2, \alpha_3\}$, forward progress (F_{ij}) = {adjacent, midway, distant} is denoted as $\{F_1, F_2, F_3\}$, and output single metric (NH) = {weakest, weaker, weak, medium, strong, stronger, strongest} as $\{H_1, H_2, H_3, H_4, H_5, H_6, H_7\}$. The ANFIS consists of 27 if-then rules related to three linguistic variables of three input variables, and these rules are developed by inspiring from Takagi-Sugeno fuzzy inference system shown in Table 1. These rules can also be expressed as

Rule 1 = if E_R is E_1 , F_{ij} is F_1 , and α is α_1 , then $H_1 = q_1 E_R + r_1 F_{ij} + s_1 \alpha + t_1$.

Rule 2 = if E_R is E_1 , F_{ij} is F_1 , and α is α_2 , then $H_2 = q_2 E_R + r_2 F_{ij} + s_2 \alpha + t_2$.

Rule 27 = if E_R is E_3 , F_{ij} is F_3 , and α is α_3 , then $H_7 = q_{27} E_R + r_{27} F_{ij} + s_{27} \alpha + t_{27}$.

Where E_1 , F_1 , and α_1 are the values of the membership function of input parameters E_R , F_{ij} , and α in antecedent (If) part, the q_1 , r_1 , s_1 , and t_1 denote linear parameters of consequent (then) part of Takagi-Sugeno model. The working process of ANFIS to produce a single metric output NH is defined by layer wise as follows.

3.3.1. Fuzzy Layer. It includes a number of nodes which are shown by square in Figure 2 and are dynamic in nature during backward pass. Every node in this layer contains a membership function which takes input as routing metrics and generates output as the degree of membership in the range 0 and 1. The triangular, trapezoidal, Gaussian, and generalized bell membership function can be used by nodes of this layer. This uses Gaussian (Eq. function). The membership function for adaptive node E_R can be given by

$$\mu_{E_k}(E_R) = \exp \left[- \left(\frac{E_R - z_k}{2x_k} \right)^2 \right]. \quad (20)$$

Similarly, the membership functions $\mu_{\alpha_k}(\alpha)$ and $\mu_{F_k}(F_{ij})$ for adaptive nodes α and F_{ij} can be determined. Where x_k and z_k are Gaussian membership functions parameters, control the shape, and slop of the functions and $k = 1, 2, 3$.

3.3.2. T-Norm Layer. This layer consists of a number of nodes, each of them is static in nature, that are shown by circle labeled with π (cf. Figure 2). At each node of this layer, the incoming signals (membership functions from layer 1) are multiplied to generate the output. The AND operator is

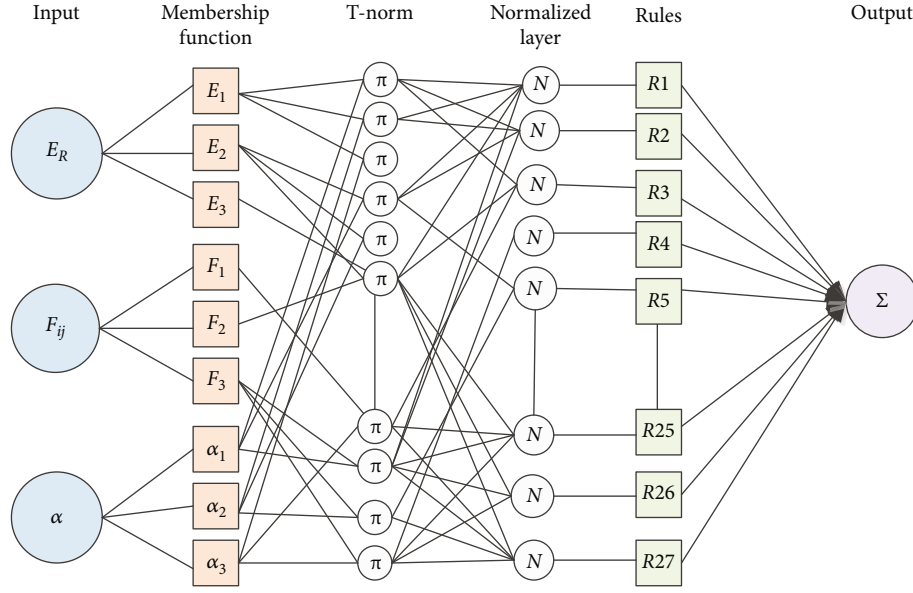


FIGURE 2: ANFIS for NH selection.

TABLE 1: Fuzzy rules.

Rule	If then			NH	Rule	If then			NH
	E_R	F_{ij}	α			E_R	F_{ij}	α	
1.	E_1	F_1	α_1	H_1	15.	E_2	F_2	α_3	H_4
2.	E_1	F_1	α_2	H_2	16.	E_2	F_3	α_1	H_1
3.	E_1	F_1	α_3	H_3	17.	E_2	F_3	α_2	H_2
4.	E_1	F_2	α_1	H_1	18.	E_2	F_3	α_3	H_2
5.	E_1	F_2	α_2	H_1	19.	E_3	F_1	α_1	H_5
6.	E_1	F_2	α_3	H_2	20.	E_3	F_1	α_2	H_6
7.	E_1	F_3	α_1	H_2	21.	E_3	F_1	α_3	H_7
8.	E_1	F_3	α_2	H_1	22.	E_3	F_2	α_1	H_4
9.	E_1	F_3	α_3	H_1	23.	E_3	F_2	α_2	H_5
10.	E_2	F_1	α_1	H_3	24.	E_3	F_2	α_3	H_6
11.	E_2	F_1	α_2	H_4	25.	E_3	F_3	α_1	H_5
12.	E_2	F_1	α_3	H_5	26.	E_3	F_3	α_2	H_7
13.	E_2	F_2	α_1	H_3	27.	E_3	F_3	α_3	H_7
14.	E_2	F_2	α_2	H_3					

used by each node in the T-norm layer to compute the antecedents/output as

$$T_k = \mu_{E_k}(E_R) * \mu_{\alpha_k}(\alpha) * \mu_{F_k}(F_{ij}), k = 1, 2, 3. \quad (21)$$

3.3.3. Normalized Layer. This contains the nodes which are nonadaptive in nature, which is also recognized as normalized node, shown by a circle labeled as N (cf. Figure 2). Each node computes the output by taking the ratio of the k th rule generated at T-norm layer to the summation of all rules produced by T-norm layer. The output at this layer can be given as

$$T_{nk} = \frac{T_k}{\sum_k T_k}, k = 1, 2, 3. \quad (22)$$

3.3.4. Defuzzy Layer. This layer contains the nodes, which are adaptive in nature and are shown by square with label R (cf. Figure 2). Each node produces the output as the product of normalized firing strength and out of individual rule. The output is given by

$$T_{nk}^{H_k} = T_{nk} H_k = T_{nk} (q_k E_R + r_k F_{ij} + s_k \alpha + t_k). \quad (23)$$

Input: E_R, F_{ij}, α and M_{epoch}

Process:

for $m=1$ to M_{epoch}

Input the fixed premise $\{E_R, F_{ij}, \alpha\}$ to fuzzy layer of Takagi- Sugeno inference engine

Fuzzy layer produces $\mu_{E_k}(E_R), \mu_{\alpha_k}(\alpha)$ and $\mu_{F_k}(F_{ij})$ for each node according to Eq. (19).

Tune the firing strength T_k of each node using Eq. (21)

Computes the firing strength T_{nk} of each node using Eq. (22).

Performs defuzzification the consequent parameter of each node using Eq. (23).

Computes the aggregated output NH using Eq. (24).

Output: NH

ALGORITHM 1:NH selection algorithm using neuro-fuzzy (NHSN).

3.3.5. *Aggregated Output Layer.* This layer contains a single nonadaptive node. The out at this node is estimated by taking the summation of all the incoming inputs to this layer [53]. The aggregated output is given by

$$NH = \sum_k T_{nk} H_k = \frac{\sum_k T_k H_k}{\sum_k T_k}. \quad (24)$$

We present Algorithm 1. NH selection algorithm is using neuro-fuzzy to explain the working of ANFIS. The gradient descent and least mean square-assisted hybrid learning algorithm have been used to train the premise and consequent parameters in two passes, namely, forward pass and backward pass. The nodes of fuzzy and defuzzy layers are updated over time. In the forward pass, the fixed premise parameters $\{E_R, F_{ij}, \alpha\}$ are static and passed through fuzzy layer to defuzzy layer in the proposed Algorithm 1. The least mean square method is used to update these fixed premise parameters. After getting the fourth layer's output which is termed ad consequent parameter, the actual output is analyzed with fourth layer's output, and the error is noted. The prime aim is to minimize the error recursively. With the backward pass, this error is sent back to fuzzy layer and membership function of fixed premise parameters is updated by employing the gradient descent method simultaneously. One execution round of the hybrid learning process (including both forward pass and backward pass) is called epoch. The algorithm is executed till it converges (the error becomes infinitesimal small) or till the maximum number of epoch (M_{epoch}).

3.3.6. *Neuro-Fuzzy Routing Approach.* The proposed neuro computes the aggregated output routing in which each sensor selects a next hop to forward the data packets. In this routing, packets are sent to sink via different routes. For each packet, a new route might be constructed which reduces energy utilization of all sensors in the WSN. The neuro-fuzzy routing approach contains three phases: neighbor discovery, metric calculation, and next hop selection using NHSN. Each sensor executes the routing algorithm to search next hop till the sink is reached. The routing algorithm is given as Algorithm 2.

- (i) *Neighbor Discovery.* Each sensor n_i broadcasts HELLO packets comprising its location information in its vicinity. Each sensors n_j , which gets this HELLO packet, answer with "ECHO" packets with its position information. On the reception of these ECHO packets, each sensor constructs its neighbor list. The only sensors which lies in the respective FSS will be added to the list
- (ii) *Metric Calculation.* The sensor n_i calculates forward progress for each sensor $n_j \in FSS_i$. Each sensor $n_j \in FSS_i$ sends containing its residual energy and degree information to the sender sensor n_i . The sensor n_i estimates NH_{ij} fusing Algorithm 1 or all the sensors $n_j \in FSS_i$
- (iii) *Next Hop Selection.* For the NH selection, the only sensors lie in FSS of the sender sensor contributes in the selection process. The sensor n_i appoints a sensor as NH which has the highest NH_{ij} value. This NH is used to forward the packet to the next NH until the packet reaches to the sink

3.3.7. *Time Complexity Analysis of NHSN and FNA Algorithms.* NHSN algorithm uses the ANFIS algorithm which combines the fuzzy algorithm and neural network. When Algorithm 1 was supplied a number of inputs, to obtain the optimum values of the parameters, it is updating the weights of the parameter continuously. The proposed rules used to modify the weight were dominant in the complexity of the algorithm. The time required to run the ANFIS algorithm depends on the number of inputs (k). The asymptotic time complexity of the algorithm is $O(k)$.

In the FNA algorithm, the neighbor discovery phase and the running of time of this phase take $O(nm)$ where n is the number of sensors in a route and m is the average number of neighbor sensors. The metric calculation needs the running time $O(m+k)$. The next hop selection phase takes the time of $O(m)$. Thus The asymptotic time complexity of the Algorithm 2 is $O(nm+k)$.

4. Simulation Results and Analysis

In this portion, the proposed ERFN routing for WSN is evaluated by conducting large-scale simulation employing

```

1. Neighbor discovery:
  I. Each sensor  $n_i \in N$  advertises HELLO packet to discover all neighbors  $n_j$ 
  II. for each neighbor  $n_j$  of  $n_i$  do
  III. Sensor  $n_j$  obtains its position information  $(x_j, y_j)$  using any localization techniques
  IV. If point  $(x_j, y_j)$  satisfies Eq. (11) then
  V. Add  $n_j$  to  $FSS_i$ 
  VI. end if
  VII. end for
2. Metric calculation:
  I. for each sensor  $n_j \in FSS_i$  do
  II. Sensor  $n_i$  computes  $F_{ij}$  using Eq. (13)
  III.  $n_i$  gets  $E_R, F_{ij}, \alpha$ 
  IV. Sensor  $n_i$  computes  $NH$  for  $n_j$  using NHSN
  end for
3. Next Hop selection:
  I.  $NH_{n_j} = \text{argmax}(NH_{ij}), n_j \in FSS_i$ 
  II. Sensor  $n_i$  sends data packet to the NH  $n_j$ 

```

ALGORITHM 2: Neuro-fuzzy routing (FNA) algorithm.

MATLAB fuzzy logic simulator tool neuro-fuzzy designer to trained ANFIS. We customize the fuzzy inference system by adding new membership functions for devised routing centric metrics to predict the next hop. The area of network field is assumed to be $300 \times 300 \text{ m}^2$, and 200 sensors are placed randomly in this field. The sink is placed in the center of the field. The initial energy of each sensor is 2J. The values of E_{elect} and $\epsilon_{f_{sp}}$ are taken as follows: 10 (nJ)/bit and 20 pJ/bit/m². The length of data packet transmitted and received by each sensor is set as 64 bits. The location of the sink node is (200, 200). The cycle time is 60 microseconds. The packet rate is 200 packets/s. The sensing and transmission ranges of each sensor are assumed to be 10 m and 20 m, respectively. Each simulation result is taken by averaging of 10 runs of each simulation, thus, measuring the performance of the ERFN.

The proposed ERFN is compared with similar position-based routing: eBPR [6] and EeBGR [9] to show its effectiveness. A number of performance metrics are deliberated to assess the performance of the developed routing approach.

4.1. Network Lifetime. It is defined in many depending on applications WSN including the time until a certain percentage of sensor dies or the time until sensors are not capable to send data to sink. This paper terms the lifetime of the network by means of the time until 50% of sensors die. The simulation process goes on till 90% of nodes are dead.

4.2. Average Residual Energy. It is defined as the ratio of the sum of the remaining energy of all alive sensors to the number of alive sensors in the network after each round. Let E_R^i is residual energy of i th sensor. The average residual energy of all the sensors for the next rounds is calculated as

$$E_{av} = \frac{1}{N} \sum_{i \in N} E_R^i. \quad (25)$$

4.3. Average Energy Consumption. It is defined as the ratio of the sum of the amount of energy consumed by all sensors to the number of sensors after each round.

4.4. Standard Deviation (SD) of Residual Energy. It is a statistical measure defined as the square root of the variance of residual energy of all the sensors. The SD of residual energy is a square root of the variance of residual energy is given by

$$\sigma(E_R) = \sqrt{\frac{1}{N} \sum_{i \in N} (E_{av} - E_R^i)^2}. \quad (26)$$

4.4.1. Network Lifetime. Figure 3 shows the lifetime in the terms of the number of alive sensors which are involved in the routing process in different rounds. The results are obtained for the proposed ERFN and compared with the state-of-the-art routing approaches: EeBGR and eBPR. At the beginning, all sensors are alive. When the routing algorithms run in rounds, sensors drain their energy, and the number of alive sensors reduces. It is noted that as the number of rounds increases, the number of alive sensors for the proposed ERFN is comparatively more than that of EeBGR and eBPR. In the proposed ERFN, the first sensor dies in about 250 rounds, whereas in EeBGR, first sensor dies at about 200 rounds, and in eBPR, the first sensor dies at about 180 rounds. Further, it is also noted that after 1000 rounds, the number of alive sensors in the proposed ERFN is about 180, whereas the number of alive sensors for EeBGR and eBPR is 150 and 170, respectively. After 2000 rounds, the number of alive sensors EeBGR, eBPR, and ERFN is about 35, 60, and 75, respectively. It is due to the fact that the proposed ERFN selects the next hop using the neuro-fuzzy system, increasing to a much longer lifetime of the network.

Figure 4 exhibits sensor death percentage for different number of rounds. It is witnessed that the proposed ERFN performs better as compared to EeBGR and eBPR. The

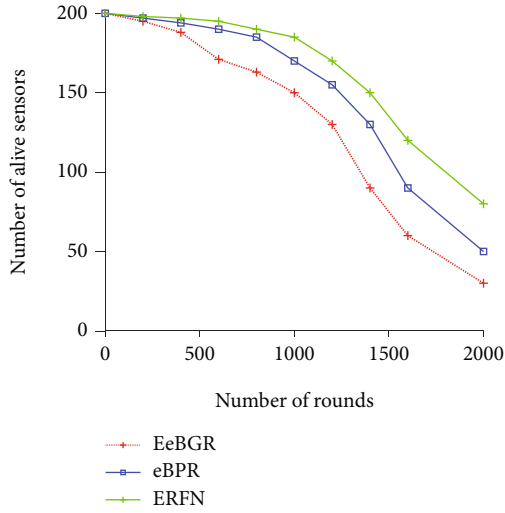


FIGURE 3: Number of alive sensors.

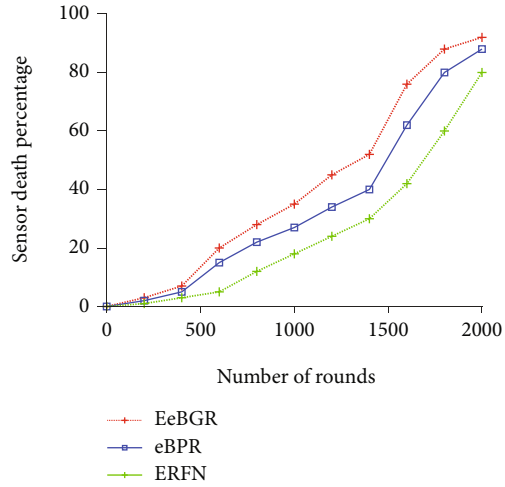


FIGURE 4: Sensor death percentage.

sensor death percentage of all the considered routing approaches is gradually increasing up to about 400 rounds. After that, the death percentage for both EeBGR and eBPR is increasing sharply as compared to that of ERFN. For example, at 700 rounds, the death percentages for both EeBGR and eBPR are 20% and 18%, respectively, whereas for ERFN, it is 5%. It is noted that the sensor death rate for ERFN is slower than that of the state-of-the-art approaches. It is due to the fact that the proposed routing uses supervised learning approach minimizes the error rate in selecting the next hop.

4.4.2. Energy Consumption. Figure 5 displays the average residual energy of all sensors for the different number of rounds. All sensors have equal that is 2 joule initially energy. As the all considered routing approaches run in rounds, after some rounds, it is seen that the ERFN saves more energy as compared to both EeBGR and eBPR. For example, after 500 rounds, the average residual energy for the ERFN

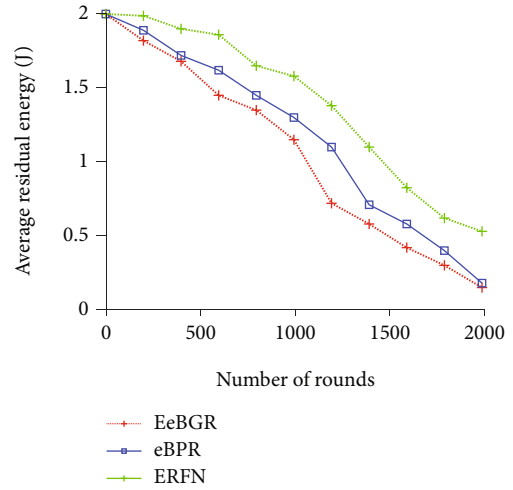


FIGURE 5: Avg. residual energy over rounds

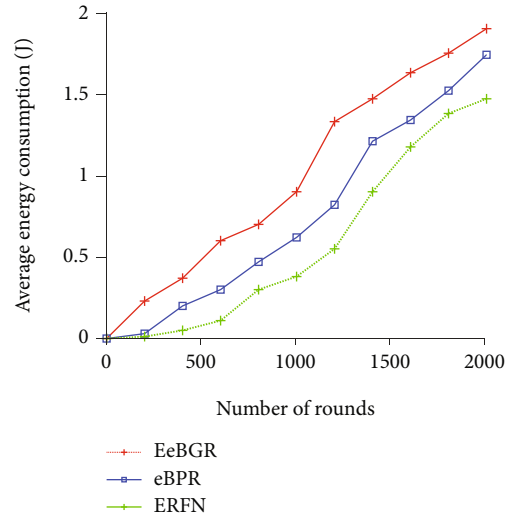


FIGURE 6: Avg. energy consumed by nodes over rounds.

is about 1.8 joule; however, at the same number of rounds, the average residual energy for both EeBGR and eBPR is 1.4 joule and 1.6 joules. It is because of the ERFN changes the routes frequently by using ANFIS where the state-of-the-art approaches do not use any learning algorithms. Thus, the ERFN conserves more energy, increasing the network lifetime.

Figure 6 displays the average energy consumption for all the sensors for different rounds. The average energy consumption is likely to be constant for ERFN and eBPR up to 250 rounds whereas it is high for EeBGR. But the ERFN consumes less energy as compared to both approaches. For example, after 500 rounds, the ERFN exhausts 0.1 joules energy, and both EeBGR and eBPR exhaust 0.25 and 0.4 energy, respectively. It noted that as the execution rounds increase, the energy consumption for all the routing also increases but this increment is less for the ERFN. It is clear that the proposed routing consumes less energy which is essential for network lifetime enhancement.

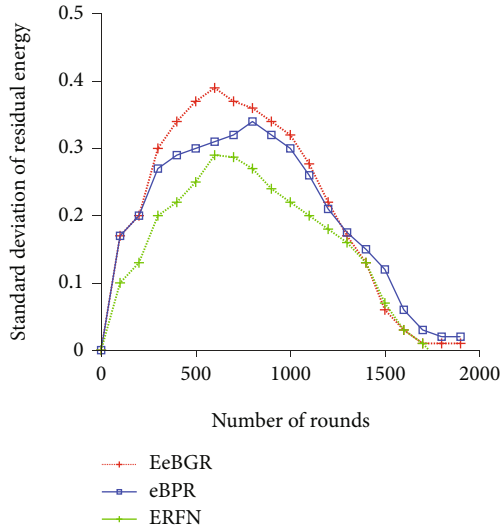


FIGURE 7: SD of residual energy.

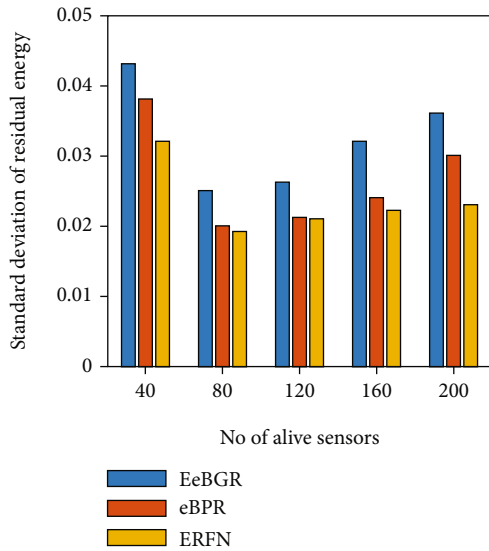


FIGURE 8: SD versus alive sensors.

4.4.3. *Standard Deviation for Residual Energy.* When WSN starts operating, each sensor begins exhausting a different amount of energy, and the SD of residual energy changes. Figure 7 exhibits the SD of residual energy among all the nodes in WSN. Low SD indicates better energy consumption balancing. Initially, all the routing approaches consume under one mean, indicating good energy consumption balancing among sensors. However, as the rounds increase, the SDs of residual energy for all considered routing approaches change. The SD with the proposed ERFN is lower than that of both EeBGR and eBPR. For example, at 500 rounds, the SD for ERFN is 0.23 whereas both EeBGR and eBPR give 0.30 and 0.38. The SD of eBPR is much closer to the ERFN as compared to EeBGR, and it is because both ERFN and eBPR take the same routing metrics. It is observed that ERFN gives much flatter graph over EeBGR and eBPR, and it is due to the fact that the ERFN uses ANFIS to select next hop which fre-

quently changes path for the data packets in each round. It is clearly noticed the ERFN achieves better energy consumption balancing than the state-of-the-art approaches.

Figure 8 displays SD of residual energy for different numbers of alive sensors. It is observed that in all cases of alive sensors, the SD for the proposed ERFN is less than that of EeBGR and eBPR. For example, 80 numbers of alive sensors, the SD for ERFN is 0.018 whereas for EeBGR and eBPR, the SDs are 0.02 and 0.025, respectively. It indicates that the ERFN obtained a better energy balance compared to EeBGR and eBPR. Further, it is observed that the proposed ERFN achieved the highest energy balance for the alive sensor equals to 80 for all the routing approaches. Thus, the proposed routing outperforms both EeBGR and eBPR in the term of SD of the residual energy.

5. Conclusion and Future Perspective

This paper proposes a new energy-efficient routing using fuzzy neural network in wireless sensor networks. Specially, an adaptive neuro-fuzzy inference system has been employed to combine the three routing-centric metrics: residual energy, forward progress, and sensors degree. The next hop selection algorithm using neuro-fuzzy to assign duty of packet forward to a neighboring sensor as next hop is presented. The neuro-fuzzy routing algorithm is presented to route the packet from source sensor to the sink. Simulation has been conducted using MATLAB fuzzy logic simulator tool neuro-fuzzy designer. The results indicate that ERFN outperforms the EeBGR and eBPR in the terms of lifetime, energy consumption, and SD of residual energy. In the future, the proposed routing will be studied using other machine learning algorithms for newer areas of applications including E-mobility route planning and information sharing in traffic environment. More energy-saving technical ideas will be incorporated such as employing duty cycling approaches in the sensor-oriented wireless communication environment.

Data Availability

Research data will be available on individual requests to the corresponding author considering research collaboration possibilities with the researcher or research team and with restrictions that the data will be used only for further research in the related literature progress.

Conflicts of Interest

The authors declare that they have no conflicts of interest

References

- [1] S. Kumar, O. Kaiwartya, M. Rathee, N. Kumar, and J. Lloret, "Toward energy-oriented optimization for green communication in sensor enabled IoT environments," *IEEE Systems Journal*, vol. 14, no. 4, pp. 4663–4673, 2020.
- [2] X. Lai, X. Ji, X. Zhou, and L. Chen, "Energy efficient link-delay aware routing in wireless sensor networks," *IEEE Sensors Journal*, vol. 18, no. 2, pp. 837–848, 2018.

- [3] M. Rathee, S. Kumar, A. H. Gandomi, K. Dilip, B. Balusamy, and R. Patan, "Ant colony optimization based quality of service aware energy balancing secure routing algorithm for wireless sensor networks," *IEEE Transactions on Engineering Management*, vol. 68, no. 1, pp. 170–182, 2021.
- [4] K. Kumar, S. Kumar, O. Kaiwartya, Y. Cao, J. Lloret, and N. Aslam, "Cross-layer energy optimization for IoT environments: technical advances and opportunities," *Energies*, vol. 10, no. 12, p. 2073, 2017.
- [5] S. Kumar, V. Kumar, O. Kaiwartya, U. Dohare, N. Kumar, and J. Lloret, "Towards green communication in wireless sensor network: GA enabled distributed zone approach," *ad hoc networks*, vol. 93, p. 101903, 2019.
- [6] V. Kumar and S. Kumar, "Position-based beaconless routing in wireless sensor networks," *wireless personal communications*, vol. 86, no. 2, pp. 1061–1085, 2016.
- [7] A. Khatri, S. Kumar, O. Kaiwartya, N. Aslam, N. Meena, and A. H. Abdullah, "Towards green computing in wireless sensor networks: controlled mobility-aided balanced tree approach," *International Journal of Communication Systems*, vol. 31, no. 7, p. e3463, 2018.
- [8] U. Dohare, D. K. Lobiyal, and S. Kumar, "Energy balanced model for lifetime maximization in randomly distributed wireless sensor networks," *Wireless Personal Communications*, vol. 78, no. 1, pp. 407–428, 2014.
- [9] H. Zhang and H. Shen, "Energy-efficient beaconless geographic routing in wireless sensor networks," *IEEE Transactions on Parallel and Distributed Systems*, vol. 21, no. 6, pp. 881–896, 2010.
- [10] S. K. Aanchal, O. Kaiwartya, and A. H. Abdullah, "Green computing for wireless sensor networks: optimization and Huffman coding approach," *Peer-to-Peer Networking and Applications*, vol. 10, no. 3, pp. 592–609, 2017.
- [11] J. Wang, Y. Gao, K. Wang, A. K. Sangaiah, and S.-J. Lim, "An affinity propagation-based self-adaptive clustering method for wireless sensor networks," *Sensors*, vol. 19, no. 11, p. 2579, 2019.
- [12] A. Jaiswal, S. Kumar, O. Kaiwartya et al., "Quantum learning enabled green communication for next generation wireless systems," *IEEE Transactions on Green Communications and Networking*, 2021.
- [13] J. Wang, Y. Gao, X. Yin, F. Li, and H. Kim, "An enhanced PEGASIS algorithm with mobile sink support for wireless sensor networks," *Wireless Communications and Mobile Computing*, vol. 2018, 9 pages, 2018.
- [14] J. Wang, C. Ju, Y. Gao, A. K. Sangaiah, and G. Kim, "A pso based energy efficient coverage control algorithm for wireless sensor networks," *Computers, Materials & Continua*, vol. 56, no. 3, pp. 433–446, 2018.
- [15] D. Gao, S. Zhang, F. Zhang, X. Fan, and J. Zhang, "Maximum data generation rate routing protocol based on data flow controlling technology for rechargeable wireless sensor networks," *Computers, Materials & Continua*, vol. 59, no. 2, pp. 649–667, 2019.
- [16] L. A. Zadeh, "Fuzzy sets," *Information and Control*, vol. 8, pp. 338–353, 1965.
- [17] T. Takagi and M. Sugeno, "Fuzzy identification of systems and its applications to modeling and control," *IEEE transactions on systems, man, and cybernetics*, vol. 15, pp. 116–132, 1985.
- [18] W. S. McCulloch and W. H. Pitts, "A logical calculus of the ideas immanent in nervous activity," *The Bulletin of Mathematical Biophysics*, vol. 5, no. 4, pp. 115–133, 1943.
- [19] F. Rosenblatt, "The perceptron: a probabilistic model for information storage and organization in the brain," *Cornell Aeronautical Laboratory, Psychological Review*, vol. 65, no. 6, pp. 386–408, 1958.
- [20] F. Rosenblatt, *Principles of neurodynamics; perceptrons and the theory of brain mechanisms*, Spartan Books, Washington DC, 1962.
- [21] F. Rosenblatt, "On the convergence of reinforcement procedures in simple perceptron," *Report VG 1196-G4*, Cornell Aeronautical Laboratory Incorporation, Buffalo, New York, 1960.
- [22] B. Widrow and M. A. Lehr, "30 years of adaptive neural networks: perceptron, madaline, and backpropagation," *Proceedings of the IEEE*, vol. 78, no. 9, pp. 1415–1442, 1990.
- [23] B. Widrow, R. G. Winter, and R. A. Baxter, "Layered neural nets for pattern recognition," *IEEE Transactions on Acoustics, Speech, and Signal Processing*, vol. 36, no. 7, pp. 1109–1118, 1988.
- [24] R. Winter and B. Widrow, "MADALINE RULE II: a training algorithm for neural networks," in *IEEE 1988 international conference on neural networks*, pp. 401–408, San Diego, CA, USA, 1988.
- [25] C.-T. Lin, "FALCON: a fuzzy adaptive learning control network," in *Fuzzy Information Processing Society Biannual Conference, 1994. Industrial Fuzzy Control and Intelligent Systems Conference, and the NASA Joint Technology Workshop on Neural Networks and Fuzzy Logic*, pp. 228–232, San Antonio, TX, USA, 1994.
- [26] C. T. Lin and C. S. G. Lee, "Neural-network-based fuzzy logic control and decision system," *IEEE Transactions on Computers*, vol. 40, no. 12, pp. 1320–1336, 1991.
- [27] H. R. Berenji and P. Khedkar, "Learning and tuning fuzzy logic controllers through reinforcements," *IEEE Transactions on Neural Networks*, vol. 3, no. 5, pp. 724–740, 1992.
- [28] D. Nauck, F. Klawon, and R. Kruse, "Neuro-fuzzy systems for function approximation," *4th international workshop fuzzy-Neuro systems*, vol. 101, pp. 261–271, 1997.
- [29] S. Tano, T. Oyama, and T. Arnold, "Deep combination of fuzzy inference," *Fuzzy Sets and System*, vol. 8, pp. 338–353, 1996.
- [30] C.-F. Juang and C.-T. Lin, "An online self-constructing neural fuzzy inference network and its applications," *IEEE Transactions on Fuzzy Systems*, vol. 6, no. 1, pp. 12–32, 1998.
- [31] M. Figueiredo and F. Gomide, "Design of fuzzy systems using neurofuzzy networks," *IEEE Transactions on Neural Networks*, vol. 10, no. 4, pp. 815–827, 1999.
- [32] D. Nauck, F. Kalwon, and R. Kruse, *Foundation of Neuro-Fuzzy Systems*, John Wiley & Sons, New York, NY, USA, 1997.
- [33] R. Jang, *Neuro-Fuzzy Modeling: Architectures, Analysis and Application*, [Ph.D. Thesis], University of California, Berkeley, 1992.
- [34] W. R. Heinzelman, A. Chandrakasan, and H. Balakrishnan, "Energy efficient communication protocol for wireless micro sensor networks," in *Proceedings of the 33rd annual Hawaii international conference on system sciences*, pp. 3005–3014, Maui, HI, USA, 2000.
- [35] W. B. Heinzelman, A. P. Chandrakasan, and H. Balakrishnan, "An application-specific protocol architecture for wireless microsensor networks," *IEEE Transaction Wireless Communication*, vol. 1, no. 4, pp. 660–670, 2002.

- [36] O. Younis and S. Fahmy, "HEED: a hybrid, energy efficient, distributed clustering approach for ad hoc sensor networks," *IEEE Transaction on Mobile Computing*, vol. 3, no. 4, pp. 366–379, 2004.
- [37] S. Lindsey and C. S. Raghavendra, "PEGASIS: power efficient gathering in sensor information systems," in *Proceedings of the IEEE Aerospace Conference*, pp. 1125–1130, Big Sky, MT, USA, 2003.
- [38] I. Gupta, D. Riordan, and S. Sampalli, "Cluster-head election using fuzzy logic for wireless sensor networks," in *3rd Annual Communication Networks and Services Research Conference (CNSR'05)*, pp. 225–260, Halifax, NS, Canada, 2005.
- [39] J. Kim, S. Park, Y. Han, and T. Chung, "CHEF: CH election mechanism using fuzzy logic in wireless sensor networks," in *Proceeding International Conference Advance Communication Technology*, pp. 654–659, Gangwon, Korea (South), 2008.
- [40] G. Ran, H. Zhang, and S. Gong, "Improving on LEACH protocol of wireless sensor networks using fuzzy logic," *Journal of Information & Computational Science*, vol. 7, pp. 767–775, 2010.
- [41] J. S. Lee and W. L. Cheng, "Fuzzy-logic-based clustering approach for wireless sensor networks using energy predication," *IEEE Sensors Journal*, vol. 12, no. 9, pp. 2891–2897, 2012.
- [42] P. Nayak and A. Devulapalli, "A fuzzy logic-based clustering algorithm for WSN to extend the network lifetime," *IEEE Sensors Journal*, vol. 16, no. 1, pp. 137–144, 2016.
- [43] J.-S. Lee and C.-L. Teng, "An enhanced hierarchical clustering approach for mobile sensor networks using fuzzy inference systems," *IEEE Internet of Things Journal*, vol. 4, no. 4, pp. 1095–1103, 2017.
- [44] H. El Alami and A. Najid, "ECH: an enhanced clustering hierarchy approach to maximize lifetime of wireless sensor networks," *IEEE Access*, vol. 7, pp. 107142–107153, 2019.
- [45] H. El Alami and A. Najid, "Energy-efficient fuzzy logic cluster head selection in wireless sensor networks," in *2016 International Conference on Information Technology for Organizations Development (IT4OD)*, pp. 1–7, Fez, Morocco, 2016.
- [46] P. Nayak, D. Anurag, and V. V. N. A. Bhargavi, "FM-SCHM: fuzzy method based super CH electio election for wireless sensor network with mobile base station (FM-SCHM)," in *in proceeding 2nd International Conference Advance Computational Methodology*, pp. 422–427, Hyderabad, India, 2013.
- [47] A. P. Abidoeye and I. C. Obagbuwa, "Models for integrating wireless sensor networks into the Internet of Things," *IET Wireless Sensor Systems*, vol. 7, no. 3, pp. 65–72, 2017.
- [48] Y. Li, Z. Sun, L. Han, and N. Mei, "Fuzzy comprehensive evaluation method for energy management systems based on an internet of things," *IEEE Access*, vol. 5, pp. 21312–21322, 2017.
- [49] R. Kasana, S. Kumar, O. Kaiwartya et al., "Fuzzy-based channel selection for location oriented services in multichannel VCPS environments," *IEEE internet of things journal*, vol. 5, no. 6, pp. 4642–4651, 2018.
- [50] Q. Hu, C. Wu, X. Zhao, X. Chen, Y. Ji, and T. Yoshinaga, "Vehicular multi-access edge computing with licensed sub-6 GHz, IEEE 802.11p and mmWave," *IEEE Access*, vol. 6, pp. 1995–2004, 2018.
- [51] O. Kaiwartya, A. H. Abdullah, Y. Cao et al., "Virtualization in wireless sensor networks: fault tolerant embedding for internet of things," *IEEE Internet of Things Journal*, vol. 5, no. 2, pp. 571–580, 2018.
- [52] O. Kaiwartya, H. A. Abdullah, Y. Cao, S. R. Raw, S. Kumar, and R. Ratan, "T-MQM: testbed based multi-metric quality measurement of sensor deployment for precision agriculture-a case study," *IEEE sensor journal*, vol. 16, no. 23, pp. 8649–8664, 2016.
- [53] J. S. R. Jang, "ANFIS: adaptive-network-based fuzzy inference system," *IEEE Transactions on Systems, Man, and Cybernetics*, vol. 23, no. 3, pp. 665–685, 1993.
- [54] Y. Cao, T. Jiang, O. Kaiwartya, H. Sun, H. Zhou, and R. Wang, "Toward pre-empted EV charging recommendation through V2V-based reservation system," *IEEE transactions on systems, man, and cybernetics: systems*, vol. 51, no. 5, pp. 3026–3039, 2019.
- [55] O. Kaiwartya and S. Kumar, "Enhanced caching for geocast routing in vehicular ad hoc network," in *In intelligent computing, networking, and informatics*, pp. 213–220, Springer, New Delhi, 2014.

Research Article

Low-Cost and Long-Range Node-Assisted WiFi Backscatter Communication for 5G-Enabled IoT Networks

Zhimin Wang ¹, Li Feng ¹, Shumin Yao,¹ Kan Xie,^{2,3} and Yuqiang Chen⁴

¹Faculty of Information Technology, Macau University of Science and Technology, Taipa, Macau 999078, China

²Information Processing and System Integration of IoT, Ministry of Education of the P.R.C., Guangzhou 510006, China

³Guangdong-HongKong-Macao Joint Laboratory for Smart Discrete Manufacturing, Guangzhou 510006, China

⁴School of Information and Communication Engineering, Guangzhou Maritime University, Guangzhou 510725, China

Correspondence should be addressed to Li Feng; lfeng@must.edu.mo

Received 9 May 2021; Revised 12 June 2021; Accepted 7 July 2021; Published 21 July 2021

Academic Editor: Xingwang Li

Copyright © 2021 Zhimin Wang et al. This is an open access article distributed under the Creative Commons Attribution License, which permits unrestricted use, distribution, and reproduction in any medium, provided the original work is properly cited.

The fifth-generation-enabled Internet of Things (5G-enabled IoT) has been considered as a key enabler for the automation of almost all industries. In 5G-enabled IoT, resource-limited passive devices are expected to join the IoT using the WiFi backscatter communication (WiFi-BSC) technology. However, WiFi-BSC deployment is currently limited due to high equipment cost and short transmission range. To address these two drawbacks, in this paper, we propose a low-cost and long-range node-assisted WiFi backscatter communication scheme. In our scheme, a WiFi node can receive backscatter signals using two cheap regular half-duplex antennas (instead of using expensive full-duplex technique or collaborating with multiple other nodes), thereby reducing the equipment cost. Besides, WiFi nodes can help relay backscatter signals to remote 5G infrastructure, greatly extending the backscatter's transmission range. We then develop a theoretical model to analyze the throughput of WiFi-BSC. Extensive simulations verify the effectiveness of our scheme and the accuracy of our model.

1. Introduction

The fifth-generation-enabled Internet of Things (5G-enabled IoT) is considered to be a key enabler for automation of almost all industries [1–5]. In a typical 5G-enabled IoT, a 5G customer premise equipment (5G-CPE) is introduced to bridge a WiFi-based IoT network and a 5G base station [6], as shown in Figure 1. In this solution, the 5G-CPE may first use its WiFi module to collect data from the WiFi-based IoT devices and then upload these data to a remote cloud server timely using its 5G module. Hence, this solution can take full advantage of 5G's high bandwidth and low latency, as well as WiFi's ubiquity.

Besides WiFi, backscatter communication (BSC) is another popular wireless technology in IoT [7]. BSC is designed for communications between tags (which are severely resource-limited and battery-free) and readers. With BSC, tags first harvest energy from ambient signals, then convey information by modulating and reflecting ambient sig-

nals (instead of generating signals by themselves), while readers are dedicatedly designed to receive the reflected signals from tags. As a recent advance, WiFi-based BSC (WiFi-BSC) [8–11] has been proposed. With WiFi-BSC, tags may harvest energy and convey information by utilizing ubiquitous WiFi signals, while WiFi nodes with self-interference cancellation capability (which is called WiFi reader) may receive the reflected signals from tags. WiFi-BSC opens up a promising opportunity for tags to join WiFi-based IoT networks, but WiFi readers are expensive because they are required to support costly full-duplex techniques or collaborate with other WiFi nodes to implement the self-interference cancellation. On the other hand, the transmission range of WiFi-BSC is very short (say, 1 m to 54 m [9, 10]). As a result, current WiFi-BSC deployment is very limited.

1.1. Motivation. In recent years, the multiuser, multi-input, and multioutput (MU-MIMO) technology has been intro-

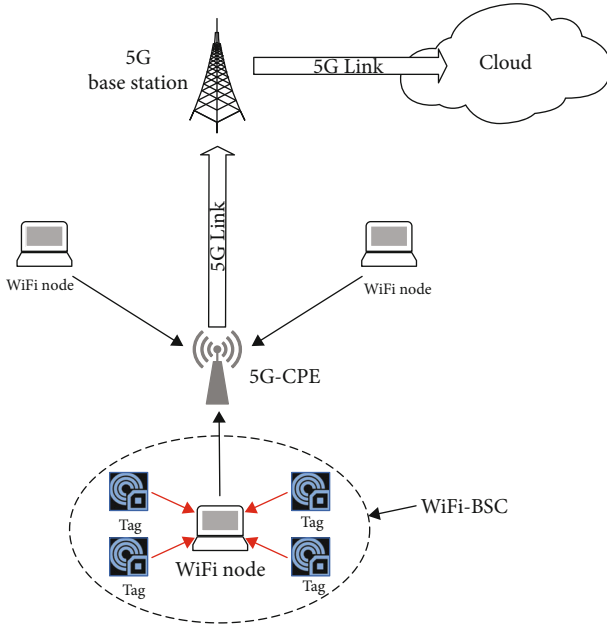


FIGURE 1: A 5G-enabled IoT network.

duced to WiFi. With MU-MIMO, a WiFi node can use regular half-duplex antennas to receive different signals from multiple nodes simultaneously and then distinguish these signals for further processing. This feature motivates us to apply MU-MIMO in WiFi-BSC for enabling conventional WiFi nodes to act as WiFi readers, without utilizing costly full-duplex technique and collaborating with other nodes.

In addition, the transmission range of WiFi (up to 1000 m [12, 13]) is much longer than that of WiFi-BSC. This motivates us to let WiFi nodes relay tags' information toward 5G-CPE, greatly extending the transmission range of the WiFi-BSC.

1.2. Contribution. In this paper, we propose a low-cost and long-range node-assisted WiFi-BSC scheme. Our contributions can be summarized as follows.

- (1) Propose a low-cost WiFi-BSC design. Our design only requires a conventional WiFi node to be equipped with two regular half-duplex antennas, so as to adopt MU-MIMO to decode the reflected signals from tags. This avoids adopting costly full-duplex technique and collaborating with other nodes for extracting reflected signals of tags, thereby saving equipment cost greatly
- (2) Propose a long-range node-assisted WiFi-BSC design. Our design lets WiFi nodes relay tags' information to a remote 5G-CPE, hence extending the transmission range of the tags significantly
- (3) Develop a theoretical model to analyze the throughput of our scheme, and verify the accuracy of our model via extensive simulations. The results show that our design significantly outperforms existing WiFi-BSC schemes in terms of throughput

1.3. Related Works. In recent years, BSC has quickly become a key technology for low-power wireless communication systems [14] and therefore has received lots of attention in the research community. Below, we present related works of BSC in terms of physical (PHY) layer and medium access control (MAC) layer schemes.

1.3.1. PHY Layer Schemes. In the PHY layer, many works are dedicated to achieving feasible BSC. For example, Liu et al. proposed ambient backscatter that enables two tags to communicate with each other by reflecting ambient TV signals [7]. However, in practical IoT systems, tags are more commonly covered by WiFi signals instead of TV signals. To this end, WiFi backscatter [10] enables tags to reflect ambient WiFi signals in their transmissions and uses an off-the-shelf WiFi device to receive and decode reflected signals. However, the decoding accuracy of this approach is low, because the WiFi node receives both the reflected signal and the ambient signal and has a difficulty in separating these two signals. To improve the decoding accuracy, BackFi [8] is proposed to enable the reader to have prior knowledge of the ambient signal. In this approach, a WiFi node equipped with a full-duplex transceiver is introduced to perform regular WiFi transmission and backscatter reception simultaneously. When decoding the reflected signals, the node adopts the self-interference cancellation (SIC) technique to cancel the ambient signals sent by itself. Nevertheless, deploying a full-duplex transceiver is costly. To avoid deploying a full-duplex transceiver, HitchHike [9] lets tags reflect ambient WiFi signals from a WiFi band to a dedicated band. At the receiving end, there are two WiFi nodes connecting to the same backend server. One node receives the reflected signal over the dedicated band, while the other node receives the regular signal over the WiFi band. Then, the server collects these two signals and extracts tags' data from the reflected signal by comparing these two signals. This design requires collaborations between multiple WiFi nodes, which is still expensive. Different from the above approaches, without deploying a full-duplex transceiver and assigning a dedicated band for BSC in our design, we enable a half-duplex WiFi node to receive and decode the backscatter signals using only two regular antennas.

Besides, some works focus on improving the PHY layer security (PLS) of BSC. For example, in [15], Li et al. investigated the impact of in-phase and quadrature-phase imbalance on the security performance of BSC systems and found out that there exists a trade-off between reliability and security. Further, they proposed a system parameter adjustment scheme to prevent BSC from being eavesdropped. Reference [16] investigated the joint effects of residual hardware impairments, channel estimation errors, and imperfect successive interference cancellation on the PLS of BSC and proposed an artificial noise scheme to prevent BSC from being eavesdropped. Reference [17] studied the PLS of BSC in the case where cognitive radio is introduced in conjunction with BSC. The authors also optimized the performance trade-off between reliability and security of BSC by adjusting system parameters. It is worth pointing out that the PLS of BSC is out of scope of this paper.

1.3.2. MAC Layer Schemes. Along with PHY layer achievements, some works focus on proposing efficient medium access control (MAC) protocol for BSC. For example, [18] proposed a distributed MAC protocol for tag-to-tag communications. When ambient signals exist, tags contend for transmissions, and the loser tags harvest energy while the winner tag performs transmissions. There are also MAC designs for tag-to-WiFi communications. Most of them assumed a full-duplex WiFi access point (AP) that can emit ambient signals and receive the reflected signals from tags simultaneously. For example, Ma et al. proposed a demand-based MAC scheme for WiFi backscatter communication [11]. In this scheme, when having a demand for collecting data from tags, the full-duplex WiFi AP ceases all WiFi transmissions and sends a period of ambient signals, and tags contend and transmit data to the AP during this period. Reference [19] proposed a rendezvous scheme for sporadic BSC. In this scheme, a full-duplex WiFi AP divides the time into frames with equal length; each frame is further divided into subperiods for coordination, WiFi transmission, and BSC, respectively. Tags perform contentions in the coordination subperiods and perform transmissions (to the AP) in the BSC subperiods. Then, this idea is extended by [20], where the full-duplex WiFi AP adopts the deep reinforcement learning technique to learn the optimal time-division strategy. Different from the above approaches, we focus on extending the range of BSC, with the assistance of regular half-duplex WiFi nodes.

The rest of this paper is organized as follows. Section 2 details our design. In Section 3, we theoretically analyze the performance of our design. Section 4 validates the accuracy of our theoretical model. Section 5 concludes this paper.

2. Our Design

In this section, we detail our low-cost and long-range node-assisted WiFi backscatter communication scheme for 5G-enabled IoT. The scheme consists of a physical (PHY) layer design and a MAC layer design. Below, we first present an overview of the scheme and then detail two designs.

2.1. Design Overview. In our design, we consider a 5G-enabled IoT network, which consists of one 5G-CPE, multiple WiFi nodes, and multiple backscatter tags. Adopting off-the-shelf hardware only, we propose a design to achieve an objective as follows. Backscatter tags first transmit data to their nearby WiFi nodes; then, the WiFi node forwards the backscatter data to the remote 5G-CPE.

In the PHY layer, whenever a WiFi signal is sent, the tag uses the signal as an excitation signal to perform a tag-to-tag communication or a tag-to-WiFi communication. During the tag-to-WiFi communication, a WiFi node can extract backscatter data from ambient WiFi signals using only two regular half-duplex antennas, instead of being equipped with expensive full-duplex receivers or collaborating with multiple nodes.

In the MAC layer, we divide the IoT network into multiple subcells (as shown in Figure 2), where each subcell consists of a WiFi node and multiple tags. We propose a MAC

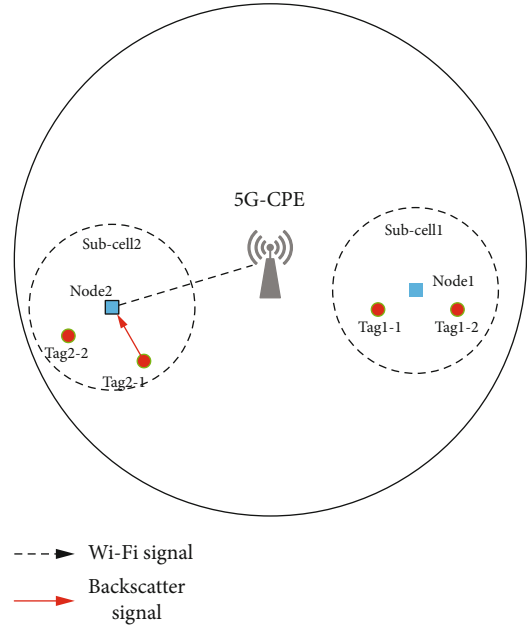


FIGURE 2: Design overview: Tag2-1 first transmits its data to Node2, and then Node2 forwards the backscatter data to the remote 5G-CPE.

layer protocol as follows. First, WiFi nodes follow the WiFi standard to contend for the channel. Then, the WiFi winner node starts a WiFi transmission, while the tags in its subcell harvest energy from the transmission signal. At the same time, other tags adopt our proposed scheme to contend and transmit data to the WiFi nodes in their subcells.

Below, we detail our PHY layer design and our MAC layer design in sequence.

2.2. PHY Layer Design. In our PHY layer design, we assume that each WiFi node has two antennas: antenna 1 (AT1) and antenna 2 (AT2). When a WiFi node transmits signals, it only activates its AT1. When a WiFi node receives signals, it activates both AT1 and AT2.

As shown in Figure 3, when a node (say, Node1) sends a WiFi signal to 5G-CPE, other nodes (say, Node2) and the tags (say, Tag2-1 and Tag2-2) can sense this signal. Using the WiFi signal as an excitation signal, a tag (say, Tag2-1) can adopt the Manchester technology to send information to other tags (say, Tag2-2). It can also adopt the M -ary phase shift keying (M -PSK) technology to perform a high-rate transmission to a WiFi node (say, Node2). Below, we detail the tag-to-tag communication and the tag-to-WiFi communication.

2.2.1. Tag-to-Tag Communication. We adopt the Manchester technology in tag-to-tag communication. Below, we introduce the Manchester modulation and demodulation under the ambient WiFi signals, respectively.

(1) *Modulation.* When performing the Manchester modulation, a tag changes the amplitude of its received WiFi signal

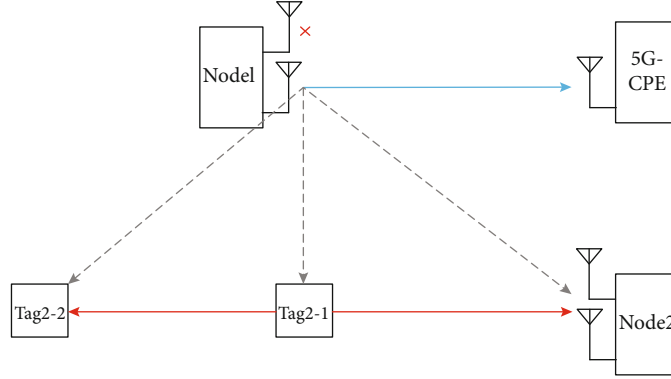


FIGURE 3: PHY overview: Node1 transmits its data to the 5G-CPE (in blue), and the transited signal (in grey) is also received by Tag2-1, Tag2-2, and Node2. Tag2-1 uses this WiFi signal as excitation signal and transmits its data to Tag2-2 and Node2 (in red).

$z(t)$ and then reflects the signal. Therefore, the backscatter signal $x_b(t)$ reflected by the tag can be expressed as follows:

$$x_b(t) = m(t) \cdot z(t), 0 \leq t < T, \quad (1)$$

where

$$m(t) = \begin{cases} s(t), & \text{bit} = 0, \\ -s(t), & \text{bit} = 1, \end{cases} \quad (2)$$

is the backscatter baseband signal and

$$s(t) = \begin{cases} 1, & 0 \leq t < \frac{T}{2}, \\ 0, & \frac{T}{2} \leq t < T. \end{cases} \quad (3)$$

(2) *Demodulation.* Each tag uses energy detection technique to demodulate a backscatter signal $y_b(t) = h_{bb}(t) * x_b(t)$ (ignoring noise) received from other tags, where $h_{bb}(t)$ is the impulse response of the channel between tags. We define

$$P_1 = \int_0^{\frac{T}{2}} (y_b(t))^2 dt, \quad (4)$$

$$P_2 = \int_{\frac{T}{2}}^T (y_b(t))^2 dt.$$

When $P_1 \geq P_2$, the tag regards that $y_b(t)$ carries a bit “0”; otherwise, it regards that $y_b(t)$ carries a bit “1.”

2.2.2. *Tag-to-WiFi Communication.* We adopt the M-PSK technology in tag-to-WiFi communication. Below, we explain M-PSK modulation on tags and the demodulation on nodes sequentially.

(1) *Modulation.* In the M-PSK scheme, bits are represented by phases of symbols. We take the 4-PSK scheme (i.e., $M = 4$) as an example to explain the modulation process. As shown in Figure 4, 4-PSK has 4 valid constellation points \mathbf{e}

$= \{e^{j\theta_1}, e^{j\theta_2}, e^{j\theta_3}, e^{j\theta_4}\}$; these constellation points correspond to bit pairs $\mathbf{B} = \{11, 01, 00, 10\}$. When performing modulation, $m(t)$ in (1) is set according to the mapping relationship between \mathbf{e} and \mathbf{B} . For example, because “10” corresponds to $e^{j\theta_4}$, when modulating “10,” we set $m(t) = e^{j\theta_4}$.

(2) *Demodulation.* In the case shown in Figure 2, Node2 receives regular WiFi signals $x_w(t)$ from Node1 and reflected signals $x_b(t)$ from Tag2-1 simultaneously. Because Node2 activates its AT1 and AT2 during its receptions, a MU-MIMO system is formed, as shown in Figure 5. In this system, Nodel’s AT1 and the Tag2-1 are the inputs, while Node2’s AT1 and AT2 are outputs. Benefitting from this system, Node2 can easily extract $m(t)$ from $x_b(t)$ and then can decode backscatter data from $m(t)$ as follows.

Step 1. Extracting the backscatter baseband signal.

Because Node2 activates two antennas in its reception, we can use a vector \mathbf{y} to represent Node2’s received signal:

$$\mathbf{y} = \begin{bmatrix} y_1(t) \\ y_2(t) \end{bmatrix}, \quad (5)$$

where $y_i(t)$ is the signal received by AT*i* and $i = 1, 2$.

Taking into account the signal fading of $x_w(t)$ and $x_b(t)$ in the MU-MIMO system, (5) can be expanded as follows:

$$\begin{aligned} \textcircled{1} \mathbf{y} &= \begin{bmatrix} x_w(t) * h_{11}(t) + x_b(t) * h_{b1}(t) \\ x_w(t) * h_{12}(t) + x_b(t) * h_{b2}(t) \end{bmatrix} \\ \textcircled{2} &= \begin{bmatrix} x_w(t) * h_{11}(t) + (m(t) \cdot z(t)) * h_{b1}(t) \\ x_w(t) * h_{12}(t) + (m(t) \cdot z(t)) * h_{b2}(t) \end{bmatrix} \\ \textcircled{3} &= \begin{bmatrix} x_w(t) * h_{11}(t) + (m(t) \cdot (x_w(t) * h_f(t))) * h_{b1}(t) \\ x_w(t) * h_{12}(t) + (m(t) \cdot (x_w(t) * h_f(t))) * h_{b2}(t) \end{bmatrix} \\ \textcircled{4} &= \begin{bmatrix} x_w(t) * h_{11}(t) + m(t) \cdot (x_w(t) * [h_f(t) * h_{b1}(t)]) \\ x_w(t) * h_{12}(t) + m(t) \cdot (x_w(t) * [h_f(t) * h_{b2}(t)]) \end{bmatrix}. \end{aligned} \quad (6)$$

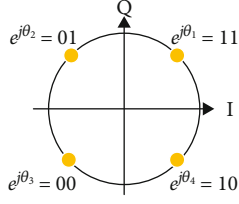


FIGURE 4: Constellation diagram of 4-PSK and bits represented by constellation points.

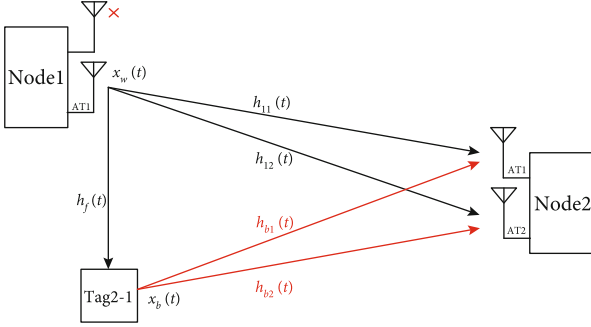


FIGURE 5: A MU-MIMO system in the tag-to-WiFi communication: Node1 and Tag2-1 are inputs, and Node2's AT1 and AT2 are outputs.

In (6), $h_{1i}(t)$ is the impulse response of the channel between Node1's AT1 and Node2's AT i , $i = 1, 2$, and $h_{bi}(t)$ is the impulse response of the channel between the tag and Node2's AT i , $i = 1, 2$. According to (1), we transform ① to ②. Then, we have ③ from ②, because $z(t)$ is $x_w(t)$ received at the tag, where $z(t) = x_w(t) * h_f(t)$ and $h_f(t)$ is impulse response of the channel between Node1's AT1 and the tag. Next, because the symbol period is much longer than the typical propagation delay in IoT (e.g., 50 ns in WiFi [8]), we can consider $m(t)$ to be a constant [8] and hence have ③ to ④. Finally, if $h_{1i}(t)$ and $h_f(t) * h_{bi}(t)$, $i = 1, 2$ in equation ④ are known, we can obtain $x_w(t)$ and $m(t)$ by combining these equations. Fortunately, benefitting from MAC layer design (see Section 2.3), $h_{1i}(t)$ and $h_f(t) * h_{bi}(t)$, $i = 1, 2$, can be estimated before demodulations.

At the receiver end, analog signals are sampled before being further processed. Hence, we can write (6) in the discrete domain as follows:

$$\mathbf{y} = \begin{bmatrix} x_w[n] \cdot h_{11} + m[n] \cdot (x_w[n] \cdot [h_f \cdot h_{b1}]) \\ x_w[n] \cdot h_{12} + m[n] \cdot (x_w[n] \cdot [h_f \cdot h_{b2}]) \end{bmatrix}. \quad (7)$$

Step 2. Decoding backscatter data.

Upon extracting $m[n]$, we perform the following operations to decode bits from it. First, we, respectively, compute the distance between $m[n]$ and each of valid constellation points in \mathbf{e} . Then, we regard $m[n]$ as the constellation point that results in the shortest distance and decode $m[n]$ as the corresponding bits. For example, if $m[n]$ is closest to $e^{j\theta_4} \in \mathbf{e}$ and "10" corresponds to $e^{j\theta_4}$, we decode $m[n]$ as "10."

2.3. MAC Layer Design. To better describe our MAC layer design, we assume an IoT network with the topology shown in Figure 2. In this topology, the IoT network comprises two subcells, i.e., subcell k , $k = 1, 2$. In subcell k , there are one WiFi node (i.e., Node k) and two tags (i.e., Tag $k - 1$ and Tag $k - 2$).

Further, we describe the MAC layer design using the example shown in Figure 6. In this example, Node1 and Node2 perform carrier sense multiple access/collision avoidance (CSMA/CA) mechanism to contend for their transmissions. Then, Node1 wins the contention and the whole network starts a process that can be divided into four periods as follows.

2.3.1. Period ①: Header Transmission. In this period, Node1 sends a WiFi PHY header (including WiFi preamble) and a MAC header. All tags (i.e., Tag1-1, Tag1-2, Tag2-1, and Tag2-2) harvest energy from the WiFi signal carrying headers. Node2 receives the PHY header and uses the WiFi preamble in the header to evaluate $h_{1i}(t)$, $i = 1, 2$, in Equation (6).

2.3.2. Period ②: Asynchronous Block ACK (AB-ACK). In this period, Node1 sends an asynchronous block ACK (AB-ACK) shown in Figure 7, which comprises a Start field (i.e., the start of the tag and WiFi transmission), a Transmit address field (TA for short, i.e., the signature of Node1), a Duration field (i.e., the number of Receive address), and n Receive address fields (RA for short, i.e., the signature of the sender of the backscattered data buffered in Node1). The length of each field is 1 microslot. In the example of Figure 6, the RA only contains the signature of Tag1-1 (i.e., $n = 1$), indicating that Node1 has only successfully received and buffered the backscatter data from Tag1-1 between its last and current transmission.

All tags receive the AB-ACK and detect the TA field in it. Tag2-1 and Tag2-2 learn from TA that the current sender node does not belong to the same subcell (i.e., is not Node2), so they read n from the duration field and then perform energy harvesting operation for a time of sending n RAs (i.e., n microslots). Meanwhile, Tag1-1 and Tag1-2 learn from TA that Node1 is the current sender node, so they continue to check the Duration and RA fields. Then, Tag1-1 detects its signature in RA and knows that its previous transmission is successful. Meanwhile, Tag1-2 does not detect its signature in RA and hence knows that its previous transmission is unsuccessful. Later, it will perform a retransmission to Node1.

Node2 keeps silent.

2.3.3. Period ③: Backscatter Contention. This period is further divided into l microslots. In each microslot, Node1 sends a predefined busy tone.

Tag1-1 and Tag1-2 perform energy harvesting and do not send data to Node1, because Node1 is performing transmission instead of reception. Meanwhile, Tag2-1 and Tag2-2 attempt to send packet to Node2; hence, they perform a contention as follows. First, they generate a random backoff counter uniformly distributed in $(0, l - 1)$. Then, they sense the channel and decrease their counters by 1 if there is no backscatter preamble (B-preamble) being transmitted. The B-preamble is a predefined special sequence transmitted

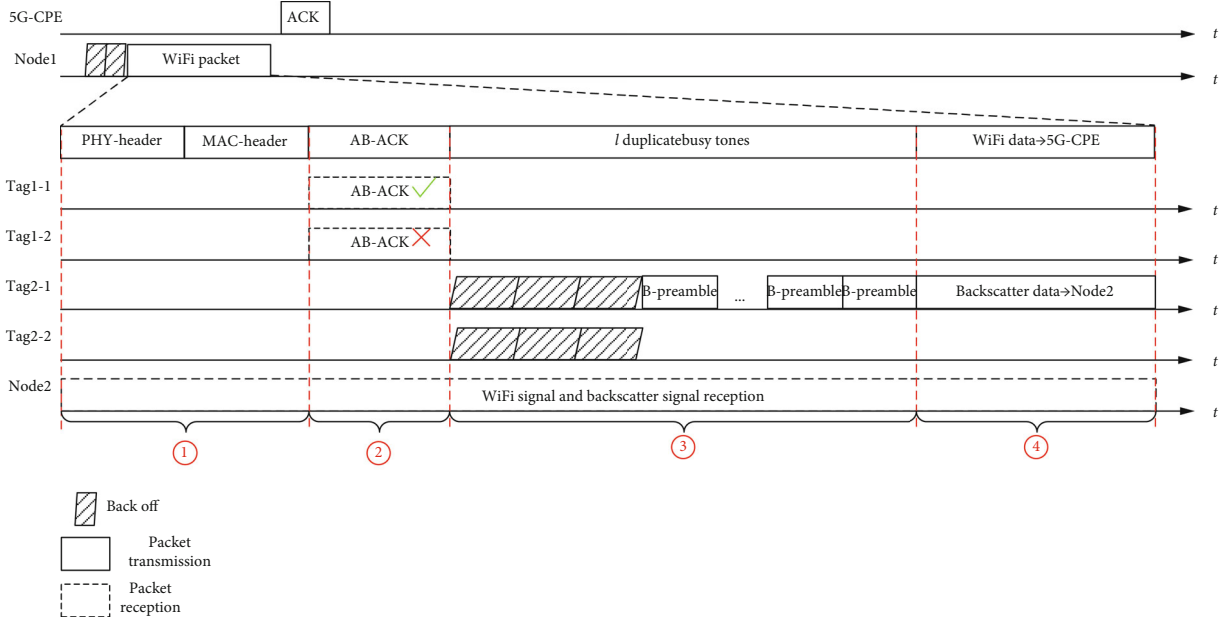


FIGURE 6: Example of transmission process in our MAC design.

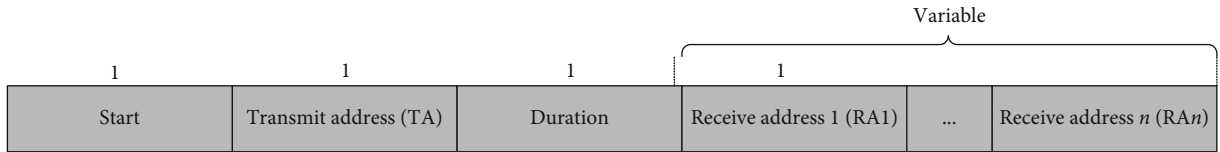


FIGURE 7: Asynchronous block ACK format.

using our tag-to-tag communication scheme and its length is 1 microslot. Then, Tag2-1's counter first reaches 0 and Tag2-1 starts to broadcast B-preamble repeatedly until the l th microslot. Tag2-2 detects Tag2-1's B-preambles, stops its backoff and transmission attempt, and performs energy harvesting.

Node2 receives a busy tone from Node1 and a B-preamble from Tag2-1 in the l th microslot. Then, it substitutes them and the $h_{1i}(t)$, $i = 1, 2$ obtained in period ① into (4) to estimate $h_f(t) * h_{bi}(t)$, $i = 1, 2$.

2.3.4. Period ④: Backscatter Transmission. In this period, Node1 follows the WiFi standard to send its data and the buffered Tag1-1's data to 5G-CPE. Tag1-1, Tag1-2, and Tag2-2 perform energy harvesting. Tag2-1 sends a packet to Node2 using our tag-to-WiFi communication scheme, where the packet consists of the tag's address and a data payload. Node2 buffers this packet and records the tag's address, and then, it forwards the packet to the 5G-CPE in its next transmission.

3. Performance Analysis

In this section, we analyze the MAC layer performance of the proposed backscatter system (namely, throughput). We consider a saturated network (i.e., all WiFi nodes and backscatter tags always have a packet to send) consisting of 1 5G-CPE

and n subcells. Each subcell consists of 1 node and g tags. That is, there are n nodes and G tags in total, where $G = n \times g$. We also assume that the nodes have the same packet size L_w and the tags have another same packet size L_b . In the following, we express the throughput in terms of WiFi and backscatter.

3.1. Throughput of WiFi. In the following, we first calculate the generic slot and then express the throughput of WiFi.

3.1.1. Calculation of the Generic Slot. Let $\tau(\gamma)$ denote the attempt rate of each WiFi node. In 802.11 networks, $\tau(\gamma)$ can be achieved through setting the minimum contention windows (CW_{\min}) and the maximum backoff stage (m) [21]. We have

$$\tau(\gamma) = \frac{2}{1 + CW_{\min} + \gamma CW_{\min} \sum_{k=0}^{m-1} (2\gamma)^k}, \quad (8)$$

where γ is the collision probability of each WiFi node and can be expressed as

$$\gamma = 1 - (1 - \tau(\gamma))^{n-1}. \quad (9)$$

Let Ω denote time duration of the generic slot that elapses for one decrement of the backoff counter. Ω depends on

TABLE 1: Main simulation parameters for PHY and MAC layers of WiFi.

Parameter	Description	Value
PHY model		
R_{data}	Data rate of MCS 4/MCS 8	3.9/7.8 Mb/s
R_{basic}	Basic rate	0.65 Mb/s
PHY header	Length of PHY header	160 μs
MAC model		
T_{SIFS}	Duration of SIFS interval	160 μs
T_{DIFS}	Duration of DIFS interval	264 μs
T_{slot}	Duration of an IEEE 802.11ah time slot	52 μs
L_{WiFi}	Length of DATA packets	1000 bytes
L_{ACK}	Length of ACK packets	14 bytes
MAC header	(40 bytes + 4 bytes)@ R_{data}	46 μs
Route header	20 bytes@ R_{data}	21 μs
T_{WiFi}	1000 bytes@ R_{data}	1026 μs
T_{ACK}	(24 bytes + 1 4bytes)@ R_{basic}	39 μs
CW_{min}	Minimum value of contention window	16
m	Maximum backoff stage	7

whether a slot is idle or interrupted by a successful or an unsuccessful WiFi transmission [22, 23]. So, Ω can be expressed as

$$\Omega = \begin{cases} \sigma, 1 - P_b, \\ T_s, P_s, \\ T_{\bar{s}}, P_b - P_s, \end{cases} \quad (10)$$

where $P_b = 1 - (1 - \tau(\gamma))^n$ is the probability of a busy slot; $P_s = n\tau(\gamma)(1 - \tau(\gamma))^{n-1}$ is the probability of a successful WiFi transmission from any of n contending nodes; σ is the duration of one time slot; and T_s and $T_{\bar{s}}$ are the mean time for a successful transmission and an unsuccessful transmission, respectively.

Let $E(\Omega)$ denote the mean value of Ω . We have

$$E(\Omega) = (1 - P_b)\sigma + P_s T_s + (P_b - P_s)T_{\bar{s}}. \quad (11)$$

3.1.2. Calculation of WiFi's Throughput. We define the throughput, Γ_w , as the number of bits that the WiFi nodes successfully transmit in $E(\Omega)$ [21–23]. We have

$$\Gamma_w = \frac{P_s L_w}{E(\Omega)}. \quad (12)$$

3.2. Throughput of Backscatter. Here, we first calculate the probability of a successful backscatter transmission and then calculate the throughput of backscatter.

3.2.1. Calculation of the Probability of a Successful Backscatter Transmission. In a subcell, when there is only one tag that wins the contention, the winner tag performs a successful

backscatter transmission. Let β denote the probability of a successful backscatter transmission. We have

$$\beta = \frac{\sum_{i=0}^{l-2} C_g^1 (C_{l-i-1}^1)^{g-1}}{(C_l^1)^g}. \quad (13)$$

In (13), the denominator represents the number of g tags' all possible contention results, while the numerator represents the number of that only one tag wins the contention. In the numerator, i is the backoff counter of the winner; $l-2$ is the maximum backoff counter that the winner can select. C_g^1 represents that any one of g contending tags wins the contention, where its backoff counter equals to i . $(C_{l-i-2}^1)^{g-1}$ represents that the other $g-1$ tags fail the contention, where their backoff counters are greater than i .

3.2.2. Calculation of Backscatter's Throughput. Each successful WiFi transmission can provide a backscatter Transmission Opportunity (TXOP) for all winner tags in other $n-1$ subcells (except the subcell of the WiFi transmitter), and then, the winners can transmit their backscatter data to the neighbouring WiFi nodes in parallel. Note that we have the same β in all subcells, because the number of tags in all subcells is the same. Therefore, we express the throughput of backscatter, Γ_b , by

$$\Gamma_b = \frac{(n-1)\beta P_s L_b}{E(\Omega)}. \quad (14)$$

Finally, we also define the total throughput, Γ_t , as the sum of WiFi's throughput and backscatter's throughput, which can be expressed as

$$\Gamma_t = \Gamma_w + \Gamma_b. \quad (15)$$

4. Performance Evaluation

In this section, we verify the accuracy of our theoretical model and make comparisons with BackFi [8].

In our design, we consider an IoT network consisting of 1 5G-CPE, n nodes, and $G(G = n \times g)$ tags, where each subcell consists of 1 node and g tags. The WiFi nodes contend to upload their data to 5G-CPE, where each WiFi transmission activates $n - 1$ backscatter transmissions in other subcells.

In BackFi, the IoT network comprises 1 5G-CPE, n nodes, and g tags, where all tags surround the 5G-CPE in the transmission range of backscatter. The 5G-CPE of BackFi contends for the channel to obtain the backscatter data. When the 5G-CPE wins the channel, it sends the excitation signal to a target tag. Then, the tag modulates the excitation signal and reflects the signal back to the 5G-CPE.

In simulation, we consider a saturated network (in both our design and BackFi). The PHY and MAC layer's default parameter settings of our design and BackFi are set according to IEEE 802.11ah [13] and listed in Table 1. The other default parameter settings of our design are shown in Table 2.

Here, we verify the accuracy of our model in terms of throughputs (which are calculated by (12) and (14)). Figure 8 plots the WiFi's throughput and backscatter's throughput, when $n = 1, \dots, 10$; $g = 5$; and $R_{\text{data}} = 3.9 \text{ Mb/s}$. From Figure 8, we have the following observations:

- (i) The theoretical curves closely match the simulation curves. This manifests that our performance model is very accurate
- (ii) As n increases, the throughput of WiFi decreases slightly, while the throughput of backscatter increases significantly. For example, the throughput of backscatter when $n = 10$ (0.68 Mb/s) is 0.7 times more than that of when $n = 5$ (0.4 Mb/s)

Here, we compare our design with BackFi in terms of WiFi's throughput, backscatter's throughput, and total throughput. Figure 9 plots the throughput of our design and BackFi as the number of nodes, n , varies, where $g = 5$ and $R_{\text{data}} = 7.8 \text{ Mb/s}$. From Figure 9, we have the following observations:

- (i) As n increases from 1 to 20, the total throughput of our design is steady at 3.0 Mb/s, while that of BackFi decreases from 3.1 Mb/s to 2.5 Mb/s
- (ii) The backscatter's throughput of our design is much higher than that of BackFi. The reasons are as follows. In our design, each WiFi transmission (whether transmitted by the 5G-CPE or the WiFi nodes) can activate $n - 1$ backscatter transmissions. However, in BackFi, only each 5G-CPE's transmission can activate one backscatter transmission
- (iii) The WiFi's throughput of our design is always 0.3 Mb/s lower than that of BackFi. This is because

TABLE 2: Main simulation parameters of our design.

Parameter	Description	Value
l	Number of microslot	8
$L_{\text{micro-slot}}$	Length of micro-slot	16 μs

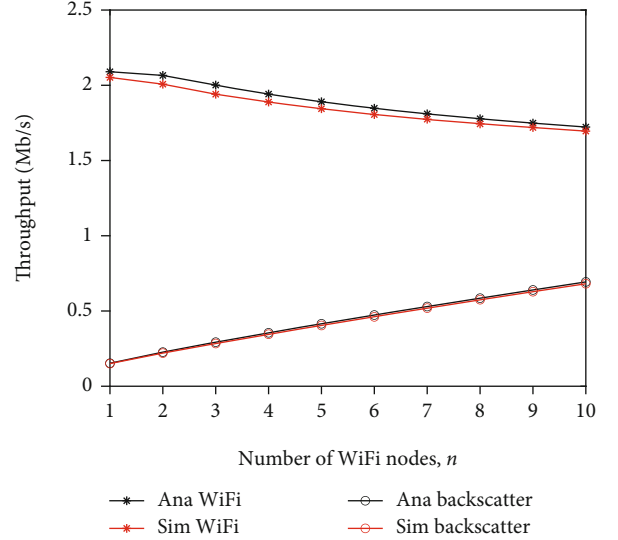


FIGURE 8: Throughput vs. number of WiFi nodes.

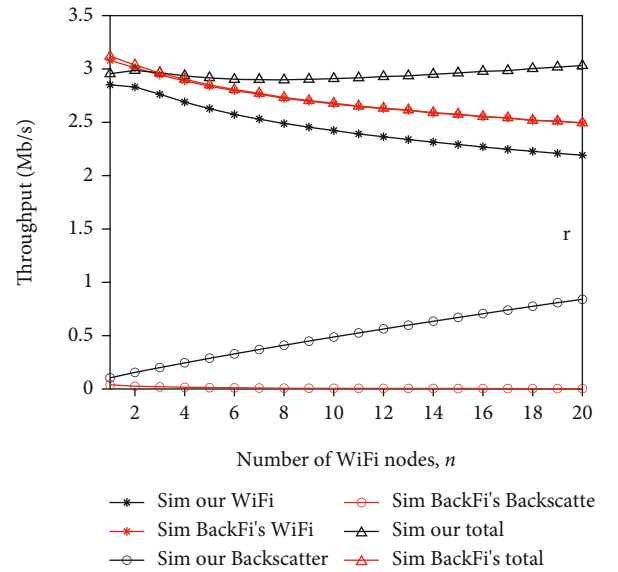


FIGURE 9: Comparison of throughput between our design and BackFi.

our design introduces the AB-ACK and the backscatter contention, which increases redundancy of WiFi packet

5. Conclusions

In this paper, we propose a low-cost and long-range node-assisted WiFi-BSC for 5G-enabled IoT. First, in the PHY

layer, we enable the off-the-shelf WiFi devices to receive and decode backscatter signals using only two regular antennas, which reduces the deployment cost of WiFi-BSC significantly. Then, in the MAC layer, we enable WiFi nodes to relay WiFi-BSC data toward the 5G-CPE, extending the communication range of WiFi-BSC greatly. Next, we model our scheme. Finally, we run extensive simulations to verify the accuracy of our model and the effectiveness of our scheme. This study shows that the WiFi-BSC has a great potential in 5G-enabled IoT.

Data Availability

The data used to support the findings of this study are available from the corresponding author upon request.

Conflicts of Interest

The authors declare that there are no conflicts of interest regarding the publication of this paper.

Acknowledgments

This work is funded in part by the National Nature Science Foundation of China (File no. 61872451 and 61872452) and in part by the Science and Technology Development Fund, Macau SAR (File nos. 0098/2018/A3, 0037/2020/A1, and 0062/2020/A2).

References

- [1] J. Ni, X. Lin, and X. S. Shen, "Efficient and secure service-oriented authentication supporting network slicing for 5G-enabled IoT," *IEEE Journal on Selected Areas in Communications*, vol. 36, no. 3, pp. 644–657, 2018.
- [2] "Minimum requirements related to technical performance for IMT-2020 radio interface(s)," <https://www.itu.int:443/en/publications/ITU-R/Pages/publications.aspx>.
- [3] "5G for connected industries and automation white paper," https://www.5g-acia.org/fileadmin/5G-ACIA/Publikationen/Whitepaper_5G_for_Connected_Industries_and_Automation/WP_5G_for_Connected_Industries_and_Automation_Download_19.03.19.pdf.
- [4] M. Simsek, A. Aijaz, M. Dohler, J. Sachs, and G. Fettweis, "5G-enabled tactile internet," *IEEE Journal on Selected Areas in Communications*, vol. 34, no. 3, pp. 460–473, 2016.
- [5] D. B. Lukic, G. B. Markovic, and D. D. Drajić, "Two-stage precoding based on overlapping user grouping approach in IoT-oriented 5G MU-MIMO systems," *Wireless Communications and Mobile Computing*, vol. 2021, Article ID 8887445, 13 pages, 2021.
- [6] J. Yang, L. Feng, T. Jin, H. Liang, F. Xu, and L. Tian, "Enabling sector scheduling for 5G-CPE dense networks," *Security and Communication Networks*, vol. 2020, Article ID 6684681, 18 pages, 2020.
- [7] V. Liu, A. Parks, V. Talla, S. Gollakota, D. Wetherall, and J. R. Smith, "Ambient backscatter: wireless communication out of thin air," *ACM SIGCOMM Computer Communication Review*, vol. 43, no. 4, pp. 39–50, 2013.
- [8] D. Bharadia, K. R. Joshi, M. Kotaru, and S. Katti, "BackFi: high throughput WiFi backscatter," *ACM SIGCOMM Computer Communication Review*, vol. 45, no. 4, pp. 283–296, 2015.
- [9] P. Zhang, D. Bharadia, K. Joshi, and S. Katti, "HitchHike: practical backscatter using commodity WiFi," in *Proceedings of the 14th ACM Conference on Embedded Network Sensor Systems CD-ROM*, pp. 259–271, Stanford, CA, USA, 2016.
- [10] B. Kellogg, A. Parks, S. Gollakota, J. R. Smith, and D. Wetherall, "Wi-Fi backscatter: internet connectivity for RF-powered devices," *ACM SIGCOMM Computer Communication Review*, vol. 44, pp. 607–618, 2014.
- [11] Z. Ma, L. Feng, and F. Xu, "Design and analysis of a distributed and demand-based backscatter MAC protocol for internet of things networks," *IEEE Internet of Things Journal*, vol. 6, no. 1, pp. 1246–1256, 2018.
- [12] E. Khorov, A. Lyakhov, A. Krotov, and A. Guschin, "A survey on IEEE 802.11ah: an enabling networking technology for smart cities," *Computer Communications*, vol. 58, pp. 53–69, 2015.
- [13] T. Adame, A. Bel, B. Bellalta, J. Barcelo, and M. Oliver, "IEEE 802.11AH: the WiFi approach for M2M communications," *IEEE Wireless Communications*, vol. 21, no. 6, pp. 144–152, 2014.
- [14] N. van Huynh, D. T. Hoang, X. Lu, D. Niyato, P. Wang, and D. I. Kim, "Ambient backscatter communications: a contemporary survey," *IEEE Communications Surveys & Tutorials*, vol. 20, no. 4, pp. 2889–2922, 2018.
- [15] X. Li, M. Zhao, Y. Liu, L. Li, Z. Ding, and A. Nallanathan, "Secrecy analysis of ambient backscatter NOMA systems under I/Q imbalance," *IEEE Transactions on Vehicular Technology*, vol. 69, no. 10, pp. 12286–12290, 2020.
- [16] X. Li, M. Zhao, M. Zeng et al., "Hardware impaired ambient backscatter NOMA systems: reliability and security," *IEEE Transactions on Communications*, vol. 69, no. 4, pp. 2723–2736, 2021.
- [17] X. Li, Y. Zheng, W. U. Khan et al., "Physical layer security of cognitive ambient backscatter communications for green Internet-of-Things," *IEEE Transactions on Green Communications and Networking*, 2021.
- [18] X. Cao, Z. Song, B. Yang, M. A. ElMossallamy, L. Qian, and Z. Han, "A distributed ambient backscatter MAC protocol for Internet-of-Things networks," *IEEE Internet of Things Journal*, vol. 7, no. 2, pp. 1488–1501, 2019.
- [19] X. Cao, Z. Song, B. Yang, M. ElMossallamy, L. Qian, and Z. Han, "A distributed MAC using Wi-Fi to assist sporadic backscatter communications," in *IEEE INFOCOM 2019-IEEE Conference on Computer Communications Workshops (INFOCOM WKSHPS)*, pp. 780–785, Paris, France, 2019.
- [20] X. Cao, Z. Song, B. Yang, X. Du, L. Qian, and Z. Han, "Deep reinforcement learning mac for backscatter communications relying on Wi-Fi architecture," in *2019 IEEE Global Communications Conference (GLOBECOM)*, pp. 1–6, Waikoloa, HI, USA, 2019.
- [21] G. Bianchi, "Performance analysis of the IEEE 802.11 distributed coordination function," *IEEE Journal on Selected Areas in Communications*, vol. 18, no. 3, pp. 535–547, 2000.
- [22] Q. Zhao, D. H. Tsang, and T. Sakurai, "A simple and approximate model for nonsaturated IEEE 802.11 DCF," *IEEE Transactions on Mobile Computing*, vol. 8, no. 11, pp. 1539–1553, 2009.
- [23] Q. Zhao, D. H. Tsang, and T. Sakurai, "Modeling nonsaturated IEEE 802.11 DCF networks utilizing an arbitrary buffer size," *IEEE Transactions on Mobile Computing*, vol. 10, no. 9, pp. 1248–1263, 2010.

Research Article

Secrecy Performance Analysis of a Cognitive Network for IoT over k - μ Channels

Junxia Li ¹, Hui Zhao ¹ and Michael Johnson²

¹The College of Information Science and Engineering, Xinjiang University, 830046 Urumqi, China

²Department of Electronic and Computer Engineering, University of Limerick, Limerick, Ireland

Correspondence should be addressed to Hui Zhao; zherryxjdx@163.com

Received 2 March 2021; Revised 14 May 2021; Accepted 1 June 2021; Published 28 June 2021

Academic Editor: Xingwang Li

Copyright © 2021 Junxia Li et al. This is an open access article distributed under the Creative Commons Attribution License, which permits unrestricted use, distribution, and reproduction in any medium, provided the original work is properly cited.

With the development of Internet of Things (IoTs), devices are now connecting and communicating together on a heretofore unheard-of scale, forming huge heterogeneous networks of mobile IoT-enabled devices. For beyond 5G- (B5G-) enabled networks, this raises concerns in terms of spectral resource allocation and associated security. Cognitive radio is one effective solution to such a spectrum sharing issue which can be adopted to these B5G networks, which works on the principle of sharing spectrum between primary and secondary users. In this paper, we develop the confidentiality of cognitive radio network (CRNs) for IoT over k - μ fading channels, with the information transmitted between secondary networks with multiple cooperative eavesdroppers, under the constraint of the maximum interference that the primary users can tolerate. All considered facilities use a single-antenna receiver. Of particular interest, the minimum limit values of secure outage probability (SOP) and the probability of strictly positive secrecy capacity (SPSC) are developed for this model in a concise form. Finally, the Monte Carlo simulations for the system are provided to support the theoretical analysis presented.

1. Introduction

With the recent roll-out of 5G technology globally, an ever-increasing number of intelligent devices are now joining the Internet including mobile IoT devices in social, industrial, healthcare, and smart-grid nature [1]. With this rapid rise in connectivity between such devices, associated security threats and challenges are also on the increase, becoming more pressing, and need to be resolved urgently.

Traditional network encryption mechanisms can resolve security problem through various encryption algorithms at the network layer and above. However, such encryption mechanisms can no longer provide perfect security for wireless communication networks due to the complexity and time-consuming nature of the problem. Fortunately, the influence of fading channel and noise actually provides the possibility for implementing physical layer security (PLS), which has been the subject of extensive research in the literature. On the basis of [2], Wyner first proposed a model to estimate the security of communication systems [3]. For the scenarios of active eavesdropping, Ai et al. pro-

vided another evaluation benchmark, namely, average secrecy capacity (ASC), over double-Rayleigh fading channels [4]. Referring to the classical Wyner eavesdropping model, SOP was given to study the security of the correlated Rician fading channels [5]. To minimize information leakage, a precoding scheme and the security of Rician fading channels were investigated by analyzing the SOP in [6]. Elsewhere, [7] studied the security capability of large-scale fading channels according to the probability of nonzero secrecy capacity (PNSC) and SOP.

The generalized fading channel can model the real transmission environment. By changing its parameters, it can represent many channel models. To account for this, a large section of the literature has studied the transmission performance and security of the generalized fading channels [8–15]. In [8], Lei et al. employed two mathematical forms to complete the derivation of the lower limit of SOP and strictly positive secrecy capacity (SPSC). Elsewhere, the ability of such a channel to resist active eavesdropping was investigated by deriving the ASC in [9]. Using a system model of decode-and-forward (DF) relay cooperation

over generalized- K channels, the exact and approximate theoretical expressions of SOP and ESC were evaluated in [10]. Using channels with the premise that the main link follows α - μ distribution and the eavesdropping link was modelled as k - μ distribution, the analytical expressions of ASC, SOP, and SPSC were derived in [11]. Sun et al. described the closed form of SOP and SPSC over other k - μ shadowed fading channels in a concise form [12] and gave an approximate analysis through the method of moment matching. The authors of [13] analyzed the security of Fox's H -function fading channels by simulating the SOP and probability of nonzero secrecy capacity (PNZ). In real-world wireless communication networks (WCNs), the correlation between antennas cannot be ignored. Based on this, the security performance analysis of correlated systems over η - μ fading channels [14] and k - μ shadowed fading channels [15] has also been investigated.

More recently, nonorthogonal multiple access (NOMA) and ambient backscatter communication technology have attracted more and more attention due to the high spectral and energy efficiency for the Internet of Things. In order to investigate the reliability and security of the ambient backscatter NOMA systems considering hardware damage, the outage probability (OP) and the intercept probability (IP) were studied [16]. More practically, the ambient backscatter NOMA system under in-phase and quadrature-phase imbalance (IQI) was taken into account in [17], where the expressions for the OP and the IP are derived in closed exact analytical form [18] and the secure performance for the future beyond 5G (B5G) networks in the presence of nonlinear energy harvesters and imperfect CSI and IQI in terms of the closed form of OP and IP was studied.

Most recently, many scholars are interested in CRNs because they can make use of scarce spectrum resources without causing decoding errors to the primary user's communication. Considering a multirelay network over Nakagami- m fading channels, the authors of [19] studied the effect of three different relay schemes on the security capacity of the channel. In [20], the SOP of the single-input multiple-output (SIMO) underlay CRNs over Rayleigh fading channels with imperfect CSI were derived and analyzed. Park et al. [21] proposed a CRN model composed of a multirelay primary network and a direct link secondary network, where the outage performance of the two networks was analyzed. The secrecy outage performance of DF-based multihop relay CRN under different parameters was investigated in the presence of imperfect CSI in [22]. The authors in [23] studied the energy distribution of CRN by analyzing spectrum sharing. Based on an underlying CRN, the derivation and analysis of SOP and SPSC are described in [24]. Combined with machine learning, a resource allocation protocol for CRN has also been proposed, and the influence of channel parameters on spectrum efficiency is presented in [25]. For conditions where the secondary network cannot interfere with the communication of the primary network, the authors in [26] took PNSC and SOP as the benchmark for studying CRN over Rayleigh fading channels. Recently, security issues are studied for popular applications such as relaying system a direct connection [27] and NOMA system [28].

As a generalized channel, k - μ fading can be equated with Rayleigh, one-sided Gaussian, Nakagami- m , and Rician fading channel [29], which can be used to simulate many wireless communication scenarios, so it is of great value to explore transmission performance. Bhargav et al. [30] analyzed the security of the wiretap system over fading channels by deriving the SOP and SPSC of the considered system. The SOP was derived based on classical Wyner's model over k - μ distribution [31]. The authors in [32] studied the statistical properties of k - μ distribution and obtained the probability density function (PDF) and cumulative distribution function (CDF) for multiple independent k - μ variables. Utilizing DF relay scheme, the SOP and SPSC in a relay system over k - μ channels were provided [33]. As an extension to [32], the authors of analyzed the secrecy outage performance of a SIMO wiretap system over k - μ channels.

1.1. Motivation and Contribution. To date, there is negligible work presented in the literature on the CRN security assessment of multiple eavesdroppers over k - μ fading channels. Motivated by the aforementioned discussions, this paper presents such an investigation into the secrecy outage performance of CRN under multiple eavesdroppers by deriving the SOP and SPSC.

The main contributions of this paper are summarized as follows:

- (i) The work presents a CRN security assessment of multiple eavesdroppers over k - μ fading channels, considering multiple eavesdroppers in the cognitive radio network. It provides theoretical analysis of SOP and studies the influence of channel parameters and other parameters on the secrecy outage performance
- (ii) The paper also presents a derivation of SPSC for such a setup, from which it can be seen that SPSC is independent of the primary channel, and this conclusion is confirmed by simulation
- (iii) To further evaluate the security for the considered system, the asymptotic analysis of SOP in the high signal-to-noise ratios (SNRs) is derived in this paper. The simulation results indicate that the secrecy diversity order is equal to the main channel parameters and is not influenced by the other parameters

1.2. Organization. The rest of this paper is organized as follows. Section 2 illustrates the proposed system model. Section 3 presents the premise, including the PDFs and CDFs of the main, primary, and wiretap channel. The SOP is derived in Section 4, the asymptotic SOP is then considered in Section 5. Section 6 introduces the associated evaluation of the SPSC. In Section 7, numerical results are presented based on the Monte Carlo method to verify the theoretical analysis presented in the preceding sections. Finally, Section 8 provides the conclusion for this paper.

1.3. Notations. In this paper, $I_m(\cdot)$ is the modified Bessel function with order m and we present $\Gamma(\cdot)$ as the Gamma

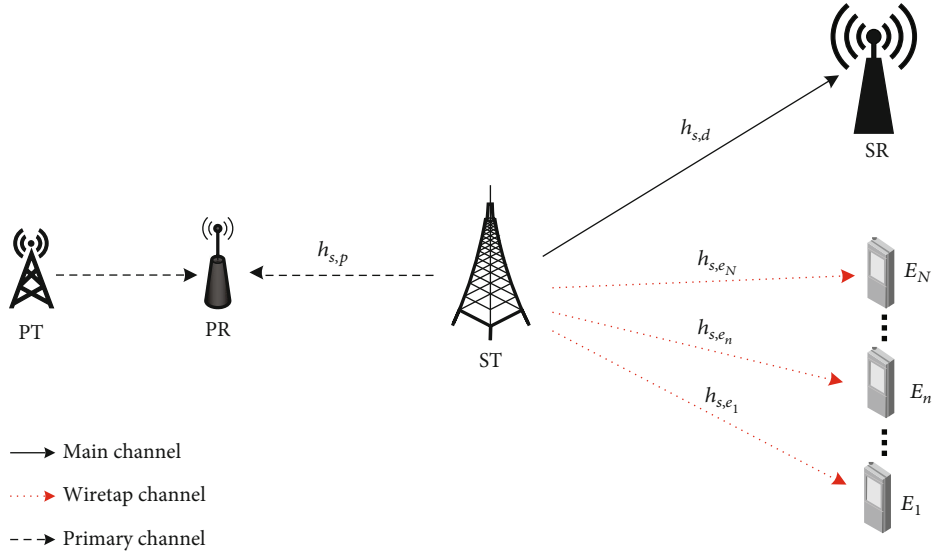


FIGURE 1: System model.

function. $\gamma(a, z)$ denotes the Pochhammer symbol. $(U)_k$ is the denotation of the generalized Laguerre polynomial. $L_k^m(\cdot)$ presents upper incomplete Gamma function. $\Psi(a, b; z)$ is the Tricomi confluent hypergeometric function defined in [33] (Equation (9.211.4)). ${}_2F_1(a, b; c; z)$ is the Gauss hypergeometric function of variable z with parameters of a , b , and c . In this paper, we represent the probability density function (PDF) in $f(\cdot)$ and the cumulative distribution function (CDF) in $F(\cdot)$.

2. System Model

The system model is presented in Figure 1. It consists of one primary transmitter (PT), one primary receiver (PR), one secondary transmitter (ST), one secondary receiver (SR), and multiple eavesdroppers ($E_i, i = 1, 2, \dots, L_E$). An effective way to realize spectrum sharing is to use cognitive radio networks (CRN). There are three types of CRN: interweave, underlay, and overlay. The model in this paper adopts the underlying CRN. The system model and analysis method can also be applied to other wireless fading channels.

In this paper, we assume that the considered network functions in underlay mode, i.e., the secondary users (SUs), concurrently are entitled to use the resources of the primary network. In underlay mode, communication among the secondary networks of the CRN can be implemented, but it must be carried out under the limitation of guaranteeing the quantity of service (QoS) of the primary network. ST tries to transmit information to SR in the presence of multiple cooperative wiretappers, without reducing the communication quality of the primary network. Hence, the transmitter power \bar{P}_s of ST is written as

$$\bar{P}_s = \min \left(\frac{I_p}{|h_{sp}|^2}, P_{\max} \right), \quad (1)$$

where I_p is the maximum interference power at PR and P_{\max} represents the peak transmit power of S restricted by designed hardware. It is assumed that there are no direct links between PT and SR and that E_i ($i = 1, 2, \dots, L_E$) can only eavesdrop on the signal from ST. All links of the considered system are independent, nonidentity, frequency flat, and subject to k - μ fading, with the coefficients of the channel unchanging during a transmission block.

Based on these assumptions, $h_{s,v}$ is the channel gain from S to v , $v \in (d, p, e_i, i \in (1, 2, \dots, L_E))$; the power gains can be denoted as a k - μ random variable with channel parameters (k_v, μ_v) , assuming that all channel coefficients are integers; finally, L_E is the number of wiretappers. Therefore, the received signals are

$$\begin{cases} y_{sp} = h_{sp}x_s + n_p, \\ y_{sd} = h_{sd}x_s + n_d, \\ y_{se_i} = h_{se_i}x_s + n_{e_i}, \end{cases} \quad (2)$$

where n_p, n_d, n_{e_i} are the additive white Gaussian noise with zero mean value and variance of σ^2 on PR, SR, and E_i . From (2), the received instantaneous SNRs are

$$\begin{cases} \gamma_p = \frac{|h_{sp}|^2 \bar{P}_s}{\sigma^2}, \\ \gamma_d = \frac{|h_{sd}|^2 \bar{P}_s}{\sigma^2}, \\ \gamma_{e_i} = \frac{|h_{se_i}|^2 \bar{P}_s}{\sigma^2}. \end{cases} \quad (3)$$

For convenience, we define $x = |h_{sp}|^2, y_d = |h_{sd}|^2$, and $y_{e_i} = |h_{se_i}|^2$. Taking into account that multiple eavesdroppers

collaborate with maximal ratio combining (MRC) technology, the total received instantaneous SNR at E is

$$\gamma_e = \sum_{i=1}^{L_E} \gamma_{e_i} = \frac{\overline{P}_s}{\sigma^2} \sum_{i=1}^{L_E} |h_{se_i}|^2. \quad (4)$$

From this, one can get the total wiretapped channel power gain as

$$\gamma_e = \sum_{i=1}^{L_E} |h_{se_i}|^2. \quad (5)$$

3. Statistical Characteristics of k - μ Fading

Since all channels of the considered system experience the independent, nonidentity k - μ fading, from [26] (Equation (10)), the k - μ power probability density function (PDF) of the link from ST to SR or E_i can be expressed as

$$\begin{aligned} f_u(z) &= \frac{\mu_u(1+k_u)^{(\mu_u+1)/2}}{k_u^{(\mu_u-1)/2} e^{\mu_u k_u \Omega_u}} \left(\frac{z}{\Omega_u} \right)^{(\mu_u-1)/2} e^{-((\mu_u(1+k_u))/\Omega_u)z} \\ &\quad \times I_{\mu_u-1} \left(2\mu_u \sqrt{\frac{k_u(1+k_u)}{\Omega_u}} z \right) \\ &= \frac{1}{e^{\mu_u k_u}} \left(\frac{\mu_u(1+k_u)}{\Omega_u} \right)^{\mu_u} e^{-((\mu_u(1+k_u))/\Omega_u)z} \\ &\quad \times \sum_{i=0}^{\infty} \frac{(k_u \mu_u)^i}{i! \Gamma(\mu_u + i)} \left(\frac{\mu_u(1+k_u)}{\Omega_u} \right)^i z^{i+\mu_u-1}, \end{aligned} \quad (6)$$

where $z \in (y_d, x)$, $u \in (p, d)$, and p , and d denote the subscripts of the channel coefficient from ST to PR or SR, respectively; y_d, x is the channel power gain of the link from ST to SR or PR, respectively; $I_m(\cdot)$ is the modified Bessel function; and $\Gamma(\cdot)$ is the Gamma function.

Utilizing ([34] Equation (8.445)), we substitute $\lambda_u = ((1+k_u)\mu_u)/\Omega_u$ into (6), and after some algebraic manipulations, (6) can be rewritten as

$$\begin{aligned} f_u(z) &= \frac{(\lambda_u)^{(\mu_u+1)/2} (z)^{(\mu_u-1)/2} e^{-\lambda_u z}}{(\mu_u k_u)^{\mu_u-1/2} e^{\mu_u k_u}} I_{\mu_u-1} \left(2\sqrt{\mu_u k_u} \sqrt{\lambda_u z} \right) \\ &= \frac{(\lambda_u)^{\mu_u}}{e^{\mu_u k_u}} \sum_{i=0}^{\infty} \frac{(k_u \mu_u \lambda_u)^i}{i! \Gamma(\mu_u + i)} z^{i+\mu_u-1} e^{-\lambda_u z}. \end{aligned} \quad (7)$$

According to the relation between the CDF and PDF, the CDF of the channel gain can now be derived as

$$\begin{aligned} F_u(z) &= 1 - \frac{1}{e^{\mu_u k_u}} \sum_{l=0}^{\infty} \frac{(k_u \mu_u)^l}{l!} \sum_{n=0}^{\mu_u+l-1} \frac{\lambda_u^n}{n!} (z)^n e^{-\lambda_u z} \\ &= \frac{1}{e^{\mu_u k_u}} \sum_{l=0}^{\infty} \frac{(k_u \mu_u)^l}{l! \Gamma(\mu_u + l)} \gamma(\mu_u + l, \lambda_u z), \end{aligned} \quad (8)$$

where $\gamma(\mu_u + l, \lambda_u z)$ denotes the lower incomplete Gamma function from ([34] Equation (8.350.1)).

In the considered system, all eavesdropping links, though independent, are not necessarily identical, and the cooperative eavesdroppers all apply MRC techniques, such that the total channel gain of all of the wiretap links is written as $\gamma_e = \sum_{i=1}^L \gamma_{e_i}$, where γ_{e_i} is the channel gain of the link from the transmitter to E_i and L is the number of eavesdroppers. Therefore, the PDF of γ_e is given by [33] (Equation (3))

$$\begin{aligned} f(\gamma_e) &= \frac{e^{-(\gamma_e/2\beta)} \gamma_e^{U-1}}{(2\beta)^U \Gamma(U)} \sum_{k=0}^{\infty} \frac{k! c_k}{(U)_k} L_k^{(U-1)} \left(\frac{U \gamma_e}{2\beta \xi} \right) \\ &= \frac{e^{-(\gamma_e/2\beta)}}{(2\beta)^U} \sum_{k=0}^{\infty} c_k \sum_{q=0}^k \frac{(-k)_q \gamma_e^{q+U-1}}{q! \Gamma(U+q)} \left(\frac{U}{2\beta \xi} \right)^q, \end{aligned} \quad (9)$$

where $(U)_k = \Gamma(U+k)/\Gamma(U)$ denotes the Pochhammer symbol [32], the series representation of the generalized Laguerre polynomial $L_k^{(U-1)}$ ([35] Equation (05.08.02.0001.01)). The efficient c_k in $f(\gamma_e)$ can be calculated as

$$\begin{aligned} c_0 &= \left(\frac{U}{\xi} \right)^U \exp \left\{ -\frac{1}{2} \sum_{i=1}^L \frac{\chi_i a_i (U - \xi)}{\beta \xi + a_i (U - \xi)} \right\} \\ &\quad \times \prod_{i=1}^L \left(1 + \frac{a_i}{\beta} \left(\frac{U}{\xi} - 1 \right) \right)^{-\mu_{e_i}}, \end{aligned} \quad (10)$$

$$c_k = \frac{1}{k} \sum_{j=0}^{k-1} c_j d_{k-j}, \quad k \geq 1, \quad (11)$$

$$\begin{aligned} d_j &= -\frac{j\beta U}{2\xi} \sum_{i=1}^L \chi_i a_i (\beta - a_i)^{j-1} \left(\frac{\xi}{\beta \xi + a_i (U - \xi)} \right)^{j+1} \\ &\quad + \sum_{i=1}^L \mu_{e_i} \left(\frac{1 - a_i/\beta}{1 + (U/\xi - 1)a_i/\beta} \right)^j \quad (j \geq 1), \end{aligned} \quad (12)$$

where $a_i = \Omega_{e_i}/[2\mu_{e_i}(1+k_{e_i})]$; $\chi_{e_i} = 2k_{e_i}\mu_{e_i}$; $U = \sum_{i=0}^L \mu_i$; L is the number of eavesdroppers; Ω_{e_i} is the average power gain of the i th wiretap link; and k_{e_i}, μ_{e_i} are the channel coefficients of the i th wiretap link. The parameters ξ and β must be carefully selected to guarantee the convergence of the series in (9). Specifically, when $\xi < U/2$ and $\beta > 0$, (9) will converge in any finite interval; if $\xi \geq U/2$, β must be chosen as $\beta > (2 - U/\xi)a_{(n)}/2$, to make certain the uniform convergence of (9) in any finite interval, where $a_{(n)} = \max \{a_i\}$ ($i = 1, \dots, L$).

4. Analysis of Secrecy Outage Probability

According to information security theory, perfect secrecy connection can be guaranteed if the rate of encoding of the confidential data into code words is lower or equal to the secrecy capacity. Otherwise, the security of the information will be compromised. In this section, we focus on analyzing the SOP, which is an important performance metric of

describing the security of the considered system; it denotes the maximum achievable rate. The secrecy capacity of CRN is

$$C_s = \begin{cases} C_D - C_E \gamma_d > \gamma_e, \\ 0 \gamma_d \leq \gamma_e, \end{cases} \quad (13)$$

where $C_D = \log_2(1 + \gamma_D)$ and $C_E = \log_2(1 + \gamma_e)$ are the instantaneous channel capacity of main and wiretap link (s), respectively.

For a CRN working in underlay mode, in order to guarantee the quality of the service for the primary network, the transmitter power of ST must be constrained by the maximum interference threshold, I_p , that the primary user can tolerate and its maximum transmitter power, P_{\max} , as

$$\bar{P}_s = \min \left\{ \frac{I_p}{x}, P_{\max} \right\}. \quad (14)$$

From the definition of SOP, it can be denoted as

$$\begin{aligned} \text{SOP} &= \Pr \{C_s \leq C_{\text{th}}\} \\ &= \Pr \left\{ C_s \leq C_{\text{th}}, x < \frac{I_p}{P_{\max}} \right\} + \Pr \left\{ C_s \leq C_{\text{th}}, x \geq \frac{I_p}{P_{\max}} \right\} \\ &= \underbrace{\Pr \{C_s \leq C_{\text{th}}, P_s = P_{\max}\}}_{\text{SOP}_1} + \underbrace{\Pr \left\{ C_s \leq C_{\text{th}}, P_s = \frac{I_p}{x} \right\}}_{\text{SOP}_2}. \end{aligned} \quad (15)$$

From expression (15), we can see that the SOP is composed of two components, with reference to SOP_1 and SOP_2 . The remainder of this section will consider these 2 terms in greater detail.

4.1. SOP_1 Analysis. When $\bar{P}_s = P_{\max}$, the work mode is the same as for a normal communication system. According to probability theory, SOP_1 can be calculated as

$$\begin{aligned} \text{SOP}_1 &= \Pr \{C_s \leq C_{\text{th}}, \bar{P}_s = P_{\max}\} \\ &= \underbrace{\Pr \{ \gamma_d \leq e^{C_{\text{th}}} \gamma_e + e^{C_{\text{th}}} - 1 \}}_{I_1} \underbrace{\Pr \left\{ x \leq \frac{I_p}{P_{\max}} \right\}}_{I_2}. \end{aligned} \quad (16)$$

Next, we derive an expression for I_1 , from (16):

$$I_1 = \Pr \{ \gamma_d \leq e^{C_{\text{th}}} \gamma_e + e^{C_{\text{th}}} - 1 \}, \quad (17)$$

where $\gamma_d = (P_s/\sigma^2)y_d$, $\gamma_e = (\bar{P}_s/\sigma^2)y_e$, and $\bar{P}_s = P_{\max}$. Rearranging terms and using mathematical methods, we can obtain

$$\begin{aligned} I_1 &= \Pr \left\{ \gamma_d \leq \Theta y_e + \frac{\Theta - 1}{\alpha} \right\} \\ &= \int_0^\alpha F_D \left(\Theta y_e + \frac{\Theta - 1}{\alpha} \right) f_E(y_e) dy_e, \end{aligned} \quad (18)$$

where $\Theta = e^{C_{\text{th}}}$ and $\alpha = P_{\max}/\sigma^2$. Taking account of the fact that $I_1 > \int_0^\alpha F_D(\Theta y_e) f_E(y_e) dy_e$, here, we derive the lower bound of I_1 as

$$I_1^L = \int_0^\alpha F_D(\Theta y_e) f_E(y_e) dy_e. \quad (19)$$

Substituting (8) and (9) into (19) and utilizing [38] (Equation (3.10.1.2)), we derived the expression of I_1^L as

$$\begin{aligned} I_1^L &= \frac{(2\beta\Theta\lambda_d)^{\mu_d}}{e^{\mu_d k_d}} \sum_{k=0}^\infty c_k \times \sum_{q=0}^k \frac{(-k)_q}{q! \Gamma(U+q)} \left(\frac{U}{\xi} \right)^q \\ &\times \sum_{i=0}^\infty \frac{(2\beta\Theta\lambda_d k_d \mu_d)^i \Gamma(\mu_d + i + q + U)}{i! \Gamma(\mu_d + i) (\mu_d + i)} \\ &\times {}_2F_1(\mu_d + i, \mu_d + i + q + U; \mu_d + i + 1; -2\beta\Theta\lambda_d). \end{aligned} \quad (20)$$

Applying (8) to this equation, we get

$$I_2 = F_p \left(\frac{I_p}{P_{\max}} \right) = \frac{1}{e^{\mu_p k_p}} \sum_{l=0}^\infty C_l. \quad (21)$$

From this, the lower bound of SOP_1 can be obtained by applying (20) and (21) as

$$\begin{aligned} \text{SOP}_1^L &= C_0 \sum_{k=0}^\infty \sum_{l=0}^\infty \sum_{q=0}^k \sum_{i=0}^\infty c_k C_i C_l C_q \Gamma(\mu_d + i + q + U) {}_2F_1(\mu_d \\ &+ i, \mu_d + i + q + U; \mu_d + i + 1; -2\beta\Theta\lambda_d), \end{aligned} \quad (22)$$

where

$$\begin{aligned} C_0 &= \frac{1}{e^{\mu_p k_p}} \frac{(2\beta\Theta\lambda_d)^{\mu_d}}{e^{\mu_d k_d}}, \\ C_i &= \frac{(2\beta\Theta\lambda_d k_d \mu_d)^i}{i! (\mu_d + i) \Gamma(\mu_d + i)}, \\ C_l &= \frac{(k_p \mu_p)^l}{l! \Gamma(\mu_p + l)} \gamma \left(\mu_p + l, \lambda_p \frac{I_p}{P_{\max}} \right), \\ C_q &= \frac{(-k)_q}{q! \Gamma(U+q)} \left(\frac{U}{\xi} \right)^q. \end{aligned} \quad (23)$$

4.2. SOP_2 Analysis. From (15), SOP_2 can be expressed as

$$\begin{aligned} \text{SOP}_2 &= \Pr \left\{ C_s \leq C_{\text{th}}, P_s = \frac{I_p}{x} \right\} \\ &= \Pr \left\{ \frac{1 + \gamma_d}{1 + \gamma_e} \leq e^{C_{\text{th}}}, x > \frac{I_p}{P_{\max}} \right\} \\ &= \Pr \left\{ \gamma_d \leq e^{C_{\text{th}}} \gamma_e + e^{C_{\text{th}}} - 1, x > \frac{I_p}{P_{\max}} \right\}. \end{aligned} \quad (24)$$

Let $\beta_2 = I_p/\sigma^2$, after some mathematical operations similar to those employed for I_1 , we obtain the following expression for SOP_2 :

$$\begin{aligned} SOP_2 &= \Pr \left\{ y_d \leq \Theta y_e + \frac{\Theta - 1}{\beta_2} x, x > \frac{I_p}{P_{\max}} \right\} \\ &= \int_{I_p/P_{\max}}^{\infty} H(x) f_p(x) dx, \end{aligned} \quad (25)$$

where $H(x) = \int_0^{\infty} F_D(\Theta y_e + ((\Theta - 1)/\beta_2)x) f_E(y_e) dy_e$. Substituting (8) into this equation, after some mathematical derivation, we can obtain $H(x)$ as

$$H(x) = 1 - I_H(x), \quad (26)$$

where

$$\begin{aligned} I_H(x) &= \frac{1}{e^{\mu_d k_d}} \sum_{i=0}^{\infty} \frac{(k_d \mu_d)^i}{i!} \sum_{n=0}^{\mu_d + i - 1} \frac{\lambda_d^n}{n!} \\ &\cdot \int_0^{\infty} e^{-\lambda_d (\Theta y_e + ((\Theta - 1)/\beta_2)x)} \left(\Theta y_e + \frac{\Theta - 1}{\beta_2} x \right)^n f_E(y_e) dy_e. \end{aligned} \quad (27)$$

Then, substituting (7) into (25), $I_H(x)$ can be given by

$$\begin{aligned} I_H(x) &= \frac{(\varphi)^U}{e^{\mu_d k_d}} \sum_{g=0}^{\infty} \frac{(k_d \mu_d)^g}{g!} \sum_{n=0}^{\mu_d + g - 1} \frac{(1 - \varphi)^n}{n!} \\ &\cdot \sum_{k=0}^{\infty} c_k \sum_{q=0}^k \frac{(-k)_q}{q! \Gamma(U + q)} \left(\frac{\varphi U}{\xi} \right)^q \\ &\times \sum_{d=0}^n C_n^d \left(\frac{\Theta - 1}{\beta_2} \right)^d (q + U - 1 + n - d)! \\ &\cdot \left(\frac{\lambda_d}{1 - \varphi} \right)^d x^d e^{-\lambda_d ((\Theta - 1)/\beta_2)x}, \end{aligned} \quad (28)$$

where $\varphi = 1/(2\beta\lambda_d\Theta + 1)$; substituting (26) into (25), SOP_2 becomes

$$SOP_2 = 1 - I_2 - \underbrace{\int_{I_p/P_{\max}}^{\infty} I_H(x) f_p(x) dx}_{I_{p_2}}. \quad (29)$$

From this, we can substitute (28) and (7) into I_{p_2} , and with the aid of binomial expansion and [34] (Equation (3.351.3)), I_{p_2} can be shown to be

$$\begin{aligned} I_{p_2} &= D_0 \sum_{i=0}^{\infty} \sum_{g=0}^{\infty} \sum_{n=0}^{\mu_d + g - 1} \sum_{k=0}^{\infty} \sum_{q=0}^k \sum_{d=0}^n D_i D_g D_n c_k D_q D_d C_n^d \\ &\cdot (q + U - 1 + n - d)! \\ &\times \Gamma \left(\mu_p + i + d, \left(\lambda_d \frac{\Theta - 1}{\beta_2} + \lambda_p \right) \frac{I_p}{P_{\max}} \right), \end{aligned} \quad (30)$$

where

$$\begin{aligned} D_0 &= \frac{\varphi^U \psi^{\mu_p}}{e^{k_d \mu_d + \mu_p k_p}}, \\ D_i &= \frac{(k_p \mu_p \psi)^i}{i! \Gamma(\mu_p + i)}, \\ D_g &= \frac{(k_d \mu_d)^g}{g!}, \\ D_n &= \frac{(1 - \varphi)^n}{n!}, \\ D_d &= \left(\frac{1 - \psi}{1 - \varphi} \right)^d, \end{aligned} \quad (31)$$

$$D_q = ((-k)_q / q! \Gamma(U + q)) (\varphi U / \xi)^q,$$

$$\psi = \lambda_p / \lambda_d ((\Theta - 1) / \beta_2) + \lambda_p.$$

$\Gamma(x, y)$ is the upper incomplete Gamma function ([34] Equation (8.350.2)). Making use of the derivation result, the lower SOP can be obtained as

$$SOP^L = 1 - I_2 - I_{p_2} + SOP_1^L. \quad (32)$$

5. Analysis of Secrecy Outage Probability Asymptotic Secure Outage Probability

Although the expressions of SOP can help us perform numerical analysis on the secrecy outage performance of the considered system, asymptotic analysis can also be used to further evaluate the system performance. Therefore, we focus on the derivation of an asymptotic expression of SOP in this section and study the impact of the maximum transmit power (P_{\max}) of ST and the maximum interference (I_p) that PU can tolerate on the secrecy communication with multiple eavesdroppers.

In the high-SNR region, the asymptotic SOP can be defined as

$$SOP^{\infty} = (G_a \Omega_d)^{-G_d} + o(\Omega_d^{-G_d}), \quad (33)$$

where $G_d = \mu_d$ denotes the secrecy diversity order and $o(\cdot)$ represents higher order terms. The secrecy array gain is

$$\begin{aligned} G_a &= \frac{1}{(1 + k_d) \mu_d} \left\{ \frac{1}{(2\beta\Theta)^U (\mu_d) e^{\mu_p k_p}} \left(\frac{\Theta - 1}{\alpha} \right)^{U + \mu_d} \right. \\ &\cdot \sum_{l=0}^{\infty} \sum_{k=0}^{\infty} \sum_{q=0}^k A_0 C_l c_k A_q \times \left(\frac{\Theta - 1}{\Theta \alpha} \right)^q \Gamma(q + U) \Psi \\ &\cdot \left(q + U, q + U + \mu_d + 1; \frac{\Theta - 1}{2\beta\Theta \alpha} \right) \\ &+ \frac{(2\beta\Theta)^{\mu_d}}{(\mu_d) e^{\mu_p k_p}} \sum_{k=0}^{\infty} \sum_{q=0}^k \sum_{d=0}^{\mu_d} \sum_{i=0}^{\infty} A_0 c_k A_q A_d A_i \Gamma \\ &\cdot \left. \left(\mu_p + i + d, \lambda_p \frac{I_p}{P_{\max}} \right) \right\}^{-1/\mu_d}, \end{aligned} \quad (34)$$

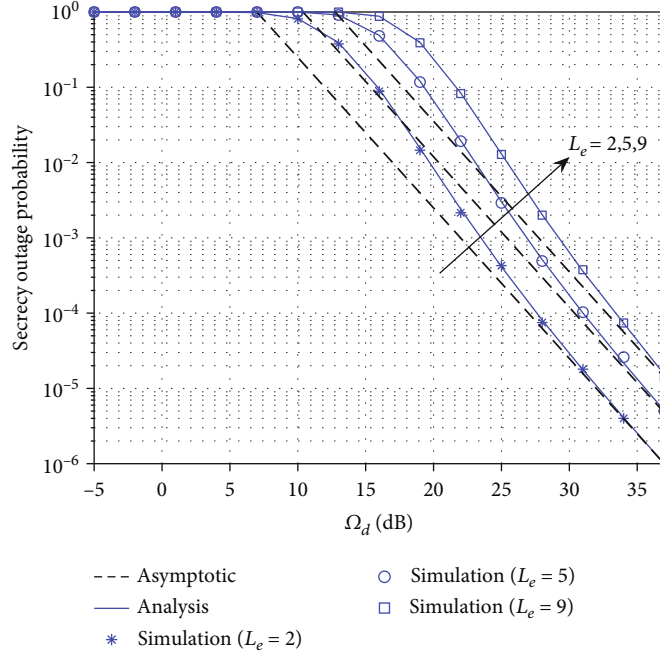


FIGURE 2: SOP with different L_e values, $\Omega_p = 2$, $\Omega_e = 4$, $I_p = 0.1$, $C_{th} = 0.1$; $(k_p, \mu_p) = (2, 2)$; $(k_d, \mu_d) = (3, 2)$; $(k_e, \mu_e) = (2, 2)$.

where

$$\begin{aligned}
 A_0 &= \frac{1}{e^{\mu_d k_d}}, \\
 A_q &= \frac{(-k)_q}{q! \Gamma(U+q)} \left(\frac{U}{\xi} \right)^q, \\
 A_d &= C_{\mu_d}^d \left(\frac{\Theta - 1}{\beta_2} \right)^d \left(\frac{1}{\lambda_p 2\beta\Theta} \right)^d (\mu_d - d + q + U - 1)!, \\
 A_l &= \frac{(k_p \mu_p \lambda_p)^l}{l! \Gamma(\mu_p + l)}.
 \end{aligned} \tag{35}$$

6. Probability of Strictly Positive Secrecy Capacity

In information theory, the absolute security of communication can be guaranteed only when the instantaneous secrecy capacity exceeds zero. Thus, SPSC is considered to be an important indicator for measuring the secure communication system, which is given by the formula

$$\text{SPSC} = \Pr \{C_s > 0\} = 1 - \Pr \{C_s \leq 0\}. \tag{36}$$

Substituting C_{th} into (16), we can get

$$\begin{aligned}
 \text{SOP} \Big|_{C_{th}=0} &= \sum_{k=0}^{\infty} \sum_{q=0}^k \sum_{i=0}^{\infty} B_0 c_k A_q A_i (2\beta)^{i+q+\mu_d} \Gamma(\mu_d + i + q + U) \\
 &\quad \times {}_2F_1(\mu_d + i, \mu_d + i + q + U; \mu_d + i + 1; -2\lambda_d \beta),
 \end{aligned} \tag{37}$$

where $\lambda_d = (\mu_d(1 + k_d))/\Omega_d$; $U = \sum_{i=0}^L \mu_{ei}$; $B_0 = \lambda_d^{\mu_d} / e^{\mu_d k_d}$; $A_i = (k_d \mu_d \lambda_d)^i / i! (\mu_d + i)!$; and A_q and A_0 are the same as mentioned above. Then, SPSC can be obtained as

$$\begin{aligned}
 \text{SPSC} &= 1 - \sum_{k=0}^{\infty} \sum_{q=0}^k \sum_{i=0}^{\infty} A_0 c_k A_q A_i (2\beta)^{i+q+\mu_d} \Gamma(\mu_d + i + q + U) \\
 &\quad \times {}_2F_1(\mu_d + i, \mu_d + i + q + U; \mu_d + i + 1; -2\lambda_d \beta).
 \end{aligned} \tag{38}$$

From this expression of SPSC, we can see that it does not rely on the primary channel gain but is only dependent on the gain of eavesdropping channel and main channel.

7. Numerical Results

In this section, the curves obtained by Monte Carlo simulation of SOP for the considered system are compared with the above mathematical analysis in order to consider the impact which the different related parameters have on the security of the cognitive networks. After verification, when the value of the variable reaches 50 times, it converges to a constant value. Infinite series does not affect the simulation results. The parameters utilised in this paper are set to $P_{\max} = 1$ and $\sigma = 1$, and the other parameter settings are as shown in the relevant figure.

Figure 2 shows the curves of the SOP for different numbers of eavesdroppers. It can be seen that the analysis results are in agreement with the simulation curves across the entire range of SNRs. In addition, the approximate curve is the tangent line of the exact theoretical results. Moreover, we can also see that the SOP will increase as the number of eavesdroppers increases. This is due to the fact that all of

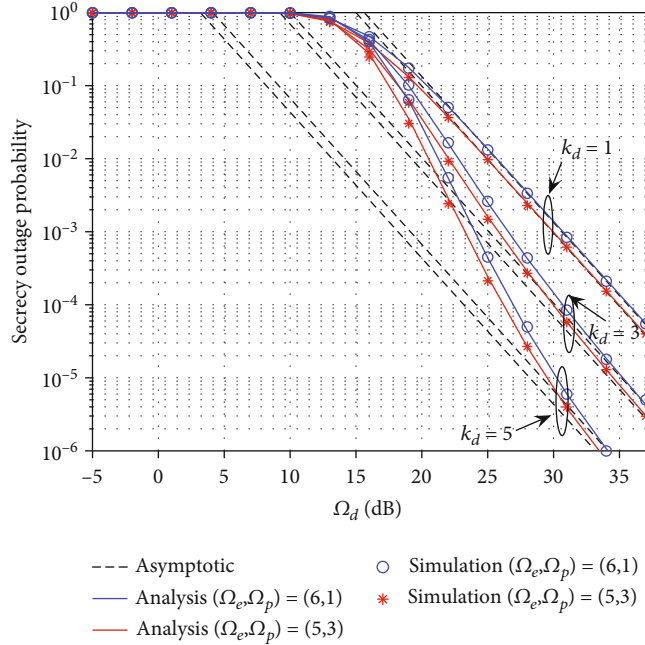


FIGURE 3: SOP with $(k_p, \mu_p) = (2, 2)$, $\mu_d = 2$; $(k_{ei}, \mu_{ei})_{i=1,2,3} = (3, 2)(5, 2)(4, 1)$; red traces $\Omega_p = 1, \Omega_e = 6$; blue traces $\Omega_p = 3, \Omega_e = 5$.

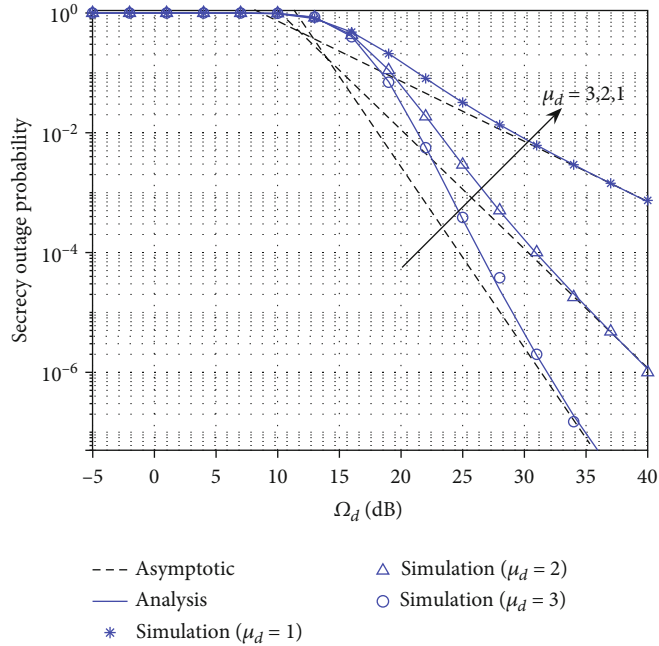


FIGURE 4: SOP with different μ_d values $\Omega_p = 2, \Omega_e = 6$; $I_p = 0.1$; $C_{th} = 0.01$; $(k_p, \mu_p) = (1, 1)$; $k_d = 3$; $(k_{ei}, \mu_{ei})_{i=1,2,3} = (2, 2)(3, 1)(2, 1)$.

the eavesdroppers cooperate with each other. The more eavesdroppers there are, the stronger the wiretapped signal strength, which means that the eavesdropper SNR increases, followed by an increase in the SOP.

Figures 3 and 4 provide the curves of SOP versus Ω_d for different values of k_d and μ_d . In order to observe the variation of SOP with k_d more clearly, two groups of experiments with different parameters were carried out and the results are

shown in Figure 3. It can be seen that SOP decreases with the increase of either k_d or μ_d . Moreover, we can see that with this increase in the value of k_d or μ_d which means the SNR at the receiver increases, the secrecy performance will improve.

Figures 5 and 6 show the influence of channel parameters (k_d, μ_d) on SOP. In Figure 6, we plot the different curves of SOP when k_d and μ_d are varied. The blue curve is the difference between $(k_d, \mu_d) = (1, 1)$ and $(k_d, \mu_d) = (1, 2)$; the red

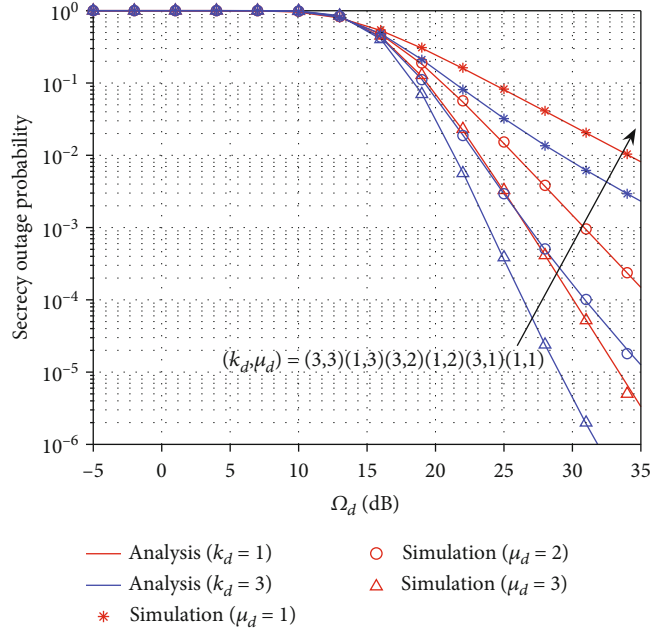


FIGURE 5: SOP with different μ_d and k_d values and $\Omega_p = 2$, $\Omega_e = 6$; $I_p = 0.1$, $C_{th} = 0.01$; $(k_p, \mu_p) = (1, 1)$; $(k_{ei}, \mu_{ei})_{i=1,2,3} = (2, 2)(3, 1)(2, 1)$.

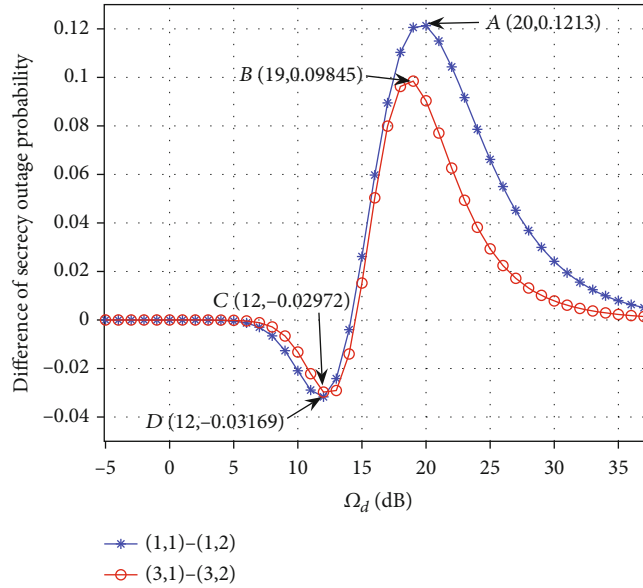


FIGURE 6: The difference of SOP between $(k_d, \mu_d) = (1, 1)$, $(k_d, \mu_d) = (1, 2)$ and $(k_d, \mu_d) = (3, 1)$, $(k_d, \mu_d) = (3, 2)$.

curve shows the difference of SOP at $(k_d, \mu_d) = (3, 1)$ and $(k_d, \mu_d) = (3, 2)$. It is worth noting that the two curves coincide together in the low Ω_d region; when Ω_d is very high, the difference is very small. When $\Omega_d = 12$, the difference of SOP is a negative peak; the corresponding positive maximum appears at $\Omega_d = 19, 20$. In other words, at these two points, the channel parameters (k_d, μ_d) have the greatest impact on the channel security performance.

From Figure 7, it can be seen that the higher the value of I_p , the better the security of the system, since ST can transmit more high power information. We can also see

that there is a limitation for the SOP in the high I_p . This is attributed to the fact that the maximum transmit power of ST (P_{max}) is equal to 1, while $I_p \rightarrow \infty$, as suggested in the above sections.

Next, without loss of generality, we plot a set of curves with different parameters to observe the effect of C_{th} on SOP. As we can see from Figure 8, the SOP for lower C_{th} outperforms the ones for the higher C_{th} . This is due to the fact that SOP is the probability that secrecy capacity C_s remains below the output threshold C_{th} . The lower the threshold C_{th} is, the smaller the corresponding probability obtained. In

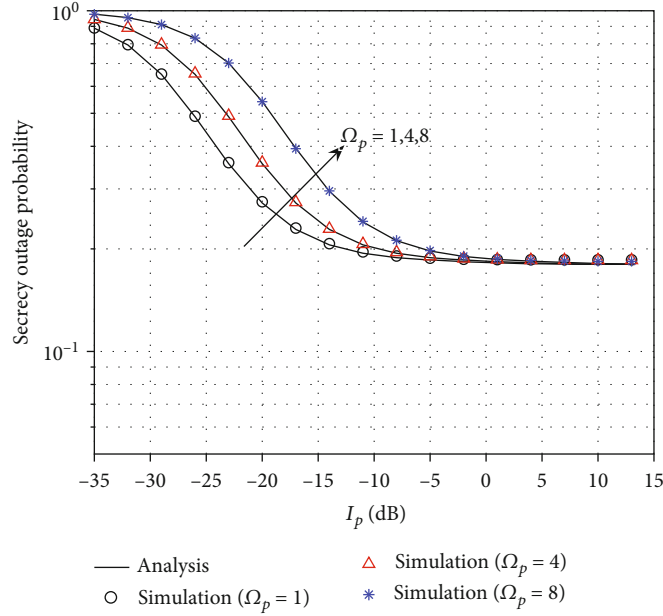


FIGURE 7: SOP versus I_p with $\Omega_d = 15$, $\Omega_e = 1$; $C_{th} = 0.1$; $(k_p, \mu_p) = (1, 1)$; $(k_d, \mu_d) = (2, 1)$; $(k_{ei}, \mu_{ei})_{i=1,2,3} = (4, 1)(5, 2)(3, 1)$.

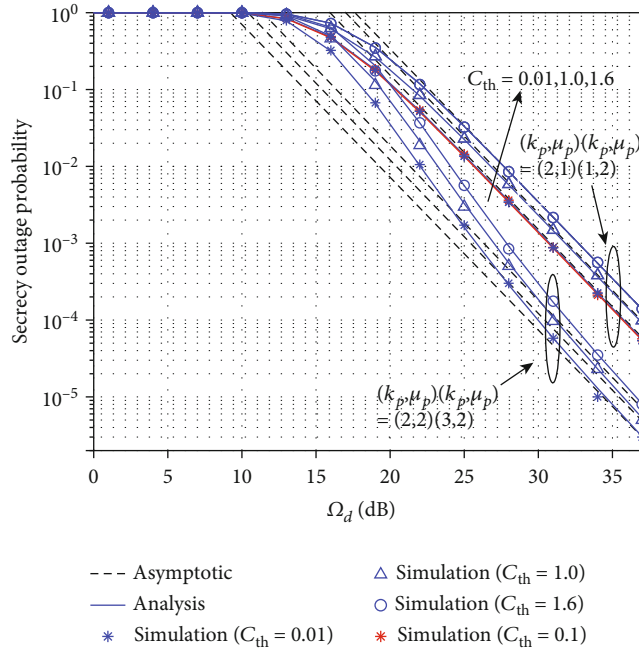


FIGURE 8: SOP versus Ω_d with $I_p = 0.1$; $(k_{ei}, \mu_{ei})_{i=1,2,3} = (4, 1)(5, 2)(3, 2)$; up ones $\Omega_p = 1$, $\Omega_e = 6$; $(k_p, \mu_p)(k_d, \mu_d) = (2, 1)(1, 2)$; down ones $\Omega_p = 3$, $\Omega_e = 5$; $(k_p, \mu_p)(k_d, \mu_d) = (2, 2)(3, 2)$.

particular, the red curve of $C_{th} = 0.01$ is almost identical to the blue curve of $C_{th} = 0.1$.

Figure 9 shows the SPSC for different values of Ω_p . From Figure 9, we can see that the SPSC decreases with the increasing values of (k_e, μ_e) . This can be explained by noting that the larger (k_e, μ_e) implies a stronger signal obtained by eavesdroppers; hence, the eavesdropper SNR increases which decreases the secrecy capacity and thereby increases the

SOP. In addition, we can also observe that the SPSC does not change with the variation of (k_p, μ_p) as discussed in (38).

To sum up, the interesting conclusion can be obtained that the improvement of the confidentiality is manifested by a larger value of SPSC and a smaller value of SOP. Therefore, a smaller number of eavesdropping antennas, a larger k_d , a larger μ_d , and a smaller C_{th} can improve the confidentiality of the CRN model.

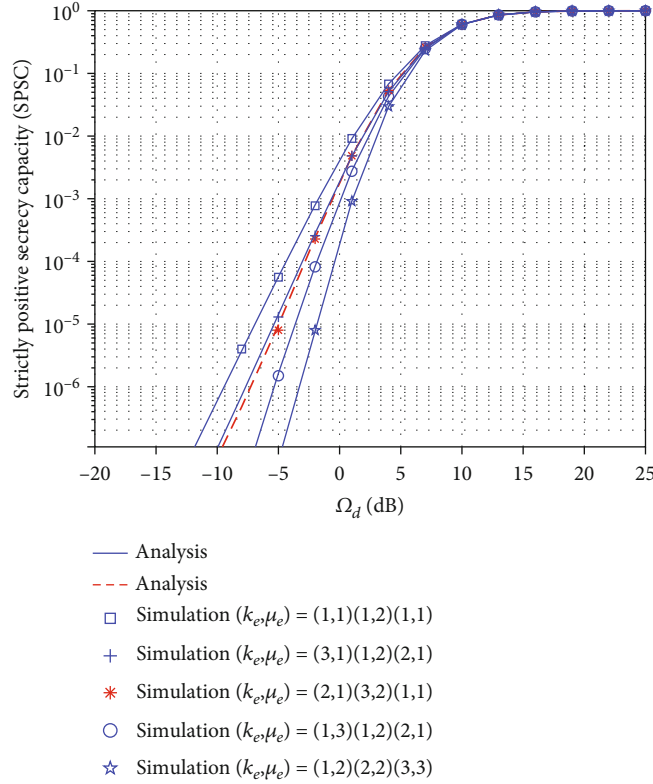


FIGURE 9: SPSC with $\Omega_p = 2, \Omega_e = 4; I_p = 0.1; \sigma = 1, P_{\max} = 1; (k_p, \mu_p) = (2, 2); (k_d, \mu_d) = (1, 2)$.

8. Conclusions

In this paper, we have investigated the security performance for CRNs which operate in underlay mode with 5G, beyond 5G, and Internet of Things (IoT) technologies, where all channels experience independent, but not necessarily identically, k - μ fading. The exact and asymptotic theoretical expressions of SOP are derived for the considered system in the presence of multiple eavesdroppers. We also derive an equivalent expression for the SPSC of such a system. These resulting formulae show that the secrecy diversity order relies on the main channel parameter. This is corroborated with simulation results, which also prove this conclusion. Finally, Monte Carlo simulation results are presented to verify these analytical expressions and illustrate the influence which factors have on the secrecy performance versus the SNR ratio (s) of the channel (s).

Data Availability

Data used to support the findings of this study are available from the corresponding author upon request.

Conflicts of Interest

The authors declare that there is no conflict of interest about the publication of this paper.

References

- [1] L. Xu, X. Yu, and T. A. Gulliver, "Intelligent outage probability prediction for mobile IoT networks based on an IGWO-Elman neural network," *IEEE Transactions on Vehicular Technology*, vol. 70, no. 2, pp. 1365–1375, 2021.
- [2] C. E. Shannon, "Communication theory of secrecy systems*," *The Bell System Technical Journal*, vol. 28, no. 4, pp. 656–715, 1949.
- [3] A. D. Wyner, "The wire-tap channel," *The Bell System Technical Journal*, vol. 54, no. 8, pp. 1355–1387, 1975.
- [4] A. Mathur and H. Lei, "On physical layer security of double Rayleigh fading channels for vehicular communications," *IEEE Wireless Communications Letters*, vol. 7, no. 6, pp. 1038–1041, 2018.
- [5] K. N. Le, "SOP under dual correlated Rician fading," in *2018 24th Asia-Pacific Conference on Communications (APCC)*, pp. 68–72, Ningbo, China, 2018.
- [6] C. Liu and R. Malaney, "Location-based beamforming and physical layer security in Rician wiretap channels," *IEEE Transactions on Wireless Communications*, vol. 15, no. 11, pp. 7847–7857, 2016.
- [7] M. Ahmed and L. Bai, "Secrecy capacity of artificial noise aided secure communication in MIMO Rician channels," *IEEE Access*, vol. 6, pp. 7921–7929, 2018.
- [8] H. Lei, C. Gao, Y. Guo, and G. Pan, "On physical layer security over generalized gamma fading channels," *IEEE Communications Letters*, vol. 19, no. 7, pp. 1257–1260, 2015.
- [9] H. Lei, I. S. Ansari, G. Pan, B. Alomair, and M. Alouini, "Secrecy capacity analysis over α - μ fading channels," *IEEE*

- Communications Letters*, vol. 21, no. 6, pp. 1445–1448, 2017.
- [10] H. Zhao, Z. Liu, L. Yang, and M. Alouini, “Secrecy analysis in DF relay over generalized- K fading channels,” *IEEE Transactions on Communications*, vol. 67, no. 10, pp. 7168–7182, 2019.
 - [11] J. M. Moualeu and W. Hamouda, “Secrecy performance analysis over mixed α - μ and κ - μ fading channels,” in *IEEE Wireless Communications and Networking Conference (WCNC)*, pp. 1–6, Barcelona, 2018.
 - [12] J. Sun, X. Li, M. Huang, Y. Ding, J. Jin, and G. Pan, “Performance analysis of physical layer security over k - μ and k - μ shadowed fading channels,” *IET Communications*, vol. 12, no. 8, pp. 970–975, 2018.
 - [13] L. Kong, G. Kaddoum, and H. Chergui, “On physical layer security over Fox’s H-function wiretap fading channels,” *IEEE Transactions on Vehicular Technology*, vol. 68, no. 7, pp. 6608–6621, 2019.
 - [14] M. K. Kundu, A. S. Sumona, A. S. M. Badrudduza, and S. Shabab, “Analysis of secrecy performance over correlated η - μ fading channels,” in *IEEE International Conference on Signal Processing, Information, Communication & Systems (SPICSCON)*, pp. 100–103, Dhaka, Bangladesh, 2019.
 - [15] J. Sun, H. Bie, X. Li, J. Zhang, G. Pan, and K. M. Rabie, “Secrecy performance analysis of SIMO systems over correlated kappa- μ shadowed fading channels,” *IEEE Access*, vol. 7, pp. 86090–86101, 2019.
 - [16] X. Li, M. Zhao, M. Zeng et al., “Hardware impaired ambient backscatter NOMA systems: reliability and security,” *IEEE Transactions on Communications*, vol. 69, no. 4, pp. 2723–2736, 2021.
 - [17] X. Li, M. Zhao, Y. Liu, L. Li, Z. Ding, and A. Nallanathan, “Secrecy analysis of ambient backscatter NOMA systems under I/Q imbalance,” *IEEE Transactions on Vehicular Technology*, vol. 69, no. 10, pp. 12286–12290, 2020.
 - [18] X. Li, H. Mengyan, Y. Liu, V. G. Menon, A. Paul, and Z. Ding, “I/Q imbalance aware nonlinear wireless-powered relaying of B5G networks: security and reliability analysis,” *IEEE Transactions on Network Science and Engineering*, 2020.
 - [19] H. Lei, H. Zhang, I. S. Ansari et al., “On secrecy outage of relay selection in underlay cognitive radio networks over Nakagami- m fading channels,” *IEEE Transactions on Cognitive Communications and Networking*, vol. 3, no. 4, pp. 614–627, 2017.
 - [20] H. Lei, J. Zhang, K. Park, I. S. Ansari, G. Pan, and M. Alouini, “Secrecy performance analysis of SIMO underlay cognitive radio systems with outdated CSI,” *IET Communications*, vol. 11, no. 12, pp. 1961–1969, 2017.
 - [21] J. Park, C. Jang, and J. H. Lee, “Outage analysis of underlay cognitive radio networks with multihop primary transmission,” *IEEE Communications Letters*, vol. 20, no. 4, pp. 800–803, 2016.
 - [22] K. Shim, N. T. Do, B. An, and S. Nam, “Outage performance of physical layer security for multi-hop underlay cognitive radio networks with imperfect channel state information,” in *International Conference on Electronics, Information, and Communications (ICEIC)*, pp. 1–4, Da Nang, 2016.
 - [23] L. Sboui, Z. Rezki, and M. Alouini, “Energy-efficient power allocation for underlay cognitive radio systems,” *IEEE Transactions on Cognitive Communications and Networking*, vol. 1, no. 3, pp. 273–283, 2015.
 - [24] C. Tang, G. Pan, and T. Li, “Secrecy outage analysis of underlay cognitive radio unit over Nakagami- m fading channels,” *IEEE Wireless Communications Letters*, vol. 3, no. 6, pp. 609–612, 2014.
 - [25] W. Lee, “Resource allocation for multi-channel underlay cognitive radio network based on deep neural network,” *IEEE Communications Letters*, vol. 22, no. 9, pp. 1942–1945, 2018.
 - [26] H. Zhao, H. Liu, Y. Liu, C. Tang, and G. Pan, “Physical layer security of maximal ratio combining in underlay cognitive radio unit over Rayleigh fading channels,” in *IEEE International Conference on Communication Software and Networks (ICCSN)*, pp. 201–205, Chengdu, 2015.
 - [27] A. Pandey, S. Yadav, D. T. Do, and R. Kharel, “Secrecy performance of cooperative cognitive AF relaying networks with direct links over mixed Rayleigh and double-Rayleigh fading channels,” *IEEE Transactions on Vehicular Technology*, vol. 69, no. 12, pp. 15095–15112, 2020.
 - [28] M. V. Nguyen and D. Do, “Evaluating secrecy performance of cooperative NOMA networks under existence of relay link and direct link,” *International Journal of Communication Systems*, vol. 33, no. 6, article e4284, 2019.
 - [29] M. D., “The κ - μ distribution and the η - μ distribution,” *IEEE Antennas & Propagation Magazine*, vol. 49, no. 1, pp. 68–81, 2007.
 - [30] S. L. Cotton and D. E. Simmons, “Secrecy capacity analysis over κ - μ fading channels: theory and applications,” *IEEE Transactions on Communications*, vol. 64, no. 7, pp. 3011–3024, 2016.
 - [31] J. M. Moualeu and W. Hamouda, “On the secrecy performance analysis of SIMO systems over κ - μ fading channels,” *IEEE Communications Letters*, vol. 21, no. 11, pp. 2544–2547, 2017.
 - [32] K. P. Peppas, “Sum of nonidentical squared k - μ variates and applications in the performance analysis of diversity receivers,” *IEEE Transactions on Vehicular Technology*, vol. 61, no. 1, pp. 413–419, 2012, Dhaka, Bangladesh, 2019, pp. 100–103.
 - [33] A. Roy, P. Maji, G. Cherukuri, and S. Kundu, “PHY layer security for IOT in κ - μ fading channel,” in *9th International Conference on Communication Systems and Networks (COMSNETS)*, pp. 472–475, Bangalore, 2017.
 - [34] I. Gradshteyn and I. Ryzik, *Table of Integrals, Series, and Products*, Academic, San Diego, CA, USA, 7th edition, 2007.
 - [35] Eq. (05.08.02.0001.01), <https://functions.wolfram.com/>.

Research Article

CR-NOMA Networks over Nakagami- m Fading: CSI Imperfection Perspective

Anh-Tu Le¹ and Dinh-Thuan Do²

¹Faculty of Electronics Technology, Industrial University of Ho Chi Minh City (IUH), Ho Chi Minh City 700000, Vietnam

²Department of Computer Science and Information Engineering, Asia University, Taichung 41354, Taiwan

Correspondence should be addressed to Anh-Tu Le; leanhtu@iuh.edu.vn

Received 30 March 2021; Revised 5 May 2021; Accepted 8 June 2021; Published 23 June 2021

Academic Editor: Mauro Femminella

Copyright © 2021 Anh-Tu Le and Dinh-Thuan Do. This is an open access article distributed under the Creative Commons Attribution License, which permits unrestricted use, distribution, and reproduction in any medium, provided the original work is properly cited.

There are high demands on both massive connections and high spectrum efficiency, and the cognitive radio-based nonorthogonal multiple access (CR-NOMA) system is developed to satisfy such demand. The unreal situation of CR-NOMA is considering the perfect channel state information (CSI) in receivers. This paper indicates impacts of imperfect CSI on outage and throughput performance. In particular, we focus on performance of the secondary network related to the imperfect CSI, and we derive closed-form expressions of outage probability and throughput for the downlink in such a CR-NOMA system. Particularly, a general form of Nakagami- m fading channel is adopted to examine the impact of fading on the performance of the CR-NOMA system. As the main achievement, we conduct extensive simulations and provide analyses to demonstrate the outage performance of the CR-NOMA system with CSI imperfections.

1. Introduction

Considering as a promising multiple access technique, non-orthogonal multiple access (NOMA) has been proposed due to the higher traffic adaptation and optimized spectral efficiency (SE) [1]. By sharing frequency/code/time resources, the NOMA-based networks serve multiple users allocated various power allocation (PA) coefficients. In particular, the users with weak channel qualities are required more power compared with the users possessing stronger channel conditions. The strong users benefit from successive interference cancellation (SIC) to detect their own messages [1]. By introducing a cooperative diversity gain, cooperative NOMA (co-NOMA) has been studied in various scenarios to highlight the performance of NOMA [2–5]. To enhance the reliability performance, a co-NOMA scheme was investigated in [5], in which relay nodes are assigned as the users with better channel conditions (namely, NOMA-strong users).

To further improve the SE, an underlay cognitive radio (CR) network is considered as another technique that allows secondary users (SUs) to transmit only if they do not result in

reducing performance of primary users (PUs) related to harmful interference [6]. To address some of the 5G challenges including spectrum efficiency and massive connectivity, it is necessary to study the combination of NOMA with CR networks while maintaining reliable transmission of primary and secondary users. In various circumstances of the underlay CR-NOMA developed in [7–10], a superimposed signal is sent by the secondary transmitter to the secondary NOMA destination users. The authors concluded that if the PA factors and target rates are accurately chosen, the performance of NOMA users can be enhanced.

The outage performance of CR NOMA systems has been investigated extensively in the literature [11–15]. Particularly, Nakagami- m fading channels are adopted in suitable systems such as [11, 15]. The authors in [16] studied overlay CR-inspired NOMA by introducing expressions of the outage probability. A similar scenario was performed in [17]; however, different from [16], only the best secondary user is chosen to forward the signal to the primary user. To assist in transmission between secondary NOMA users and a secondary base station (SBS), many relays are deployed [18].

In such a system, it is beneficial as the selected relay with the strongest link with the SBS is required to forward signals to the secondary receivers [18]. However, these papers assumed that channel state information (CSI) is available and exact estimation at the receivers. In practice, imperfect CSI occurs as the main reason of degraded performance. It motivates us to study the new system performance analysis for CR-NOMA over Nakagami- m fading. In particular, we evaluate numerous new challenges when compared to previous works. These main challenges are summarized as follows.

- (i) A cooperative scheme needs to be deployed in the context of NOMA transmission. Such a NOMA scheme has been recognized as a crucial approach to further improve spectral efficiency in CR-NOMA, especially for users with poor channel condition
- (ii) Spectrum sharing is required at the secondary network in CR-NOMA; then, transmit power constraint is necessary since the SUs are permitted to reuse the licensed spectrum bands belonging to the PU. Spectrum sharing performs well under the conditions that the interference to the PU is guaranteed to be less than an assigned threshold
- (iii) Outage performance of CR-NOMA network depends on the estimated channels at receiver. However, imperfect CSI make crucial impacts on SNR and then outage probability becomes worse

To address these challenges, we propose the CR-NOMA under a scenario of imperfect CSI by considering the Nakagami- m fading channel model. The proposed system in this research is challenging and more realistic compared with [19]. On the comprehensiveness, we implement our proposed method through simulations. We summarize the main contributions of this research as follows.

- (i) It need be improved performance of far NOMA users in CR-NOMA. Due to poor channel condition, the far user requires to assign a higher power allocation factor. Particularly, the secondary network is affected by interference from the primary nodes; then, relaying scheme should be implemented to achieve expected system improvement
- (ii) Impacts of interference among two networks in CR-NOMA are considered. Degraded performance can be accepted under the limitation of interference satisfied. In particular, outage probability and throughput are the two most important metrics and we derive the concrete expressions of these metrics under the constraints of transmit power and separated target rates of NOMA users
- (iii) Simulation results show the performance of the proposed CR-NOMA model using Nakagami- m fading channel models with respect to different variable conditions. We mainly focus on the trade-off between the system outage performance and other characteristic parameters such as level of CSI imper-

fections, total transmit power, and target rates. The results illustrate that the system outage behavior has a satisfied value within a certain range

2. System Model

We examine a general NOMA model as a system model shown in Figure 1 wherein a downlink of CR-NOMA scenario. The relay is necessary to serve two NOMA users U_1 and U_2 which can operate in the secondary network (SN) containing secondary source (BS) intends and relay R . Moreover, the relay operates in a decode-and-forward (DF) mode. It is noted that such SN deals with interference to the primary transmitter (PT) and primary destinations (PD) are operated in the primary network (PN). The transmit source BS in the SN is limited by transmit power of the PN. It is assumed that all nodes are equipped single antenna and operated in half-duplex mode. The Nakagami- m fading channel coefficients are adopted in the considered system with parameter m . In such a CR-NOMA system, we denote wireless channels from node a to node b as g_{ab} . In the second hop of the SN, we denote g_1 and g_2 denote the links from relay to user U_1 and U_2 , respectively. To guarantee NOMA fairness characteristic, let a_1 and a_2 be the power allocation factors. It is noted that we can assume that $a_1 > a_2$ with $a_1 + a_2 = 1$ [20, 21]. n_R , n_1 , and n_2 are denoted as Additive White Gaussian Noise (AWGN) with variance of N_0 .

In a real scenario, the imperfect CSI-related channels are known at the receivers; it is given by [22]

$$g_j = \hat{g}_j + e_j, \quad (1)$$

where $j \in \{SR, 1, 2\}$, \hat{g}_j represents the estimated channel factor, and e_j stands for the channel estimation error. Moreover, $I_p \sim \text{CN}(0, N_0\mu)$ is denoted as the interference from the PN to SN, and μ is the scaling coefficient of I_p . The CSI of primary transmitters is not available at the secondary receivers as reported in [19].

To enable functions of CR in the context of the CR-NOMA system, the transmit power of secondary node Q is restricted as [19] $P_Q \leq \min(I_{th}/|g_{QP}|^2, P_Q)$, $Q \in \{S, R\}$. We denote P_Q as the maximum average allowed transmit power, with I_{th} denoted as the interference temperature constraint (ITC) at node PD.

There are two phases in transmission at the SN. The received signal at the relay R in the first phase is computed by

$$\begin{aligned} y_{SR} &= (\hat{g}_{SR} + e_{SR})\sqrt{P_S}(\sqrt{a_1}x_1 + \sqrt{a_2}x_2) + I_p + n_R \\ &= \hat{g}_{SR}\sqrt{P_S}(\sqrt{a_1}x_1 + \sqrt{a_2}x_2) \\ &\quad + \underbrace{e_{SR}\sqrt{P_S}(\sqrt{a_1}x_1 + \sqrt{a_2}x_2)}_{\text{effective noise}} + I_p + n_R. \end{aligned} \quad (2)$$

To further evaluate performance, the signal-to-interference-plus-noise ratio (SINR) and signal-to-noise ratio (SNR) before and after performing SIC can be obtained to

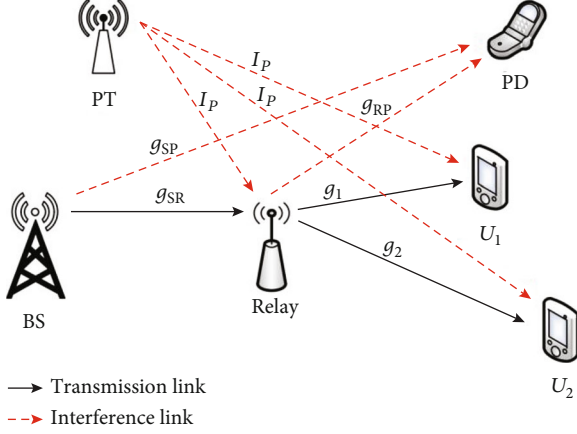


FIGURE 1: System model of CR-NOMA.

detect signal x_1 and x_2 , respectively, at R and they are given by

$$\begin{aligned} \gamma_{R,1} &= \frac{P_S |g_{\wedge_{SR}}|^2 a_1}{P_S |g_{\wedge_{SR}}|^2 a_2 + P_S |e_{SR}|^2 (a_1 + a_2) + N_0 \mu + N_0} \\ &= \frac{(P_S/N_0) |g_{\wedge_{SR}}|^2 a_1}{(P_S/N_0) |g_{\wedge_{SR}}|^2 a_2 + (P_S/N_0) |e_{SR}|^2 + \mu + 1} \\ &= \frac{|g_{\wedge_{SR}}|^2 a_1 \rho_S}{|g_{\wedge_{SR}}|^2 a_2 \rho_S + |e_{SR}|^2 \rho_S + \mu + 1}, \end{aligned} \quad (3)$$

$$\gamma_{R,2} = \frac{|g_{\wedge_{SR}}|^2 a_2 \rho_S}{|e_{SR}|^2 \rho_S + \mu + 1}, \quad (4)$$

where $\rho_S = P_S/N_0$ is defined as the transmit SNR at the BS.

In the second phase, the received signals in U_i , $i \in \{1, 2\}$, can be expressed by

$$\begin{aligned} y_i &= (\hat{g}_i + e_i) \sqrt{P_R} (\sqrt{a_1} x_1 + \sqrt{a_2} x_2) + I_P + n_i \\ &= \hat{g}_i \sqrt{P_R} (\sqrt{a_1} x_1 + \sqrt{a_2} x_2) + e_i \sqrt{P_R} (\sqrt{a_1} x_1 + \sqrt{a_2} x_2) + I_P + n_i. \end{aligned} \quad (5)$$

Considering signal at U_1 , the SINR to detect its signal x_1 is given by

$$\gamma_{U_1,1} = \frac{|g_{\wedge_1}|^2 a_1 \rho_R}{|g_{\wedge_1}|^2 a_2 \rho_R + \rho_R |e_1|^2 + \mu + 1}. \quad (6)$$

Similarly, to detect signal x_1 , x_2 , we compute the corresponding SINR at user U_2 as

$$\gamma_{U_2,1} = \frac{|g_{\wedge_2}|^2 a_1 \rho_R}{|g_{\wedge_2}|^2 a_2 \rho_R + \rho_R |e_2|^2 + \mu + 1}, \quad (7)$$

$$\gamma_{U_2,2} = \frac{|g_{\wedge_2}|^2 a_2 \rho_R}{\rho_R |e_2|^2 + \mu + 1}. \quad (8)$$

3. Performance Analysis

To compute the outage probability (OP) for users U_i , these functions are necessary, and they include the probability density function (PDF) and the cumulative distribution function (CDF) of dedicated Nakagami- m channel, respectively, as [15]

$$f_{|g_j|^2}(x) = \frac{x^{m_j-1} e^{-x/\Omega_j}}{\Gamma(m_j) (\Omega_j)^{m_j}}, \quad (9)$$

$$F_{|g_j|^2}(x) = 1 - \frac{\Gamma(m_j, x/\Omega_j)}{\Gamma(m_j)} = \frac{\gamma(m_j, x/\Omega_j)}{\Gamma(m_j)} = 1 - e^{-x/\Omega_j} \sum_{i=0}^{m_j-1} \frac{1}{i!} \left(\frac{x}{\Omega_j}\right)^i, \quad (10)$$

where $\Gamma(\alpha) = \int_0^\infty x^{\alpha-1} e^{-x} dx$, $\gamma(\alpha, x) = \int_0^x x^{\alpha-1} e^{-x} dx$, and $\Gamma(\alpha, x) = \int_x^\infty x^{\alpha-1} e^{-x} dx$ represent for the Gamma function, the lower and upper incomplete Gamma function, respectively ([23], Equations 8.310.1, 8.350.1, and 8.350.2).

It is noted that the PDF of $|e_j|^2$ is given as $f_{|e_j|^2}(x) = x^{m_{e_j}-1} e^{-x/\Omega_{e_j}} / (\Gamma(m_{e_j}) (\Omega_{e_j})^{m_{e_j}})$, in which $\Omega = \lambda/m$, m , and λ stand for the fading severity factor and mean, respectively. Regarding Nakagami fading, we also assume m is an integer number.

3.1. Outage Probability of User U_1 . The OP is determined by SNR, i.e., $\gamma_{thi} = 2^{2R_{thi}} - 1$ with R_{thi} being the target rate at user U_i , $i = 1, 2$, and its unit is BPCU (BPCU is short for bit per channel use). Then, it can be computed the OP of U_1 as [19]

$$\begin{aligned} P_{out}^1 &= 1 - \Pr(\min(\gamma_{R,1}, \gamma_{U_2,1}, \gamma_{U_1,1}) > \gamma_{th1}) \\ &= 1 - \underbrace{\Pr(\gamma_{R,1} > \gamma_{th1})}_{\Psi_1} \underbrace{\Pr(\gamma_{U_2,1} > \gamma_{th1})}_{\Psi_2} \underbrace{\Pr(\gamma_{U_1,1} > \gamma_{th1})}_{\Psi_3}. \end{aligned} \quad (11)$$

Lemma. The first term of (11) Ψ_1 is formulated by

$$\begin{aligned} \Psi_1 &= \sum_{i_{SR}=0}^{m_{SR}-1} \sum_{k_{SR}=0}^{i_{SR}} \binom{m_{e_{SR}} + i_{SR} - k_{SR} - 1}{m_{e_{SR}} - 1} \\ &\cdot \frac{\Theta^{k_{SR}} \Omega_{SR}^{m_{e_{SR}}} \beta_I^{i_{SR}} (1 - (\Gamma(m_{SP}, \rho_I/\rho_S \Omega_{SP})/\Gamma(m_{SP}))) e^{-\beta_I \Theta/\Omega_{SR}}}{k_{SR}! \Omega_{SR}^{k_{SR}} (\beta_I + \Omega_{SR})^{m_{e_{SR}} + i_{SR} - k_{SR}}} \\ &+ \sum_{i_{SR}=0}^{m_{SR}-1} \sum_{k_{SR}=0}^{i_{SR}} \binom{m_{e_{SR}} + i_{SR} - k_{SR} - 1}{m_{e_{SR}} - 1} \\ &\cdot \frac{\beta_I^{i_{SR}} \Omega_{SR}^{m_{e_{SR}}}}{k_{SR}! \Gamma(m_{SP}) (\beta_I + \Omega_{SR})^{m_{e_{SR}} + i_{SR} - k_{SR}}} \times \Gamma \\ &\cdot \left(m_{SP} + k_{SR}, \frac{(\beta_I \Theta \Omega_{SP} + \Omega_{SR}) \rho_I}{\Omega_{SR} \Omega_{SP} \rho_S}\right) \left(\frac{\Omega_{SR}}{\Theta \Omega_{SP}}\right)^{m_{SP}} \\ &\cdot \left(\beta_I + \frac{\Omega_{SR}}{\Theta \Omega_{SP}}\right)^{-m_{SP} - k_{SR}}. \end{aligned} \quad (12)$$

Proof. See the appendix.

Base on (7), we can write Ψ_2 as

$$\begin{aligned}\Psi_2 &= \Pr\left(\frac{|g\Lambda_2|^2 a_1 \rho_R}{|g\Lambda_2|^2 a_2 \rho_R + \rho_R |e_2|^2 + \mu + 1} > \gamma_{th1}\right) \\ &= \Pr\left(\frac{|g\Lambda_2|^2 a_1 \rho_R}{|g\Lambda_2|^2 a_2 \rho_R + |e_2|^2 \rho_R + \mu + 1} > \gamma_{th1}, \rho_R < \frac{\rho_I}{|g_{RP}|^2}\right) \\ &\quad + \Pr\left(\frac{|g\Lambda_2|^2 a_1 \rho_I}{|g\Lambda_2|^2 a_2 \rho_I + |e_2|^2 \rho_I + |g_{RP}|^2 (\mu + 1)} > \gamma_{th1}, \rho_R > \frac{\rho_I}{|g_{RP}|^2}\right).\end{aligned}\quad (13)$$

With the help of (9), (10), and some transform, it can be expressed as

$$\begin{aligned}\Psi_2 &= \sum_{i_1=0}^{m_1-1} \sum_{k_1=0}^{i_1} \binom{m_{e_1} + i_1 - k_1 - 1}{m_{e_1} - 1} \\ &\quad \cdot \frac{\Theta^{k_1} \Omega_1^{m_{e_1}} \beta_1^{i_1} (1 - (\Gamma(m_{RP}, \rho_I / \rho_R \Omega_{RP}) / \Gamma(m_{RP}))) e^{-\beta_1 \Theta / \Omega_1}}{k_1! \Omega_1^{k_1} (\beta_1 + \Omega_1)^{m_{e_1} + i_1 - k_1}} \\ &\quad + \sum_{i_1=0}^{m_1-1} \sum_{k_1=0}^{i_1} \binom{m_{e_1} + i_1 - k_1 - 1}{m_{e_1} - 1} \frac{\beta_1^{i_1} \Omega_1^{m_{e_1}}}{k_1! \Gamma(m_{RP}) (\beta_1 + \Omega_1)^{m_{e_1} + i_1 - k_1}} \\ &\quad \times \Gamma\left(m_{RP} + k_1, \frac{(\beta_1 \Theta \Omega_{RP} + \Omega_1) \rho_I}{\Omega_1 \Omega_{RP} \rho_R}\right) \left(\frac{\Omega_1}{\Theta \Omega_{RP}}\right)^{m_{RP}} \\ &\quad \cdot \left(\beta_1 + \frac{\Omega_1}{\Theta \Omega_{RP}}\right)^{-m_{RP} - k_1},\end{aligned}\quad (14)$$

where $\Omega_i = \Omega_i / \Omega_{e_i}$. Similarly, putting (6) into (11) and the close form of Ψ_3 can be obtained as

$$\begin{aligned}\Psi_3 &= \sum_{i_2=0}^{m_2-1} \sum_{k_2=0}^{i_2} \binom{m_{e_2} + i_2 - k_2 - 1}{m_{e_2} - 1} \\ &\quad \cdot \frac{\Theta^{k_2} \Omega_2^{m_{e_2}} \beta_1^{i_2} (1 - (\Gamma(m_{RP}, \rho_I / \rho_R \Omega_{RP}) / \Gamma(m_{RP}))) e^{-\beta_1 \Theta / \Omega_2}}{k_2! \Omega_2^{k_2} (\beta_1 + \Omega_2)^{m_{e_2} + i_2 - k_2}} \\ &\quad + \sum_{i_2=0}^{m_2-1} \sum_{k_2=0}^{i_2} \binom{m_{e_2} + i_2 - k_2 - 1}{m_{e_2} - 1} \frac{\beta_1^{i_2} \Omega_2^{m_{e_2}}}{k_2! \Gamma(m_{RP}) (\beta_1 + \Omega_2)^{m_{e_2} + i_2 - k_2}} \\ &\quad \times \Gamma\left(m_{RP} + k_2, \frac{(\beta_1 \Theta \Omega_{RP} + \Omega_2) \rho_I}{\Omega_2 \Omega_{RP} \rho_R}\right) \left(\frac{\Omega_2}{\Theta \Omega_{RP}}\right)^{m_{RP}} \\ &\quad \cdot \left(\beta_1 + \frac{\Omega_2}{\Theta \Omega_{RP}}\right)^{-m_{RP} - k_2}.\end{aligned}\quad (15)$$

Putting the result of Lemma (12), (14), and (15) into (11), the OP of x_1 is written as

$$P_{out}^1 = \begin{cases} 1 - \Psi_1 \times \Psi_2 \times \Psi_3, & \text{if } \gamma_{th1} < \frac{a_1}{a_2}, \\ 1, & \text{otherwise.} \end{cases}\quad (16)$$

□

3.2. *Outage Probability of x_2* . Similarly, it can be obtained outage probability for x_2 as

$$\begin{aligned}P_{out}^2 &= 1 - \Pr\left(\min(\gamma_{R,2}, \gamma_{U,2}) > \gamma_{th2}\right) \\ &= 1 - \underbrace{\Pr(\gamma_{R,2} > \gamma_{th2})}_{\Psi_4} \underbrace{\Pr(\gamma_{U,2} > \gamma_{th2})}_{\Psi_5}.\end{aligned}\quad (17)$$

Then, with the (4), Ψ_4 can be expressed as

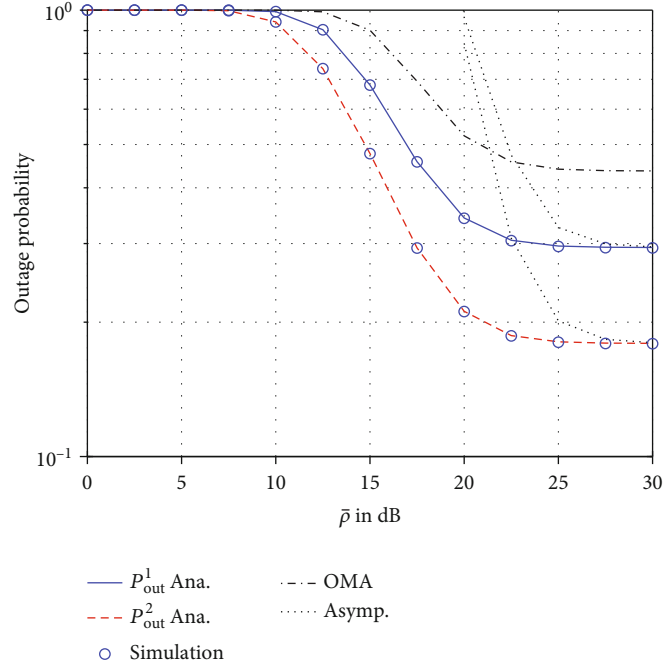
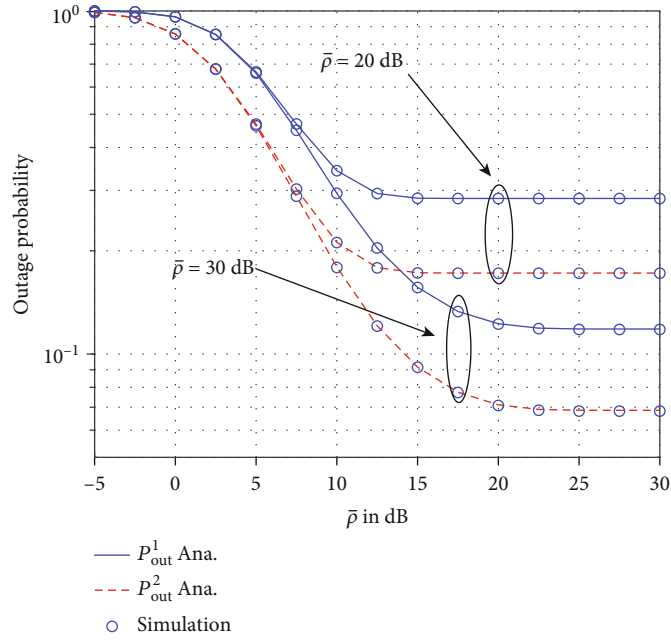
$$\begin{aligned}P_{out}^2 &= \Pr\left(\frac{|g\Lambda_{SR}|^2 a_2 \rho_S}{|e_2|^2 \rho_S + \mu + 1} > \gamma_{th1}\right) \\ &= \Pr\left(\frac{|g\Lambda_{SR}|^2 a_2 \rho_S}{|e_{SR}|^2 \rho_S + \mu + 1} > \gamma_{th1}, \rho_S < \frac{\rho_I}{|g_{SP}|^2}\right) \\ &\quad + \Pr\left(\frac{|g\Lambda_{SR}|^2 a_2 \rho_I}{|e_{SR}|^2 \rho_I + |g_{SP}|^2 (\mu + 1)} > \gamma_{th1}, \rho_S > \frac{\rho_I}{|g_{SP}|^2}\right).\end{aligned}\quad (18)$$

Similarly, the close form of Ψ_4 is expressed as

$$\begin{aligned}\Psi_4 &= \sum_{i_{SR}=0}^{m_{SR}-1} \sum_{k_{SR}=0}^{i_{SR}} \binom{m_{e_{SR}} + i_{SR} - k_{SR} - 1}{m_{e_{SR}} - 1} \\ &\quad \cdot \frac{\Theta^{k_{SR}} \Omega_{SR}^{m_{e_{SR}}} \beta_2^{i_{SR}} (1 - (\Gamma(m_{SP}, \rho_I / \rho_S \Omega_{SP}) / \Gamma(m_{SP}))) e^{-\beta_2 \Theta / \Omega_{SR}}}{k_{SR}! \Omega_{SR}^{k_{SR}} (\beta_2 + \Omega_{SR})^{m_{e_{SR}} + i_{SR} - k_{SR}}} \\ &\quad + \sum_{i_{SR}=0}^{m_{SR}-1} \sum_{k_{SR}=0}^{i_{SR}} \binom{m_{e_{SR}} + i_{SR} - k_{SR} - 1}{m_{e_{SR}} - 1} \\ &\quad \cdot \frac{\beta_2^{i_{SR}} \Omega_{SR}^{m_{e_{SR}}}}{k_{SR}! \Gamma(m_{SP}) (\beta_2 + \Omega_{SR})^{m_{e_{SR}} + i_{SR} - k_{SR}}} \\ &\quad \cdot \Gamma\left(m_{SP} + k_{SR}, \frac{(\beta_2 \Theta \Omega_{SP} + \Omega_{SR}) \rho_I}{\Omega_{SR} \Omega_{SP} \rho_S}\right) \left(\frac{\Omega_{SR}}{\Theta \Omega_{SP}}\right)^{m_{SP}} \\ &\quad \cdot \left(\beta_2 + \frac{\Omega_{SR}}{\Theta \Omega_{SP}}\right)^{-m_{SP} - k_{SR}},\end{aligned}\quad (19)$$

where $\beta_2 = \gamma_{th2} / \alpha_2$. Then, Ψ_5 is written as

$$\begin{aligned}\Psi_5 &= \sum_{i_2=0}^{m_2-1} \sum_{k_2=0}^{i_2} \binom{m_{e_2} + i_2 - k_2 - 1}{m_{e_2} - 1} \\ &\quad \cdot \frac{\Theta^{k_2} \Omega_2^{m_{e_2}} \beta_2^{i_2} (1 - (\Gamma(m_{RP}, \rho_I / \rho_R \Omega_{RP}) / \Gamma(m_{RP}))) e^{-\beta_2 \Theta / \Omega_2}}{k_2! \Omega_2^{k_2} (\beta_2 + \Omega_2)^{m_{e_2} + i_2 - k_2}} \\ &\quad + \sum_{i_2=0}^{m_2-1} \sum_{k_2=0}^{i_2} \binom{m_{e_2} + i_2 - k_2 - 1}{m_{e_2} - 1} \frac{\beta_2^{i_2} \Omega_2^{m_{e_2}}}{k_2! \Gamma(m_{RP}) (\beta_2 + \Omega_2)^{m_{e_2} + i_2 - k_2}} \\ &\quad \times \Gamma\left(m_{RP} + k_2, \frac{(\beta_2 \Theta \Omega_{RP} + \Omega_2) \rho_I}{\Omega_2 \Omega_{RP} \rho_R}\right) \left(\frac{\Omega_2}{\Theta \Omega_{RP}}\right)^{m_{RP}} \\ &\quad \cdot \left(\beta_2 + \frac{\Omega_2}{\Theta \Omega_{RP}}\right)^{-m_{RP} - k_2}.\end{aligned}\quad (20)$$


 FIGURE 2: The OP of two users versus transmit SNR with $m = 2$ and $\lambda_e = 0.01$.

 FIGURE 3: Outage performance versus transmit ρ_1 varying ρ with $m = 2$ and $\lambda_e = 0.01$.

Finally, the closed-form outage probability of x_2 is formulated as

$$P_{\text{out}}^2 = 1 - \Psi_4 \times \Psi_5. \quad (21)$$

3.3. Asymptotic Analysis. To obtain the insight about CR-NOMA systems, the asymptotic outage probability is presented in high SNR regimes $\rho = \rho_S = \rho_R \rightarrow \infty$ based on the outage probability. In high SNR, we use $e^{-x} \approx 1 - x$.

Moreover, we can write the incomplete Gamma function as

$$\gamma(a, bx) \stackrel{x \rightarrow 0}{\approx} \frac{(bx)^a}{a}. \quad (22)$$

Base on analysis, the asymptotic outage probability of x_1 is obtained as

$$P_{\text{out},\infty}^1 = 1 - \Psi_1^\infty \times \Psi_2^\infty \times \Psi_3^\infty, \quad (23)$$

where Ψ_1^∞ , Ψ_2^∞ , and Ψ_3^∞ are expressed, respectively, as

$$\begin{aligned} \Psi_1^\infty &= \sum_{i_{SR}=0}^{m_{SR}-1} \sum_{k_{SR}=0}^{i_{SR}} \binom{m_{e_{SR}} + i_{SR} - k_{SR} - 1}{m_{e_{SR}} - 1} \\ &\cdot \frac{\Theta^{k_{SR}} \Omega_{SR}^{m_{e_{SR}}} \beta_1^{i_{SR}} (\beta_1 + \Omega_{SR})^{k_{SR} - m_{e_{SR}} - i_{SR}}}{\Gamma(m_{SP} + 1) k_{SR}! \Omega_{SR}^{k_{SR}}} \left(1 - \frac{\beta_1 \Theta}{\Omega_{SR}}\right) \left(\frac{\rho_I}{\rho_S \Omega_{SP}}\right)^{m_{SP}} + \sum_{i_{SR}=0}^{m_{SR}-1} \sum_{k_{SR}=0}^{i_{SR}} \\ &\cdot \binom{m_{e_{SR}} + i_{SR} - k_{SR} - 1}{m_{e_{SR}} - 1} \frac{\Gamma(m_{SP} + k_{SR}) \beta_1^{i_{SR}} \Omega_{SR}^{m_{e_{SR}}}}{k_{SR}! \Gamma(m_{SP}) (\beta_1 + \Omega_{SR})^{m_{e_{SR}} + i_{SR} - k_{SR}}} \left(\frac{\Omega_{SR}}{\Theta \Omega_{SP}}\right)^{m_{SP}} \\ &\times \left(1 - \frac{1}{\Gamma(m_{SP} + k_{SR} + 1)} \left(\frac{(\beta_1 \Theta \Omega_{SP} + \Omega_{SR}) \rho_I}{\Omega_{SR} \Omega_{SP} \rho_S}\right)^{m_{SP} + k_{SR}}\right) \\ &\cdot \left(\beta_1 + \frac{\Omega_{SR}}{\Theta \Omega_{SP}}\right)^{-m_{SP} - k_{SR}}, \end{aligned}$$

$$\begin{aligned} \Psi_2^\infty &= \sum_{i_1=0}^{m_1-1} \sum_{k_1=0}^{i_1} \binom{m_{e_1} + i_1 - k_1 - 1}{m_{e_1} - 1} \frac{\Theta^{k_1} \Omega_1^{m_{e_1}} \beta_1^{i_1} (\beta_1 + \Omega_1)^{k_1 - m_{e_1} - i_1}}{\Gamma(m_{RP} + 1) k_1! \Omega_1^{k_1}} \\ &\cdot \left(1 - \frac{\beta_1 \Theta}{\Omega_1}\right) \left(\frac{\rho_I}{\rho_R \Omega_{RP}}\right)^{m_{RP}} + \sum_{i_1=0}^{m_1-1} \sum_{k_1=0}^{i_1} \binom{m_{e_1} + i_1 - k_1 - 1}{m_{e_1} - 1} \\ &\cdot \frac{\Gamma(m_{RP} + k_1) \beta_1^{i_1} \Omega_1^{m_{e_1}}}{k_1! \Gamma(m_{RP}) (\beta_1 + \Omega_1)^{m_{e_1} + i_1 - k_1}} \left(\frac{\Omega_1}{\Theta \Omega_{RP}}\right)^{m_{RP}} \left(\beta_1 + \frac{\Omega_1}{\Theta \Omega_{RP}}\right)^{-m_{RP} - k_1} \\ &\times \left(1 - \frac{1}{\Gamma(m_{RP} + k_1 + 1)} \left(\frac{(\beta_1 \Theta \Omega_{RP} + \Omega_1) \rho_I}{\Omega_1 \Omega_{RP} \rho_R}\right)^{m_{RP} + k_1}\right), \end{aligned}$$

$$\begin{aligned} \Psi_3^\infty &= \sum_{i_2=0}^{m_2-1} \sum_{k_2=0}^{i_2} \binom{m_{e_2} + i_2 - k_2 - 1}{m_{e_2} - 1} \frac{\Theta^{k_2} \Omega_2^{m_{e_2}} \beta_2^{i_2} (\beta_2 + \Omega_2)^{k_2 - m_{e_2} - i_2}}{k_2! \Omega_2^{k_2} \Gamma(m_{RP} + 1)} \\ &\cdot \left(1 - \frac{\beta_2 \Theta}{\Omega_2}\right) \left(\frac{\rho_I}{\rho_R \Omega_{RP}}\right)^{m_{RP}} + \sum_{i_2=0}^{m_2-1} \sum_{k_2=0}^{i_2} \binom{m_{e_2} + i_2 - k_2 - 1}{m_{e_2} - 1} \\ &\cdot \frac{\Gamma(m_{RP} + k_2) \beta_2^{i_2} \Omega_2^{m_{e_2}}}{k_2! \Gamma(m_{RP}) (\beta_2 + \Omega_2)^{m_{e_2} + i_2 - k_2}} \left(\frac{\Omega_2}{\Theta \Omega_{RP}}\right)^{m_{RP}} \left(\beta_2 + \frac{\Omega_2}{\Theta \Omega_{RP}}\right)^{-m_{RP} - k_2} \\ &\times \left(1 - \frac{1}{\Gamma(m_{RP} + k_2 + 1)} \left(\frac{(\beta_2 \Theta \Omega_{RP} + \Omega_2) \rho_I}{\Omega_2 \Omega_{RP} \rho_R}\right)^{m_{RP} + k_2}\right). \end{aligned} \quad (24)$$

Similarly, the asymptotic outage probability of x_2 is expressed as

$$P_{\text{out},\infty}^1 = 1 - \Psi_4^\infty \times \Psi_5^\infty, \quad (25)$$

where

$$\begin{aligned} \Psi_4^\infty &= \sum_{i_{SR}=0}^{m_{SR}-1} \sum_{k_{SR}=0}^{i_{SR}} \binom{m_{e_{SR}} + i_{SR} - k_{SR} - 1}{m_{e_{SR}} - 1} \\ &\cdot \frac{\Theta^{k_{SR}} (\beta_2 + \Omega_{SR})^{k_{SR} - m_{e_{SR}} - i_{SR}}}{k_{SR}! \Omega_{SR}^{k_{SR}} \Gamma(m_{SP} + 1) \Omega_{SR}^{m_{e_{SR}}} \beta_2^{-i_{SR}}} \left(1 - \frac{\beta_2 \Theta}{\Omega_{SR}}\right) \left(\frac{\rho_I}{\rho_S \Omega_{SP}}\right)^{m_{SP}} \\ &+ \sum_{i_{SR}=0}^{m_{SR}-1} \sum_{k_{SR}=0}^{i_{SR}} \binom{m_{e_{SR}} + i_{SR} - k_{SR} - 1}{m_{e_{SR}} - 1} \\ &\cdot \frac{\Gamma(m_{SP} + k_{SR}) \beta_2^{i_{SR}} \Omega_{SR}^{m_{e_{SR}}}}{k_{SR}! \Gamma(m_{SP}) (\beta_2 + \Omega_{SR})^{m_{e_{SR}} + i_{SR} - k_{SR}}} \left(\beta_2 + \frac{\Omega_{SR}}{\Theta \Omega_{SP}}\right)^{-m_{SP} - k_{SR}} \\ &\times \left(1 - \frac{1}{\Gamma(m_{SP} + k_{SR} + 1)} \left(\frac{(\beta_2 \Theta \Omega_{SP} + \Omega_{SR}) \rho_I}{\Omega_{SR} \Omega_{SP} \rho_S}\right)^{m_{SP} + k_{SR}}\right) \left(\frac{\Omega_{SR}}{\Theta \Omega_{SP}}\right)^{m_{SP}}, \end{aligned}$$

$$\begin{aligned} \Psi_5^\infty &= \sum_{i_2=0}^{m_2-1} \sum_{k_2=0}^{i_2} \binom{m_{e_2} + i_2 - k_2 - 1}{m_{e_2} - 1} \frac{\Theta^{k_2} \Omega_2^{m_{e_2}} \beta_2^{i_2} (\beta_2 + \Omega_2)^{k_2 - m_{e_2} - i_2}}{k_2! \Omega_2^{k_2} \Gamma(m_{RP} + 1)} \\ &\cdot \left(1 - \frac{\beta_2 \Theta}{\Omega_2}\right) \left(\frac{\rho_I}{\rho_R \Omega_{RP}}\right)^{m_{RP}} + \sum_{i_2=0}^{m_2-1} \sum_{k_2=0}^{i_2} \binom{m_{e_2} + i_2 - k_2 - 1}{m_{e_2} - 1} \\ &\cdot \frac{\beta_2^{i_2} \Omega_2^{m_{e_2}} \Gamma(m_{RP} + k_2)}{k_2! \Gamma(m_{RP}) (\beta_2 + \Omega_1)^{m_{e_2} + i_2 - k_2}} \left(\frac{\Omega_2}{\Theta \Omega_{RP}}\right)^{m_{RP}} \left(\beta_2 + \frac{\Omega_2}{\Theta \Omega_{RP}}\right)^{-m_{RP} - k_2} \\ &\times \left(1 - \frac{1}{\Gamma(m_{RP} + k_2 + 1)} \left(\frac{(\beta_2 \Theta \Omega_{RP} + \Omega_2) \rho_I}{\Omega_2 \Omega_{RP} \rho_R}\right)^{m_{RP} + k_2}\right). \end{aligned} \quad (26)$$

3.4. Consideration on Throughput. The achieved outage probability leads to computations on throughput to indicate the ability of transmission at fixed target rates. As an extra metric, overall throughput can be given as

$$T_{\text{total}} = (1 - P_{\text{out}}^1) R_{th1} + (1 - P_{\text{out}}^2) R_{th2}. \quad (27)$$

4. Simulation Result

The main parameters in simulation are provided in detail. First, the fixed power allocation factors are assigned for two NOMA users, $a_1 = 0.8$, $a_2 = 0.2$. In addition, we set channel gains as $\lambda_{SR} = 1$, $\lambda_{SP} = \lambda_{RP} = 0.1$, $\lambda_1 = 1$, $\lambda_2 = 2$, $R_{th} = R_{th1} = R_{th2} = 1$ (BPCU), $\lambda_e = \lambda_{e_{SR}} = \lambda_{e_1} = \lambda_{e_2}$, $m = m_{SR} = m_1 = m_2 = m_{SP} = m_{RP}$, $\mu = 0.1$, and $\rho_I = 10$ dB except for specific cases.

In Figure 2, we consider the OP versus transmit SNR at the SN. Different OP values are seen for two users at the SN due to different power allocation factors assigned to U_i . As the main achievement, the exact matching can be seen between analytical results and simulation results. Secondly, the OP of two users are better than the OMA case in the whole range of SNR ρ , which confirms the benefit of the CR-NOMA model. In addition, the OP can be improved as increasing of transmit SNR at the BS, which confirms the necessity of improving the quality of transmit signal.

In Figure 3, two cases of ρ which makes impacts on the OP of two users versus the transmit SNR at secondary source are studied. It can be seen clearly that $\rho = 30$ dB is a better case. The main reason is that $\rho = 30$ dB leads to higher SINR and then OP will be improved.

Figure 4 plots OP of two users in different fading parameters; $m = 1$, $m = 3$, and $m = 3$ are the better outage behavior. It can be seen clearly that $m = 3$ leads to a better channel which plays an important role to improve the performance of destinations. The main reason is that main expressions of SINR depend on channel gains. Therefore, higher channel gains result in higher SINR and the corresponding outage performance can be enhanced. When $m = 3$, such outage performance meets saturation lines sooner for the case of $m = 1$, which confirms that the outage performance can not be adjusted by increasing SNR at the base station at high SNR region.

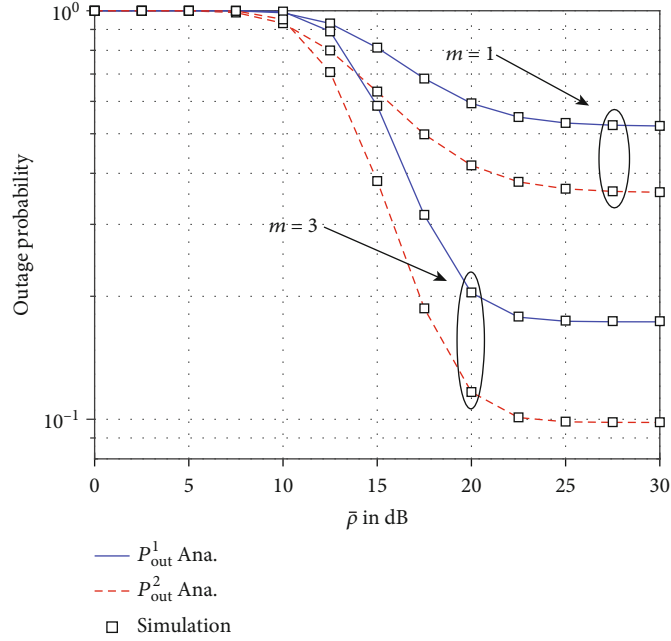


FIGURE 4: Outage performance versus SNR varying m with $\lambda_e = 0.01$.

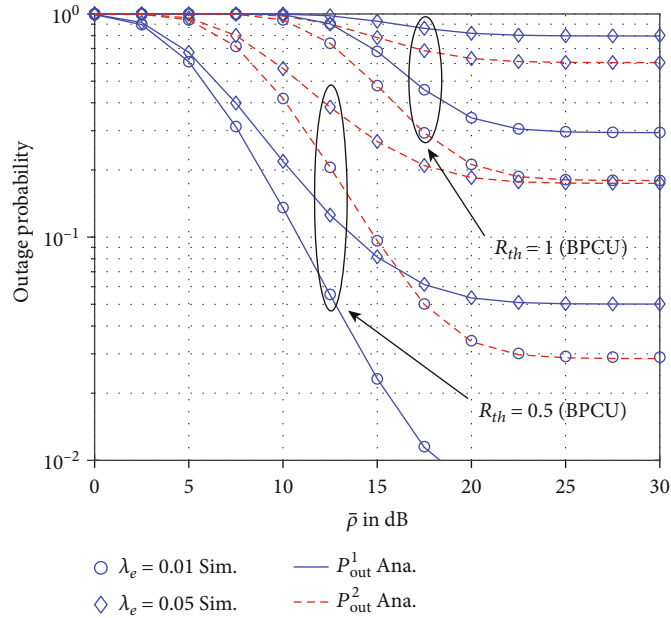


FIGURE 5: The OP versus transmit SNR as varying λ_e and R_{th} with $m = 2$.

Moreover, other trend of OP is similar as previous cases.

In Figure 5, the OP decreases significantly for the case of $R_{th} = 0.5$ and $\lambda_e = 0.01$. Two factors make influence on OP performance which is confirmed in this figure. It is important to examine OP under the impact of imperfect CSI. Therefore, λ_e related to the level of imperfect CSI is controlling parameter to target best outage performance for two users. The lower target rate R_{th} is required at lower CSI imperfection CSI that provides better outage performance. It can be observed the lowest case is the OP of user U_1 that corresponds to $\lambda_e = 0.01$ and $R_{th} = 0.5$.

Regarding impacts of power allocation factors on OP performance, Figure 6 requires we perform simulation for case of $a_1 > 0.5$. Figure 5 shows the different trends of OPs for two users U_i when we change power factor as $0.5 < a_1 < 1$. Looking at case $a_1 < 0.7$, the OP of the user U_2 is better than that of U_1 . However, opposite trend happens as $a_1 > 0.7$. The main reason is that power level allocated to each user is strictly related to the OP.

To look on throughput performance, m fading parameter makes influence on the performance of two users of such a CR-NOMA, all observations as Figure 7. It can be observed

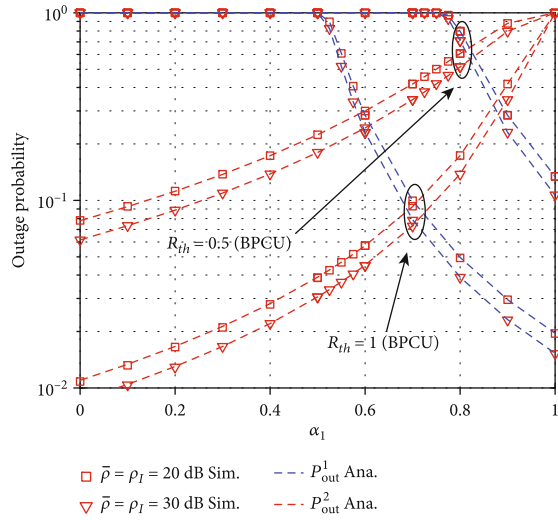


FIGURE 6: The OP versus power allocation factor α_1 with $m = 2$ and $\lambda_e = 0.01$.

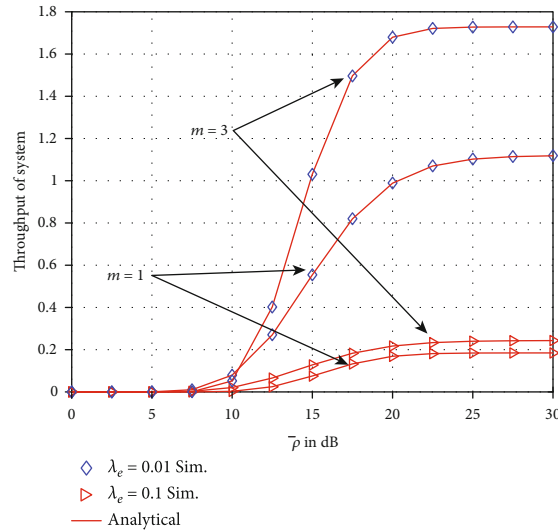


FIGURE 7: Throughput of system versus transmit SNR at BS with varying λ_e and m .

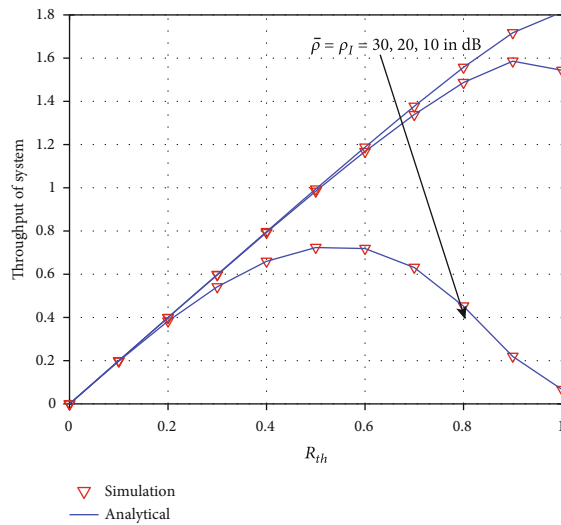


FIGURE 8: Throughput of system versus R_{th} with varying $\rho = \rho_I$.

that the highest throughput occurs at $\lambda_e = 0.01$ and $m = 3$. The ceiling throughput is also seen at a high region on transmit SNR as SNR is greater than 25 dB. Interestingly, the existence of R_{th} corresponds to maximal throughput as simulation reported in Figure 8.

5. Conclusions

In this paper, we have studied the impact of imperfect CSI on the CR-NOMA as a possible realistic scenario. Two users are evaluated in terms of outage performance to show advantages of a developed CR-NOMA system wherein NOMA users cooperate with the relay nodes. In particular, we derived the closed-form expressions of outage probabilities and throughput to show performance gaps among two NOMA users. Our simulation analysis confirms that the target rates and power allocation factors are main impacts on these metrics. The further simulation results show that CR-NOMA yields better outage performance once we limit imperfect CSI at low level and proper power allocation factor achieved.

Appendix

Proof of Lemma

Next, we further examine the outage event at the BS for x_2 and it can be formulated by the following.

It can be recalled that

$$\begin{aligned} \Xi_1 = & \Pr \left(\frac{|g_{SR}|^2 a_1 \rho_S}{|g_{SR}|^2 a_2 \rho_S + |e_{SR}|^2 \rho_S + \mu + 1} > \gamma_{th1}, \rho_S < \frac{\rho_I}{|g_{SP}|^2} \right) \\ & + \Pr \left(\frac{|g_{SR}|^2 a_1 \rho_I}{|g_{SR}|^2 a_2 \rho_I + |e_{SR}|^2 \rho_I + |g_{SP}|^2 (\mu + 1)} > \gamma_{th1}, \rho_S > \frac{\rho_I}{|g_{SP}|^2} \right), \end{aligned} \quad (A.1)$$

where $\rho_S = P_S/N_0$, $\rho_R = P_R/N_0$, and $\rho_I = I_{th}/N_0$. Then, we determine the first and second term of (A.1) which are denoted as C_1 and C_2 , respectively. Firstly, C_1 can be rewritten as

$$C_1 = \Pr \left(|g_{SR}|^2 > \beta_1 |e_{SR}|^2 + \beta_1 \Theta \right) \Pr \left(|h_{SP}|^2 < \frac{\rho_I}{\rho_S} \right), \quad (A.2)$$

where $\beta_1 = \gamma_{th1}/a_1 - \gamma_{th1}a_2$ and $\Theta = \mu + 1/\rho_S$.

Then, the first term of C_1 is denoted as C_{11} and it can be obtained as

$$C_{11} = \int_0^\infty f_{|e_{SR}|^2}(x) \int_{\beta_1 x + \beta_1 \Theta}^\infty f_{|g_{SR}|^2}(y) dx dy. \quad (A.3)$$

With the help of (9) and after some manipulations, it can be further achieved as

$$\begin{aligned} C_{11} = & \sum_{i_{SR}=0}^{m_{e_{SR}}-1} \sum_{k_{SR}=0}^{i_{SR}} \binom{m_{e_{SR}} + i_{SR} - k_{SR} - 1}{m_{e_{SR}} - 1} \\ & \times \frac{\Omega_{e_{SR}}^{m_{e_{SR}}} \Omega_{SR}^{-k_{SR}} \Theta^{k_{SR}} \beta_1^{i_{SR}} e^{-\beta_1 \Theta / \Omega_{e_{SR}}}}{k_{SR}! (\beta_1 + \Omega_{SR})^{m_{e_{SR}} + i_{SR} - k_{SR}}}, \end{aligned} \quad (A.4)$$

where $\Omega_{SR} = \Omega_{SR}/\Omega_{e_{SR}}$. Then, the second term (A.2) is so-called as C_{12} . With the help of (10), C_{12} can be given as

$$C_{12} = 1 - \frac{\Gamma(m_{SP}, \rho_I/\rho_S \Omega_{SP})}{\Gamma(m_{SP})}. \quad (A.5)$$

The second component is computed as

$$C_2 = \Pr \left(|g_{SR}|^2 > \beta_1 |e_{SR}|^2 + \beta_1 \Theta |g_{SP}|^2, |g_{SP}|^2 > \frac{\rho_I}{\rho_S} \right), \quad (A.6)$$

in which $\Theta = (\mu + 1)/\rho_I$. Similarly, C_2 is rewritten as

$$\begin{aligned} C_2 = & \int_{\rho_I/\rho_S}^\infty f_{|g_{SP}|^2}(z) \int_0^\infty f_{|e_{SR}|^2}(x) \int_{\beta_1 x + \beta_1 \Theta z}^\infty f_{|g_{SR}|^2}(y) dy dx dz \\ = & \sum_{i_{SR}=0}^{m_{e_{SR}}-1} \sum_{k_{SR}=0}^{i_{SR}} \binom{m_{e_{SR}} + i_{SR} - k_{SR} - 1}{m_{e_{SR}} - 1} \\ & \cdot \frac{\Omega_{e_{SR}}^{m_{e_{SR}}} \rho_I^{i_{SR}}}{k_{SR}! (\beta_1 + \Omega_{SR})^{m_{e_{SR}} + i_{SR} - k_{SR}} \Gamma(m_{SP})} \times \left(\frac{\Omega_{SR}}{\Theta \Omega_{SP}} \right)^{m_{SP}} \\ & \cdot \left(\beta_1 + \frac{\Omega_{SR}}{\Theta \Omega_{SP}} \right)^{-m_{SP} - k_{SR}} \Gamma \left(m_{SP} + k_{SR}, \frac{(\beta_1 \Theta \Omega_{SP} + \Omega_{SR}) \rho_I}{\Omega_{SR} \Omega_{SP} \rho_S} \right). \end{aligned} \quad (A.7)$$

Putting (A.4), (A.5), and (A.7) into (A.1), we can obtain (12). It completes the proof.

Data Availability

No data were used to support this study.

Conflicts of Interest

The authors declare that they have no conflicts of interest.

References

- [1] Z. Ding, X. Lei, G. K. Karagiannidis, R. Schober, J. Yuan, and V. K. Bhargava, "A survey on non-orthogonal multiple access for 5G networks: research challenges and future trends," *IEEE Journal on Selected Areas in Communications*, vol. 35, no. 10, pp. 2181–2195, 2017.
- [2] D.-T. Do and A.-T. Le, "NOMA based cognitive relaying: transceiver hardware impairments, relay selection policies and outage performance comparison," *Computer Communications*, vol. 146, pp. 144–154, 2019.
- [3] T.-L. Nguyen and D.-T. Do, "Power allocation schemes for wireless powered NOMA systems with imperfect CSI: an application in multiple antenna-based relay," *International*

- Journal of Communication Systems*, vol. 31, no. 15, article 3789, 2018.
- [4] T.-L. Nguyen and D.-T. Do, "Exploiting impacts of intercell interference on SWIPT-assisted non-orthogonal multiple access," *Wireless Communications and Mobile Computing*, vol. 2018, Article ID 2525492, 12 pages, 2018.
 - [5] H.-P. Dang, M. S. van Nguyen, D.-T. Do, H.-L. Pham, B. Selim, and G. Kaddoum, "Joint relay selection, full-duplex and device-to-device transmission in wireless powered NOMA networks," *IEEE Access*, vol. 8, pp. 82442–82460, 2020.
 - [6] S. Arzykulov, G. Naurzybayev, T. A. Tsiftsis, B. Maham, and M. Abdallah, "On the outage of underlay CR-NOMA networks with detect-and-forward relaying," *IEEE Transactions on Cognitive Communications and Networking*, vol. 5, no. 3, pp. 795–804, 2019.
 - [7] Y. Liu, Z. Ding, M. ElKashlan, and J. Yuan, "Non-orthogonal multiple access in large-scale underlay cognitive radio networks," *IEEE Transactions on Vehicular Technology*, vol. 65, no. 12, pp. 10152–10157, 2016.
 - [8] D. T. Do, A. T. le, and B. M. Lee, "NOMA in cooperative underlay cognitive radio networks under imperfect SIC," *IEEE Access*, vol. 8, pp. 86180–86195, 2020.
 - [9] Y. Song, W. Yang, Z. Xiang, N. Sha, H. Wang, and Y. Yang, "An analysis on secure millimeter wave NOMA communications in cognitive radio networks," *IEEE Access*, vol. 8, pp. 78965–78978, 2020.
 - [10] G. Im and J. H. Lee, "Outage probability for cooperative NOMA systems with imperfect SIC in cognitive radio networks," *IEEE Communications Letters*, vol. 23, no. 4, pp. 692–695, 2019.
 - [11] J. Men, J. Ge, and C. Zhang, "Performance analysis of non-orthogonal multiple access for relaying networks over Nakagami- m fading channels," *IEEE Transactions on Vehicular Technology*, vol. 66, no. 2, pp. 1200–1208, 2017.
 - [12] X. Wang, J. Wang, L. He, and J. Song, "Outage analysis for downlink NOMA with statistical channel state information," *IEEE Communications Letters*, vol. 7, no. 2, pp. 142–145, 2018.
 - [13] J. Lee, H. Wang, J. G. Andrews, and D. Hong, "Outage probability of cognitive relay networks with interference constraints," *IEEE Transactions on Wireless Communications*, vol. 10, no. 2, pp. 390–395, 2011.
 - [14] Y. Zou, Y.-D. Yao, and B. Zheng, "Outage probability analysis of cognitive transmissions: impact of spectrum sensing overhead," *IEEE Transactions on Wireless Communications*, vol. 9, no. 8, pp. 2676–2688, 2010.
 - [15] C. Zhong, T. Ratnarajah, and K.-K. Wong, "Outage analysis of decode-and-forward cognitive dual-hop systems with the interference constraint in Nakagami- m fading channels," *IEEE Transactions on Vehicular Technology*, vol. 60, no. 6, pp. 2875–2879, 2011.
 - [16] L. Lv, J. Chen, Q. Ni, and Z. Ding, "Design of cooperative non-orthogonal multicast cognitive multiple access for 5G systems: user scheduling and performance analysis," *IEEE Transactions on Communications*, vol. 65, no. 6, pp. 2641–2656, 2017.
 - [17] L. Lv, J. Chen, and Q. Ni, "Cooperative non-orthogonal multiple access in cognitive radio," *IEEE Communications Letters*, vol. 20, no. 10, pp. 2059–2062, 2016.
 - [18] L. Bariah, S. Muhaidat, and A. Al-Dweik, "Error performance of NOMA-based cognitive radio networks with partial relay selection and interference power constraints," *IEEE Transactions on Communications*, vol. 68, no. 2, pp. 765–777, 2020.
 - [19] S. Arzykulov, T. A. Tsiftsis, G. Naurzybayev, and M. Abdallah, "Outage performance of cooperative underlay CR-NOMA with imperfect CSI," *IEEE Communications Letters*, vol. 23, no. 1, pp. 176–179, 2019.
 - [20] X. Li, Q. Wang, M. Liu et al., "Cooperative wireless-powered NOMA relaying for B5G IoT networks with hardware impairments and channel estimation Errors," *IEEE Internet of Things Journal*, vol. 8, no. 7, pp. 5453–5467, 2021.
 - [21] X. Li, Q. Wang, Y. Liu, T. A. Tsiftsis, Z. Ding, and A. Nallanathan, "UAV-aided multi-way NOMA networks with residual hardware impairments," *IEEE Wireless Communications Letters*, vol. 9, no. 9, pp. 1538–1542, 2020.
 - [22] Z. Yang, Z. Ding, P. Fan, and G. K. Karagiannidis, "On the performance of non-orthogonal multiple access systems with partial channel information," *IEEE Transactions on Communications*, vol. 64, no. 2, pp. 654–667, 2016.
 - [23] D. Zwillinger, *Table of Integrals, Series, and Products, 7 Ed*, Academic Press, 2007.

Research Article

Relay Selection for Security Improvement in Cognitive Radio Networks with Energy Harvesting

Khuong Ho-Van ^{1,2} and **Thiem Do-Dac** ^{1,2,3}

¹Ho Chi Minh City University of Technology (HCMUT), 268 Ly Thuong Kiet Street, District 10, Ho Chi Minh City, Vietnam

²Vietnam National University Ho Chi Minh City, Linh Trung Ward, Thu Duc District, Ho Chi Minh City, Vietnam

³Thu Dau Mot University, 6 Tran Van On Street, Phu Hoa Ward, Thu Dau Mot City, Binh Duong Province, Vietnam

Correspondence should be addressed to Thiem Do-Dac; thiemdd@tdmu.edu.vn

Received 22 March 2021; Revised 20 April 2021; Accepted 13 May 2021; Published 21 June 2021

Academic Editor: Xingwang Li

Copyright © 2021 Khuong Ho-Van and Thiem Do-Dac. This is an open access article distributed under the Creative Commons Attribution License, which permits unrestricted use, distribution, and reproduction in any medium, provided the original work is properly cited.

This paper selects an unlicensed relay among available self-powered relays to not only remain but also secure information transmission from an unlicensed source to an unlicensed destination. The relays harvest energy in signals of the unlicensed source and the licensed transmitter. Then, they spend the harvested energy for their relaying operation. Conditioned on the licensed outage restriction, the peak transmission power restriction, Rayleigh fading, and the licensed interference, the current paper proposes an exact closed-form formula of the secrecy outage probability to quickly evaluate the secrecy performance of the proposed relay selection method in cognitive radio networks with energy harvesting. The proposed formula is corroborated by computer simulations. Several results illustrate the effectiveness of the relay selection in securing information transmission. Additionally, the security capability is saturated at large peak transmission powers or large preset outage probabilities of licensed users. Furthermore, the security capability depends on many specifications among which the power splitting ratio, the relays' positions, and the time switching ratio can be optimally selected to obtain the best security performance.

1. Introduction

In cognitive radio networks, unlicensed users are supported to use opportunistically the allotted frequencies of licensed users to improve significantly the spectrum utilization efficiency, which is currently low [1]. Amidst three typical operation mechanisms of cognitive radios (interweave, underlay, overlay), the underlay one has received more attention because of its low system design complexity [2]. Following this trend, our work also considers this mechanism. The underlay mechanism requires the power allotment for unlicensed users strictly subject to the licensed outage constraint (This paper uses “constraint” and “restriction” interchangeably) inflicted by communication reliability of licensed users and the peak transmission power restriction imposed by hardware design [3]. These power constraints bound the transmission power of unlicensed users, inducing insufficient power to reliably transmit information directly from an unlicensed source to an unlicensed destination. Additionally,

severe wave propagation conditions (heavy path-loss, strong shadowing, and severe fading) induce communication outage for the direct channel between the unlicensed source-destination pair. Therefore, exploiting unlicensed relays in this direct link can significantly mitigate these severe wave propagation conditions and eliminate the need of large transmission power over a wide coverage range. Consequently, the relays can play a role as a bridge for the source information to reach the destination. Instead of exploiting all available relays which either transmit simultaneously in one orthogonal channel or sequentially in several orthogonal channels, selecting one relay among them according to a certain criterion is considered as an efficient-and-economical solution in terms of complexity, power, and bandwidth [4–11]. However, as an assistant, the selected relay may be unwilling to consume its individual energy for assistant activity. Nowadays, advanced technologies allow wireless users to power their operations by the harvested radio frequency (RF) energy [12–15]. As a result, the selected relay can extend

the coverage range of the unlicensed source with the harvested energy, better maintaining reliable source-to-destination communications. Nevertheless, the harvested energy is limited and, thus, the issue is whether the selected relay can ensure secure-and-reliable communication for source data against the eavesdropping of wire-tappers in the viewpoint of information theory. This viewpoint affirms that the positive subtraction of the wire-tap channel capacity from the main channel capacity ensures the secured communications [16]. The current paper solves such an issue.

1.1. Previous Works. While most recent publications focused on securing direct transmission (i.e., without relaying [17–23]) and relaying transmission (i.e., without relay selection [24–28]) in cognitive radio networks with energy harvesting (CRNwEH) by the physical layer security technique (e.g., [29–33]), to the best of our understanding only three works in [34–36] mentioned the relay selection in these networks. To be specific, [34] studied the security capability of the conventional reactive relay selection in CRNwEH in terms of the secrecy outage probability (SOP) through Monte-Carlo simulations under the (peak transmission and interference) power constraints. The conventional reactive relay selection selects one relay which produces the highest signal-to-noise ratio (SNR) to the destination as compared to all remaining relays. Additionally, [34] considered the time switching protocol for energy harvesting, which enables the relay to harvest energy from merely the unlicensed source signal. To improve the security capability, [35] suggested a link selection method in which the link (A link is a multihop communication link through which the unlicensed source transmits information to the unlicensed destination via multiple unlicensed relays) of the largest capacity is adopted. Also, [35] permitted the relays to scavenge the energy in the beacon signals with the time switching protocol. Furthermore, [35] solely analyzed the connection outage probabilities (The connection outage probability indicates the possibility that the received SNR is smaller than a target value) of the wire-tapper and the unlicensed destination. Recently, ([37] is the conference version of [36]. In [37], a part of the results of [36] was briefly presented without any proof. However, the direct link was considered in [37] but not in [36]) [36] suggested a relay selection method where the adopted relay must successfully recover the unlicensed source’s information and minimize the SNR at the wire-tapper. In [36], the (peak transmission and interference) power constraints were imposed on the unlicensed transmission power, and the power splitting protocol was considered for energy harvesting. Additionally, [36] only analyzed the intercept outage probability (The intercept outage probability signifies the possibility that the SNR at the wire-tapper is lower than a target value). In addition, [34–36] neglected the interference from the licensed transmitter (shortly, licensed interference). In general, the licensed interference should be considered in the underlay mechanism because both licensed and unlicensed users transmit on the same wireless channel. Moreover, the licensed interference is useful for energy harvesting at relays. Furthermore, none of [34–36] neither investigated the licensed outage constraint nor analyzed the SOP, a key security capability indicator in the viewpoint of information theory.

1.2. Motivations. This paper extends [34, 36] with the following remarkable differences (Since the system models in [34, 36] and ours are completely different, it is impossible to compare their security performance under the same system parameters):

- (i) The relays work solely as they are able to recover successfully the unlicensed source’s information. Such an operation of the relays avoids the error propagation (e.g., [34])
- (ii) The proposed relay selection method (It is obvious that this paper completely differs [35] because the former proposed the relay selection while the latter proposed the link selection) selects one relay which produces the largest maximum secrecy rate (As recommended by the reviewer, “maximum secrecy rate” should be used in this paper instead of “secrecy capacity” which is normally used in the literature) as compared to activated relays. On the contrary, [34] selects one relay which produces the largest SNR to the unlicensed destination as compared to all remaining relays, and [36] selects one relay which produces the smallest SNR to the wire-tapper as compared to activated relays. Therefore, the relay selection method in [34] only concentrated on improving the main (the unlicensed selected relay to the unlicensed destination) channel capacity while that in [36] merely focused on degrading the wire-tap (the unlicensed selected relay to the wire-tapper) channel capacity. It is reminded that the subtraction of the wire-tap channel capacity from the main channel capacity is the maximum secrecy rate [16]. Accordingly, our relay selection is more complete than [34, 36] in improving and evaluating the security performance in the viewpoint of information theory
- (iii) The licensed interference is investigated in analyzing the security performance of the relay selection in CRNwEH while [34, 36] ignored this interference. Considering this interference complicates the performance analysis but valuable because the licensed interference should not be neglected in the underlay mechanism in general
- (iv) The relays take advantage of the licensed interference for energy harvesting. Apparently, converting unexpected signals to advantageous energy sources is valuable and this also distinguishes [34, 36] where the energy in the licensed interference is not harvested at relays
- (v) The power splitting based energy harvesting method is employed in this paper while [34] uses the time switching based energy harvesting method
- (vi) Our work suggests the precise closed-form SOP analysis that distinguishes [34] where merely simulation results were provided and [36] where the intercept outage probability (IOP) was analyzed. It

is reminded that the SOP analysis in this paper is more complete than the IOP analysis in [36] because the former considers both the wire-tap and main channels while the latter only investigated the wire-tap channel. Moreover, our SOP analysis considers the licensed outage constraint while [34, 36] ignored it

1.3. *Contributions.* Our work contributes the following:

- (i) Propose the relay selection method for securing the unlicensed source-to-destination information transmission in case that their direct link is blocked. The proposed method maximizes the maximum secrecy rate in the information processing stage, and the relays are able to scavenge the energy in both signals of the licensed transmitter and the unlicensed source based on the power splitting protocol. Moreover, the relays must correctly restore the unlicensed source's information before relaying it
- (ii) Propose exact closed-form expressions for principal security capability indicators including the SOP, the intercept probability (IP), the probability of strictly positive maximum secrecy rate (PSPMSR) under both licensed outage restriction and peak transmission power restriction, and the licensed interference to quickly assess the secrecy performance of the relay selection in CRNweH without the need of exhaustive simulations
- (iii) Exploit the suggested formulas to optimally select pivotal system parameters
- (iv) Supply multiple results to achieve helpful insights into the security capability; for example, the minimum SOP accomplishable with reasonable selection of the time switching ratio, the relays' positions, and the power splitting ratio; the secrecy performance saturation at high peak transmission powers or high preset outage probabilities of licensed users

1.4. *Paper Structure.* The next part describes maximum secrecy rate, signal model, system model, unlicensed power allocation, and relay selection. Part 3 presents the detailed derivation of essential performance indicators including the IP, the SOP, and the PSPMSR. Part 4 shows analytical/simulated results, and Part 5 closes our work.

2. System Description

2.1. *System Model.* Figure 1 demonstrates the relay selection in CRNweH. A complete communication from the unlicensed source (US) to the unlicensed destination (UD) with the help of the selected unlicensed relay (UR_b) comprises two stages as depicted in Figure 2(a).

In Stage I, both the licensed transmitter (LT) and US concurrently transmit their legitimate information to the licensed receiver (LR) and UD, correspondingly, inducing mutual interferences between the unlicensed and licensed networks. The unlicensed interferences (i.e., in the unli-

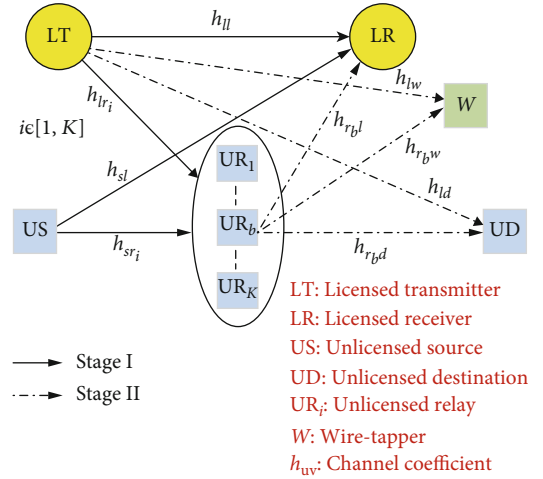


FIGURE 1: System model.

censed to licensed direction) are well investigated in open literature but the licensed interferences (i.e., in the licensed to unlicensed direction) are normally ignored (e.g., [5, 6, 8, 17, 21–26, 28, 34–37]). As such, by integrating these mutual interferences into the system model, the current paper is undoubtedly more general than published ones yet the performance analysis is more complicated. The wire-tapper (W) purposely eavesdrops the US's information. Due to bad propagation conditions, the US's signals are unable to be reliably received by UD and W . Therefore, it is advisable to ask the unlicensed relays (UR_i), $i \in [1, K]$, in the transmission range of US for relaying the US's information to UD. In order to save bandwidth and power, this paper just selects one relay, namely, UR_b , from a subset of relays which successfully decodes the US's information. Moreover, in order to avoid the waste of energy for relaying operation, the relays are assumed to relay with the energy scavenged from the RF signals. The energy harvesting is implemented with the power splitting protocol (e.g., [38, 39]) as seen in Figure 2(b). More specifically, the signals of LT and US provide the RF energy for UR_i to harvest. Accordingly, this paper exploits even the interference from LT as a useful energy supply. The power of UR_i 's received signal is split into two portions: one for restoring the US's information (Most previous works (e.g., [5, 12, 17–19, 21–28, 34–39]) omitted the power consumption of the information decoder. The current paper also follows this assumption) and another for harvesting the energy.

In Stage II, the adopted relay UR_b restores the US's information and forwards the decoded information to UD at the same time that LT transmits its information to LR, which again induces mutual interference between the licensed and unlicensed networks. At the end of Stage II, UD attempts to restore while W wire-taps the US's information from UR_b 's transmit signal.

2.2. *Signal Model.* In Figure 1, $h_{uv} \in \{h_{ll}, h_{lw}, h_{ld}, h_{lr}, h_{sl}, h_{sr}, h_{rl}, h_{rb}, h_{rd}\}$ symbolizes the channel coefficient between a transmitter-receiver pair (The global channel state information

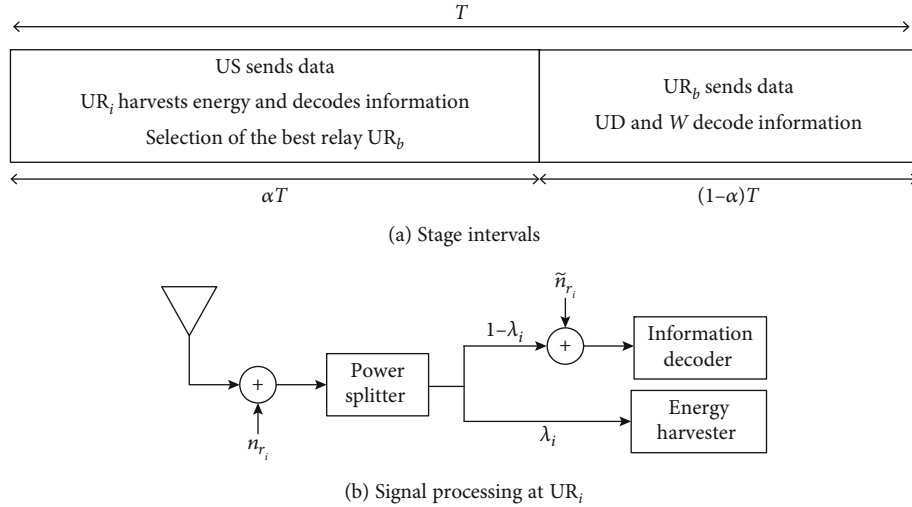


FIGURE 2: Signal processing.

is assumably available in this paper, which is similar to [6, 8, 21]. How to obtain such global channel state information is beyond our scope but rather we focus on the SOP analysis for the proposed relay selection in CRNwEH). Under the assumption of Rayleigh fading, h_{uv} is modelled as a zero-mean μ_{uv} -variance circular symmetric complex Gaussian distribution, i.e., $h_{uv} \sim \mathcal{CN}(0, \mu_{uv})$. Integrating path-loss into channel characteristics, μ_{uv} , is deputized as $\mu_{uv} = \tau_{uv}^{-\omega}$ with ω symbolizing the path-loss exponent and τ_{uv} symbolizing the transmitter u -receiver v distance. Therefore, it is naturally accepted in the following that the cumulative distribution function (CDF) and the probability density function (PDF) of the channel gain $|h_{uv}|^2$ are correspondingly represented as $F_{|h_{uv}|^2}(x) = 1 - e^{-x/\mu_{uv}}$ and $f_{|h_{uv}|^2}(x) = e^{-x/\mu_{uv}}/\mu_{uv}$.

In Figure 2, α with $\alpha \in (0, 1)$, λ_i with $\lambda_i \in (0, 1)$, and T symbolize the time switching ratio, the power splitting ratio, and the total duration for transmission from US to UD through UR_b , respectively. Given these notations in Figure 2, one can model the signals as follows.

UR_i and LR receive signals in Stage I, correspondingly, as

$$y_{r_i} = h_{sr_i} \sqrt{P_s} x_s + h_{lr_i} \sqrt{P_l} x_l + n_{r_i}, \quad (1)$$

$$y_{l1} = h_{sl} \sqrt{P_s} x_s + h_{ll} \sqrt{P_l} x_l + n_{l1}, \quad (2)$$

where x_s and x_l are respectively the unity-power transmit symbols of US and LT; the receive antennas of UR_i and LR generate the noises $n_{r_i} \sim \mathcal{CN}(0, \sigma_{r_i}^2)$ and $n_{l1} \sim \mathcal{CN}(0, \sigma_{l1}^2)$, respectively; the transmission powers of US and LT are P_s and P_l , respectively.

As shown in Figure 2(b), the relay UR_i divides the received signal y_{r_i} into two portions: one portion of $\sqrt{\lambda_i} y_{r_i}$ passes through the energy harvester and another portion of $\sqrt{1-\lambda_i} y_{r_i}$ passes through the information decoder. Based

on $\sqrt{\lambda_i} y_{r_i}$, the energy that UR_i scavenges in the Stage I is computed as

$$E_{r_i,m} = \eta_i \Xi \left\{ \left| \sqrt{\lambda_i} y_{r_i} \right|^2 \right\} \alpha T = \eta_i \lambda_i \left(P_s \mu_{sr_i} + P_l \mu_{lr_i} + \sigma_{r_i}^2 \right) \alpha T, \quad (3)$$

where $\Xi\{\cdot\}$ symbolizes the statistical average and η_i with $\eta_i \in (0, 1)$ symbolizes the energy conversion efficiency.

The UR_i consumes the scavenged energy in (3) to transmit information in Stage II with the peak transmission power as

$$P_{r_i,m} = \frac{E_{r_i,m}}{(1-\alpha)T} = \frac{\alpha \eta_i \lambda_i}{1-\alpha} \left(P_s \mu_{sr_i} + P_l \mu_{lr_i} + \sigma_{r_i}^2 \right). \quad (4)$$

According to the operation principle in Figure 2(b), one can represent the input signal of the information decoder as $\tilde{y}_{r_i} = \sqrt{1-\lambda_i} y_{r_i} + \tilde{n}_{r_i}$ where the passband-to-baseband signal converter creates the noise $\tilde{n}_{r_i} \sim \mathcal{CN}(0, \tilde{\sigma}_{r_i}^2)$. Inserting (1) in \tilde{y}_{r_i} yields $\tilde{y}_{r_i} = \sqrt{(1-\lambda_i)P_s} h_{sr_i} x_s + \sqrt{(1-\lambda_i)P_l} h_{lr_i} x_l + \sqrt{1-\lambda_i} n_{r_i} + \tilde{n}_{r_i}$, which creates the SINR (signal-to-interference plus noise ratio) for decoding x_s as

$$\gamma_{sr_i} = \frac{(1-\lambda_i)P_s |h_{sr_i}|^2}{(1-\lambda_i)P_l |h_{lr_i}|^2 + (1-\lambda_i)\sigma_{r_i}^2 + \tilde{\sigma}_{r_i}^2} = \frac{P_s |h_{sr_i}|^2}{P_l |h_{lr_i}|^2 + \tilde{\sigma}_{r_i}^2}, \quad (5)$$

where $\tilde{\sigma}_{r_i}^2 = \sigma_{r_i}^2 + (\tilde{\sigma}_{r_i}^2/(1-\lambda_i))$.

Generally, the relay UR_i , which is scheduled to transmit in Stage II, will result in the received signals at UD, W, and LR, respectively, as

$$y_{r,d} = h_{r,d} \sqrt{P_{r_i}} x_{r_i} + h_{ld} \sqrt{P_l} x_l + n_d, \quad (6)$$

$$y_{r,w} = h_{r,w} \sqrt{P_{r_i}} x_{r_i} + h_{lw} \sqrt{P_l} x_l + n_w, \quad (7)$$

$$y_{r,l} = h_{r,l} \sqrt{P_{r_i}} x_{r_i} + h_{ll} \sqrt{P_l} x_l + n_{l2}, \quad (8)$$

where the receive antennas of UD, W , and LR create the noises $n_d \sim \mathcal{CN}(0, \sigma_d^2)$, $n_w \sim \mathcal{CN}(0, \sigma_w^2)$, and $n_{l2} \sim \mathcal{CN}(0, \sigma_l^2)$, correspondingly; P_{r_i} is the transmission power of the relay UR_i . It is noted that because LT transmits the signal x_l at the same time that UR_i transmits the signal x_{r_i} , the terms ($h_{ld} \sqrt{P_l} x_l$, $h_{lw} \sqrt{P_l} x_l$, $h_{ll} \sqrt{P_l} x_l$) are the interferences induced by LT to UD and W , respectively. Furthermore, in order to decrease the number of notations without loss of generality, equations in (1), (2), (6), (7), and (8) supposed that merely one licensed transmitter-receiver pair are communicating to each other in both stages. That is why the same set of notations (h_{ll} , P_l , x_l) is used for both stages in (1), (2), (6), (7), and (8). The case of different licensed transmitter-receiver pairs in two stages is straightforwardly extended.

2.3. Maximum Secrecy Rate. Assuming that the relay UR_i is scheduled to transmit information in Stage II. Then, (6) and (7) yield the SINRs at UD and W as

$$\gamma_{r,d} = \frac{P_{r_i} |h_{r,d}|^2}{P_l |h_{ld}|^2 + \sigma_d^2}, \quad (9)$$

$$\gamma_{r,w} = \frac{P_{r_i} |h_{r,w}|^2}{P_l |h_{lw}|^2 + \sigma_w^2}. \quad (10)$$

From (9) and (10), channel capacities that UD and W achieve through the assistance of UR_i are respectively given by [40]

$$\begin{aligned} C_{r,d} &= (1 - \alpha) \log_2(1 + \gamma_{r,d}), \\ C_{r,w} &= (1 - \alpha) \log_2(1 + \gamma_{r,w}), \end{aligned} \quad (11)$$

where the duration of Stage II of $(1 - \alpha)T$ indicates the prelog factor of $(1 - \alpha)$.

The subtraction of the (UR_i to W) wire-tap channel capacity from the (UR_i to UD) main channel capacity is the maximum secrecy rate [16]. Therefore, with the assistance of UR_i , the maximum secrecy rate can be achieved as

$$C_{r_i} = [C_{r,d} - C_{r,w}]^+ = (1 - \alpha) \left[\log_2 \frac{1 + \gamma_{r,d}}{1 + \gamma_{r,w}} \right]^+, \quad (12)$$

where $[x]^+$ denotes $\max(x, 0)$.

2.4. Licensed Power Allocation. From (2), one can compute the SINR at LR in Stage I as

$$\gamma_{l1} = \frac{P_l |h_{ll}|^2}{P_s |h_{sl}|^2 + \sigma_l^2}, \quad (13)$$

from which the channel capacity that LR can obtain in Stage I is

$$C_{l1} = \alpha \log_2(1 + \gamma_{l1}). \quad (14)$$

Similarly, the SINR at LR in Stage II under the activation of the relay UR_i is inferred from (8) as

$$\gamma_{l2i} = \frac{P_l |h_{ll}|^2}{P_{r_i} |h_{r,i}|^2 + \sigma_l^2}, \quad (15)$$

from which the channel capacity that LR can obtain in Stage II under the activation of the relay UR_i is

$$C_{l2i} = (1 - \alpha) \log_2(1 + \gamma_{l2i}). \quad (16)$$

In cognitive radio networks, the reliability of the licensed users is of paramount importance. Therefore, the unlicensed transmitters (US and UR_i) must guarantee the reliability of the licensed users while they operate. In this paper, the reliability of the licensed users is represented by the outage probability of the licensed receiver. As such, the transmission powers of the unlicensed users must be controlled for the outage probability of the licensed receiver not to exceed a preset value ε . To be specific, P_s and P_{r_i} must be subject to

$$\Pr \{C_{l1} \leq C_2\} \leq \varepsilon, \quad (17)$$

$$\Pr \{C_{l2i} \leq C_2\} \leq \varepsilon, \quad (18)$$

where C_2 is the target spectral efficiency of LR.

Restrictions in (17) and (18) are named as the licensed outage restrictions.

The transmission powers of US and UR_i are also upper-bounded by their peak transmission powers, P_{sm} and $P_{r,m}$, correspondingly, that are due to the hardware design and the energy harvester, respectively. As such, P_s and P_{r_i} are constrained by

$$P_s \leq P_{sm}, \quad (19)$$

$$P_{r_i} \leq P_{r,m}. \quad (20)$$

Restrictions in (19) and (20) are named as the peak transmission power restrictions.

The solution of the equation system (i.e., the qualities hold for (17) and (19)) is the transmission power of P_s as

$$P_s = \min \left(\frac{P_l \mu_{ll}}{\gamma_{21} \mu_{sl}} \left[\frac{1}{1 - \varepsilon} e^{-\gamma_{21} \sigma_l^2 / P_l \mu_{ll}} - 1 \right]^+, P_{sm} \right), \quad (21)$$

where $\gamma_{21} = 2^{C_2/\alpha} - 1$.

Similarly, the solution of the equation system (i.e., the qualities hold for (18) and (20)) is the transmission power of P_{r_i} as

$$P_{r_i} = \min \left(\frac{P_l \mu_{ll}}{\gamma_{22} \mu_{r_i l}} \left[\frac{1}{1 - \varepsilon} e^{-\gamma_{22} \sigma_l^2 / P_l \mu_{ll}} - 1 \right]^+, P_{r_i m} \right), \quad (22)$$

where $\gamma_{22} = 2^{C_2/(1-\alpha)} - 1$.

The equations in (21) and (22) are derived similarly as ([3], eq. (17)) and ([3], eq. (19)).

2.5. Relay Selection. According to information theory, UR_i can achieve the channel capacity in Stage I as $C_{sr_i} = \alpha \log_2(1 + \gamma_{sr_i})$ bps/Hz where the reason for the appearance of the prelog factor α is that the duration of Stage I is αT . Moreover, according to information theory, UR_i can recover the US's information as long as C_{sr_i} exceeds the target spectral efficiency of SUs, C_1 , i.e., $C_{sr_i} \geq C_1$. Equivalently, x_s is correctly restored at UR_i if $\gamma_{sr_i} \geq \gamma_1$ where $\gamma_1 = 2^{C_1/\alpha} - 1$.

Let \mathcal{D} be the set of relays that correctly restored the US's message, i.e.,

$$\mathcal{D} = \{UR_i : C_{sr_i} \geq C_1\}. \quad (23)$$

Among relays in \mathcal{D} , the relay, namely, UR_b , that maximizes the maximum secrecy rate is chosen to relay the US's information in Stage II. According to this relay selection method, the maximum secrecy rate that CRNweH can achieve is given by

$$C_{\text{sec}} = \max_{r_i \in \mathcal{D}} C_{r_i} = \max_{r_i \in \mathcal{D}} (1 - \alpha) \left[\log_2 \left(\frac{1 + \gamma_{r_i d}}{1 + \gamma_{r_i w}} \right) \right]^+, \quad (24)$$

which is essential to derive the performance metric for the proposed relay selection method in CRNweH.

3. SOP Analysis

In the viewpoint of information theory, the most appropriate performance metric for evaluating the security capability of wireless transmission is the SOP, which is the possibility that C_{sec} is below a target security degree \bar{C}_3 . Therefore, the lower SOP indicates the more secure wireless transmission. This part derives elaborately the SOP for the suggested relay selection method in CRNweH. The derived closed-form expression of the SOP facilitates in evaluating the secrecy performance without time-consuming simulations and in deriving other paramount security capability indicators, e.g., the PSPMSR and the IP.

The SOP of the relay selection in CRNweH is expressed as

$$\mathcal{U}(\bar{C}_3) = \Pr \{C_{\text{sec}} < \bar{C}_3\} = \Pr \left\{ \max_{r_i \in \mathcal{D}} (1 - \alpha) \left[\log_2 \left(\frac{1 + \gamma_{r_i d}}{1 + \gamma_{r_i w}} \right) \right]^+ < \bar{C}_3 \right\}. \quad (25)$$

Because the number of relays which restore correctly the US's message in Stage I varies from 0 to K , according to the total probability principle, (25) can be decomposed as

$$\begin{aligned} \mathcal{U}(\bar{C}_3) &= \Pr \{0 < \bar{C}_3 \mid |\mathcal{D}| = 0\} \Pr \{|\mathcal{D}| = 0\} + \sum_{k=1}^K \Pr \\ &\cdot \left\{ \max_{r_i \in \mathcal{D}} (1 - \alpha) \left[\log_2 \left(\frac{1 + \gamma_{r_i d}}{1 + \gamma_{r_i w}} \right) \right]^+ < \bar{C}_3 \mid |\mathcal{D}| = k \right\} \Pr \{|\mathcal{D}| = k\}, \end{aligned} \quad (26)$$

where $|\cdot|$ symbolizes the cardinality of the set.

The target security degree \bar{C}_3 is nonnegative and hence, (26) can be simplified as

$$\mathcal{U}(\bar{C}_3) = \underbrace{\Pr \{|\mathcal{D}| = 0\}}_{\mathcal{Q}_1} + \sum_{k=1}^K \sum_{m=1}^{\binom{K}{k}} \underbrace{\Pr \left\{ \max (1 - \alpha) \left[\log_2 \left(\frac{1 + \gamma_{r_i d}}{1 + \gamma_{r_i w}} \right) \right]^+ < \bar{C}_3 \right\}}_{\mathcal{Q}_2} \underbrace{\Pr \{S_m^k\}}_{\mathcal{Q}_3}. \quad (27)$$

In (27), $\binom{K}{k} = K!/k!(K-k)!$ denotes the binomial coefficient and \mathcal{S}_m^k stands for the m^{th} combination among $\binom{K}{k}$ combinations, each comprising k distinct elements taken from the set of K different elements. For instance, $\mathcal{S}_1^2 = \{1, 2\}$, $\mathcal{S}_2^2 = \{1, 3\}$, $\mathcal{S}_3^2 = \{2, 3\}$ for $k=2$ and $K=3$.

In order to represent (27) in closed-form, the triplet $(\mathcal{Q}_1, \mathcal{Q}_2, \mathcal{Q}_3)$ will be solved sequentially as follows.

The quantity \mathcal{Q}_1 is the possibility which all relays fail to restore the US's information in Stage I. As such, \mathcal{Q}_1 can be computed as

$$\mathcal{Q}_1 = \Pr \left\{ \bigcap_{i=1}^K \left\{ \gamma_{sr_i} < \gamma_1 \right\} \right\}. \quad (28)$$

Because of the statistical independence of γ_{sr_i} , $i = \{1, \dots, K\}$, one can rewrite (28) as

$$\mathcal{Q}_1 = \prod_{i=1}^K \underbrace{\Pr \left\{ \gamma_{sr_i} < \gamma_1 \right\}}_{\mathcal{F}_i}, \quad (29)$$

where \mathcal{F}_i has the precise closed form as

$$\mathcal{F}_i = 1 - O_i \frac{e^{-G_i \gamma_1}}{\gamma_1 + O_i}, \quad (30)$$

with

$$O_i = \frac{\mu_{sr_i} P_s}{\mu_{lr_i} P_l}, \quad (31)$$

$$G_i = \frac{\hat{\sigma}_{r_i}^2}{\mu_{sr_i} P_s}. \quad (32)$$

The proof of (30) is presented in Appendix A.

The quantity \mathcal{Q}_3 is the probability that the relays belonging to the set \mathcal{S}_m^k successfully decode the US's information while the relays not belonging to the set \mathcal{S}_m^k unsuccessfully decode the US's information. Therefore, \mathcal{Q}_3 is represented in closed-form as

$$\mathcal{Q}_3 = \Pr \left\{ \bigcap_{i \in \mathcal{S}_m^k} \left\{ \gamma_{sr_i} \geq \gamma_1 \right\}, \bigcap_{j \notin \mathcal{S}_m^k} \left\{ \gamma_{sr_j} < \gamma_1 \right\} \right\}. \quad (33)$$

Because of the statistical independence of γ_{sr_i} , $i = \{1, \dots, K\}$, one can rewrite (33) as

$$\mathcal{Q}_3 = \prod_{i \in \mathcal{S}_m^k} (1 - \mathcal{F}_i) \prod_{j \notin \mathcal{S}_m^k} \mathcal{F}_j, \quad (34)$$

where \mathcal{F}_i is given by (30) while \mathcal{F}_j is also given by (30) with i being replaced by j .

The last quantity \mathcal{Q}_2 is decomposed as

$$\mathcal{Q}_2 = \Pr \left\{ \bigcap_{r_i \in \mathcal{S}_m^k} \left\{ \left[\log_2 \left(\frac{1 + \gamma_{r_i d}}{1 + \gamma_{r_i w}} \right) \right]^+ < \frac{\bar{C}_3}{1 - \alpha} \right\} \right\}. \quad (35)$$

Terms $(1 + \gamma_{r_i d})/(1 + \gamma_{r_i w})$ are statistically dependent because they contain two common variables ($|h_{ld}|^2$ and $|h_{lw}|^2$). To decorrelate them, one applies the conditional probability as

$$\mathcal{Q}_2 = \mathbb{E}_{|h_{ld}|^2, |h_{lw}|^2} \left\{ \prod_{r_i \in \mathcal{S}_m^k} \underbrace{\Pr \left\{ \left[\log_2 \left(\frac{1 + \gamma_{r_i d}}{1 + \gamma_{r_i w}} \right) \right]^+ < C_3 \mid |h_{ld}|^2, |h_{lw}|^2 \right\}}_{\mathcal{G}_i} \right\}, \quad (36)$$

where

$$C_3 = \frac{\bar{C}_3}{1 - \alpha}. \quad (37)$$

The term \mathcal{G}_i is represented in closed-form as

$$\mathcal{G}_i = 1 - \frac{(C_i |h_{lw}|^2 + D_i) e^{-(2^{C_3-1})(A_i |h_{ld}|^2 + B_i)}}{2^{C_3} (A_i |h_{ld}|^2 + B_i) + C_i |h_{lw}|^2 + D_i}, \quad (38)$$

where

$$A_i = \frac{P_l}{\mu_{r_i d} P_{r_i}}, \quad (39)$$

$$B_i = \frac{\sigma_d^2}{\mu_{r_i d} P_{r_i}}, \quad (40)$$

$$C_i = \frac{P_l}{\mu_{r_i w} P_{r_i}}, \quad (41)$$

$$D_i = \frac{\sigma_w^2}{\mu_{r_i w} P_{r_i}}. \quad (42)$$

The proof of (38) is presented in Appendix B. For simplicity, one lets

$$X = |h_{ld}|^2, \quad (43)$$

$$Y = |h_{lw}|^2, \quad (44)$$

$$a_i = \frac{(C_i Y + D_i) e^{-(2^{C_3-1})(A_i X + B_i)}}{2^{C_3} (A_i X + B_i) + C_i Y + D_i}. \quad (45)$$

Then, \mathcal{G}_i in (38) has a compact form as

$$\mathcal{G}_i = 1 - a_i. \quad (46)$$

Inserting (46) into (36), one has

$$\mathcal{Q}_2 = \Xi_{X,Y} \left\{ \prod_{r_i \in \mathcal{S}_m^k} (1 - a_i) \right\}. \quad (47)$$

Using the following equality ([3], eq. (30))

$$\begin{aligned} \prod_{k=1}^L (1 - a_k) &= 1 + \sum_{u=1}^{L-1} (-1)^u \sum_{v_1=1}^{L-u+1} \sum_{v_2=v_1+1}^{L-u+2} \cdots \sum_{v_u=v_{u-1}+1}^L \prod_{k \in \mathcal{M}} a_k \\ &\quad + (-1)^L \prod_{k \in \mathcal{R}} a_k, \end{aligned} \quad (48)$$

with $\mathcal{R} = \{1, 2, \dots, L\}$ and $\mathcal{M} = \{\mathcal{R}[v_1], \dots, \mathcal{R}[v_u]\}$ to expand (48) as

$$\begin{aligned} \mathcal{Q}_2 &= 1 + \sum_{u=1}^{|\mathcal{S}_m^k|-1} (-1)^u \sum_{v_1=1}^{|\mathcal{S}_m^k|-u+1} \sum_{v_2=v_1+1}^{|\mathcal{S}_m^k|-u+2} \cdots \sum_{v_u=v_{u-1}+1}^{|\mathcal{S}_m^k|} \underbrace{\Xi_{X,Y} \left\{ \prod_{i \in \mathcal{A}} a_i \right\}}_{\mathcal{Q}_{2\mathcal{A}}} \\ &\quad + (-1)^{|\mathcal{S}_m^k|} \underbrace{\Xi_{X,Y} \left\{ \prod_{i \in \mathcal{S}_m^k} a_i \right\}}_{\mathcal{Q}_{2\mathcal{S}_m^k}}, \end{aligned} \quad (49)$$

where $\mathcal{A} = \{\mathcal{S}_m^k[v_1], \dots, \mathcal{S}_m^k[v_u]\}$.

To obtain the closed form of \mathcal{Q}_2 , one needs to evaluate a common expression

$$\mathcal{Q}_{2\mathcal{W}} = \Xi_{X,Y} \left\{ \prod_{i \in \mathcal{W}} a_i \right\}, \quad (50)$$

where $\mathcal{W} = \{\mathcal{A}, \mathcal{S}_m^k\}$.

Inserting (45) into (50), one obtains

$$\begin{aligned} \mathcal{Q}_{2\mathcal{W}} &= \Xi_{X,Y} \left\{ \prod_{i \in \mathcal{W}} \frac{(C_i Y + D_i) e^{-(2^{C_3-1})(A_i X + B_i)}}{2^{C_3} A_i X + C_i Y + 2^{C_3} B_i + D_i} \right\} \\ &= e^{-2^{C_3-1} \sum_{i \in \mathcal{W}} B_i} \left(\prod_{i \in \mathcal{W}} \frac{1}{2^{C_3} A_i} \right) \Xi_{X,Y} \left\{ e^{-X(2^{C_3-1}) \sum_{i \in \mathcal{W}} A_i} \prod_{i \in \mathcal{W}} \frac{C_i Y + D_i}{X + 2^{-C_3} (C_i/A_i) Y + (B_i + 2^{-C_3} D_i)/A_i} \right\} \\ &= e^{-2^{C_3-1} \sum_{i \in \mathcal{W}} B_i} \left(\prod_{i \in \mathcal{W}} \frac{1}{2^{C_3} A_i} \right) \times \Xi_Y \left\{ \underbrace{\left[\prod_{i \in \mathcal{W}} (C_i Y + D_i) \right]}_{\mathcal{K}} \underbrace{\left\{ e^{-X(2^{C_3-1}) \sum_{i \in \mathcal{W}} A_i} \prod_{i \in \mathcal{W}} \left[X + 2^{-C_3} \frac{C_i}{A_i} Y + \frac{B_i + 2^{-C_3} D_i}{A_i} \right]^{-1} \right\}}_{\mathcal{H}} \right\}. \end{aligned} \quad (51)$$

The term \mathcal{K} can be rewritten in an explicit form as

$$\begin{aligned} \mathcal{K} &= \int_0^\infty \frac{1}{\mu_{ld}} e^{-x/\mu_{ld}} e^{-x(2^{C_3-1}) \sum_{i \in \mathcal{W}} A_i} \prod_{i \in \mathcal{W}} \left[x + 2^{-C_3} \frac{C_i}{A_i} Y + \frac{B_i + 2^{-C_3} D_i}{A_i} \right]^{-1} dx \\ &= \frac{1}{\mu_{ld}} \int_0^\infty e^{-x} \left[\frac{1}{\mu_{ld} + (2^{C_3-1}) \sum_{i \in \mathcal{W}} A_i} \right] \sum_{i \in \mathcal{W}} H_i / \left(x + 2^{-C_3} \frac{C_i}{A_i} Y + \frac{B_i + 2^{-C_3} D_i}{A_i} \right) dx, \end{aligned} \quad (52)$$

where

$$H_i = \prod_{j \in \mathcal{W}, j \neq i} \left[2^{-C_3} \left(\frac{C_j}{A_j} - \frac{C_i}{A_i} \right) Y + \frac{B_j + 2^{-C_3} D_j}{A_j} - \frac{B_i + 2^{-C_3} D_i}{A_i} \right]^{-1}, \quad (53)$$

which is obtained from the partial fraction decomposition.

By exchanging the summation and the integration, one obtains

$$\begin{aligned} \mathcal{K} &= \frac{1}{\mu_{ld}} \sum_{i \in \mathcal{W}} H_i \int_0^\infty \frac{e^{-[1/\mu_{ld} + (2^{C_3-1}) \sum_{i \in \mathcal{W}} A_i] x}}{x + 2^{-C_3} (C_i/A_i) Y + (B_i + 2^{-C_3} D_i)/A_i} dx \\ &= -\frac{1}{\mu_{ld}} \sum_{i \in \mathcal{W}} H_i e^{\left[\frac{1}{\mu_{ld} + (2^{C_3-1}) \sum_{i \in \mathcal{W}} A_i} \right] \left(2^{-C_3} \frac{C_i}{A_i} Y + \frac{B_i + 2^{-C_3} D_i}{A_i} \right)} \\ &\quad \times Ei \left(-\left[\frac{1}{\mu_{ld}} + (2^{C_3-1}) \sum_{i \in \mathcal{W}} A_i \right] \left(2^{-C_3} \frac{C_i}{A_i} Y + \frac{B_i + 2^{-C_3} D_i}{A_i} \right) \right), \end{aligned} \quad (54)$$

where $Ei(\cdot)$ is the exponential integral in [41], and the

integral in the first equality is achieved from the following result:

$$\Omega(a, b) = \int_0^\infty \frac{e^{-ax}}{x+b} dx = -e^{ab} Ei(-ab). \quad (55)$$

Inserting H_i in (53) into (54) and performing simplifications, one reduces \mathcal{H} to

$$\mathcal{H} = -\frac{1}{\mu_{ld}} \sum_{i \in \mathcal{W}} L_i \left(\prod_{\substack{j \in \mathcal{W} \\ j \neq i}} \frac{1}{Y + M_j} \right) e^{V_i Y} Ei(-V_i Y - U_i), \quad (56)$$

where $U_i = [1/\mu_{ld} + (2^{C_3} - 1) \sum_{i \in \mathcal{W}} A_i] (B_i + 2^{-C_3} D_i) / A_i$, $V_i = [1/\mu_{ld} + (2^{C_3} - 1) \sum_{i \in \mathcal{W}} A_i] 2^{-C_3} C_i / A_i$, $M_j = ((B_j + 2^{-C_3} D_j) / A_j - (B_i + 2^{-C_3} D_i) / A_i) 2^{C_3} (C_j / A_j - C_i / A_i)^{-1}$, and $L_i = e^{U_i} \prod_{\substack{j \in \mathcal{W} \\ j \neq i}} 2^{-C_3} (C_j / A_j - C_i / A_i)$.

The term \mathcal{H} in (51) can be written in an explicit form as

$$\begin{aligned} \mathcal{H} &= \int_0^\infty \frac{1}{\mu_{lw}} e^{-y/\mu_{lw}} \left\{ \prod_{i \in \mathcal{W}} (C_i y + D_i) \right\} \mathcal{H} dy \\ &= -\int_0^\infty \frac{1}{\mu_{lw}} e^{-y/\mu_{lw}} \left\{ \prod_{i \in \mathcal{W}} (C_i y + D_i) \right\} \frac{1}{\mu_{ld}} \sum_{i \in \mathcal{W}} L_i \\ &\quad \cdot \left\{ \prod_{\substack{j \in \mathcal{W} \\ j \neq i}} \frac{1}{y + M_j} \right\} e^{V_i y} Ei(-V_i y - U_i) dy \\ &= -\frac{\prod_{i \in \mathcal{W}} C_i}{\mu_{lw} \mu_{ld}} \sum_{i \in \mathcal{W}} L_i \int_0^\infty e^{-(1/\mu_{lw} - V_i)y} \left(y + \frac{D_i}{C_i} \right) \\ &\quad \cdot \left\{ \prod_{\substack{j \in \mathcal{W} \\ j \neq i}} \frac{y + D_j/C_j}{y + M_j} \right\} Ei(-V_i y - U_i) dy. \end{aligned} \quad (57)$$

By denoting $\mathcal{X} = \mathcal{W} \setminus i$, one can rewrite \mathcal{H} as

$$\begin{aligned} \mathcal{H} &= -\frac{\prod_{i \in \mathcal{W}} C_i}{\mu_{lw} \mu_{ld}} \sum_{i \in \mathcal{W}} L_i \int_0^\infty e^{-(1/\mu_{lw} - V_i)y} \left(y + \frac{D_i}{C_i} \right) \\ &\quad \cdot \left\{ \prod_{j \in \mathcal{X}} \left(1 - \frac{M_j - D_j/C_j}{y + M_j} \right) \right\} Ei(-V_i y - U_i) dy. \end{aligned} \quad (58)$$

Using (48) to decompose \mathcal{H} as

$$\begin{aligned} \mathcal{H} &= -\frac{\prod_{i \in \mathcal{W}} C_i}{\mu_{lw} \mu_{ld}} \sum_{i \in \mathcal{W}} L_i \int_0^\infty e^{-(1/\mu_{lw} - V_i)y} \left(y + \frac{D_i}{C_i} \right) Ei(-V_i y - U_i) \\ &\quad \times \left\{ 1 + \sum_{q=1}^{|\mathcal{X}|-1} (-1)^q \sum_{u_1=1}^{|\mathcal{X}|-q+1} \sum_{u_2=u_1+1}^{|\mathcal{X}|-q+2} \cdots \sum_{u_q=u_{q-1}+1}^{|\mathcal{X}|} \prod_{j \in \mathcal{Z}} b_j + (-1)^{|\mathcal{X}|} \prod_{k \in \mathcal{X}} b_k \right\} dy, \end{aligned} \quad (59)$$

where $\mathcal{Z} = \{\mathcal{X}[u_1], \dots, \mathcal{X}[u_q]\}$ and

$$b_j = \frac{M_j - D_j/C_j}{y + M_j}. \quad (60)$$

One can further simplify (59) as

$$\begin{aligned} \mathcal{H} &= -\frac{\prod_{i \in \mathcal{W}} C_i}{\mu_{lw} \mu_{ld}} \sum_{i \in \mathcal{W}} L_i \\ &\quad \cdot \left\{ \Phi_\emptyset + \sum_{q=1}^{|\mathcal{X}|-1} (-1)^q \sum_{u_1=1}^{|\mathcal{X}|-q+1} \sum_{u_2=u_1+1}^{|\mathcal{X}|-q+2} \cdots \sum_{u_q=u_{q-1}+1}^{|\mathcal{X}|} \Phi_{\mathcal{Z}} + (-1)^{|\mathcal{X}|} \Phi_{\mathcal{X}} \right\}, \end{aligned} \quad (61)$$

where

$$\Phi_\emptyset = \int_0^\infty e^{-(1/\mu_{lw} - V_i)y} \left(y + \frac{D_i}{C_i} \right) Ei(-V_i y - U_i) dy, \quad (62)$$

$$\Phi_{\mathcal{B}} = \int_0^\infty e^{-(1/\mu_{lw} - V_i)y} \left(y + \frac{D_i}{C_i} \right) Ei(-V_i y - U_i) \left\{ \prod_{j \in \mathcal{B}} b_j \right\} dy, \quad (63)$$

with $\mathcal{B} = \{\mathcal{Z}, \mathcal{X}\}$.

The following solves Φ_\emptyset and $\Phi_{\mathcal{B}}$ in closed forms to finish the computation of \mathcal{H} . First of all, Φ_\emptyset can be represented in terms of two special functions as

$$\Phi_\emptyset = \Psi \left(\frac{1}{\mu_{lw}} - V_i, V_i, U_i \right) + \frac{D_i}{C_i} \Theta \left(\frac{1}{\mu_{lw}} - V_i, V_i, U_i \right), \quad (64)$$

where $\Psi(b, c, d)$ and $\Theta(b, c, d)$ are respectively defined as

$$\begin{aligned} \Psi(b, c, d) &= \int_0^\infty x e^{-bx} Ei(-cx - d) dx, \\ \Theta(b, c, d) &= \int_0^\infty e^{-bx} Ei(-cx - d) dx. \end{aligned} \quad (65)$$

Applying ([42], eq. (16)) with appropriate substitutions yields the closed form of $\Theta(b, c, d)$ as

$$\Theta(b, c, d) = \frac{Ei(-d)}{b} + \frac{e^{-d}}{b} \Omega \left(b + c, \frac{d}{c} \right), \quad (66)$$

where $\Omega(\cdot, \cdot)$ is the function defined in (55).

TABLE 1: Key specifications.

Specification	Value
Coordinate of LR	LR at (0.7, 0.6)
Coordinate of LT	LT at (0.2, 0.8)
Coordinate of UD	UD at (1.0, 0.0)
Coordinate of UR ₁	UR ₁ at (0.3402,0.0421)
Coordinate of UR ₂	UR ₂ at (0.2063,0.1785)
Coordinate of UR ₃	UR ₃ at (0.3132,0.1696)
Coordinate of UR ₄	UR ₄ at (0.3954,-0.1489)
Coordinate of UR ₅	UR ₅ at (0.2534,0.0243)
Coordinate of US	US at (0.0, 0.0)
Coordinate of W	W at (1.0, 0.4)
Energy conversion efficiency	$\eta = 0.9$
Path-loss exponent	$\omega = 4$

Similarly, applying ([43], eq. (29)) with appropriate substitutions yields the closed form of $\Psi(b, c, d)$ as

$$\Psi(b, c, d) = \frac{Ei(-d)}{b^2} + \frac{e^{-d}}{b(b+c)} + \frac{e^{-d}}{b} \left(\frac{1}{b} - \frac{d}{c} \right) \Omega \left(b+c, \frac{d}{c} \right). \quad (67)$$

Inserting (60) into (63), one obtains

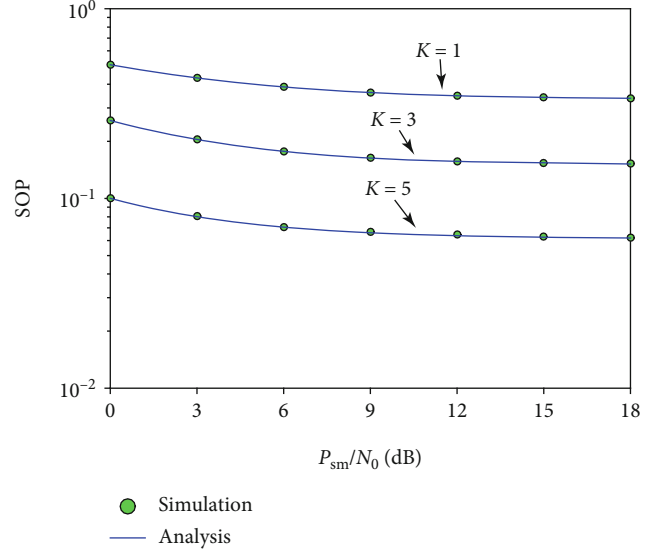
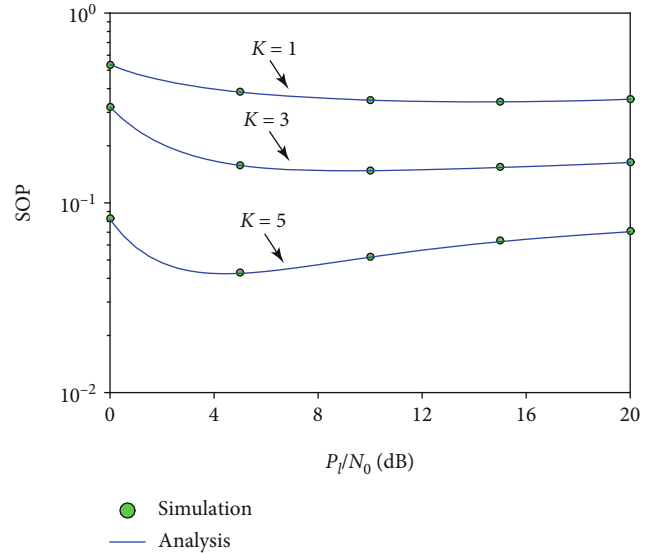
$$\Phi_{\mathcal{B}} = \int_0^{\infty} e^{-(1/\mu_{lw}-V_i)y} \left(y + \frac{D_i}{C_i} \right) Ei(-V_i y - U_i) \prod_{j \in \mathcal{B}} \frac{M_j - D_j/C_j}{y + M_j} dy. \quad (68)$$

Performing the partial fraction decomposition, one simplifies (68) as

$$\Phi_{\mathcal{B}} = \left\{ \prod_{j \in \mathcal{B}} \left(M_j - \frac{D_j}{C_j} \right) \right\} \int_0^{\infty} e^{-(1/\mu_{lw}-V_i)y} \left(y + \frac{D_i}{C_i} \right) Ei(-V_i y - U_i) \left(\sum_{j \in \mathcal{B}} \frac{Q_j}{y + M_j} \right) dy, \quad (69)$$

where $Q_j = \prod_{g \in \mathcal{B}, g \neq j} 1/(M_g - M_j)$.

$$\begin{aligned} \Phi_{\mathcal{B}} &= \left\{ \prod_{j \in \mathcal{B}} \left(M_j - \frac{D_j}{C_j} \right) \right\} \sum_{j \in \mathcal{B}} Q_j \int_0^{\infty} e^{-(1/\mu_{lw}-V_i)y} \frac{y + D_i/C_i}{y + M_j} Ei(-V_i y - U_i) dy \\ &= \left\{ \prod_{j \in \mathcal{B}} \left(M_j - \frac{D_j}{C_j} \right) \right\} \sum_{j \in \mathcal{B}} Q_j \left\{ \underbrace{\int_0^{\infty} e^{-(1/\mu_{lw}-V_i)y} Ei(-V_i y - U_i) dy}_{\Theta \left(\frac{1}{\mu_{lw}} - V_i, V_i, U_i \right)} + \left(\frac{D_i}{C_i} - M_j \right) \underbrace{\int_0^{\infty} \frac{e^{-(1/\mu_{lw}-V_i)y}}{y + M_j} Ei(-V_i y - U_i) dy}_{\Lambda \left(\frac{1}{\mu_{lw}} - V_i, M_j, V_i, U_i \right)} \right\}, \end{aligned} \quad (70)$$

FIGURE 3: SOP versus P_{sm}/N_0 .FIGURE 4: SOP versus P_l/N_0 .

By exchanging the summation and the integration, (69) is reduced to

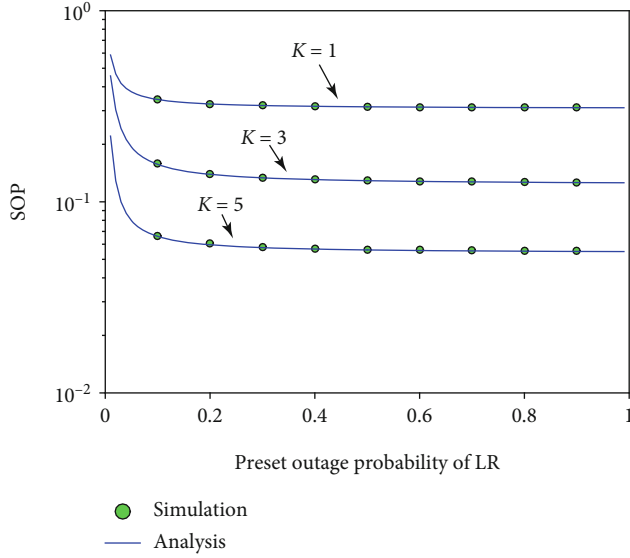


FIGURE 5: SOP versus the preset outage probability of licensed user.

where

$$\Lambda(b, c, g, l) = \int_0^{\infty} \frac{e^{-bx}}{x+c} Ei(-gx-l) dx. \quad (71)$$

The function $\Lambda(b, c, g, l)$ has an accurate closed form as ([42], eq. (19)) by setting the argument a of ([42], eq. (19)) to zero. Therefore, the precise closed form of $\Lambda(b, c, g, l)$ should not be summarized in this paper for brevity.

Given the exact closed forms of Φ_{\emptyset} in (64) and $\Phi_{\mathcal{B}}$ in (70), it is apparent that \mathcal{H} in (61) is solved in a precise closed form. Therefore, $\mathcal{Q}_{2\mathcal{W}}$ in (51) is presented in an exact closed form. Consequently, \mathcal{Q}_2 in (49) is also presented in an exact closed form.

Because \mathcal{Q}_1 in (29), \mathcal{Q}_2 in (49), and \mathcal{Q}_3 in (34) are all represented in precise closed forms, the SOP of the relay selection in CRNwEH in (27) is found in an exact closed form. The derived SOP formula is helpful to quickly rate the security performance without exhaustive simulations. Upon our knowledge, this formula is novel. Furthermore, some paramount security performance indicators including the PSPMSR and the IP are easily obtained from this formula. To be more specific, the IP indicates the probability of the negative maximum secrecy rate:

$$\phi = \Pr \{C_{\text{sec}} < 0\} = \mathcal{W}(0). \quad (72)$$

Moreover, the PSPMSR indicates the possibility of the strictly positive maximum secrecy rate:

$$\kappa = \Pr \{C_{\text{sec}} > 0\} = 1 - \Pr \{C_{\text{sec}} < 0\} = 1 - \mathcal{W}(0). \quad (73)$$

4. Illustrative Results

This part presents analytical/simulated results to rate the secrecy performance of the relay selection in CRNwEH through key specifications where (27) generates analytical

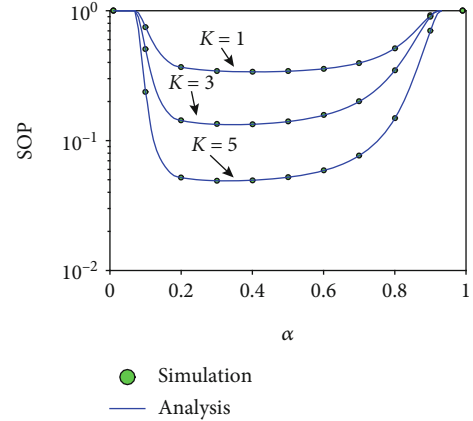


FIGURE 6: SOP versus the time switching ratio.

results, and the computer simulation produces simulated results. Key specifications under consideration are tabulated in Table 1. To limit case studies, equal noise variances, equal power splitting ratios, and equal energy conversion efficiencies are supposed, i.e., $\sigma_l^2 = \sigma_d^2 = \sigma_w^2 = \sigma_{r_i}^2 = \tilde{\sigma}_{r_i}^2 = N_0$, $\eta_i = \eta$, $\lambda_i = \lambda$ for $i \in [1, K]$.

Figure 3 shows the SOP versus P_{sm}/N_0 for $\bar{C}_3 = 0.1$ bps/Hz, $\alpha = 0.6$, $\varepsilon = 0.1$, $C_1 = 0.2$ bps/Hz, $P_l/N_0 = 15$ dB, $\lambda = 0.8$, and $C_2 = 0.3$ bps/Hz. The results confirm the precision of (27) owing to the assortment between the analysis and the simulation. Furthermore, the SOP reduces with the increase in the number of relays ($K=1$ reduces our system model to relaying transmission (i.e., without relay selection [24–28]) in CRNwEH.). This exposes the effectuality of the relay selection in securing CRNwEH. Moreover, the SOP reduces with the increase in P_{sm}/N_0 . This originates from the truth that the increase in P_{sm}/N_0 creates UR_i more chances to correctly restore the US's data and to harvest more RF energy from the US's signal, ultimately mitigating the SOP in Stage II. However, the SOP is saturated at large P_{sm}/N_0 . Such saturation comes from the power allotment for US and UR_i in (21) and (22) in which transmission powers of US and UR_i do not depend on P_{sm}/N_0 at high P_{sm}/N_0 (i.e., the peak transmission power restriction is relaxed at high P_{sm}/N_0), causing the saturated SOP.

Figure 4 shows the SOP versus P_l/N_0 for $\alpha = 0.6$, $\varepsilon = 0.1$, $C_1 = 0.2$ bps/Hz, $P_{sm}/N_0 = 15$ dB, $\bar{C}_3 = 0.1$ bps/Hz, $\lambda = 0.8$, and $C_2 = 0.3$ bps/Hz. The results corroborate (27) since the simulation coincides with the analysis. Moreover, the SOP reduces with increasing number of relays, again exposing the effectuality of the relay selection in securing CRNwEH. Furthermore, the SOP is minimum at a moderate value of P_l for a specific number of relays. Here are reasons for this observation. For low values of P_l , the interference from LT is small but the unlicensed users must transmit with low power to guarantee the QoS of LR to be fixed at $\varepsilon = 0.1$. Therefore, the SOP is large. For high values of P_l , the interference from LT is large but the unlicensed users must transmit with high power to guarantee the QoS of LR to be fixed at $\varepsilon = 0.1$. The increase in the interference from LT may surpass the increase in the unlicensed users' the

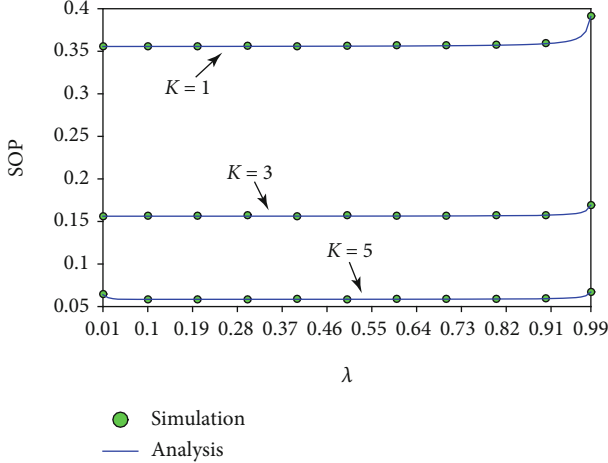


FIGURE 7: SOP versus the power splitting ratio.

transmission power and thus, the SOP is large for high values of P_l . As such, a moderate value of P_l creates the minimum SOP.

Figure 5 shows the SOP versus ε for $P_{sm}/N_0 = 15$ dB, $\alpha = 0.6$, $C_1 = 0.2$ bps/Hz, $P_l/N_0 = 17$ dB, $\bar{C}_3 = 0.1$ bps/Hz, $\lambda = 0.8$, and $C_2 = 0.3$ bps/Hz. The results confirm the precision of (27) owing to the assortment between the simulation and the analysis. In addition, the SOP reduces with increasing number of relays as expected. Furthermore, the SOP decreases with increasing the preset outage probability of licensed receiver. The reason is that the increase in ε permits licensed receivers to tolerate more interference from unlicensed transmitters. Consequently, unlicensed transmitters are able to send signals with larger powers, intimately tempering the outage in Stage II. However, the saturated SOP occurs at large ε (e.g., $\varepsilon > 0.5$). The reason for the SOP saturation is the power allotment in (21) and (22) in which the second term in P_s (or P_{r_i}) does not depend on ε . Consequently, large values of ε make P_s (or P_{r_i}) unchanged, resulting in the saturated SOP.

Figure 6 shows the SOP versus α for $P_{sm}/N_0 = 8$ dB, $\varepsilon = 0.1$, $C_1 = 0.2$ bps/Hz, $\bar{C}_3 = 0.1$ bps/Hz, $P_l/N_0 = 12$ dB, $\lambda = 0.8$, and $C_2 = 0.3$ bps/Hz. The results verify the accuracy of (27) because the simulation exactly agrees with the analysis. Additionally, the SOP decreases with increasing number of relays as expected. Furthermore, the appropriate selection of α , namely, α_{opt} , minimizes the SOP. Here are the reasons for the existence of α_{opt} . Increasing α extends the duration of the Stage I and hence, UR_i scavenges more energy and restores correctly the US's data with a larger possibility. Nonetheless, the increase in α also mitigates the maximum secrecy rate in the Stage II and therefore, the SOP accretes. As a result, the trade-off between the durations of two stages is optimized with α_{opt} for the minimum SOP.

Figure 7 demonstrates the SOP versus the power splitting ratio λ for $\bar{C}_3 = 0.1$ bps/Hz, $P_{sm}/N_0 = 8$ dB, $C_1 = 0.2$ bps/Hz, $\alpha = 0.6$, $C_2 = 0.3$ bps/Hz, $P_l/N_0 = 12$ dB, and $\varepsilon = 0.1$. The results expose that the simulation matches the analysis, corroborating (27). In addition, the security capability is enhanced with increasing number of relays as expected. Furthermore, the security performance is optimized by optimally adopting λ . Here are reasons for the existence

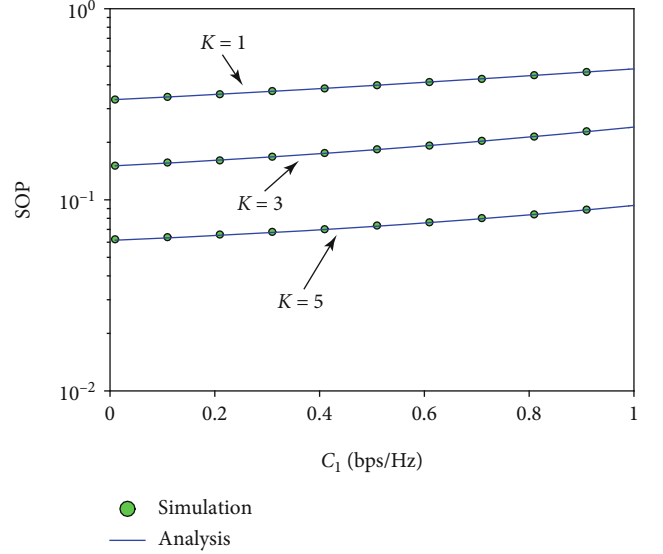


FIGURE 8: SOP versus the target spectral efficiency of unlicensed users.

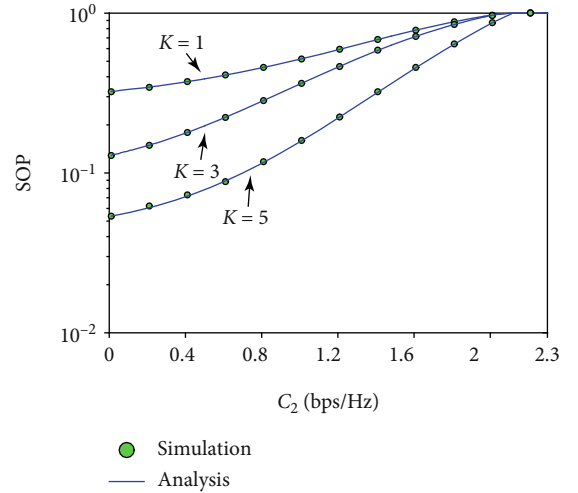


FIGURE 9: SOP versus the target spectral efficiency of licensed users.

of the optimum value of λ for the best security performance. The increase in λ allows UR_i to harvest more energy and hence, UR_i improves its communication reliability in the Stage II, eventually reducing the SOP. However, the increase in λ also mitigates the energy for the message decoder, deteriorating the possibility that UR_i decodes successfully the US's data in the Stage I and inducing more secrecy outage in Stage II. As such, λ can be optimally selected to compromise the communication reliability of US and UR_i in both stages.

Figure 8 illustrates the SOP versus C_1 for $P_{sm}/N_0 = 10$ dB, $\lambda = 0.8$, $\alpha = 0.6$, $\bar{C}_3 = 0.1$ bps/Hz, $\varepsilon = 0.1$, $C_2 = 0.3$ bps/Hz, and $P_l/N_0 = 15$ dB. The results show the assortment between the analysis and the simulation, corroborating (27).

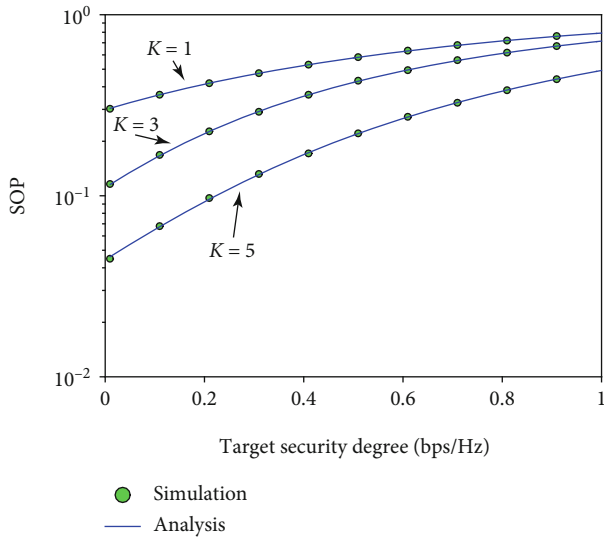


FIGURE 10: SOP versus the target security degree.

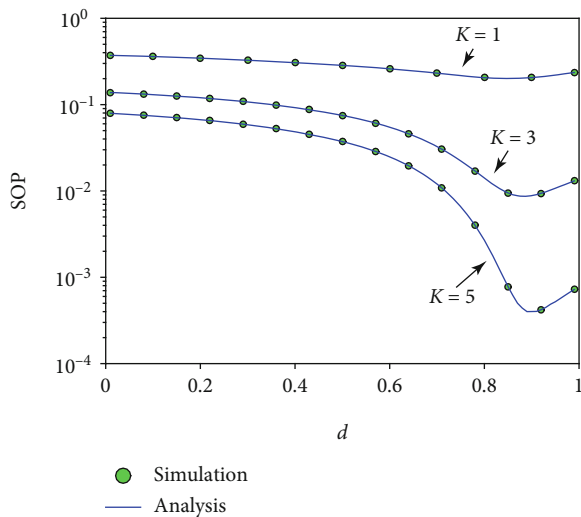


FIGURE 11: SOP versus the relays' positions.

Additionally, the security performance is enhanced with increasing number of relays as expected. Furthermore, the security performance reduces with the increase in C_1 . This is obvious since the higher target spectral efficiency the unlicensed users expect, the lower the possibility for the relays to exactly recover the US's data and thus, the higher the outage probability in Stage II.

Figure 9 demonstrates the SOP versus C_2 for $P_{sm}/N_0 = 10$ dB, $\lambda = 0.8$, $\alpha = 0.6$, $\bar{C}_3 = 0.1$ bps/Hz, $\epsilon = 0.1$, $C_1 = 0.2$ bps/Hz, and $P_l/N_0 = 15$ dB. The results verify the agreement between the analysis and the simulation, corroborating the accuracy of (27). Additionally, the SOP reduces with increasing number of relays as expected. Moreover, the security performance is worse with the increase in C_2 . Here are reasons for this. For a certain value of ϵ in (17) and (18), the larger

target spectral efficiency the licensed users expect, the smaller the interference at licensed users induced by unlicensed users must be and thus, the smaller transmission power the unlicensed users must transmit with, causing the larger SOP. However, the system outage always occurs at high values of C_2 . Here are the reasons for this. Relied on (21) and (22), we see that γ_{21} and γ_{22} (or C_2) are inversely proportional to the terms inside $[\cdot]^+$. Therefore, the increase in C_2 up to some value (e.g., 2.13 bps/Hz) induces $[\cdot]^+ = 0$ and thus, $P_s = 0$ and $P_{r_i} = 0$ always happen as C_2 is above a threshold, inducing the system outage with the probability of 1.

Figure 10 plots the SOP versus \bar{C}_3 for $P_{sm}/N_0 = 10$ dB, $= 0.6\lambda = 0.8$, $\epsilon = 0.1$, $C_1 = 0.2$ bps/Hz, $C_2 = 0.1$ bps/Hz, and $P_l/N_0 = 15$ dB. The results affirm the preciseness of (27) since the simulation agrees with the analysis. Additionally, the security capability is enhanced with increasing number of relays as expected. Moreover, the security performance is worse with the increase in \bar{C}_3 . The reason is since conditioned on specifications, and the higher target security degree causes the higher SOP.

Figure 11 assumes all relays to be located at $(d, 0)$ to demonstrate the SOP versus the relays' positions for $\bar{C}_3 = 0.1$ bps/Hz, $P_{sm}/N_0 = 15$ dB, $\epsilon = 0.1$, $C_1 = 0.2$ bps/Hz, $\alpha = 0.6$, $P_l/N_0 = 17$ dB, $\lambda = 0.8$, and $C_2 = 0.3$ bps/Hz. The results corroborate (27) owing to the assortment between the simulation and the analysis. Furthermore, the security performance improves with increasing number of relays, again demonstrating the efficacy of the relay selection in securing CRNwEH. Note that the secrecy outage event occurs as UR_b is unable to exactly restore the US's data (i.e., US is far away from UR_b) or UR_b is unable to transmit reliably the restored source data to UD (i.e., UD is far away from UR_b). Consequently, it is natural that the relays' optimum positions always exist. This optimum position optimally compromises the probability that UR_b can precisely decode the US's data with the possibility that UR_b is able to transmit reliably the recovered source data to UD to maximize the security performance. Figure 11 verifies this observation that the best security performance is obtained when UR_b is $d_{opt} = 0.85, 0.87, 0.91$ away from US for $K = 1, 3, 5$, correspondingly.

5. Conclusions

The current paper performed the secrecy performance analysis for the relay selection in CRNwEH by deriving the precise closed-form formula of the SOP under investigation of the licensed outage restriction, Rayleigh fading, the licensed interference, and the peak transmission power restriction. The preciseness of the suggested formula was confirmed by computer simulations. Numerous results illustrated that the relay selection dramatically improves the security capability. Furthermore, the secrecy performance is saturated at large peak transmission power or large target outage probability of licensed user. Additionally, the secrecy performance of the relay selection in CRNwEH depends on several key specifications among which the power splitting ratio, the time switching ratio, and the relays' positions can be optimally adopted to achieve the best information security.

Appendix

A. Proof of (30)

\mathcal{F}_i in (29) is rewritten after invoking (5) as

$$\begin{aligned}
\mathcal{F}_i &= \Pr \left\{ \gamma_{sr_i} < \gamma_1 \right\} = \Pr \left\{ \frac{P_s |h_{sr_i}|^2}{P_l |h_{lr_i}|^2 + \hat{\sigma}_{r_i}^2} < \gamma_1 \right\} \\
&= \mathbb{E}_{|h_{lr_i}|^2} \left\{ \Pr \left\{ |h_{sr_i}|^2 < \frac{\gamma_1}{P_s} (P_l |h_{lr_i}|^2 + \hat{\sigma}_{r_i}^2) \mid |h_{lr_i}|^2 \right\} \right\} \\
&= \mathbb{E}_{|h_{lr_i}|^2} \left\{ 1 - e^{-\frac{\gamma_1}{P_s \mu_{sr_i}} (P_l |h_{lr_i}|^2 + \hat{\sigma}_{r_i}^2)} \right\} \\
&= 1 - \int_0^\infty e^{-\gamma_1 / P_s \mu_{sr_i} (P_l x + \hat{\sigma}_{r_i}^2)} \frac{1}{\mu_{lr_i}} e^{-x / \mu_{lr_i}} dx \\
&= 1 - \frac{e^{-\hat{\sigma}_{r_i}^2 \gamma_1 / P_s \mu_{sr_i}}}{\mu_{lr_i} \left((P_l \gamma_1 / P_s \mu_{sr_i}) + (1 / \mu_{lr_i}) \right)}. \tag{A.1}
\end{aligned}$$

Given O_i and G_i in (31) and (32), respectively, one can reduce (A.1) to (30), finishing the proof.

B. Proof of (38)

By considering two scenarios, $\log_2((1 + \gamma_{r,d})/(1 + \gamma_{r,w})) \geq 0$ and $\log_2((1 + \gamma_{r,d})/(1 + \gamma_{r,w})) < 0$, one can decompose \mathcal{G}_i as

$$\begin{aligned}
\mathcal{G}_i &= \Pr \left\{ \log_2 \left(\frac{1 + \gamma_{r,d}}{1 + \gamma_{r,w}} \right) < C_3 \mid \log_2 \left(\frac{1 + \gamma_{r,d}}{1 + \gamma_{r,w}} \right) \right. \\
&\geq 0, |h_{ld}|^2, |h_{lw}|^2 \left. \right\} \times \Pr \left\{ \log_2 \left(\frac{1 + \gamma_{r,d}}{1 + \gamma_{r,w}} \right) \right. \\
&\geq 0 \mid |h_{ld}|^2, |h_{lw}|^2 \left. \right\} + \Pr \left\{ 0 < C_3 \mid |h_{ld}|^2, |h_{lw}|^2 \right\} \Pr \left\{ \log_2 \left(\frac{1 + \gamma_{r,d}}{1 + \gamma_{r,w}} \right) \right. \\
&< 0 \mid |h_{ld}|^2, |h_{lw}|^2 \left. \right\}, \tag{B.1}
\end{aligned}$$

where C_3 is given in (37).

Due to the positive target security degree (i.e., $C_3 > 0$), (B.1) is simplified as

$$\begin{aligned}
\mathcal{G}_i &= \Pr \left\{ \frac{1 + \gamma_{r,d}}{1 + \gamma_{r,w}} < 2^{C_3} \mid |h_{ld}|^2, |h_{lw}|^2 \right\} \\
&= \Pr \left\{ \gamma_{r,d} < 2^{C_3} (1 + \gamma_{r,w}) - 1 \mid |h_{ld}|^2, |h_{lw}|^2 \right\} \tag{B.2} \\
&= \int_0^\infty \int_0^{2^{C_3}(1+x)-1} f_{\gamma_{r,w}, \gamma_{r,d}}(x, y \mid |h_{ld}|^2, |h_{lw}|^2) dy dx.
\end{aligned}$$

Conditioned on $|h_{ld}|^2$ and $|h_{lw}|^2$, $\gamma_{r,d}$ and $\gamma_{r,w}$ are uncorrelated and hence, their joint PDF is symbolized as the multiplication of their marginal PDFs, i.e., $f_{\gamma_{r,w}, \gamma_{r,d}}(x, y \mid |h_{ld}|^2, |h_{lw}|^2) = f_{\gamma_{r,w}}(x \mid |h_{lw}|^2) f_{\gamma_{r,d}}(y \mid |h_{ld}|^2)$. Therefore, (B.2) is further decomposed as

$$\begin{aligned}
\mathcal{G}_i &= \int_0^\infty \left[\int_0^{2^{C_3}(1+x)-1} f_{\gamma_{r,d}}(y \mid |h_{ld}|^2) dy \right] f_{\gamma_{r,w}}(x \mid |h_{lw}|^2) dx \\
&= \int_0^\infty F_{\gamma_{r,d}}(2^{C_3}[1+x] - 1 \mid |h_{ld}|^2) f_{\gamma_{r,w}}(x \mid |h_{lw}|^2) dx. \tag{B.3}
\end{aligned}$$

To achieve the closed form for (B.3), the CDF of $\gamma_{r,d}$, $F_{\gamma_{r,d}}(z \mid |h_{ld}|^2)$, and the PDF of $\gamma_{r,w}$, $f_{\gamma_{r,w}}(z \mid |h_{lw}|^2)$, are found first.

The CDF of $\gamma_{r,d}$ is

$$\begin{aligned}
F_{\gamma_{r,d}}(z \mid |h_{ld}|^2) &= \Pr \left\{ \gamma_{r,d} \leq z \mid |h_{ld}|^2 \right\} \\
&= \Pr \left\{ \frac{P_{r_i} |h_{r,d}|^2}{P_l |h_{ld}|^2 + \sigma_d^2} \leq z \mid |h_{ld}|^2 \right\} \tag{B.4} \\
&= \Pr \left\{ |h_{r,d}|^2 \leq \frac{z}{P_{r_i}} (P_l |h_{ld}|^2 + \sigma_d^2) \mid |h_{ld}|^2 \right\} \\
&= 1 - e^{-z \mu_{r,d} P_{r_i} (P_l |h_{ld}|^2 + \sigma_d^2)}.
\end{aligned}$$

The PDF of $\gamma_{r,w}$ is straightforwardly obtained from the PDF of $|h_{r,w}|^2$ by using the variable change and hence, the PDF of $\gamma_{r,w}$ can be reduced to

$$\begin{aligned}
f_{\gamma_{r,w}}(z \mid |h_{lw}|^2) &= \frac{(P_l |h_{lw}|^2 + \sigma_w^2)}{P_{r_i}} f_{|h_{r,w}|^2} \left(z \frac{P_l |h_{lw}|^2 + \sigma_w^2}{P_{r_i}} \right) \\
&= \frac{P_l |h_{lw}|^2 + \sigma_w^2}{\mu_{r,w} P_{r_i}} e^{-z (P_l |h_{lw}|^2 + \sigma_w^2) / \mu_{r,w} P_{r_i}}. \tag{B.5}
\end{aligned}$$

Inserting (B.4) and (B.5) with appropriate variable substitutions into (B.3) results in

$$\begin{aligned}
\mathcal{G}_i &= \int_0^\infty \left\{ 1 - e^{-(2^{C_3}[1+x]-1) / \mu_{r,d} P_{r_i} (P_l |h_{ld}|^2 + \sigma_d^2)} \right\} \frac{(P_l |h_{lw}|^2 + \sigma_w^2)}{\mu_{r,w} P_{r_i}} e^{-x (P_l |h_{lw}|^2 + \sigma_w^2) / \mu_{r,w} P_{r_i}} dx \\
&= 1 - \frac{P_l |h_{lw}|^2 + \sigma_w^2}{\mu_{r,w} P_{r_i}} e^{-(2^{C_3}-1) / \mu_{r,d} P_{r_i} (P_l |h_{ld}|^2 + \sigma_d^2)} \int_0^\infty e^{-(2^{C_3} (P_l |h_{ld}|^2 + \sigma_d^2) / \mu_{r,d} + (P_l |h_{lw}|^2 + \sigma_w^2) / \mu_{r,w}) x / P_{r_i}} dx \\
&= 1 - \frac{P_l |h_{lw}|^2 + \sigma_w^2}{\mu_{r,w} P_{r_i}} e^{-(2^{C_3}-1) / \mu_{r,d} P_{r_i} (P_l |h_{ld}|^2 + \sigma_d^2)} \frac{P_{r_i}}{2^{C_3} \left((P_l |h_{ld}|^2 + \sigma_d^2) / \mu_{r,d} \right) + \left((P_l |h_{lw}|^2 + \sigma_w^2) / \mu_{r,w} \right)}. \tag{B.6}
\end{aligned}$$

Given A_i , B_i , C_i , and D_i in (39), (40), (41), and (42), respectively, one can shorten (B.6) as (38). This completes the proof.

Data Availability

The authors declare that all data used to support the findings of this study are included within the article

Conflicts of Interest

The authors declare that they have no conflicts of interest.

Acknowledgments

This research is funded by Viet Nam National University Ho Chi Minh City (VNU-HCM) under grant number B2021-20-01. We would like to thank Ho Chi Minh City University of Technology (HCMUT), VNU-HCM for the support of time and facilities for this study.

References

- [1] Z. Tian, S. Yi, P. Zhiwen, L. Nan, and Y. Xiaohu, "Matching theory based physical layer secure transmission strategy for cognitive radio networks," *IEEE Access*, vol. 9, pp. 46201–46209, 2021.
- [2] K. Ho-van, L. Pham-Hong, S. Vo-Que, and T. Luu-Thanh, "On the performance of opportunistic relay selection in cognitive radio networks with primary user's interference and direct channel," *Wireless Personal Communications*, vol. 91, no. 1, pp. 345–367, 2016.
- [3] K. Ho-Van, "Outage analysis of opportunistic relay selection in underlay cooperative cognitive networks under general operation conditions," *IEEE Transactions on Vehicular Technology*, vol. 65, no. 10, pp. 8145–8154, 2016.
- [4] A. Bletsas, A. Khisti, D. P. Reed, and A. Lippman, "A simple cooperative diversity method based on network path selection," *IEEE Journal on Selected Areas in Communications*, vol. 24, no. 3, pp. 659–672, 2006.
- [5] J. He, S. Guo, F. Wang, and Y. Yang, "Relay selection and outage analysis in cooperative cognitive radio networks with energy harvesting," in *2016 IEEE International Conference on Communications (ICC)*, pp. 1–6, Kuala Lumpur, Malaysia, 2016.
- [6] L. Jiang and H. Tian, "Energy-efficient relay selection scheme for physical layer security in cognitive radio networks," *Mathematical Problems in Engineering*, vol. 2015, Article ID 587104, 9 pages, 2015.
- [7] B. M. ElHalawany, M. Elsabrouty, O. Muta, A. Abdelrahman, and H. Furukawa, "Joint energy-efficient single relay selection and power allocation for analog network coding with three transmission phases," in *2014 IEEE 79th Vehicular Technology Conference (VTC Spring)*, pp. 1–7, Seoul, Korea, 2014.
- [8] H. Lei, H. Zhang, I. S. Ansari et al., "On secrecy outage of relay selection in underlay cognitive radio networks over Nakagami-m fading channels," *IEEE Transactions on Cognitive Communications and Networking*, vol. 3, no. 4, pp. 614–627, 2017.
- [9] C. Wang, H.-M. Wang, and X.-G. Xia, "Hybrid opportunistic relaying and jamming with power allocation for secure cooperative networks," *IEEE Transactions on Wireless Communications*, vol. 14, no. 2, pp. 589–605, 2015.
- [10] H.-M. Wang and X.-G. Xia, "Enhancing wireless secrecy via cooperation: signal design and optimization," *IEEE Communications Magazine*, vol. 53, no. 12, pp. 47–53, 2015.
- [11] X. Li, Q. Wang, M. Liu et al., "Cooperative wireless-powered NOMA relaying for B5G IoT networks with hardware impairments and channel estimation errors," *IEEE Internet of Things Journal*, vol. 8, no. 7, pp. 5453–5467, 2021.
- [12] T.-T. Chan and T.-M. Lok, "Utilizing interference by network coding for simultaneous wireless information and power transfer," *IEEE Wireless Communications Letters*, 2021.
- [13] R. Parekh, U. Shah, and K. George, "Experimental study on 3D fractal base antennas design for efficient Wi-Fi energy harvesting," in *2021 IEEE 11th Annual Computing and Communication Workshop and Conference (CCWC)*, pp. 1459–1463, NV, USA, 2021.
- [14] H. Zheng, K. Xiong, P. Fan, Z. Zhong, and K. B. Letaief, "Age of information-based wireless powered communication networks with selfish charging nodes," *IEEE Journal on Selected Areas in Communications*, vol. 39, no. 5, pp. 1393–1411, 2021.
- [15] K. Ma, Z. Li, P. Liu et al., "Reliability-constrained throughput optimization of industrial wireless sensor networks with energy harvesting relay," *IEEE Internet of Things Journal*, 2021.
- [16] A. D. Wyner, "The wire-tap channel," *Bell System Technical Journal*, vol. 54, no. 8, pp. 1355–1387, 1975.
- [17] L. Ni, X. Da, H. Hu, Y. Yuan, Z. Zhu, and Y. Pan, "Outage-constrained secrecy energy efficiency optimization for CRNs with non-linear energy harvesting," *IEEE Access*, vol. 7, pp. 175213–175221, 2019.
- [18] N. Pham-Thi-Dan, T. Do-Dac, K. Ho-Van, S. Vo-Que, and S. Pham-Ngoc, "Effect of Nakagami-m fading on secrecy outage of energy scavenging underlay cognitive networks," in *2019 International Conference on Advanced Technologies for Communications (ATC)*, pp. 287–291, Hanoi, Vietnam, October 2019.
- [19] D. Wang and S. Men, "Secure energy efficiency for NOMA based cognitive radio networks with nonlinear energy harvesting," *IEEE Access*, vol. 6, pp. 62707–62716, 2018.
- [20] F. Wang and X. Zhang, "Secure resource allocation for cooperative cognitive radio networks with dedicated energy sources," in *2018 IEEE International Conference on Communications (ICC)*, pp. 1–6, Kansas City, MO, USA, May 2018.
- [21] H. Lei, M. Xu, I. S. Ansari, G. Pan, K. A. Qaraqe, and M. S. Alouini, "On secure underlay MIMO cognitive radio networks with energy harvesting and transmit antenna selection," *IEEE Transactions on Green Communications and Networking*, vol. 1, no. 2, pp. 192–203, 2017.
- [22] A. Singh, M. R. Bhatnagar, and R. K. Mallik, "Secrecy outage performance of SWIPT cognitive radio network with imperfect CSI," *IEEE Access*, vol. 8, pp. 3911–3919, 2020.
- [23] R. Tan, Y. Gao, H. He, and Y. Cao, "Secrecy performance of cognitive radio sensor networks with an energy-harvesting based eavesdropper and imperfect CSI," in *2018 Asian Hardware Oriented Security and Trust Symposium (AsianHOST)*, pp. 80–85, Hong Kong, China, December 2018.
- [24] N. Pham-Thi-Dan, K. Ho-Van, T. Do-Dac, S. Vo-Que, and S. Pham-Ngoc, "Security analysis for cognitive radio network with energy scavenging capable relay over Nakagami-m fading channels," in *2019 International Symposium on Electrical and Electronics Engineering (ISEE)*, pp. 68–72, Ho Chi Minh City, Vietnam, October 2019.

- [25] M. Bouabdellah, F. el Bouanani, P. C. Sofotasios et al., "Cooperative energy harvesting cognitive radio networks with spectrum sharing and security constraints," *IEEE Access*, vol. 7, pp. 173329–173343, 2019.
- [26] T. V. Nguyen and B. An, "Cognitive multihop wireless powered relaying networks over Nakagami-m fading channels," *IEEE Access*, vol. 7, pp. 154600–154616, 2019.
- [27] W. Zhao, R. She, and H. Bao, "Security energy efficiency maximization for two-way relay assisted cognitive radio NOMA network with self-interference harvesting," *IEEE Access*, vol. 7, pp. 74401–74411, 2019.
- [28] N. Pham-Thi-Dan, T. Do-Dac, K. Ho-Van, S. Vo-Que, and S. Pham-Ngoc, "On security capability of cooperative communications in energy scavenging cognitive radio networks," in *2019 International Conference on Advanced Technologies for Communications (ATC)*, pp. 89–93, Hanoi, Vietnam, October 2019.
- [29] H. M. Wang, T. X. Zheng, J. Yuan, D. Towsley, and M. H. Lee, "Physical layer security in heterogeneous cellular networks," *IEEE Transactions on Communications*, vol. 64, no. 3, pp. 1204–1219, 2016.
- [30] C. Wang and H. M. Wang, "On the secrecy throughput maximization for MISO cognitive radio network in slow fading channels," *IEEE Transactions on Information Forensics and Security*, vol. 9, no. 11, pp. 1814–1827, 2014.
- [31] H. Lei, R. Gao, K. H. Park, I. S. Ansari, K. J. Kim, and M. S. Alouini, "On secure downlink NOMA systems with outage constraint," *IEEE Transactions on Communications*, vol. 68, no. 12, pp. 7824–7836, 2020.
- [32] X. Li, M. Zhao, M. Zeng et al., "Hardware impaired ambient backscatter NOMA systems: reliability and security," *IEEE Transactions on Communications*, vol. 69, no. 4, pp. 2723–2736, 2021.
- [33] X. Li, M. Zhao, Y. Liu, L. Li, Z. Ding, and A. Nallanathan, "Secrecy analysis of ambient backscatter NOMA systems under I/Q imbalance," *IEEE Transactions on Vehicular Technology*, vol. 69, no. 10, pp. 12286–12290, 2020.
- [34] P. Maji, B. Prasad, S. D. Roy, and S. Kundu, "Secrecy outage of a cognitive radio network with selection of energy harvesting relay and imperfect CSI," *Wireless Personal Communications*, vol. 100, no. 2, pp. 571–586, 2018.
- [35] T. D. Hieu, T. T. Duy, and S. G. Choi, "Performance enhancement for harvest-to-transmit cognitive multi-hop networks with best path selection method under presence of eavesdropper," in *2018 20th International Conference on Advanced Communication Technology (ICACT)*, pp. 323–328, Chunchon, Korea (South), February 2018.
- [36] K. Ho-van and T. Do-Dac, "Security enhancement for energy harvesting cognitive networks with relay selection," *Wireless Communications and Mobile Computing*, vol. 2020, Article ID 8867148, 13 pages, 2020.
- [37] N. Pham-Thi-Dan, K. Ho-Van, T. Do-Dac, S. Vo-Que, and S. Pham-Ngoc, "Energy harvesting cooperative cognitive networks: relay selection for information security," in *2019 International Symposium on Electrical and Electronics Engineering (ISEE)*, pp. 93–96, Ho Chi Minh City, Vietnam, October 2019.
- [38] K. Ho-Van and T. Do-Dac, "Overlay networks with jamming and energy harvesting: security analysis," *Arabian Journal for Science and Engineering*, 2021.
- [39] P. Nguyen-Huu and K. Ho-van, "Bidirectional relaying with energy harvesting capable relay: outage analysis for Nakagami-m fading," *Telecommunication Systems*, vol. 69, no. 3, pp. 335–347, 2018.
- [40] E. Biglieri, J. Proakis, and S. Shamai, "Fading channels: information-theoretic and communications aspects," *IEEE Transactions on Information Theory*, vol. 44, no. 6, pp. 2619–2692, 1998.
- [41] I. S. Gradshteyn et al., *Table of Integrals, Series and Products*, Academic Press, San Diego, CA, USA, 6th edition, 2000.
- [42] K. Ho-van and T. Do-Dac, "Reliability-security trade-off analysis of cognitive radio networks with jamming and licensed interference," *Wireless Communications and Mobile Computing*, vol. 2018, Article ID 5457176, 15 pages, 2018.
- [43] K. Ho-Van, "On the performance of maximum ratio combining in cooperative cognitive networks with proactive relay selection under channel information errors," *Telecommunication Systems*, vol. 65, no. 3, pp. 365–376, 2017.

Research Article

Physical Layer Secrecy Analysis of Multihop Hybrid Satellite-Terrestrial Relay Networks with Jamming

Xiaoqi Wang , Hanwei Zhang , and Zheng Hou 

School of Surveying and Land Information Engineering, Henan Polytechnic University, Jiaozuo 454003, China

Correspondence should be addressed to Zheng Hou; housheng.com@163.com

Received 12 March 2021; Revised 3 May 2021; Accepted 20 May 2021; Published 10 June 2021

Academic Editor: Yuan Ding

Copyright © 2021 Xiaoqi Wang et al. This is an open access article distributed under the Creative Commons Attribution License, which permits unrestricted use, distribution, and reproduction in any medium, provided the original work is properly cited.

This paper explores the secrecy analysis of a multihop hybrid satellite-terrestrial relay network (HSTRN) with jamming, where one satellite source is aimed at communicating with destination users via multihop decode-and-forward (DF) terrestrial relays, in the existence of an eavesdropper. All the destination users are deployed randomly following a homogeneous Poisson point process (PPP) based on stochastic geometry. Each relay operates not only as a conventional DF relay to forward the received signal but also as a jammer to generate intentional interference to degrade the eavesdropper link, considering shadowed-Rician fading for legitimate link and wiretap link while Rayleigh fading for jamming link. To characterize the secrecy performance of the considered network, the accurate analytical expression for the secrecy outage probability (SOP) is derived. In order to reveal further insights on the achievable diversity order of the network, the asymptotic behavior of SOP expression at high signal-to-noise ratio (SNR) region is deduced. Moreover, the throughput of the system is discussed to characterize the secrecy performance. Finally, the theoretical results are validated through comparison with simulation results and show that (1) the secrecy performance of the considered network gets better with the decreasing of the hops and with the decreasing severity of the channel fading scenario, (2) the relay of the network operating as a jammer can provide better secrecy performance without extra network resources, and (3) small hops and high SNR can yield to high throughput of the system.

1. Introduction

With the development of wireless communication towards high-speed and broadband, there are great challenges for wireless communication to support massive and seamless connection under limited spectrum, while satellite communication has become much popular on account of its high transmission quality, wide coverage at low cost, and easy deployment [1–3], and it has various applications in navigation, military defence, disaster response, and other remote or dangerous areas. Unfortunately, between the satellite and the terrestrial terminal, masking effect caused by some obstacles and shadowing will make the line-of-sight (LOS) communication unstable even unavailable, and the performance of the satellite network will be affected seriously. Therefore, relay technology has drawn increasing attention by researchers due to its improvement in the reliability and coverage of the networks [4–9].

Satellite communication with joined relay forms a new framework of hybrid satellite-terrestrial relay networks

(HSTRN) [10–13]. This framework can provide satellite services to handheld devices, which has been incorporated in the DVB-SH standard [14]. In HSTRN, the relay transmits the signal from satellite to the destination. That cooperative technique has been an important approach in relay communication for its advantage of providing diversity gain, enhancing coverage, and reducing power consumption [15]. Amplify-and-forward (AF) and decode-and-forward (DF) are two cooperative diversity protocols in common. Based on different relay protocols, more and more researchers have paid attention to improving the performance of HSTRN from different views [12, 16, 17]. An et al. [12] investigated the outage probability (OP) performance and the ergodic capacity of an AF HSTRN. Sakarellos et al. [16] examined the OP performance of a HSTRN using the maximal ratio combining (MRC) technique based on DF relaying. The authors of [17] focused their research on the performance of a multiantenna HSTRN with multiple cochannel interferes at both the terrestrial relay and destination.

However, the transmission security of HSTRN is hardly involved. Recently, the security of wireless communication has become much important to evaluate a communication system. In the beginning, the security of satellite communication mainly bases on the traditional encryption method at upper layers, but there is a great challenge for this method because of its complex algorithm and without consideration of the error transmission at the physical layer. To solve this problem, Wyner characterized fading channels to achieve physical layer security based on information-theoretic approach [18]. And yet, research on physical layer secrecy in HSTRN is limited [19–24]. In [19], the authors explored the physical layer secrecy analysis of multiuser HSTRN by deriving accurate and asymptotic expressions for secrecy outage probability (SOP) and deducing the expression for probability of nonzero secrecy capacity. Huang et al. [20] investigated the secrecy performance of HSTRN by comparing AF and DF protocols, revealing that the system secrecy performance with the DF protocol was always better than that with the AF protocol. And on this basis, Bankey and Upadhyay [21] studied the physical layer security of a downlink HSTRN with multiantenna satellite, multiple terrestrial destinations, multiple relays, and multiple eavesdroppers. Guo et al. [22] presented a joint relay selection and a user scheduling scheme based on jammer to balance the system performance and actual implementation. In order to enhance the secrecy of the system under the total power constraint of relays, Yan et al. [23] investigated cooperative jamming by the relays to maximize the secrecy rate. Likewise, Yan et al. [24] maximized the secrecy rate of HSTRN through the joint optimization of the relay beamforming vector and the covariance matrix of artificial noise. In addition, the authors of [25] proposed an unmanned aerial vehicle (UAV) to ground communication system with spatially random eavesdropper account on both ground and airspace and investigated the secrecy performance of the system.

In general, the present physical layer secrecy studies mostly have focused on the HSTRN with dual-hop relaying [19, 20] or multiple users without consideration of their distribution [19], while multihop communication has been proved to extend the coverage of a wireless network effectively as well as to combat the adverse effects of wireless fading channels without more network resources [26]. Given its indoor coverage and service availability, especially in highly shadowed regions like shopping malls, office buildings, and dense residential areas, where the users of complicated distribution do not have LOS communication with the satellite due to masking effect, the investigation is explored in this paper.

In view of the aforementioned discussion, the secrecy performance of a multihop HSTRN is investigated, where a satellite source communicates with destination users via multihop relays in the presence of an eavesdropper. The relays use the DF protocol to forward the received signal and jam the reception of the eavesdropper simultaneously, while the ground users are deployed randomly. Both of the legitimate link (including satellite link and terrestrial link) and wiretap link experience shadowed-Rician fading [27, 28], while jamming link undergoes Rayleigh fading [29]. The main works we have done can be summed up as follows:

- (1) A multihop HSTRN with jamming is proposed, in which all the destination users are deployed randomly following a homogeneous Poisson point process (PPP) distribution based on stochastic geometry. The probability density functions (PDFs) and the cumulative distribution functions (CDFs) of the channel gain between the relay and users are deduced
- (2) The accurate analytical SOP expression of the considered network is derived
- (3) The asymptotic behavior of the SOP expression at high SNR region is explored, and the throughput of the system is obtained
- (4) The simulation is carried out to verify the theoretical results, which reveal that the performance of a multihop HSTRN depends on the hops, secrecy rate, jammer, and shadowing severity of the considered network

The rest of this paper proceeds as follows. The system model and channel model are presented in Section 2. The secrecy analysis of the network is provided in Section 3, where the accurate, asymptotic SOP formulas and the throughput of the system have been derived. Numerical and simulation results are given in Section 4, and conclusions are drawn in Section 5.

Notations 1. In this paper, $|\cdot|$ denotes the absolute value of a scalar, $E[\cdot]$ denotes the expectation operator, $n!$ symbolizes the factorial of n , $f_X(\cdot)$ and $F_X(\cdot)$ represent the PDF and CDF, respectively, and $\Pr(\cdot)$ means the probability for a random variable.

2. HSTRN Description

2.1. System Model. Considering the configuration of a downlink multihop HSTRN is shown in Figure 1, where one satellite source (S) communicates with destination users (D) via $L - 1$ DF terrestrial relays $\{R_l\}_{l=1}^{L-1}$, in the existence of an eavesdropper (E). Each relay operates as a conventional DF relay, which can fully decode the received confidential signal and then forward it to the next legitimate node. Meanwhile, at each hop, the eavesdropper also attempts to decode the message over an eavesdropper channel. On the other hand, each relay operates as a jammer mode to generate intentional interference to degrade the eavesdropper link. And all the ground destination users are deployed randomly following a homogeneous PPP based on stochastic geometry. Here, it is assumed that each node has only one antenna. In the long distance communication between the satellite and the terrestrial terminal, masking effect caused by severe shadowing and heavy obstacles (such as clouds, hills, and mountains) will make the LOS communication unstable even unavailable, and the performance of the satellite network will be affected seriously [19, 21]. Therefore, in view of masking effect and heavy fading, we assume that the direct link between S and D as well as between S and E is unavailable [12, 30, 31]. The legitimate link ($S \rightarrow R_l \rightarrow D$) and wiretap link

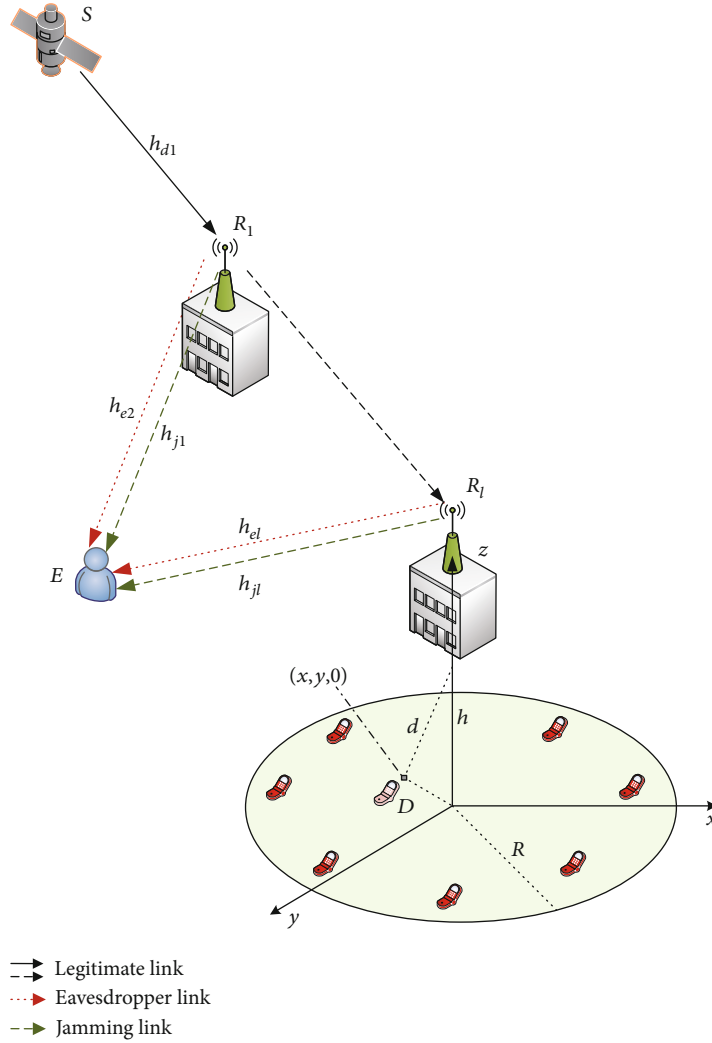


FIGURE 1: System model of a multihop HSTRN.

($R_l \rightarrow E$) are assumed to undergo Shadowed-Rician fading while jamming link follows Rayleigh fading. (Here, the statistical characterization for fading channels of terrestrial link can be changed with the parameter variation of Shadowed-Rician fading distribution.) All the receivers are affected by additive white Gaussian noise (AWGN) with zero mean and variance.

Without loss of generality, the total communication is divided into l hops.

In the first hop, the satellite source transmits its signal $x_{s_0}(t)$ with $E[|x_{s_0}(t)|^2] = 1$ to the first relay R_1 . Then, the relay forwards its received signal $\{x_{s_l}(t)\}_{l=1}^{L-1}$ with $E[|x_{s_l}(t)|^2] = 1$ to the next relay until the destination in the next hops. During the next periods, each relay performs both as a relay and a jammer, so it can fully decode the received signal and then forward the signal to the next node and use some of its available power to transmit jamming signal simultaneously. Meanwhile, the eavesdropper also attempts to decode the signal. For simplicity, we assume that the intended receiver has an a priori knowledge of the artificial jamming signal and hence is able to eliminate the effects while decoding the orig-

inal signal [32]. So all the jamming signals are well known by the next relay or the destination, and the signal received at the relay or the destination at hop l is given as

$$y_{d,l} = \sqrt{P_{l-1}} h_{d,l} x_{s_{l-1}}(t) + n_{d,l}, \quad (1 \leq l \leq L), \quad (1)$$

where P_{l-1} is the transmission power (P_0 being the transmission power at S) and $h_{d,l}$ represents the channel coefficient between $R_{l-1} \rightarrow R_l(D)$ ($h_{d,0}$ corresponding to $S \rightarrow R_1$), while $n_{d,l}$ is the AWGN variable at the destination.

Here, for simplicity, we assume that the eavesdropper cannot do joint decoding, which can be realized by using randomized code books at each hop to confuse the eavesdropper in practice [26, 32]. Therefore, the eavesdropper receives the signal only from R_{l-1} at hop l , and considering the unavailability between S and E as well as the jamming signal, the signal received at the eavesdropper at hop l can be obtained as

$$y_{e,l} = \sqrt{P_{l-1}} h_{e,l} x_{s_{l-1}}(t) + \sqrt{P_{j,l-1}} h_{j,l} x_{s_{l-1}}(t) + n_{e,l}, \quad (2 \leq l \leq L), \quad (2)$$

where $P_{j,l-1}$ is the jamming power at R_{l-1} , $h_{e,l}$ and $h_{j,l}$ denote the, respectively, channel coefficient of wiretap and jamming link between $R_{l-1} \rightarrow E$, and $n_{e,l}$ is the AWGN variable at the eavesdropper.

Thus, the instantaneous received SNRs at $R_l(D)$ and E can be expressed as

$$\gamma_{d,l} = \frac{P_{l-1}}{\sigma^2} |h_{d,l}|^2 = \eta_s |h_{d,l}|^2, \quad (1 \leq l \leq L), \quad (3)$$

$$\gamma_{e,l} = \frac{P_{l-1} |h_{e,l}|^2}{P_{j,l-1} |h_{j,l}|^2 + \sigma^2} = \frac{\gamma_{re,l}}{\gamma_{je,l} + 1}, \quad (2 \leq l \leq L), \quad (4)$$

where $\gamma_{re,l} = \eta_e |h_{e,l}|^2$ and $\gamma_{je,l} = \eta_j |h_{j,l}|^2$, with $\eta_e = P_{l-1}/\sigma^2$ and $\eta_j = P_{j,l-1}/\sigma^2$.

2.2. Channel Model. According to most of the related works, such as [19, 28], the legitimate link and wiretap link follow the independent shadowed-Rician distribution, and the PDF of $|h_\rho|^2$, $\rho = \{s, e\}$ (s, e , respectively, corresponding to the legitimate link and wiretap link), is given by

$$f_{|h_\rho|^2}(x) = \alpha_\rho \sum_{k=0}^{m_\rho} \zeta(k) x^k e^{-(\beta_\rho - \delta_\rho)x}, \quad (5)$$

where $\alpha_\rho = (2b_\rho m_\rho / (2b_\rho m_\rho + \Omega_\rho))^{m_\rho} / 2b_\rho$, $\beta_\rho = 1/2b_\rho$, $\delta_\rho = \Omega_\rho / 2b_\rho (2b_\rho m_\rho + \Omega_\rho)$, and $\zeta(k) = (-1)^k (1 - m_\rho)_k \delta_\rho^k / (k!)^2$, with b_ρ , m_ρ , and δ_ρ being the multipath components, the fading severity parameter, and the average power of LOS, respectively, and $(\cdot)_n$ being the Pochhammer symbol [33].

After applying the transformation of variable, the PDF of γ_ρ is given by

$$f_{\gamma_\rho}(x) = \alpha_\rho \sum_{k=0}^{m_\rho-1} \frac{\zeta(k)}{\binom{\eta_\rho}{k+1}} x^k e^{-((\beta_\rho - \delta_\rho)/\eta_\rho)x}. \quad (6)$$

By integrating the PDF in Equation (6), the CDF of γ_ρ can be given as

$$F_{\gamma_\rho}(x) = 1 - \alpha_\rho \sum_{k=0}^{m_\rho-1} \frac{\zeta(k)}{\binom{\eta_\rho}{k+1}} \sum_{p=0}^k \frac{k!}{p!} \left(\frac{\beta_\rho - \delta_\rho}{\eta_\rho} \right)^{-(k+1-p)} x^p e^{-((\beta_\rho - \delta_\rho)/\eta_\rho)x}. \quad (7)$$

For the jamming link, the channel coefficient $|h_{j,l}|$ follows Rayleigh fading distribution (Rayleigh distributions are usually used to model multipath fading without LOS paths. For simplicity, we assumed Rayleigh fading for the jamming link. And other fading models are applicable here.) with the CDF and PDF of $\gamma_{je,l}$ given, respectively, by

$$F_{\gamma_{je,l}}(x) = 1 - e^{-x/\overline{\gamma_{je,l}}}, \quad (8)$$

$$f_{\gamma_{je,l}}(x) = \frac{1}{\overline{\gamma_{je,l}}} e^{-x/\overline{\gamma_{je,l}}}, \quad (9)$$

where $\overline{\gamma_{je,l}}$ is the average SNR of the jamming link.

3. Performance Analysis

In this subsection, the exact closed-form SOP expression is deduced, the asymptotic behavior of the SOP is analysed, and the throughput of the considered system is discussed.

3.1. SOP Analysis. We start with the instantaneous capacity of the legitimate link and the wiretap link at hop l , which is given by

$$C_{d,l} = \frac{1}{L} \log_2(1 + \gamma_{d,l}), \quad (1 \leq l \leq L), \quad (10)$$

$$C_{e,l} = \frac{1}{L} \log_2(1 + \gamma_{e,l}), \quad (2 \leq l \leq L).$$

The achievable secrecy capacity of the network is defined as the difference between the capacity of the legitimate link and the wiretap link. Therefore, the secrecy capacity at hop l is expressed as

$$C_{s,l} = [C_{d,l} - C_{e,l}]^+ = \left[\frac{1}{L} \log_2 \left(\frac{1 + \gamma_{d,l}}{1 + \gamma_{e,l}} \right) \right]^+, \quad (2 \leq l \leq L), \quad (11)$$

where $[x]^+ = \max(x, 0)$.

To facilitate the analysis, we denote the secrecy SNR of hop l by $\gamma_l = (1 + \gamma_{d,l})/(1 + \gamma_{e,l})$ and Equation (11) can be expressed as

$$C_{s,l} = \left[\frac{1}{L} \log_2 \gamma_l \right]^+, \quad (2 \leq l \leq L). \quad (12)$$

For multihop DF relaying, secrecy outage of the network occurs whenever the data transmission in any hop is either unsuccessfully decoded or imperfectly secure. Given the assumption that the direct link between S and D is unavailable and considering the fact that the secrecy outage decisions are taken on each hop, the secrecy SNR of the network can be expressed as

$$\gamma_{\text{sys}} = \min_{2 \leq l \leq L} \{\gamma_l\}, \quad (13)$$

where $\gamma_1 = \gamma_{d,1}$.

As can be seen, the form is similar to that of conventional multihop DF relay networks. However, secrecy SNR is used here instead of instantaneous SNR. It is due to the fact that the system secrecy performance is dominated by the weakest hop in view of security.

Thus, we can obtain the secrecy capacity as

$$C_{\text{sys}} = \min_{2 \leq l \leq L} \{C_{s,l}\}. \quad (14)$$

The network is defined to be secrecy outage when the

secrecy capacity C_{sys} is lower than a predefined secrecy rate γ_{th} , namely,

$$P_{\text{sec}} = \Pr (C_{\text{sys}} < \gamma_{\text{th}}), \quad (15)$$

which can be expressed as

$$P_{\text{sec}} = \Pr (\gamma_{\text{sys}} < \gamma_0), \quad (16)$$

where $\gamma_0 = 2^{L\gamma_{\text{th}}}$.

Assuming that all γ_l are independent of each other and invoking Equation (13) into Equation (16), the SOP of the network can be obtained as

$$P_{\text{sec}} = 1 - \left[1 - F_{\gamma_1}(\gamma_0) \right] \prod_{l=2}^{L-1} \left[1 - F_{\gamma_l}(\gamma_0) \right] \left[1 - F_{\gamma_L}(\gamma_0) \right]. \quad (17)$$

To proceed further, we require $F_{\gamma_1}(\gamma_0)$, $F_{\gamma_l}(\gamma_0)$, and $F_{\gamma_L}(\gamma_0)$, respectively.

According to Equation (7), $F_{\gamma_1}(\gamma_0)$ can be obtained as

$$F_{\gamma_1}(\gamma_0) = 1 - \alpha_s \sum_{k=0}^{m_s-1} \frac{\zeta(k)}{(\eta_s)^{k+1}} \sum_{p=0}^k \frac{k!}{p!} \left(\frac{\beta_s - \delta_s}{\eta_s} \right)^{-(k+1-p)} \gamma_0^p e^{-((\beta_s - \delta_s)/\eta_s)\gamma_0}. \quad (18)$$

Then, we need to express the CDF of γ_l .

Theorem 2. *The CDF of γ_l can be expressed as Equation (19), where $\Phi = ((\beta_s - \delta_s)/\eta_s)\gamma_0 + ((\beta_e - \delta_e)/\eta_e)$ and $\delta_i = \cos [((2i - 1)\pi)/2N]$.*

$$\begin{aligned} F_{\gamma_l}(\gamma_0) &= 1 - \alpha_s \sum_{k=0}^{m_s-1} \sum_{p=0}^k \frac{\zeta(k)}{\eta_s^{k+1}} \frac{k!}{p!} \frac{\gamma_0^p}{((\beta_s - \delta_s)/\eta_s)^{k+1-p}} \\ &\cdot \alpha_e \sum_{k_i=0}^{m_e-1} \frac{\zeta(k_i)}{\eta_e^{k_i+1}} (p + k_i)! \Phi^{-p-k_i-1} \\ &- \frac{\pi \alpha_s}{2N} \sum_{i=0}^N e^{-2(i/\gamma_{\text{rel}}(\delta_i+1)) + (1/\gamma_{\text{rel}})} \sum_{k=0}^{m_s-1} \frac{\zeta(k)}{\eta_s^{k+1}} \\ &\cdot \left(\frac{\delta_i + 1}{2} \right)^k \sqrt{1 - \delta_i^2} \gamma_0^{k+1} \alpha_e \sum_{k_i=0}^{m_e-1} \frac{\zeta(k_i)}{\eta_e^{k_i+1}} \\ &\cdot (k + k_i + 1)! \Phi^{-k-k_i-2}. \end{aligned} \quad (19)$$

Proof. See Appendix A.

In the last hop, the channel coefficient $h_{d,L}$ between the last relay γ_{L-1} and the destination user D is denoted as

$$h_{d,L} = \frac{h_{d,L}^*}{\sqrt{1 + d^\nu}}, \quad (20)$$

where d represents the distance between the last relay γ_{L-1} and the user D , ν denotes the path loss exponent, and the coordinates of γ_{L-1} and the user D are symbolized by $(0, 0, h)$ and $(x, y, 0)$. Hence, the distance is represented as

$$d = \sqrt{x^2 + y^2 + h^2}. \quad (21)$$

As can be seen the distance is related to the location of the last relay γ_{L-1} and the user D . Assuming that all users are modeled independently and identically distributed in the area following a homogeneous PPP [2], denoted by Λ , the PDF of Λ is given by

$$f_\Lambda(\Lambda) = \frac{1}{\pi R^2}, \quad (22)$$

where R is the radius of the area.

Theorem 3. *Based on stochastic geometry, the CDF of $\gamma_{d,L}$ is given by*

$$\begin{aligned} F_{\gamma_{d,L}}(x) &= 1 - \frac{2}{R^2} \alpha_s \sum_{k=0}^{m_s-1} \zeta(k) \sum_{p=0}^k \frac{k!}{p!} \sum_{t=0}^p \binom{p}{t} \\ &\cdot \sum_{n=0}^{\infty} (\beta_s - \delta_s)^{n-k+p-1} \left(\frac{1}{\eta_s} \right)^{p+n} \frac{(-1)^n}{n!(\nu t + \nu n + 2)} \\ &\cdot \left((R^2 + h^2)^{((\nu t + \nu n)/2) + 1} - h^{\nu t + \nu n + 2} \right) e^{-((\beta_s - \delta_s)/\eta_s)x} x^{n+p}. \end{aligned} \quad (23)$$

Proof. Combining Equations (7) and (22), the CDF of $|h_{d,L}|^2$ is derived as Equation (24), where $\Upsilon(\cdot, \cdot)$ represents the lower incomplete Gamma function.

$$\begin{aligned} F_{|h_{d,L}|^2}(x) &= \int_1 \left(F_{|h_{d,L}|^2}(x(1 + d^\nu)) \right) f_\Lambda(\Lambda) d\Lambda = \int_h^{\sqrt{R^2 + h^2}} \\ &\cdot \left(1 - \alpha_s \sum_{k=0}^{m_s-1} \zeta(k) \sum_{p=0}^k \frac{k!}{p!} (\beta_s - \delta_s)^{-(k-p+1)} x^p \right. \\ &\cdot \left. (1 + r^\nu)^p e^{-(\beta_s - \delta_s)x(1+r^\nu)} \right) \frac{2r}{R^2} dr \\ &= 1 - \frac{2\alpha_s}{R^2} \sum_{k=0}^{m_s-1} \sum_{p=0}^k \sum_{t=0}^p \zeta(k) \binom{p}{t} \\ &\cdot \frac{k!}{p!} (\beta_s - \delta_s)^{-(k-p+1+t+(2/\nu))} \nu^{-1} x^{p-t-(2/\nu)} \\ &\cdot e^{-(\beta_s - \delta_s)x} \times \left(\Upsilon\left(\frac{\nu t + 2}{\nu}, (\beta_s - \delta_s)x(R^2 + h^2)^{\nu/2}\right) \right. \\ &\cdot \left. - \Upsilon\left(\frac{\nu t + 2}{\nu}, (\beta_s - \delta_s)xh^\nu\right) \right). \end{aligned} \quad (24)$$

Based on Equation (24), using series exploration of $\Upsilon(\cdot, \cdot)$ and applying the transformation of variable [33], Equation (23) can be obtained.

By derivation of Equation (23), the PDF of $\gamma_{d,L}$ can be obtained as

$$f_{\gamma_{d,L}}(x) = \xi(k, p, t, n) e^{-((\beta_s - \delta_s)/\eta_s)x} \left(-\frac{\beta_s - \delta_s}{\eta_s} x^{n+p} + (n+p)x^{n+p-1} \right), \quad (25)$$

where

$$\begin{aligned} \xi(k, p, t, n) = & -\frac{2}{R^2} \alpha_s \sum_{k=0}^{m_s-1} \zeta(k) \sum_{p=0}^k \frac{k!}{p!} \sum_{t=0}^p \binom{p}{t} \\ & \cdot \sum_{n=0}^{\infty} (\beta_s - \delta_s)^{n-k+p-1} \left(\frac{1}{\eta_s} \right)^{p+n} \frac{(-1)^n}{n!(vt + vn + 2)} \\ & \cdot \left((R^2 + h^2)^{((vt+vn)/2)+1} - h^{vt+vn+2} \right). \end{aligned} \quad (26)$$

Theorem 4. The CDF of γ_L can be obtained as Equation (29), where

$$\begin{aligned} \Xi_1 = & -\frac{\beta_s - \delta_s}{\eta_s} \left(\frac{\delta_i + 1}{2} \right)^{n+p} \gamma_0^{p+n+1} (k_1 + p + n + 1)! \\ & \cdot \left(\frac{\beta_s - \delta_s}{\eta_s} \frac{\delta_i + 1}{2} \gamma_0 + \frac{\beta_e - \delta_e}{\eta_e} \right)^{-k_1 - p - n - 2}, \end{aligned} \quad (27)$$

$$\begin{aligned} \Xi_2 = & (n+p) \left(\frac{\delta_i + 1}{2} \right)^{n+p-1} \gamma_0^{p+n} (k_1 + p + n)! \\ & \cdot \left(\frac{\beta_s - \delta_s}{\eta_s} \frac{\delta_i + 1}{2} \gamma_0 + \frac{\beta_e - \delta_e}{\eta_e} \right)^{-k_1 - p - n - 1}, \end{aligned} \quad (28)$$

$$\begin{aligned} F_{\gamma_L}(\gamma_0) = & 1 - \frac{2\alpha_s \alpha_e}{R^2} \sum_{k=0}^{m_s-1} \sum_{p=0}^k \sum_{t=0}^p \sum_{n=0}^{\infty} \sum_{k_1=0}^{m_e-1} \frac{\zeta(k) \zeta(k_1) k!}{\eta_e^{k_1+1} p!} \\ & \cdot \binom{p}{t} (\beta_s - \delta_s)^{n-k+p-1} \left(\frac{1}{\eta_s} \right)^{p+n} \frac{(-1)^n}{n!(vt + vn + 2)} \\ & \cdot \left((R^2 + h^2)^{((vt+vn)/2)+1} - h^{vt+vn+2} \right) \\ & \cdot \left(\frac{\gamma_0^{n+p} (n+p+k_1)!}{\Phi^{(n+p+k_1+1)}} - \frac{\pi}{2N} e^{-((2/(\gamma_{jcl}(\delta_i+1)))+(1/\gamma_{jcl}))} \right) \\ & \cdot \sum_{i=0}^N \sqrt{1 - \delta_i^2} (\Xi_1 + \Xi_2). \end{aligned} \quad (29)$$

Proof. See Appendix B.

Theorem 5. The SOP of the network can be formulated as

$$\begin{aligned} P_{\text{sec}} = & 1 - \alpha_s \sum_{k=0}^{m_s-1} \sum_{p=0}^k \frac{\zeta(k) k!}{(\eta_s)^{k+1} p!} \left(\frac{\beta_s - \delta_s}{\eta_s} \right)^{-(k+1-p)} \gamma_0^p e^{-((\beta_s - \delta_s)/\eta_s)\gamma_0} \\ & \cdot \left(\alpha_s \sum_{k=0}^{m_s-1} \sum_{p=0}^k \frac{\zeta(k) k!}{\eta_s^{k+1} p!} \frac{\gamma_0^p}{((\beta_s - \delta_s)/\eta_s)^{k+1-p}} \alpha_e \sum_{k_1=0}^{m_e-1} \frac{\zeta(k_1)}{\eta_e^{k_1+1}} (p+k_1)! \Phi^{-p-k_1-1} \right)^{L-2} \\ & \cdot \left(+ \frac{\pi \alpha_s}{2N} \sum_{i=0}^N e^{-((2/(\gamma_{jcl}(\delta_i+1)))+(1/\gamma_{jcl}))} \sum_{k=0}^{m_s-1} \frac{\zeta(k) \alpha_e}{\eta_s^{k+1}} \left(\frac{\delta_i + 1}{2} \right)^k \sqrt{1 - \delta_i^2} \gamma_0^{k+1} \sum_{k_1=0}^{m_e-1} \frac{\zeta(k_1)}{\eta_e^{k_1+1}} (k+k_1+1)! \Phi^{-k-k_1-2} \right) \\ & \times \frac{2\alpha_s \alpha_e}{R^2} \sum_{k=0}^{m_s-1} \sum_{p=0}^k \sum_{t=0}^p \sum_{n=0}^{\infty} \sum_{k_1=0}^{m_e-1} \frac{\zeta(k) \zeta(k_1) k!}{\eta_e^{k_1+1} p!} \binom{p}{t} (\beta_s - \delta_s)^{n-k+p-1} \left(\frac{1}{\eta_s} \right)^{p+n} \frac{(-1)^n}{n!(vt + vn + 2)} \\ & \cdot \left((R^2 + h^2)^{((vt+vn)/2)+1} - h^{vt+vn+2} \right) \left(\frac{\gamma_0^{n+p} (n+p+k_1)!}{\Phi^{(n+p+k_1+1)}} - \frac{\pi}{2N} e^{-((2/(\gamma_{jcl}(\delta_i+1)))+(1/\gamma_{jcl}))} \right) \sum_{i=0}^N \sqrt{1 - \delta_i^2} (\Xi_1 + \Xi_2). \end{aligned} \quad (30)$$

Proof. Invoking Equations (18), (19), and (29) into Equation (17), Equation (30) can be obtained.

3.2. Asymptotic Behavior. To get better insights on the secrecy performance of the network, the asymptotic secrecy outage behavior at high SNR region is investigated. Here, we examine the asymptotic SOP analysis at high SNR region ($\eta_s \rightarrow \infty$).

Corollary 6. The diversity order of the network at high SNR region can be obtained easily as

$$d = - \lim_{\eta_s \rightarrow \infty} \frac{\log(P_{\text{sec}}^{\infty})}{\log \eta_s} = 1. \quad (31)$$

Proof. As in [19], at high SNR region, assuming $\eta_s \rightarrow \infty$ and applying the Maclaurin series expansion of the exponential

TABLE 1: Table of parameter settings for numerical results.

Monte Carlo simulations	10 ⁶ iterations
Shadowing-Rician fading parameters (heavy shadowing)	$m_\rho = 1$, $b_\rho = 0.063$, and $\Omega_\rho = 0.0007$
Shadowing-Rician fading parameters (average shadowing)	$m_\rho = 5$, $b_\rho = 0.251$, and $\Omega_\rho = 0.279$
The transmit SNR of the wiretap link	$\eta_e = 10$ dB
The height of the last relay	$h = 100$ m
The radius of the area	$R = 500$ m
The path loss exponent	$\nu = 3$

function [33], the PDF f_{γ_ρ} can be approximated as

$$f_{\gamma_\rho}(x) \approx \frac{\alpha_\rho}{\eta_\rho}, \quad (32)$$

and by integrating Equation (32), the asymptotic behavior of F_{γ_ρ} can be given as

$$F_{\gamma_\rho}(x) \approx \frac{\alpha_\rho}{\eta_\rho} x. \quad (33)$$

Therefore, we can derive $F_{\gamma_1}(\gamma_0) \approx (\alpha_s/\eta_s)\gamma_0$ and

$$F_{\gamma_1}(\gamma_0) \approx \frac{\alpha_s \alpha_e \gamma_0}{\eta_s} \left(1 - \frac{e^{1/\overline{\gamma_{je,l}}} \pi}{2N} \sum_{i=0}^N e^{-2/(\overline{\gamma_{je,l}}(\delta_i+1))} \sqrt{1-\delta_i^2} \right) \cdot \sum_{k_1=0}^{m_e-1} \frac{\zeta(k_1)}{\eta_e^{k_1+1}} (k_1+1)! \left(\frac{\beta_e - \delta_e}{\eta_e} \right)^{-k_1-2}, \quad (2 \leq l \leq L). \quad (34)$$

Now, invoking $F_{\gamma_1}(\gamma_0)$ and Equation (34) into Equation (17), the asymptotic expression for the SOP can be derived as

$$P_{asy}^{so} = 1 - \left(1 - \frac{\alpha_s}{\eta_s} 2^{Lr_{th}} \right) \left(1 - \frac{\alpha_s}{\eta_s} 2^{Lr_{th}} \left(1 - \frac{e^{1/\overline{\gamma_{je,l}}} \pi}{2N} \sum_{i=0}^N e^{-2/(\overline{\gamma_{je,l}}(\delta_i+1))} \sqrt{1-\delta_i^2} \right) \cdot \sum_{k_1=0}^{m_e-1} \frac{\zeta(k_1)}{\eta_e^{k_1+1}} (k_1+1)! \left(\frac{\beta_e - \delta_e}{\eta_e} \right)^{-k_1-2} \right)^{L-1}. \quad (35)$$

On invoking Equation (35) into Equation (31) and doing some algebraic manipulations, the diversity order of 1 can be acquired.

Remark 7. Through the asymptotic analysis of the SOP, we can reveal that the diversity order of the multihop network at high SNR region is 1. Importantly, it remains unaffected by the hops, secrecy rate, or other channel parameters.

3.3. Throughput Analysis. In order to estimate the secrecy performance of the network further, the throughput of the overall system is explored. According to [34], the throughput

is defined as

$$R_{thr} = \frac{\gamma_{th}}{L} \times [1 - P_{sec}(\gamma_{th})], \quad (36)$$

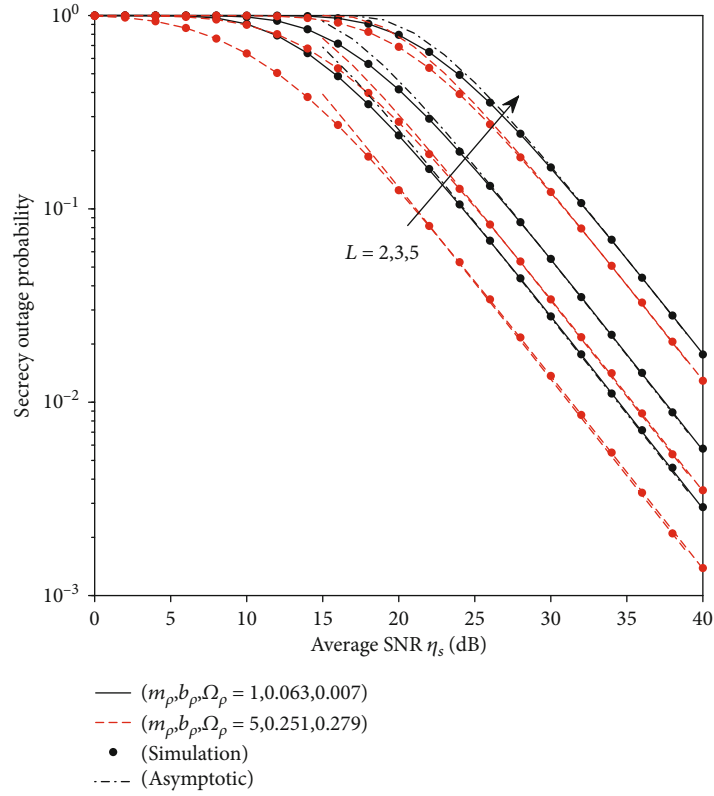
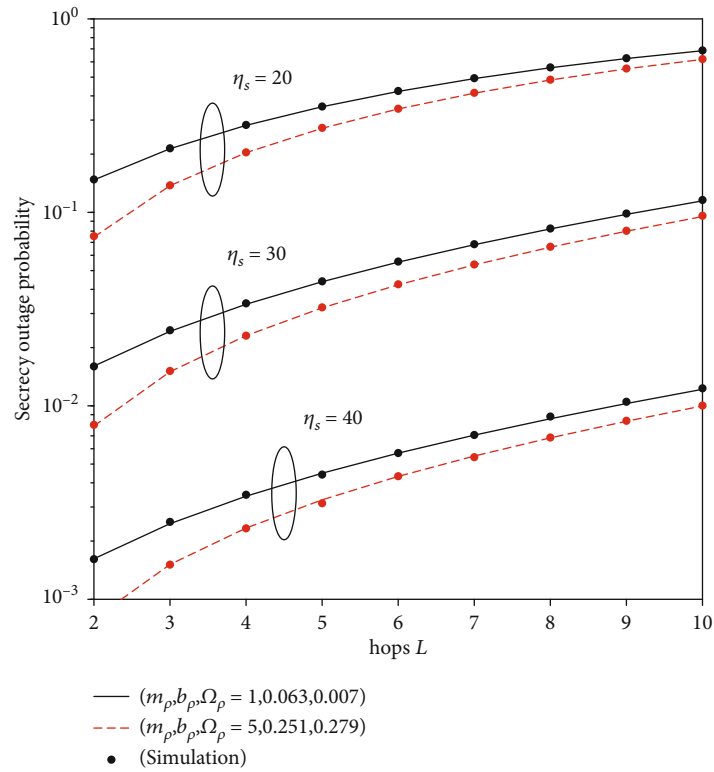
where the constant $1/L$ indicates that the communication process is divided into L hops, γ_{th} represents the secrecy rate, and $P_{sec}(\gamma_{th})$ can be obtained from the previous section. Thus, by substituting Equation (30) into Equation (36), the analytical throughput expression of the system is derived.

4. Numerical Results

In this section, the theoretical analysis results obtained from Section 3 are presented through comparison with Monte Carlo simulations. Monte Carlo simulations are carried out in order to verify the accuracy of the theoretical derivation. In particular, the SOP and throughput analysis are examined under various channel settings. Unless otherwise stated, channel parameters of the legitimate link are the same with those of the wiretap link and the parameter settings are used as shown in Table 1 [2, 19, 27, 35, 36].

Figure 2 shows the results of the SOP versus η_s for different hops under heavy and average shadowing scenarios of shadowing-Rician fading. The numerical results obtained from Equations (30) and (35) ($\gamma_{th} = 0.5$, $\overline{\gamma_{je,l}} = 1$ dB) agree well with the Monte Carlo simulation results, which confirm the correctness of the analysis. From the figure, it can be observed that the curves of the asymptotic SOP almost overlap with the analytical ones at the moderate and high SNR region. Moreover, it is obvious that the SOP performance of the network under average shadowing scenarios is better than that under heavy shadowing scenarios and it gets worse with the increasing hops. This is because the communication distance gets increasing with the increasing hops. This figure also indicates that the achievable diversity order does not change with different hops.

Figure 3 investigates the SOP performance of the network versus hops for $\eta_s = 20, 30, 40$ under heavy and average shadowing scenarios. Herein, we set $\gamma_{th} = 0.1$ and $\overline{\gamma_{je,l}} = 1$ dB. It is obviously found that theory results sufficiently coincide with the Monte Carlo simulation results. And as can be seen from Figure 3, the SOP performance of the network is getting worse with the increasing severity of the channel fading scenario and it gets better with the decrease of the hops L .

FIGURE 2: SOP versus η_s for different hops.FIGURE 3: SOP versus hops for different η_s .

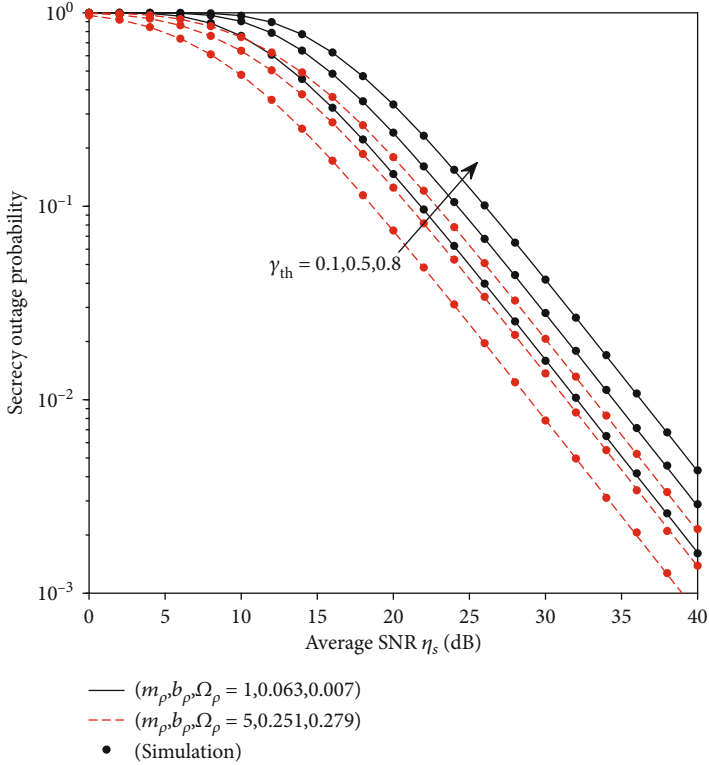


FIGURE 4: SOP versus η_s for different γ_{th} .

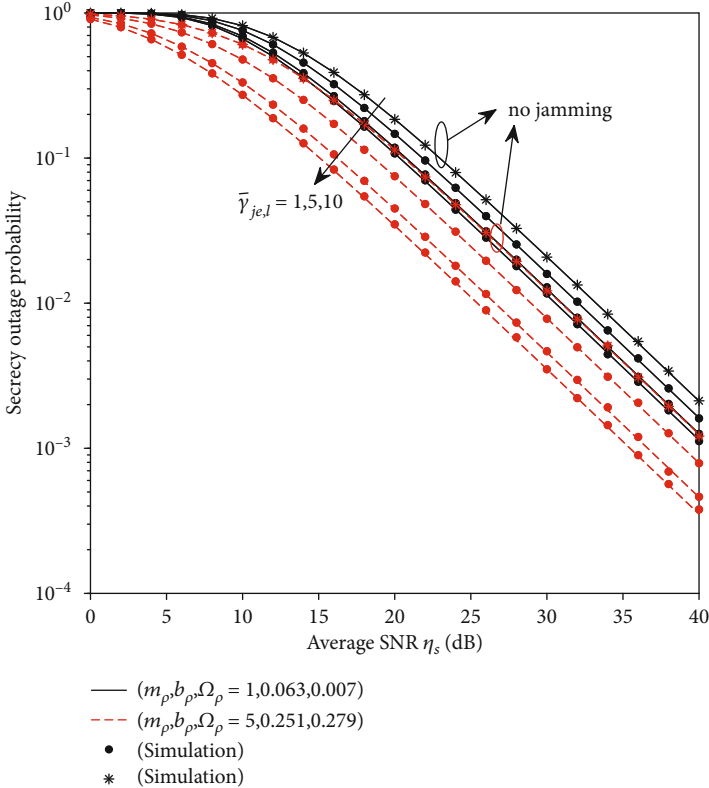


FIGURE 5: SOP versus η_s for different $\bar{\gamma}_{je,l}$.

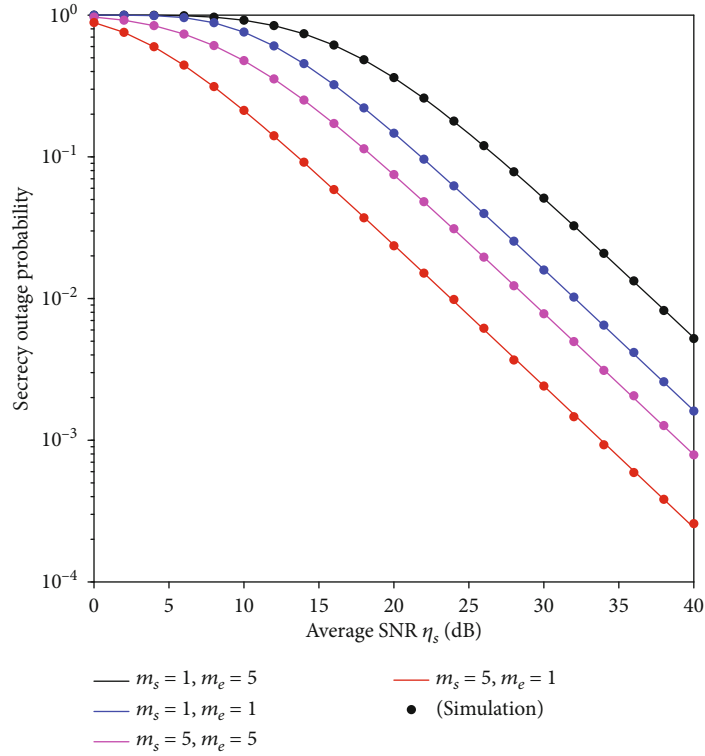


FIGURE 6: SOP versus η_s in different shadowing scenarios.

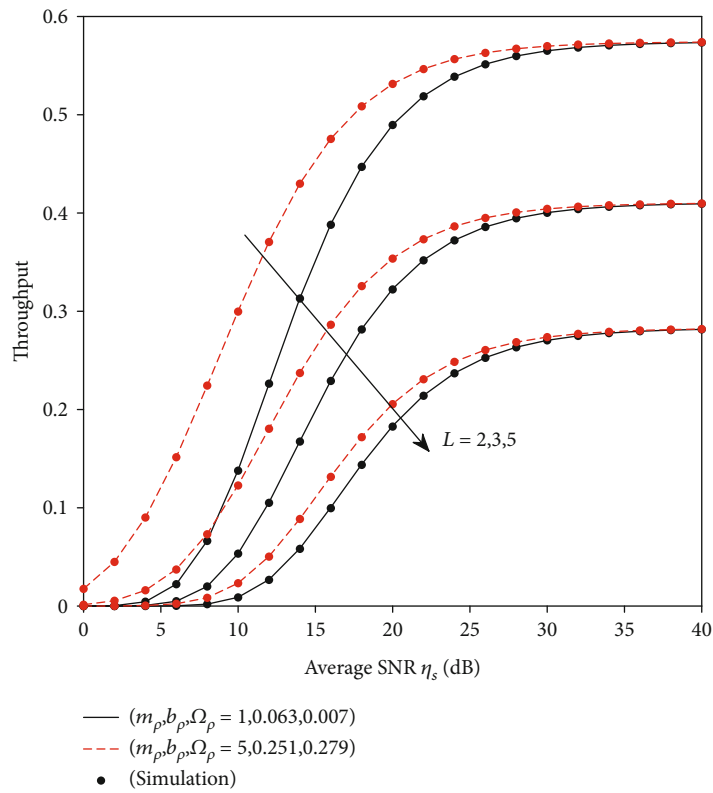


FIGURE 7: System throughput versus η_s for different hops.

Figure 4 plots the results of the SOP versus η_s for different secrecy rate γ_{th} under heavy and average shadowing scenarios of shadowing-Rician fading. Here, it is assumed that the received signal from the satellite experiences 2 hops and $\overline{\gamma_{je,l}} = 1$ dB. As is expected, the SOP performance of the network gets worse with the secrecy rate increasing.

Figure 5 shows the SOP performance comparison of the network versus η_s for different average SNR of the jamming link $\overline{\gamma_{je,l}}$ under heavy and average shadowing scenarios of shadowing-Rician fading. Also, the performance comparison of HSTRN without jamming is presented. Here, we suppose that the communication process experiences 2 hops and $\gamma_{th} = 0.1$. As shown in the figure, the SOP performance of the network with jamming is better than that without jamming obviously. And when the average SNR of the jamming link $\overline{\gamma_{je,l}}$ gets increasing, the SOP performance of the network improves correspondingly. This can be attributed to the jammer. The stronger the jamming signal gets, the weaker the wiretap signal becomes. Hence, the jammer has a great effect on the SOP performance of the network.

Figure 6 depicts the SOP performance comparison of the network versus η_s based on different channel settings of the legitimate link and wiretap link. Here, we still set $\gamma_{th} = 0.1$, $\overline{\gamma_{je,l}} = 1$ dB, and $L = 2$. As can be seen from the figure, when the legitimate link is under heavy shadowing scenarios ($m_s = 1$) and the wiretap link is under average shadowing ($m_e = 5$), the SOP performance of the network is the worst. While the legitimate link is under average shadowing scenarios ($m_s = 5$) and the wiretap link is under heavy shadowing ($m_e = 1$), the network has the best SOP performance.

Figure 7 presents the system throughput versus η_s ($\gamma_{th} = 0.1$, $\overline{\gamma_{je,l}} = 1$ dB). As can be noted, the throughput increases with η_s increasing and then trends to a fixed constant based on the same hop. This can be explained by the fact that SOP will approach to zero at high SNR region. Also, the throughput of system degrades with hops increasing, and it is better under average shadowing scenarios than that under heavy shadowing scenarios, which is consistent with the SOP performance seen from Figure 2.

5. Conclusions

In this work, the secrecy analysis of a multihop DF HSTRN with jamming has been investigated. Considering shadowed-Rician fading for legitimate link and wiretap link while considering Rayleigh fading for jamming link, the accurate SOP formula of the considered network has been derived. The asymptotic behavior of the SOP expression at high SNR region is explored, and the throughput of the system is discussed. Finally, simulation results are given as verification of the theoretical results and illustrate that some key system parameters have great impacts on the SOP performance of the considered network. The results reveal that the hops and the jammer play important parts in the secrecy performance of the multihop DF HSTRN with jamming. In the future, multiantenna satellite, multiantenna relay, and multiple eavesdroppers in such system could be our further research.

Appendix

A. Proof of Theorem 2

After the approximation $(1+x)/(1+y) \approx x/y$ and the substitution of Equation (4), γ_l can be obtained as

$$\gamma_l \approx \frac{\gamma_{d,l}(\gamma_{je,l} + 1)}{\gamma_{re,l}}. \quad (\text{A.1})$$

Therefore, $F_{\gamma_l}(\gamma_0)$ can be expressed as

$$\begin{aligned} F_{\gamma_l}(\gamma_0) &\approx \Pr\left(\frac{\gamma_{d,l}(\gamma_{je,l} + 1)}{\gamma_{re,l}} < \gamma_0\right) = \Pr(A < \gamma_0 \gamma_{re,l}) \\ &= \int_0^{\infty} F_A(\gamma_0 \gamma_{re,l}) f_{\gamma_{re,l}}(\gamma_{re,l}) d\gamma_{re,l}, \end{aligned} \quad (\text{A.2})$$

where $A = \gamma_{d,l}(\gamma_{je,l} + 1)$.

To proceed, we require $F_A(z)$, and it is derived as

$$F_A(z) = \Pr(A < z) = \int_0^z F_{\gamma_{je,l}}\left(\frac{z}{\gamma_{d,l}} - 1\right) f_{\gamma_{d,l}}(\gamma_{d,l}) d\gamma_{d,l}. \quad (\text{A.3})$$

Invoking Equations (6) and (8) into Equation (A.3), doing some algebra processing and applying the approximation of the Gaussian-Chebyshev quadrature [37], $F_A(z)$ can be formulated as

$$\begin{aligned} F_A(z) &\approx 1 - \alpha_s \sum_{k=0}^{m_s-1} \frac{\zeta(k)}{\eta_s^{k+1}} \sum_{p=0}^k \frac{k!}{p!} \left(\frac{\beta_s - \delta_s}{\eta_s}\right)^{-(k+1-p)} \\ &\quad \cdot z^p e^{-((\beta_s - \delta_s)/\eta_s)z} - \frac{\pi\alpha_s}{2N} \sum_{i=0}^N e^{-2/(\overline{\gamma_{je,l}}(\delta_i+1))} + (1/\overline{\gamma_{je,l}}) \\ &\quad \cdot \sum_{k=0}^{m_s-1} \frac{\zeta(k)}{\eta_s^{k+1}} \left(\frac{\delta_i + 1}{2}\right)^k \sqrt{1 - \delta_i^2} z^{k+1} e^{-((\beta_s - \delta_s)/\eta_s)((\delta_i+1)/2)z}. \end{aligned} \quad (\text{A.4})$$

Now, substituting Equations (A.4) and (6) into Equation (A.2), Equation (19) can be obtained.

B. Proof of Theorem 4

Like Equation (A.2), $F_{\gamma_L}(\gamma_0)$ can be expressed as

$$F_{\gamma_L}(\gamma_0) \approx \int_0^{\infty} F_{A_L}(\gamma_0 \gamma_{re,L}) f_{\gamma_{re,L}}(\gamma_{re,L}) d\gamma_{re,L}, \quad (\text{B.1})$$

where $A_L = \gamma_{d,L}(\gamma_{je,L} + 1)$.

And $F_{A_L}(z)$ can be derived as

$$F_{A_L}(z) = \Pr(A_L < z) = \int_0^z F_{\gamma_{j_e,L}} \left(\frac{z}{\gamma_{d,L}} - 1 \right) f_{\gamma_{d,L}}(\gamma_{d,L}) d\gamma_{d,L}. \quad (\text{B.2})$$

Invoking Equations (25) and (8) into Equation (B.2), doing some algebra processing like Equation (A.4), $F_{A_L}(z)$ can be obtained as

$$\begin{aligned} F_{A_L}(z) \approx & 1 - \frac{2\alpha_s}{R^2} \sum_{k=0}^{m_s-1} \sum_{p=0}^k \frac{\zeta(k)k!}{p!} \sum_{t=0}^p \binom{p}{t} \\ & \cdot \sum_{n=0}^{\infty} (\beta_s - \delta_s)^{n-k+p-1} \times \left(\frac{1}{\eta_s} \right)^{p+n} \frac{(-1)^n e^{-((\beta_s - \delta_s)/\eta_s)z} z^{n+p}}{n!(vt + vn + 2)} \\ & \cdot \left((R^2 + h^2)^{((vt+vn)/2)+1} - h^{vt+vn+2} \right) - \xi(k, p, t, n) \frac{\pi e^{1/\gamma_{j_e,L}}}{2N} \\ & \cdot \sum_{i=0}^N \sqrt{1 - \delta_i^2} e^{-2i/(\gamma_{j_e,L}(\delta_i+1))} \\ & \cdot \left(\begin{aligned} & -\frac{\beta_s - \delta_s}{\eta_s} \left(\frac{\delta_i + 1}{2} \right)^{n+p} z^{p+n+1} e^{-((\beta_s - \delta_s)/\eta_s)((\delta_i+1)/2)z} \\ & + (n+p) \left(\frac{\delta_i + 1}{2} \right)^{n+p-1} z^{p+n} e^{-((\beta_s - \delta_s)/\eta_s)((\delta_i+1)/2)z} \end{aligned} \right). \quad (\text{B.3}) \end{aligned}$$

Then, substituting Equations (B.3) and (6) into Equation (B.1), doing some algebra processing, Equation (29) can be obtained.

Data Availability

The data used to support the findings of this study are available from the corresponding author upon request.

Conflicts of Interest

The authors declare that there is no conflict of interest regarding the publication of this paper.

Acknowledgments

This work was supported by the National Natural Science Foundation of China (41474021 and 41931075), key scientific and technological project of Henan province (212102310436), Fundamental Research Funds for the Universities of Henan Province (NSFRF210329), and doctoral fund of Henan Polytechnic University (B2021-18).

References

- [1] A. Vanelli-Coralli, G. Corazza, G. Karagiannidis, T. Mathiopoulos, and S. Scalise, "Satellite communications: research trends and open issues," in *2007 International Workshop on Satellite and Space Communications*, pp. 71–75, Salzburg, Austria, 2007.
- [2] X. Li, Q. Wang, H. Peng et al., "A unified framework for HS-UAV NOMA networks: performance analysis and location optimization," *IEEE Access*, vol. 8, pp. 13329–13340, 2020.
- [3] K. Guo, D. Guo, Y. Huang, X. Wang, and B. Zhang, "Performance analysis of a dual-hop satellite relay network with hardware impairments," in *2016 25th Wireless and Optical Communication Conference (WOCC)*, pp. 1–5, Chengdu, China, 2016.
- [4] S. W. Peters and R. W. Heath, "The future of wimax: multihop relaying with IEEE 802.16j," *IEEE Communications Magazine*, vol. 47, no. 1, pp. 104–111, 2009.
- [5] X. Li, J. Li, Y. Liu, Z. Ding, and A. Nallanathan, "Residual transceiver hardware impairments on cooperative NOMA networks," *IEEE Transactions on Wireless Communications*, vol. 19, no. 1, pp. 680–695, 2020.
- [6] X. Li, J. Li, and L. Li, "Performance analysis of impaired SWIPT NOMA relaying networks over imperfect Weibull channels," *IEEE Systems Journal*, vol. 14, no. 1, pp. 669–672, 2020.
- [7] X. Li, M. Zhao, M. Zeng et al., "Hardware impaired ambient backscatter NOMA systems: reliability and security," *IEEE Transactions Communications*, vol. 69, no. 4, pp. 2723–2736, 2021.
- [8] X. Li, "Secrecy analysis of ambient backscatter NOMA systems under I/Q imbalance," *IEEE Transactions on Vehicular Technology*, vol. 69, no. 10, pp. 12286–12290, 2020.
- [9] X. Li, Q. Wang, Y. Liu, T. A. Tsiftsis, Z. Ding, and A. Nallanathan, "UAV-aided multi-way NOMA networks with residual hardware impairments," *IEEE Wireless Communications Letters*, vol. 9, no. 9, pp. 1538–1542, 2020.
- [10] B. Evans, M. Werner, E. Lutz et al., "Integration of satellite and terrestrial systems in future multimedia communications," *IEEE Wireless Communication*, vol. 12, no. 5, pp. 72–80, 2005.
- [11] S. Kim, H. W. Kim, K. Kang, and D. S. Ahn, "Performance enhancement in future mobile satellite broadcasting services," *IEEE Communications Magazine*, vol. 46, no. 7, pp. 118–124, 2008.
- [12] K. An, M. Lin, and T. Liang, "On the performance of multiuser hybrid satellite-terrestrial relay networks with opportunistic scheduling," *IEEE Communications Magazine*, vol. 19, no. 10, pp. 1722–1725, 2015.
- [13] Y. Bu, M. Lin, K. An, J. Ouyang, and C. Yuan, "Performance analysis of hybrid satellite-terrestrial cooperative systems with fixed gain relaying," *Wireless Personal Communications*, vol. 89, no. 2, pp. 427–445, 2016.
- [14] *Digital video broadcasting (DVB); system specifications for satellite services to handheld services (SH) below 3 GHz*, European Telecommunications Standards Institute (ETSI), 2008, ETSI EN 102 585 V1.1.2.
- [15] X. Li, M. Liu, J. Deng, J. Li, and Q. Yu, "Power beacon assisted wireless power cooperative relaying using NOMA with hardware impairments and imperfect CSI," *International Journal of Electronics and Communications*, vol. 108, pp. 275–286, 2019.
- [16] V. K. Sakarellos, C. Kourogorgas, and A. D. Panagopoulos, "Cooperative hybrid land mobile satellite-terrestrial broadcasting systems: outage probability evaluation and accurate simulation," *Wireless Personal Communications*, vol. 79, no. 2, pp. 1471–1481, 2014.
- [17] K. An, M. Lin, T. Liang et al., "Performance analysis of multi-antenna hybrid satellite-terrestrial relay networks in the presence of interference," *IEEE Transactions on Communications*, vol. 63, no. 11, pp. 4390–4404, 2015.

- [18] A. D. Wyner, "The wire-tap channel," *Bell System Technical Journal*, vol. 54, no. 8, pp. 1355–1387, 1975.
- [19] V. Bankey and P. K. Upadhyay, "Physical layer secrecy performance analysis of multi-user hybrid satellite-terrestrial relay networks," *CSI Transactions on ICT*, vol. 6, no. 2, pp. 187–193, 2018.
- [20] Q. Huang, M. Lin, K. An, J. Ouyang, and W. P. Zhu, "Secrecy performance of hybrid satellite-terrestrial relay networks in the presence of multiple eavesdroppers," *IET Communications*, vol. 12, no. 1, pp. 26–34, 2018.
- [21] V. Bankey and P. K. Upadhyay, "Physical layer security of multiuser multirelay hybrid satellite-terrestrial relay networks," *IEEE Transactions on Vehicular Technology*, vol. 68, no. 3, pp. 2488–2501, 2019.
- [22] K. Guo, K. An, B. Zhang, Y. Huang, and D. Guo, "Physical layer security for hybrid satellite terrestrial relay networks with joint relay selection and user scheduling," *IEEE Access*, vol. 6, pp. 55815–55827, 2018.
- [23] S. Yan, X. Wang, Z. Li, B. Li, and Z. Fei, "Cooperative jamming for physical layer security in hybrid satellite terrestrial relay networks," *China Communications*, vol. 16, no. 12, pp. 154–164, 2019.
- [24] Y. Yan, B. Zhang, D. Guo, S. Li, H. Niu, and X. Wang, "Joint beamforming and jamming design for secure cooperative hybrid satellite-terrestrial relay network," in *2016 25th Wireless and Optical Communication Conference (WOCC)*, pp. 71–75, Chengdu, China, 2016.
- [25] J. Ye, C. Zhang, G. Pan, Y. Chen, and Z. Ding, "Secrecy analysis for spatially random UAV systems," in *2018 IEEE Globecom Workshops (GC Wkshps)*, pp. 1–6, Abu Dhabi, United Arab Emirates, 2018.
- [26] X. He and A. Yener, "End-to-end secure multi-hop communication with untrusted relays," *IEEE Transactions on Wireless Communications*, vol. 12, no. 1, pp. 1–11, 2013.
- [27] V. Bankey, P. K. Upadhyay, D. B. da Costa, P. S. Bithas, A. G. Kanas, and U. S. Dias, "Performance analysis of multi-antenna multiuser hybrid satellite-terrestrial relay systems for mobile services delivery," *IEEE Access*, vol. 6, pp. 24729–24745, 2018.
- [28] A. Abdi, W. C. Lau, M. S. Alouini, and M. Kaveh, "A new simple model for land mobile satellite channels: first- and second-order statistics," *IEEE Transactions on Wireless Communications*, vol. 2, no. 3, pp. 519–528, 2003.
- [29] M. Lin, Y. Jiang, J. Ouyang, and K. An, "The performance of a hybrid satellite-terrestrial cooperative networks with interferences," *Acta Electronica Sinica*, vol. 46, no. 1, pp. 8–14, 2018.
- [30] A. Pandey and S. Yadav, "Physical layer security in cooperative AF relaying networks with direct links over mixed Rayleigh and double-Rayleigh fading channels," *IEEE Transactions on Vehicular Technology*, vol. 67, no. 11, pp. 10615–10630, 2018.
- [31] L. Fan, N. Yang, T. Q. Duong, M. ElKashlan, and G. K. Karagiannis, "Exploiting direct links for physical layer security in multiuser multirelay networks," *IEEE Transactions on Wireless Communications*, vol. 15, no. 6, pp. 3856–3867, 2016.
- [32] E. R. Alotaibi and K. A. Hamdi, "Secure relaying in multihop communication systems," *IEEE Wireless Communications Letters*, vol. 20, no. 6, pp. 1120–1123, 2016.
- [33] I. S. Gradshteyn and I. M. Ryzhik, *Tables of Integrals, Series and Products*, Academic Press, New York, NY, USA, 6th edition, 2000.
- [34] K. Guo, B. Zhang, Y. Huang, and D. Guo, "Performance analysis of two-way satellite terrestrial relay networks with hardware impairments," *IEEE Wireless Communications Letters*, vol. 6, no. 4, pp. 430–433, 2017.
- [35] K. Guo, K. An, B. Zhang et al., "On the performance of the uplink satellite multiterrestrial relay networks with hardware impairments and interference," *IEEE Systems Journal*, vol. 13, no. 3, pp. 2297–2308, 2019.
- [36] C. Loo, "A statistical model for a land mobile satellite link," *IEEE Transactions On Vehicular Technology*, vol. 34, no. 3, pp. 122–127, 1985.
- [37] D. D. Tran and D. B. Ha, "Secrecy performance analysis of QoS-based non-orthogonal multiple access networks over Nakagami-m fading," in *2018 2nd International Conference on Recent Advances in Signal Processing, Telecommunications & Computing (SigTelCom)*, pp. 187–191, Ho Chi Minh City, Vietnam, 2018.

Review Article

Application Status and Prospects of 5G Technology in Distribution Automation Systems

Zhaoyun Zhang^{1,2} and Qitong Wang^{1,2}

¹Electronic Engineering and Intelligence College, Dongguan University of Technology, Dongguan, China

²Automation College, Guangdong University of Technology, Guangzhou, China

Correspondence should be addressed to Zhaoyun Zhang; 18927491998@163.com

Received 19 January 2021; Revised 25 February 2021; Accepted 19 March 2021; Published 5 April 2021

Academic Editor: Yuan Ding

Copyright © 2021 Zhaoyun Zhang and Qitong Wang. This is an open access article distributed under the Creative Commons Attribution License, which permits unrestricted use, distribution, and reproduction in any medium, provided the original work is properly cited.

With the continuous development of 5G (5th generation mobile networks) communication technology, increasing attention has been paid to the integration of 5G technology and vertical industry. Based on the consideration of power security, the large-scale application of 5G in the power industry will start from the distribution grid and gradually extend to the high-voltage power grid. There have been some powerful attempts to apply 5G technology in distribution grid automation, distribution grid relay protection, and distribution grid monitoring. This article will summarize the application of 5G technology in these fields, focuses on the analysis of possible problems in technical standards, network security, application costs, and signal coverage, and will propose reasonable prospects and thoughts on the integration of 5G technology and distribution grids.

1. Introduction

The electric power communication network is a valuable foundation supporting the development of the country's electric power capacity. The emergence of 5G communication technology will qualitatively improve all aspects of the electric power communication network. 5G technology is expected to play the role of "connecting everything" in the power communication network [1, 2]. Compared with the previous generation of mobile communication technology, 5G technology, that is, fifth-generation mobile communication technology, has the characteristics of larger bandwidth, lower latency, higher capacity, and wider connections [3]. It has become a key technical basis for establishing a "three-type two-net" strategy in China. Under the influence of the "two-net" strategy, the distribution grid will be deeply integrated with 5G technology in the future, and higher requirements for the economy, safety, and reliability of the operation of the distribution grid will be implemented [4]. The construction of the ubiquitous power Internet of Things runs through all links of the power system and requires a great extent of detection and control for each node of the distribu-

tion grid. Regardless of the method, it is essential to carry out real-time detection and control of the operation status of the distribution network, transmit the control signals sent by the cloud server in a timely manner to each link of the distribution network, and execute the method quickly [5].

Further research on 5G technology will accelerate the development of distribution grid automation [6]. Due to the access of a large number of distributed power sources, the increasing demand of users for power reliability and the high management costs and low efficiency of traditional power distribution methods, distribution grid automation has gradually developed. The construction and development of distribution grid automation will largely alleviate the problems of power waste and uneven power distribution [7]. There are a large number of measurement and control objects in the distribution grid, such as substations, subsection posts, distribution stations, distribution transformers, and section switches. There are usually hundreds or even tens of thousands of sites [8]. Although China has achieved data connections to important nodes, there are still large-scale user-side data and edge data that have not yet been obtained. In terms of distribution grid terminals, most of the terminal

equipment is located in a very harsh geographic environment, so buried optical fibers and power wireless private networks have now become the major power communication methods for terminals [9]. Because of the high cost of optical fiber communication and the lack of optical fiber access conditions in some areas, large-scale buried optical fiber communication cannot be implemented on a large scale. The power wireless private network can only be used to realize the connection of most terminals. In recent years, 3G and 4G power wireless private networks have achieved remarkable results in the “last mile” of the power communication network, but some of the performance indicators of 4G still fail to meet the national strategic target requirements, unlike 5G communication technology [10]. The realization of feeder automation (FA) has gradually transitioned from a noncommunication method achieved through recloser timing adjustment to a centralized intelligent FA method that uses a feeder terminal unit (FTU) or distribution terminal unit (DTU) for fault detection and communication technology for fault isolation and restoration of power supply in nonfaulty sections [11, 12], but the operation effect of the pilot project of distributed intelligent FA is not good. Due to the distrust of the system and equipment, the feeder is semiautomatic, manual, and not fully automatic. In January 2019, the China Southern Power Grid took the lead in completing the 5G network distributed differential protection service test in Shenzhen. This test showed that 5G technology fully meets the various services of grid control under the condition of ultralow latency. In May of the same year, Shenzhen completed the first domestic and foreign field synthesis of synchronous vector measurement based on a 5G distribution grid, smoothly solving the problem of absolute time synchronization and delay between devices. 5G technology will play a vital role in the development of the distribution grid in the near future.

This article will start from the concept, structure, core features, and core technology of 5G technology; summarize the current integration technology of 5G technology in distribution grid automation, distribution grid relay protection, distribution grid monitoring, and vital node monitoring; analyze the challenges that 5G technology and the distribution grid will face; and finally provide a new outlook for the future integration of 5G technology and the distribution grid.

2. 5G Communication Technology

2.1. Concept and Structure of 5G Communication Technology. 5G (5th generation mobile networks) communication technology is the same as the traditional communication network, and it is also a type of cellular mobile communication technology [13]. A schematic diagram of the 5G communication system is shown in Figure 1. The content of a transmission is converted into a bit torrent by a digital analog converter.

The 5G communication system is composed of a core net, macrobase station and microbase station. Compared with microbase stations, macrobase stations have higher transmit power and broader coverage areas. Although the coverage of a single microbase station is limited, a large number of microbase stations will ensure the signal strength of the

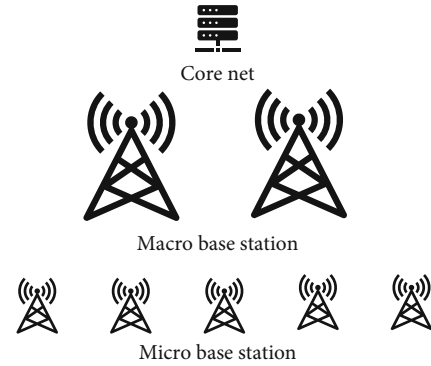


FIGURE 1: 5G communication system.

area where it is located, making the wireless network more reliable. Microbase stations, macrobase stations, and users are mainly receivers, and the data of all receivers come from the core network. The core network is centrally responsible for the control and data transmission of the entire system and is the core “brain” of the whole system [14].

2.2. 5G Core Features. The core features of 5G are shown in Figure 2 and Table 1. 5G communication technology has a transmission speed far exceeding that of 4G communication technology and has a greater capacity to connect more devices. At the same time, the bandwidth, delay, and reliability of 5G communication technology are five times, ten times, and one hundred times those of 4G communication technology [13]. The emergence of 5G technology will dramatically change electric power.

5G communication technology has an ultrahigh-speed transmission rate incomparable with that of traditional communication technology; that is, the peak speed of the uplink reaches 10 Gbps, and the peak speed of the downlink reaches 20 Gbps. In some tests, a peak transmission speed of 20 Gbit/s for single user equipment has been achieved [15]. There are three main reasons why 5G communication technology can achieve a transmission speed nearly ten times that of 4G communication technology. 5G technology directly increases its spectrum range to above 6 GHz; it adopts massive antenna technology represented by massive multiple input multiple output (MIMO) [16] and improves the transmission rate through 3D beamforming [17].

Another notable feature of 5G technology is that the number of connections has increased from 10,000 to 1,000,000 per square kilometer, and it supports a data transmission capacity of 10 Mbps per square meter. Due to the increase in its spectrum width and the extensive application of microbase stations, it can support more device connections. The improvement in spectrum width provides conditions for connecting more devices on this basis. Microbase stations were implemented in the 4G communication era, and their effect is very significant. Therefore, in the future 5G era, more microbase stations will be implemented, thereby increasing the connection density and capacity.

5G technology fundamentally changes the network architecture, including the core network and wireless access network, and reduces the air interface transmission delay and

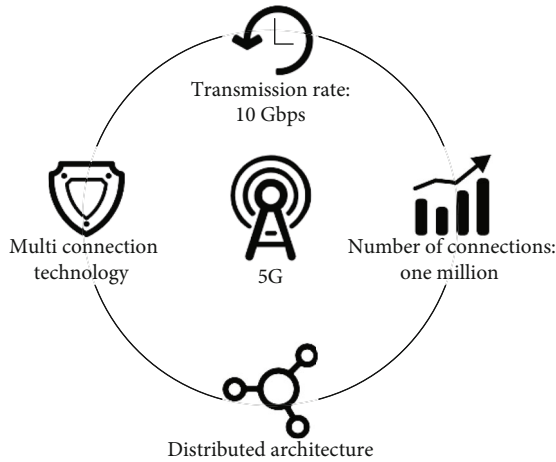


FIGURE 2: 5G core features.

TABLE 1: Comparison between 4G and 5G technology.

	4G	5G
Peak transmission rate	100~150 Mb/s	20480 Mb/s
Device connection density	10000/km ²	1000000/km ²
Delay	40~60 ms	10 ms

distance between the source and the node; that is, the core network has changed from traditional centralized to distributed, physically shortening the distance from the user so that 5G technology has a millisecond delay [14].

5G communication technology also has the core characteristics of high reliability, and the performance index for the packet loss rate has reached 0.001%. Multiconnection technology is the reason for the high reliability of 5G communication technology. It provides users with high-reliability communication by combining the wide coverage range and mobility of low-frequency bands with the large bandwidth and high speed of high-frequency bands.

2.3. 5G Core Technology. In addition to its high-profile core features, 5G core technology has also caused heated discussions. 5G technology has many core technologies. Among them, the superior adaptability of edge computing and network slicing in electric power has become a hot topic of research and discussion by scholars.

Due to the emergence of 5G technology, edge computing has returned to everyone's field of vision as the core technology of 5G. Edge computing is based on the completely centralized management and automatic operation of cloud infrastructure. Cloud computing can store a large amount of data in the cloud, so users can dynamically obtain what they need [18]. With the gradual increase in the amount of user equipment, cloud data will become increasingly large and complex, and various performance indicators of cloud computing will be greatly challenged. With the emergence of edge computing, the computing function in the cloud can sink part of the computing authority, which can share the large amount of data and calculations for the cloud.

Moreover, the traditional cloud-to-end distance is long, and edge computing can shorten the distance to the end, endowing edge computing with the characteristics of faster calculation speeds and lower latency [19].

The service objects of the network have gradually developed from the original mobile phones to various types of equipment, and higher requirements have been proposed for the network. Reference [20] proposes a reliable partition solution for the 5G transmission network based on virtual network embedding and provides special protection in elastic optical networks. Network slicing technology is another core technology of 5G technology. Network slicing technology refers to logically cutting a physical network into multiple virtual networks to achieve end-to-end connections. According to different business requirements and security requirements [21], the virtual network can be cut and personalized on demand. When the virtual network in a certain application scenario fails or is abnormal, it will not affect other virtual networks.

3. Application of 5G Technology in the Distribution Grid

3.1. Distribution Grid Automation and Relay Protection. At present, 2.5G dedicated wireless communication is mostly used for low-voltage switch cabinets in distribution grids, and a small number of switch stations use optical fiber communication. The automatic fault diagnosis and isolation of a medium-voltage distribution grid cannot be guaranteed. The low-voltage distribution grid has a low degree of automation and requires many workforce and material resources for maintenance.

3.1.1. Accurate Fault Location. Traditional fault location technology is mainly divided into two methods: one method locates the fault based on additional equipment, and the other method locates the fault based on the measurement information of the distribution line. The fault location of additional equipment is mainly determined by the sectionalizer and recloser method [22] and the fault indicator method [23]. In the second method, the accuracy of the fault location is based on the measurement information of the distribution line [24]. The decisive factor is the need for sufficient measurement information for analysis to achieve accurate fault location determination. Current fault location technology achieves accurate fault location determination through algorithm optimization or by predicting the passage of accident collectors. In the literature [25], an FTU is established at the circuit breaker and section switch so that the fault current is detected, and the algorithm is used to locate the fault. Reference [26] collects the status of fault indicators and smart meters through the control center and uses a multihypothesis method to quickly identify faults and activate protection devices. This easily shows that for current precise fault location technology, most of the analysis methods are continuously optimized after various measurement information has been collected.

The core features of 5G technology are large bandwidth and low latency, which can greatly reduce the collection time

of key information in the distribution grid. At the same time, the distribution grid can be combined with the edge computing capability of 5G technology, and this low-latency computing business can be delegated to an edge computer room. At the same time, edge computer rooms are close to the access side, reducing the data transmission distance from the physical level and increasing the fault removal speed. The large bandwidth and low latency of 5G technology extend the precise fault location technology in the distribution grid. In the literature [27], distributed power distribution fault detection based on edge computing is introduced. In the fault detection system of this work, the network layer uses mostly 4G networks and optical fiber power private networks. Current 4G communication technology is far inferior to 5G communication technology in terms of latency and bandwidth, and optical fiber networks cannot be widely used due to their cost and environmental conditions. In the near future, a 5G power local area network will be the main communication method in the distribution grid.

3.1.2. Fault Isolation. FA plays an important role in fault isolation in distribution grid automation. At present, centralized FA applies simple principles and mature strategies, and distributed FA has gradually evolved due to the large number of distributed energies needing access.

The most significant feature of centralized FA is that it needs to upload measurement information to the master station when a permanent fault occurs. The feeder monitoring terminal of each switch or ring network cabinet must communicate with the power distribution master station, which is controlled by the master station. After that, the dispatcher isolates the fault and applies self-healing schemes for different situations [28]. Reference [29] introduced a centralized intelligent feeder automation system based on IEC61850 and explained the information sequence diagram of fault isolation and fault detection for centralized FA in detail. The continuous interaction of this information is very complicated. The document does not give a reliable communication method that can support such a complicated information exchange process and the time to successfully isolate the fault. In such a continuous isolation solution that requires uploading and downloading, only a 5G network with large bandwidth, low latency, and strong reliability can provide communication technology support and improve the efficiency of fault isolation on the original basis.

The greatest difference between distributed FA and centralized FA is that distributed FA does not rely on the global information of the master station, completes fault location identification and isolation through mutual communication and cooperation between terminals, and reports the results and process of processing. Although the distribution grid has been continuously connected to various distributed loads in recent years, distributed FA has the characteristics of one-time fault handling and a strong ability to adapt to the line, which makes the distribution grid more reliable; thus, distributed FA has become a current research hotspot and direction. Reference [30] introduced a method for implementing intelligent distributed feeder automation in active distribution grids, which can isolate faults within milliseconds and

realize power supply in nonfaulty areas within seconds. According to the technical requirements of distributed intelligent feeder automation proposed in the literature, rapid fault isolation achieved through remote control, and smart electronic equipment is desired, so the main communication method in the literature chooses the optical fiber-based communication method. However, due to the cost of optical fibers and because some areas are not suitable for dedicated optical fibers, this will become the main reason restricting their large-scale application. The wireless network provided by 5G communication technology can reduce the power communication network's reliance on optical fibers, cover a wide range of smart electronic devices, and complete remote control more accurately and quickly. Due to the superior characteristics of 5G technology, its cost will be greatly reduced, and its core technology edge computing capability can be applied to the application of distributed FA, reducing the time delay from the physical distance.

3.1.3. Differential Protection. Due to its selectivity and efficiency, differential protection has become a reliable selective main protection method for power system equipment [31–33]. Differential protection is based on Kirchoff's current law (KCL), which compares the incoming and outgoing currents of the relays at both ends of its protection section to determine internal and external faults and act. The reliability of differential protection depends entirely on the communication system at both ends of the line [34]. The greatest limitation of early differential protection systems with buried cables and overhead lines used as communication media is that the protection length is limited and the relays at both ends will lose their original functions when the line is disconnected. After that, differential protection that uses optical fibers and digital communication networks as the communication medium [35] appeared and is still in use today, which makes up for the previous generation of differential protection and, to a large extent, guarantees the shortcomings of relay function loss due to line disconnection. Reference [36] pointed out that wireless networks have a unique position and advantages in many communication media; that is, they have a lower cost and faster response time than cable optical fibers. At the same time, relays can also ignore system parameter changes; the construction of a 30 km differential protection scheme is proposed by connecting the relays used in differential protection to the relays at the sending end and the receiving end through a wireless transmission network. 5G technology is about to be applied in wireless communication [37]. Because of its large capacity and wide coverage, 5G technology will allow more relay connections, especially due to its superior time delay characteristics, to allow information and data to be transmitted more accurately and quickly.

3.2. Distribution Grid Monitoring

3.2.1. Power Distribution Room Monitoring. The primary need is to ensure the safety and stability of the environment inside power distribution rooms. Through the sensors installed in distribution rooms and 5G communication technology, indoor temperature, humidity, and the presence of

dangerous gases (SF_6/O_3 etc.) can be transmitted to on-duty personnel in real time, and appropriate schemes can be arranged to ensure the normal operation of all equipment in the distribution room within a standard range.

Second, it is necessary to conduct real-time monitoring of important equipment in power distribution rooms. Some important equipment, such as transformers, switch cabinets, power distribution cabinets, and DTUs, exists in power distribution rooms. In traditional power distribution room management, it is necessary to arrange personnel to regularly inspect and monitor equipment. With the emergence of 5G technology and the development of sensors, 5G technology can be combined with existing sensors. For example, multiple sensors are installed around the transformer to obtain data such as the operating temperature of the transformer, the vibration acceleration of the transformer tank, and the electrical output of the transformer and then monitor and analyze these data. After that, the data are uploaded to the monitoring personnel in real time through the 5G communication network. When an abnormality occurs, the alarm from the power distribution room can be received in the shortest time, and a set of suitable fault solutions can be automatically generated and calculated. In this way, the normal operation of the equipment in the power distribution room can be ensured to the greatest extent, the efficiency of monitoring and maintenance of the power distribution room can also be improved, and the monitoring cost can be reduced.

Because of its small size, convenient installation, and low cost, medium-voltage distribution grid phasor measurement units (PMUs) bring a qualitative improvement in fault diagnosis and fault location technology to the distribution grid [38, 39]. The combination of PMUs and 5G technology will gradually develop in the direction of visualizing the operation of the distribution grid. This will depend on the core features and core technology of 5G technology [40]. Power distribution rooms can build a 5G cellular network and rely on the large bandwidth, low latency, and large capacity of 5G technology. Power distribution rooms can not only monitor the operation of the distribution grid in real time but also obtain a large amount of accurate terminal data and bus information, as well as equipment operating status [41]. The large amount of data is visually fed back to the client for real-time monitoring and control. 5G technology can provide faster upload and download speeds to support the data transmission of high-definition video and pictures during repair processes; at the same time, these data will be returned to the center in real time. 5G communication technology not only provides a possibility for the visualization of the distribution grid but also improves the efficiency of the daily inspection of the distribution grid, reduces costs, and improves efficiency.

The ring main unit is an important part and key link in the automation of the distribution grid, so it is of great significance to integrate automatic monitoring and detection in the ring main unit of a distribution room. The traditional ring main unit mostly relies on the connection of cables or optical fibers to realize multipoint detection and control. Wired data transmission will increase the complexity of the line inside a ring main unit and increase security risks. Compared with

wireless public network, 5G is more expensive. The real-time standard of on-line ring main unit monitoring is very strict. Because of its outstanding core characteristics, 5G technology can replace the existing data transmission of wired and wireless public networks. It can ensure real-time monitoring and reduce cost without increasing the complexity of the ring main unit. Multiple units in a ring main unit will also better complete their functions with the integration of 5G communication technology. For example, the signal processing unit inside a ring main unit needs to control the returned telemetry signal, remote signal, and other control devices while also simultaneously realizing visual online real-time detection for the ring main unit.

3.2.2. Online Monitoring. 5G technology lays the foundation for the future application of online monitoring technology in smart grids [42]. A distribution transformer is important basic equipment for distribution grid operation, so monitoring its data is necessary. The transformer terminal unit (TTU) is an important core device for the automatic online monitoring of distribution grids. Depending on the TTU used for the real-time monitoring data of distribution transformers, the abnormal operation status of distribution transformers can be discovered and solved in time.

TTUs have stringent standards for communication networks. It is necessary to pay attention to the cost-effectiveness and real-time performance of communication networks to ensure high reliability. Optical communication meets the requirements of reliability and real time, and due to the large number of TTU devices and their wide distribution, it is obviously impossible to use optical communication for a wide range of purposes. At present, more communication modes are power line carriers and wireless communication networks. The main disadvantage of a power line carrier is that when the distribution transformer is abnormal, the speed of data transmission for monitoring is slow, and it is also vulnerable to harmonics and electromagnetic interference between power lines. 5G communication technology, to a large extent, meets the stringent requirements of TTU devices for communication. When a distribution transformer is in abnormal operation conditions, the abnormal operation data can be quickly transmitted, and the low latency of the data can be guaranteed. At the same time, 5G's superior coverage ensures the connection of multiple TTU devices in some areas. 5G communication technology is of great significance for future online TTU monitoring.

3.2.3. Intelligent Interconnection of Power Distribution Equipment. Distribution grids contain a large number of power electronic devices, such as series-shunt compensators, contactless switches, and active power filters. These devices often operate in an independent form to meet the growing demand of distribution grids [43]. With the introduction of increasingly more distributed energy, power electronic devices are gradually developing toward interconnection. Reference [44] introduces several communication methods used in distribution grids to connect power and electronic devices, among which cellular networks are a mature communication technology. However, traditional cellular

communication technology is conducive to communication between smart meters and distribution stations or remote nodes, but as a public platform, the cellular network will have the drawbacks of network congestion and long delays. In the future, power electronic devices in the distribution grid may be interconnected and integrated through 5G cellular networks or network slicing technology to achieve the integration of energy information.

3.3. Important Node Monitoring. Knowing the trend direction [45] requires unified detection and the control of a large number of connected distributed energy sources in distribution grid automation. However, the greatest difficulty with distributed energy monitoring is that the topology of the distribution grid cannot be identified [46]. Research on sensors, such as topology sensors and high-precision phasor units of μ PMUs, largely solves the problem of topology identification [47, 48]. Subsequently, reference [49] assumes that the nodes of the distribution grid are measurable, measures and controls the nodes of the distribution grid, realizes the identification of the distribution grid topology through node data, and successfully identifies the access points of the distributed energy. Regardless of which method is used, the nodes are arranged and calculated from the nodes in the distribution grid. There are many nodes in the distribution grid. To achieve multipoint collaborative computing and ensure data delay, a 5G wireless network and distribution grid nodes can be combined. Wireless intelligent devices are placed on important nodes in 5G communication technology, such as connecting sensors and the intelligent terminals of the distribution grid of a 5G network. Because the coverage of the 5G signal is wide enough, the sensors in a region can be interconnected. At the same time, an edge computer room combined with 5G edge computing can realize the identification of distributed energy access and distribution grid topology in a region.

4. Challenges of Distribution Grids with 5G Technology

4.1. 5G Technical Standard Maturity Match. In the first half of 2020, the technical freeze of the release 16 (R16) standard for 5G technology and the establishment of ultrareliable and low-latency communication (URLLC) standards were completed. Smart grids have just been established in 3GPP release 18 (R18), which is the first definition of a 5G+ smart grid end-to-end standard architecture. Research on how 5G technology can support the business needs of distribution grids and even power grids is still in the initial stage, and it will take a long time to freeze the R18 technical standard. Due to the lack of certain technical standards, the application of 5G technology in distribution grid-related business is still in the initial stage of exploration, and the large-scale application of 5G technology needs further exploration.

All distribution terminals will be integrated with 5G technology in the future; for example, the communication module of 5G technology will be embedded in the distribution terminal. At present, relevant research on 5G communication terminals is still in progress. The market of intelligent

communication terminals has been saturated before. Although the emergence of 5G technology gives communication terminals the opportunity to reenter the market, the relevant supporting industries of 5G technology are unable to support the development of 5G communication terminals and mass manufacturing [50].

4.2. 5G Network Slicing Security Issues. Reference [51] provides a simple key generation and key management scheme that provides a quantum secure key hierarchy in the 5G scenario for Internet of Things devices. The security of network slicing technology in 5G communication technology needs to be solved. Currently, there are many new security issues in network slicing specially tailored to the distribution grid. For new network attack, this indicates whether the network can resist attack from outside when network slicing is implemented. Network defense means of network slicing need further research and exploration. Since the formation of network slicing is achieved by several virtual networks separated by physical networks, it is possible to achieve mutual noninfluence mentioned in network slicing. However, the degree of independence of a single sliced network and the associated problems with other networks will lead to new network security problems, such as information and data leakage in the slice. Only by ensuring the operational safety of the distribution grid can we further promote and apply network slicing technology in the distribution grid.

4.3. Network Cost Performance. Another problem to be considered in the application of 5G technology is the cost performance of a network, that is, the choice of a public network or a private network. Compared with public networks, private networks have the advantages of network security, information data transmission speed, and relatively smooth signal switching and reselection, but their construction cost is incomparable to that of public networks. 5G technology has a high transmission speed, and its data transmission is also more expensive. A problem with network construction is that the network must be reasonably arranged within the range of acceptable costs. It is obviously unreasonable to choose only one of them. Therefore, if the operators can flexibly open the network architecture system in the future and cooperate to discuss a set of suitable network selection schemes, the scheme can also be used to reasonably design different business requirements for the distribution grid. To ensure safety, flexibility, and reliability, the distribution grid and 5G technology can be integrated in depth.

4.4. 5G Signal Penetration. The signal problem of 5G technology has always been a hot topic; that is, how to improve the speed without sacrificing signal strength is of interest. In the era of 4G-LTE systems, because its wavelength is approximately 8 m, 5G mainly uses millimeter waves, so its antenna length is greatly shortened, and more antennas can be arranged in space to improve the transmission rate at one time. However, the signal strength of the 5G millimeter wave is weak; that is, signal attenuation in the transmission process is very serious. For the signal penetration problem of 5G communication technology, although the uplink and

downlink decoupling technology of “downlink 5G frequency, uplink 4G frequency” has been proposed, the construction of a large number of microbase stations and application of massive MIMO technology to base stations are design schemes to be adopted in cities. For the distribution terminals applied to some harsh environmental conditions, such as terminals built in remote areas, the construction level of base stations cannot reach the scale of base stations in cities and the cables buried in the ground, so the reception effect of signals may not be good. Therefore, to apply 5G technology to terminals to complete data collection and transmission or achieve remote functions in the distribution grid, only technical theory can be achieved, but for specific technology implementation, it is still far from reaching this goal.

5. Conclusions

The emergence of 5G technology will change the architecture of traditional mobile communication and its security. The existing communication network was not achieved overnight. The relevant 5G technical standard, R18, is still being studied. Even if the standard is completely frozen, it is impossible to deploy 5G in an all-around way. Only using the original special power network can the existing optical fiber network be retained. For some distribution grids, 5G communication technology can be combined, and a set of network structures combining private networks and public networks can be developed with operators to pave the way for transition. For example, [52] introduces a kind of low-cost, data-centric next-generation lightless network, and Gigabit wireless LAN technology based on an optical fiber wireless network to meet the requirements of a 5G communication network. In addition, we also need to consider the location of constructed 5G base stations, signal, security, and anti-interference issues. Further research programs and plans for the integration of 5G technology into the distribution grid are needed.

Data Availability

The data used to support the findings of this study are included within the article.

Conflicts of Interest

The authors declare that there is no conflict of interests regarding the publication of this paper.

References

- [1] Y. Wang, Q. X. Chen, N. Zhang, C. Feng, F. Teng, and M. Y. Sun, “Fusion of the 5G communication and the ubiquitous electric Internet of Things: application analysis and research prospects,” *Power System Technology*, vol. 43, no. 5, pp. 1575–1585, 2019.
- [2] J. Tao, M. Umair, M. Ali, and J. Zhou, “The impact of Internet of Things supported by emerging 5G in power systems: a review,” *CSEE Journal of Power and Energy Systems*, vol. 6, no. 2, pp. 344–352, 2019.
- [3] B. L. Risteska Stojkoska and K. V. Trivodaliev, “A review of Internet of Things for smart home: Challenges and solutions,” *Journal of Cleaner Production*, vol. 140, pp. 1454–1464, 2017.
- [4] S. Wang, L. Zhu, Z. Zhang, and S. Zhang, “Research on single phase grounding fault detection technology of distribution grid based on intelligent variable terminal,” *Power System Technology*, vol. 43, no. 12, pp. 4291–4298, 2019.
- [5] J. Liu, L. Chen, and Z. Zhang, “Estimation of static parameters testability for distribution grid considering the effect of measurement errors,” *Power System Technology*, vol. 44, no. 4, pp. 1481–1487, 2020.
- [6] S. Hu, X. Chen, W. Ni, X. Wang, and E. Hossain, “Modeling and analysis of energy harvesting and smart grid-powered wireless communication networks: a contemporary survey,” in *IEEE Transactions on Green Communications and Networking*, vol. 4, no. 2, pp. 461–496, 2020.
- [7] W. Tao, K. Dou, F. Chen, C. Fang, J. Liu, and M. Ding, “Comparison and technical analysis of phasor data access modes in distribution grid,” *Power System Technology*, vol. 43, no. 3, pp. 784–792, 2019.
- [8] J. Liu, J. Ni, and L. Xu, “Management of distribution automation system (DAS),” *Power System Technology*, vol. 8, pp. 3–5, 1998.
- [9] Y. Wu, H. Gao, B. Xu, K. Gengqiang, W. Zhigang, and W. Ning, “Distributed fault self-healing scheme and its implementation for active distribution grid,” *Automation of Electric Power Systems*, vol. 43, no. 9, pp. 140–155, 2019.
- [10] L. Lin, B. Qi, B. Li, X. Ye, and W. Mei, “Requirements and developing trends of electric power communication network for new services in electric Internet of Things,” *Power System Technology*, vol. 44, no. 8, pp. 3114–3130, 2020.
- [11] Z. Zhu, B. Xu, T. Yip, Y. Che, and Y. Li, “IEC 61850 based models for distributed feeder automation system,” *Automation of Electric Power Systems*, vol. 42, no. 23, pp. 148–156, 2018.
- [12] A. Ghosh, A. Maeder, M. Baker, and D. Chandramouli, “5G evolution: a view on 5G cellular technology beyond 3GPP release 15,” *IEEE Access*, vol. 7, pp. 127639–127651, 2019.
- [13] M. Shafi, A. F. Molisch, P. J. Smith et al., “5G: a tutorial overview of standards, trials, challenges, deployment, and practice,” *IEEE Journal on Selected Areas in Communications*, vol. 35, no. 6, pp. 1201–1221, 2017.
- [14] I. Parvez, A. Rahmati, I. Guvenc, A. I. Sarwat, and H. Dai, “A survey on low latency towards 5G: RAN, core network and caching solutions,” *IEEE Communications Surveys & Tutorials*, vol. 20, no. 4, pp. 3098–3130, 2018.
- [15] J. G. Andrews, S. Buzzi, W. Choi et al., “What will 5G be?,” *IEEE Journal on Selected Areas in Communications*, vol. 32, no. 6, pp. 1065–1082, 2014.
- [16] M. Agiwal, A. Roy, and N. Saxena, “Next generation 5G wireless networks: a comprehensive survey,” *IEEE Communications Surveys & Tutorials*, vol. 18, no. 3, pp. 1617–1655, 2016.
- [17] Q. Zheng, *Research on 3D Beamforming Technology Based on Massive MIMO Networks*, Beijing University of Posts and Telecommunications, Beijing, 2018.
- [18] H. Tian, S. Fan, X. C. Lü, P. T. Zhao, and S. He, “Mobile edge computing for 5G requirements,” *Journal of Beijing University of Posts and Telecommunications*, vol. 40, no. 2, pp. 1–10, 2017.
- [19] T. Zhu, A. Qian, X. He et al., “An overview of data-driven electricity consumption behavior analysis method and application,” *Power System Technology*, vol. 44, no. 9, pp. 3497–3507, 2020.

- [20] N. Shahriar, S. Taeb, S. R. Chowdhury et al., "Reliable slicing of 5G transport networks with bandwidth squeezing and multi-path provisioning," *IEEE Transactions on Network and Service Management*, vol. 17, no. 3, pp. 1418–1431, 2020.
- [21] X. Yong, W. Haowen, W. Zongyi, and W. Yan, "Communication service optimization of demand response for interruptible load control," *Automation of Electric Power Systems*, vol. 44, no. 15, pp. 36–43, 2020.
- [22] W. Zhang, G. B. Song, M. Dou et al., "A quick fault location and isolation method in distribution network based on adaptive reclosure," *Power System Protection and Control*, vol. 47, no. 18, pp. 60–67, 2019.
- [23] J. Liu, X. Zhang, X. Tong, Z. Zhang, H. Du, and Y. Chen, "Fault location for distribution system with distributed generations," *Automation of Electric Power Systems*, vol. 37, no. 2, pp. 36–42, 2013.
- [24] S. Jamali, A. Bahmanyar, and S. Ranjbar, "Hybrid classifier for fault location in active distribution networks," *Protection and Control of Modern Power Systems*, vol. 2, pp. 84–92, 2020.
- [25] G. Zhuangzhi, X. Qixing, H. Junjie, and M. Xiaoming, "Integer linear programming based fault section diagnosis method with high fault-tolerance and fast performance for distribution network," *Proceedings of the Chinese Society of Electrical Engineering*, vol. 37, no. 3, pp. 786–795, 2017.
- [26] Y. Jiang, C.-C. Liu, M. Diedesch, E. Lee, and A. K. Srivastava, "Outage management of distribution systems incorporating information from smart meters," *IEEE Transactions on Power Systems*, vol. 31, no. 5, pp. 4144–4154, 2016.
- [27] W. Huo, F. Liu, L. Wang, Y. Jin, and L. Wang, "Research on distributed power distribution fault detection based on edge computing," *IEEE Access*, vol. 8, pp. 24643–24652, 2020.
- [28] Z. Wang, X. Wen, C. Yu, and P. S. Guangzhou, "Information model of centralized feeder automation based on IEC 61850," *Automation of Electric Power Systems*, vol. 41, no. 8, pp. 133–137, 2017.
- [29] J. Liu, B. Yun, Q. Cui, L. He, and J. Zheng, "A distributed intelligent feeder automation system with fast self-healing performance," *Automation of Electric Power Systems*, vol. 34, no. 10, pp. 62–66, 2010.
- [30] S. Borkar and H. Pande, "Application of 5G next generation network to Internet of Things," in *2016 International Conference on Internet of Things and Applications (IOTA)*, pp. 443–447, Pune, 2016.
- [31] C. Tang, Z. Yang, B. Song, and Z. Yajun, "A method of intelligent distributed feeder automation for active distribution grid," *Automation of Electric Power Systems*, vol. 39, no. 9, pp. 101–106, 2015.
- [32] J. Ying, Y. Cai, H. Du, M. Liu, S. Feng, and J. Yao, "Secondary verification method of distribution network model," *Automation of Electric Power Systems*, vol. 43, no. 7, pp. 185–192, 2019.
- [33] Z. Guo, S. Shui, T. Xu, Q. Zhang, J. Chen, and J. Chen, "Mechanism analysis on differential protection action caused by short-circuit fault of current transformer secondary circuit," *Automation of Electric Power Systems*, vol. 37, no. 2, pp. 130–133, 2013.
- [34] S. M. Hashemi and M. Sanaye-Pasand, "Current-based out-of-step detection method to enhance line differential protection," *IEEE Transactions on Power Delivery*, vol. 34, no. 2, pp. 448–456, 2019.
- [35] P. Fubin, C. Yu, W. Yi, L. Yong, and G. Hailong, "A signal attenuation calculation method of high frequency protection for," *Power System Technology*, vol. 43, no. 6, pp. 2187–2194, 2019.
- [36] K. M. Abdel-Latif, M. M. Eissa, A. S. Ali, O. P. Malik, and M. E. Masoud, "Laboratory investigation of using Wi-Fi protocol for transmission line differential protection," *IEEE Transactions on Power Delivery*, vol. 24, no. 3, pp. 1087–1094, 2009.
- [37] F. Sun, N. Xie, C. Wang, M. Fan, and Z. Zhang, "Review of CIRED 2017 on power distribution system planning," *Power System Technology*, vol. 42, no. 9, pp. 2733–2741, 2018.
- [38] L. Yu, J. Zaibin, W. Xiaopeng, C. Wei, and D. Feng, "Accurate fault location scheme and key technology of medium-voltage distribution network with synchrophasor measurement units," *Automation of Electric Power Systems*, vol. 44, no. 18, pp. 30–38, 2020.
- [39] S. Deepa, S. J. S. Kumar, and S. S. Biju, "Micro-synchro phasor based special protection scheme for distribution system automation in a smart city," *Protection and Control of Modern Power Systems*, vol. 5, no. 1, pp. 97–110, 2020.
- [40] N. Zhang, J. Yang, Y. Wang, Q. Chen, and C. Kang, "5G communication for the ubiquitous Internet of Things in electricity: technical principles and typical applications," *Proceedings of the Chinese Society for Electrical Engineering*, vol. 39, no. 14, pp. 4015–4025, 2019.
- [41] P. H. Gadde, M. Biswal, S. Brahma, and H. Cao, "Efficient compression of PMU data in WAMS," *IEEE Transactions on Smart Grid*, vol. 7, no. 5, pp. 2406–2413, 2016.
- [42] T. A. Zerihun, M. Garau, and B. E. Helvik, "Effect of Communication Failures on State Estimation of 5G-Enabled Smart Grid," *IEEE Access*, vol. 8, pp. 112642–112658, 2020.
- [43] Z. Ma, A. Ting, and S. Yuwei, "State of the art and development trends of power distribution technologies," *Proceedings of the Chinese Society for Electrical Engineering*, vol. 36, no. 6, pp. 1552–1567, 2016.
- [44] X. He, Z. Sheng, J. Wu, and R. Zhao, "Technologies of power electronic equipment interconnecting and networking in distribution grids," *Proceedings of the Chinese Society of Electrical Engineering*, vol. 34, no. 29, pp. 5162–5170, 2014.
- [45] X. Zhu, H. Xueshan, M. Yang, Y. Xu, S. Wang, and B. Li, "A layered time-varying optimization tracking algorithm for active distribution networks," *Proceedings of the Chinese Society of Electrical Engineering*, vol. 39, no. 24, pp. 7093–7106, 2019.
- [46] Y. Liao, Y. Weng, and R. Rajagopal, "Urban distribution grid topology reconstruction via Lasso," in *2016 IEEE Power and Energy Society General Meeting (PESGM)*, pp. 1–5, Boston, MA, 2016.
- [47] G. Cavarro, R. Arghandeh, G. Barchi, and A. von Meier, "Distribution network topology detection with time-series measurements," in *2015 IEEE Power & Energy Society Innovative Smart Grid Technologies Conference (ISGT)*, pp. 1–5, Washington, DC, 2015.
- [48] A. von Meier, D. Culler, A. McEachern, and R. Arghandeh, "Micro-synchro phasors for distribution systems," in *ISGT 2014*, pp. 1–5, Washington, DC, 2014.
- [49] Y. Weng, Y. Liao, and R. Rajagopal, "Distributed energy resources topology identification via graphical modeling," *IEEE Transactions on Power Systems*, vol. 32, no. 4, pp. 2682–2694, 2017.
- [50] C. Wanliang, *A Research on Working Capital Management of H Company Based on Stakeholders*, University of Electronic Science and Technology of China, Sichuan, 2019.

- [51] R. Arul, G. Raja, A. O. Almagrabi, M. S. Alkathiri, S. H. Chauhdary, and A. K. Bashir, "A quantum-safe key hierarchy and dynamic security association for LTE/SAE in 5G scenario," *IEEE Transactions on Industrial Informatics*, vol. 16, no. 1, pp. 681–690, 2020.
- [52] H. Beyranvand, M. Levesque, M. Maier, J. A. Salehi, C. Verikoukis, and D. Tipper, "Toward 5G: FiWi enhanced LTE-A HetNets with reliable low-latency fiber backhaul sharing and WiFi offloading," *IEEE/ACM Transactions on Networking*, vol. 25, no. 2, pp. 690–707, 2017.